

PROCEEDINGS: Twenty-Seventh Workshop on Geothermal Reservoir Engineering
Stanford University, Stanford, California, January 28-30, 2002
SGP-TR-171

Soil Mineralogy Anomaly Detection in Dixie Valley, Nevada using Hyperspectral Data

Gregory D. Nash and Glenn W. Johnson

Energy & Geoscience Institute
University of Utah
423 Wakara Way, Suite 300
Salt Lake city, UT 84108
gnash@egi.utah.edu & gjohnson@egi.utah.edu

ABSTRACT

Anomalous soil mineralogy can indicate buried geologic structures and zones of permeability. Hyperspectral data can be used to map these anomalies in geothermal exploration efforts. This paper describes work done in Dixie Valley, Nevada, in this regard. Dixie Valley, which lies in the Great Basin, west-central Nevada, is host to a structurally controlled deep-circulation geothermal system. Caithness Energy, LLC operates a 65 Megawatt geothermal power plant in the northwest corner of the valley. This study took advantage of archive AVIRIS (Advanced Visible and Infrared Imaging Spectrometer) airborne hyperspectral imagery of the area adjacent to the power plant. Two spectral unmixing methods were employed to separate minerals from other components of a given pixel (ground unit in computer terms). The first was a supervised learning method (which requires the use of a training data set of known or suspected mineral spectra). The second method, polytopic vector analysis (PVA), is an unsupervised classification method, which allows spectral fingerprints to be derived based on analysis of ambient data. Both methods produced useful spectral end-members. The supervised methodology facilitated mapping of a strong calcium carbonate anomaly that exists in an area where fumaroles appeared shortly after the image was acquired.

INTRODUCTION

This paper addresses the initial results of work regarding the development of data processing methodologies to facilitate the use of hyper-spectral data for mapping soil mineralogy anomalies that may be related to hydrothermal convection systems. In particular, this study has focused on development of methods that can be replicated by industry. This effort has been focused on Dixie Valley, Nevada.

The detection of subtle soil anomalies can be useful in detecting blind geothermal systems, buried structures, and zones of permeability. Soil mineralogy anomalies can result from many conditions, including: (1) parent material consisting of hydrothermally altered regolith produced from buried faults or (2) fumarolic activity generated from relatively short-term perturbations in reservoir pressure, which can be caused by steam production or seismic events, and produce reservoir boiling. Dixie Valley was an excellent study area as reduced reservoir pressures created prerequisite conditions for soil mineralogy anomaly formation in the mid 1990s.

Hyperspectral data has been shown to be useful in a number of past mineralogical studies and was, therefore, believed to be a good resource for the detection and mapping of soil mineralogy anomalies. However, the proper processing of this type of data is critical for accurate interpretation and several considerations must be kept in mind. The spatial resolution of hyperspectral data is such that most, if not all, pixels represent mixtures of surface materials. Thus, spectral unmixing is a necessary part of the processing flow. Both unsupervised and supervised unmixing methods were tested to determine which would be the most effective in terms of cost, ease of use, and results. Additionally, before attempting hyperspectral data processing and analysis, the data must undergo atmospheric correction and conversion to apparent reflectance.

DATA PREPROCESSING

The dataset used in this study was NASA Jet Propulsion Lab's (JPL) Airborne Visible/Infrared Imaging Spectrometer (AVIRIS), which was acquired on May 20, 1995 (Figure 1). This data had 224 channels, with a sampling interval of approximately 10 nm, ranging from 383 nm to 2508 nm. The spatial resolution of the dataset (pixel footprint size) was 20 m.

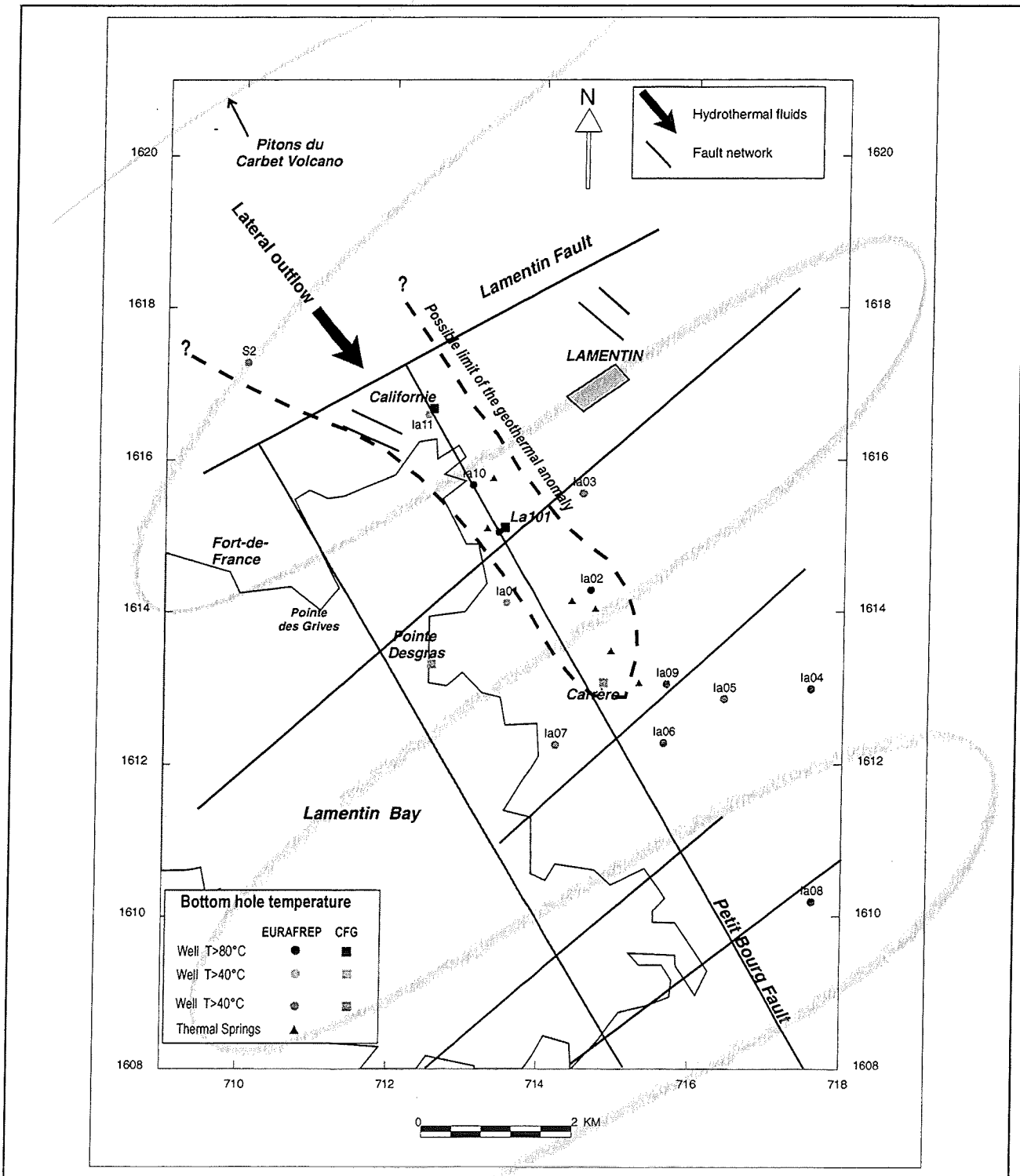


Figure 8. Interpretative model of the low temperature geothermal system showing the lateral outflow in the northern part of the Lamentin graben. The N115E California faults as well as the NW-SE Petit Bourg fault are interpreted as the main structures responsible for the fluid circulation.



Figure 1. AVIRIS RGB image of the Dixie Valley study area.

Due to the inherent nature of airborne or satellite hyperspectral data, atmospheric effects are present and must be minimized. Additionally, hyperspectral data are generally not supplied as reflectance data. Therefore, the data needs to undergo conversion from radiance to apparent reflectance to better facilitate accurate interpretation. This conversion is generally an integrated part of most atmospheric correction procedures.

In an ideal situation spectral data collected on the ground, during hyperspectral data collection overflights, can serve to aid in the determination and correction of atmospheric effects. However, as a field effort is not always possible during data collection, techniques have been developed to allow post data-capture processing. Three of these methods were tested in this study including (1) IAR Reflectance (Kruse, 1988) - the conceptually simplest method, which uses the internal average spectrum of a data set to derive relative reflectance and to minimize atmospheric effects, (2) Atmosphere REMoval Program (ATREM) (Bo-Cai et al, 1993; Bo-Cai et al, 1997) which uses radiative transfer modeling, and (3) Atmospheric CORrection Now (ACORN) which also uses radiative transfer modeling (more information about ACORN can be found at <http://www.aigllc.com/acorn/intro.asp>).

Figure 2 shows a single spectrum, from the AVIRIS data, processed using each of the above three techniques. The three spectra all clearly show distinctive kaolinite absorptions at 2.165 μm and 2.205 μm , and would, therefore, be useful for mapping said mineral. However, in comparing the

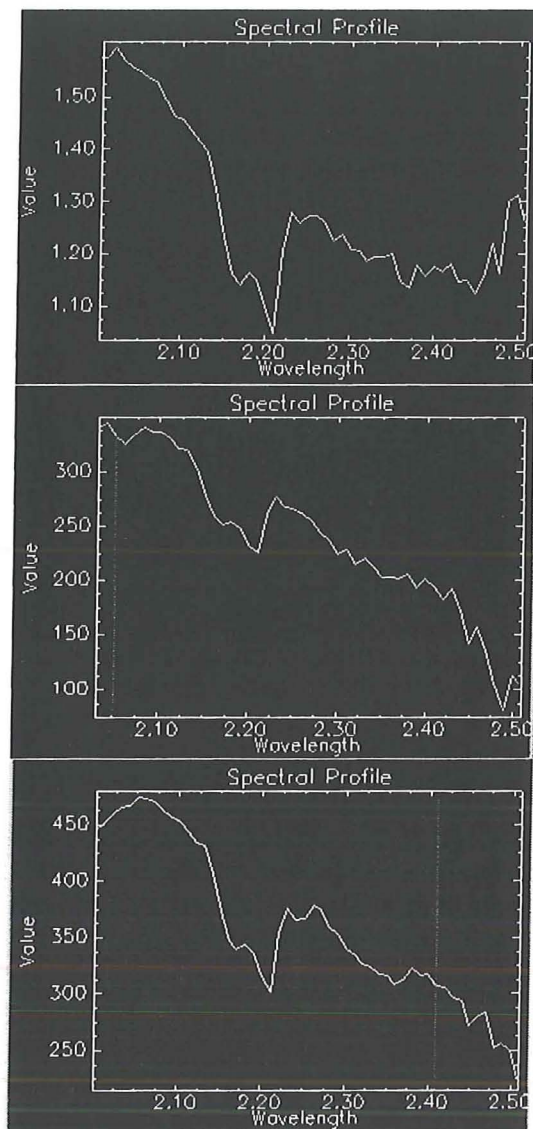


Figure 2. AVIRIS data derived kaolinite spectra, IAR, ATREM, and ACORN processed from top to bottom.

three processed AVIRIS spectra with a laboratory kaolinite spectrum (Figure 3), it becomes evident that the ACORN processed data gives the closest match. The ATREM processed data is also close and could probably be used adequately to accomplish the goals of this project. However, ATREM code is no longer supported or distributed, therefore, its future use is problematic unless one is already in possession of the code. For general purposes, such as mapping only major mineral, occurrences the IAR method should work in most cases. This method is built into the commonly used software packages Imagine™ and RSI ENVI™. This method is also fast and easy. The

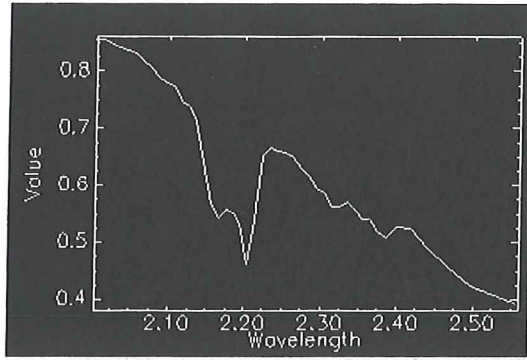


Figure 3. Laboratory kaolinite spectrum.

user needs little background in remote sensing to utilize it. However, radiative transfer model based atmospheric correction would be recommended for use for mapping detailed mineralogy.

To further illustrate this, Figure 4 shows another example of a spectrum, taken from the same pixel, processed with IAR, ATREM, and ACORN, from top to bottom respectively. Again, all three spectra show distinctive kaolinite absorption features. However, in the ATREM processed spectrum, an absorption feature at 2.350 μm (which is clearly shown in the ACORN processed spectrum and to a lesser degree in the IAR processed spectrum) is minimized. This absorption is likely to be indicative of another mineral, such as muscovite, which is mixed within the pixel with kaolinite, although not necessarily within the same rock. This being the case, the ACORN processed data would be more useful for detailed mineralogy mapping. The only drawback to ACORN is that the user needs to have a reasonable understanding of hyperspectral data processing.

DATA PROCESSING

The AVIRIS data, after preprocessing for atmospheric correction and conversion to apparent reflection, were processed to (1) extract mineral end-member spectra and (2) to map the relative abundance of these minerals. This was done in two ways. The first was an unsupervised method – polytopic vector analysis (PVA). This technique was tested because unsupervised methods could be more easily applied by the geothermal industry/exploration personnel with minimal training in remote sensing technologies. The second method tested, supervised unmixing and classification, on the other hand, is more complicated and difficult to use.

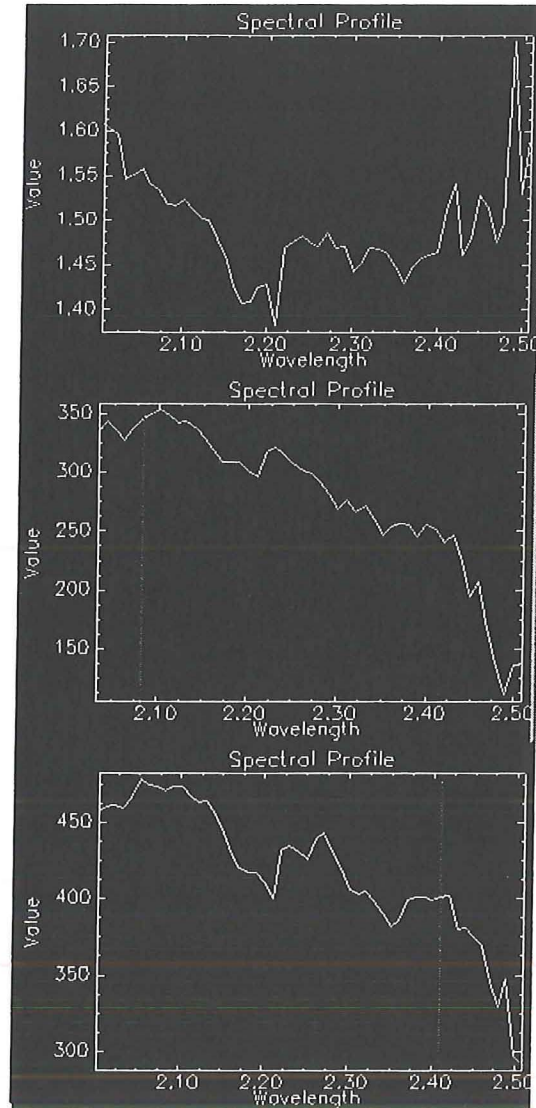


Figure 4. Kaolinite and unknown mineral mixed spectrum.

Unsupervised Classification – Polytopic Vector Analysis

PVA is a multivariate method developed in the earth sciences for analysis of mixtures. PVA is an unsupervised classification method and also referred to as a “self-training classifier.” In other words, with PVA, the analyst does not need to know, or assume, the composition of contributing end-member spectra. This is advantageous because it allows feasible end-members to be inferred in areas where little ground-truth data exists. Given samples from a mixed system, PVA is used to resolve three parameters of interest: (1) the number of end-members contributing to the mixture; (2) the spectral composition of each end-member (i.e. the spectral

“fingerprint”); and (3) the relative proportion of each end-member in each sample. PVA has been used extensively for analysis of multivariate mixtures in the earth and environmental sciences. Johnson et al. (2002) outline its development and formalism. It is a relatively new tool in remote sensing applications, but it has been applied to the analysis of Dixie Valley AVIRIS data (Johnson & Nash, 1998) in a vegetation study focused within a small subset of the study area.

For this study PVA was implemented using software coded in the programming language MATLAB (The Mathworks, Inc., Natick, MA). A commercial version of the PVA software is available through Tramontane, Inc. (<http://www.etrumontane.com>). One modification to the PVA algorithm was made for this study: After the principal components analysis step and determination of the number of end-members, the DENEG algorithm of Full et al., (1981) was applied only to those pixels located on the convex hull of the reduced dimensional data cloud. This increased the speed of the DENEG algorithm because it operates on a very small subset of the original number of pixels (161 of > 300,000 pixels) while yielding an identical solution as the analysis of the full data set.

For the unsupervised classification exercise, it was concluded that the library of reference spectra (used for comparison to derived end-member spectra) should be from published mineral spectra from other study areas (rather than using site-specific spectra from the field area). We wanted to simulate conditions where the analyst had minimal *a priori* knowledge of site geology. In such a situation, a user would likely be forced to rely on published spectra. The spectra used were from the USGS Digital Spectral Library (Clark et al., 2000). Derived end-member compositions were compared to this library by visual inspection/comparison, and by calculation of the cosine theta ($\cos \theta$) similarity metric (Davis, 1986). The values of $\cos \theta$ range from 0 (for two completely dissimilar spectra) to 1.0 (for two identical samples).

Supervised Classification

Unlike PVA, the supervised unmixing and classification requires a number of different processing steps. These included the following:

1. Minimum noise fraction (MNF) transformation;
2. Pixel purity index (PPI) generation;
3. Selection of mineral spectra end-members from the PPI;

4. Mixture tuned matched filtering (MTMF); and
5. Color enhancement (optional).

ATREM and ACORN processed data were classified in the project with the results of the ACORN processed data being reported here.

RSI ENVI™ image analysis software (<http://www.rsinc.com/envi/index.cfm>) was used for data processing and interpretation. It is not known if other image analysis packages allow the specific processing flow described here, however, other packages do have specific hyperspectral data processing and analysis capabilities.

The first step, the MNF transformation is, in practice, a pair of cascaded principal components (PCA) transforms, with the first using an estimated noise covariance matrix with the second being a standard PCA transform (Green et al., 1988; Boardman and Kruse, 1994). The most significant difference in the result from a standard PCA is that the data output bands are ordered by noise. When using a standard principal components transform this is generally not the case. The noise bands resulting from the MNF transform are easily recognized both visually and by observing the resultant eigenvalues. Noise bands can be removed from further processing. A way to further reduce the dataset is to use only the bands necessary to achieve the desired results, as input to the MNF transform. As hydroxyl bearing minerals and calcium carbonate were the primary targets of interest in this study, the input data set was reduced to only those bands in the 2.0 μm to 2.5 μm range.

The second step used the MNF transformed data, minus the noise bands, as input to create an ENVI™ PPI image. The PPI image indicates the most spectrally pure pixels in the MNF transformed image. The PPI image and the atmospherically corrected apparent reflectance data set can be linked on the computer screen so that, as each potential end-member pixel on the PPI image is checked, the spectrum can also be viewed. Figure 5 shows Dixie Valley apparent reflectance image on top of a PPI image along with a chlorite end-member that was found using the PPI image. It must be noted, however, that not every pixel identified in a PPI image is going to produce a useful end-member. Each potential end-member must be validated in step three.

The third step is to identify the end-members produced in the PPI image. To aid in the

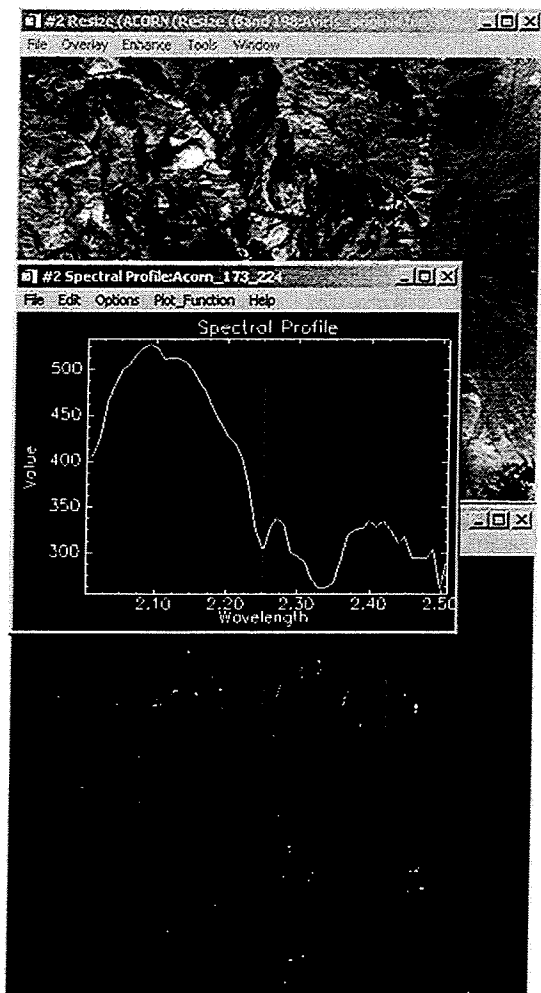


Figure 5. Dixie Valley apparent reflectance image on top of a PPI image and chlorite spectral end-member.

identification of spectral end-members, mineral spectral libraries can be used for comparisons. Additionally, statistical correlations can be done to help identify library spectra that is similar to that identified as an end-member by the PPI image. The software used in this study facilitated this through several algorithms found in its "Spectral Analyst" feature.

The fourth step is to use the ENVI™ MTMF capability to create end-member distribution maps. To accomplish this, the end-members that have been identified are extracted from the MNF image and used as input along with the MNF image. This results in an image that contains double the number of bands as input end-members. These consist of a matched filter score and a infeasibility band for each end-member. The use of the two bands can help eliminate

false positives. Figure 6 shows a matched filter score band (top) and an infeasibility band (bottom) for kaolinite. Bright pixels indicate high scores.

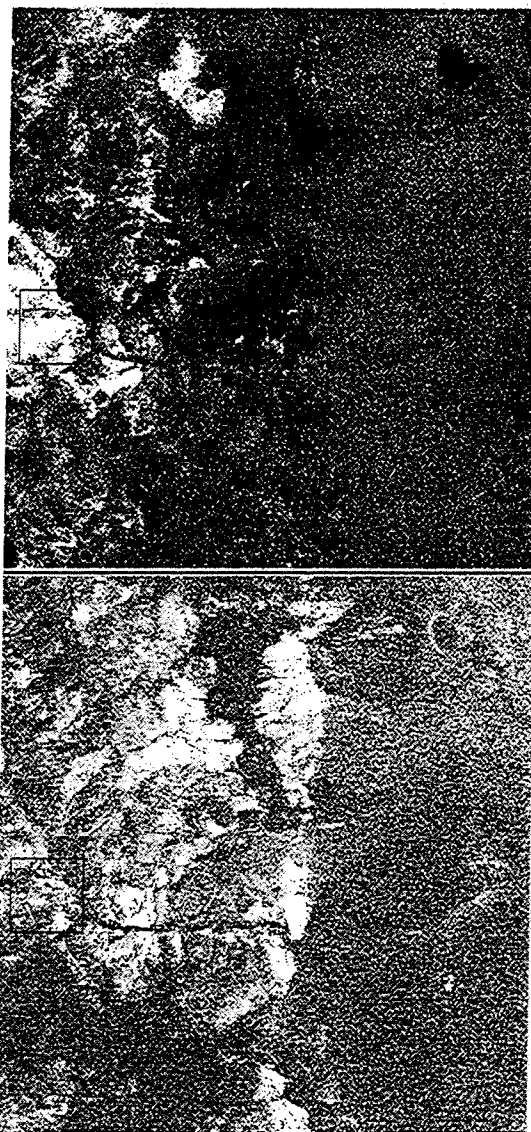


Figure 6. MTMF results. The matched filter score results are on top and the infeasibility scores on the bottom. Bright pixels indicate high scores.

Figure 7 shows a spectrum from a pixel with a matched filter score of 0.233 out of a possible 1.0 (highest score in this example) and an infeasibility score of 7.88, where the highest score was 214.1. The spectrum indicates that kaolinite is indeed present in area of the selected pixel, although not pure.

Step 5 is simply using a gradational color scheme to emphasize the areas that are determined to contain at

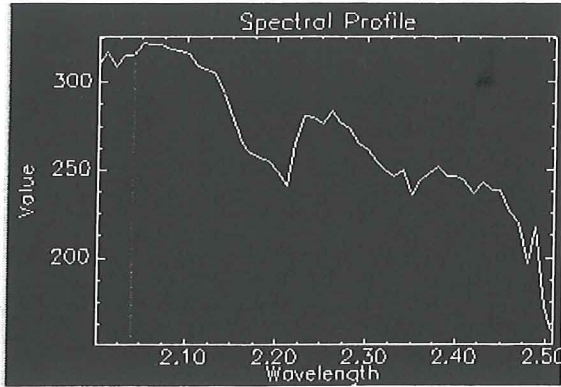


Figure 7. Kaolinite spectrum derived using the matched filter score image from Figure 6.

least some proportion of the spectral end-member in question and to indicate the relative the purity.

RESULTS

PVA Unsupervised Method

Prior to PVA implementation, the AVIRIS image data were preprocessed by (1) atmospheric correction using ATREM; and (2) reduction to 44 bands in the 2.0309 μm to 2.4592 μm range. This range was chosen as it eliminates strong water and vegetation signatures but includes important hydroxyl absorption features found in many hydrothermal alteration minerals.

Initial analyses of data processed with PVA showed that ATREM resulted in abhorrent data values in many surface water pixels, particularly in pond pixels. This was due to residual effects of the atmospheric correction as water absorption bands are used in the process. Thus surface water pixels were also removed from the image. This resulted in removal of 551 of the original 314368 pixels. The image analyzed by PVA was 313817 pixels and 44 bands.

The number of end-members in the model were determined using method outlined by Johnson et al., 2002, in particular, the CD scatter plot method (Miesch, 1976; Johnson et al., 2000). Based on these goodness of fit diagnostics, a five end-member model was chosen. The model was resolved using the DENEG algorithm of Full et al., (1981), modified as described in the methods section, above. Resolved end-member spectra were consistent with published mineral spectra (Clark et al., 2000). The PVA model resolved end-member patterns fairly consistent with those chosen in the supervised method (kaolinite, chlorite, and muscovite). However, in addition

spectra were also resolved that were consistent with water absorption and several mafic minerals (olivine, hypersthene). The full model will be presented in a subsequent paper. For the purposes of this paper, we will focus on just one of the five end-members (End-Member 2), as it illustrates an important caveat for application of unsupervised classification methods. The spectrum and geographic distribution of EM-2 is illustrated on Figure 8.

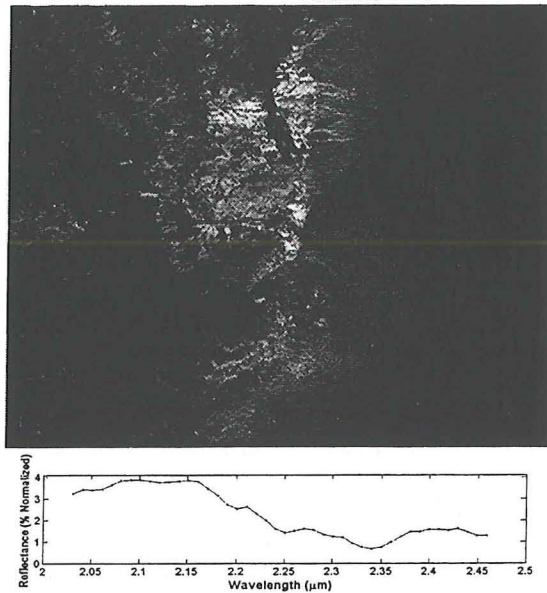


Figure 8. PVA End-Member 2 gray-scale abundance map, and spectra. Black pixels on map indicate absence of this spectrum. White pixels indicate maximum observed in the image (59%).

The EM-2 spectral pattern shows high reflectance in the shorter wavelengths, and an absorption feature at 2.33 - 2.34 μm . Unfortunately, there are several minerals that exhibit this character (Figure 9).

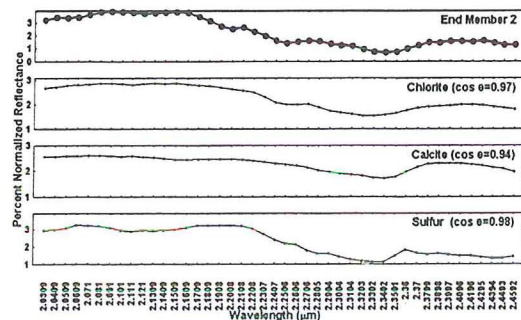


Figure 9. Comparison of End-Member 2 to mineral spectra in the USGS library. Spectra PVA EM-2 shows high similarity to three mineral spectra known to be present in the Dixie Valley study area.

Three of those (chlorite, calcite and sulfur) are shown in comparison to EM-2. All three minerals are known to be present in the study area, and when compared to EM-2, all three exhibit a $\cos \theta$ value greater than 0.94. Retention of more than five end-members did not result in differentiation of chlorite, calcite or sulfur. Therefore, it is likely that this “end-member” itself is a mixture, which represents the contribution of more than one mineral spectra. The problem illustrated here is known as “colinearity.” That is, multiple minerals exhibit very similar spectral patterns within in the chosen wavelength range. Colinearity is a well-known problem in application of mixing models. Given collinear contributing end-members, it is difficult for any multivariate method to discriminate between those patterns.

Colinearity is a concern for both supervised and unsupervised methods. However, in supervised methods, assuming that the analyst has correctly chosen the contributing spectra, the colinearity problem is not as severe, because the analyst is forcing the method to differentiate between the those similar patterns (in this case: chlorite and calcite). Furthermore, if minerals with similar spectra are known to be important constituents of a study, the colinearity problem may be minimized by *a priori* selection of spectral bands that maximize the contrast between those spectra (elimination of variables that are nearly collinear). However, both examples assume the analyst has considerable *a priori* knowledge.

In PVA, the colinearity problem may be dealt with additional data preprocessing, or by selection of spectral bands after review of results of the initial unsupervised model. This is the approach that will be taken in subsequent PVA analyses of the Dixie Valley image. Now that we know that calcite and chlorite (and to a lesser extent, sulfur) are important spectral components of the image, subsequent PVA models may be improved by picking a wavelength range that extends down into shorter wavelengths. Figure 10 shows the full 224 band spectra for chlorite, calcite and sulfur. There is significant contrast between these spectra at lower wavelengths. However, subsequent analyses will likely not extend into the visible spectrum, because of the potential for interference from vegetation spectra. Subsequent PVA models will however extend down into the 1.75 μm range, where there is a notable contrast between these minerals (Figure 10).

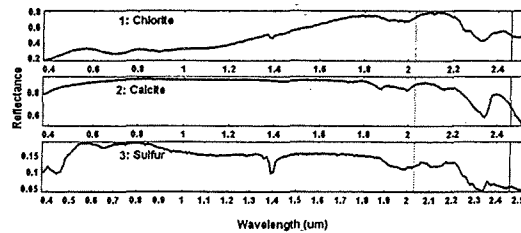


Figure 10. Full 224-band spectra for minerals similar to EM-2. Vertical lines at 2.03 and 2.46 μm show spectral range of present PVA model.

This study highlights the advantage of unsupervised methods in situations where the analyst has little or no *a priori* information, but it also points out a caveat; that we must recognize and be able to take into account colinearity of contributing spectra.

Supervised Method

Following the steps outlined in the Data Processing section above, four excellent end-member spectra were derived and used in the MTMF process. This allowed the creation of four matched filter and infeasibility score images for kaolinite, muscovite, chlorite, and calcite.

As for soil mineralogy anomalies, there were no significant anomalies for kaolinite, muscovite, or chlorite. However, a significant calcite anomaly (Figure 11) exists adjacent to an area where a hydrothermal convection related vegetation die-off occurred and along a path where fumarolic activity began a short time after the image was acquired, clearly indicating a buried structure and a zone of permeability. The image has not been georeferenced



Figure 11. Soil calcium carbonate anomaly bounded by a dark black outline.

as this process tends to degrade the spectra, however the anomaly trends NNE.

Work is now being done to refine this classification methodology to include additional minerals. Samples, collected from the study area, are undergoing X-ray diffraction to determine their bulk compositions. These results will act as ground truth to determine what minerals may have been missed in the first pass of analysis.

CONCLUSIONS

Both supervised and unsupervised unmixing and classification techniques could be useful for detecting soil mineralogy anomalies in geothermal exploration efforts. PVA provides a set of interpretable end-members very quickly and can be used with no prior knowledge of the geology of a study area. In this study five readily interpretable end-members were generated, but the contribution of more than one mineral per end-member, precluded discrimination between calcite and chlorite. Several options are now being considered as solutions for the colinearity problem. The obvious first step in solving such problem is recognizing that they exist: thus, the importance of finding comprehensive spectral libraries such as that of Clark et al., (2000). Beyond that the solution to such problems is usually project-specific. In this case modification of the wavelength range used (provided it does not extend down into the visible range).

Supervised unmixing and classification techniques, although more time consuming and difficult to use, may prove more useful where detailed information is needed as it is likely that additional end-members can be identified. However, this amount of detail may not always be necessary for exploration efforts. This methodology leads to the mapping of a soil calcium carbonate anomaly that is directly related to the hydrothermal convection systems and that indicates a zone of permeability and a buried structure.

REFERENCES

Boardman, J. W., and F. A. Kruse (1994), "Automated Spectral Analysis: A Geologic Example Using Aviris Data, North Grapevine Mountains, Nevada" in *Proceedings of the Tenth Thematic Conference on Geologic Remote Sensing*, May 9-12, San Antonio, TX., I-407 to I-418.

Clark, R.N, G.A. Swayze, A. Gallagher, T.V.V. King, and W. M. Calvin (2000), "USGS Digital Spectral Library", File downloaded contains AVIRIS 1995, 224 channel wavelengths & resolution. <http://speclab.cr.usgs.gov/spectral-lib.html>

Full, W.E., R. Ehrlich, J.E. Klovan (1981), "EXTENDED QMODEL - Objective Definition Of External End Members In The Analysis Of Mixtures" in *Math. Geol.* **13**, 331-344.

Gao, B-C, K. B. Heidebrecht, and A.F.H. Goetz (1993), "Derivation Of Scaled Surface Reflectances From AVIRIS Data" in *Remote Sensing of the Environment*, **44**: 2, 165-178.

Gao, B-C, K. B. Heidebrecht, and A.F.H. Goetz (1997), "Atmosphere Removal Program (ATREM) Version 3.0 Users Guide", *Center for the Study of Earth from Space, University of Colorado, Boulder*, 27.

Green, A. A., M. Berman, P. Switzer, and M. D. Craig (1988), "A Transformation For Ordering Multispectral Data In Terms Of Image Quality With Implications For Noise Removal", in *IEEE Transactions on Geoscience and Remote Sensing*, **26**: 1, 65-74.

Johnson, G.W., Ehrlich, R., and Full, W. (2002), "Principal Components Analysis And Receptor Models In Environmental Forensics", in *An Introduction to Environmental Forensics* (Murphy and Morrison, Editors), Academic Press, San Diego, 461-515.

Johnson, G.W., Jarman, W.M., Bacon, C.E., Davis, J.A., Ehrlich, R., and Risebrough, R. (2000), "Resolving Polychlorinated Biphenyl Source Fingerprints In Suspended Particulate Matter Of San Francisco Bay", *Environ. Sci. Technol.*, **34**, 552-559.

Johnson, G. W. and G. D. Nash (1998), "Unmixing of AVIRIS Hyperspectral Data from Dixie Valley, Nevada", *Proceedings: Twenty-Third Workshop on Geothermal Reservoir Engineering*, Stanford University, Stanford, California, **23**, 240-245.

Miesch, A.T. (1976), "Q-Mode Factor Analysis Of Geochemical And Petrologic Data Matrices With Constant Row Sums", *U.S. Geological Survey Professional Paper 574-G*, 47.

Regional Hydrology of the Dixie Valley Geothermal Field, Nevada: Preliminary Interpretations of Chemical and Isotopic Data

Gregory Nimz¹, Cathy Janik², Fraser Goff³, Charles Dunlap⁴,
Mark Huebner², Dale Counce³, and Stuart D. Johnson⁵

¹Lawrence Livermore National Laboratory, Livermore CA 94550

²U.S. Geological Survey, Menlo Park CA 94025

³Los Alamos National Laboratory, Los Alamos NM 87545

⁴University of California, Santa Cruz CA 95064

⁵Oxbow Power Services Incorporation, Reno NV 89511

ABSTRACT

Chemical and isotopic analyses of Dixie Valley regional waters indicate several distinct groups ranging in recharge age from Pleistocene (<20 ka) to recent (<50a). Valley groundwater is older than water from perennial springs and artesian wells in adjacent ranges, with Clan Alpine range (east) much younger (most <50a) than Stillwater range (west; most >1000a). Geothermal field fluids (~12-14 ka) appear derived from water similar in composition to non-thermal groundwater observed today in valley artesian wells (also ~14 ka). Geothermal fluid interaction with mafic rocks (Humboldt Lopolith) appears to be common, and significant reaction with granodiorite may also occur. Despite widespread occurrence of carbonate rocks, largescale chemical interaction appears minor. Age asymmetry of the ranges, more extensive interaction with deep-seated waters in the west, and distribution of springs and artesian wells suggest the existence of a regional upward hydrologic gradient with an axis in proximity to the Stillwater range.

Introduction

Dixie Valley is located in the western Basin and Range Province in west-central Nevada between the Stillwater (SW) and Clan Alpine-Augusta (CAA) mountain ranges (Figure 1). Both the valley and ranges are characterized by artesian wells and abundant perennial springs. The Humboldt Salt Marsh covers a wide area in the center of the valley. The Dixie Valley geothermal field (DVGF) is located in the northwest part of the valley, along the SW range front. Operation of the power plant began in 1988 and has a production of 62 MWe. Fluids are produced from ~2500-3000m depth at a temperature of ~250°C. The present production field covers ~20 km². The Oxbow Geothermal Corporation owns and operates the plant and its geothermal wells.

The purpose of this paper is to discuss chemical and isotopic data obtained from waters in the Dixie Valley and surrounding areas that pertain to the regional hydrologic system, including the geothermal field. Samples were collected from both cold and thermal wells and springs in Dixie Valley and the SW-CAA ranges. Samples were analyzed for elemental

compositions, $\delta^{13}\text{C}$, δD , $\delta^{18}\text{O}$, ^{14}C , $^{36}\text{Cl}/\text{Cl}$, and $^{87}\text{Sr}/^{86}\text{Sr}$. The objective is to characterize the hydrologic relations between the regional groundwaters, valley hot springs, and the geothermal production fluids.

Geologic Setting

Dixie Valley basin is bounded on the west by the tectonically active Stillwater Fault (earthquakes in 1915 and 1954, $M \approx 7$; Okaya and Thompson, 1985). The basin is bounded on the east by step faults, some of which are observed in the valley by linear N-NE trending arrays of springs. Valley sedimentary fill exceeds 2000m in the west and thins towards the CAA range to the east.

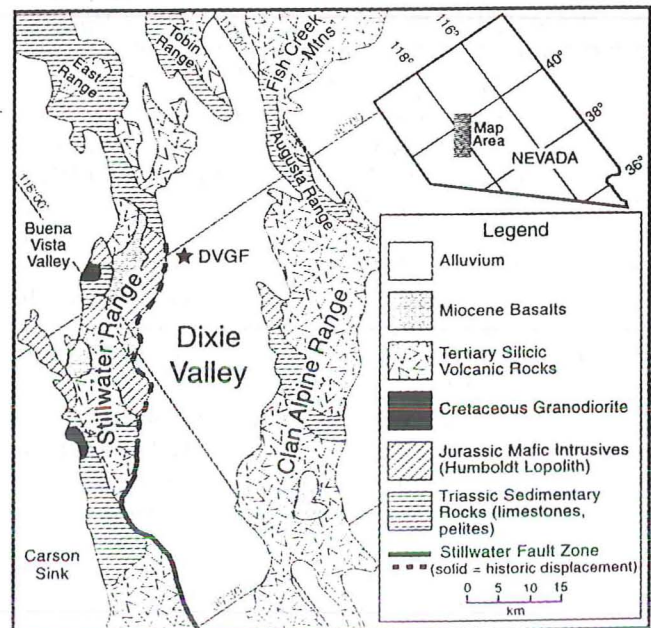


Figure 1. Dixie Valley Region. Water samples collected throughout map area. DVGF = Dixie Valley Geothermal Field.

The oldest common rocks in the hydrologic basin are Mesozoic marine sequences. In the CAA range, upper Triassic sections occur as thick units of pelites, quartz arenites, clastic and micritic limestones, and dolomites. Lithologically similar sequences of slightly older age (early Triassic) are the oldest rocks in the SW range. The SW upper Triassic section is a thick sequence of pelitic rocks overlain by late Triassic-Jurassic calcareous pelites. Thin units of lower Jurassic, heavily deformed carbonates, calcarenites, and pelitic rocks overlie these or are in thrust fault contact. The Jurassic Humboldt Lopolith overlies the SW-range Triassic section in thrust-fault contact (Speed, 1976). It is of mafic composition (coarse-grained gabbros, picrites, anorthosites), and locally reaches thicknesses in excess of 1200m (Speed, 1976). The entire Mesozoic sequence was intruded by several Cretaceous (69-104 Ma) granodioritic bodies of unknown subsurface extent. They crop out on the lower slopes of the western SW range and are encountered in the footwall of the Stillwater fault by DVGF boreholes (~3300m depth). Moderately thick mid-Cenozoic silicic tuffs occur in both ranges. They are found above the lopolith section in DVGF boreholes. Seismic data indicate depth to pre-Tertiary basement in the valley exceeds ~2500m near the DVGF. Late-Cenozoic basalts cap both ranges, and form areally extensive units. In DVGF boreholes they occur just beneath the valley fill units at ~2100-2400m.

Hydrologic Setting

Dixie Valley is an enclosed basin with a surface drainage of ~5200km² (Parchman and Knox, 1981). Pleistocene-age shorelines and lake deposits exist ("Lake Dixie"), and vertical recharge probably occurred at that time. (Thompson and Burke, 1973; Bell and Katzer, 1990). Today, water enters the basin during winter and spring from streams draining the SW and CAA ranges. Subsurface water movement within the ranges is probably controlled by fracture flow and geologic structure. However, very little is actually known about the hydrology of these ranges.

The valley fill holds an unknown number of aquifers. A shallow unconfined aquifer certainly occurs near the Humboldt Salt Marsh. Irrigation wells in the north valley draw water from deeper basin fill, but the thickness or confinement state of these aquifers is unknown. Dixie settlement domestic wells are under artesian head, implying confinement. Basalts underlying the basin fill host an aquifer that is a secondary DVGF production zone; seismic data indicate they are continuous throughout the valley and dip slightly westward. Tertiary ash-flows underlying the basalts are encountered in DVGF boreholes where they occur as thin units (<200m) with poor aquifer characteristics. They are probably not significant valley aquifers. The intersection of the SW fault zone with the lopolith creates the largest DVGF producing zone. However, boreholes away from the fault zone indicate low permeability in the lopolith, with lower temperature gradients than the overlying volcanic units (Williams et al., 1997). Lopolith lithologies are not naturally porous, and flow must be fracture dominated. Spatially variable hydrologic properties are to be expected. Subsurface aquifer characteristics of the Triassic units are unknown. Cementation often substantially reduces porosity in such lithologies. A borehole

penetrating these units north of the DVGF shows low hydraulic pressure and low temperature gradients indicative of low porosity (Williams et al., 1997). Triassic units in the SW and CAA ranges are substantially fractured only where adjacent to major fault zones (Speed, 1976). The Cretaceous granodiorite has low permeability when encountered during drilling. Like the lopolith, flow in this igneous body must be fracture dominated and highly variable (Nordstrom et al., 1989).

Previous hydrochemical and $\delta D/\delta^{18}O$ investigations using several of the wells and springs reported in this paper were conducted by Bohm et al. (1980) and Karst et al. (1988). Our expanded data set has led to several conclusions that differ from these previous studies.

Chemical and Isotopic Characterization

Chemical Groups

Major ion chemical compositions are shown on a trilinear diagram in Figure 2. Waters from the SW and CAA ranges can be distinguished by high-Cl and high-HCO₃ fields respectively. Fluids from the DVGF lie in a low-(Ca, Mg) and high-Cl field. Hot spring and valley samples are not specifically associated with either field, although valley waters are more commonly associated with the CAA field. Only Dixie Hot Spring has major ion chemistry similar to thermal wells. The Cl-HCO₃-SO₄ triangular diagram is perhaps most diagnostic of water type (Figure 2), and leads to a more general characterization of waters into High-HCO₃/Cl and Low-HCO₃/Cl groups (Figure 3). A third trend of very high HCO₃/Cl also occurs.

The δD and $\delta^{18}O$ compositions of SW and CAA waters are similar, but are distinct from valley, hot spring, and reservoir fluids (Figure 4). Isotopically heavy (less negative) δD and $\delta^{18}O$ compositions imply warmer conditions of recharge (summer, low altitude). Groundwater in the ranges would not be expected

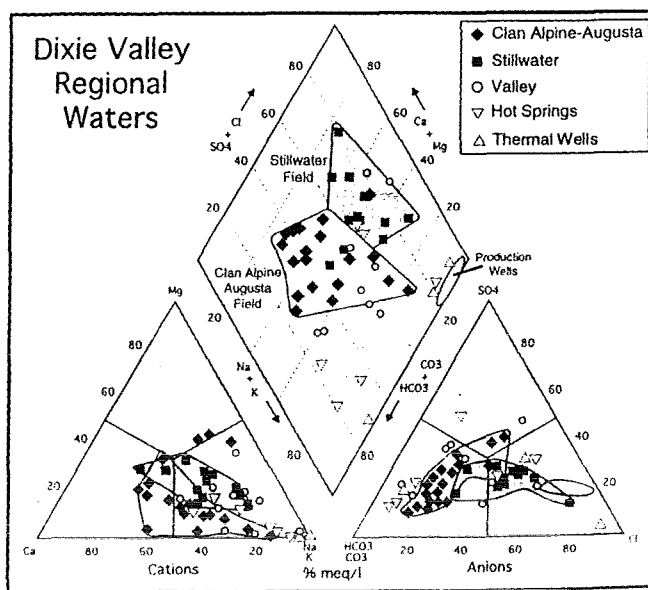


Figure 2. Trilinear diagram showing major ion relationships of the Dixie Valley regional waters. Thermal wells shown are wells not in production at the DVGF.

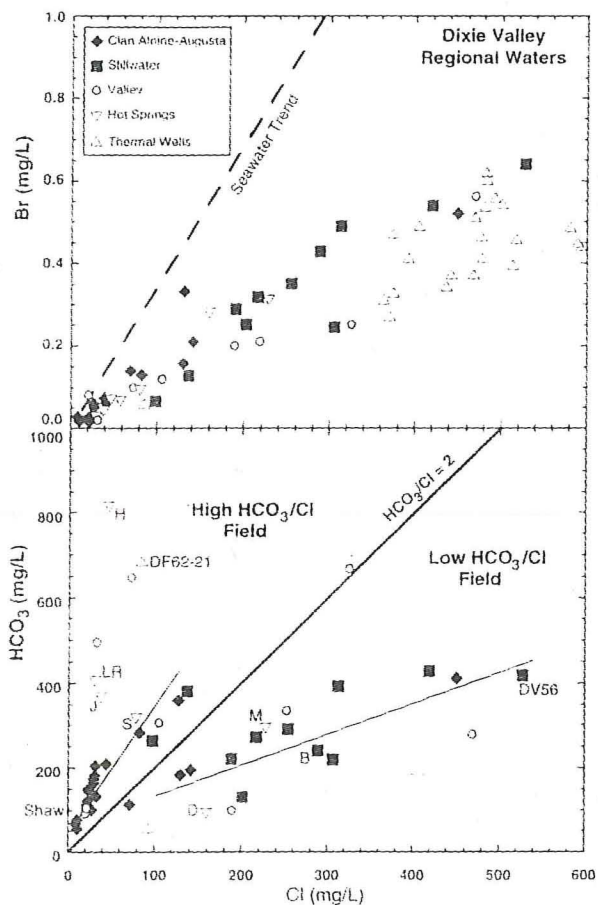


Figure 3. Bicarbonate-chloride-bromide relations for Dixie Valley regional waters. DVGF production wells not plotted on HCO₃⁻-Cl diagram. Select wells and springs discussed in text are identified. B = Bolivia artesian well. Hot springs: D = Dixie, H = Hyder, J = Jersey, LR = Lower Ranch, M = McCoy, S = Sou.

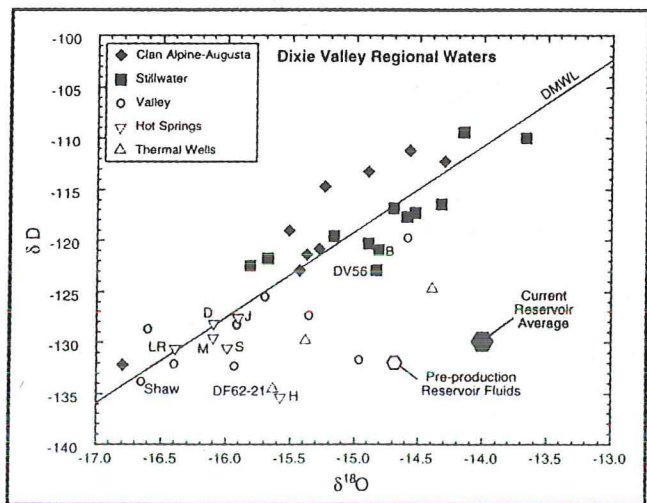


Figure 4. Oxygen-hydrogen isotopic compositions of Dixie Valley regional waters. The Dixie Valley meteoric water line (DMWL) represents the linear regression through SW, CAA, and valley waters. Sample identifiers are the same as Figure 3.

to be isotopically heavier than that in the valley. This occurrence suggests that the valley waters, including hot springs, were recharged during a colder climate. Noting similar relations in other Great Basin waters, Flynn and Buchanan (1993) suggest that the lighter waters are late-Pleistocene in age (10-30 ka). The position of pre-production reservoir fluid in Figure 4 is based on water collected in 1986-87. The position of the current reservoir average results from mixing with reinjection water that has become heavier due to evaporation in the cooling tower. The δD values of the reservoir fluids indicate that they are not fluids similar to those currently seen in the SW or CAA ranges. This does not mean that they were not recharged in the ranges, only that they were recharged during a colder climate. Likewise, the valley waters could have been recharged in the ranges during an earlier but cooler time.

Development of Chemical Compositions

Origin of Chloride. The sources of the Cl become apparent by examining ³⁶Cl/Cl (Figure 5). Much of the Cl in the High-HCO₃/Cl waters was derived directly from precipitation (concentrated in soil by evaporation), as indicated by the nuclear weapons testing (high) ³⁶Cl/Cl ratios (Bentley et al., 1982). These waters, mostly CAA samples, mostly 50 years old. The Cl in the Low-HCO₃/Cl group, mostly SW and valley waters, was derived through a combination of pre-1950's precipitation (³⁶Cl/Cl ≈ 300E-15; Bentley et al., 1986) and dissolution of Cl from rock (Figure 5). Typical rock ³⁶Cl/Cl values are shown in Table 1. DVGF fluids have ³⁶Cl/Cl ratios of about (51±3)E-15 (based on analysis of 24 samples; see Figure 5). The uniformity of the ³⁶Cl/Cl ratio suggests that this is the ratio

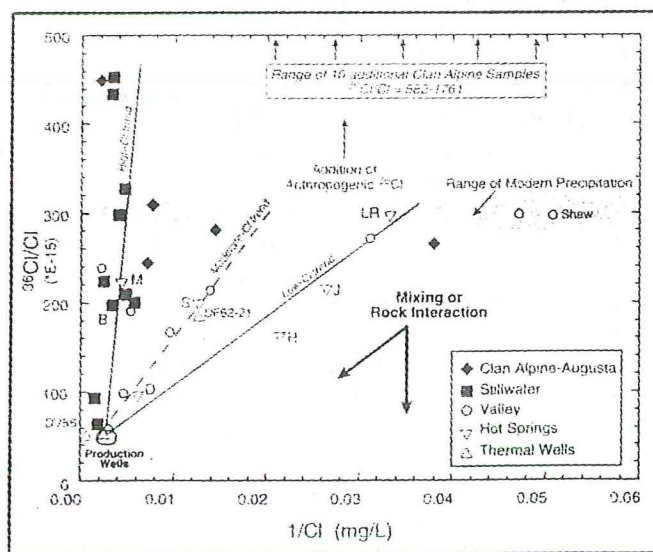


Figure 5. Chloride-³⁶Cl/Cl relationships in Dixie Valley regional waters. Range for modern precipitation represents expected variation of ³⁶Cl/Cl ratios in precipitation chloride based on calculations of Bentley et al. (1986), and direct measurement of one Dixie Valley rain sample. The range is not intended to represent the range of precipitation Cl concentration. Anthropogenic ³⁶Cl represents globally distribute ³⁶Cl due to nuclear weapons testing, 1950's-60's. Sample identifiers are the same as Figure 3.

in the rock from which their Cl was derived. The only lithology thought to abundantly occur in the subsurface with $^{36}\text{Cl}/\text{Cl}$ values typically of this magnitude is the Cretaceous granodiorite (Table 1; see Nimz et al., 1997)

Table 1. Characteristic $^{36}\text{Cl}/\text{Cl}$ values for common rock types.

Rock:		Basalt	Andesite	Granitic	Rhyolite	Arkose	Limestone	Shale
SiO ₂	%ox	49.5	59.0	67.2	67.2	77.1	0.8	62.8
Al ₂ O ₃		15.0	17.4	16.0	16.0	8.7	0.3	18.9
MgO		6.5	3.5	1.8	1.8	0.5	2.1	2.2
Na ₂ O		3.0	3.5	3.8	3.0	1.5	0.0	1.2
K ₂ O		1.0	1.4	2.8	2.2	2.8	0.0	3.7
F	ppm	200	350	700	600	220	112	560
Li		16	20	40	32	15	5	75
B		5	15	15	12	35	55	100
Sm		5.0	3.5	4.2	3.4	3.1	3.8	5.6
Gd		5.0	3.3	4.2	3.4	2.7	3.8	4.7
Th		3.0	6.9	18.7	16.8	5.7	2.0	14.6
U		0.8	1.8	5.8	5.3	1.5	1.0	3.1
phi (n/cm ² /a)		449	1184	3293	3142	715	274	1095
$^{36}\text{Cl}/\text{Cl}$ (E-15)		6.5	17.1	47.5	45.3	10.3	4.0	15.8

Origin of Bicarbonate. Figure 6 shows $\delta^{13}\text{C}$, ^{14}C , and $^{87}\text{Sr}/^{86}\text{Sr}$ values that provide some information on HCO_3^- origins for the Low- HCO_3^-/Cl and very high HCO_3^-/Cl groups. All very high HCO_3^-/Cl samples fall into the high $\delta^{13}\text{C}$ cluster on Figure 6. These samples appear to lie on a line between atmospheric values and values we have measured in Triassic marine limestones of the SW and CAA ranges. Low- HCO_3^-/Cl samples lie along another line between atmospheric $\delta^{13}\text{C}$ and a value intermediate between the limestones and fracture-fill vein calcite we have measured from the SW range. All of the geothermal wells we have measured lie on the "calcite" line, while all of the hot springs except for Dixie Hot Springs lie on the "limestone" line. Most of the waters have interacted with subsurface carbonates that have added HCO_3^- , altered the original atmospheric $\delta^{13}\text{C}$ values, and artificially increased their ^{14}C age. It is not completely apparent what the carbonate endmembers are, despite the measured limestone and calcite $\delta^{13}\text{C}$ values. First, the Br-Cl trend of the Dixie Valley samples is unlike the seawater trend (Figure 3). Significant interaction with marine carbonates should produce a seawater Br-Cl trend. Second, the $^{87}\text{Sr}/^{86}\text{Sr}$ composition in the waters seems largely controlled by carbonate dissolution ($\delta^{13}\text{C}$; Figure 6). Projecting the $^{87}\text{Sr}/^{86}\text{Sr}$ trend to an endpoint at the limestone $\delta^{13}\text{C}$ value produces a value of 0.7095. This is too high for Mesozoic or even Paleozoic seawaters (which are <0.7088), suggesting that the endmember may not be a marine carbonate (Burke et al., 1982).

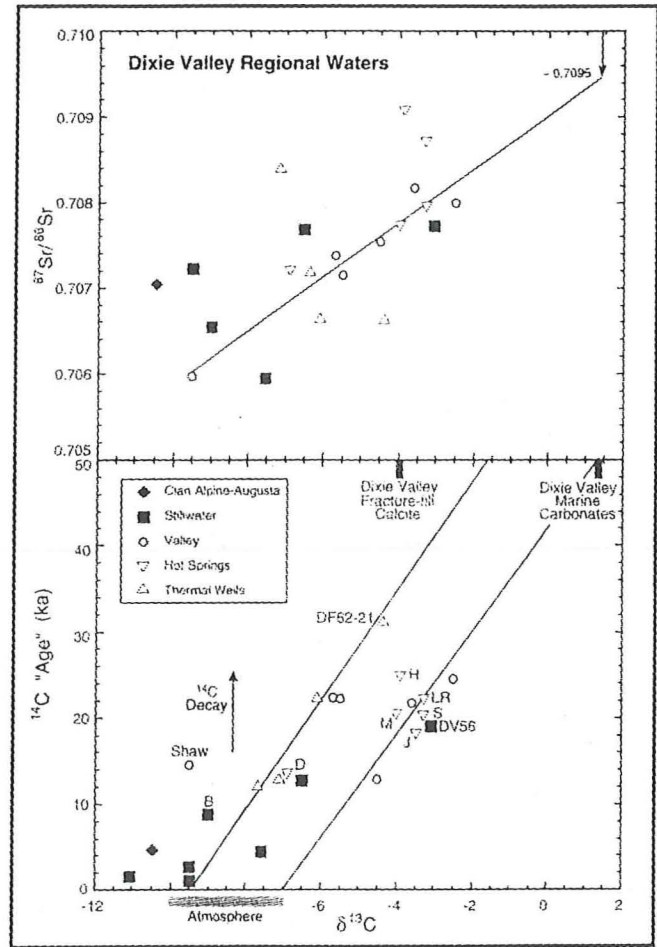


Figure 6. $\delta^{13}\text{C}$ - ^{14}C - Sr isotope relations in Dixie Valley regional waters. ^{14}C "age" positioning of carbonate and calcite endmembers represents the approximate upper age limit of detection for the ^{14}C technique (~50 ka). Samples with $\delta^{13}\text{C}$ values more negative than atmosphere indicate addition of biologically mediated carbon. Sample identifiers are the same as Figure 3.

Water Recharge Ages

More specific ages than those derived from $\delta\text{D}-\delta^{18}\text{O}$ can be estimated using ^{14}C , provided attention is paid to carbonate chemistry, especially $\delta^{13}\text{C}$ (Figure 6). The oldest reliable measured CAA age is ~5 ka. However, the CAA $^{36}\text{Cl}/\text{Cl}$ values indicate most waters are <50a. The oldest reliable SW range age is ~9 ka. Sample DV56, a SW cold spring, gives an uncorrected age of ~19 ka, and is sufficiently like valley hot springs in HCO_3^- and $\delta^{13}\text{C}$ that it reasonably could be Pleistocene. Its δD value is low enough to make this plausible. The youngest reliable SW age based on ^{14}C is ~900a, although a few bomb-pulse $^{36}\text{Cl}/\text{Cl}$ samples occur. It is noteworthy that very young waters are rare in the SW compared to the CAA range.

The oldest reliable age for a non-thermal water measured in the valley is ~14 ka (Shaw well; Figure 6). Ages for samples reacting with subsurface carbonate can be regarded as *maxi-*

ages, since this process makes samples appear older. The maximum age for a valley hot spring is ~25 ka (Hyder), for a thermal well is ~31 ka (DF62-21), and for a DVGF production fluid is ~13 ka. A simple-minded reconstruction of their $\delta^{13}\text{C}$ values, following the limestone-calcite interaction lines on Figure 6, suggests these samples are 5-20 ka. However, this is probably over-simplified. The youngest maximum age for a hot spring sample is ~13 ka (Dixie), and for a thermal well is ~12 ka. Based on this evidence, the range in $\delta^{13}\text{C}$ values, and the $\delta\text{D}-\delta^{18}\text{O}$ values, it is reasonable to believe that most of the thermal water in the region is ~12-14 ka. It is notable that the oldest reliable non-thermal valley age is of similar magnitude (Shaw well). It is perhaps also significant that two wells not in the DVGF have older max ages (DF62-21 and DF45-14).

Evidence of Water Mixing

Evidence of mixing between or within chemical/isotopic or age groups can be a guide to understanding hydrologic flow. Samples with intermediate chemical compositions are apparent on the figures. However, samples intermediate on one diagram are usually not those that are intermediate on other diagrams. Widespread mixing between groups is therefore not evident. Within groups, the system most suggestive of mixing is $^{36}\text{Cl}/\text{Cl}$. Figure 5 shows linear arrays radiating from a high-concentration/low-ratio composition, forming various trends. Mixing calculations indicate that the amounts of the high-Cl endmember are small. For example, the hot springs would be predominantly a low-Cl, presumably surface-water, endmember with small and variable amounts of a high-Cl, possibly reservoir-like, endmember: Lower Ranch <3%, Jersey <5%, Sou \approx 5%, Hyder \approx 5%, Dixie \approx 25%. McCoy Hot Spring requires a significantly more concentrated surface-water endmember (~180-210 mg/L Cl), although the mixing percentage would be similar to the other hot springs (~15% reservoir-like water).

Chemical interaction with rock - Cl dissolution - would also produce similar arrays (Figure 7). With the available data set, it is difficult to discriminate between mixing and dissolution processes for the Dixie Valley waters. The trajectories for samples within single chemical or age groups on Figure 7 are perhaps closer to the trajectories of the mixing lines, particularly at high Cl concentrations. For this reason it is felt that while rock interaction does occur, some mixing with high-Cl low- $^{36}\text{Cl}/\text{Cl}$ endmembers is partly responsible for producing the observed lower $^{36}\text{Cl}/\text{Cl}$ ratios within the SW, valley and hot springs groups.

Figure 7 also provides some insight into the origin and evolution of the low- $^{36}\text{Cl}/\text{Cl}$ endmember. Assuming the water recharged with an atmospheric $^{36}\text{Cl}/\text{Cl}$ ratio (~300E-15), it must have begun reacting with rock when it still had a very low Cl concentration, similar to the valley Shaw well. That is, virtually none of the Cl was derived from the soil column where it was concentrated through evaporation (and still be ~300E-15). If it had originated with concentrations similar to SW range waters, where soil Cl must be a factor, the dissolution trajectories indicate it would not have achieved its present $^{36}\text{Cl}/\text{Cl}$ together with its present Cl concentration.

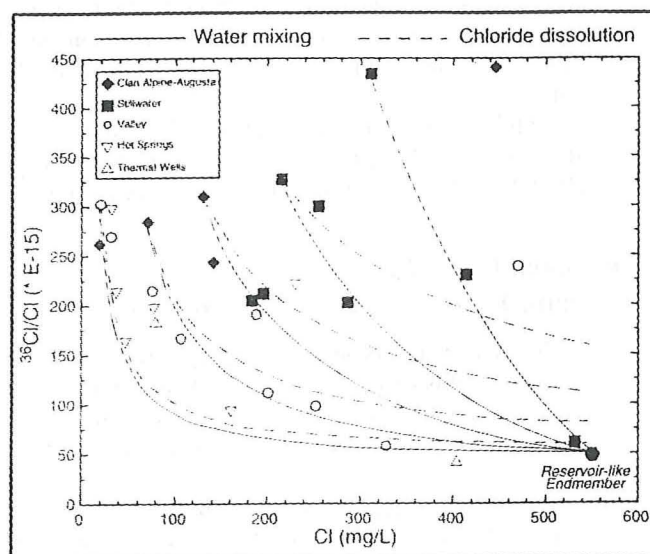


Figure 7. Mixing and Cl dissolution curves for various Dixie Valley water endmembers. Low- $^{36}\text{Cl}/\text{Cl}$ endmember represents reservoir-like fluid compositions, but with chloride contents higher than pre-production values (see Kennedy et al., 1999). Cl dissolution curves are not a function of the Cl concentrations in the "rock" endmembers, since the model adds chlorine until reservoir $^{36}\text{Cl}/\text{Cl}$ values are achieved (curves continue off of diagram to higher Cl contents). Measured Dixie Valley samples are used for high- $^{36}\text{Cl}/\text{Cl}$ endmembers.

Observations and Implications

Based on the chemical and isotopic measurements, there are several observations that can be made concerning the relations among the hydrochemical groups and regional hydrologic flow.

Dixie Valley Regional Waters: Characterization and Chemical Relations

- Valley groundwaters, hot springs, and DVGF fluids recharged during colder conditions than SW-CAA waters, suggesting a late-Pleistocene age that is supported by ^{14}C (~12-14 ka).
- Most of the water observed in the CAA range is very young, <50a.
- Most of the water observed in the SW range is much older than CAA water (e.g., ~9 ka), even though they have similar δD values.
- Some Pleistocene-age valley waters have remained or become very dilute (e.g., Shaw).
- The lowest- $^{36}\text{Cl}/\text{Cl}$ waters (DVGF fluids, DV56) may not derive the bulk of their Cl from their current host rocks, the Triassic marine sequences or Humboldt Lopolith. The only lithology in the region with $^{36}\text{Cl}/\text{Cl}$ similar to these waters is the Cretaceous granodiorite.
- $^{36}\text{Cl}/\text{Cl}$ modeling suggests that reservoir fluids evolved from dilute surface waters like those of the Shaw well, rather than from more concentrated surface waters like those in the SW range.

- $\delta^{13}\text{C}$ values suggest that the very high HCO_3/Cl group has interacted with marine carbonates; in comparison, based on $\delta^{13}\text{C}$ -calcite trends, the low- HCO_3/Cl group apparently has not.
- Very limited mixing *between* chemical groups may occur. *Within* groups, internal mixing with low- $^{36}\text{Cl}/\text{Cl}$ endmembers (DVGF- or DV56-like fluids) appears more common.

Regional Fluid Flow:

Origins, Relative Rates, and Flowpaths

- If the Cl in the reservoir fluids is derived from granodiorite, then either this rock occurs at depth beneath the valley, the bulk of the Cl is incorporated within the fault zone at the granodiorite contact, or fluid flow is across the SW fault zone.
- Average subsurface flow from the ranges into the valley is not rapid; valley water is still Pleistocene in age. Simplistic flow-line analysis would suggest $<1\text{m/a}$ flow rates.
- Controls on flow paths vary greatly within the regional hydrologic system. Evidence includes:
 - Artesian dilute Shaw-type waters and the DVGF fluids are the same age.
 - Flow rates to reservoir depths exceed 0.25m/a , assuming 3000m depth and an age of 12 ka.
 - Flow rates to valley shallow domestic wells are $<0.03\text{m/a}$, assuming vertical piston flow, $<300\text{m}$ depth, and an age of 12 ka (non-vertical flow paths require even slower flow rates).
 - Old ages and high-TDS in SW waters suggest a deep source and a regional upward hydrologic gradient with an axis in the SW range; this may also affect the valley.
 - Despite the upward gradient, hot springs contain only a small fraction of reservoir-like water.

Acknowledgments

This research was supported by the Geothermal Technology Division under the Assistant Secretary for Energy Efficiency and Renewable Energy of the U.S. Department of Energy. We thank Oxbow Power Services Incorporated, and Dick Benoit in particular, for very significant help with field work logistics, background chemical data, and providing access to geothermal field wells. Work by LLNL authors was performed under the auspices of the U.S. Department of Energy by Lawrence Livermore National Laboratory under contract W-7405-Eng-48.

References

- Bell, J.W. and Katzer, T. (1990) "Timing of late Quaternary faulting in the 1954 Dixie Valley earthquake area, central Nevada." *Geology*, 18:622-615.
- Bentley, H.W., Phillips, F.M., and Davis, S.N. (1986) "Chlorine-36 in the terrestrial environment." In: P. Fritz and J.-Ch. Fontes (Editors), *Handbook of Environmental Geochemistry*. Elsevier, Amsterdam, p. 427-480.
- Bentley, H.W., Phillips, F.M., Davis, S.N., Gifford, S., Elmore, D., Tubbs, L.E., and Gove, H.E. (1982) "Thermonuclear ^{36}Cl pulse in natural waters." *Nature*, 300: 737-740.
- Bohm, B.W., Jacobson, R.L., Campana, M.E., and Ingraham, N.L. (1980) "Hydrology and Hydrogeochemistry." *Geothermal Reservoir Assessment Case Study, Northern Basin and Range Province, Northern Dixie Valley, Nevada*. Mackey Minerals Research Institute, v.1, p. 159-186.
- Burke, W.H., Denison, R.E., Hetherington, E.A., Koepnick, R.B., Nelson, H., and Otto, J.B. (1982) "Variation of seawater $^{87}\text{Sr}/^{86}\text{Sr}$ throughout Phanerozoic time." *Geology*, 10:516-519
- Flynn, T. and Buchanan, P.K. (1993) "Pleistocene origin of geothermal fluids in the Great Basin, western United States." *Resource Geol. Spec. Issue*, 16:60-68.
- Karst, G.B., Campana, M.E., and Jacobson, R.L. (1988) "A mixing-cell model of the hydrothermal flow system, northern Dixie Valley, Nevada." *Geothermal Resources Council Transactions*, 12:167-174.
- Kennedy, B.M., Janik, C., Benoit, D., and Shuster, D.L. (1999) "Natural geochemical tracers for injectate fluids at Dixie Valley." *Proceeding of the 24th Workshop on Geothermal Reservoir Engineering*, Stanford University.
- Nimz, G.J., Moore, J.N., and Kasameyer, P.W. (1997) " $^{36}\text{Cl}/\text{Cl}$ ratios in geothermal systems: Preliminary measurements from the Coso field." *Geothermal Resources Council Transactions*, 21:211-217.
- Nordstrom, D.K., Olsson, T., Carlsson, L., Fritz, P. (1989) "Introduction to the hydrogeological investigations within the International Stripa Project. *Geochim. et Cosmochim. Acta* 53:1717-1726.
- Okaya, D.A. and Thompson, G.A. (1985) "Geometry of the Cenozoic extensional faulting, Dixie Valley, Nevada." *Tectonics* 4:107-125.
- Parchman, W.L. and Knox, J.W. (1981) "Exploration for geothermal resources in Dixie Valley, Nevada." *Geothermal Resources Council Bull.* June, 1991.
- Speed, R.C. (1976) Geologic Map of the Humboldt Lopolith, scale 1:81050, GSA Map Chart Series, MC-14.
- Thompson, G.A. and Burke, D.B. (1973) "Rate and direction of spreading in Dixie Valley, Basin and Range Province, Nevada." *Geol. Soc. Am. Bull.* 84:627-632.
- Williams, C.F., Sass, J.H., and Grubb, F.V. (1997) "Thermal signature of subsurface fluid flow in the Dixie Valley geothermal field, Nevada." *Stanford Geothermal Workshop Proceedings*, SGP-TR-155, 22:77-85.

GEOMETRY OF CENOZOIC EXTENSIONAL
FAULTING: DIXIE VALLEY, NEVADA

David A. Okaya and George A. Thompson

Department of Geophysics, Stanford
University, Stanford, California

Abstract. Precise definition of geometric relationships between individual basins and ranges may help to reveal the mechanical processes of Basin and Range Cenozoic extensional faulting at depth. Previous studies have attempted to identify simple horsts and grabens, tilted crustal blocks with planar faulting, or tilted crustal blocks with listric faulting in the shallow crust. Normal faults defining these crustal blocks may root (1) individually in the ductile lower crust, (2) in regional or local low-angle detachment faults, or (3) in igneous intrusions or decoupling surfaces produced by the intrusions. The present study, in Dixie Valley, west-central Nevada, makes use of a seismic reflection survey, gravity models, seismograms from earthquakes occurring on December 16, 1954, and geometrical block models. These data show a structurally asymmetric basin bounded by a single zone of faulting on the northwest and by a downbowed and step-faulted floor to the southeast. The northwest bounding fault is moderately dipping (50°) and planar to a depth of 3 km. The southeast boundary is step-faulted, and altogether the faults indicate an extension of 20% across the valley at the rate of 0.38 mm/y for the

last 8 my. Synthetic earthquake seismograms confirm a focal depth of 15 km and fault dip of 62° for the Fairview Peak earthquake and suggest that the focal depth of the Dixie Valley earthquake was also 15 km instead of the previously reported 40 km. Local microearthquakes cluster around 10-15 km. The geometrical block models indicate that crustal horst-graben faulting and planar, high-angle normal faults rooted in a low-angle detachment surface do not readily account for development of the subsidiary (step) faults found in Dixie Valley. Extension of the crust by intrusion may develop high-angle faults and, with further intrusion, may develop the subsidiary faults and produce a complex, sagged, asymmetric graben like Dixie Valley.

INTRODUCTION

Formation of the basins and ranges in the northern Basin and Range province represents a late stage of Cenozoic crustal extension. While the shallow Basin and Range structure is generally known from geologic studies, geophysical methods have only recently begun to reveal the structure at greater depth. In particular, extensional normal faults which separate the crustal blocks defining the basins and ranges are steeply dipping ($>50^\circ$) near the surface; geophysical measurements are necessary to define the deeper geometry of the crustal blocks and

Copyright 1985
by the American Geophysical Union.

Paper number 4T0980.
0278-7407/85/004T-0980\$10.00

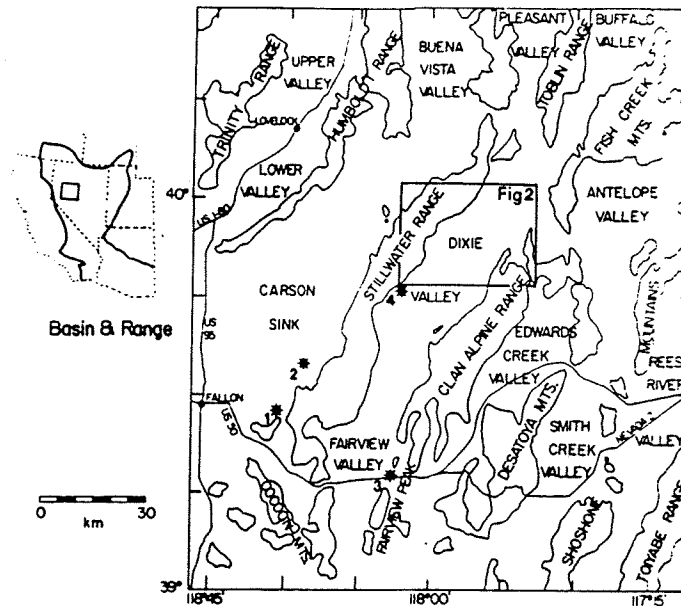


Fig. 1. Outline of ranges and basins in west-central Nevada showing location of Dixie Valley. Stars locate epicenters of major earthquakes in 1954: (1) Fallon, July 6; (2) Stillwater, August 23; (3) Fairview Peak, December 16; (4) Dixie Valley, December 16.

to provide insights to the processes of crustal extension.

Crustal extension may be accommodated by brittle (elastic to the point of failure) and ductile (yielding, creeping, or visco-elastic) attenuation of the crust [Bott, 1980a; Eaton, 1982]. The topographic basins and ranges are expressions of dominantly brittle attenuation, which presumably gives way to ductile attenuation in the lower crust [Fletcher and Hallet, 1983]. As seismic activity is associated with brittle deformation, the base of the seismogenic zone of the crust marks the transition from brittle to ductile deformation [Sibson, 1982].

Crustal response to brittle attenuation has been to form horst, graben, and rotated crustal blocks [Stewart, 1980]. Litrictic, tilted planar, or steeply dipping planar normal faults separate these blocks [Effimoff and Pinezich, 1981; Anderson et al., 1983]. These faults may have associated conjugate or second-order faults which produce secondary structural features within the crustal blocks. The major faults may root within a detachment zone in the seismogenic crust [McDonald, 1976]; within a zone of decoupling in the ductile crust [Bott, 1980b; Wallace, 1980]; within lower crustal magmatic in-

trusions [Thompson, 1959]; or penetrate to the asthenosphere [Wernicke, 1981].

Geophysical evidence may reveal how these extensional faults root at depth. First, however, upper crustal fault geometry must be well understood to provide constraints to lower crustal geometry. Dixie Valley, in west-central Nevada, offers a unique opportunity to examine the basin's fault geometry. Previous studies have used seismic refraction, aeromagnetism, electrical potential, and gravity to study upper crustal structure. Large and small earthquakes have provided evidence of continued tectonic displacement within the deeper crust. This study presents the findings of new seismic reflection, gravity, and teleseismic data in conjunction with previous studies in order to delineate the geometry of late Cenozoic extensional faulting in Dixie Valley.

DIXIE VALLEY

Dixie Valley is located in the west-central portion of the Basin and Range province (Figure 1). Bounded by the Stillwater Range to the northwest and the Clan Alpine Range to the southeast, the asymmetric valley is still tectonically active, as evidenced by microearthquakes,

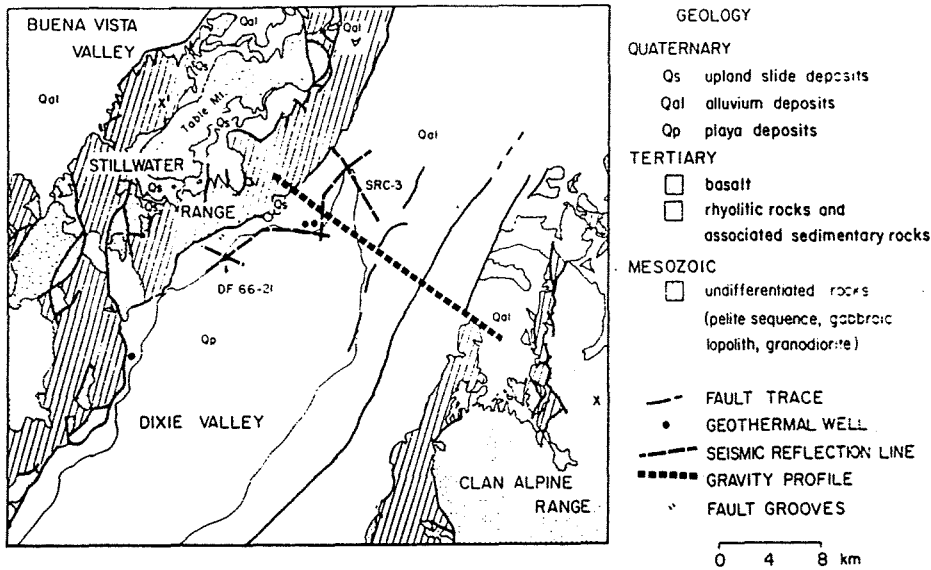


Fig. 2. Geology of Northern Dixie Valley region and location map for geophysical data. Geology from Speed [1976] and Hastings [1979]. Faults in Dixie Valley are from aerophotographic studies by Burke [1967] and Whitney [1980]. Fault grooves along the Stillwater Range-front are oriented at $N40^{\circ}W$ with plunge 50° . X-X' denotes cross section of Figure 10.

modern fault scarps, and major earthquakes as recent as 1954. The estimated direction of extension within Dixie Valley is $N55^{\circ}W-S55^{\circ}E$, and the established rate is 0.4 mm/yr over the last 15 m.y. and 1 mm/yr over the last 12,000 years [Thompson and Burke, 1973]. In the area of the present study (Figure 2), exposures of the major normal fault separating the Stillwater Range from Dixie Valley show a dip of 50° and fault grooves oriented $N40^{\circ}W$. The closest seismic refraction determination of Moho depth is 22 km at Antelope Valley, northeast of the Clan Alpine Range [Stauber and Boore, 1977].

GEOLOGY OF THE NORTHERN DIXIE VALLEY REGION

In the northern Dixie Valley region (Figure 2), the Mesozoic "basement" is composed of sedimentary rocks, mainly pelites, and intrusive gabbros and granodiorites. This basement is unconformably overlain by a Tertiary volcanoclastic sequence topped by basalt. Dixie Valley is filled with late Cenozoic alluvial, lacustrine, and playa deposits. Geologic studies have been carried out by Page [1965] in the Stillwater Range; by Riehle et al. [1972] in a volcanic center within the

southern Clan Alpine Range; by Speed [1976] in the gabbro complex, or Humboldt lopolith; and by Stewart and Carlson [1976] in the broad region of west-central Nevada. Structural and tectonic analyses of Dixie Valley have been made using a variety of geologic and geophysical data, including seismic refraction [Thompson et al., 1967; Meister, 1967]; seismic reflection [Anderson et al., 1983]; aeromagnetism [Smith, 1968]; aerophotographs [Burke, 1967; Whitney, 1980]; geodetic information [Meister et al., 1968]; and earthquake seismology [Romney, 1957; Ryall and Malone, 1971; Stauber and Ryall, 1967; Westphal and Lange, 1967; Zoback et al., 1981]. A geothermal study combining hydrology, geochemistry of hot springs, heat flow, magnetotellurics, resistivity, and well logging was performed by Parchman and Knox [1981]. A similar but more detailed study was conducted by Bell et al. [1980].

The oldest rocks recognized in the Mesozoic basement are Triassic to lower Jurassic mudstones, wackes, and carbonates deposited in what has been interpreted as an early Mesozoic basinal shelf [Speed, 1976]. Thrust over these sedimentary units are lower to mid-Jurassic mudstones, siltstones, quartz sandstones, carbonates, and calcareous breccias intruded by gabbro

and diorite. This intrusive "Humboldt lopolith" [Speed, 1976] extends laterally across most of the northern Dixie Valley region and constitutes the basement for geophysical purposes. Overlying Mesozoic volcanics include basaltic lava.

Unconformably overlying the Mesozoic basement is a Tertiary volcanoclastic sequence divided by Hastings [1979] into three distinct units of calc-alkaline tuffs and flows, fluvio-lacustrine deposits, and a capping basalt. The volcanic center for the tuffs and flows is speculated to be in the southern Clan Alpine Range [Riehle et al., 1972]. Scattered radiometric age dating by Hastings [1979] yielded an age of 30-17 m.y. for the tuffs and flows and 8 (+ 4) m.y. for the capping basalt. Hastings suggests that the basalt was deposited on a surface of low relief and predates the extensional faulting that formed Dixie Valley; i.e., the Tertiary volcanoclastic sequence forms the subvalley floor.

Quaternary lacustrine and playa deposits in Dixie Valley are 2 km thick. The modern playa is located near the Stillwater Range, reflecting the structural asymmetry of the valley. Fans off the Stillwater Range extend 1 to 2 km from the range and the fan gravels reach a depth of up to 2 km as determined by seismic profiles and gravity modeling. Fans off the Clan Alpine Range slope less steeply and extend several kilometers farther into the valley; these fan gravels are also less thick than those adjacent to the Stillwater Range.

Structural models for northern Dixie Valley have been presented by Smith [1968], Thompson and Burke [1973, 1974], Bell et al. [1980], and Parchman and Knox [1981]. These models are refinements of models suggested by Thompson et al. [1967] and Burke [1967], which are based on gravity, aeromagnetic, and seismic refraction information. Dixie Valley was proposed to have asymmetric graben-within-graben structure with several opposing faults. Bell et al. [1980] speculate the steep faults root within a ductile crust-mantle interface.

SEISMIC REFLECTION PROFILE

During the course of geothermal exploration in northern Dixie Valley, the Southland Royalty Co. obtained 28 km of high-resolution seismic reflection data. The four seismic lines, recorded by

Petroleum Geophysical Co. and processed by Western Geophysical Co., represent a detailed cross section of the northwestern side of northern Dixie Valley. Revealed in the seismic survey are the basin sediments, the alluvial fan deposits off the Stillwater Range, and the Mesozoic "basement" found both in the ranges and under the valley floor.

Recording parameters of the seismic survey include a Vibroseis (registered trademark of Conoco, Inc.) source, group spacing of 110 feet (33.5 m), a shot-to-geophone spacing ratio of 2:1, and a 96-channel split-spread arrangement yielding 24-fold coverage. A normal processing sequence has been performed, including deconvolution, velocity analysis, elevation and residual statics, stacking, filtering, and finite difference migration.

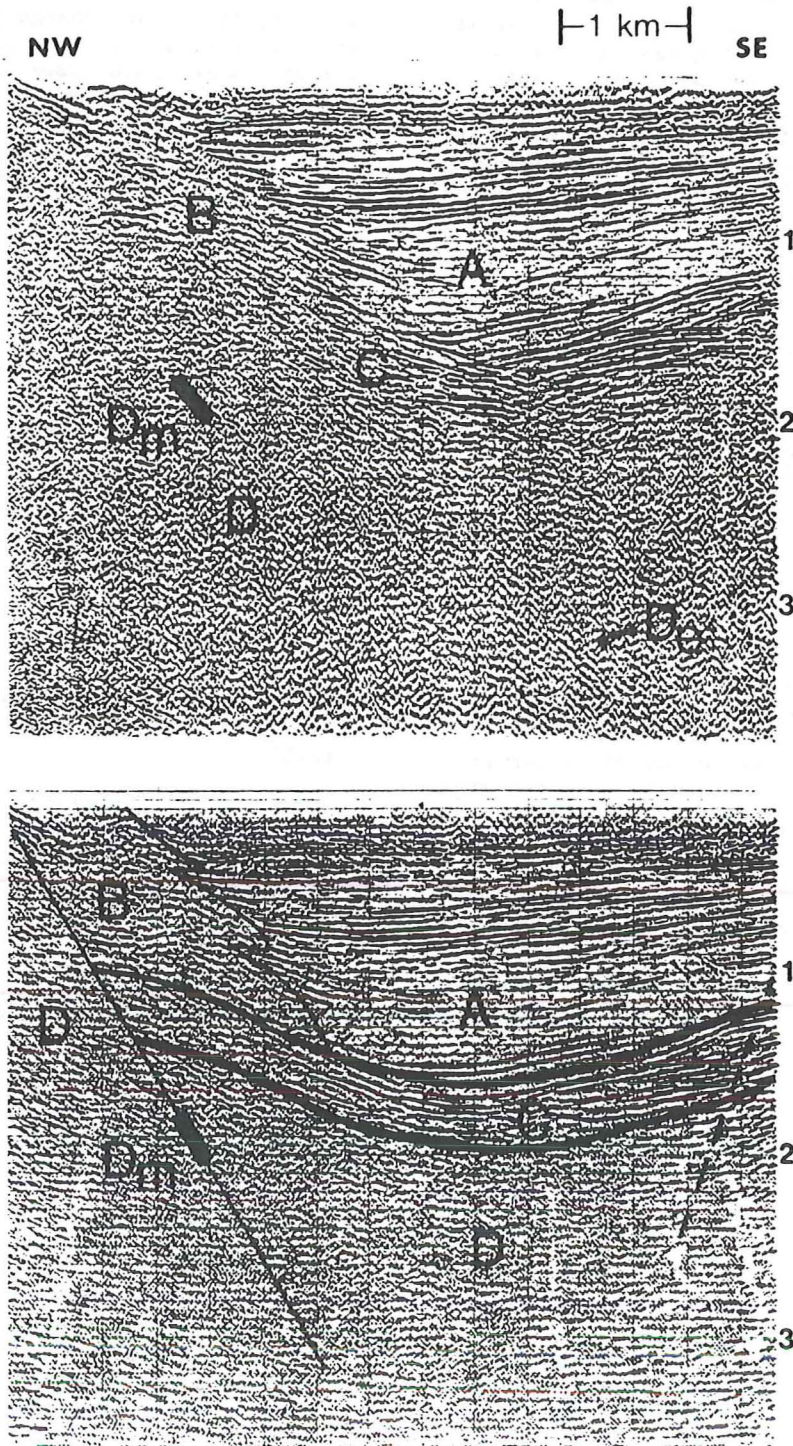
Two of the four seismic lines are parallel to the Stillwater Range. The remaining two lines are oblique to nearly perpendicular to the range-front; line SRC-3 is within 15° of being a true dip line (Figure 2). This seismic line starts within the alluvial fan 150 m from the bedrock of the range and extends six km into Dixie Valley, presenting a cross section of roughly half of the valley; it is also nearly parallel to a gravity traverse located less than 3 km to the southwest.

Seismic Line SRC-3

The seismic reflections of line SRC-3 may be divided into four zones based on seismic character. Zone A (Figure 3) shows subhorizontal reflections, zone B has discontinuous, relatively chaotic reflections, zone C shows particularly strong, layered reflections, and zone D is comparatively transparent. Variation in seismic character between zones is related to geology.

The reflections of zone A extend to a maximum of 1.4 s. Large amplitude horizons are interlayered with horizons of low energy. The lateral extent of zone A near the surface corresponds to the known limit of the Quaternary lacustrine and playa deposits of Dixie Valley. Interval thinning to the southeast is exhibited within the overall zone of reflections. The seismic reflections reveal a northwesterly migrating basinal axis which is currently 3 km from the range front; this migration is due to tilting or sagging of the basin during deposition.

only to
SRC-3



ask Denise

Fig. 3. Seismic line SRC-3, (top) stacked and (bottom) interpreted finite difference migration. Reflection symbols: A, lacustrine and playa deposits; B, alluvial fan; C, Tertiary volcanoclastic sequence; D, Mesozoic basement; D_e, steeply dipping fault plane reflections; D_m, hand migration of event D_e. Calculated fault dip from the hand migration is 50°.

The discontinuous reflections of zone B extend from near surface to about 1.1 s, and the lateral extent correlates with the large alluvial fan originating from Cottonwood Canyon in the Stillwater Range; intertonguing of alluvial fan and lacustrine/playa reflections may be seen at depth. The comparatively chaotic nature of fan reflections is due to the marked lateral heterogeneity of fan deposits.

In Carson Sink, on the other side of the Stillwater Range, results from reconnaissance exploration by the petroleum industry reveal a seismic profile similar to line SRC-3 [Hastings, 1979]. Deep, layered strong amplitude events are proven by drilling to be reflections off the Tertiary volcanoclastic sequence; the uppermost strong reflection represents the capping basalt layer. Mapping by Page [1965] and Speed [1976] shows similar geology on both sides of the Stillwater Range. As the deep, layered reflections in Carson Sink are similar to the reflections of zone C in line SRC-3, Dixie Valley appears to be underlain by the same Tertiary volcanoclastic sequence. Quality of these Tertiary volcanoclastic reflections deteriorates under the alluvial fan reflections due to attenuation of seismic signal by the fan material. Dips of these reflections appear steeper under the fan reflections due to velocity pull-up caused by the higher velocity of the alluvial fan relative to the lacustrine/playa deposits. The disruption of reflections to the extreme southeast of the seismic line is possibly due to a northwest dipping normal fault.

Zone D is interpreted as the Mesozoic basement. This zone is nearly transparent except for a steeply dipping event on the stacked, unmigrated seismic section at 3.2 s approximately 4.4 km from the range front (event D_e in Figure 3a). Hand migration of this event using an average velocity of 7500 ft/s derived from a seismic refraction study by Thompson et al. [1967] and from sonic well logs from the Dixie Federal 66-21 geothermal exploratory well (T. 24N, R. 36E, sec. 21) moves the event to 1.8 s located 1.5 km from the range front. The hand-migrated event D_m is interpreted as a reflection off the range-front fault for the following reasons: Connecting the surface outcrop of the fault with D_m yields a dip of 50° for the fault; this is in agreement with surface

dip observations. Interpretation of this event as a fault reflection is substantiated by the abrupt change from alluvial fan chaotic reflections to the basically transparent Mesozoic basement across the fault. Event D_e does not appear in the 45° -finite difference migration section.

In summary, seismic line SRC-3 reveals a basin composed of an alluvial fan, lacustrine deposits, and the Tertiary volcanoclastic sequence, separated from the Stillwater Range by a major normal fault dipping at 50° . A minor "down-to-the-northwest" normal fault may be present southeast of the basin axis near the edge of the seismic section. The basin axis at various times was located 2-3 km from the range front, which confirms the present topographic asymmetry of the basin. Internal reflections in the lake deposits show updip thinning, due to tilting or sagging of the basin during deposition. The Mesozoic basement of the range also underlies the valley floor. Depths and thicknesses of the geologic units obtained from seismic arrival times and velocities can be supplemented and extended by interpretation of gravity information.

GRAVITY

Previous interpretations of gravity data in Dixie Valley have showed an asymmetric graben-within-graben structure [Speed, 1976; MicroGeophysics Corp., unpublished data, 1981]. A uniform density contrast between valley fill and bedrock was used, however, and no attempt was made to distinguish intrabasinal features. Modeling of gravity data in conjunction with the seismic data in the present study reveals an asymmetric, slightly tilted basin with one major southeast-dipping normal fault. On the other side of the valley, three smaller northwest-dipping normal faults satisfy the gravity data and correlate with surface fault traces. Complete Bouguer gravity anomaly values, which were obtained from MicroGeophysics Corp., traverse northern Dixie Valley (see Figure 2) with end stations anchored within the Stillwater and Clan Alpine Ranges. These values are in agreement with readings from a similar traverse by G. A. Thompson (unpublished data, 1967).

Features observed within seismic line SRC-3, located 3 km to the northeast and nearly parallel to the gravity traverse, were incorporated into the gravity model

TABLE 1. Average Densities of Rock Samples Collected in the Dixie Valley Region

Type of Rock	1959 Series Number of Samples (Density Range)	1967 Series Number of Samples (Density Range)	Average Density gm/cc
granitic	5 (2.61-2.68)	...	2.65
altered granitic	1	...	2.51
amphibolite schist	2 (2.78-2.82)	...	2.80
hornfels	1	...	2.94
limestone & marble	4 (2.70-2.86)	...	2.79
chert	1 (2.58)	1 (2.34)	2.46
basalt, vesicular	1	...	2.62
andesite	7 (2.23-2.66)	...	2.54
welded tuff, rhyolite	11 (2.32-2.57)	9 (2.24-2.57)	2.45
tuff	2 (1.86-1.91)	...	1.89
sandstones, volcanic	4 (1.46-1.91)	3 (1.87-2.26)	1.82
diatomite	1	...	1.21
obsidian	...	1	2.34

by projecting depths and boundaries along strike. Evidence of faults on the southeast side of the basin are taken from surface outcrop and aerophotographic studies by Whitney [1980] and Burke [1967]. Water-saturated bulk density values were obtained from Speed [1976], Thompson [1959], and previously unpublished measurements of samples collected in the Dixie Valley region by Thompson (Table 1). The observed complete Bouguer anomaly values

are shown in Figure 4 along with the density model of Dixie Valley and the calculated gravity anomalies. Interpretation of the faults on both sides of the basin is strengthened by the modeling; faults on the southeast side of the basin were modeled as dipping to the northwest at 60° .

To determine the sensitivity of the gravity model to changes in the geometry of the faults, the dip of the major Still-

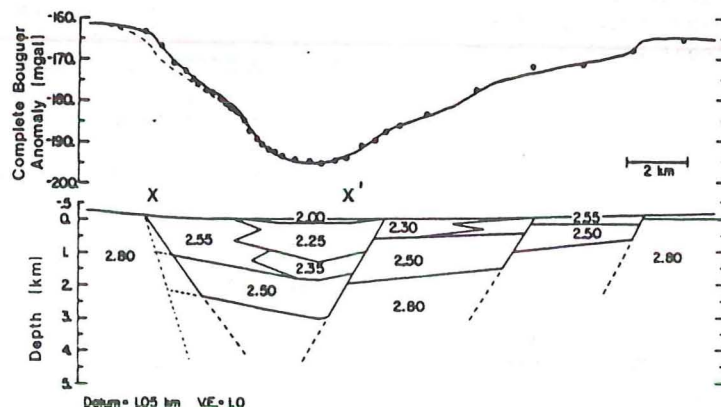


Fig. 4. Gravity model across Dixie Valley. (top) Observed stations (points) and calculated curve. Dashed alternative curve represents values from a fault with dip of 70° . (bottom) model of Dixie Valley; densities in gm/cm^3 , depths in km. X-X' represents the projection of seismic line SRC-3 onto the model. Stillwater Range-front fault dip is 50° ; thin dashed lines represent projection of the model for a dip of 70° . Other faults dip at 60° . Densities: lacustrine/playa range = 2.00 to 2.35 gm/cm^3 ; alluvial fan = 2.55 gm/cm^3 ; Tertiary volcanoclastic sequence = 2.50 gm/cm^3 ; Mesozoic basement = 2.80 gm/cm^3 .

water Range-bounding fault was increased to 70° . The change in the calculated gravity is shown in Figure 4; adjustment of layer geometries or densities for the entire model would be needed to fit the observed values.

In summary, gravity modeling suggests an asymmetric basin terminated by one major zone of faulting to the northwest and cut by three smaller faults to the southeast, all dipping toward the axis of the basin. As shown in Figure 4, alluvial fan deposits enter the basin from both bounding ranges to a maximum depth of 1.5 km. Valley sediments in the axis of the basin reach 1.8 km; the valley is underlain by the Tertiary volcanoclastic sequence which reaches a depth of 3 km.

EARTHQUAKES

Since 1860, the Basin and Range province in Nevada has experienced over two dozen major earthquakes and numerous smaller ones [Byerly, 1956]. Several occurred in the Dixie Valley region, including four in 1954 (Figure 1). The Fallon-Stillwater earthquakes of July 6 and August 23, 1954, both of magnitude (M_L) 6.8 [Byerly, 1956], were accompanied by as much as 30 cm of vertical offset [Tocher, 1956]. The Fairview Peak earthquake of December 16, 1954 was followed about 4 min later by the Dixie Valley earthquake approximately 50 km to the north (Figure 5). The two earthquakes had magnitudes (M_L) 7.1 and 6.8, respectively [Tocher, 1957]. Examination of the P-pP arrivals by Romney [1957] indicated a focal depth of 15 km

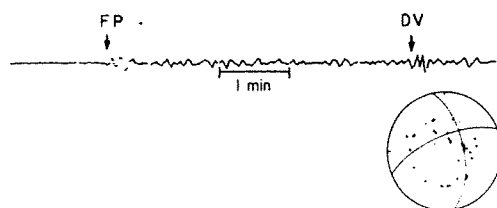


Fig. 5. Vertical component seismogram of the Fairview Peak-Dixie Valley double earthquake recorded at Strasbourg, France on December 16, 1954. The Dixie Valley (DV) earthquake occurred 4 min 20 s after the Fairview Peak (FP) earthquake. Also shown is the focal mechanism for the Fairview Peak earthquake using data from Romney [1957]. Fault plane strikes $N11^{\circ}W$, dips $62^{\circ}E$, with motion plunging $S65^{\circ}E$ at 24° .

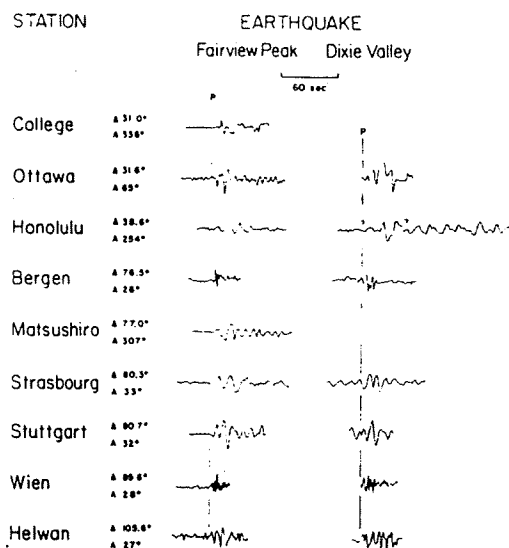


Fig. 6. Comparison of initial P arrivals from the Fairview Peak and Dixie Valley earthquakes for various seismographic stations. The two earthquakes have similar waveforms recorded at each station even though Fairview Peak later arrivals are superimposed over Dixie Valley initial arrivals. All stations vertical component except Honolulu (N-S) and Ottawa (E-W). Δ , angular distance from earthquake to station; A, azimuth of station clockwise with respect to north.

for the Fairview Peak earthquake and 40 km for the Dixie Valley earthquake. Study of the focal mechanism of the Fairview Peak event by Romney revealed a fault plane striking $N11^{\circ}W$ and dipping $62^{\circ}E$ (the nodal plane corresponding to surface faulting, Figure 5). Direction of movement along the fault was $S65^{\circ}E$ at a plunge of 24° . A focal mechanism solution for the Dixie Valley earthquake was not determined by Romney.

Seismic Body Wave Modeling

In view of the shallow crustal thickness for the west-central Basin and Range (22 km; Stauber and Boore [1977]), the focal depth of 40 km for the Dixie Valley earthquake as determined by Romney [1957] is suspect. The focal depth was calculated using the difference in P and pP arrival times. However, the identification of these arrivals is made difficult by the interference of continuing waves from the preceding Fairview Peak earthquake; thus

the reliability of the Dixie Valley focal depth is less than that of the Fairview Peak earthquake.

Comparison of the initial P arrivals of both the Fairview Peak and Dixie Valley earthquakes reveals a reasonably good correlation between the arrival waveforms, despite later Fairview Peak waves superimposed on the Dixie Valley arrivals (Figure 6). As the two earthquakes occurred approximately 50 km and 4 1/3 min apart, the similarity in initial waveforms suggests similar focal mechanisms and depths for the two earthquakes. It is possible to infer that the focal depth of the Dixie Valley earthquake is similar to that of the Fairview Peak earthquake provided that a change in focal depth from 15 to 40 km would appreciably modify the initial waveforms. The effects of focal depth on waveform is examined next.

Teleseismic body wave modeling based on first motion ray approximation as outlined by G. C. Kroeger and R. J. Geller (unpublished manuscript, 1984) provides a method to examine focal depths in relation to their corresponding seismograms. A synthetic seismogram for a given seismographic station can be generated using:

$$y(t) = S(t) * NSS(t) * E(t) * RS(t) * I(t)$$

where $y(t)$ is the synthetic seismogram; $S(t)$ is the far-field source time function; $NSS(t)$ is the near-field source time function and is dependent on the near-source earth model, the fault strike and dip, fault slip, and source depth; $E(t)$ is the earth propagation effect; $RS(t)$ is the receiver structure; $I(t)$ is the seismometer instrument response; and a superior asterisk denotes convolution. Using Romney's values for strike, dip, slip, and depth, a seismogram of the initial arrivals (P, pP, sP, and all other intermediary waves) of the Fairview Peak earthquake may be generated for a given seismographic station. Any of these four focal parameters may then be modified in order to view resulting changes to the synthetic seismogram. Validity of the synthetic seismogram may be tested by comparing the synthetic seismogram to the actual station seismogram.

Requests for seismograms from nearly forty seismographic stations distributed world-wide resulted in less than a dozen recordings with visible seismic waveforms, the best of which are displayed in Figure 6. Though only two seismograms maintained

layer	depth	Vp	Vs	density
valley fill	1.9	2.1	1.5	2.1
basement	22.9	6.0	3.5	2.65
mantle		7.0	4.0	3.0

(km km/s km/s gm/cc)

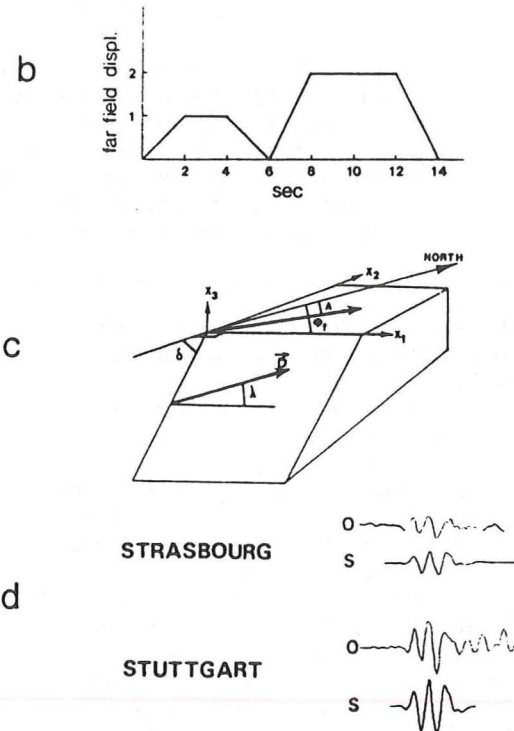


Fig. 7. Teleseismic body wave modeling. Input parameters are (a) earth model; (b) far field source time function (describing earthquake wavelet); (c) focal parameters: ϕ_f , strike of fault with respect to north, λ , azimuth of seismographic station with respect to north, δ , dip of fault from horizontal, D , direction of motion of hanging wall block with respect to foot wall block, λ , counter-clockwise angle between D and horizontal in the plane of the fault. Fairview Peak earthquake focal parameters: $\phi_f=349^\circ$ (N11⁰W); $\delta=62^\circ$; $\lambda=206^\circ$; depth=15 km. (d) Synthetic seismograms of the Fairview Peak earthquake for the Strasbourg and Stuttgart stations. O is observed seismogram, S is synthetic seismogram.

sufficient waveform resolution for body wave modeling and their stations are of similar epicentral distance (Δ) and azimuth, waveform modeling was attempted, nonetheless, to obtain as much information

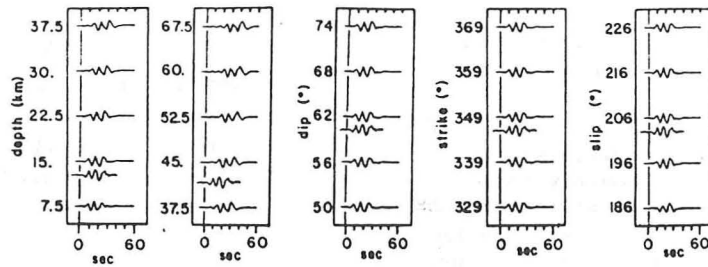


Fig. 8. Effects of changing focal mechanism parameters on the resulting Fairview Peak synthetic seismograms for Strasbourg. Each focal parameter (depth, dip, strike, and slip) is varied while the remaining three parameters are held fixed. The observed seismogram is plotted adjacent to the synthetic seismograms which use Romney's calculated parameters in addition to this study's preferred depth. Focal depth is the only parameter which changes widely over the calculated intervals.

as possible from the two seismograms. The original seismograms used by Romney are now lost.

For the seismographic stations located in Strasbourg, France, and Stuttgart, West Germany, the earth model, earthquake source time function, and synthetic and original Fairview Peak arrivals are shown in Figure 7. The earth model includes 2 km of basin fill underlain by a 20 km crystalline crust and a mantle "halfspace." Resolution does not increase with further subdivision of the crystalline crust. The earthquake source time function describes the rate of slip as a function of time. For the Strasbourg and Stuttgart seismograms, the best synthetic seismogram incorporates a double source time function; the earthquake slipped in two pulses. Focal parameters used in the modeling are strike, $N11^{\circ}W$; dip, $62^{\circ}E$; slip, 24° ; and depth, 15 km.

In order to test the sensitivity of seismograms to changes in focal parameters, seismograms for Strasbourg were regenerated. Each focal parameter was varied widely from Romney's values while preserving the remaining three parameters (Figure 8). Of the four focal parameters, only changes in depth are significant; changes in fault plane strike, dip, or slip have negligible effect. The synthetic seismograms most similar to the original seismograms are those with a depth of 15 km, verifying Romney's calculated depth. Note that for a depth of 40 km, the pP and sP arrivals are appreciably delayed behind the P arrival and thus the waveforms for the two depths are not similar.

Synthetic body wave seismograms for Strasbourg and Stuttgart verify the focal parameters as determined by Romney. The depth of the Fairview Peak earthquake is 15 km; as the early arrivals of the Dixie Valley seismogram are similar to those of the Fairview Peak seismogram, the Dixie Valley depth is not 40 km but about 15 km.

Local Seismicity

Foci of microearthquakes in the Fairview Peak region during 1966 were found to lie predominantly on a plane striking $N10^{\circ}W$ and dipping $57^{\circ}E$ [Stauder and Ryall,

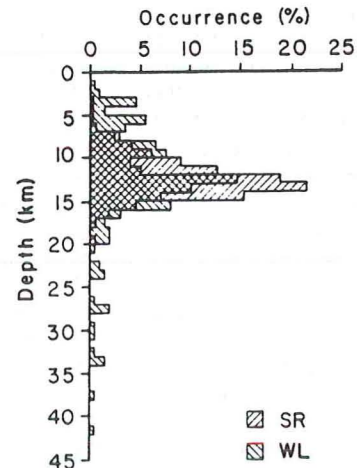


Fig. 9. Distribution of microearthquakes in the Fairview Peak region during 1966 as a function of depth. SR represents 308 events [Stauder and Ryall, 1967]; WL represents 199 events [Westphal and Lange, 1967].

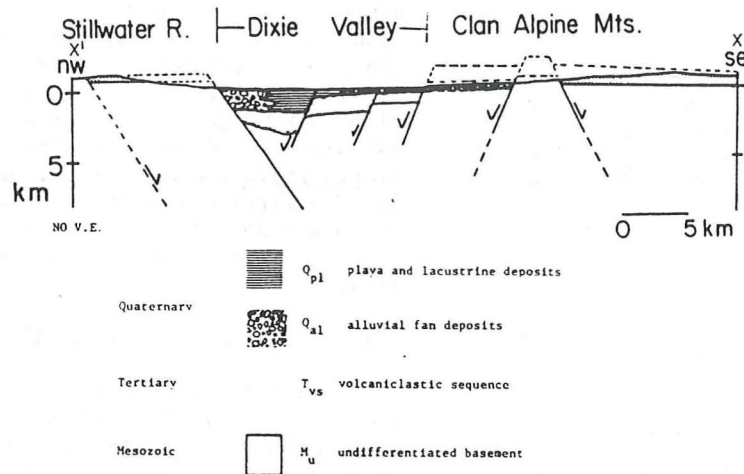


Fig. 10. Shallow crustal structure of Dixie Valley.

1967], this is in excellent agreement with Romney's fault plane solution. A plot of the depth data presented by Stauder and Ryall reveal that 73% of all recorded events occurred between 10-15 km and 99% of all events occurred above 16 km (Figure 9). Data from a similar study by Westphal and Lange [1967] show that 44% of recorded events occurred between 10-15 km and 85% occurred shallower than 16 km. Further microearthquake studies by Ryall and Malone [1971] found lateral variation in focal mechanisms due to variations in fault trends relative to the constant regional extensional direction.

In summary, examination of the teleseismic and microearthquake data reveals that (1) the depth of the Dixie Valley earthquake is about 15 instead of 40 km and (2) seismicity is concentrated in the upper two thirds of the 22-km crust found in this region. This suggests that some type of ductile deformation dominates within the lower third of the crust [Sibson, 1982].

DISCUSSION

Upper Crust

The interpretation and modeling of seismic reflection and gravity data combined with previous geologic and geophysical studies produce a well constrained upper crustal model for Dixie Valley (Figure 10).

The vertical component of offset along the Stillwater Range-front fault can be determined by correlating the basalt at

the top of the Tertiary volcanoclastic sequence buried in the basin with the basalt exposed in the Stillwater Range (Table Mountain, so named for the level top formed by the capping basalt; Figure 2). Field mapping by Speed [1976] suggests minimal dip for the exposed basalt; thus, vertical offset is about 2.2 km. Accounting for additional basin sag or fault drag makes the combined structural relief due to faulting and bending about 2.9 km. Similar calculations for the three smaller faults cutting the southeastern side of Dixie Valley were made by matching the base of the Tertiary volcanoclastic sequence and yield vertical offsets of 1.0, 0.5, and 0.5 km (northwest to southeast).

The extensional components corresponding to these vertical offsets sum to a net extension of 3.0 km across the basin (20% extension). If the Tertiary volcanoclastic sequence and the upper capping basalt unit are pre-Basin and Range as suggested by Hastings [1979], then Hastings' radiometric basalt age of 8 (+ 4) m.y. results in an average extension rate of 0.38 mm/yr (0.25 to 0.76 mm/yr using the age date error range). This extension rate is in good agreement with 0.4 mm/yr over the previous 15 m.y. as estimated by Thompson and Burke [1973].

Lower Crust

Given the well constrained upper crustal fault pattern, a variety of alternative lower crustal geometries for Dixie Valley need to be considered. Examined here are geometrical models involving: (1)

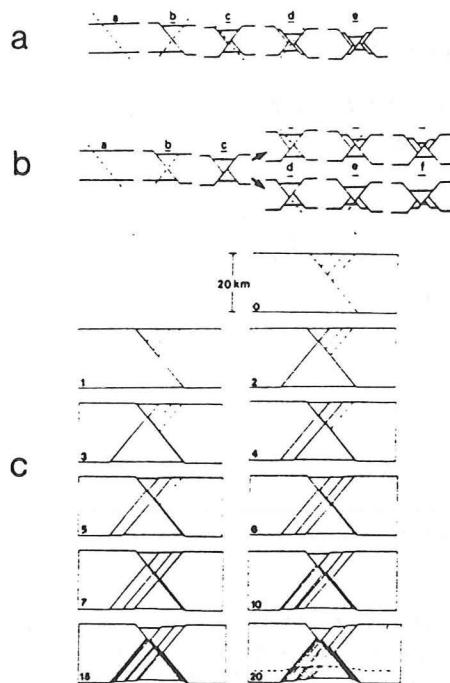


Fig. 11. Alternate conjugate faults: (a) creation of entirely new fault planes (Freund, adapted from Horsefield [1980]); (b) extension of truncated fault planes (adapted from Horsefield [1980]). In both (a) and (b), fault blocks are alternately faulted. In each case, only one block remains stationary but grows progressively smaller. Horizontal bars represent original elevation. (c) Extrapolation of Dixie Valley fault geometry down to the lower crust. Number in lower left corner of each block indicates number of fault offsets that have taken place. Offsets along Stillwater Range-front (SR) fault alternate with offsets along subsidiary faults which have opposite dip; amount of offset for each fault movement is 200 m. 0: restoration of faults as evidenced in upper crust. 1: offset along SR fault. 2: offset along inner subsidiary fault: SR fault plane has been crosscut. 3: offset along SR fault: inner fault plane has been crosscut (Odd numbers indicate offset along SR fault). 4: offset along middle subsidiary fault. 6: offset along outer subsidiary fault. 7: steps 1-6 begin again. 10: after 10 fault offsets; 7% extension. 15: after 15 fault offsets; 10% extension. 20: after 20 fault offsets; 15% extension; graben floor resembles Dixie Valley basement floor. Note repeated faulting along SR fault has created a broad fault zone. Actual fault motion may tend to flatten in

crosscutting conjugate faults; (2) simple horst and graben blocks; (3) detachments within the seismogenic crust, ductile crust, or brittle-to-ductile transition zone; and (4) faults and detachments associated with igneous intrusions. While the earth's crust does not behave strictly as simple rigid blocks, block models are useful for first order, quantitative studies. Plausible models in which the blocks are also internally deformed may then be suggested.

Constraints to Faulting in the Lower Crust

Earthquake data in the Dixie Valley-Fairview Peak region give four major constraints for the deeper structure. First, focal mechanisms and depths of earthquakes suggest that the Stillwater Range-front fault is not listric but is steeply dipping to a depth of at least 15 km. Second, microearthquakes occur predominantly within the upper 15 km of the crust. Evidently the transition from a brittle seismogenic upper crust to a more ductile lower crust begins about this depth. Third, no current seismicity is associated with the northwest-dipping step faults. Fourth, the northwest-dipping faults project toward the Stillwater Range-front fault and should either crosscut it or root within that fault zone at depths considerably less than 15 km. Relative to the fourth constraint, planar or listric antithetic faults can root in a major listric fault zone, as demonstrated by growth faults in the Gulf of Mexico. Development of planar antithetic faults which root within a planar fault zone is volumetrically more difficult, if not impossible. Moreover, the northwest-dipping faults are planar, as listric faulting would produce tilted basin blocks with dip opposite to the slight northwest dip observed in the seismic reflection and gravity data (Figure 4).

Rigid Block Models

Figures 11c and 12a-12c show simple rigid block models for Dixie Valley. These four models are constructed to fit the ob-

this less coherent zone. Approximate location of the top of the brittle-to-ductile transition zone is shown by the dashed line; fault motion may also flatten due to ductile deformation.

served fault geometry of the shallow crust. The first and second major fault constraints help define each model; as discussed below, the third and fourth constraints limit the applicability of each model.

In addition to the four constraints, definition of major crustal blocks by faulting must be considered. Seismic reflection data presented by Hastings [1979] suggests a major range-front fault bounding the northwestern side of the Stillwater Range and dipping under Buena Vista Valley and Carson Sink. Thus, the Stillwater Range appears to be a horst-shaped crustal block. No major range-front fault separates Dixie Valley from the Clan Alpine Mountains to the southeast, suggesting that Dixie Valley is not a separate graben block but a structural feature occurring on the edge of the Clan Alpine "horst" or "tilt" crustal block.

Model 1: Conjugate Normal Faults. The geometry of contemporaneous conjugate faults that mutually displace each other has been examined by Freund [1974] and Horsefield [1980], among others. Movement along each fault in a conjugate pair offsets the other fault, requiring successive faulting either to create entirely new fault surfaces (Freund; Figure 11a) or to extend truncated fault surfaces into previously unfaulted material (Horsefield; Figure 11b).

Extrapolation of the Dixie Valley fault geometry (Figure 10) down to the lower crust using a multiple-conjugate fault mechanism patterned after Horsefield is shown in Figure 11c. For this reconstruction, each fault has 200 m of offset before motion on a crosscutting fault commences. Offset along the Stillwater Range-front fault alternates with offset along each of the smaller faults which dip opposite to the Stillwater Range-front fault. For simplicity, the three smaller faults move in the sequence of inner, middle, and outer faults. These sequential movements preserve the relative fault offsets observed in Dixie Valley but do not necessarily represent an evolutionary sequence. In the model successive faulting creates 200-600 m thick fault slices within the lower crust.

The formation of such closely spaced faults on a crustal scale seems mechanically unlikely because it would require much more energy than a simpler fault system. In the model, simplistic assumptions have been made, but in the earth, new

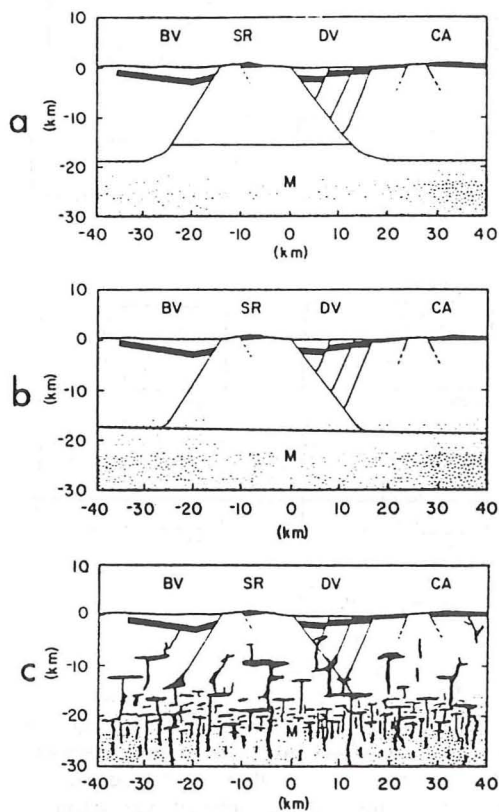


Fig. 12. Simple rigid block models. The models were constructed to preserve the shallow crust geometry found in Dixie Valley and to meet the first two of four major fault constraints. Black horizon in shallow crust is the Tertiary volcanoclastic sequence. The ductile lower crust begins below 15 km (dots). The Moho discontinuity is at a depth of about 23 km (stipple). BV, SR, DV, and CA represent Buena Vista Valley, Stillwater Range, Dixie Valley, and Clan Alpine Mountains, respectively. (a) Crustal horsts and grabens which float above the ductile lower crust. (b) High-angle extensional faults bounding the Stillwater Range root within a low-angle detachment surface at depth. The detachment is shown in the ductile crust where movement is aseismic. (c) Intrusion into the crust. Magma is derived from the upper mantle and intrudes predominantly into the lower crust. Extension of the lower crust may rotate dikes to subhorizontal positions. Intrusion into the lower crust allows for initial graben formation; subsequent intrusion into the upper crust allows for smaller grabens to develop, with differential displacement along the subsidiary faults.

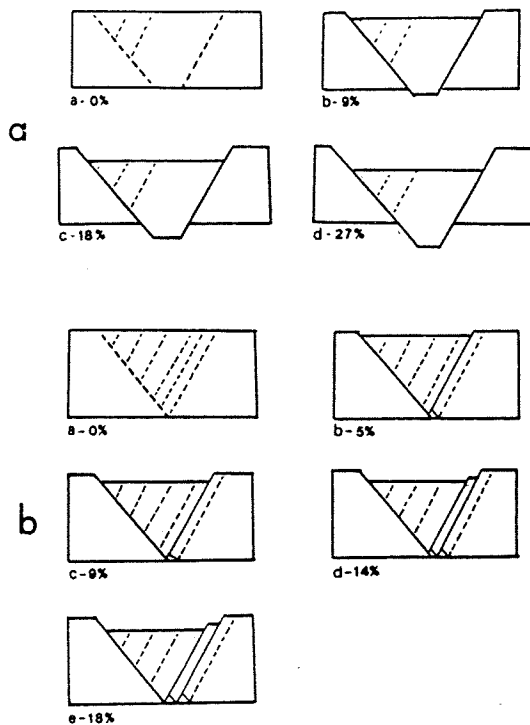


Fig. 13. Block diagrams illustrating the difficulty in creating the "step" geometry found in Dixie Valley for rigid horst-grabens and upper plate extension along a detachment surface. Percents indicate amount of lateral extension. (a) Pure horst-graben development. A subsidiary fault will not show separate offset until the fault ceases to root in the master high-angle fault. (b) Block response to pure lateral extension. Assuming planar faulting, subsidiary faults rooted in the detachment zone will show no offset with extension (a to b). Trailing blocks formed by subsidiary faults rooted in the master high-angle fault will move as one large downthrown block; the subsidiary faults will show no offset (b to e). Faults which initially root in the major high-angle fault but come to root within the detachment zone will show differential offset (d, e). Note the space problem at the detachment surface.

faults may preferentially shallow into the old fault zone rather than cut new material. Note that the fault slices (or the broad fault zone) would be found in the lower crust but not in the upper crust. Given the fact that ductile deformation should predominate below a depth of about

15 km geometry of conjugate faults. These models of crosscutting conjugate faults are not convincing.

Model 2: Horsts-Grabens. Although blocks might conceivably be bounded by faults which cut the crust or even the entire lithosphere and root within the mantle or asthenosphere, it seems more likely that the faults penetrate only the brittle crust and root within the ductile lower crust [Bott, 1980b]. Dixie Valley may be examined in light of this model (Figure 12a). The faults extend to a depth of at least 15 km based on earthquake depths and presumably die out within the ductile crust above the Moho discontinuity.

The block diagrams of Figure 13a illustrate a volumetric problem if one assumes that the inner graben faults root at the master graben-bounding fault (fourth constraint). As extension occurs, the graben block is downthrown with little or no tilt; only after an inner graben fault roots in ductile lower crust will displacement occur on that fault and "step" structure be exhibited on the graben surface. Since the inner graben faults in Dixie Valley would root in the Stillwater Range-front fault well above the brittle-ductile transition zone, models like those in Figure 13 are not attractive for Dixie Valley.

Model 3: Detachments. Within the upper plate of a low angle detachment zone, offsets on high-angle normal faults may produce basin-range topography. These high-angle faults may be planar or listric and may root within the detachment zone.

Extensional detachment surfaces may extend from near surface, as evidenced by seismic reflection data in the Sevier Desert [McDonald, 1976] to depths of more than 15 km [Allmendinger et al., 1983]. Evidently they are not confined to brittle upper crust nor to the ductile lower crust. Wallace [1980] postulated a decoupling zone at the transition from brittle to ductile extension and Wernicke [1981] suggested dipping detachments that penetrate the entire crust. Geometric models yield some insights applicable to the Dixie Valley region.

Figure 12b shows a deep-seated detachment zone in the ductile lower crust. In this detachment model, Dixie Valley and the Clan Alpine Mountains together are represented by a +30 km wide upper plate crustal block, with a broken trailing edge forming Dixie Valley. With continued lateral extension, the toes of the trailing

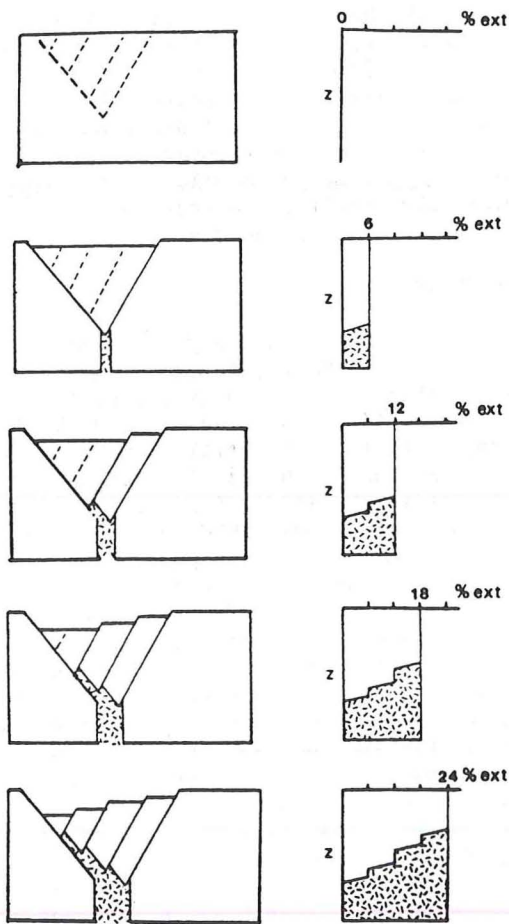


Fig. 14. Block diagrams illustrating the ability of crustal intrusion to (1) extend the crust, and (2) develop differential displacement along the subsidiary faults within the major downthrown block. Associated with each block diagram is a chart revealing the percentage of lateral extension which has occurred. The portion of the lateral extension due to intrusion is highlighted in stipple; the remainder is due to normal faulting. The sequence a-e is not necessarily a time sequence.

blocks slip down the Stillwater Range-front fault.

Two difficulties arise from this detachment model, both involving the subsidiary faults within Dixie Valley. First, while the Stillwater Range-front fault is seismically active, no activity is known to be associated with either the subsidiary (antithetic) faults or a detachment zone (third constraint). The second difficulty comes from the differential dis-

placement along the subsidiary faults (fourth constraint). These faults define trailing blocks whose movements help compensate for volume or mass deficiency created by lateral extension. The block models in Figure 13b illustrate lateral extension along a detachment of two upper plate blocks (representing Stillwater and Clan Alpine) separated by a master normal fault. The downdropped block is broken by subsidiary faults (like those in Dixie Valley) which create trailing blocks. With extension, the toes of the trailing blocks slide down along the master normal fault; however, there can be little or no displacement along the subsidiary faults, which initially root in the master fault zone, until they come to root in the detachment zone (d of Figure 13b). Geophysical data in Dixie Valley indicate the subsidiary faults would root in the master fault shallower than any likely detachment zone and should therefore show little or no displacement. "Step" geometry, however, is exhibited in the basin floor and suggests that some other fault mechanism in the upper crust is needed.

Model 4: Intrusion. Basin and Range normal faults rooted within magmatic intrusions, analogous to mid-ocean rifts, have been suggested by Thompson [1959] and Thompson and Burke [1974]. This style of normal faulting might account for the formation of the Stillwater Range-front fault (Figure 12c). In addition, further intrusion into the shallow crust along this major normal fault might allow for the different subsidiary fault displacements. The block diagrams of Figure 14 demonstrate a quantitative relation between lower crust intrusion and upper crust normal faulting for various amounts of extension. It should be mentioned that there is no surface expression of young igneous activity; geothermal activity in Dixie Valley can be explained by deep circulation of ground water [Parchman and Knox, 1981].

Magmatic intrusion may allow the development of decoupling surfaces on a local or regional level, separating lower crustal intrusion from shallow crustal faulting. For Dixie Valley, the constraints for detachments discussed above also apply to the model of a detachment caused by magmatic intrusion. The detachment should be at a depth of at least 15 km to satisfy earthquake data, and extension by magmatic intrusion might predominate at greater depth. A leaky detach-

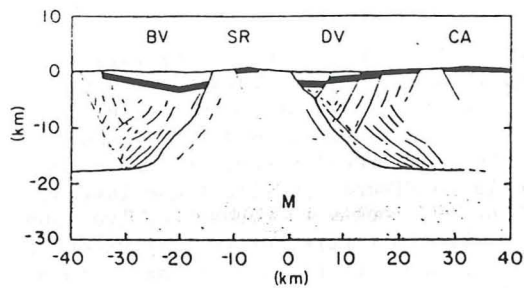


Fig. 15. Combination of rigid and nonrigid models to describe late Cenozoic extensional faulting in the Dixie Valley region. Many small faults associated with nonrigid deformation accommodate faulting and sagging of Dixie Valley in the lower to intermediate crust. Intrusion of the crust is not shown but plays a major role in the development of the basin.

a faulty ^{detachment} ment would allow for isolated shallower intrusion; intrusion along the Stillwater Range-front fault would allow subsidiary faults with differential displacement to develop.

Nonrigid Models

We have used rigid block models to provide a framework for analyzing first-order problems of extensional faulting, but of course we recognize that the earth is not rigid. The spatial and temporal continuum of fracture development in clay slabs [Cloos, 1968; Stewart, 1971] suggests graben models that contain more of the complexity of the real earth. The clay deforms on myriad small fractures and also bends and flows. Nevertheless the volume and boundary constraints must still be satisfied, as in our block models. Cloos' mechanism for extension of the clay consists of laterally moving horizontal plates at the lower boundary of the clay. Fractures extend to the base of the clay slab, rooting, in effect, in the artificial slip surface. This is exactly analogous to extension above a low-angle detachment surface.

A combination of rigid and nonrigid deformation above a detachment is pictured in the model of Figure 15. For simplicity, magmatic intrusions have not been shown in the model but could be significant. Extension of the lower crust, below the detachment, may be accomplished by intrusion, and intrusion into the upper crust under Dixie Valley may accommodate

some of the antithetic faulting. Faults which break the basin floor bifurcate or merge with varying offset toward southern Dixie Valley [Thompson et al., 1967], creating a varying fault pattern both laterally and with depth. A diagrammatic crustal cross section through southern Dixie Valley would be similar to but not necessarily identical to that for the northern portion of the basin.

CONCLUSION

Seismic reflection and gravity data reveal that Dixie Valley is an asymmetric basin filled with 1.8 km of alluvial fan and lacustrine/playa deposits. The basin is separated from the Stillwater Range by one major range-front fault dipping to the southeast at 50° and on its opposite side is stepped down from the Clan Alpine Range by three smaller faults dipping to the northwest at about 60° ; no major fault separates Dixie Valley from the Clan Alpine Mountains. Recorded seismicity is associated with the range-front fault but not with the smaller faults. On the Clan Alpine side of the basin the Tertiary volcanoclastic sequence and basin fluviolacustrine deposits dip northwestward about 6° and thin southeastward (updip); this suggests that sagging or slight tilting of the basin has taken place. Thinning and truncation of bedding indicates erosion of the volcanoclastic sequence before alluvial deposition began. Restoration of the pre-Basin and Range basalt member of the Tertiary volcanoclastic sequence reported to be 8 m.y. old reveals 20% extension in Dixie Valley at an average rate of 0.38 mm/yr.

Seismic activity, in conjunction with the other subsurface data, produces four main constraints to possible fault geometries at depth. First, large and small earthquakes indicate that the Stillwater Range-front fault is not listric but extends steeply to a depth of at least 15 km. Second, the brittle-to-ductile transition zone begins below this depth. Third, contemporary tectonic movement is associated with the Stillwater Range-front fault. Fourth, stratal tilt that would be produced by listric faults is not present; the subsidiary faults are evidently also planar.

Conceptual block models help to define processes to account for the faulting in Dixie Valley; the alternative models include (1) mutually crosscutting conjugate

normal faults; (2) horsts and grabens that root in a ductile zone; (3) high angle normal faults that root in low angle detachment surfaces; and (4) high angle faults, with or without detachment surfaces, that are related to magmatic intrusion. The fourth model presents the fewest difficulties and is favored here.

Clay models by Cloos [1968] help to simulate the complexity of the real earth. The clay model which formed an asymmetric half-graben similar to Dixie Valley originated from extension on an artificial low-angle detachment at the base of the clay. However, that model produced mainly warping instead of the step-faulting seen on the southeast side of Dixie Valley.

Future imaging of the crust by reflection seismology in concert with other techniques may reveal the relative importance of high angle faults, detachment faults, and magmatic intrusions. In turn, such evidence will suggest the underlying mechanisms of continental rift features as seen in the Basin and Range province.

Acknowledgements. John Nicholl provided gravity measurements by Microgeophysics Corp.; computing was carried out on facilities of the Stanford Exploration Project directed by Jon Claerbout. Carl Romney kindly supplied notes from his original work on the Fairview Peak-Dixie Valley earthquakes. Thanks are extended to Glenn Kroeger for having the patience to explain earthquake body wave modeling, to Bob Geller for use of the computing facilities, and to the many people worldwide who responded to our request for seismograms. Discussions with Jack Stewart and Tsvi Meidav were fruitful. The manuscript was reviewed by R. B. Smith and J. H. Stewart. This work was supported by National Science Foundation grant EAR81-09294.

REFERENCES

- Allmendinger, R. W., J. W. Sharp, D. Von Tish, L. Serpa, L. Brown, S. Kaufman, J. Oliver, and R. B. Smith, Cenozoic and Mesozoic structure of the eastern Basin and Range from COCORP seismic reflection data, *Geology*, **11**, 532-536, 1983.
- Anderson, R. E., M. L. Zoback, and G. A. Thompson, Implications of selected subsurface data on the structural form and evolution of some basins in the northern Basin and Range province, Nevada and Utah, *Geol. Soc. Am. Bull.*, **94**, 1055-1072, 1983.
- Bell, E. J., M. E. Campana, R. L. Jacobson, L. T. Larson, D. B. Slemmons, T. R. Bard, B. W. Bohm, N. L. Ingraham, R. W. Juncal, and R. A. Whitney, Geothermal reservoir assessment case study, Northern Basin and Range province, Northern Dixie Valley, Nevada, Report, 223 pp., Mackay Miner. Res. Inst., Univ. of Nev., Reno, Nev., 1980.
- Bott, M. H. P., Mechanisms of subsidence at passive continental margins, in *Dynamics of Plate Interiors, Geodyn. Ser.*, vol. 1, edited by A. W. Bally et al., pp. 27-35, AGU, Washington, D. C., 1980a.
- Bott, M. H. P., Crustal doming and the mechanism of continental rifting, *Tectonophysics*, **73**, 1-8, 1980b.
- Burke, D. B., Aerial photography survey of Dixie Valley, Nevada, Geophysical Study of Basin-Range Structure, Dixie Valley Region, Nevada, edited by G. A. Thompson et al., 1-36, *U.S. Air Force Cambridge Res. Lab. Spec. Rep.*, **66-848**, part IV, 1967.
- Byerly, P., The Fallon-Stillwater earthquakes of July 6, 1954, and August 23, 1954, *Bull. Seismol. Soc. Am.*, **46**, 1-3, 1956.
- Cloos, E., Experimental analysis of Gulf Coast fracture patterns, *Am. Assoc. Pet. Geol. Bull.*, **52**, 420-444, 1968.
- Eaton, G. P., The Basin and Range Province: origin, and tectonic significance, *Ann. Rev. Earth Planet. Sci.*, **10**, 409-440, 1982.
- Effimoff, I., and A. R. Pinezich, Tertiary structural development of selected valleys based on seismic data, Basin and Range province, northeastern Nevada, *Philos. Trans. R. Soc. London Ser. A*, **A300**, 435-442, 1981.
- Fletcher, R. C., and B. Hallet, Unstable extension of the lithosphere: A mechanical model for Basin-and-Range structure, *J. Geophys. Res.*, **88**, 7457-7466, 1983.
- Freund, R., Kinematics of transform and transcurrent faults, *Tectonophysics*, **21**, 93-134, 1974.
- Hastings, D. D., Results of exploratory drilling, northern Fallon Basin, Western Nevada, in *Basin and Range Symposium*, edited by G. W. Newman and H. D. Good, pp. 515-522, Rocky Mountain Association of Geologists-Utah Geological Association, Denver, Colo., 1979.
- Horsefield, W. T., Contemporaneous movement along crossing conjugate normal

- faults, *J. Struct. Geol.*, 2, 305-310, 1980.
- McDonald, R. E., Tertiary tectonics and sedimentary rocks along the transition: Basin and Range Province to Plateau and Thrust Belt, Utah, in *Geology of the Cordilleran Hingeline, Rocky Mountain Association of Geologists Symposium*, edited by J. G. Hill, pp. 281-317, Rocky Mountain Association of Geologists, Denver, Colo., 1976.
- Meister, L. J., Seismic refraction study of Dixie Valley, Nevada, in *Geophysical Study of Basin-Range Structure, Dixie Valley Region, Nevada*, edited by G. A. Thompson, et al., 1-72, *U.S. Air Force Cambridge Res. Lab. Spec. Rep. 66-848*, part I, 1967.
- Meister, L. J., R. O. Burford, G. A. Thompson, and R. L. Kovach, Surface strain changes and strain energy release in the Dixie Valley-Fairview Peak area, Nevada, *J. Geophys. Res.*, 73, 5981-5994, 1968.
- Page, B. M., Preliminary geologic map of a part of the Stillwater Range, Churchill County, Nevada, map 28, Nev. Bur. Mines and Geol., Reno Nev., 1965.
- Parchman, W. L., Jr., and J. W. Knox, Exploration for geothermal resources in Dixie Valley, Nevada: A case history, *Geotherm. Resour. Coun. Bull.*, 10, 3-6, June 1981.
- Riehle, J. R., E. H. McKee, and R. C. Speed, Tertiary volcanic center, west-central Nevada, *Geol. Soc. Am. Bull.*, 83, 1383-1396, 1972.
- Romney, C., Seismic waves from the Dixie Valley-Fairview Peak earthquakes, *Bull. Seismol. Soc. Am.*, 47, 301-319, 1957.
- Ryall, A., and S. D. Malone, Earthquake distribution and mechanism of faulting in the Rainbow Mountain-Dixie Valley-Fairview Peak area, Central Nevada, *J. Geophys. Res.*, 76, 7421-7428, 1971.
- Sibson, R. H., Fault zone models, heat flow, and the depth distribution of earthquakes in the continental crust of the United States, *Bull. Seismol. Soc. Am.*, 72, 151-163, 1982.
- Smith, T. E., Aeromagnetic measurements in Dixie Valley, Nevada: Implications on Basin-Range structure, *J. Geophys. Res.*, 73, 1321-1331, 1968.
- Speed, R., *Geology of Humboldt Lopolith & vicinity*, Geol. Soc. of Am. map MC-14, Boulder, Colo., 1976.
- Stauber, D., and D. M. Boore, Crustal structure in the Battle Mountain heat flow high from seismic refraction experiments (abstract), *Eos Trans. AGU*, 58(12), 12, p 1238, 1977.
- Stauber, W., and A. Ryall, Spatial distribution and source mechanism of microearthquakes in central Nevada, *Seismol. Soc. Am. Bull.*, 57, 1317-1345, 1967.
- Stewart, J. H., Basin and Range structure: A system of horsts and grabens produced by deep-seated extension, *Geol. Soc. Am. Bull.*, 82, 1019-1044, 1971.
- Stewart, J. H., Basin-range structure in western North America: A review, *Cenozoic Tectonics and Regional Geophysics of the Western Cordillera*, edited by R. B. Smith and G. P. Eaton, *Mem. Geol. Soc. Am.*, 152, 1-31, 1978.
- Stewart, J. H., Regional tilt patterns of late Cenozoic basin-range fault blocks, western United States, *Geol. Soc. Am. Bull.*, 91, part I, 460-464, 1980.
- Stewart, J. H., *Geology of Nevada*, *Spec. Publ. 4*, Nev. Bur. Mines and Geol., 136 pp., 1981.
- Stewart, J. H., and J. E. Carlson, Geologic map of North-Central Nevada, map 50, Nev. Bur. of Mines and Geol., Reno, Nev., 1976.
- Thompson, G. A., Gravity measurements between Hazen and Austin, Nevada: A study of basin-range structure, *J. Geophys. Res.*, 64, 217-229, 1959.
- Thompson, G. A., and D. B. Burke, Rate and direction of spreading in Dixie Valley, Basin and Range province, Nevada, *Geol. Soc. Am. Bull.*, 84, 627-632, 1973.
- Thompson, G. A., and D. B. Burke, Regional geophysics of the Basin and Range province, *Annu. Rev. Earth Planet. Sci.*, 2, 213-238, 1974.
- Thompson, G. A., L. J. Meister, A. T. Herrington, T. E. Smith, D. B. Burke, R. L. Kovach, R. O. Burford, I. A. Salehi, and M. D. Wood, Geophysical study of Basin-Range structure, Dixie Valley region, Nevada, *U.S. Air Force Cambridge Res. Lab. Spec. Rep. 66-848*, 244 pp., 1967.
- Tocher, D., Movement on the Rainbow Mountain Fault, *Bull. Seismol. Soc. Am.*, 46, 10-14, 1956.
- Tocher, D., The Dixie Valley-Fairview Peak Earthquakes of December 16, 1954: Introduction, *Bull. Seismol. Soc. Am.*, 47, 299-300, 1957.
- Wallace, R. E., Tectonic Analysis of Active Faults, *Rep. 9900-01270*, pp. 233-235, U.S. Geol. Surv., Menlo Park, Calif., 1980.
- Wernicke, B., Low-angle normal faults in

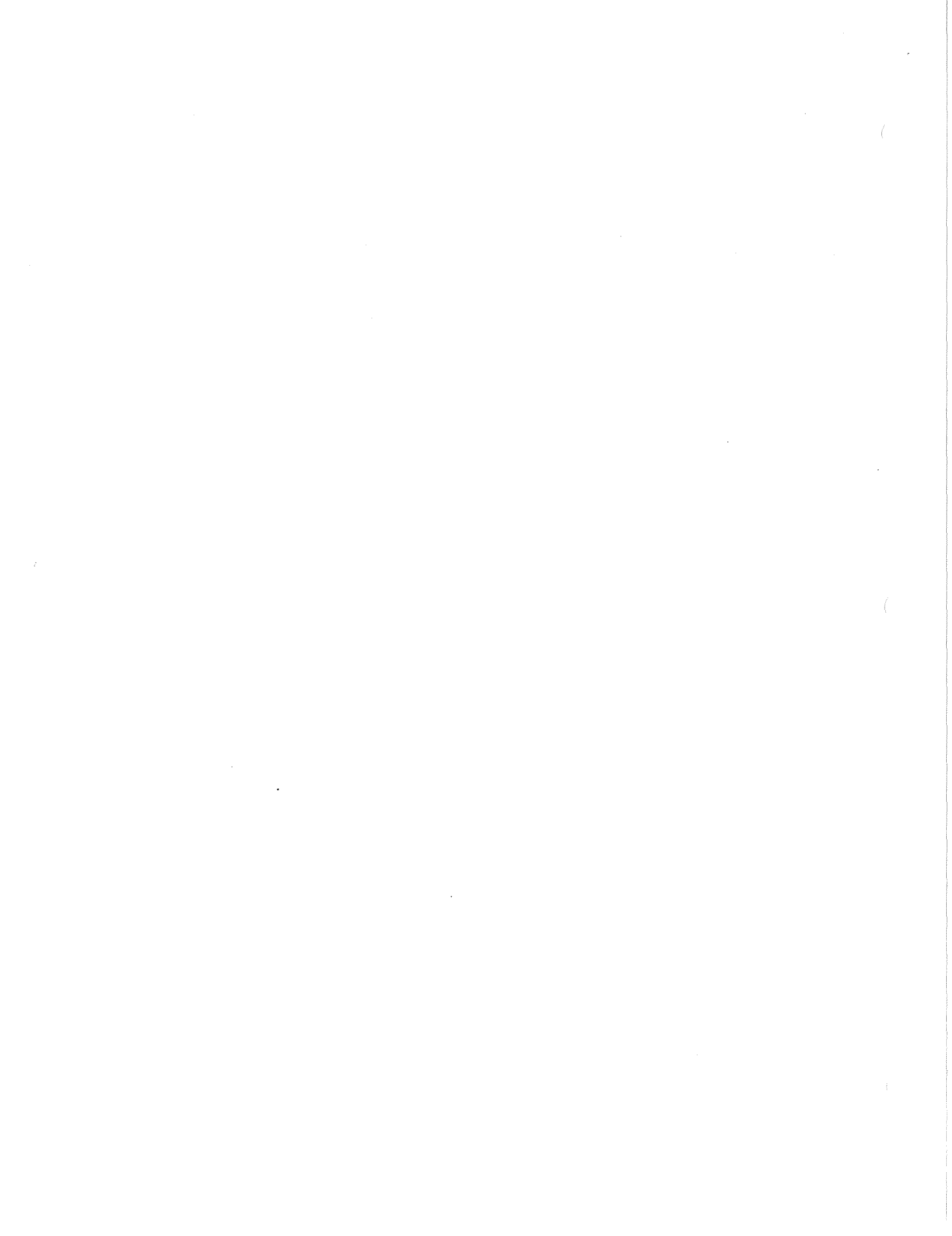
the Basin and Range province: Nappe tectonics in an extending orogen, Nature London, 291, 645-648, 1981.

Westphal, W. H., and A. L. Lange, Local seismic monitoring- Fairview Peak area, Nevada, Seismol. Soc. Am. Bull., 57, 1279-1298, 1967.

Whitney, R. A., Structural-tectonic analysis of Northern Dixie Valley, Nevada, M.S. thesis, 65 pp., Univ. of Nevada, Reno, Nev., 1980.

Zoback, M. L., R. E. Anderson, and G. A. Thompson, Cainozoic evolution of the state of stress and style of tectonism of the Basin and Range province of the western United States, Philos. Trans. R. Soc. London Ser. A, A300, 407-434, 1981.

(Received May 18, 1983;
revised May 2, 1984;
accepted July 16, 1984.)



2. INTRODUCTION

2.1 Project Description.

Oxbow Geothermal Corporation is developing a 50 megawatt (MW) net geothermal electrical generating facility in Dixie Valley, Nevada. The Dixie Valley geothermal field and power plant site are located along the northwest margin of Dixie Valley at the foot of the Stillwater Range, in northeastern Churchill County. The Dixie Valley project site lies 110 miles northeast of Reno and is reached from U. S. Highway 50 via 60 miles of paved and graded road (Fig. 2.1).

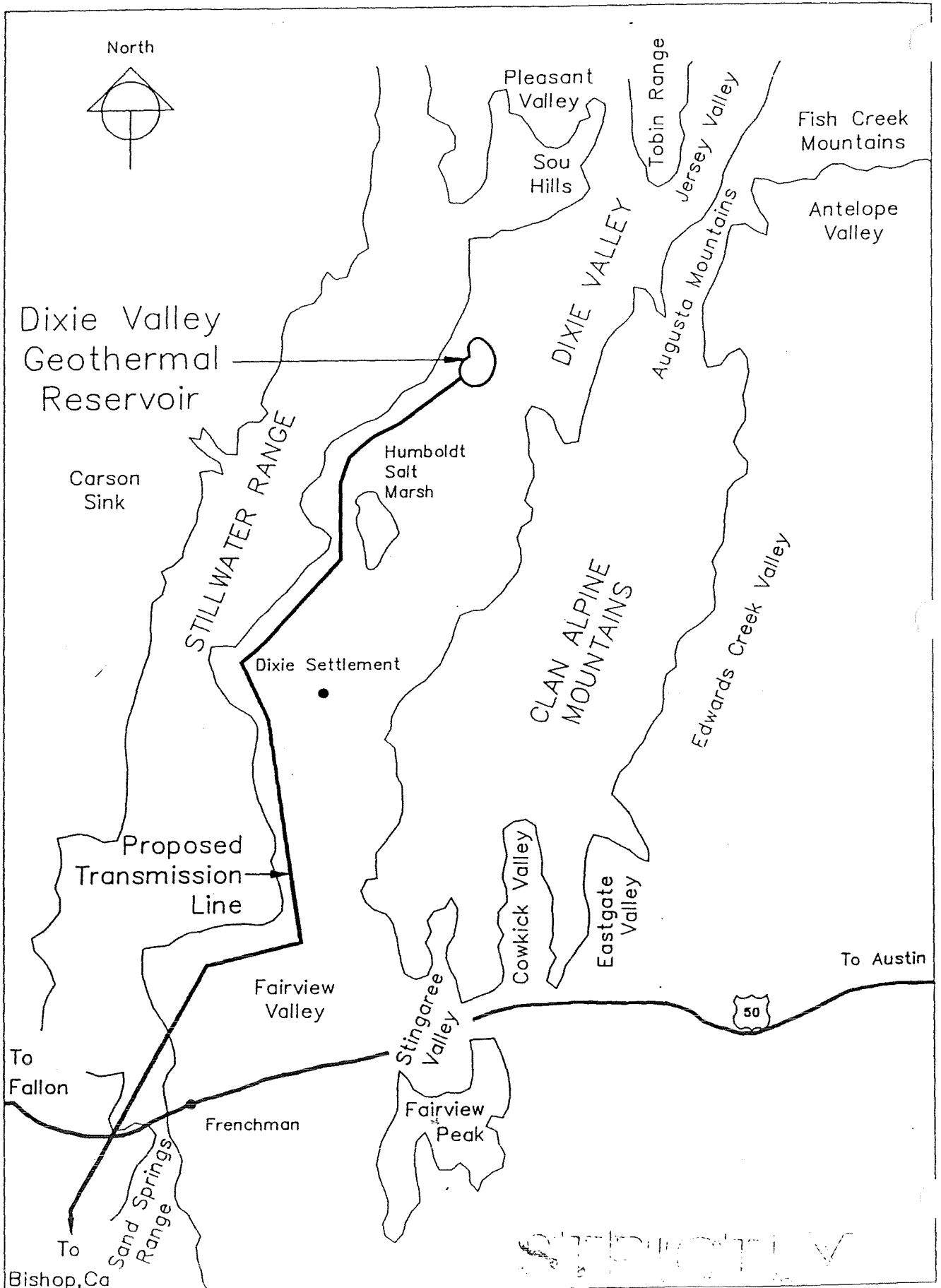
The electricity generated by the Dixie Valley geothermal project will be sold to Southern California Edison (SCE) at the SCE substation in Bishop, California (Fig. 2.1). Electricity from the project will be wheeled by a 230 kilovolt (kV) radial transmission line extending a distance of 217 miles from the project site to the SCE substation. The project is scheduled to go on-line in early 1988 at a total cost, including field development, power plant construction, and transmission line construction of \$165 million. A detailed description of the economics, budget, organization, and schedule of the Dixie Valley project is presented in the Oxbow project prospectus entitled "Dixie Valley Development" (March, 1986).

To date 16 wells have been drilled within or near the Dixie Valley geothermal reservoir ranging in depth from 7500 feet to over 12,500 feet. Two other wells, 45-14 and 66-21, are located to the southwest of the area shown on Figure 2.2. The producing wells are divided geographically into three clusters (Fig. 2.2) which are distributed along a northeast trend parallel to the strike of the Stillwater range-front fault. The southwestern cluster is referred to as the Section 18 wells, the central cluster as the Section 7 wells and the northeastern cluster as the Section 33 wells. This nomenclature is used throughout this document. The wells have encountered a liquid-dominated reservoir below a depth of 7000 feet and extending to depths below 10273 feet which is the deepest production encountered in the field to date. The downhole flowing temperatures in the field range from 400 deg.F to 480 deg.F with the Section 7 and Section 33 wells producing a higher temperature fluid than the Section 18 wells.

The wells are generally prolific producers with production rates varying from 300,000 to 1.7 million lbs/hr. The most prolific wells have mass flow rates equivalent to an electric power output of over 20 MWe each. The initial flow capability

STRICTLY

CONFIDENTIAL



of all existing wells at a wellhead pressure of 100 psig is approximately 7.5 million lbs/hr. This total flow rate is sufficient to produce 100 MWe using a dual flash power cycle.

2.2 Purpose of the Reservoir Assessment.

The purpose of this reservoir assessment is to provide a prediction of reservoir and individual well behavior over the 30-year life of the proposed 50 MW net power plant based on the best geologic and reservoir engineering data available. The 50 MW net power plant will require a continuous geothermal fluid mass flow of approximately 4.3 million lbs/hour. Sound management, design, and financing decisions for the project are dependent on an accurate assessment of the capacity of the geothermal reservoir to supply the required mass flow at sufficient pressure and temperature for power plant operation over the life of the project. This document presents a quantitative assessment of the productive capability of the Dixie Valley geothermal reservoir. The primary results of the assessment are:

1. To prepare a comprehensive geological, geochemical, and hydrological model of the Dixie Valley geothermal reservoir and surrounding area.
2. To determine the existing and future production characteristics of the individual wells.
3. To determine the probable pressure and temperature depletion characteristics of the Dixie Valley geothermal reservoir for the first 50 MW net power plant.
4. To determine the effect of reinjection on reservoir behavior and to determine which among the various reinjection options will provide optimum pressure support.
5. To provide a preliminary estimate of the rate of infill drilling required to maintain full plant capacity during the thirty year life of the first 50 MW plant.
6. To provide an assessment of silica and calcium carbonate scaling potential in production and reinjection wells and in surface equipment.
7. To provide an assessment of risk of damage to production and injection wells due to seismic activity.

8. To outline possible reinjection strategies that will lead to full reinjection in a period of less than three years from power plant startup.

2.3 Scope of the Reservoir Assessment.

The Dixie Valley geothermal reservoir as discussed in this document is defined by the region contained within the 4 deg.F/100' thermal gradient anomaly (Fig. 2.2). Deep production drilling within this region has confirmed that the near-surface thermal anomaly correlates closely with an active hydrothermal system with temperatures exceeding 400 deg.F as shallow as 5,700 feet.

A large body of geotechnical data relating to the Dixie Valley Field has been accumulated by Oxbow and by developers preceding Oxbow, primarily SUNEDCO and Trans-Pacific Geothermal Inc. (TGI). The Oxbow geologic staff assimilated this large data set into a comprehensive geologic model of the geothermal reservoir. The geologic model was then converted into a computerized numerical reservoir model by assigning observed hydrologic characteristics of the reservoir derived from extensive well and interference testing to the various lithologic and structural entities which make up the reservoir.

A detailed description of the work plan used to synthesize the geotechnical data base into the conceptual reservoir model is given in Appendix A: "Scope of Work, Dixie Valley Geothermal Reservoir Model".

The following geotechnical data sets were used to create the conceptual reservoir model:

1. Subsurface Geology: All lithologic and structural data available from production drilling, surface mapping, and seismic reflection profiles were integrated into a geologic model of the reservoir. Well logs and drilling logs were used to identify production zones, dips, and formation changes.
2. Static Pressure and Temperature: Static pressure and temperature profiles were obtained for all available deep wells in the area to establish the natural thermal and hydrologic state of the reservoir and surrounding area.
3. Brine Chemistry and Hydrology: Fluid chemistry from production wells, hot springs, perennial streams, and

shallow aquifers was examined to determine reservoir recharge zones, mixing zones, and discharge zones. Flow patterns within the reservoir were established by matching natural state hydrologic data with fluid chemistry patterns. Isotope geochemistry of reservoir fluids and gases and surrounding hot spring and non-thermal surface waters was used to identify possible local and regional sources of recharge. Bench testing of production fluid, caliper logging of well bores, and observation of surface brine handling equipment after long flow periods provided information regarding silica and calcium carbonate scaling.

4. Seismic Reflection Profile Reprocessing: Seismic reflection profiles provided by SUNEDCO were reprocessed to enhance resolution of structure adjacent to the range-front fault in production zones.
5. Tectonic Activity and Fracturing within the Reservoir: The nature of ongoing tectonic activity that is creating permeability in the reservoir was examined using low sun angle aerial photography and first motion studies of local seismic events.
6. Assessment of Seismic Hazard: Operating histories of geothermal fields throughout the world were reviewed for the purpose of indentifying the number and nature of seismic events that have caused mechanical or hydrologic damage to production and injection wells. These histories were related to observed Dixie Valley seismicity to assess the probability of damage to Dixie Valley wells by seismic activity.

Summaries and interpretations resulting from the examination of each of the geotechnical data sets are presented in Chapters 3, 4, 5, and 6.

Well and reservoir testing procedures and results from tests performed by Oxbow and others are described in Chapter 7. Included for each well are test results, flow characteristics, and casing design. Reservoir pressure response during production and shut-in are also presented. These data are used to produce an analytical model of the reservoir based on an idealized reservoir configuration. Future behavior of individual wells is predicted by use of a computer simulation of wellbore flow characteristics as reservoir pressure and enthalpy decline during the 30 year production history of the field. This analytical model is used as a simplified check of

the far more complex numerical model described in Chapter 8.

The conceptual reservoir model derived from the geologic data sets and reservoir test data are synthesized in Chapter 8 to produce the computer generated numerical reservoir model. This computer model provides a simulation of reservoir behavior under various conditions of production and reinjection.

The accuracy of the predictions provided by the simulation is dependent on the accuracy of the underlying geotechnical data used to create the conceptual model and the duration of reservoir testing.

2.4 Contributors.

The following investigators contributed to the reservoir assessment.

Dick Benoit - Execution of well and reservoir testing, electric log interpretation, measurement of scaling, chief editor.

Mr. Benoit (M.S. geology) has been involved in the geological aspects of geothermal development for 13 years, primarily in the Basin and Range province in Nevada. He played a key role in the discovery and development of the Desert Peak geothermal field. He has also either worked with or evaluated almost every other high-temperature geothermal reservoir in the Basin and Range province.

Gudmundur Bodvarsson - Numerical reservoir modeling

Mr. Bodvarsson (Ph. D. reservoir engineering) has been involved in geothermal reservoir engineering and modeling for 9 years. He is currently a staff scientist with the Lawrence Berkeley Laboratory specializing in numerical modeling and reservoir engineering in fractured porous media. He has modeled and evaluated geothermal reservoirs throughout the world and has published numerous articles in professional journals.

Bill Desormier - Execution of well and reservoir testing and compilation of data bases.

Mr. Desormier (M. S. geology) has been involved in the geological aspects of geothermal development for 11

years. He played a key role in the discovery of the Steamboat Springs and Humboldt House geothermal reservoirs in western Nevada. Most of his geothermal experience is in the Basin and Range province.

Chris Doughty - Numerical reservoir modeling
Ms. Doughty (B. S. engineering physics) is a staff scientist with the Lawrence Berkeley Laboratory involved in mathematical modeling of geothermal reservoirs. She has an extensive list of professional publications to her credit.

Roger Harrison - Reservoir engineering including design of reservoir test and analytical analysis of results.

Mr. Harrison (M. E.) has 12 years of experience in all aspects of geothermal drilling and reservoir and production engineering at most of the major geothermal resources in the United States and many of the high-temperature resources around the world. He has been associated with the Dixie Valley reservoir since 1983.

Stu Johnson - Geochemistry of reservoir fluids.

Mr. Johnson (M. S. geology) has been involved in both geology and geochemistry in both geothermal exploration and development for 13 1/2 years. He has evaluated many of the high-temperature geothermal areas in the Basin and Range province. His most extensive experience is at the Roosevelt geothermal field in Utah.

Tsvi Meidav - Assessment of seismic hazard.

Mr. Meidav (Ph. D. geophysics) has been involved in geothermal exploration and development for 19 years in academic, administrative, and developer roles. He has published numerous articles on geothermal areas throughout the United States and the world.

David Okaya - Seismic reflection profile reprocessing.
Mr. Okaya (Ph. D. geophysics) is a guest scientist at the Lawrence Berkeley Laboratory and a research associate professor at the University of Southern California.. He specializes in seismic reflection processing and interpretation of crustal structures. He has published

papers on faulting and seismic profiling at Dixie Valley.

Bill Peppin - Structural interpretation of local seismic events.

Mr. Peppin (Ph. D. seismology) is a research seismologist at the University of Nevada. He has authored numerous seismological papers including an analysis of seismicity at the Geysers in California.

Bill Teplow - Design of the reservoir assessment program, development of the structural and conceptual geological models.

Mr. Teplow (B. A. geology) has been involved in geological aspects of geothermal exploration and development for 5 1/2 years and has 4 years of experience in Dixie Valley. He was responsible for locating the two Section 33 wells while working for Trans-Pacific Geothermal Inc. In addition, he played a key role in the discovery of the high-temperature Fish Lake Valley geothermal prospect in Nevada.

Al Waibel - Reservoir lithology, stratigraphy, and hydrothermal mineralization.

Mr. Waibel (B. S. anthropology) has been involved in geological aspects of geothermal exploration for 13 years and has worked extensively in Dixie Valley for over 6 years. In addition he has experience in many areas in the western United States, Mexico, and Africa.

Bob Whitney - Aerial photo interpretation of surface faulting.

Mr. Whitney (Ph. D. expected 1987 in geology) has been involved with numerous structural and seismic evaluations throughout the United States and in Argentina. In addition he has previous structural experience in Dixie Valley as part of the Mackay Mineral Research Institute study in 1980.

Doug Willier - Graphics Design

Mr. Willier (M.S. Public Administration) has over 6 years of experience in energy and related fields.

Frank Yeamans - Hydrology

Mr. Yeamans (M. S. Water Resources) has been involved in hydrologic aspects of geothermal exploration and development for 7 years. He has worked extensively on geothermal systems in the Basin and Range province, including Steamboat Springs, Desert Peak, and Roosevelt.

3. GEOLOGY

3.1 Regional Geology

The regional geology of west-central Nevada including Dixie Valley has been described by Willden and Speed (1974). The local geology has been extensively studied by Speed (1976). The complex structural history is described in the MMRI (1980) Geothermal Reservoir Assessment Case Study. The major geologic features of the region are shown in Figure 3.1 which is a simplified NW-SE cross section of west-central Nevada passing through the Dixie Valley geothermal reservoir. The major stratigraphic and structural features seen in the cross section can be summarized as follows.

1. The deepest sedimentary rocks underlying the Dixie Valley region are probably carbonate and silicic clastic sediments, characteristic of the eastern Nevada shelf facies, ranging in age from Cambrian to Triassic. These units have not yet been encountered in the Dixie Valley wells, due to the great thickness of the overlying Triassic-Jurassic marine sediments, but are exposed to the east of Dixie Valley in the Clan Alpine and Shoshone Mountains.

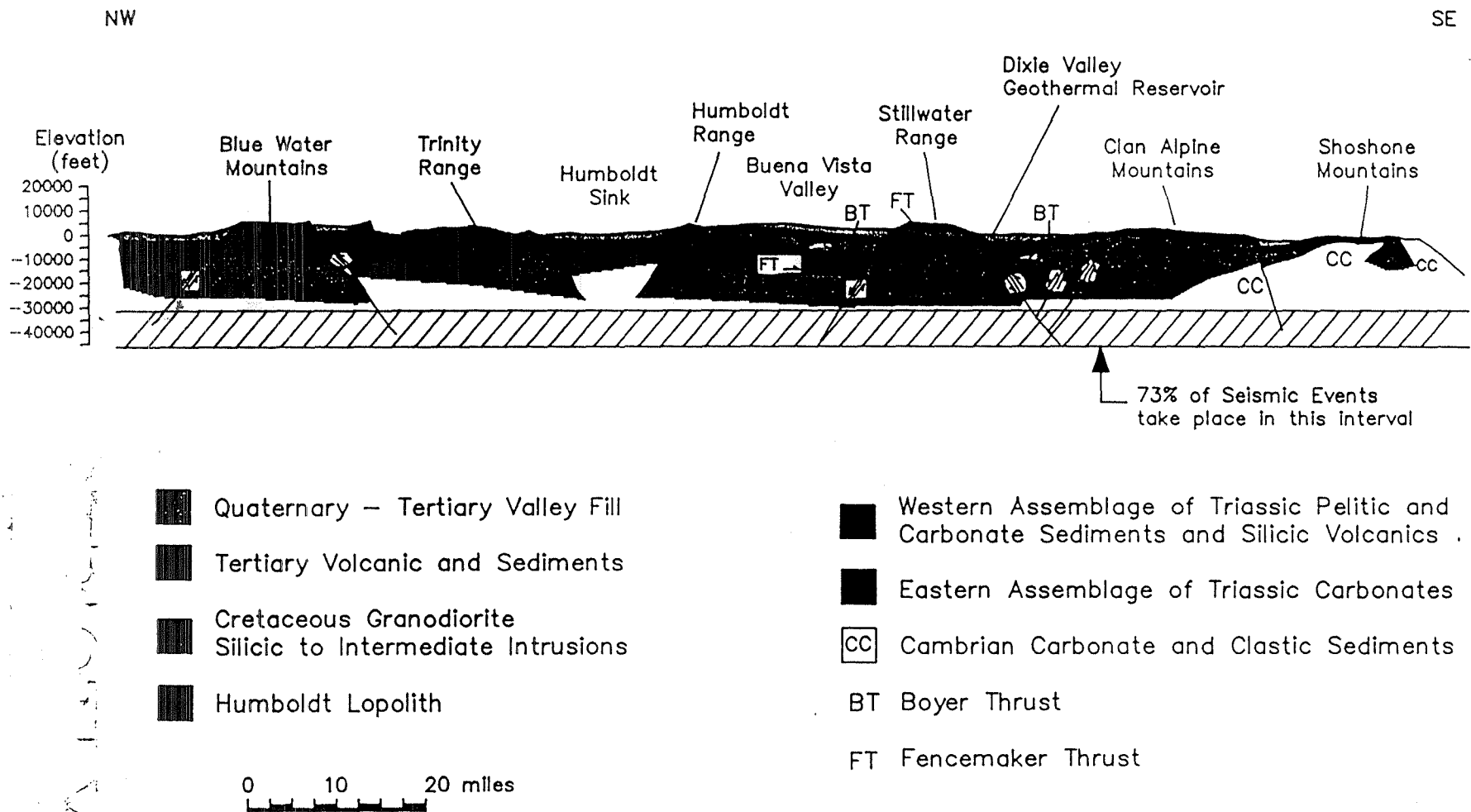
2. A sheet of Triassic marine sediments and silicic volcanics ranging in thickness from 10,000 to 40,000 feet blankets most of west-central Nevada. This sheet has been thrust over the Cambrian-Triassic section along the Fencemaker thrust fault from the west. Dixie Valley is located near the leading edge of the thrust so this unit pinches out within the deep part of the Dixie Valley graben at the northern end of the production well field in the vicinity of well 45-33. The Triassic marine sediments are dominated by siltstone and shale with less than 30 percent interbedded carbonates and sandstone.

3. A Jurassic oceanic crust complex consisting of gabbros, diorites, and basalts intruding marine clastic and carbonate sediments overlies the Triassic section over an area of several hundred square miles in and surrounding Dixie Valley. This complex, which is termed the Humboldt Lopolith, has a thickness of up to 4000 feet near its center and thins gradually toward the margins. The complex is thrust over the Triassic marine sediments along the Boyer Thrust.

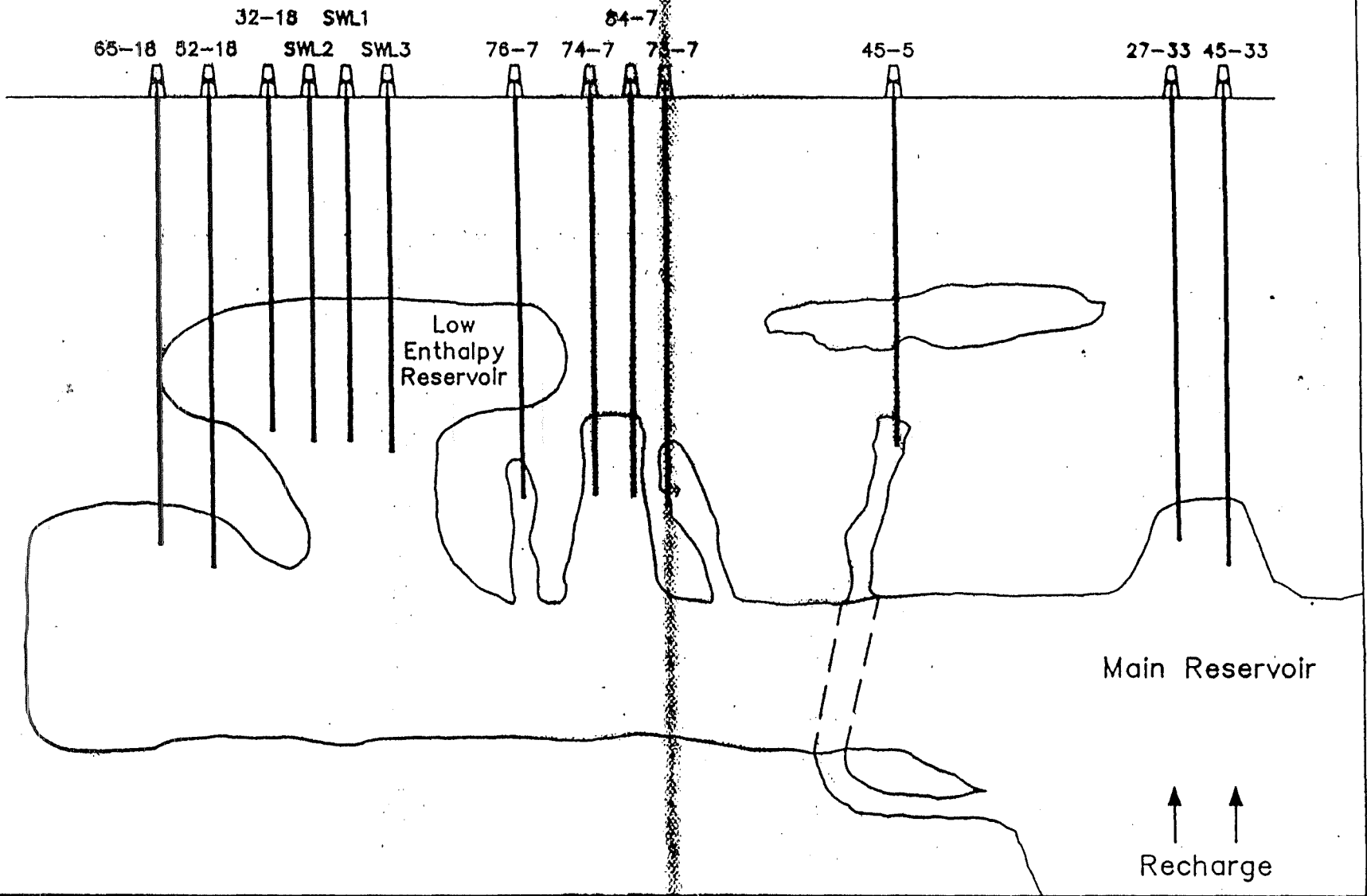
STRICTLY

CONFIDENTIAL

Simplified Geologic Cross Section West Central Nevada



Schematic Reservoir Model



OXBOW

Figure 1

Fig 3.27

4. The imbricated Paleozoic-Mesozoic marine sedimentary and oceanic crustal thrust sheets were intruded by Cretaceous intermediate to silicic magmas similar to those of the Sierra Nevada batholith. These intrusions are exposed in isolated outcrops throughout the region and have been encountered in the deeper wells in Dixie Valley that penetrate into the Stillwater Range block. These intrusives probably become more abundant at depth than is apparent from the extent of surface outcrops.

5. During middle to late Tertiary time several thousand feet of silicic, intermediate, and basaltic volcanic and volcanoclastic rocks were deposited over most of the region. These volcanic events occurred prior to and during incipient Basin and Range extension and block faulting.

6. East-west crustal extension of up to 30 percent during the last 8 million years has resulted in the formation of the horst and graben structural features which currently dominate the regional geomorphology. Northeast-trending horst block mountain ranges are separated from the graben blocks by range-front faults with dips of 50 to 60 degrees. Earthquake focal points along these faults indicate that brittle fracturing takes place to a maximum depth of approximately 49,000 (Fig. 3.1). Most seismic events occur in the depth interval between 33,000 and 49,000 feet. Basins created by this extensional faulting have accumulated up to 10,000 feet of late Tertiary and Quaternary lacustrine, volcanoclastic, and alluvial deposits.

3.2 Geology of the Dixie Valley Geothermal Reservoir

3.2.1 Introduction

This description of the geology of the Dixie Valley geothermal reservoir has been excerpted from a comprehensive report prepared for Oxbow by Al Waibel.

The stratigraphy, in the order encountered in the majority of the drill holes, includes basin filling sediments (Qal), silicic tuff-rich sediments (Tts), Miocene basalt (Tb), Miocene sediments (Ts), Oligocene silicic volcanics (Tsv), Jurassic oceanic crust (Js & Jpg), Jurassic marine sediments (Jms), Cretaceous granodiorite (Kgd), and Triassic marine sediments (Trc). The letter designations are those employed in the drill hole lithologies shown in Figure 3.2 and geologic cross sections shown in subsequent Figures.

The distribution of hydrothermal aquifers in the geothermal drill holes is also shown in Figure 3.2. The location of

these currently or recently active aquifers has been determined from secondary mineralization and the effects of the host rock interacting with geothermal fluid and gas. Analyses by the Argonne National Labs suggest that the geothermal system may have been active for as much as 150,000 to 300,000 years.

The structural history of the area now occupied by the geothermal field is complex. Jurassic oceanic crustal rocks have been thrust over carbonaceous marine sediments of Triassic age. Siliceous and mafic rocks of Tertiary age unconformably overlie the pre-Tertiary rocks. North-striking normal faulting occurred in this area in the Miocene, followed by a superimposed NNE striking set of normal faults. The Dixie Valley graben and the Stillwater Range are artifacts of the most recent episode of faulting. Highly fractured areas hosting geothermal production appear to have best developed in tensional zones resulting from strike-slip and normal faulting along the two generations of normal faults.

3.2.2 Lithology

Triassic Marine Sedimentary Rocks (Trc)

These are the deepest and oldest rocks encountered by a few of the wells in Dixie Valley. They are primarily calcareous carbonaceous shale, siltstone, and silty carbonates. The carbonaceous marine sediments are correlative to the Favret Formation, a lower member of the Star Peak Group. Geological and geochemical evidence indicates that the Favret Fm. is the primary reservoir at Dixie Valley; i.e., the fluid recovered from the deep production wells apparently reached thermal and chemical equilibrium within this unit and then has moved rather rapidly to the producing intervals.

Affection of dolomite by contact metamorphism?

Mechanically the Triassic sediments will deform rather than fracture when subjected to strain. Dolomite bearing horizons form secondary serpentine during deformation. These characteristics make this formation an unlikely host for geothermal production. However, it is not necessary for this unit to be capable of giving up large volumes of fluid in short times. As a geothermal reservoir rock it is necessary to have substantial storage capacity and the ability to slowly release fluids into small fractures over time. The large producing fractures are found overlying

these Triassic sediments in much more competent igneous rocks.

The Favret Fm. is rich in hydrocarbons and is apparently undergoing metamorphism which is liberating gases such as CH₄, H₂S, N₂, NH₃, and CO₂. Chemical reactions involving these gases, particularly CH₄ and H₂S, control rock-water-gas reactions in the shallower production portion of the geothermal system.

Jurassic Formations (Jms Js Jpg)

From a production viewpoint, the Jurassic rocks are the most important rocks in the Dixie Valley field as it is these formations which contain most of the large productive fractures. Wells 74-7, 73-7, and 84-7 produce from the Jurassic oceanic crust (Js and Jpg) as do the deeper productive wells in Section 18 (52-18 and 65-18). Wells 27-33 and 45-33 produce from the Jurassic marine sediments.

Jurassic Marine Sediments (Jms)

Jurassic shallow marine sediments overlie the Triassic marine sediments and are separated from each other by the Fencemaker thrust fault. Compositionally these sediments consist of carbonate, quartzite, and minor conglomerate. Willden and Speed (1974) refer to these sediments as the Boyer Ranch Formation. Thrusting of the Jurassic oceanic crust clearly involved the Boyer Ranch Formation. Portions of the sediments can be observed in the Stillwater Range as overlying, overridden by, and mechanically incorporated into the allochthonous oceanic crust.

The quartz arenite portion of the Boyer Ranch Formation is a well-lithified, competent rock that tends to host open permeability along fault planes. However, outcrop evidence suggests that it is not prone to extensive fracture propagation. The rock is composed largely of lithified quartz grains and should be chemically and mineralogically stable in the geothermal system. The only extensive occurrences of this quartz arenite in the geothermal wells are in 27-33 and 45-33 where it forms the foot wall of a fault.

Jurassic Oceanic Crust (Js & Jpg)

The Jurassic oceanic crust section consists primarily of mafic igneous rocks that have undergone extensive sodium

metasomatism. The dominant rock types vary from spillites, basalts, keratophyres, and trondhjemites to albitites, plagiogranites, and gabbro. Locally, lenses of sedimentary rock, most commonly siltstone, are observed within the igneous series.

Willden and Speed (1974) and Speed (1976) describe the Jurassic igneous rock as a locally intruding lopolith. Autochthonous thrusting has been associated with the intrusion of the lopolith. Al Waibel and others, however, have concluded that the entire Jurassic igneous section is most probably an allochthonous fragment of oceanic crust, thrust over Triassic marine shelf and slope sediments. The most obvious points leading to this reinterpretation include pervasive sodium metasomatization, pervasive secondary calcite, and abundant lamellar plates, lenses, and nappes markedly disrupting specific lithologic and stratigraphic continuity. The "lopolith" is remarkably similar to igneous portions of ophiolites observed in many places throughout the world.

The large blocks of spilite, keratophyre, and trondhjemite rock tend to be very brittle and are capable of maintaining good fracture permeability. The albitite and plagiogranite are somewhat less prone to host good fracture permeability. The prevailing mineral assemblage, albite, calcite, chloritized hornblende, chloritized biotite, and chloritized augite, tends to be stable in the chemical and thermal environment of the currently active geothermal system.

The mineral suite is not mechanically stable in the cataclastic environment of thrust faulting, shear planes, and nappes. The mafic minerals are usually altered to serpentine and chlorite; the albite tends to be broken up into small angular fragments and the calcite tends to recrystallize as a matrix mineral. The resulting effect is lenses of mechanically unstable rock within the more competent formation. While these lenses have the potential of hosting permeability, the permeability does not always have good communication with major geothermal production, and the formation tends to slough when produced. The serpentinized zones in two of the legs of well 82-5 are the result of thrust related alteration.

Cretaceous Granodiorite (Kgd)

A quartz monzonite to granodiorite intrusive pluton has been penetrated in several of the deeper wells in Dixie Valley. The mineralogy of the rock is distinctly different from the igneous rocks of the Jurassic oceanic crust. Where least

I should look at this attention to see if quartzite or contact metamorphism or Jurassic faulting related.

altered this rock consists of quartz, plagioclase, biotite, muscovite, hornblende, and minor K-feldspar. Where altered the mineralogy is albite, chlorite, K-feldspar, epidote, and calcite. The mafic minerals usually are slightly chloritized.

The genetic and structural relationship of this silicic intrusive to other igneous rocks in the area is not totally clear. It is typically observed as the foot wall in fault contact with Jurassic rock. In the first leg of well SWL-2 it is in fault contact with Miocene basalt. At no place in the Jurassic rocks cropping out in the Stillwater Range is rock this potassic observed. The mineralogy and texture more closely resemble intrusives cropping out along the west side of the Stillwater Range in the New York Canyon area that have been dated as late Cretaceous. This would place the intrusive event after the allochthonous thrust faulting and would explain the apparent thin fingers or layers of granodiorite within thrust-fault zones as intrusive sills.

Where do they see these? While granitic rocks in other reservoirs in the Basin and Range province have excellent productive intervals no commercial production has been developed from the granodiorite in the Dixie Valley geothermal field. The rock is mechanically competent and should fracture when under stress. Fracture permeability would tend to seal in the unaltered granodiorite as calcic plagioclase altered to albite and calcite. The albite-chlorite-epidote-K-feldspar altered granodiorite would be in chemical/mechanical equilibrium with geothermal fluids. Fracture permeability is more stable here, though the rock at this grade of alteration is usually observed in fault zones containing mechanically incompetent fault gouge. Perhaps fracturing has simply not occurred in the footwall of the Stillwater fault where the granodiorite is located or the fault gouge does not allow any fracturing stresses to be transmitted into the granodiorite.

Oligocene Silicic Volcanics (Tsv)

Oligocene silicic volcanic tuffs in excess of 4000 feet thick dominate the Clan Alpine Range to the east of the Dixie Valley geothermal field, and are a few hundred feet thick in the Stillwater Range just west of the geothermal field. These volcanics are only rarely encountered in the geothermal drill holes, however. In most of the geothermal wells in Dixie Valley the Oligocene volcanic section has been faulted out (e.g., 65-18 and 84-7) by basin-bounding normal faults. The single good example of these silicic tuffs in the wells is observed in 74-7, where a 180 foot

section of predominantly welded biotite-quartz-sanidine tuff is overlain by Miocene sediments.

Welded portions of the Oligocene silicic tuffs are brittle and generally fracture when subjected to strain. Poorly welded and cemented aspects of the tuff sequence are generally soft and undergo plastic deformation rather than structural failure when subjected to strain. Fracture permeability within Oligocene silicic volcanics may or may not be significantly affected by interaction with the current geothermal system depending upon the individual rock type.

Miocene Sediments (Ts)

The Miocene lacustrine sedimentary section conformably overlies the silicic volcanic tuffs of late Oligocene age. The formation is composed of intercalated volcanoclastic sediments, carbonaceous siltstone, and silicic volcanoclastic tuff. The section is usually observed in a truncated form in many of the drill holes in Dixie Valley due to normal faulting. The thickest sections observed in drill holes are seen in 27-33 (1040 ft) and in 45-33 (1300 ft).

The upper portion of the sediments consists of intercalated volcanoclastic sediments and carbonaceous siltstone. The volcanoclastic sediments appear to be derived predominantly from silicic volcanics and tuffs. The lower portion of the sedimentary section is composed of reworked silicic tuffaceous sediments with only minor carbonaceous siltstone horizons. The basal boundary of this sedimentary unit is not distinct. In well 74-7 a downward progression is observed from reworked silicic tuffs to possibly primary devitrified silicic tuff to primary welded Oligocene silicic tuff.

Clays represent the dominant mineralogy in this sedimentary section. As a result, tectonic strain tends to cause plastic deformation rather than brittle failure and rock breakage.

Rock-water-gas interaction between the sediments and the geothermal system is limited due to the low potential for porosity and permeability.

Miocene Basalt (Tb)

After the Jurassic rocks the Miocene basalt is the second major producing formation. Wells 76-7, 32-18, SWL-1 and

SWL-3 produce from this unit. Of these wells only 76-7 is regarded as a high enthalpy well.

The Miocene basalt overlies Miocene lacustrine sediments and is overlain by as much as 6000 to 7000 feet of basin filling sediments in the area of the geothermal field. These basalts crop out as high as 8000 feet elevation in the Stillwater Range which indicates an offset on the Stillwater fault of 12,000 feet since these basalts were deposited. A K-Ar date from a sample from the Stillwater Range analyzed for SUNEDCO in 1981 shows an age of $8.5 \pm .4$ million years. The basalt section as observed in geothermal drill holes is often abbreviated due to normal faulting. Observed thicknesses in the drill holes range from less than 300 ft (45-33) to greater than 1900 ft (65-18).

Two distinct alteration mineral suites are observed in the Miocene basalt section in drill holes. The effects of weathering are plainly visible in portions of the basalt chips recovered during drilling. Other portions of the basalt show a later overprinting of alteration resulting from interaction with geothermal fluid and gas with a low oxygen activity. Precipitation of quartz, chlorite, and occasionally epidote into open fractures indicates that this later alteration is likely associated with conductive cooling geothermal fluids. No mineral-chemical evidence for mixing of geothermal and nongeothermal water in the basalt is found in any of the drill holes.

Basin Filling Sediments (Qal & Tts)

Subsequent to the eruption of the Miocene basalts, horst and graben tensional structural features developed in the area of the Stillwater Range and Dixie Valley. Sediments accumulated in the grabens, unconformably overlying the Miocene basalt flows. The current Dixie Valley basin is asymmetrical with the deepest portions occurring in the northwest margin along the Stillwater Range. In the wells 74-7 and 76-7 the basin filling sediments are in excess of 7000 feet thick. Seismic data suggest that toward the center and along the eastern portion of Dixie Valley these sediments are no more than 2000 to 3000 feet thick.

The composition of the fill which makes up the basin sediments is somewhat variable from place to place. Toward the center and along the eastern portions of the valley the entire sedimentary section is dominated by reworked silicic tuffs eroding from the Clan Alpine Range. Along the Stillwater Range the contributing rock types are more varied. Reworked silicic tuffs tend to dominate the deepest

(earliest) sediments in the geothermal production area. With decreasing depth the sediments are usually variations on a pebble conglomerate with clay matrix. Near the discharge of major Stillwater Range drainages (i.e. Cottonwood Canyon) conglomerates are most common and horizons of clay and silt are minor. Areas away from major drainages have basin filling sediment sections dominated by clay, silt, and sand size particles with less common conglomerate horizons.

3.2.3 Structural History

Three structural patterns are recognized in the vicinity of the Dixie Valley Geothermal Field. The first of these is thrust faulting associated with crustal shortening. The second and third are both normal faulting associated with crustal extension. Geothermal production in Dixie Valley is related to an extended complex network of fault and fracture permeability. The combined tectonic history is, therefore, quite important to interpreting the production potential of any given location within the geothermal field.

Thrust faulting of Jurassic oceanic crustal rocks over Triassic shelf-related marine sediments is observed in the Stillwater Range. This thrust faulting event is one of the last in a series of crustal shortening events that involved allochthonous thrusting of deep marine strata over older rocks (Antler Orogeny, Devonian-Mississippian; Sonoma Orogeny, Triassic; and Nevadan Orogeny, Jurassic-Cretaceous).

The Jurassic oceanic rock has undergone differential movement along horizontal planes within the overthrusting block resulting in horizontal cataclastic zones and inclusions of marine sediments into the thrusting Jurassic plate. Serpentinization of portions of the Jurassic mafic igneous rocks and of Triassic dolomitic sediments is common within melange-like features created by zones of turbulence along the leading edge of the thrust block.

The Dixie Valley area of Nevada appears to have been structurally quiet from the Cretaceous through the Oligocene. Subsequent to the silicic volcanism in the late Oligocene a series of north-striking normal faults developed. The best surface expressions of these faults can be observed along the western edge of the Clan Alpine Range and in the White Rock Canyon area in the Stillwater Range. Seismic line data show similar north-striking patterns to be present beneath the alluvium in Dixie Valley. The surface

expressions of this episode of normal faulting show evidence of rotation, suggesting that these were listric faults which flatten with depth. The relationship between the timing of the late Miocene basalt eruptions and the north-striking normal faulting is unclear. Both Jurassic and Oligocene rocks were affected by this fault movement. No outcrops of Miocene basalt show a similar rotational relationship.

The current high-angle NNE-striking normal faulting that defines the Stillwater Range and Dixie Valley physiographic features is relatively young, and is superimposed over the earlier two tectonic features. The uplift of the Stillwater Range occurred after the late Miocene basalt eruptions, as is evidenced by the flat lying basalt flows and palagonite tuffs which occupy some of the highest elevations within the range. The onset of this last episode of faulting, therefore, can be no older than very early Pliocene. Historic earthquakes along the basin-range boundaries attest to the continuing activity of this latest structural feature.

3.2.4 Hydrothermal Mineralogy

Multiple thermal and metasomatic events have left a mineralogical signature in the host rocks in the Dixie Valley area. The temperatures of most of these metasomatic events have ranged from 120 to 500 deg. F., similar to the range of temperatures in the currently active geothermal system. As a result many of the secondary minerals are stable in the present geothermal environment and may be representative of more than one thermal event. The mineralogical effects of fossil thermal systems must be distinguished from those of the active system before any interpretations pertaining to this current system can be made.

The earliest thermal and metasomatic event recognized in the Dixie Valley area involves the Jurassic oceanic crustal rocks. The pre-alteration rocks of this group were basalt, diabase, gabbro, and locally more leucocratic fractionations of this suite. Extensive sodium metasomatization is manifested in nearly complete albitization and local scapolitization of plagioclase. Extensive secondary calcite occurs within the rock and in veins, an effect of the pervasive sodium metasomatization. Chloritization of mafic minerals is ubiquitous, and varies in degree from minor to near complete replacement of the mafics. Additional secondary minerals, including epidote, pyrite and chrysotile, are irregularly distributed throughout portions of the Jurassic igneous suite. The post-alteration rock

suite consists of spilite, keratophyre, trondhjemite, albitite, and plagiogranite.

The spilitic rock suite of the Jurassic section is typical of the igneous rock suites observed in many ophiolite complexes. The sodium metasomatization most likely had to occur while this section was still in a marine environment. The only reasonable sodium reservoir to support this type of extensive alteration would be sea water.

A second metasomatic event, confined to the Jurassic oceanic rocks, involves silica and iron oxides and is represented by quartz-filled veins in association with specular hematite replacement of spilitic rock.

The timing and possible relationship between the two events has not been determined. Both of these secondary features may have developed at or near the same time, while these rocks were still part of an ocean environment.

Additional thermal and metasomatic events in the Dixie Valley-Stillwater Range area include contact metamorphism associated with Cretaceous plutonic intrusives and Oligocene silicic volcanism. In the Dixie Valley region these thermal events have concentrated both base and precious metals to the extent that mining districts are rather common.

The most recent vulcanism in the Dixie Valley area is the late Miocene basaltic eruptions and associated subvolcanic dikes. Contact metamorphic effects are usually limited to a few tens of centimeters away from the edge of the intrusives and consist mainly of chloritization. No hydrothermal activity has been observed to be associated with this intrusive event.

Hydrothermal mineralization associated with the active geothermal system varies with temperature and host rock type. The fluid has low oxygen activity, low total dissolved solids, and limited sulfur and carbonate activity. Precipitation mineralization in the deeper production from Jurassic igneous rock is usually limited to quartz. Host rock alteration by the hot fluid is limited to pyrite forming at the expense of Fe-Ti oxide. The Jurassic igneous rock is already at a chlorite-albite grade of greenschist metamorphism and is chemically stable in the presence of the hot fluid.

Hydrothermal mineral reactions within the Miocene basalt are substantially different from the reactions observed in formations underlying the basalt. Here, chlorite, pyrite,

albite, calcite, and locally epidote are present as hydrothermal alteration products of the formerly hematite altered basalt. Hydrothermal precipitation minerals in these basalts include quartz, chlorite, pyrite, calcite, epidote, laumontite, and rarely wairakite.

The marked difference between the hydrothermal mineral assemblages in the two mafic igneous units is the combined result of the stable mineral phases prior to the introduction of the geothermal fluids and the gas content of the geothermal system. The Miocene basalt is oxidized where unaffected by geothermal fluids, with reddish hematite as a major stable Fe mineral. The Jurassic spilitic series has been albitized and partially chloritized prior to the current geothermal activity. The significant change within the geothermal fluid as it passes through the Jurassic section is limited to conductive heat loss. This results in slight but steady silica oversaturation, manifested by the precipitation of druse quartz forming along fracture surfaces.

3.2.5 Mineralogic and Lithologic Characteristics of Geothermal Production Zones

Geothermal production in the Dixie Valley field is defined by fault and fracture permeability. Rather than being strata bound, permeability is defined by and varies with the physical characteristics of each rock type. The production potential of a rock is best defined by its mechanical and mineral-chemical stability. Open fractures are dependent on brittle rock that will fail rather than deform under tectonic strain. Producing fractures are, therefore, most likely to occur in brittle igneous rock and least likely to occur in soft, clay-rich sedimentary rock. Subsequent to fracturing, the longevity of permeability is dependent upon the mineral and chemical stability of the rock in the presence of geothermal fluid and gas.

The occurrence of faults or fractures within a brittle rock does not automatically guarantee production. Fault planes are not always "planer". Normal faults associated with extensional tectonics in Dixie Valley tend to undulate, which results in portions of the fault plane being under high compression and impermeable, regardless of the rock type involved. Conversely other portions of the fault plane will be under tension and contain open spaces possibly tens of centimeters wide. An example of the former would be the fault zone intersected by SWL 3 from 8730 to 8880 feet; and example of the latter would be the fault zone intersected by 76-7 between 7332 and 7334 feet.

The two most common host formations of geothermal production in Dixie Valley are the Miocene basalt and the Jurassic oceanic crust. The basalt contains cooling fractures and flow breccias that can complement fault-related fracturing and provide additional production permeability. The pervasive mineralogy within the basalt, secondary hematite, zeolite, and clay, is not stable in the presence of the geothermal fluids and gas. Interaction between the basalt and the geothermal system results in chloritization. With extreme chloritization fractures tend to seal and the rock becomes less competent. Fracture production within the basalt tends to be in zones of very fresh to moderately chloritized rock. The typical hydrothermal mineralogy includes alteration chlorite, pyrite, albite, and minor calcite; and precipitation quartz, chlorite, minor calcite, and locally epidote. Fracture production from basalt is not associated with rock strongly dominated by hematite, zeolite, and clay alteration. Loss of drilling fluid or the occurrence of methane are not, by themselves, reliably distinct indicators of geothermal production fractures in the basalt.

Geothermal production from fault zones in the Miocene basalt is usually associated with chlorite and pyrite alteration minerals and quartz, chlorite, ± epidote precipitation minerals. Major to total loss of drilling fluid is always, though not uniquely, associated with fault production in the basalt. Permeable fault zones are much less susceptible to the subtle nuances of physical rock characteristics of the basalt than are fracture zones.

The Jurassic oceanic crust rocks have undergone a substantially different history from the Miocene basalt as evidenced by the mineralogical and mechanical rock characteristics. The rocks range from spilite and keratophyre to trondhemite and rarely to gabbro, albitite, and plagiogranite. Physically the rocks range from competent blocks to cataclastized horizontal shear zones. The rock is pervasively albitized and variably chloritized, a mineral assemblage that is generally in equilibrium with the geothermal fluids. The more mafic portions (spilite, keratophyre, trondhemite) fracture under tectonic strain and the fractures tend to remain open. The rocks dominated by feldspar and calcite (albitite and plagiogranite) are less brittle and tend to be poorer hosts for fracture and fault permeability. Cataclastized zones resulting from Jurassic-age thrust faulting are much more ductile than the equivalent uncataclastized rock, and are less likely to host current production.

The physical parameters of rock likely to host production in Dixie Valley are easy to define. These features are not strata bound, however. In coal fields or sedimentary basins structural and stratigraphic projections can be made for kilometers with some degree of accuracy. Crustal thrusting, two episodes of normal faulting, and volcanic stratigraphy render analogies between layer-cake sedimentary basin geology and the Dixie Valley geothermal field meaningless. Projection of the general formations and normal faults within the Dixie Valley geothermal field can be approximated for short distances with the well controls and seismic data now in hand. Predicting exact locations of production zones within these formations is more problematic. Evaluation of the production potential in any well in any given formation is most effectively done at the well site as drilling is underway.

3.2.6 Determination of Production Zones by Electrical Logging and Drilling Records.

Production zones for each producible well have been defined using a combination of electric logging and physical drilling parameters. Methods employed for each well and the resulting definition of production zones is detailed in Appendix B. These production zones are shown graphically in Figure 3.2 and are summarized on Table 3.1.

3.2.7 Age of the Geothermal System

Age estimates have been made on two hydrothermal silica specimens from the geothermal system using the ionium/thorium method. The facilities at the Argonne National Laboratories in Argonne, Illinois were used. The first sample is of dense clear cryptocrystalline silica from a silicious sinter hot spring deposit in section 15, T24N, R36E located 2 miles southwest of the Section 18 wells along the range-front fault. The hot spring is no longer active and the area has been uplifted by ongoing normal faulting along the Stillwater Range front. Total uplift since the hot springs deposits formed may be as much as 200 feet. The estimated age of this deposit is determined to be 9,000 ± 2,000 years.

A second sample was collected for dating from hydrothermally precipitated cryptocrystalline silica from near the Senator Fumaroles in section 32, T24N, R37E. This sample formed near the boiling plane below the topographic surface. Subsequent uplift by normal faulting along the Stillwater Range from the time of silica deposition until now positions

this rock 250 feet above the Dixie Valley floor. The age of this sample is much less definitive, with a maximum possible age of 300,000 years and a minimum possible age of 150,000 years.

3.3 Structure of the Dixie Valley Geothermal Reservoir

Structure within the Dixie Valley geothermal reservoir has been defined using well bore geology and electric logging techniques, coupled with seismic reflection profiling. Stratigraphy, faulting, and deformation are defined with high precision within the existing well field. The stratigraphy, faulting, and deformation can then be followed several miles to the north, south, and east using seismic reflection profiles run by SUNEDCO and Southland Royalty.

Structure within the productive portions of the reservoir is dominated by the Stillwater range-front fault and associated secondary sympathetic and antithetic faults. Three styles of faulting are observed in the productive part of the field. These styles are shown in cross section in Figures 3.3.1-3.3.3. The locations of these cross sections are shown in Figure 2.2. The transition between the three regions is probably gradational.

MISSING!

The Section 18 area (Fig. 3.3.1) is characterized by numerous sympathetic and antithetic faults of relatively small displacement. These intersecting secondary faults form a rubble zone of high permeability and relatively high fracture porosity. The high density of fracturing appears to be most strongly developed in the Miocene basalt (Tb). This style of fracturing extends northeastward through well 76-7. Wells 84-7 and 73-7 further to the northeast show decreasing fracture permeability in the basalt. Wells 82-5, 27-33, and 45-33 at the northeast terminus of the field encountered no permeable fractures in the basalt.

The northwest-southeast width of the highly faulted area appears to decrease from the Section 18 area to the vicinity of well 82-5. The region extending from well 84-7 to 82-5 is characterized by the existence of one or two secondary faults which parallel the main range-front fault surface. These faults separate the down-dropped graben block into two or three slivers with vertical offsets of several hundred feet between each sliver. This style of faulting is shown in Figure 3.3.2. Within this region, commercially productive fractures are encountered between the slivers. Seismic reflection profile No. 6 which passes through well 84-7 perpendicular to the range-front fault, shows two

relatively large slivers and their relationship to the major down-dropped graben block (Fig. 3.3.4)

The range-front fault system becomes more coherent north of 82-5 as the secondary faults appear to die out and all offset between the two blocks is confined to the main range fault (Fig. 3.3.3). Drilling results from 45-33 and 27-33 confirm this structural interpretation which was originally developed by Okaya and Thompson (1985) using a seismic reflection profile passing through 27-33 perpendicular to the strike of the range-front fault.

Development of the differing faulting styles may be related to the relative magnitude of dip - slip and strike - slip movement in the fault planes as discussed in Appendix D. The increasing component of strike-slip movement going south from 27-33 to the Section 18 area is predicted for the corresponding change in strike of the range-front fault. As the range-front fault strike swings farther to the west in the Section 18 area, increased strike-slip movement causes dilation of the down-dropped block. This dilation breaks the down-dropped block into numerous smaller slivers, thereby producing the abundant permeable fractures observed in the production zones. Apparent decrease in the magnitude of strike-slip movement north of 84-7 results in less tensional force so that fault movement tends to be confined to a single fault zone with a thickness of less than 200 feet when measured perpendicular to the plane of the fault.

MISSING! The attitude of bedding within the fault slivers has been determined from seismic reflection profiles and dipmeter logging runs. Dips derived from the dipmeter survey in 73-7 are shown in Figure 3.3.2. Dips in the 5000 foot to 8300 foot depth interval range from 20 to 36 degrees to the south and southeast. These dips are confirmed by Sunmark Seismic Profile No. 6 as shown in Figure 3.3.4.

Thickening of the Tertiary section (Tts, Tb, and Ts) in the northwest to southeast direction is evident from seismic reflection profiles. Seismic reflection profile No. 6 (Fig. 3.3.4) shows a thickening from approximately 1500 feet adjacent to the range-front fault to a thickness of 3000 feet at the apex of the graben located approximately 2000 feet southeast of 65-18. Apparent thicknesses observed in the production wells are affected both by stratigraphic thickening and by thinning resulting from normal fault extension. The thinning effect of normal faulting is much greater than the lateral increase in thickness in the southwest direction, thereby causing an apparent net thinning of the Tertiary section in the Section 18 and

Section 7 wells. Section 33 wells show a full stratigraphic thickness in the Tertiary section of approximately 3000 feet which indicates an absence of secondary normal faulting.

3.4 References Cited

Speed, R.C., 1976, Geologic map of the Humboldt Lopolith: Geol. Soc. Amer. Map Series MC-14.

Willden, R. and Speed, R.C., 1974, Geology and mineral deposits of Churchill County, Nevada: Nevada Bur. Mines Bull. 83.

Okaya, D. and George Thompson, 1985, Geometry of Cenozoic extensional faulting: Dixie Valley, Nevada, Tectonics, V.4, no. 1, pp. 107-126.

4. GROUND WATER HYDROLOGY

4.1 Regional Hydrologic Setting

The Dixie Valley basin is topographically the lowest of seven valleys that constitute a closed shallow ground water hydrologic unit. This unit includes Fairview Valley, which is a topographically closed basin, and Dixie Valley with the five smaller valleys that drain into Dixie Valley--Jersey, Pleasant, Eastgate, Cowkick, and Stingaree Valleys (Figure 2.1) (Cohen and Everett, 1963). Shallow ground water flow within Dixie Valley is toward the Humboldt Salt Marsh (Figures 4.1.1 and 4.1.2) which is the topographic low point of the seven valley system and is the ultimate destination or sink for both surface and ground water.

According to Cohen and Everett (1963), precipitation within the seven valley system is the source of virtually all of the surface and ground water in the system. The estimated average annual natural recharge to and discharge from the ground water reservoir in the entire seven valley system is on the order of 18,000 acre-feet. Precipitation within Dixie Valley accounts for about 40 percent of the average annual recharge. Recharge to the shallow ground water system from the Dixie Valley geothermal reservoir was not taken into account by Cohen and Everett.

For the ground water system, approximately 90 percent of the 18,000 acre-feet per year estimated perennial yield, is discharged by transpiration from phreatophytes and evaporation from bare soil within the Humboldt Salt Marsh.

Under Dixie Valley climatic conditions, evapotranspirative potential is approximately five feet of water per year, and is defined by the 3440 foot elevation contour line. This area is characterized by numerous seeps, springs, artesian wells, and large areas of exposed moist playa and standing water. The surface area contained within this contour is approximately 146 square miles so that evapotranspirative potential is approximately 467,000 acre-feet of water per year. The potential for discharge of fluid from the ground water system to the atmosphere is therefore about 26 times greater than the observed recharge to the basin. Because of the great imbalance between recharge to the system and potential for loss from the system, minor contributions of geothermal waters could be discharging into shallow aquifers without creating obvious hydrothermal surface manifestations such as prolific boiling springs.

Potentiometric Relationship Between Geothermal & Ground Water Systems

Elevation (feet)

8500

7500

6500

5500

4500

3500

2500

Zone of Recharge

Zone of Lateral Flow

Zone of Increasing Ground Water Potential

Zone of Active Ground Water Discharge

Stillwater Range

● Height to which water will rise in a well cased to its total depth

Regional Saturation

Ground Surface

Air-Water Interface

Humboldt Salt Marsh (elev. 3380')

Flow Lines

Geothermal System 3100'

Equipotential Lines

4700

4400

3800

3600

3500

3450

3425

100-110-111-112-113-114-115-116-117-118-119-120-121-122-123-124-125-126-127-128-129-130-131-132-133-134-135-136-137-138-139-140-141-142-143-144-145-146-147-148-149-150-151-152-153-154-155-156-157-158-159-160-161-162-163-164-165-166-167-168-169-170-171-172-173-174-175-176-177-178-179-180-181-182-183-184-185-186-187-188-189-190-191-192-193-194-195-196-197-198-199-200-201-202-203-204-205-206-207-208-209-210-211-212-213-214-215-216-217-218-219-220-221-222-223-224-225-226-227-228-229-230-231-232-233-234-235-236-237-238-239-240-241-242-243-244-245-246-247-248-249-250-251-252-253-254-255-256-257-258-259-260-261-262-263-264-265-266-267-268-269-270-271-272-273-274-275-276-277-278-279-280-281-282-283-284-285-286-287-288-289-290-291-292-293-294-295-296-297-298-299-300-301-302-303-304-305-306-307-308-309-310-311-312-313-314-315-316-317-318-319-320-321-322-323-324-325-326-327-328-329-330-331-332-333-334-335-336-337-338-339-340-341-342-343-344-345-346-347-348-349-350-351-352-353-354-355-356-357-358-359-360-361-362-363-364-365-366-367-368-369-370-371-372-373-374-375-376-377-378-379-380-381-382-383-384-385-386-387-388-389-390-391-392-393-394-395-396-397-398-399-400-401-402-403-404-405-406-407-408-409-410-411-412-413-414-415-416-417-418-419-420-421-422-423-424-425-426-427-428-429-430-431-432-433-434-435-436-437-438-439-440-441-442-443-444-445-446-447-448-449-450-451-452-453-454-455-456-457-458-459-460-461-462-463-464-465-466-467-468-469-470-471-472-473-474-475-476-477-478-479-480-481-482-483-484-485-486-487-488-489-490-491-492-493-494-495-496-497-498-499-500-501-502-503-504-505-506-507-508-509-510-511-512-513-514-515-516-517-518-519-520-521-522-523-524-525-526-527-528-529-530-531-532-533-534-535-536-537-538-539-540-541-542-543-544-545-546-547-548-549-550-551-552-553-554-555-556-557-558-559-560-561-562-563-564-565-566-567-568-569-570-571-572-573-574-575-576-577-578-579-580-581-582-583-584-585-586-587-588-589-590-591-592-593-594-595-596-597-598-599-600-601-602-603-604-605-606-607-608-609-610-611-612-613-614-615-616-617-618-619-620-621-622-623-624-625-626-627-628-629-630-631-632-633-634-635-636-637-638-639-640-641-642-643-644-645-646-647-648-649-650-651-652-653-654-655-656-657-658-659-660-661-662-663-664-665-666-667-668-669-670-671-672-673-674-675-676-677-678-679-680-681-682-683-684-685-686-687-688-689-690-691-692-693-694-695-696-697-698-699-700-701-702-703-704-705-706-707-708-709-710-711-712-713-714-715-716-717-718-719-720-721-722-723-724-725-726-727-728-729-730-731-732-733-734-735-736-737-738-739-740-741-742-743-744-745-746-747-748-749-750-751-752-753-754-755-756-757-758-759-760-761-762-763-764-765-766-767-768-769-770-771-772-773-774-775-776-777-778-779-780-781-782-783-784-785-786-787-788-789-790-791-792-793-794-795-796-797-798-799-800-801-802-803-804-805-806-807-808-809-810-811-812-813-814-815-816-817-818-819-820-821-822-823-824-825-826-827-828-829-830-831-832-833-834-835-836-837-838-839-840-841-842-843-844-845-846-847-848-849-850-851-852-853-854-855-856-857-858-859-860-861-862-863-864-865-866-867-868-869-870-871-872-873-874-875-876-877-878-879-880-881-882-883-884-885-886-887-888-889-890-891-892-893-894-895-896-897-898-899-900-901-902-903-904-905-906-907-908-909-910-911-912-913-914-915-916-917-918-919-920-921-922-923-924-925-926-927-928-929-930-931-932-933-934-935-936-937-938-939-940-941-942-943-944-945-946-947-948-949-950-951-952-953-954-955-956-957-958-959-960-961-962-963-964-965-966-967-968-969-970-971-972-973-974-975-976-977-978-979-980-981-982-983-984-985-986-987-988-989-990-991-992-993-994-995-996-997-998-999-1000

Potentiometric Relationship Between Hydrologic Systems – Thermal & Non-Thermal Northern Nevada

Elevation
(feet)

6000'

5000'

4000'

3000'

2000'

Cottonwood
Canyon

Cottonwood
Canyon

Soda Lake
4100'

Stillwater
3900'+

Humboldt Sink
3890'

Carson Sink
3870'

Dixie H.S.
3428'

DF 45-14
3400'+

DF 66-21
3415'+

Humboldt Salt Marsh
3380'

62-21
3480'+

SWL-3
3133'

Brinkerhoff Well
3450'

Hyder H.S.
3586'

Sou H.S.
3700'

Lamb Windmill
3428'

Lower Ranch H.S.
3960'

McCoy H.S.
3720'

Leach H.S.
4700'

Kyle H.S.
4500'

Beowawe
Hot Springs

General North, South Orientation

4.2 Deuterium and Oxygen Isotopes

The hydrologic system of the deep geothermal reservoir in Dixie Valley appears to have very limited interaction with the shallow ground water system. This limited interaction is indicated by isotope, chemical, and pressure data available from various aquifers within Dixie Valley.

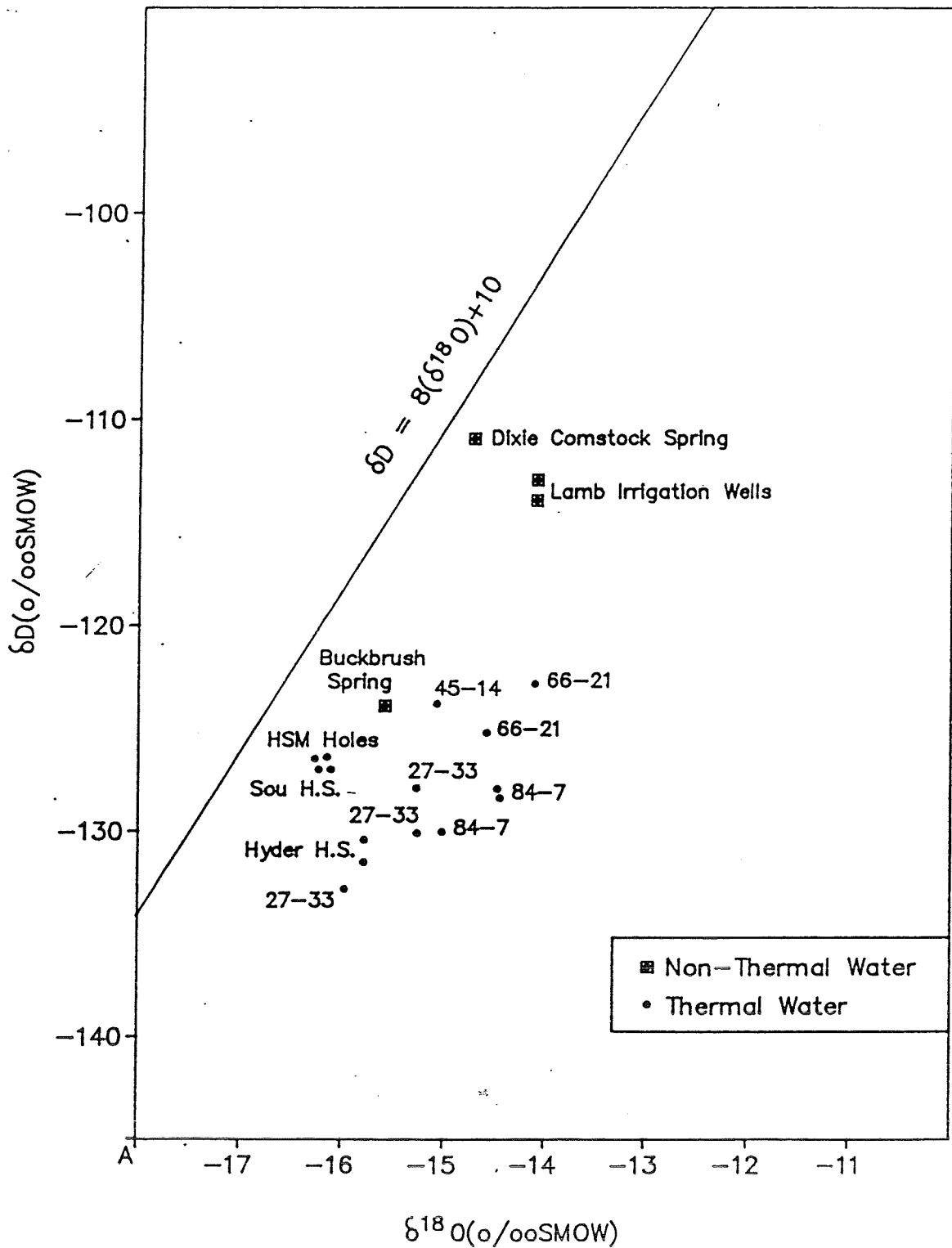
Deuterium and oxygen isotope data can be used to delineate, in a general manner, possible recharge zones and/or recharge mechanisms. Deuterium values for the deep geothermal system are very close to those of numerous surrounding hot springs (compare Figures 4.2.1 and 4.2.2). The deuterium values are centered around a value of -130 ‰ . Note that hot springs with similar deuterium value extend as far as the Beowawe geothermal system that is 90 miles northeast of the Dixie Valley reservoir.

The existence of similar deuterium values does not necessarily prove a common recharge zone for all of the geothermal systems exhibiting similar values. However, it does suggest that the recharge mechanisms in operation for the widely separated systems share common characteristics, resulting in similar deuterium values for the various geothermal waters.

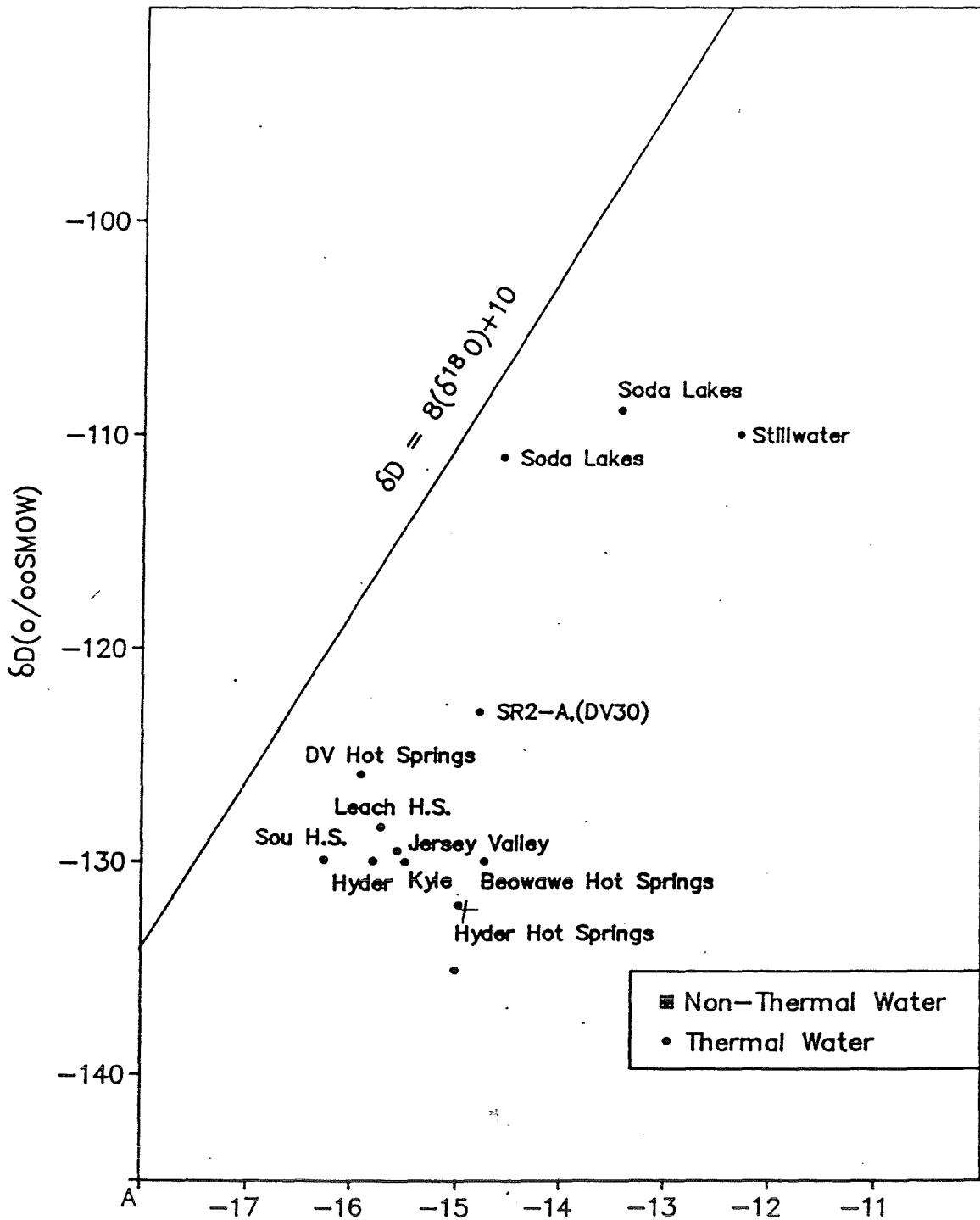
The geothermal fluids have consistently greater negative deuterium values (i.e., "lighter") than those for the nonthermal waters from the nearby eastern slope of the Stillwater Range or the Clan Alpine and Augusta Mountains (Figure 4.2.3). A similar isotopic relationship between thermal and nonthermal waters was observed by Welch *et al.* (1981) at the Leach Hot Springs in southern Grass Valley, 48 miles north of the Dixie Valley reservoir. Welch *et al.* (1981) suggest that this isotopic disparity either results from modern-day recharge from precipitation at an elevation higher than that in the immediate vicinity of the Leach Hot Springs or the present discharge was recharged during an earlier, colder climatic period.

Elevation zones where modern precipitation would have the same deuterium value as the Leach Hot Springs are so far away (100 miles) that under a flow rate of 30 feet/year, the infiltration event could have occurred up to 16,000 years ago and thus the recharge water still would be considered "paleowater" (Welch *et al.*, 1981). Young and Lewis (1980) suggest present-day discharge from the Bruneau-Grand View geothermal system in Idaho was recharged during late Pleistocene glacial advances when the climate averaged 6-10 deg. F colder than at present.

Dixie Valley Oxygen and Deuterium Isotope Values Thermal, Non-Thermal & Geothermal Wells



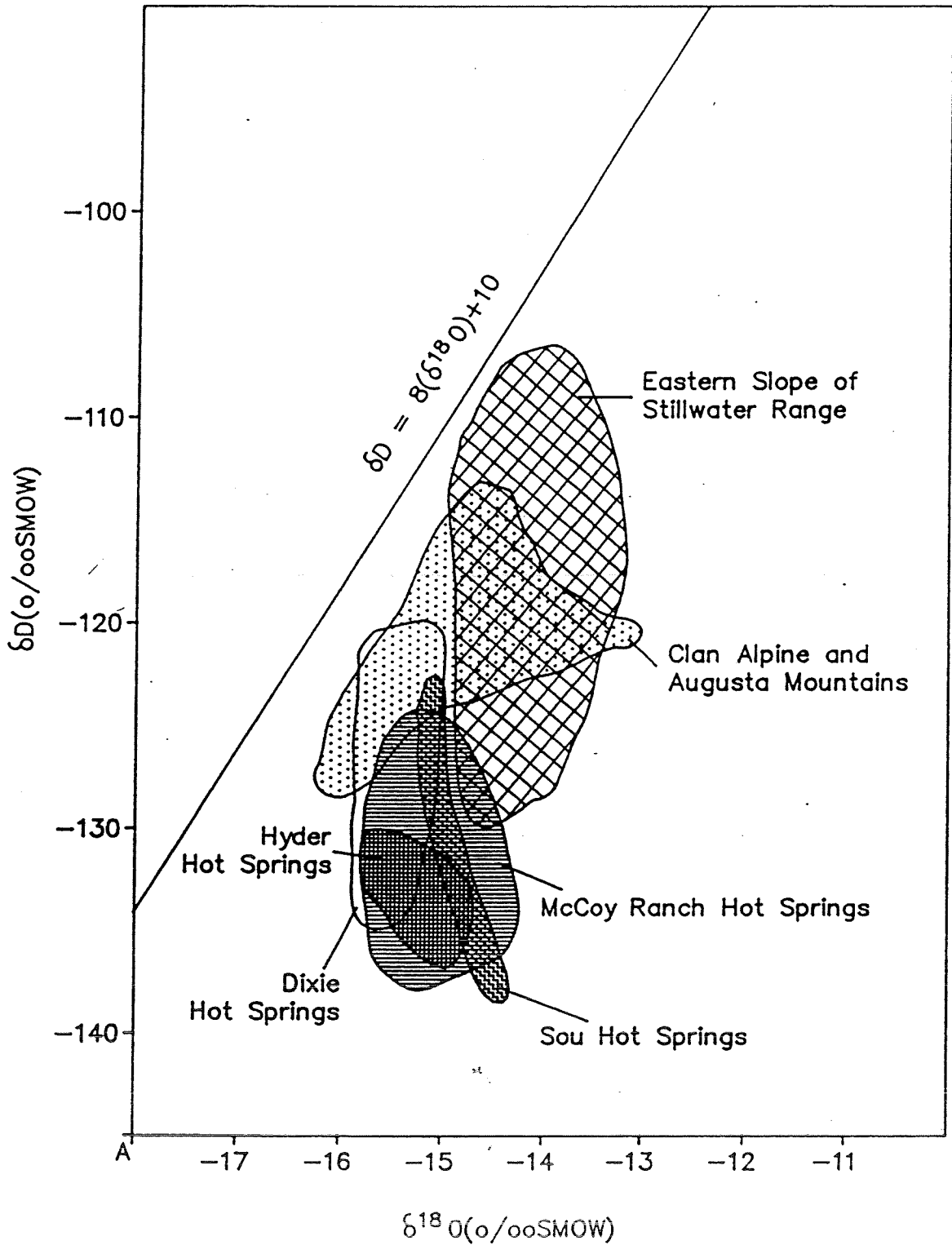
Regional Oxygen and Deuterium Isotope Values



$\delta^{18}O(\text{‰ SMOW})$

STRICTLY

Local Oxygen and Deuterium Isotope Values



The deep Dixie Valley geothermal system presents the same situation. The closest mountains significantly higher than the 8,000-9,000 foot heights of the Stillwater and Clan Alpine Ranges are in the Toiyabe Range, some 60 miles to the east. The climatologic influence may therefore be the dominant factor in creating the regional isotope characteristics, as at Bruneau-Grand View. Lower average temperatures during the late Pleistocene, when Lake Lahontan reached its maximum extent and abundant surface water was available for recharge of deep aquifers, may have resulted in the isotope characteristics of the thermal waters now observed throughout the region.

4.3 Carbon and Sulfur Isotopes

Geothermal well fluids, hot springs waters, and rock chip cuttings from geothermal production zones were analyzed for the $^{13}\text{C}/^{12}\text{C}$ and $^{34}\text{S}/^{32}\text{S}$ isotope ratios. A gas sample from well 27-33 was analyzed for ^{14}C , hydrogen/deuterium, and $^{15}\text{N}/^{14}\text{N}$ isotope analysis.

The stable isotopes of carbon and sulfur can be used in a general manner to delineate separate or common subsurface flow systems, much in the same manner as the hydrogen/deuterium and $^{18}\text{O}/^{16}\text{O}$ isotope data.

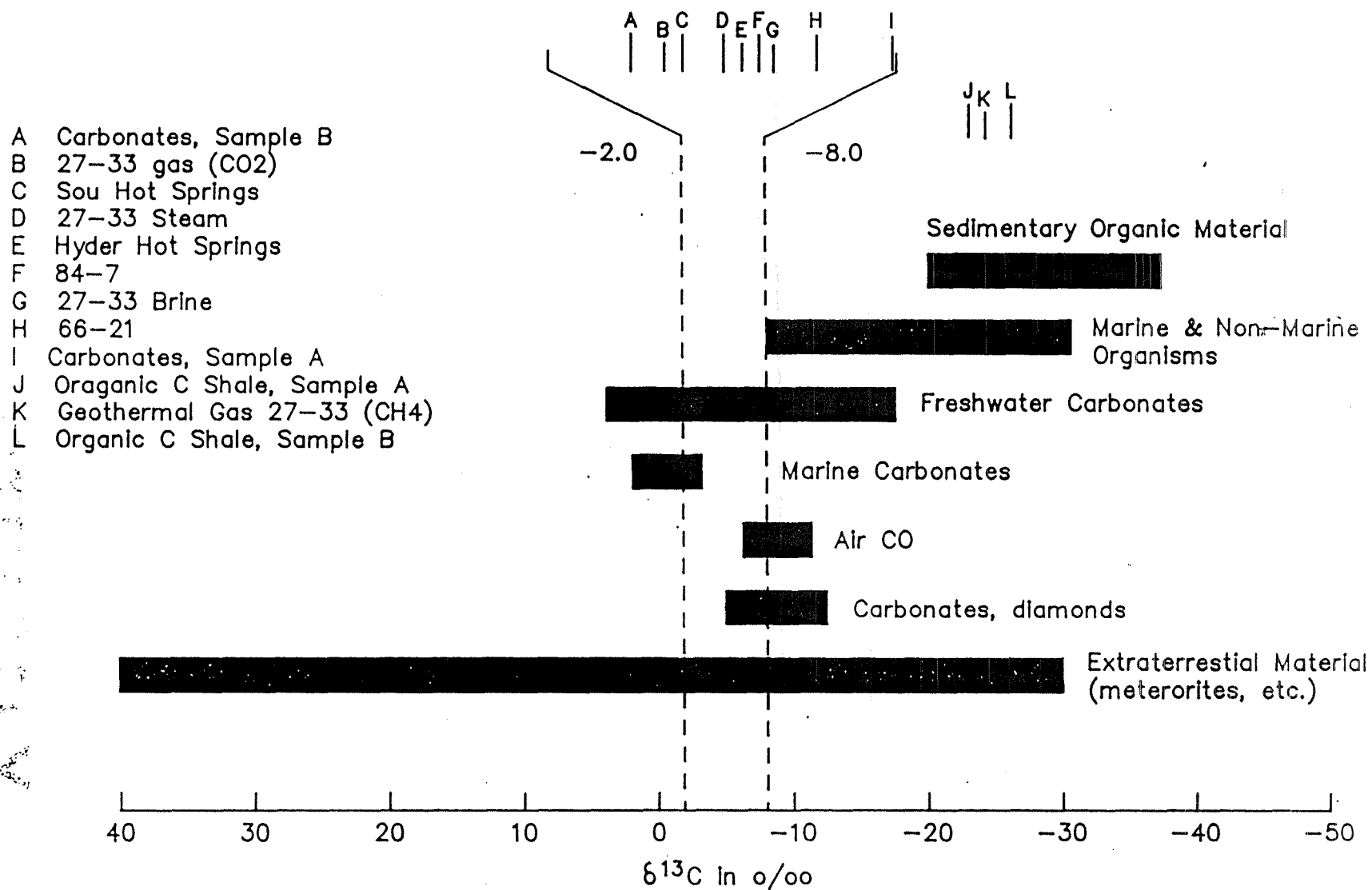
As with the hydrogen/deuterium data, the carbon and sulfur isotope data suggest, in a very broad manner, a common flow path, in part, between the Hyder and Sou Hot Springs and the deep high temperature geothermal system in Dixie Valley. A regional flow system can be inferred from the data but the volumetric extent of such a system remains unquantified.

Carbon Isotope Data

The $^{13}\text{C}/^{12}\text{C}$ ratios for the carbonate ions in the geothermal fluids from the deep geothermal wells and the hot springs show a tight clustering around a ^{13}C value of -5.0 ‰ (Fig. 4.3.1) The absolute difference between geothermal wells 27-33 and 84-7 and the Sou and Hyder Hot Springs is less than 2.0 ‰. With well 66-21 included, the absolute difference is still less than 3.0 ‰. Thus, like the similarity of the deuterium values, the similarity of the carbon isotope values suggests a common factor between the high- and low-temperature geothermal systems in northern Dixie Valley.

Two rock chip samples (A and B) were analyzed for their carbon and sulfur isotope ratios. The samples consisted of shale cuttings from the Favret Formation from wells 62-21

$^{13}\text{C}/^{12}\text{C}$ Ratios for Geothermal Wells & Hot Springs Compared to Ratios in Geologically Important Materials



and 45-33 (Al Waibel, personal communication). Sample B with a ^{13}C value of -3.4 ‰ and Sample A with a ^{13}C value of -7.9 ‰ completely bracket the carbon isotope values for the sampled geothermal fluids (Fig. 4.3.1). A possible conclusion is that both the high and low-temperature geothermal systems have reached a carbon isotopic equilibrium with the carbonate minerals in the Favret Formation.

Carbon isotopes were determined from carbon dioxide (CO_2) and methane (CH_4) from well 27-33. For the CO_2 the ^{13}C value is -4.0 ‰. This is within the values measured from the liquid phase and indicates a CO_2 (gas)/ HCO_3 (liquid) equilibrium.

The CO_2 gas from well 27-33 also was analyzed for a ^{14}C age determination. The activity level of the ^{14}C was below the detection limit of 1.2% of the standard activity. The age is therefore greater than 35,700 ^{14}C years before present (Geochem Laboratories Division of Krueger Enterprises Inc., rpt. of 6/9/86).

The ^{13}C value for the CO_2 gas radiometrically dated was -4.1 ‰, almost identical to the ^{13}C value of -4.0 ‰ previously mentioned. These values are close enough to the ^{13}C values from the liquid phase to be considered representative of the unflushed geothermal fluid.

Carbon in the methane gas has a ^{13}C value of -23.8 ‰. This is very close to and bracketed by the values for organic carbon in the Favret Formation shale cuttings. Samples A and B had ^{13}C values of -25.4 ‰ and -22.8 ‰ respectively. This suggests the methane is a product of the thermal maturation of organic carbon in the Favret Formation.

The similar ^{13}C values for both the deep high-temperature fluids and the hot springs fluids suggest a similar source environment for fluids from both systems. This is consistent with the deuterium values for the two systems as discussed above. The similarity suggests a common regional factor which may be the Favret Formation where the ^{13}C values for two geothermal production zone cuttings narrowly bracket the ^{13}C values for geothermal fluids from both the deep high-temperature system and the hot springs. Such a concurrence may result from the deep geothermal system and the hot spring fluids coming into ^{13}C isotopic equilibrium with that of the Favret Formation during their subsurface circulation.

Sulfur Isotope Data

The sulfur isotope data are presented in Figure 4.3.2. Once again there is a tight grouping of isotope values for both the deep geothermal system and the hot springs. Well 27-33 is the "heaviest" with a ^{34}S value of +20.6 ‰. The other geothermal fluids are clustered around a ^{34}S value of +15 ‰.

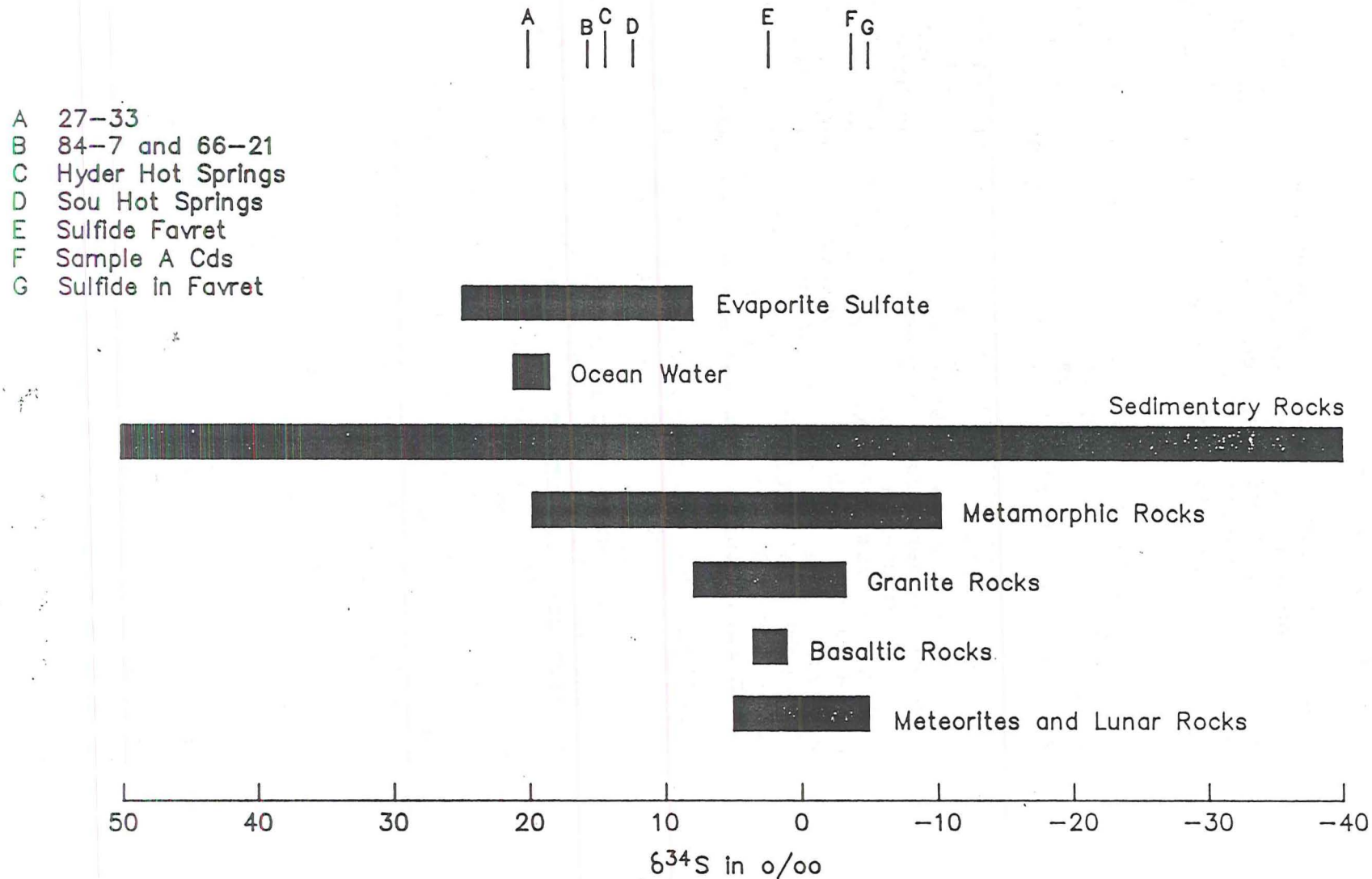
Sulfides from the Favret shale cuttings were analyzed for their ^{34}S . These samples are significantly depleted in ^{34}S relative to the fluid samples. The sulfides have ^{34}S values ranging between +3.4 ‰ and -2.3 ‰.

The difference between fluid and mineral ^{34}S isotopic values may be related to temperature-dependent fractionation processes. Hoefs (1980) reviewed the literature and noted several papers that suggested that at high temperatures isotopic exchange should lead to sulfides being depleted in ^{34}S up to 75% relative to sulfates. The Dixie Valley data agree with such a temperature-dependent fractionation process. The ^{34}S isotope values for the sulfide minerals in the geothermal production zones are from 12% to 23% lighter than the ^{34}S values from the sulfate ions in the deep geothermal fluids from wells 27-33 and 84-7.

Note that the relative difference between ^{34}S values for the sulfide minerals and those for the sulfate minerals in geothermal fluids decreases directly as the predicted maximum subsurface temperatures decrease. The maximum difference is found in 27-33 where the maximum predicted temperature is 459 F by both the quartz and the Na/K geothermometers (Table 5.2). Sou Hot Springs, with the smallest relative difference, 11%, has a maximum predicted geothermal temperature of only 237 deg.F. No sulfide minerals from the Sou Hot Springs deposits have been analyzed for their ^{34}S values. If there were subsurface mixing between thermal and non-thermal waters this could possibly alter the isotope ratios.

Although the sulfur isotope data are not as amenable to interpretation as the carbon isotope data, a generalized interpretation is consistent with that given for the carbon isotope data. Where the higher temperature fluids are in contact with sulfide-bearing minerals, the sulfide minerals are depleted in ^{34}S relative to the ^{34}S isotope in the sulfate ions of the geothermal fluids. Lesser differences are noted between the sulfide minerals and the lower temperature hot spring fluids. Such relationships can exist if the hot spring fluids have circulated through the same

$^{34}\text{S}/^{32}\text{S}$ Ratios for Geothermal Wells & Hot Springs Compared to Ratios in Geologically Important Materials



sulfide-bearing Favret Formation shale but at lower temperatures than the deep high-temperature geothermal fluids. *- great uncertainty*

Based on the isotopic data, it is possible to conclude that the potential recharge area for the deep geothermal system in Dixie Valley is regional in extent. In theory, any body of water in northern Nevada has the hydraulic potential to recharge the geothermal system. Ongoing tectonic activity is capable of maintaining deep, permeable flow paths for recharge.

Isotope data suggest a long-lasting system with present discharge having been recharged at least 35,000 years ago. Source rock for transport and storage of the recharge fluid may be early Mesozoic carbonates and shales which extend over thousands of square miles in west-central Nevada. Isotopic patterns of recharge correspond well with the regional hydrologic setting of the geothermal system as described below.

4.4 Deep Temperature Profiles

49-18
 Static temperature profiles for the production wells (Figures 4.4.1-4.4.11) are characteristic of conductive heat flow from the producing fractures at depths of 7000 to 10,000 feet up to the surface. Only the section 18 wells have convecting zones and these are the producing zones near the bottom of the wells.

45-33
 Thermal gradients for all the productive wells with the exception of 45-33 are tightly grouped around the average gradient of 4.7 deg.F/100 feet (Fig 4.4.12). Well 45-33 has a significantly lower conductive gradient of 4.2 deg.F/100 feet in the vertical portion of the hole to a depth of 7530 feet. The vertical open-hole leg of this well encountered very low fracture permeability in the range-front fault fracture system in contrast to other production wells. The low thermal gradient is consistent with the drilling results and indicates that the wellhead location is over a part of the range-front fault which is effectively sealed and does not contain an active hydrothermal system. Production from 45-33 is encountered in the deviated open hole at a horizontal distance of 1600 feet southwestward from the surface location at a depth of approximately 9500 feet (Fig. 2.2).

The absence of significant changes in slope, reversals, and isothermal intervals in the production well temperature profiles indicates that no major outflow zones exist below a

Temperature/Pressure Survey

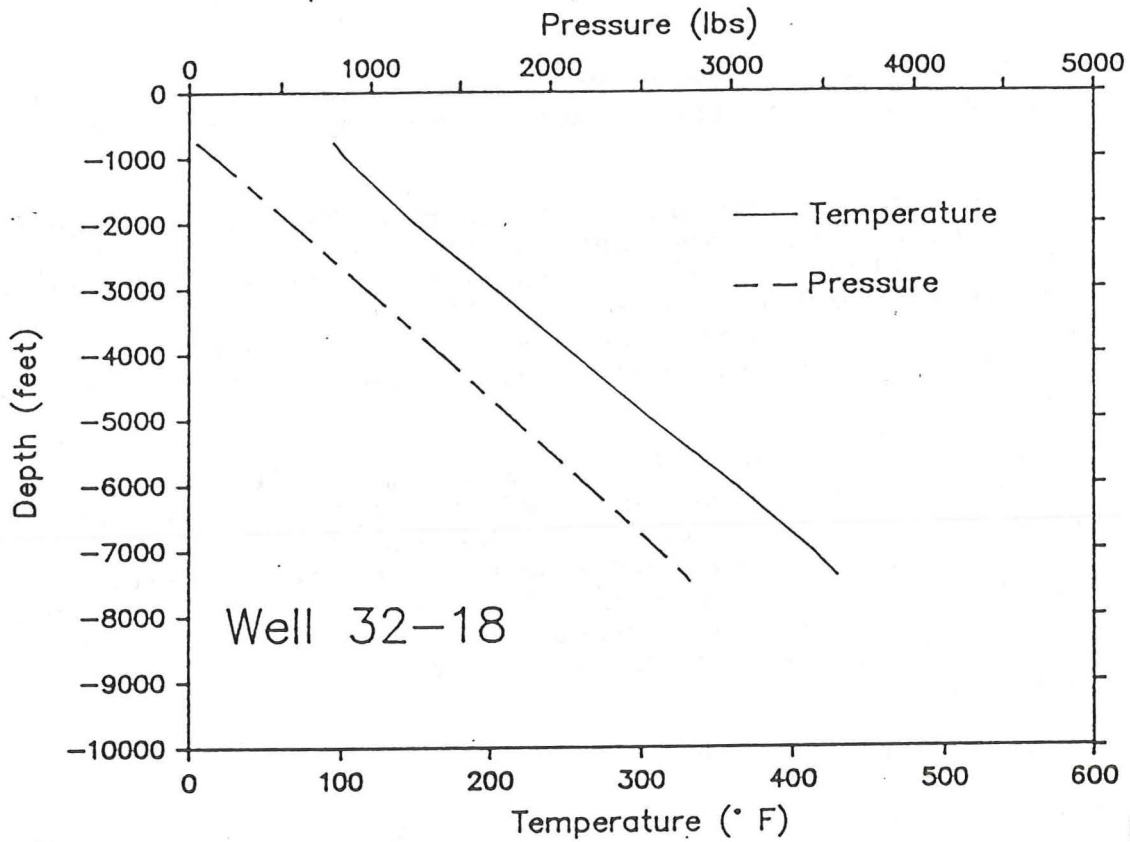


Figure 4.4.1

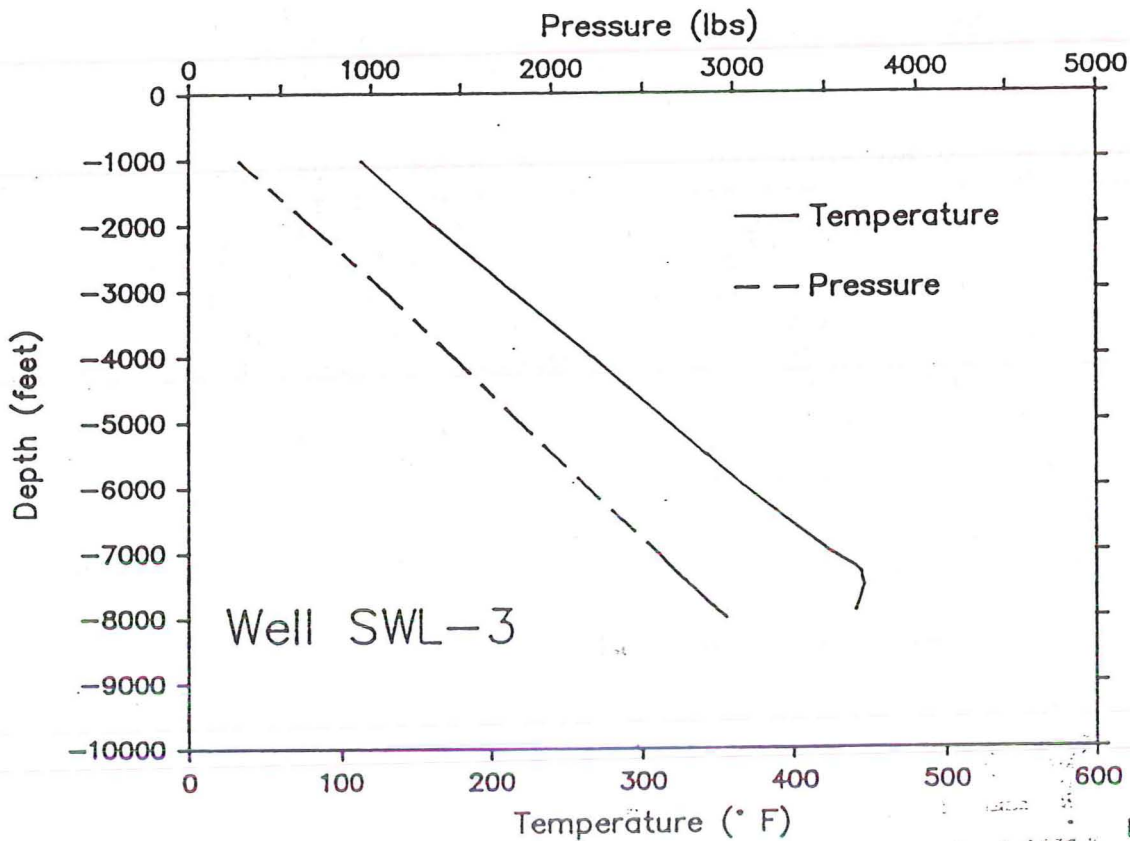


Figure 4.4.2

Temperature/Pressure Survey

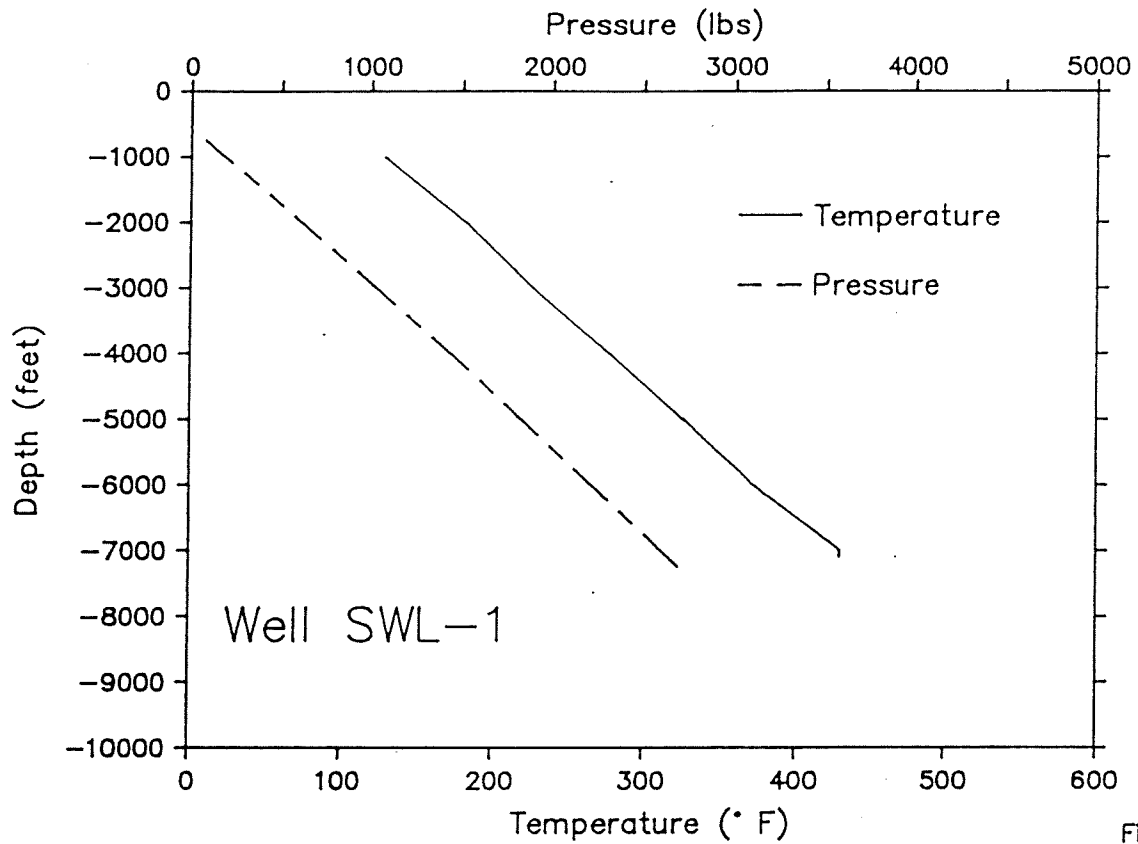


Figure 4.4.3

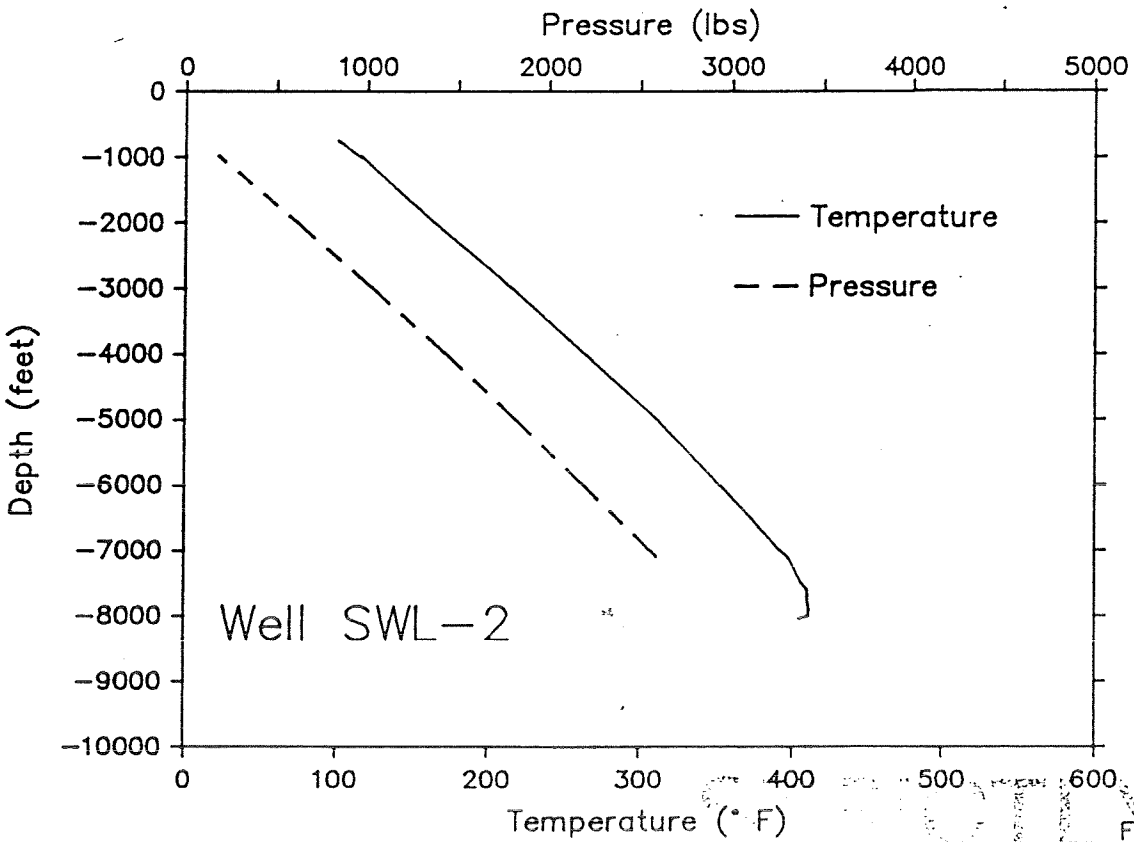


Figure 4.4.4

Temperature/Pressure Survey

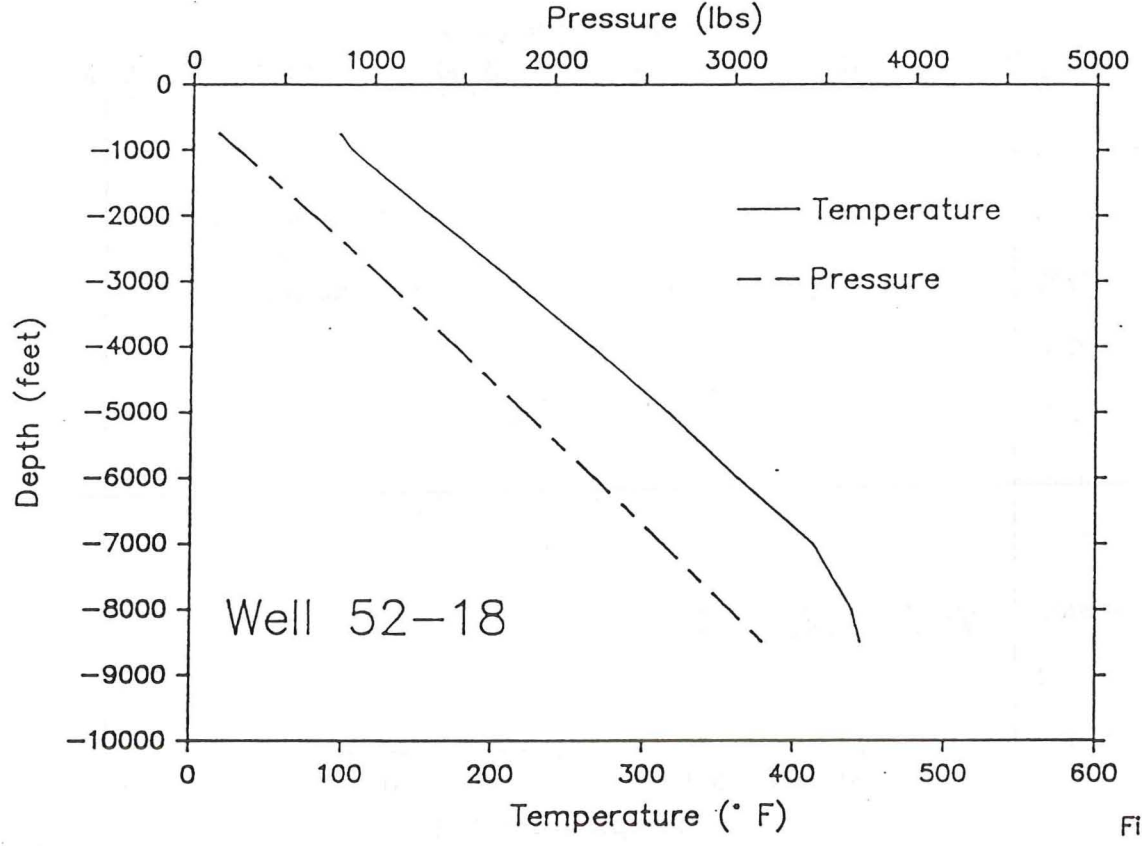


Figure 4.4.5

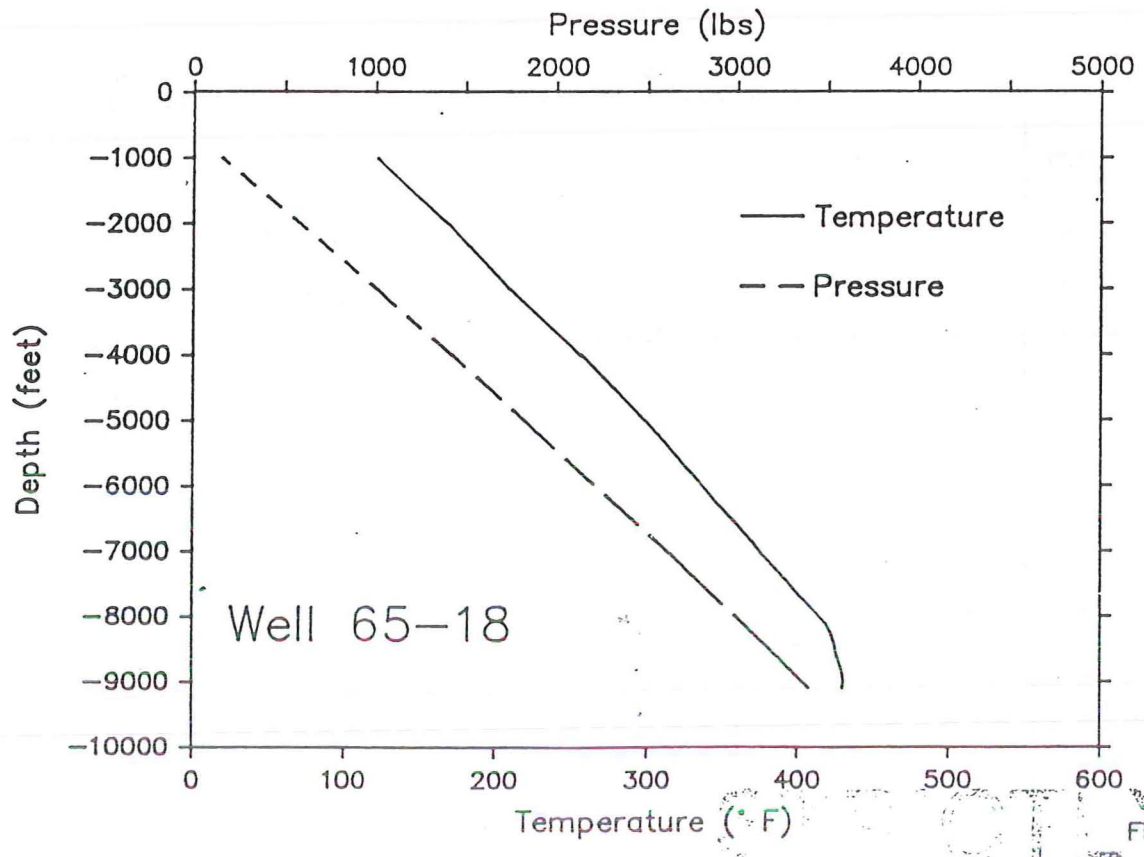


Figure 4.4.6

Temperature/Pressure Survey

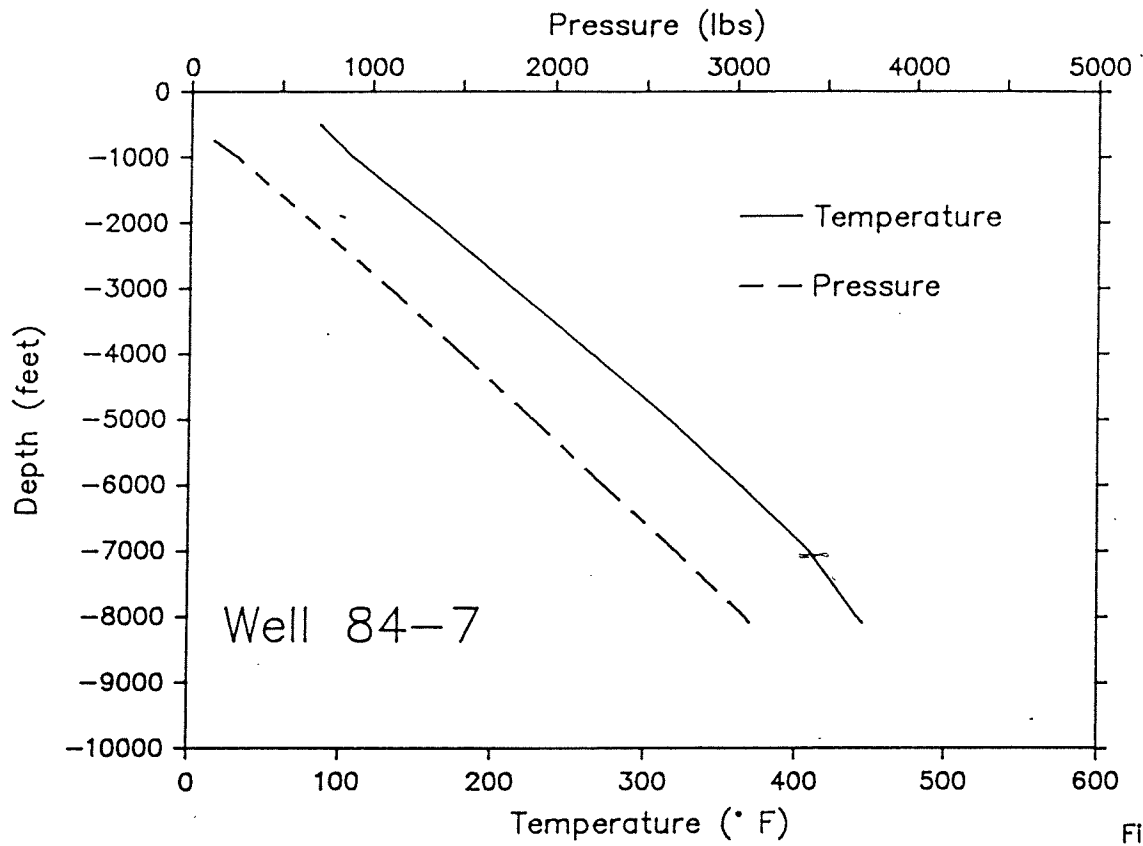


Figure 4.4.7

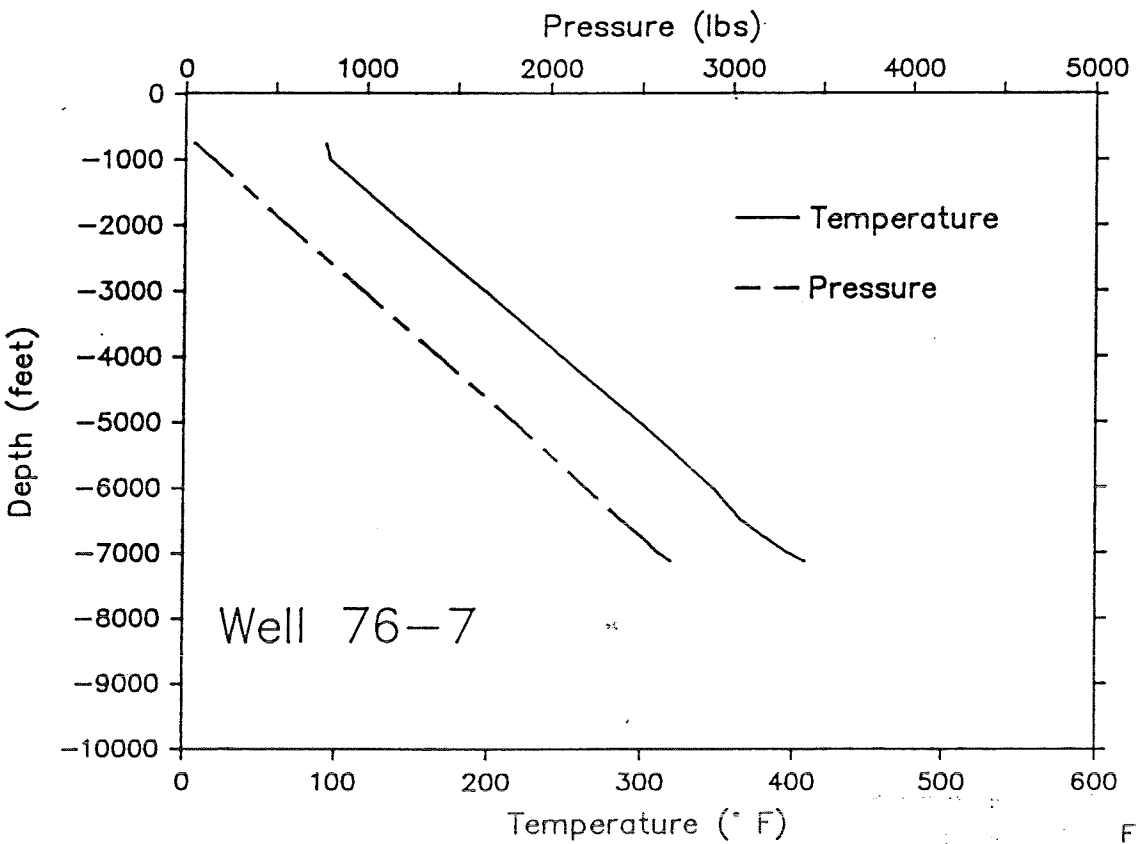


Figure 4.4.8

Temperature/Pressure Survey

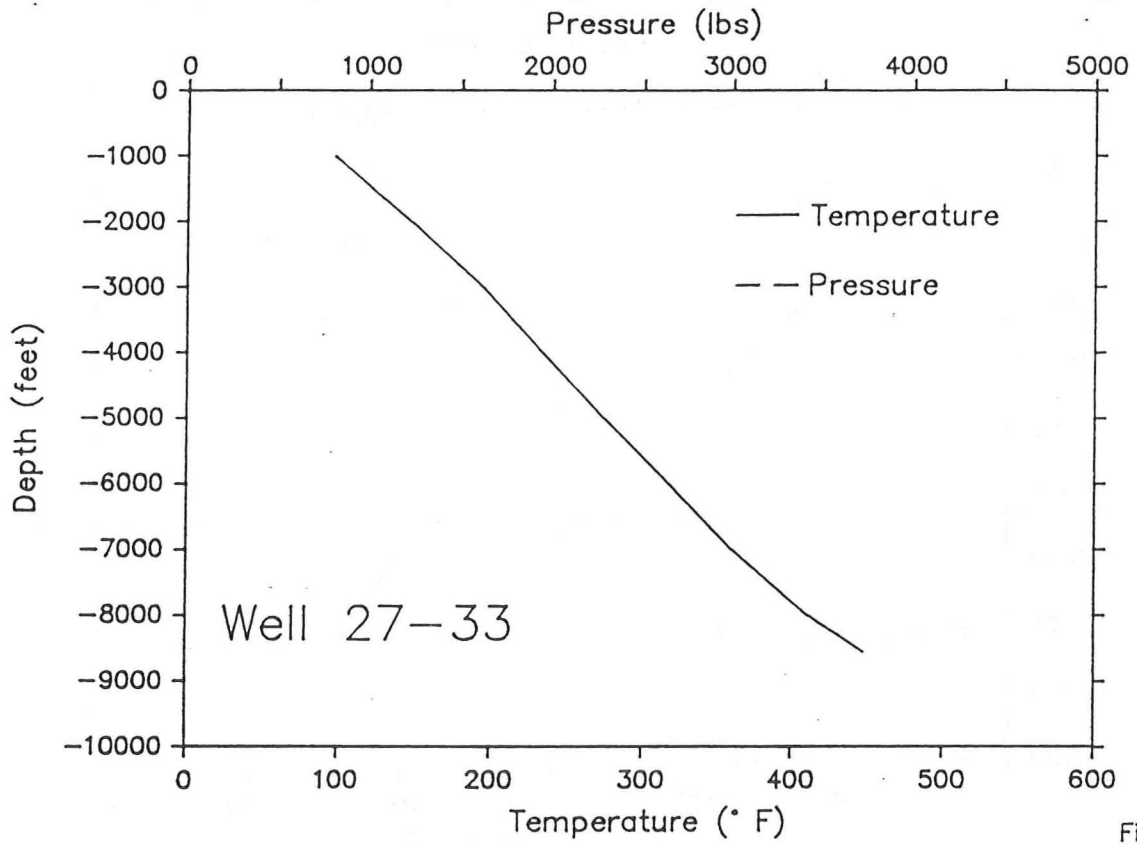


Figure 4.4.9

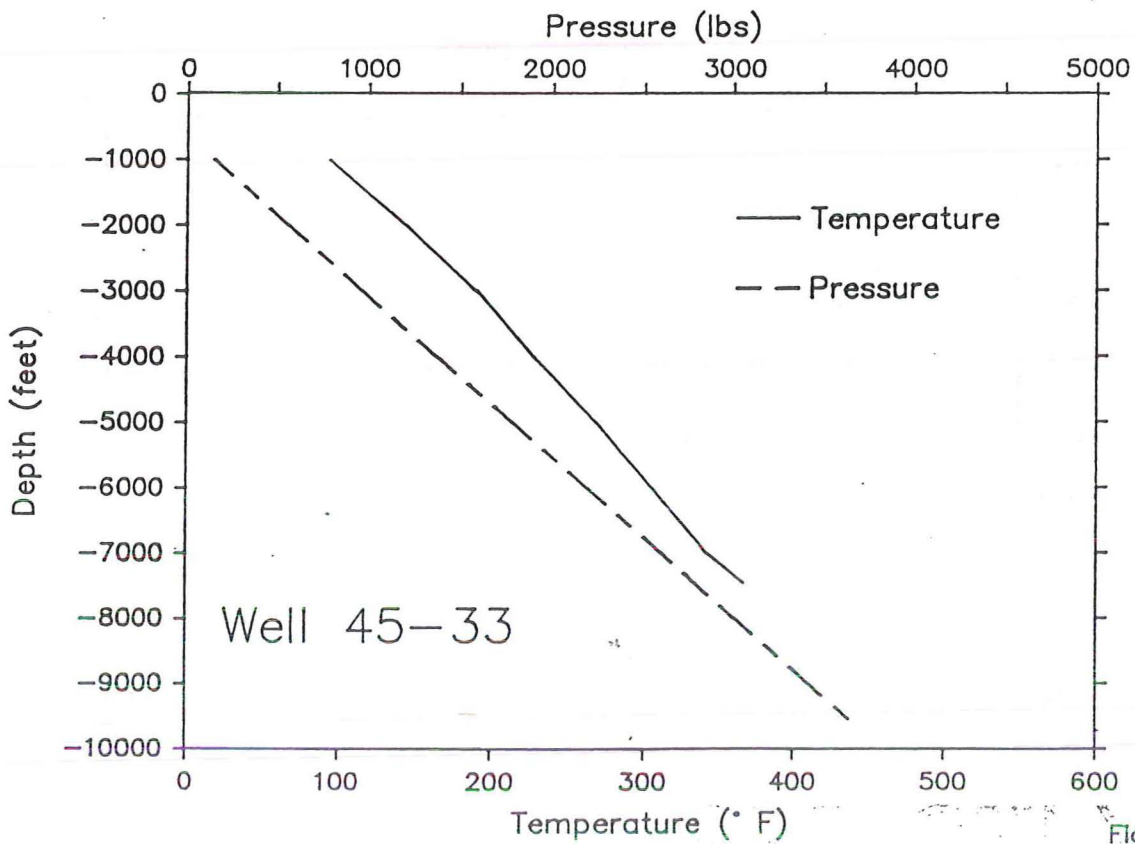
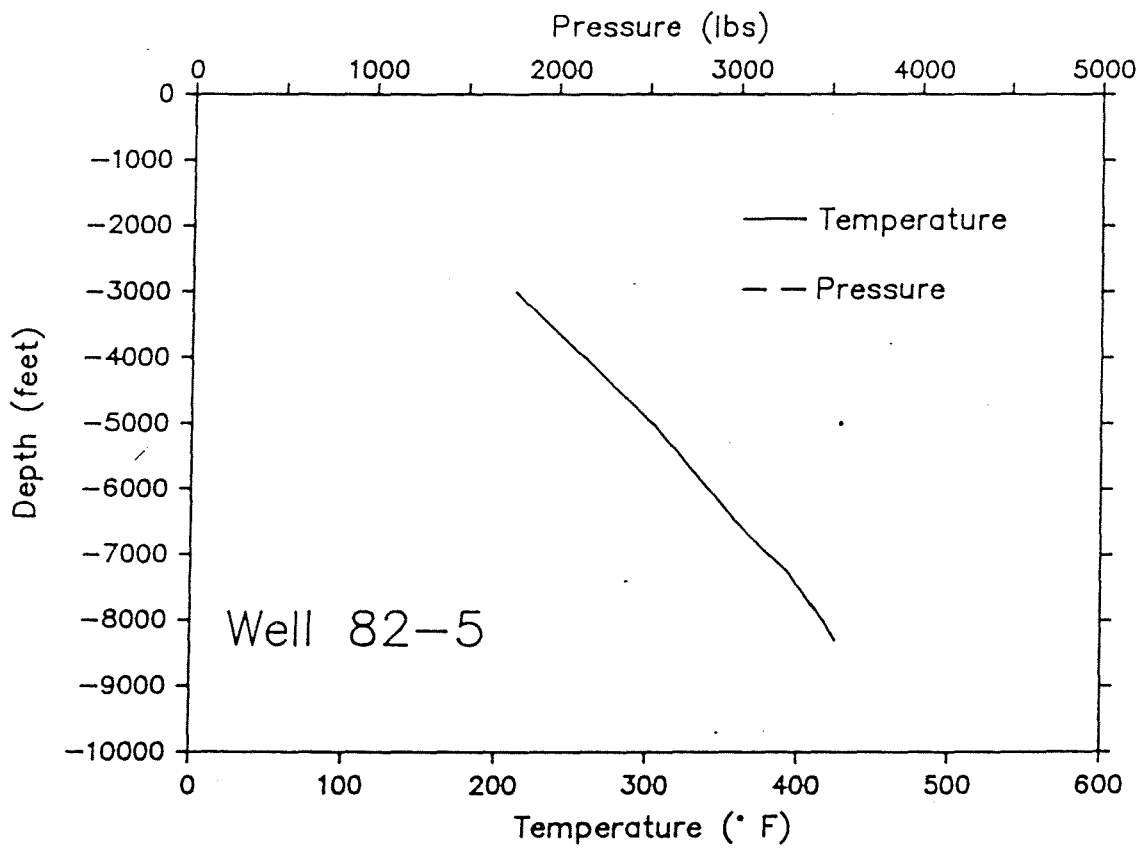
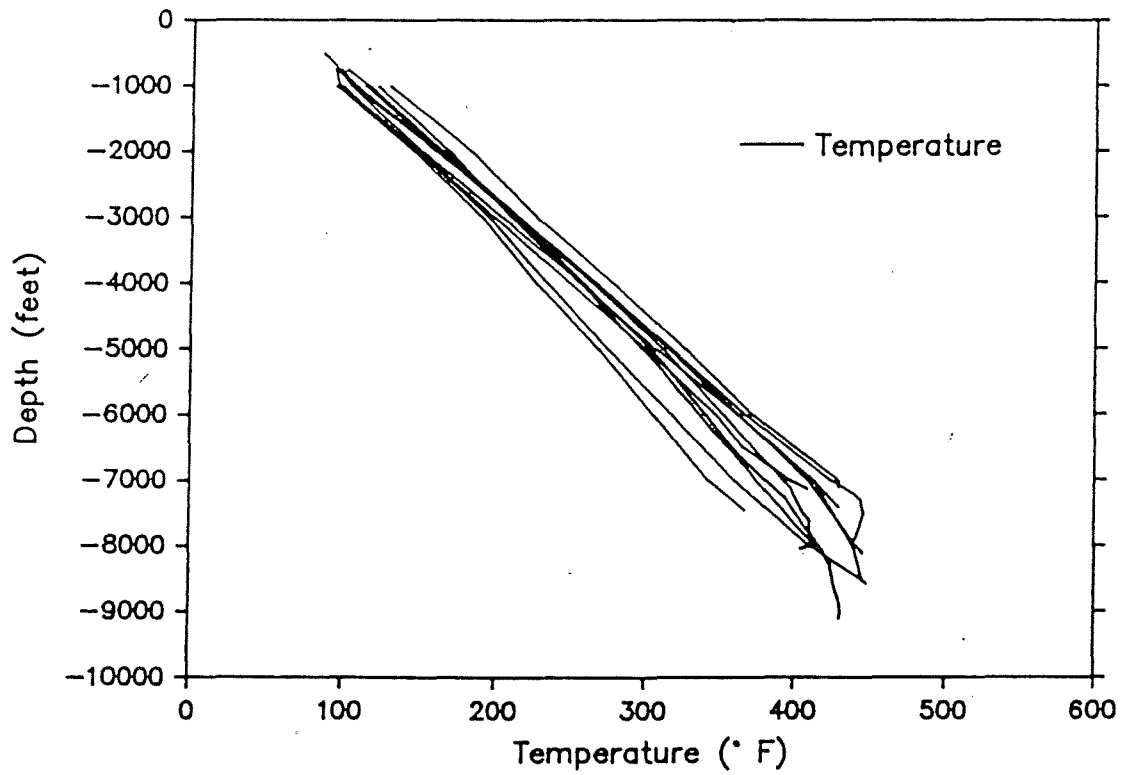


Figure 4.4.10

Temperature/Pressure Survey



Temperature Survey Section 18, 7, 5, and 33 Wells



depth of 1000 feet that would allow significant hot fluid transport away from the range-front fault. This observation is consistent with the lack of fluid entries during air drilling and the absence of fluid loss during mud drilling through several thousand feet of Quaternary-Tertiary sediments and volcanoclastics.

4.5 Deep Hydrostatic Pressure Distribution

The regional distribution of hydrostatic pressure at a depth of 5000 feet below mean sea level (MSL) is shown in Figure 4.5. Static pressure profiles for production wells are shown in Figure 4.4.1-4.4.11. Static reservoir pressures within the high temperature production zones of the Dixie Valley reservoir range from 3130 to 3160 psi. Wells 62-21 and 66-21, which lie 3-5 miles away from the productive part of the field, have pressures at the -5000 foot MSL datum of 3631 and 3440 psi respectively. Geothermal production wells to the west of the Stillwater Range in and around the Carson Sink have pressures within the range of 62-21 and 66-21 (Figure 4.5). This indicates that the deep geothermal waters outside the highly permeable Dixie Valley production zones are in regional pressure equilibrium over an area of several thousand square miles.

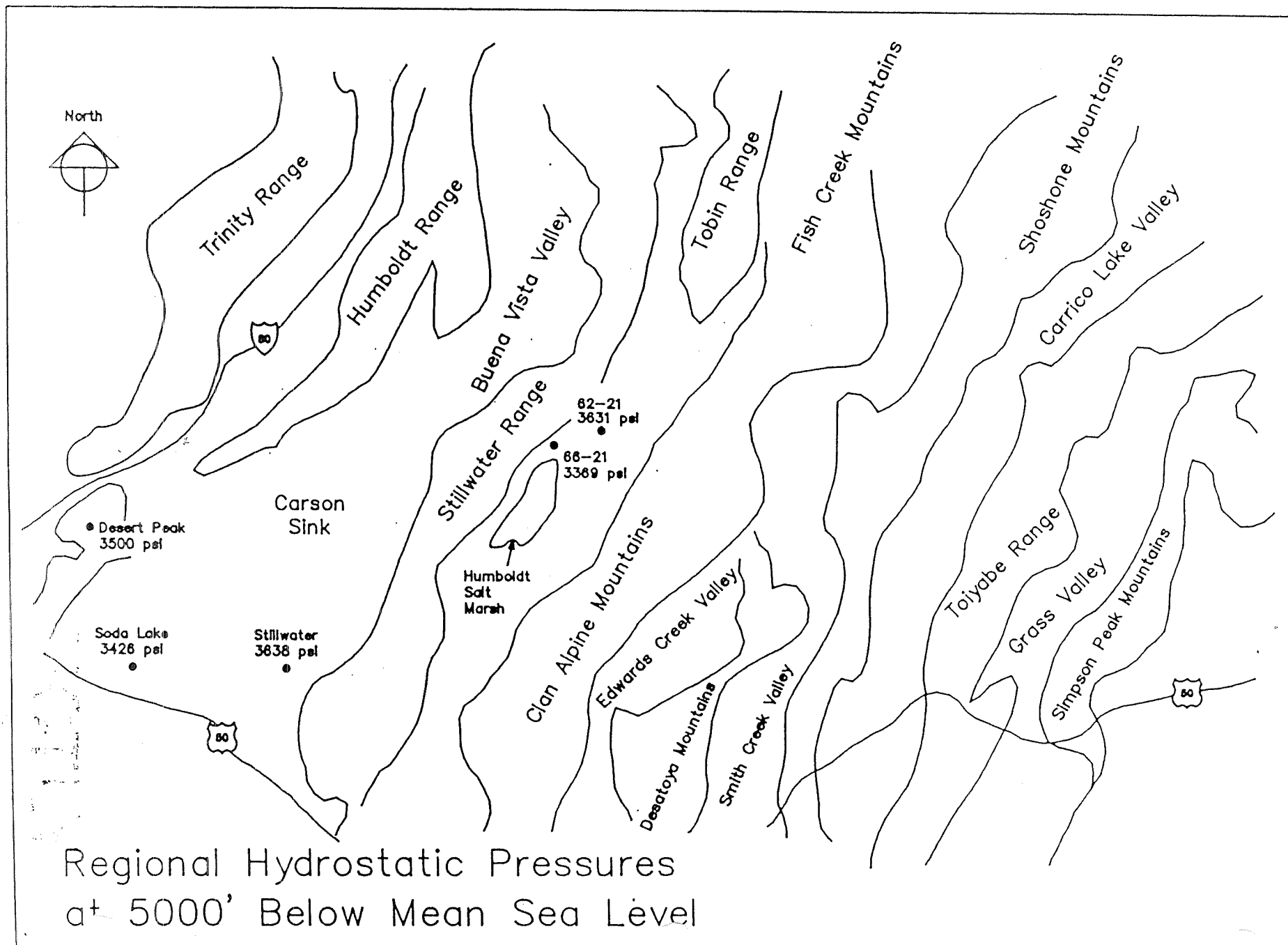
The static temperature gradients observed in 62-21 and deep wells drilled in the Carson Sink area range from 2.7 to 3.0 deg.F/100 feet. Water stored below a depth of 14,000 feet below MSL will obtain a temperature of 480 deg.F which is characteristic of the high-temperature fluid produced from the Dixie Valley reservoir. The regional geologic cross section (Fig 3.1) shows that much of the Triassic-Jurassic marine sedimentary section in west-central Nevada lies at a depth below the 480 deg.F isotherm.

Non-thermal groundwater as observed in irrigation wells in the vicinity of the geothermal reservoir has a projected hydrostatic pressure of 3621 psi at the -5000 foot datum which indicates that the shallow groundwater aquifers are in hydrostatic equilibrium with the deep aquifers penetrated in 62-21 and by wells in the Carson Sink.

The regional and local pressure data therefore demonstrate that the high-temperature production zones of the Dixie Valley reservoir have pressures 300 to 500 psi below the regional and shallow groundwater pressures extrapolated to production depths.

Pressure - hydro head

hi T, low P



4.6 Thermo-artesian Pressure Gradients

Penetration of geothermal fluid with an initial temperature of 480 deg.F to shallow depths along the range-front fault fracture system can create significant pressure gradients between fluid in the fracture system and fluid in the surrounding aquifers. This mechanism for developing a local horizontal pressure differential is shown graphically in Figure 4.6. Temperatures in excess of 400 deg. F. measured in well 45-5 at a depth of 5700 feet and near-surface boiling water that supplies steam to Senator Fumarole demonstrate that high-temperature fluid does penetrate to the near-surface along the range front fault.

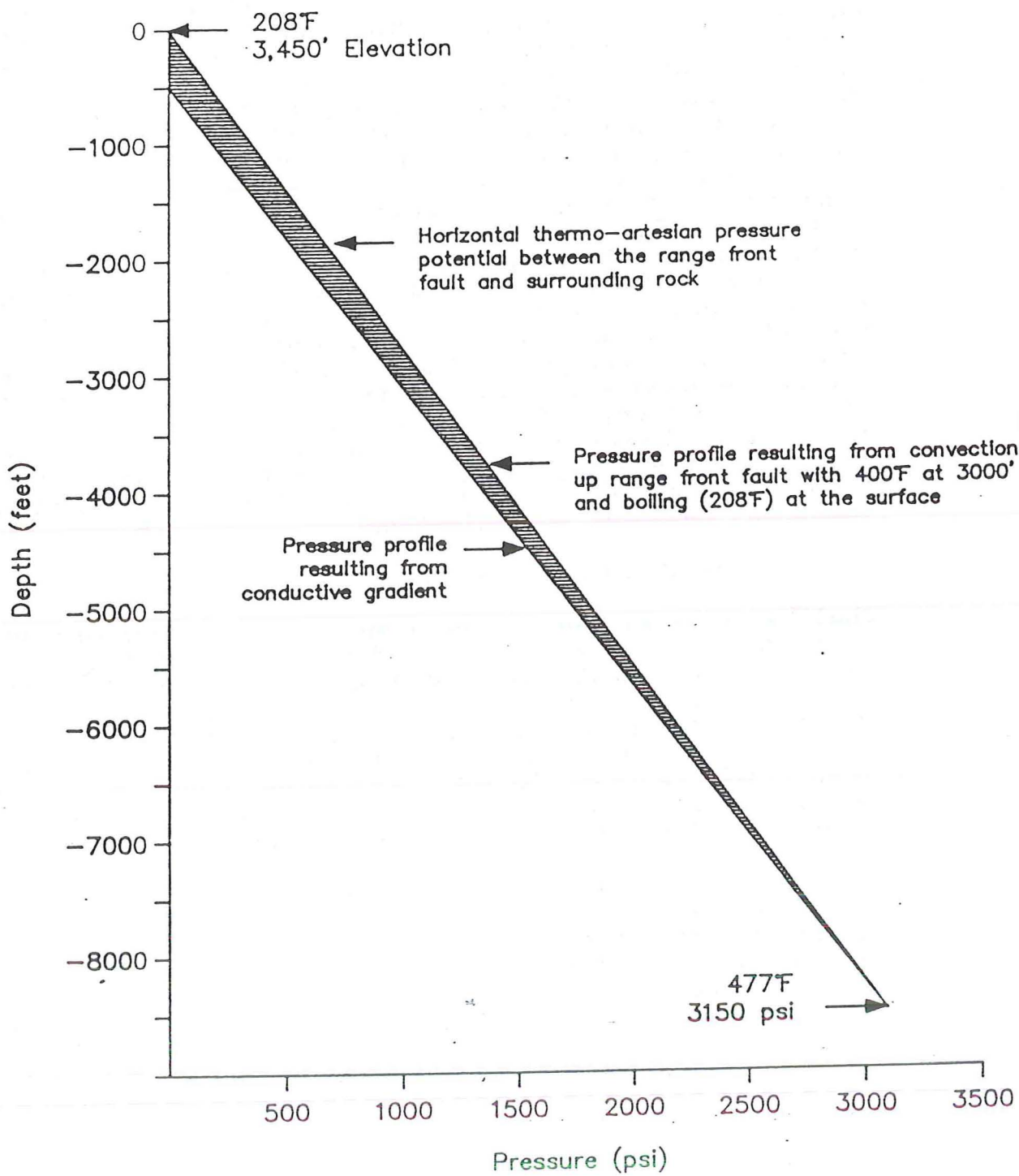
Penetration of high temperature to shallow depths creates higher pressures within the range-front fracture system in comparison to the surrounding cooler aquifers despite the low reservoir pressure feeding the fractures from below. Because these pressures exceed the local groundwater hydrostatic pressures at all depths above the reservoir (Fig. 4.6), water penetrates from the fracture system into the surrounding aquifers. Evidence for this outflow is seen in the chemistry of shallow warm aquifers overlying the reservoir. Elevated levels of K, Si, B, Li, Sr, NH⁺, Cl, and F clearly show mixing of high-enthalpy fluid from the high temperature reservoir with shallow ground water (Johnson, personal communication).

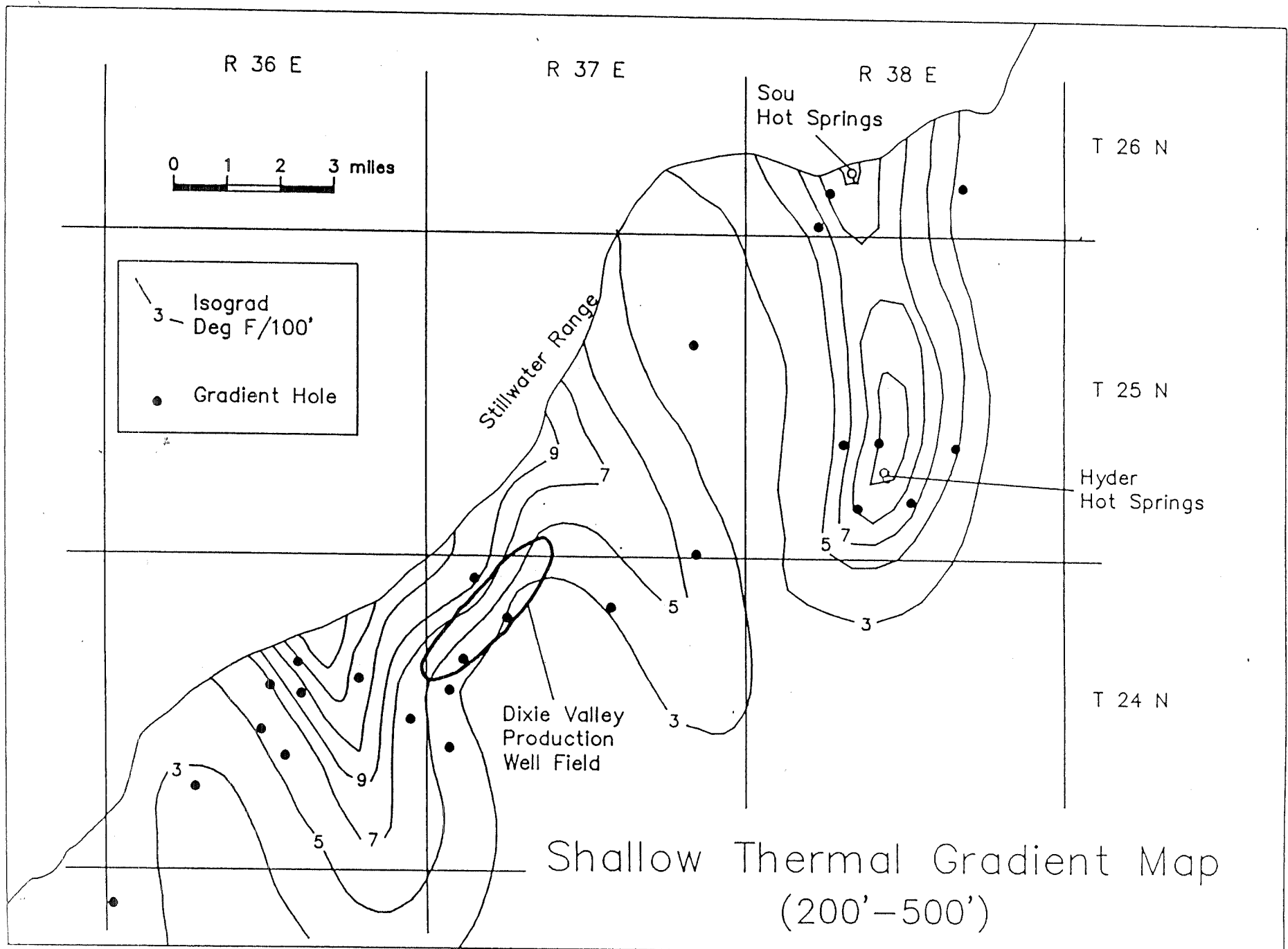
water table

4.7 Shallow Thermal Anomalies

Shallow thermal anomalies overlying and surrounding the Dixie Valley reservoir are evidence for hot water discharge from the deep geothermal system into the shallow alluvial aquifers. Heat flow anomalies that may represent leakage of fluid from the deep reservoir are defined by the 4 deg.F/100 isograd measured to a depth of 500 feet as shown in Fig. 4.7. The anomaly which surrounds the Dixie Valley geothermal reservoir exhibits two southeast trending lobes with a total surface area of approximately 39 square miles. A separate anomaly associated with Sou and Hyder Hot Springs trends southward from the Sou Hills and has an areal extent of approximately 28 square miles. The combined area of these shallow anomalies is similar to other commercial geothermal reservoirs in Nevada though it may be of lower overall intensity. Desert Peak exhibits a heat flow anomaly of approximately 75 square miles contained within the 4 deg.F/100 feet isograd. The Stillwater anomaly has an area of 54 square miles within the 4 deg.F/100 feet isograd.

Mechanism for Development of Thermo-Artesian Pressure in the Dixie Valley Reservoir





Morgan (1982) has calculated that the geothermal recharge to the Stillwater system is approximately 55 kg/sec. Approximately 2/3 of the heat contribution from this recharge is lost due to shallow (<2000 feet) subsurface flow and only 1/3 is lost due to conduction. Chemistry of the shallow thermal discharge zones in Stillwater is identical to that of the deep reservoir recharging the system. A major temperature reversal in the 900 to 1500 foot depth range is observed in all the Stillwater production wells. This discharge plume, defined both chemically and thermally, confirms Morgan's assertion that most of the heat loss from the system is due to shallow subsurface flow of reservoir fluid as opposed to conductive heat loss. The shallow thermal water in Dixie Valley, by contrast, contains only a small component of reservoir fluid which is estimated by Johnson (1986, personal communication) to be on the order of 5%. These shallow thermal waters must therefore acquire most of the observed heat through conductive heat contribution from the reservoir. The small chemical component of reservoir fluid in the shallow thermal water and lack of reversals or isothermal temperature profiles verify that the contribution of reservoir fluid to the shallow ground water system must be very small. Because the Dixie Valley near-surface thermal anomaly is primarily conductive, the actual throughput of reservoir fluid may only be a small fraction of the 55 kg/sec flow calculated for the Stillwater anomaly though it is of similar areal extent.

The Sou-Hyder thermal anomaly appears to be separated from the anomaly centered around the Lamb Ranch by a north-south trending strip of low heat flow one to three miles wide. However, stratigraphic continuity between the deep reservoir and the Sou-Hyder anomaly may provide a conduit for supplying water to the hot springs and surrounding area. Permeable Tertiary volcanic rocks that contain water at temperatures above 400 deg.F within the reservoir form a continuous pathway for hot fluids to migrate up-dip to the eastern and northern margins of the valley. These Tertiary volcanic and volcanoclastic units are located at a depth of 6000 to 8000 feet within the reservoir. The units are tilted upward to the east and surface close to Sou and Hyder Hot Springs. Southwest-dipping step faults with tens to hundreds of feet of displacement in the Tertiary volcanic rocks allow thermal fluid moving northeastward to penetrate to the surface, creating the hot springs. Isotope data discussed previously indicate that the high-temperature reservoir fluid and fluid discharging from Sou and Hyder Hot Springs share some common ancestry.

4.8 Summary and Conclusions Regarding the Hydrologic System

1. Hydrostatic pressures in the -5000 to -9000 foot MSL depth range within a radius of 3 to 5 miles of the Dixie Valley productive area are in equilibrium with regional thermal and non-thermal aquifers over an area of several thousand square miles.

2. Commercially productive high-temperature zones within the Dixie Valley geothermal field have hydrostatic pressures of up to 500 psi below those observed in the surrounding regional aquifers in the -5000 to -9000 foot MSL depth range.

3. Isotope data indicate that the high-temperature reservoir fluid is in equilibrium with Triassic-Jurassic carbonate rocks which are distributed over several thousand square miles surrounding the Dixie Valley reservoir. Much of this stratigraphic section is found at depths below the 480 deg.F isotherm over a large region surrounding the reservoir. The age of the fluid produced from these rocks is greater than 35,000 years.

4. Shallow thermal anomalies overlying and surrounding the Dixie Valley reservoir may represent discharge of high-temperature fluid from the deep production zones to the near-surface alluvial aquifers, though the actual discharge rate is small compared to other major Basin and Range hydrothermal systems.

5. Evapotranspirative potential of the Humboldt Salt Marsh and surrounding playas is several times greater than the total supply of groundwater and geothermal fluid to the basin.

6. Linear temperature profiles in production wells show the absence of significant hot water movement in the depth interval from 1000 feet to the production zones in the 7000 to 10,000 foot depth range.

4.9 References

Cohen, P. and D. E. Everett, 1963, A brief appraisal of the groundwater hydrology of the Dixie Valley-Fairview Valley area, Nevada: Dept. of Conservation and Natural Resources, Ground-Water Resources Reconnaissance Series, Report 23.

Hoefs, J., 1980, Stable isotope geochemistry; Springer-Verlag, New York, New York, 208 p.

Morgan, D. S., 1982, Hydrogeology of the Stillwater geothermal area, Churchill County, Nevada:, USGS Open File Report 82-345.

Welch, A. H., Sorey, M. L., and Olmsted, F. H., 1981, The hydrothermal system in southern Grass Valley, Pershing County, Nevada: U. S. Geological Survey Open-File Report 81-915, 193 p.

Young, H. W., and Lewis, R. E., 1980, Hydrology and geochemistry of thermal ground water in southwestern Idaho and north-central Nevada: U. S. Geological Survey Open-File Report 80-2043, 40 p.

5. GEOCHEMISTRY

The deep wells at Dixie Valley produce fluids with a downhole enthalpy range of 405 to 462 btu/lb. These fluids are all fairly similar chemically but there are apparently real chemical differences between most of the wells. These differences can be used to formulate a geochemical model which can shed light on the origin of the different enthalpies. Enthalpy differences can be caused by conductive gain or loss of heat or by gain or loss of heat through mixing fluids with different enthalpies. An important subset of the latter method would be by the addition or loss of steam. The geochemical data from Dixie Valley indicate the enthalpy variations are the result of mixing of up to 5 separate fluids, each with a distinct enthalpy.

5.1 Analytical Quality

The available data from Dixie Valley are highly variable in quality. For many of the early analyses performed by SUNEDCO the sampling conditions were either not recorded or not passed on to Oxbow. The analytical quality of some analyses is in question as there are large variations between different labs. Some analyses are incomplete so that no charge balances can be performed to verify the analytical quality. Unfortunately several of the wells have not been recently tested so there has been no opportunity to obtain data of a higher quality. Consequently, use of this earlier data is limited to calculation of ratios of conservative elements which are not affected by steam separation.

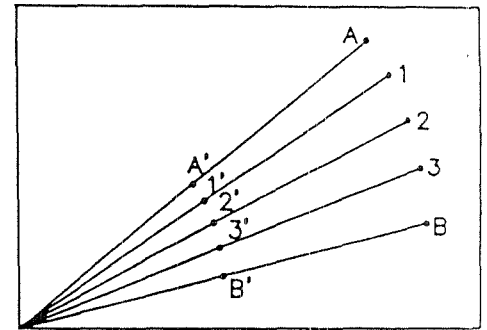
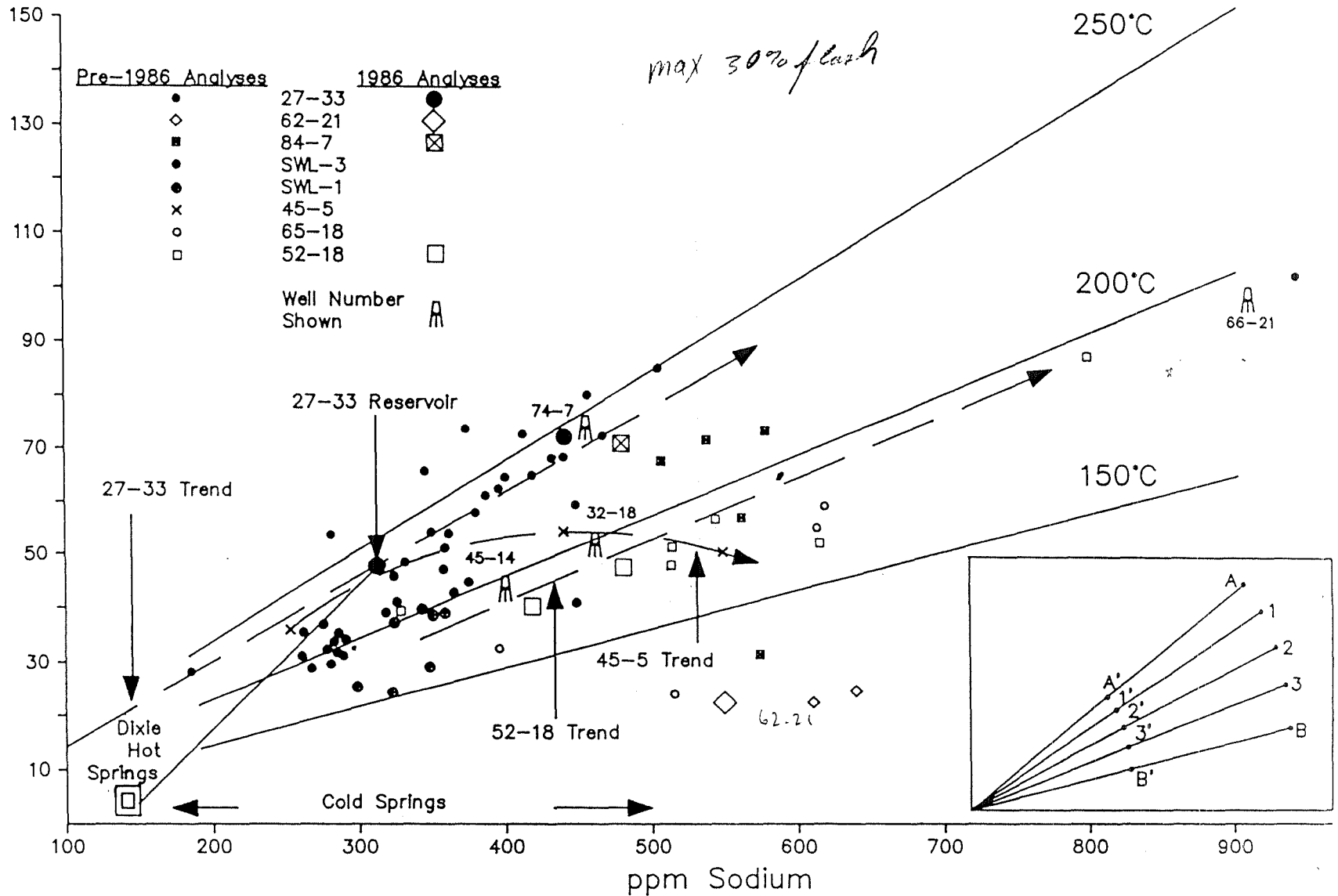
5.2 Definition of Populations

The approach to this geochemical modeling has been to define populations of water types and then to compare the different populations to find common characteristics which might show relationships between the populations. These populations are then examined in terms of geothermometry and enthalpy relationships to further clarify the relationships. Finally the populations are grouped as to the degree of shared ancestry, and spatial relationships are defined.

The populations are defined on a sodium - potassium (Na - K) cross plot (Figure 5.2). This plot shows the trends most

Sodium - Potassium Cross Plot

ppm Potassium



clearly and has the advantage of providing a visual impression of reservoir temperatures as a geothermometer overlay is included. The data on the Na - K plot have not been corrected for steam loss, hence a given well composition will plot as a linear feature trending away from the origin, *i.e.*, trends A-A' or B-B' on Figure 5.2. Constant proportion mixtures or single source end members will also plot as linear trends through the origin, *i.e.* trends 1-1', 2-2', or 3-3' on Figure 5.2. However, variable proportion mixtures of end members with different enthalpies will plot as curved trends that will not project through the origin, *i.e.* trend B', 1', 2', 3', A' which arises from mixing along A-B and flashing to a constant pressure (Figure 5.2). If the pressure were variable this last trend would be smeared out along one or more of the trend lines radial to the origin.

The pre-1986 data suggest that well 27-33 produces a constant composition fluid along the trend labeled "27-33". The geochemical data from well 45-33 are virtually identical to those from well 27-33, as expected from the close bottomhole spacing, so only the 27-33 data are discussed. The Berkeley Group calculated a reservoir composition that is both shown on the trend and summarized in Table 5.1. The higher concentrations along the trend are due to greater steam loss; the lower concentrations are suspected to be due to sampling errors, *i.e.* steam enrichment, since no shift in the Na - K ratio is apparent. The 1986 data from well 27-33 also plot on this trend, thus confirming the original interpretation. The 1986 data for wells 74-7 and 84-7 also plot on or close to this trend.

A separate trend was defined by the pre-1986 data and is labeled as the "52-18" trend. It is about 50 deg. C lower in temperature than the 27-33 trend. If the spread of the 52-18 trend was created solely by steam loss it would require at least a 40% steam loss, which is far too great to be accounted for by the low measured enthalpy of this fluid (Table 5.2). In addition the great depths and pressures where these fluids are found rule out any steam separation processes. The 52-18 trend suggests that a higher salinity end member mixes with a lower salinity end member to create this compositional variation.

Waters from wells SWL-1 and SWL-3 plot at the low salinity end of the 52-18 trend and may be a low salinity end member. The SWL-1 and SWL-3 waters tend to overlap both the 52-18 and 27-33 trends. However, a tight cluster of SWL-3 analyses near 275 ppm sodium may hold the key to the proper interpretation of these waters. They are clearly lower in

Table 5.1
Total Calculated Reservoir Water Composition

SPECIES	WEIR WATER (mg/kg)	SEPARATOR STEAM (mg/kg)	RESERVOIR WATER (mg/kg)
SiO ₂	710		512
H ₃ BO ₃ (from B)	(8.45)		34.8 (6.09)
Na ⁺	438		316
K ⁺	69.7		50.2
Li ⁺	2.98		2.13
Ca ⁺⁺	0.99		0.71
Mg ⁺⁺	0.01		0.01
Sr ⁺⁺	0.17		0.12
Cl ⁻	352		254
F ⁻	15.2		11.0
HS ⁻			48.9
(from S=)	(0.07)		(0.05)
(from SO ₄ =)	(139)		(100)
(from H ₂ S)		(87.9)	(15.4)
HCO ₃ ⁻			3,080
(from CO ₂)		(12,900)	(2,260)
(from HCO ₃ ⁻)	(278)		(200)
(from CO ₃ =)	(16.8)		(12.1)
NH ₄ ⁺			2.00
(from NH ₃)		(10.8)	(1.89)
N ₂			2273

Table 5.1

SPECIES	WEIR WATER (mg/kg)	SEPARATOR STEAM (mg/kg)	RESERVOIR WATER (mg/kg)
CH4		16.7	2.93
Ar		3.17	0.556
He		0.444	0.0779
H2		0.0605	0.0106

Note: The composition of reservoir water is given in terms of the major species, and contributing species are shown in parentheses below.

SECRET

$$F = 1.8^{\circ}C + 32$$

$$F - 32 = 1.8^{\circ}C$$

$$\frac{F - 32}{1.8} = ^{\circ}C$$

Table 5.2

TABLE 5.2
COMPARISON OF CHEMICAL VERSUS MEASURED ENTHALPY

WELL	MEASURED STATIC TEMP	MEASURED FLOWING TEMP	MEASURED DOWNHOLE ENTHALPY	MEASURED WELLHEAD ENTHALPY	PREDICTED Na-K ENTHALPY	PREDICTED SILICA ENTHALPY
45-33	N/A	477	461	446		
27-33	448	477	461	443	459	459
45-5	404	401	376	322		
84-7	445	477	461	443	444	467
74-7	452	478	462	450	459	464
52-18	443	446	426	417	332	384
32-18	443	427	405	395	367	440
SWL-3	453	N/A (Probably 428)	406	395	382	384
SWL-1	429	428	406	402	379	414
65-18	430	438	417	410	336	483
62-21		356 = 180°C	328 = 164°C			
66-21					357 = 181°C	404 = 207°C

::

salinity than the 27-33 reservoir fluid. Thus, unless they are the result of steam enrichment during sampling, they cannot be derived from 27-33 type waters by conductive heat loss. If this is the case the SWL-3 waters are the low salinity end member on the 52-18 trend. The SWL-1 waters form two possible sub-populations based on potassium content. The lower potassium waters will be discussed with the 62-21 well.

While the 27-33 fluids cannot be the parent for the SWL-3 fluids, the converse is not true. Heating and a slight increase in salinity could produce a 27-33 type fluid. A second possibility to explain the SWL-3 type waters would be to invoke a very dilute water such as a Dixie Hot Spring type to dilute the 27-33 type water. The involvement of SWL-3 waters in the 52-18 trend is shown by the high salinity (975 ppm sodium) sample and several other SWL-3 analyses along the trend.

7 slides of manuscript!

The high salinity end member for the 52-18 mixing trend is water from well 66-21. This unflashed fluid, collected when the well was on bleed, is believed to be representative of the far southern portion of the Dixie Valley system. It is sodium chloride-rich and represents the most mature water type for this basin, in that carbonates and sulfate have been replaced by chloride, probably through precipitation reactions, indicating longer residence. It has a predicted Na-K temperature of 194 deg. C and has also been produced from the 52-18 and SWL-3 wells, as indicated by the presence of fluids produced from these wells plotting at the high salinity end of this trend.

Well 62-21 produces a low-enthalpy fluid from near the center of the basin. It is thought to be typical of the water which fills much of the basin at depths greater than a few thousand feet. For the identified water types in the study, the salinity of 62-21 makes it a potential parent water only for the 66-21 well, as its salinity exceeds that of the higher enthalpy fluids and as such could not parent such waters. As a potential mixing end member this well has much more significance. Wells 65-18, 45-5, SWL-1, and 84-7 have produced fluids which appear to have a 62-21 component. Mixtures of SWL-1 and 62-21 may account for the lower potassium cluster of SWL-1 subtype on Figure 5.2. The pre-1986 analyses of 84-7 also show a curved mixing trend with 62-21 end member (2 enthalpy mixing type curve).

Fluid from well 84-7 has in the 1986 tests shown a consistently close affinity to 27-33 fluids. The earlier data show that this well is connected to the deep basin

62-21 system and to the 66-21 type waters which are the end member for the 52-18 trend. The latter relationship is even more strongly supported when the Piper plot is examined (Figure 5.3.3).

Well 45-5 has three available analyses which suggest that the well began to produce a SWL-3 type fluid, but quickly became more strongly influenced by the 62-21 waters. The abrupt shift indicates mixing very near the wellbore. The shift is known to be abrupt because the well was only flowed for a total of 18 days. It should be made clear that no distinction can be made between multiple production zones that have been encountered by individual wells and the concept that fluids produced from a given well may be the result of several fluids mixing within the natural environment. The close spacing of producing intervals in most of the wells tends to argue against multiple production zones with different chemistries being a common feature.

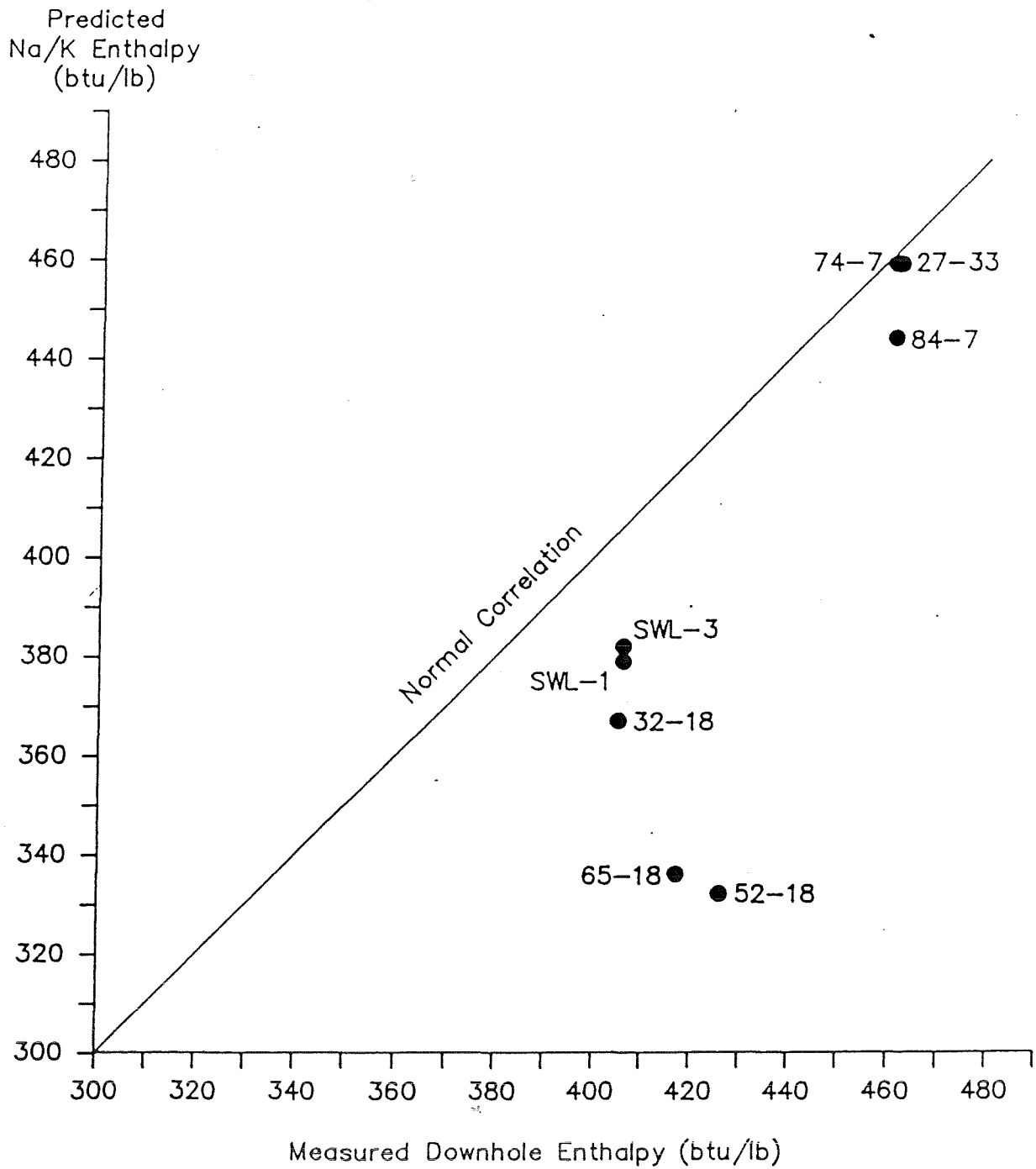
Recent analyses of wells 45-14 and 32-18 indicate that both belong to the 52-18 compositional mixing trend with a 66-21 compositional component.

Recent analyses of well 74-7 show this fluid to belong with 27-33 fluid type. There is no evidence for mixing with other fluids.

5.3 Measured and Geochemically Predicted Enthalpies

The previous discussion in a qualitative sense has implied that the chemical evidence offers little support for the premise that the widely varying enthalpies in the Dixie Valley wells result from conductive cooling of fluids. This lack of support for conductive cooling can be quantified by comparison of the geothermometer estimates of reservoir enthalpy with the measured enthalpy for each well (Table 5.2). If conductive cooling were the main factor affecting enthalpy, the Na - K estimate of enthalpy would be expected to be greater than the measured enthalpy as a consequence of the relatively slow re-equilibration of the Na-K geothermometer in response to falling temperatures. Instead, the Na - K estimates of all of the lower enthalpy wells are much lower than the measured downhole flowing enthalpies (Figure 5.3.1). This situation is a result of logarithmic increase in relative amounts of sodium in lower enthalpy fluids. When these fluids are mixed with higher enthalpy fluids, the heat contents are balanced linearly but a disproportionate amount of sodium will be present and an abnormally low Na-K temperature will be an expected result. Note that the high enthalpy wells are in close agreement

Measured Downhole Enthalpy vs Predicted Na/K Enthalpy



between measured downhole flowing enthalpy and the Na-K predicted enthalpy, whereas the lower enthalpy wells have large discrepancies (Figure 5.3.1).

The plot of silica predicted enthalpy versus downhole flowing measured enthalpy is less diagnostic, but also suggests mixing. Since silica increases as a log function with increasing enthalpy, mixed waters are expected to have a slightly higher silica enthalpies than the measured enthalpy. This is because the enthalpies of mixtures are nearly linear projections of the mixing ratio, whereas silica concentrations are skewed toward the higher enthalpy end member. Silica estimates of enthalpy of a mixture are in error on the high side. This is the case for wells 65-18 and 32-18, but others have a low silica enthalpy (Figure 5.3.2). These low discrepancies may be due to loss of silica between sampling and analysis. In conductively cooled systems, the silica equilibration kinetics are rapid enough that a close correlation between silica and measured enthalpies is expected. Since a close correlation is not seen in this data, cooling by mixing is believed to be the mechanism for the enthalpy loss. Again, the high enthalpy wells have close agreement between measured enthalpy and the silica-predicted enthalpy, while the lower enthalpy wells are subject to large differences.

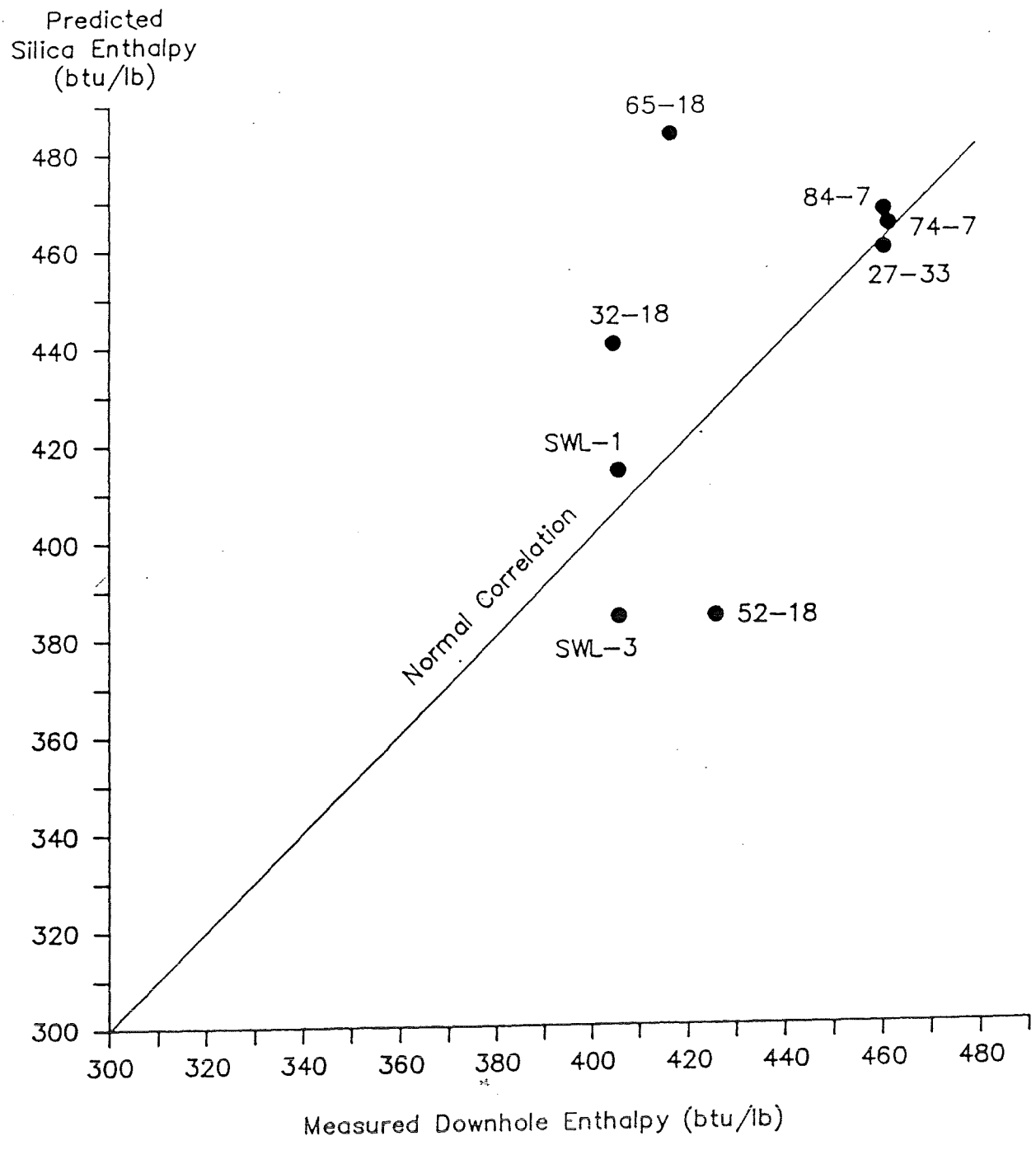
The enthalpy considerations agree well with mixing of geothermal fluids with varying enthalpies at Dixie Valley. //

5.4. Multivariate Analysis

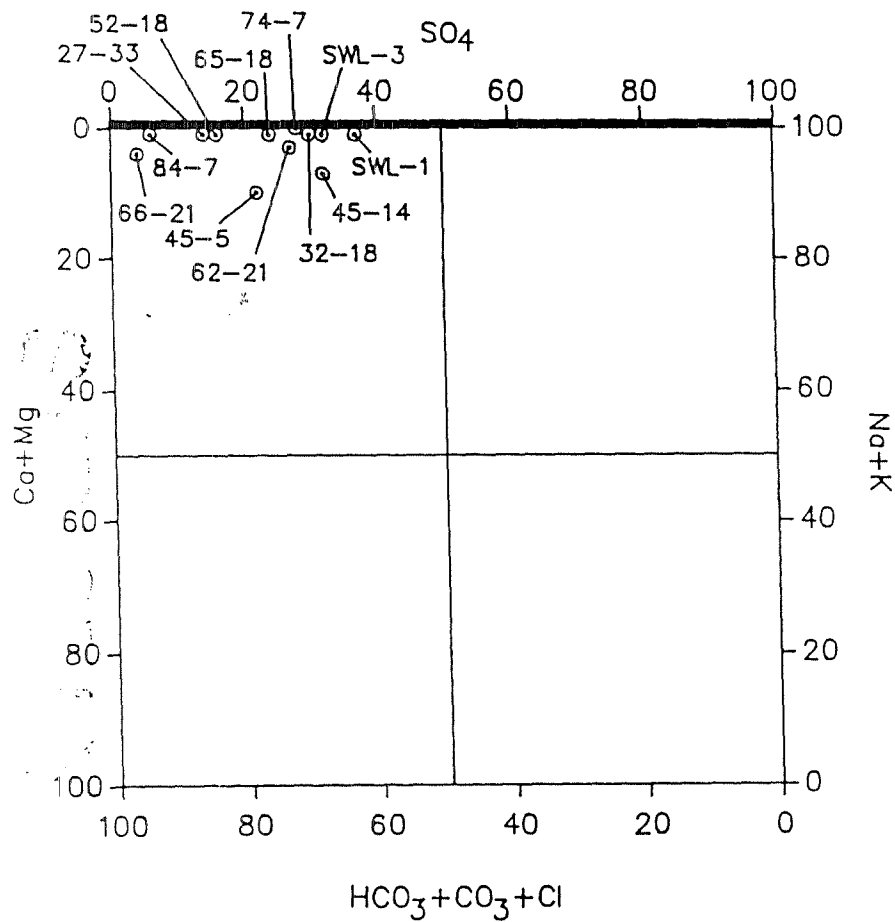
All of the deep thermal waters in Dixie Valley are exceptionally dilute given the high temperatures at which they have equilibrated. Water from well 66-21 is the most saline by far and it barely exceeds 3000 ppm. The other well waters are generally between 1200 and 2000 ppm in total dissolved solids (Figure 5.3.3). The major chemical variation is a change in sulfate relative to chloride and bicarbonate as shown on a Piper plot with sulfate isolated (Figure 5.3.3).

The Piper plot is incapable of showing salinity variations or relationships. To add this capability it is necessary to construct a separate diagram known as a three-dimension composition space. Basically this is a slice across a Piper plot that tapers up to an apex which is defined as zero salinity. Any convenient taper can be chosen for the sides of the three-dimension composition space. Salinity increases away from the apex. Another way to imagine this is to view the Piper plot as a horizontal slice through a

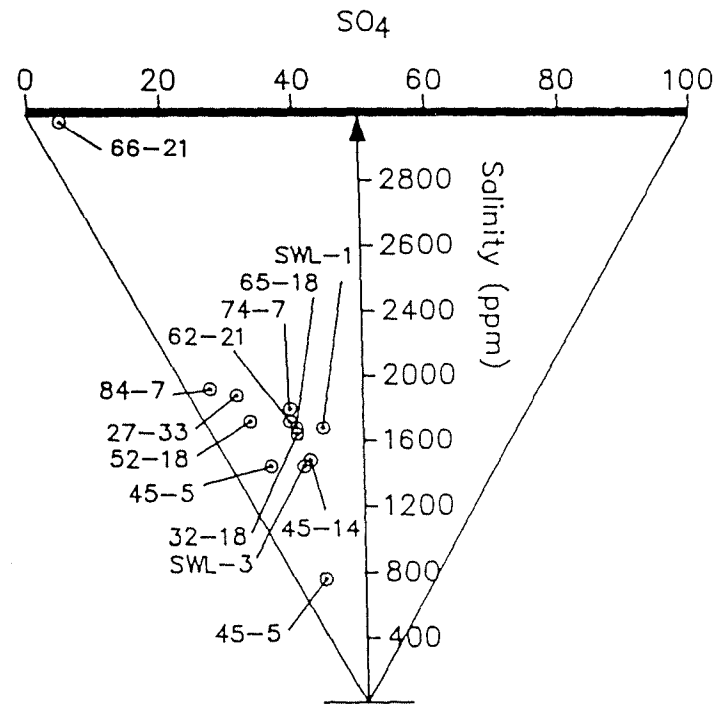
Measured Downhole Enthalpy vs Predicted Silica Enthalpy



Piper Plot (Sulfate Isolated)



Three Dimension Composition Space



pyramid with the apex of the pyramid representing zero salinity. The lower one cuts the slice horizontally across the pyramid the greater the salinity becomes. Figure 5.3.3 contains a three-dimension composition space drawn along the anion margin (top) of the Piper plot.

For purposes of this discussion the following three points are deemed most important from the trends shown on Figure 5.3.3.

1. There is a general increase in chloride from 62-21 to 66-21 shown on the Piper plot and all higher enthalpy wells lie within this trend.
2. Well 84-7 shows the strongest affinity to the 66-21 type of fluid on the Piper plot.
3. On the basis of salinity and cation ratios (highest calcium contents), wells 45-5 and 45-14 are most strongly skewed toward dilute surface water compositions.

These relationships lend support for the conceptual geochemical model which will be considered next.

5.5 Conceptual Geochemical Model of the Flow System

The conceptual model includes a mechanism for the mixing of geothermal fluids into the dilute surface waters; however, since wells 45-5 and 45-14, which show this relationship, are not being considered for production, this topic was not pursued. The purpose of the conceptual model is to define the probable chemical relationships by mixing fluids encountered in various production wells in Dixie Valley. The geologic-hydrologic context of these relationships is of course a critical factor in the commercial development of this resource. The following fluid types have been identified for purposes of the conceptual model.

1. The 27-33 high-enthalpy fluid. This system shows little compositional variation and is the high enthalpy parent of the SWL-3 water. The temperature of this fluid is near 250 deg.C.
2. The SWL-3 moderate-enthalpy fluid. These waters form by mixing of 27-33 fluids with dilute cooler waters. Temperatures range from about 215 to 240 deg.C.
3. The 66-21 lower-enthalpy system. These waters are

more mature than either of the above types in that the sulfate content is much lower. This is based on the assumption that as waters mature, insoluble sulfates precipitate and sulfate is lost from the system. This maturity, however, has been attained in a lower temperature environment of about 194 C. These waters are significantly more saline than any other fluid type.

4. The 62-21 deep basin waters. These fluids are similar to types 1 and 2 above in salinity but have matured in a lower enthalpy environment. Although mostly chloride in character they have a maximum temperature of only 167 C. They appear to have only this moderate temperature imprint and have never attained higher temperatures.
5. Surface waters. The requirement for more dilute waters is clear in the case of the hot spring systems present and possibly to explain the SWL-3 fluids. Also, these may influence the composition of 45-5 and 45-14 fluids.

The spatial-physical relationships of these fluids can be explained as a result of the mixing of 27-33 type fluid with various populations of cooler fluid stored with the basin. This mixing takes place within or in close proximity to the plane of the range-front fault. This plane of convection is broken into sub-cells at permeability nodes which extend out into the basin. These nodes are probably zones of high fracture density which serve as conduits for high enthalpy fluids from the range-front fault to penetrate into and mix with cooler fluids stored in the deep basin to the east and south.

The main source of high enthalpy fluid is centered near the Section 7 and 33 wells and serves as the thermal driving force for the system. The high-enthalpy fluid creates pressure differentials within the reservoir as a consequence of the density contrasts due to thermal expansion (See Section 4.5 and 4.6). Absence of temperature decline during flow testing of the high-enthalpy wells confirms that hot water preferentially flows upward along the range-front fault and penetrates into cooler aquifers to produce the observed mixing. Convection due to discharge of low-density thermal fluids to the shallower alluvium with loss by evapotranspiration serving as the ultimate sink for the net throughput of the system. Basin fluids are drawn into the convection cells at permeability nodes along the range-front fault and this results in the observed mixing of different

chemical populations.

Three distinct zones of fluid storage are defined by fluid chemistry. These zones are the 66-21 type fluid, the SWL-3 type fluid and the 27-33 type fluid. The southern-most cell, the 66-21 cell, is an end member compositionally and has a component of flow in the direction of the Section 18 wells to the northeast and a flow component to the south-southwest towards 45-14. The resultant mixtures of SWL-3 type fluids and the 66-21 type fluids provide what has been previously referred to as the 52-18 compositional trend. This trend would include the following wells, listed in order of an increasing component of 66-21 fluids: SWL-3, SWL-1, 45-14, 32-18, and 52-18. This mixing process is driven by the large regional pressure gradient which exists between 66-21 and the producing part of the field. Fluid from wells 52-18 and 65-18 shows significant mixing with fluid from the deep basin represented by 62-21. This mixing is also consistent with the observed pressure gradient between 62-21 and the production zones in 52-18 and 65-18.

The chemistry of the high-enthalpy fluid observed in wells 84-7 and 74-7 is nearly identical to that of 27-33. Only a very slight component of 66-21 is seen in the fluid, indicating that these wells are tapping directly into the same fluid source supplying 27-33 with only very slight mixing. Well 84-7 shows less sulfate than 27-3, but in terms of salinity it could have only a small component of 66-21 for the average produced mixture. It is thus closely related to 27-33.

5.6 Scaling

5.6.1 Silica Scale

Bench testing of produced geothermal fluid for silica scaling was performed by TGI during the flow testing of 45-33 in 1984. This testing is summarized in Appendix E, "Chemistry of Silica in Dixie Valley Brine" by Oleh Weres, 1984.

These experiments have demonstrated that if the separated brine is kept near the boiling point, silica polymerization is slow. This is in large part a function of the high pH of the Dixie Valley geothermal fluid, which is 8.43 at 96 deg.C. Even if the dissolved silica does polymerize to colloidal silica, the colloidal silica does not flocculate, and does not appear to adhere to solid surfaces. Therefore,

the silica in the brine is stable in two important respects.

If brine handling and reinjection procedures are designed to preserve this stability throughout the system, there will be no problem with silica scaling or injection well damage.

If the brine is maintained near the boiling point (205 deg. F), polymerization is very slow. Polymerization is also slow at 176 deg. F. If temperature is reduced to about 140 deg. F, the silica begins to polymerize within minutes. Reducing brine pH to 7.7 caused fairly rapid polymerization at 176 deg. F. These results suggest the lowest "safe" temperature for injecting the brine is about 176 deg. F. If, however, the pH of the brine is reduced, the minimum safe temperature will be higher, perhaps near the boiling point.

These results are sufficient to prescribe a safe and conservative brine handling and injection procedure: (a) Minimize heat loss at the surface by not exposing the brine to air and keeping pipelines insulated and/or short. (b) Do not decrease the brine pH, for example, by contacting it with condenser vent gas. (c) Inject the brine into a stratum where the temperature is 176 deg. F or higher. There is little doubt that the separated brine can safely be injected into the geothermal reservoir without requiring preinjection treatment.

The conclusion summarized above applies in full only to a brine that has been flashed to atmospheric pressure in one step. Extracting heat from the brine otherwise will produce brine in a different chemical state, possibly with different silica scaling potential; in particular, the "minimum safe temperature" may be different. If the steam is separated in two stages, the second at atmospheric pressure, the pH of the brine will be slightly higher, and the minimum safe temperature may be lower. As the Dixie Valley power plant is a dual flash plant this should further minimize any silica scaling problems. No silica precipitation was observed on surface brine handling equipment including the atmospheric flash tank and weir box used for several thousand hours of flow testing. This verifies conclusions made from the bench tests that silica does not tend to precipitate at temperatures above approximately 200 deg. F.

The idea of injecting the brine into shallower formations that have much lower temperature and different brine from the geothermal reservoir raises other, more difficult questions. If the receiving formation contains swellable clays, the injected brine may dispense and mobilize the

clays, causing formation damage. If the brine in the receiving formation is more saline and more acid, mixing it with the injection brine may accelerate polymerization and flocculation of the silica. However, Oxbow intends to inject the spent brine back into the reservoir for pressure maintainance so these problems should not occur.

Preliminary results from the silica scaling test skid on well 74-7 during the six well flow test have confirmed that silica scaling need not be a problem at Dixie Valley. After a month of flowing through the skid, designed to simulate a reinjection system, only traces of scale had formed on carbon steel components in the skid. The stainless steel mesh had absolutely no silica deposition.

5.6.2 Carbonate Scaling

Carbonate scale deposits in the bores of production wells during flowing. A volumetric measure of scaling was made in wells 27-33 and 84-7 using caliper logging before and after long term flow tests. The results of this study are described in Appendix E. The scaling rates observed in the 9-5/8" casing string for both wells would required cleanout at three to six month intervals. The time between cleanout could be lengthened by varying wellhead pressures so that the flash point would move up or down the well. This movement of the flash point would distribute the scale buildup over a greater area per unit volume of scale deposition, thereby reducing the rate of effective well bore diameter constriction.

The 13 3/8" wells will not need nearly as many scale cleanouts as the 9 5/8" wells. Experience at other geothermal reservoirs in the Basin and Range province suggests that the 13 3/8" wellbores will flow between 3 and 4 times as long as the 9 5/8" bores before a cleanout is necessary. It is anticipated that wells 74-7 and 76-7 will need about one cleanout per year and the 10 3/4" casing in well 73-7 will need to be cleaned out about twice a year under maximum flow conditions.

The mechanical properties of the carbonate scale appear to be amenable to reaming. The scale tends to be friable, breaking into small fragments which are easily cleared from the well bore during reaming under flowing conditions.

6. CONCEPTUAL RESERVOIR MODEL

The geotechnical data described in Chapters 3, 4, and 5 are sufficient to develop a well-constrained conceptual model of the Dixie Valley geothermal reservoir. This conceptual model is a necessary step in converting the geotechnical data base into a representative numerical model. The accuracy with which the conceptual model represents the natural system is expressed in the relative ease with which the numerical model can be made to match observed reservoir behavior. Accuracy of the conceptual model also determines the accuracy of long term predictions made by the numerical model for periods of time and for reservoir volumes which are well beyond those observed during actual flow testing.

The conceptual model of the Dixie Valley reservoir incorporates the following geologic, geochemical, and hydrologic features as discussed previously:

1. Distribution of formation permeability must be consistent with observed structure and stratigraphy. High permeability is apparently confined to the range-front fault fracture system and Tertiary basalt aquifer. The Quaternary-Tertiary-Jurassic section comprising the rocks of the graben block above a depth of 9700 feet must have low vertical permeability to account for the observed conductive thermal gradients. Lack of water entries during air drilling through unfractured Tertiary and Jurassic sections verifies the existence of low intergranular permeability within the down-dropped block.

2. The production intervals must be supplied from an aquifer located at depths greater than 10,000 feet beneath the valley floor in order to supply 480 deg.F water to the deep production wells. No evidence of recent volcanism is found in the region that could supply heat to the system. Consequently, deep circulation of water to depths below the 480 deg.F isotherm is the only remaining mechanism that could create the observed high-enthalpy fluid. Isotope data indicate that this water is distributed regionally at depth over a minimum of several thousand square miles and is older than 35,000 years, indicating very slow rates of flow through the system. Gas and isotope characteristics of the high-enthalpy fluid indicate a source in the Triassic marine sediments which correspond to the depth of circulation required to produce the observed 480 deg.F temperatures (Section 4.3).

3. The geochemistry of reservoir fluids with varying enthalpies indicate that the temperature distribution within the productive portions of the reservoir must be accounted for by mixing of fluids as opposed to conductive heat loss. The highest-enthalpy fluids (from wells 27-33, 45-33, and 84-7) appear to be unmixed with cooler fluids. These wells therefore define the zone of upwelling of high-enthalpy fluid from the postulated regional aquifer described in 4.3. Fluids from outlying wells 66-21 and 62-21 appear to represent the cooler chemical end members that are available for mixing with higher-enthalpy fluid from depth to produce the wide range of temperatures observed in the reservoir (Section 5.5).

4. The distribution of permeability surrounding the reservoir and the natural rate of fluid flow in and out of the reservoir must be consistent with the observed regional and local pressure distribution. A pressure drop of 350 to 500 psi at -5000 foot MSL is observed between the regional deep aquifer system and the producing portion of the reservoir. Deep wells 62-21 and 66-21 appear to be in equilibrium with pressures observed in the deep geothermal reservoirs in the Carson Sink on the west side of the Stillwater Range. The low observed pressures within the producing portion of the reservoir appear to be constrained horizontally by these two wells which lie 3 and 6 miles respectively from the producing zones.

5. Horizontal pressure gradients created by thermo-artesian pressure within the producing fracture systems cause penetration of high-enthalpy fluids from production zones observed in Section 7 and Section 33 wells into lower-enthalpy production zones observed in the Section 18 wells. This produces the observed chemical and enthalpy mixing (Sections 4.6 and 5.5).

6. Thermo-artesian pressure caused by leakage of high-temperature fluid to the near-surface along the range-front fault must be sufficient to allow for penetration of reservoir fluid into the shallow ground water system to produce the observed surface heat flow anomaly. The quantity of near-surface and surface discharge must be consistent with the relatively weak heat flow anomaly and very small amounts of silica sinter observed at the surface. (Section 4.7).

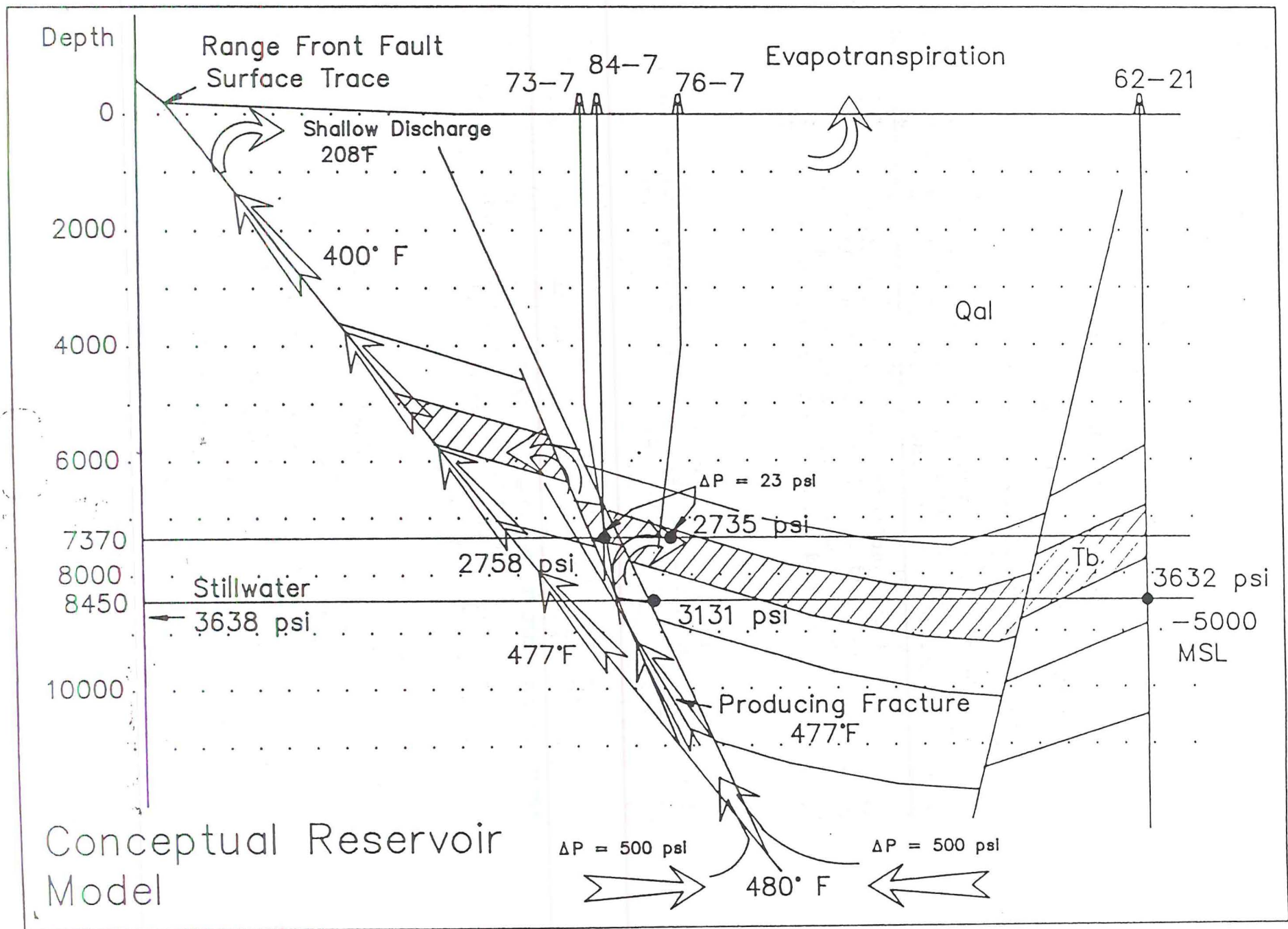
→ creates older Etz Umi in sediments Section

7. Natural discharge from the geothermal reservoir is readily accounted for by evapotranspiration from the Humboldt Salt Marsh and surrounding playa. The evapotranspirative potential of the Salt Marsh exceeds

probable natural geothermal discharge by three orders of magnitude. As a result of the essentially unlimited discharge potential, natural flow of water through the system is constrained only by thermo-artesian pressure gradients and the fracture and intergranular permeability of the reservoir and overlying rock.

The observed phenomena described above are shown schematically on the cross section shown in Figure 6.1. The conceptual model of the Dixie Valley geothermal system derived from these observations can be described as follows:

1. Pore water stored in the Triassic pelitic and carbonate sediments deeper than 10,000 feet below ground level attain a temperature in excess of 480 deg.F due to the relatively high regional thermal gradients in west-central Nevada. The high-temperature fluid is in hydrostatic equilibrium throughout the high heat flow region.
2. A rapidly dilating fracture system associated with the Stillwater range-front fault in the Section 18 area allows high-temperature fluid from the deep regional aquifer to penetrate into shallower fracture zones. Continuous fracturing of rock adjacent to the range-front fault creates significant fracture permeability and porosity storage of high temperature fluid in close proximity to the range-front fault system.
3. High vertical permeability in the fracture system allows a thermo-artesian pressure differential to develop in the 5,000-8,000 foot depth range thereby driving high-temperature fluid from depth into the cooler aquifers in the Tertiary basalt. The moderate-temperature reservoir of mixed fluid encountered in the Tertiary basalt is created by this mechanism.
4. Penetration of hot fluid along the range-front fault to the near-surface creates thermo-artesian pressure which overcomes cold water hydrostatic pressures thereby creating hydrothermal discharge plumes at the margins of the field. Water discharged from the plumes is lost to evapotranspiration in the Humboldt Salt Marsh.
5. Net loss of fluid from the system due to vertical flow and loss at the surface creates the large pressure drop between the high-temperature regional aquifer and the highly fractured zones which make up the productive part of the reservoir.



7. WELL AND RESERVOIR TESTING

7.1 Well Completions and Histories

The Dixie Valley geothermal well field considered in this assessment consists of 9 production wells and 5 non-commercial wells as shown in Figure 2.2. Two outlying noncommercial wells, 66-21 and 62-21, were also used in this study for background pressure and temperature data. The physical characteristics of each well are summarized in Table 7.1 and the geologic and flow characteristics of each well are summarized in Table 7.2. The following is a brief discussion of the drilling history, completion and flow characteristics, and current and projected uses of each well in the field.

SWL-1

Well SWL-1, the discovery well in Dixie valey, was completed by SUNEDCO on November 29, 1978 to a total depth of 7255 feet (Figure 7.1.1). SWL-1 produces from the Miocene basalt between depths of 7191^{2142m} and 7255^{7211m} feet. Numerous flow tests of this well have been conducted by SUNEDCO. The most recent flow test of SWL-1 was a 7 hour test on March 27, 1986. The well flowed 252,000 lbs/hr with a wellhead pressure of 56 psig. Casing partings or collapse have occurred in SWL-1 in the 13 5/8", 9 5/8," and 7" casing strings. SWL-1 is not suitable for production. It will be used for observation purposes and conceivably could also be used as an injection well.

SWL-2

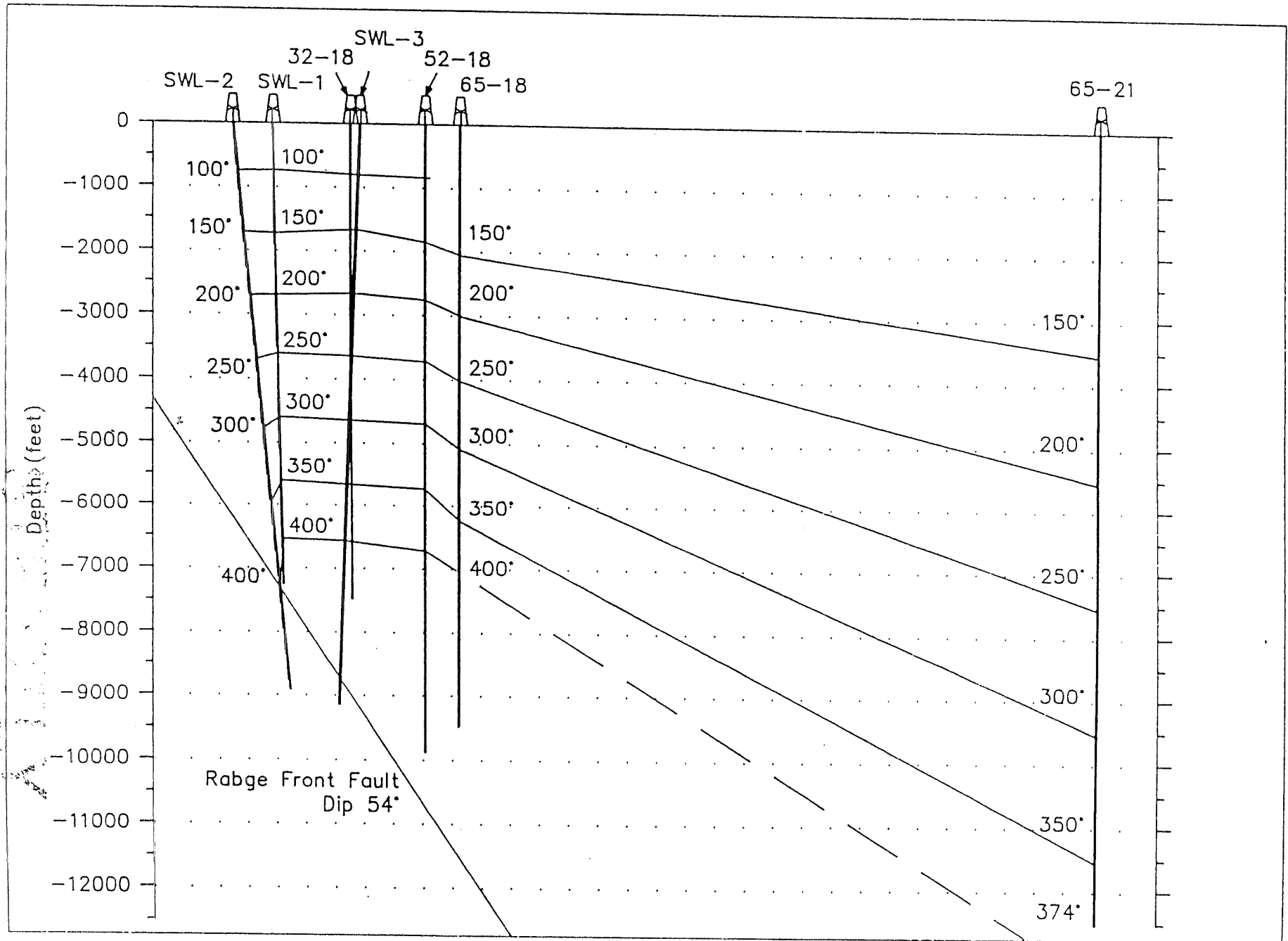
Well SWL-2 was completed by SUNEDCO on August 25, 1979 to a total depth of 8588 feet (Figure 7.1.2). The well produced from the 6570 to 8290 foot interval located within the Miocene basalt. The existing leg of SWL-2 is the second leg of the well and was drilled because the original leg was a dry hole completed in Cretaceous granodiorite. After completion the existing leg would not flow. In November 1979 a slotted 5" liner was run from 7994-8455 feet. SWL-2 was flow tested during January and February 1980 but would not sustain flow unassisted. The maximum flow acheived was 50,000 lbs/hr with a wellhead pressure of 38 psig. SWL-2 is currently being used for pressure observation purposes and this appears its only use.

Max. Flowrate lb/hr	MPEMax. Flowrate psig	Enthalpy BTU/lb	Down Hole Flow Temp. deg. F	Stat. Prod. Int. Temp. deg. F	Stat. Pres. @ -5000' MSL
50000	38	397	428	410	3048
609000	65	322	401	404	
	NA			NA	
1100000	118		○	Unknown	
1350000	162	450	478	452	3151
1700000	148				3219
650000	128	443	477	445	3221
934000	93	395	427	443	3122
263000	90	417	^{= 230°C} 446	443	3149
819000	107	410	438	430	3156
252000	56	402	428	429	3143
300000	90	395		453	3153
720000	104	443	^{= 180°C} 356 477	448	3302
904000	131	446	477		3190
	NA			NA	
	NA			NA	
250000	28			Unknown	
	NA			NA	
	25		436	Unknown	
	NA			NA	
300000	NA			406	

✓ RD-3 ←



Last Workover	Workover type	Last Flowed	Well Status
11/27/79.	Run Liner-Test	01-Feb-80	P Monitoring
None	NA	01-Jul-81	P Monitoring
None	NA		Shut in-Dry
09/04/86	Repr Csg Clapse	18-Sep-86	Flowing
None	NA	18-Sep-86	Flowing
None	NA	18-Sep-86	Flowing
05/29/82	Scale Removal	07-Apr-86	P Monitoring
None	NA	12-Sep-86	P Monitoring
02/19/86	Scale Removal	05-Mar-86	P Monitoring
03/11/86	Clean/Deepen	18-Sep-86	Flowing
03/25/86	P Test Casing	27-Mar-86	P Monitoring
05/12/82	Scale Removal	03-Jun-80	P Monitoring
None	NA		S.I. Non-Comm.
03/20/86	Clean/Deepen	04-Apr-86	P Monitoring
06/24/86	Mill Csg/Deepen	18-Sep-86	Flowing
None	NA		Abandoned
None	NA		Abandoned
None	NA		Abandoned
None	NA	04-Jun-86	Abandoned
None	NA		Abandoned
None	NA	25-Nov-85	Abandoned
None	NA		Abandoned
None	NA	14-Jul-79	Abandoned



SWL-3

Well SWL-3 was completed by SUNEDCO on November 26, 1979 to a total depth of 9126 feet (Figure 7.1.3). SWL-3 produces through perforations in the 9 5/8" casing from the Miocene basalt in the 7070 to 7450 foot interval. SWL-3 has been flow tested several times, the most recent being in 1983. It will produce 300,000 lbs/hr with a wellhead pressure of 90 psig. Currently this well is being used for pressure observation purposes. It could also be used for injection purposes. In its current state it is incapable of commercial production.

52-18

Well 52-18 was completed by SUNEDCO on May 8, 1980 to a total depth of 9860 feet (Figure 7.1.4). The well produces from the 9055 to 9289 foot interval located within the Jurassic spilite sequence. The well has only been a marginal producer and this is believed to be due to the producing fractures being damaged by mud during drilling. The well has been flowed several times, the most recently being for 9 days in February and March 1986. During this sequence of flow tests the maximum flowrate was 263,000 lbs/hr at a wellhead pressure of 90 psig. Currently this well is being used for pressure observation purposes. It may be possible to use this as an injection well in the future.

62-21

Well 62-21 was completed by SUNEDCO on October 31, 1980 to a total depth of 12,500 feet (Figure 7.1.5). Well 62-21 produces from argillaceous sedimentary rocks in the 9040-12,500 foot interval. The small flow rate is artesian at a maximum temperature of 246 degrees F. The maximum static temperature in the well is probably near 380 deg. F. The shut-in wellhead pressure is approximately 73 psig. To date there is no evidence that well 62-21 has intersected the reservoir. This well is currently being used for pressure observation purposes.

84-7

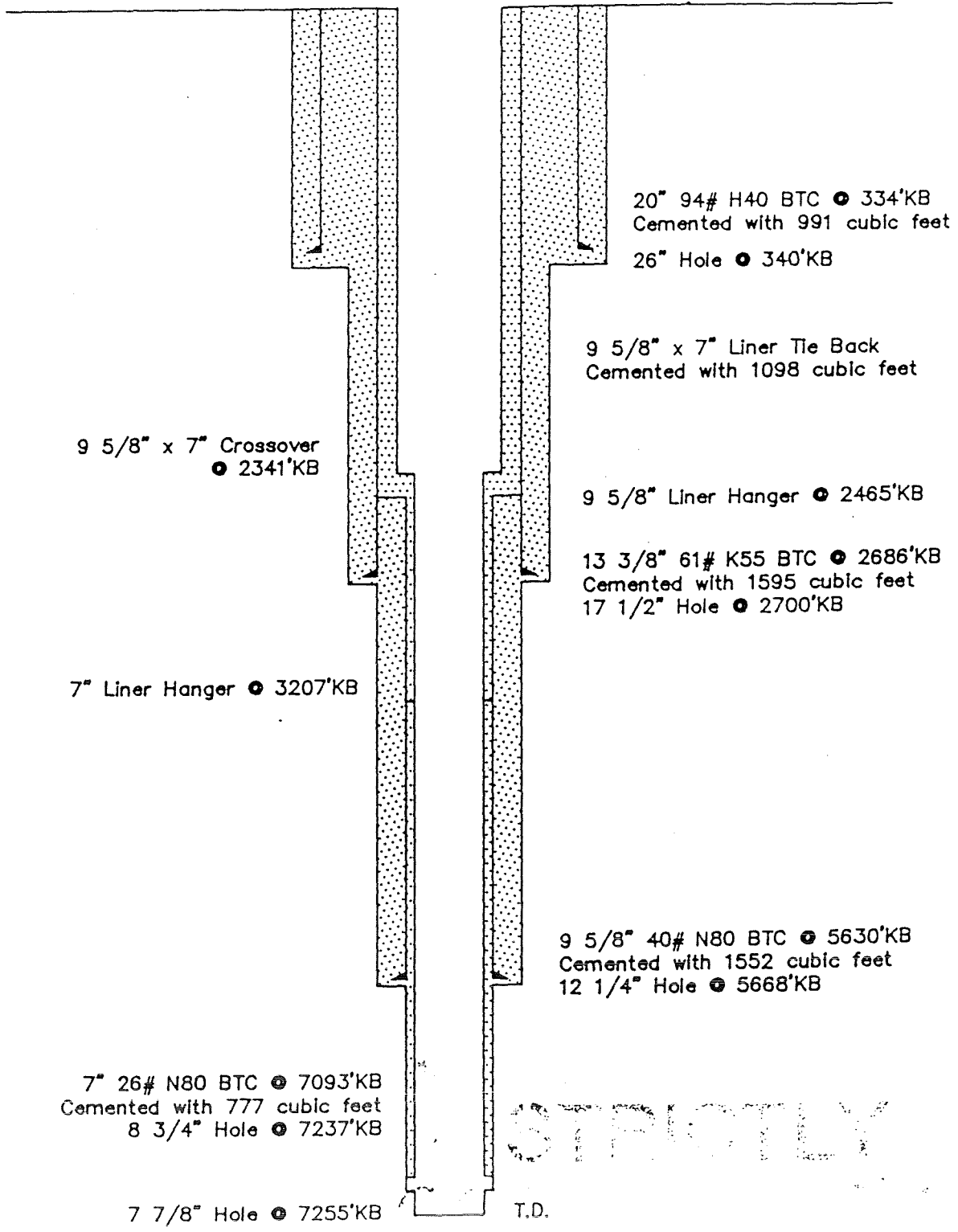
Well 84-7 was completed by SUNEDCO on January 17, 1981 to a total depth of 8142 feet (Figure 7.1.6). The well produces from the Jurassic spilitic sequence between depths of 8055 and 8142 feet. The production zone is associated with the range front fault. The well was most recently flow tested for 75 days during early 1986 as part of Oxbow's reservoir

Well Completion Diagram Well SWL-1

Location: NW-NW-NW Section 18-24N-37E
Churchill County, Nevada

Datum: 3496' KB, 16' Above Ground Level

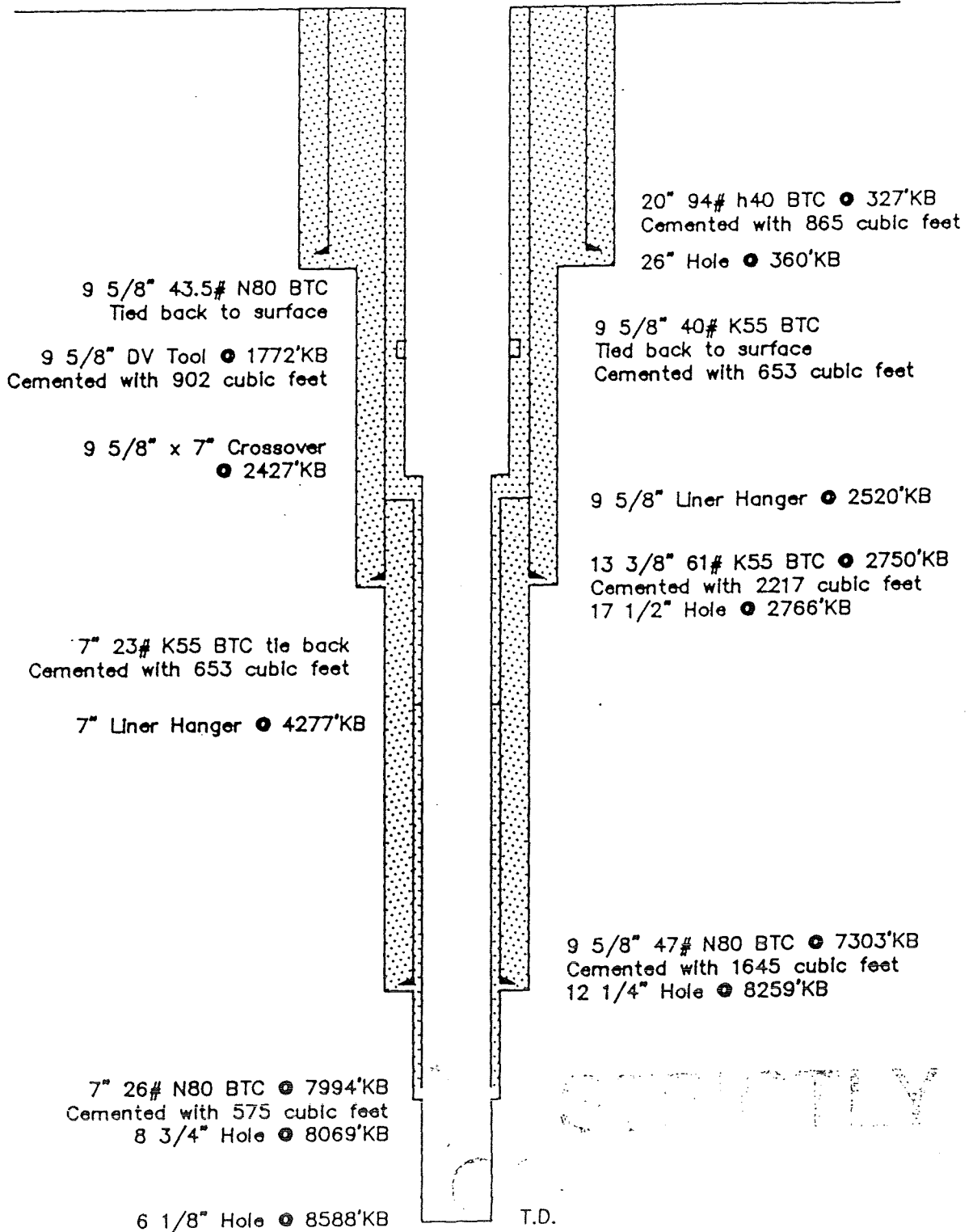
Drilled: 11/29/78



Well Completion Diagram Well SWL-2

Location: SE-NE-NE Section 13-24N-36E
Churchill County, Nevada

Datum: 3490.5' KB, 22' Above Ground Level
Drilled: 08/24/79

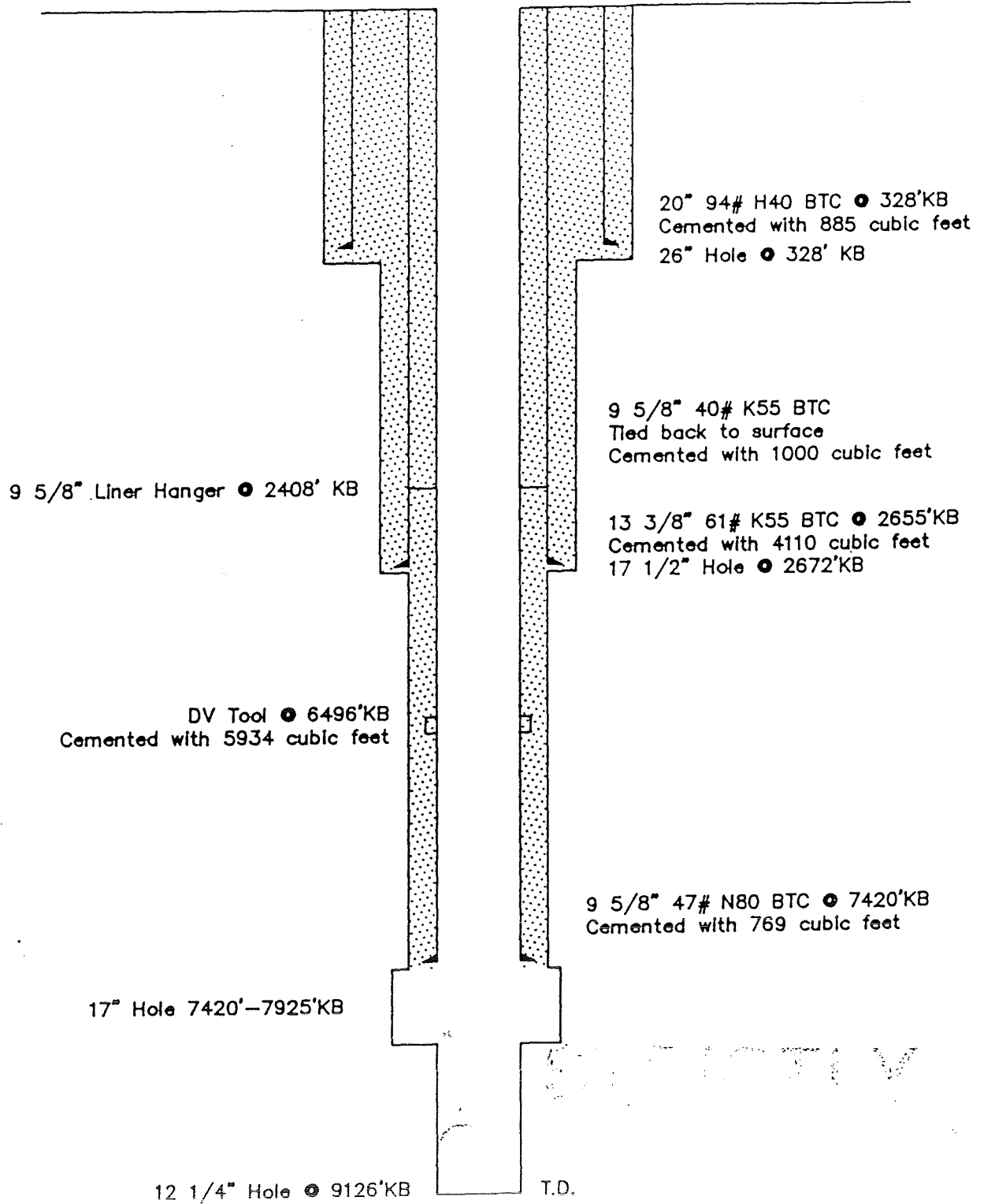


Well Completion Diagram Well SWL-3

Location: SW-NE-NW Section 18-24N-37E
Churchill County, Nevada

Datum: 3493' KB, 25' Above Ground Level

Drilled: 11/25/79



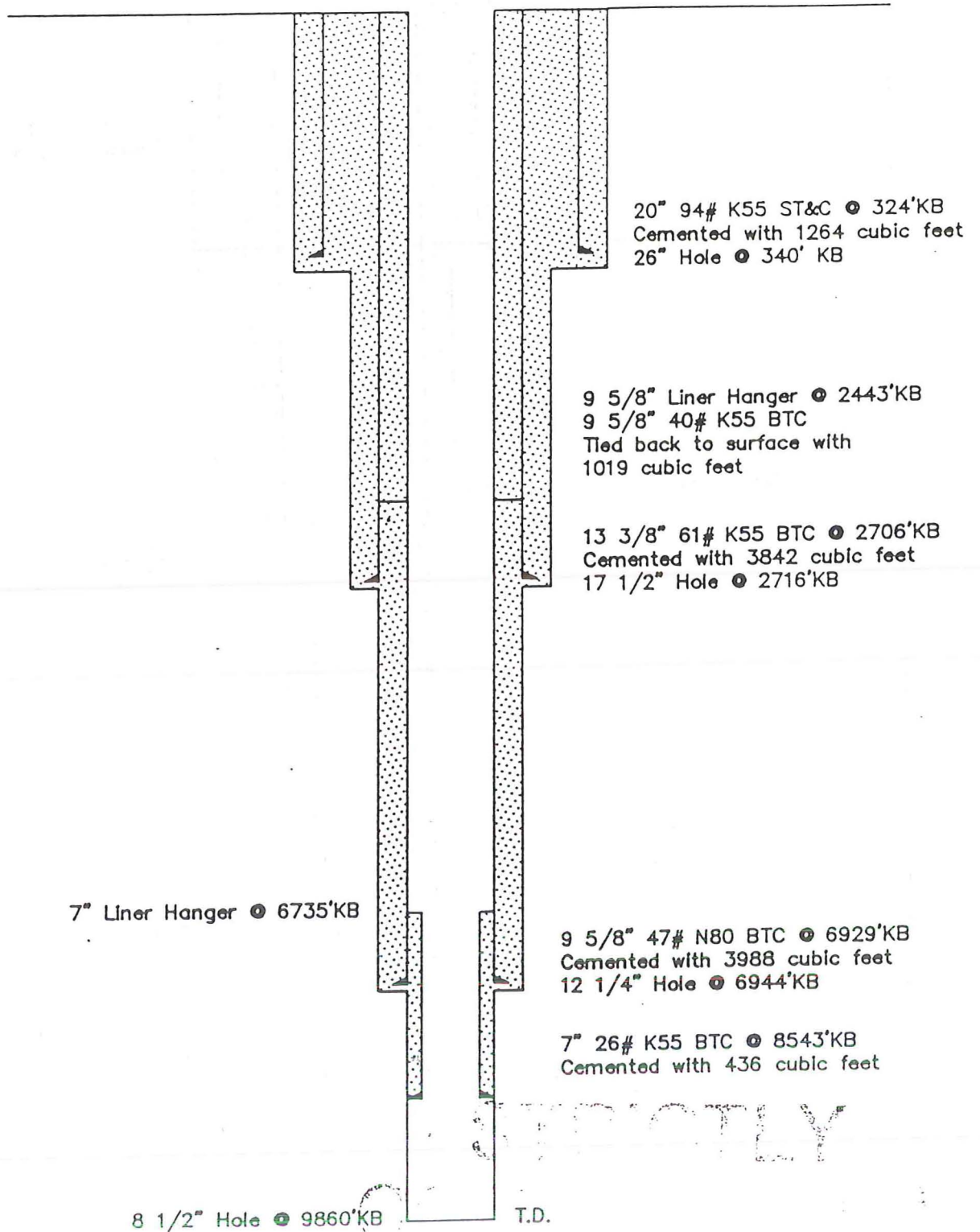
Well Completion Diagram Well 52-18

Location: NE-NE-NW Section 18-24N-37E

Churchill County, Nevada

Datum: 3486.5' KB, 25.5 Above Ground Level

Drilled: 02/08/80

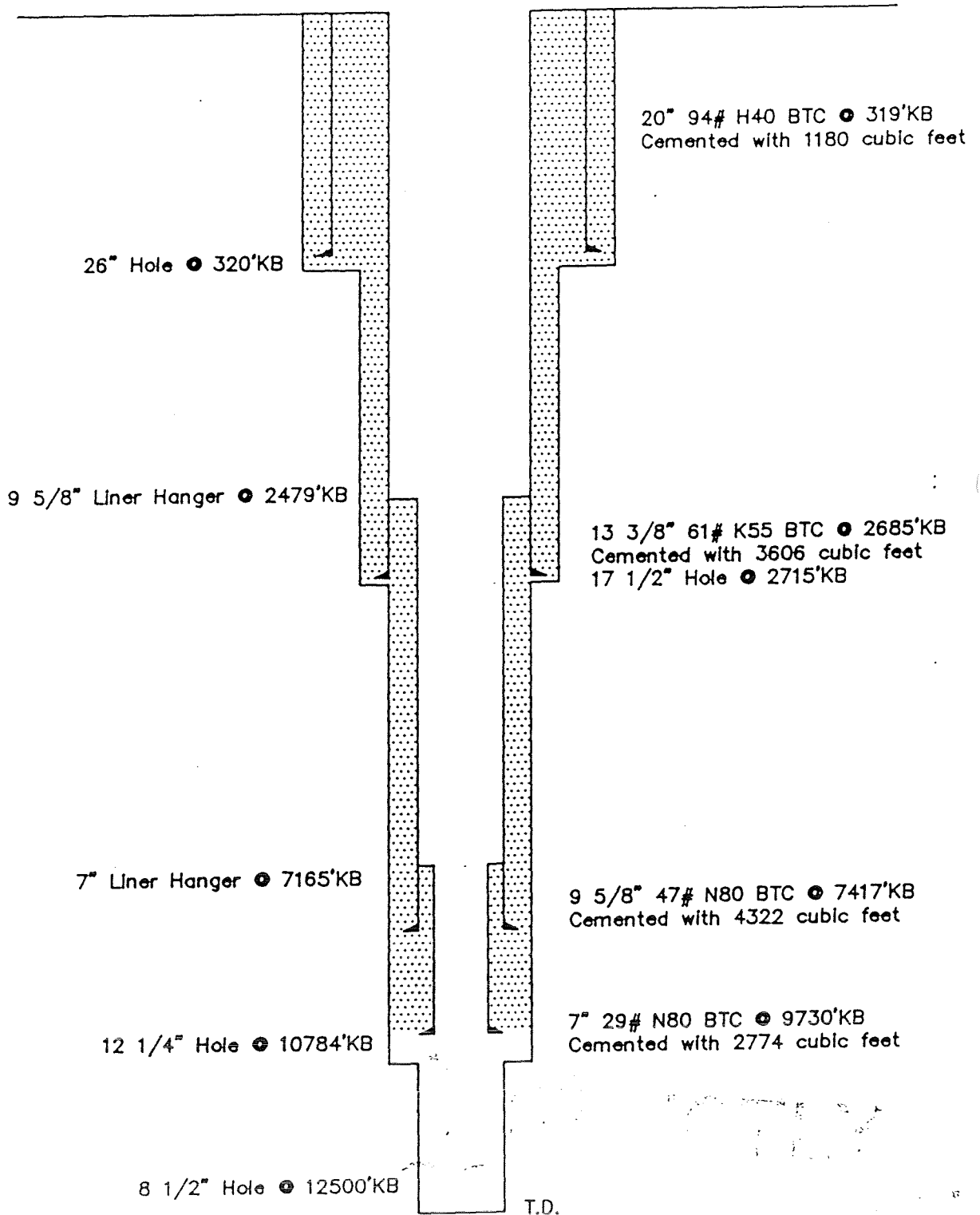


Well Completion Diagram Well 62-21

Location: NE-NE-NW Section 21-24N-37E
Churchill County, Nevada

Datum: 3471' KB, 25.5 Above Ground Level

Drilled: 10/31/86

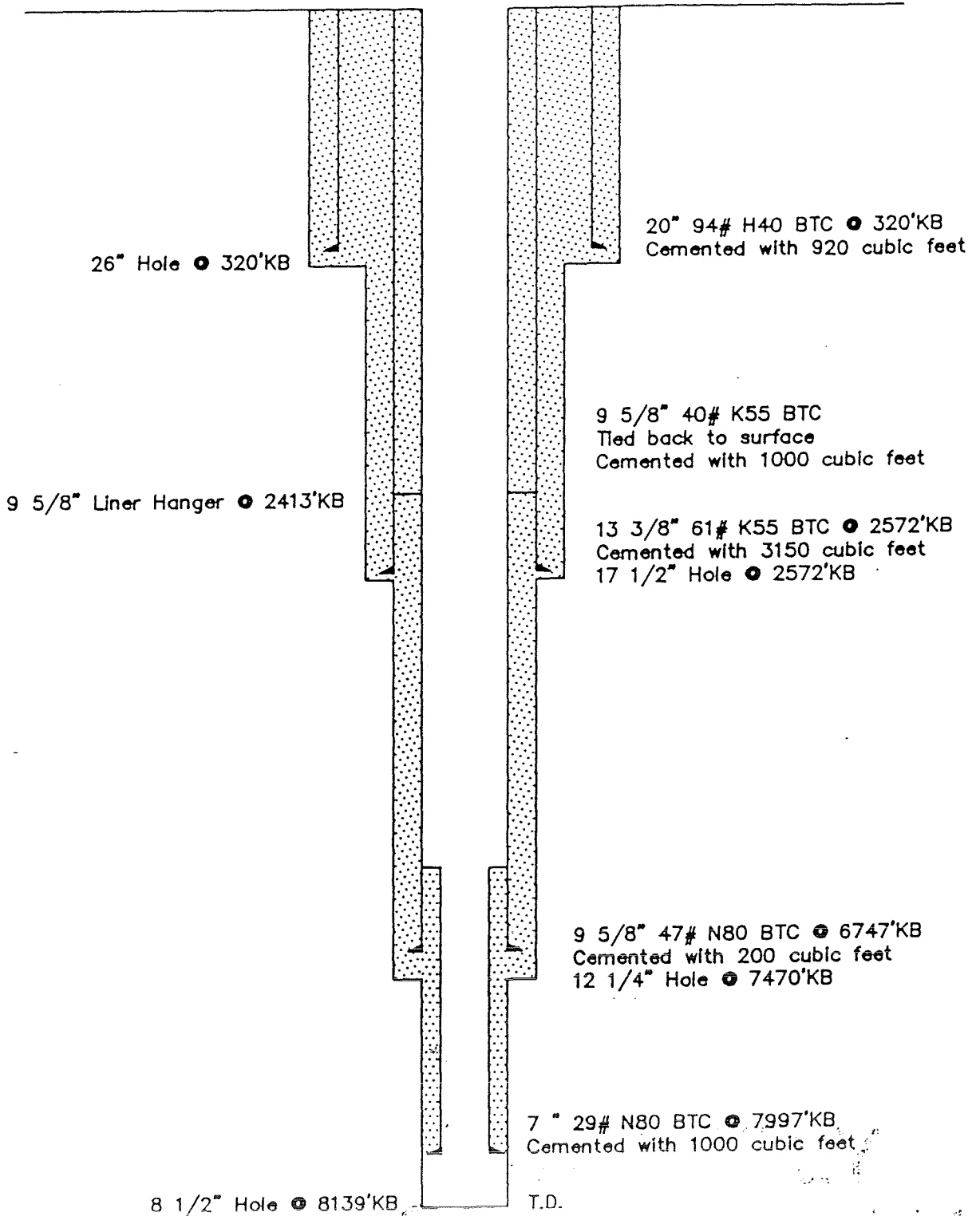


Well Completion Diagram Well 84-7

Location: NE-SW-NE Section 7-24N-37E
Churchill County, Nevada

Datum: 3498.5' KB, 25.5' Above Ground Level

Drilled: 01/17/81



assessment. During this flow test well 84-7 produced 650,000 lbs/hr of fluid at a wellhead pressure of 128 psig. Currently this well is being used as a pressure observation hole for the 6 well flow test. Future plans for this well include a cleanout and deepening to intersect additional fractures and increase its flow rate.

65-18

Well 65-18 was completed by SUNEDCO on March 30, 1981 to a total depth of 9305 feet. The well was subsequently deepened to 9466 feet during the March 1986 workover by Oxbow (Figure 7.1.7). Well 65-18 produces from the Jurassic spilitic sequence between depths of 9265 and 9417 feet. The well was flow tested twice during early 1981 and late 1982. During the latter part of 1981 and early 1982 the well was used as an injector. After the 1986 workover the well produced at flow rates up to 800,000 lbs/hr at a wellhead pressure of 100 psig. This is one of the wells flowed during the 6 well flow test. In the future well 65-18 will be evaluated as a possible injector.

45-5

Well 45-5 was completed by SUNEDCO on June 24, 1981 to a total depth of 8261 feet (Figure 7.1.8). The well produced from the Miocene basalt in the 6020 to 6200 foot interval. The production zone is associated with the range-front fault at a relatively shallow depth. Although the well produced up to 609,000 lbs/hr, the enthalpy (322 btu/lb) and wellhead pressure (65 psig) are abnormally low. The well has only been flow tested for three days in May, 1981, and fifteen days in July, 1981. Currently well 45-5 is being used for pressure observation purposes. In the near future well 45-5 will be evaluated as a possible injection well.

27-33

Well 27-33 was completed by TGI on August 30, 1983 to a total depth of 9051 feet. The well was subsequently deepened to 9110 feet during the March 1986 workover by Oxbow (Figure 7.1.9). Well 27-33 produces from the Jurassic marine sedimentary rocks in the 8862 to 9110 foot interval. The well was extensively flow tested prior to the 1986 workover. After the workover its flow rate increased from 370,000 lbs/hr to 720,000 lbs/hr. Currently this well is being used for pressure observation purposes in the 6 well test. This will be one of the wells supplying the power plant.

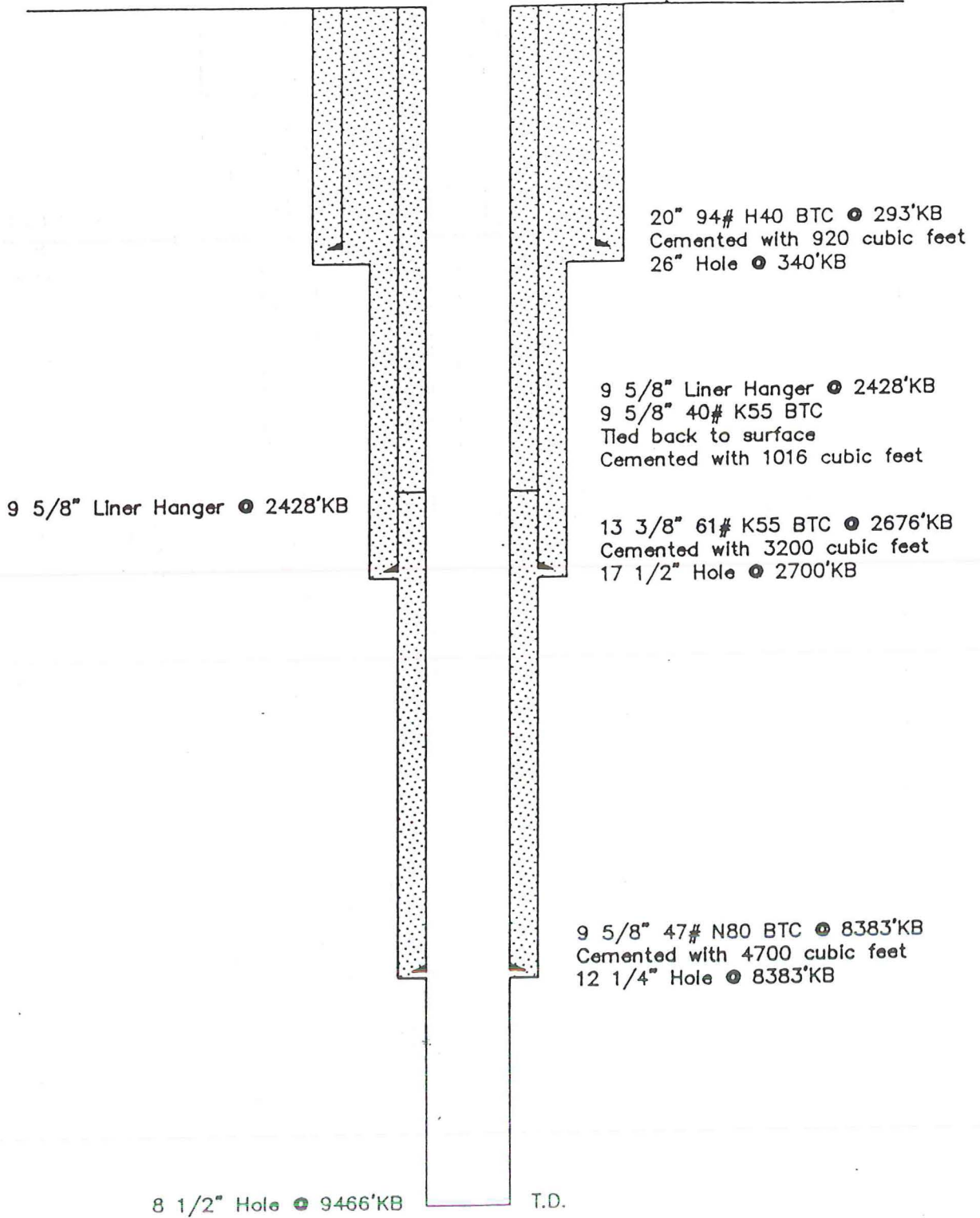
Well Completion Diagram Well 65-18

Location: NW-NW-SE Section 18-24N-37E

Churchill County, Nevada

Datum: 3469' KB, 32' Above Ground Level

Drilled: 01/21/81



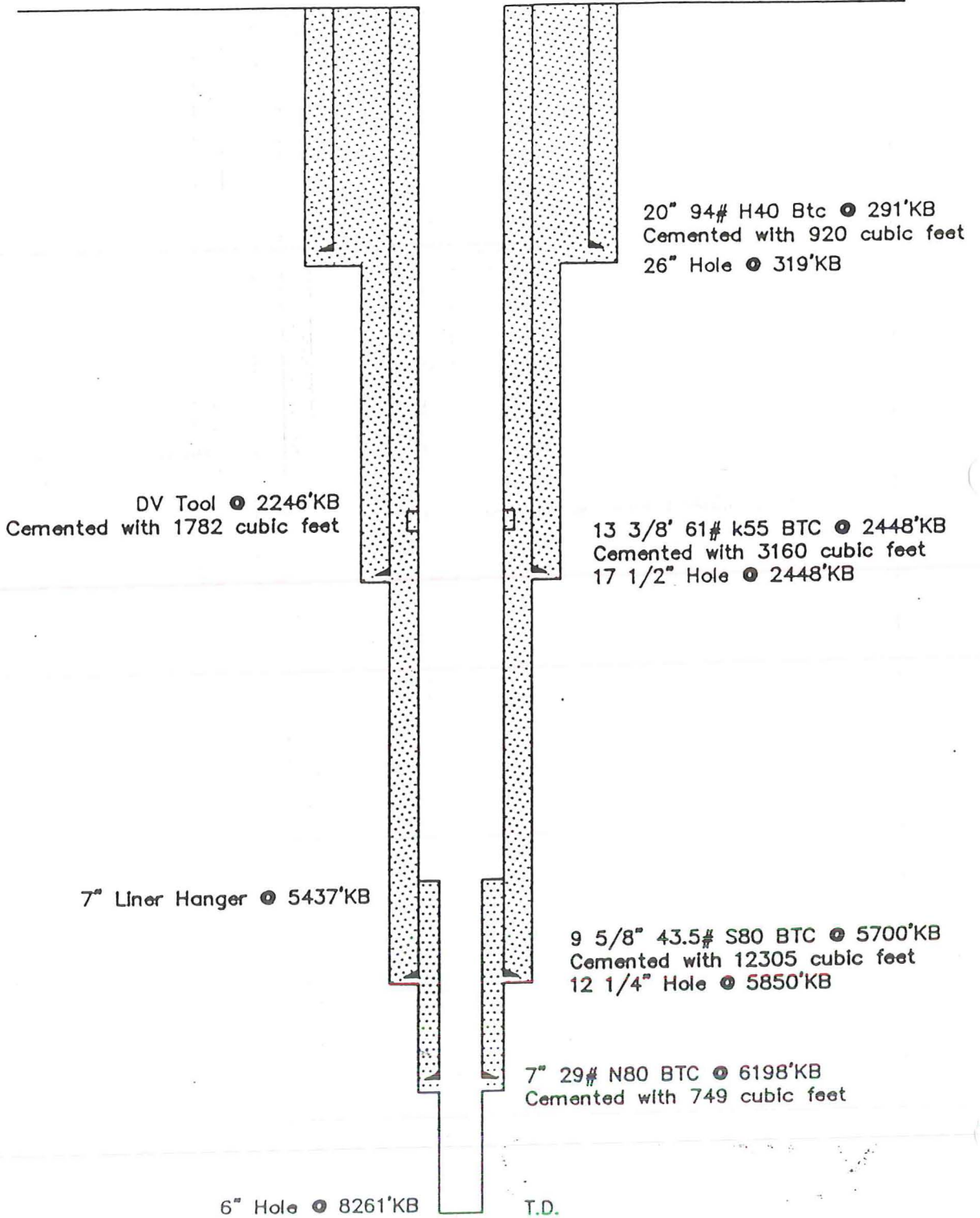
Well Completion Diagram Well 45-5

Location: SE-SW-NW Section 5-24N-37E

Churchill County, Nevada

Datum: 3478' KB, 27' Above Ground Level

Drilled: 06/24/81

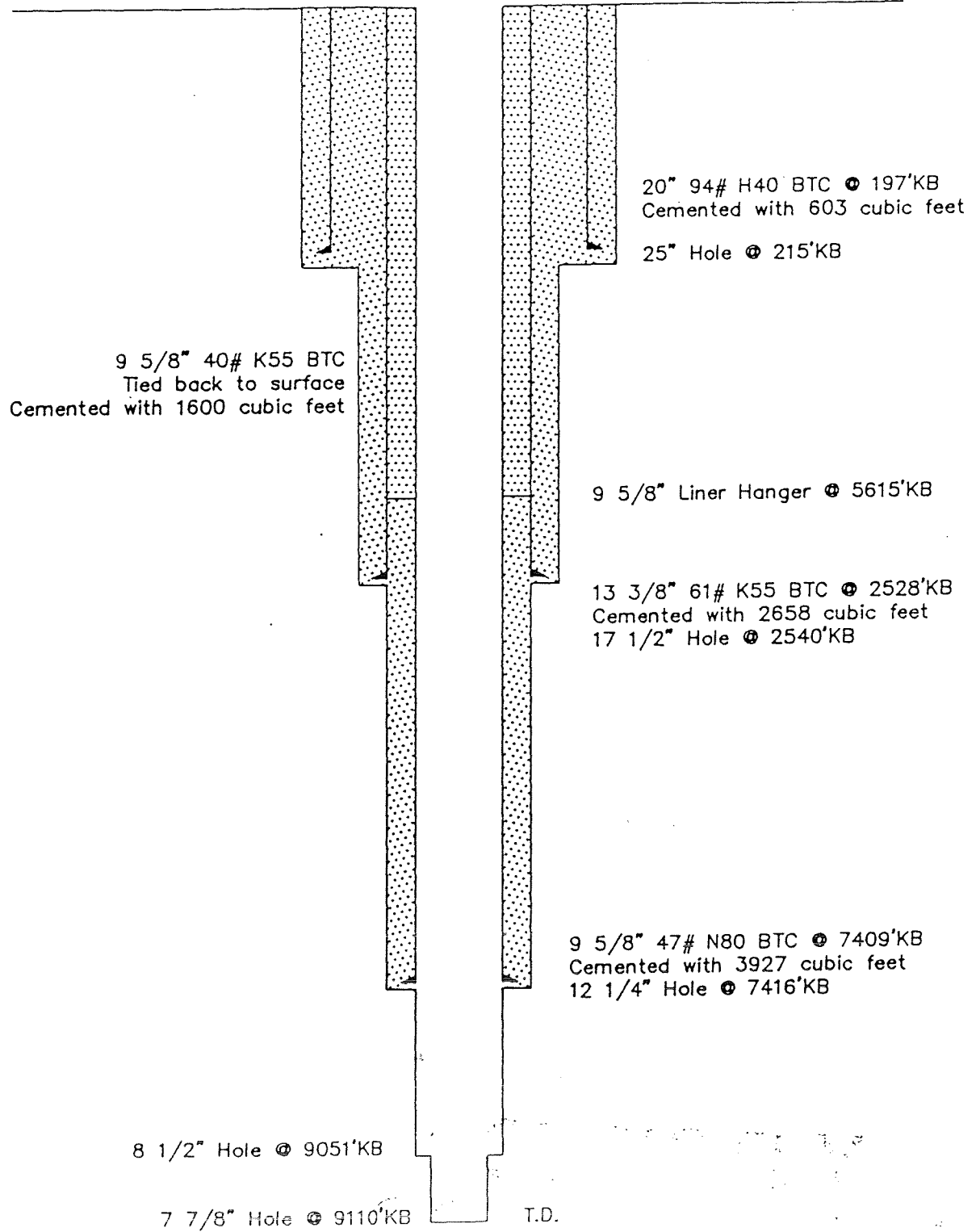


Well Completion Diagram Well 27-33

Location: NE-SW-SW Section 33-25N-37E
Churchill County, Nevada

Datum: 3469' KB, 23' Above Ground Level

Drilled: 08/31/83



45-33

Well 45-33 was completed by TGI on December 31, 1983 to a total depth of 10,212 feet. The well was subsequently deepened to 10,266 feet during the June 1986 workover by Oxbow (Figure 7.1.10). The workover was conducted to mill out two casing collapse zones located within the 9 5/8" casing. The well produces from the Jurassic marine sedimentary rocks in the 10,058 to 10,240 foot interval. The well was extensively flow tested prior to the Oxbow workover. Since the workover the flow rate for well 45-33 has increased from 610,000 lbs/hr to about 1,000,000 lbs/hr. Oxbow is currently flowing this well as part of the 6 well flow test. Well 45-33 is one of the wells that will be supplying the power plant.

82-5

Well 82-5 was completed by Oxbow on February 18, 1986, to a total depth of 9384 feet (Figure 7.1.11). The existing leg of 82-5 is the fourth leg of the well and is a dry hole completed in Cretaceous granodiorite. Only leg two of 82-5 was capable of production and this was at a wellhead pressure of 25 psig. Currently this well is idle. Future plans call for cleaning out the well so it can be evaluated as a long term pressure observation well.

74-7

Well 74-7 was completed by Oxbow on March 29, 1986, to a total depth of 8890 feet (Figure 7.1.12). The well produces from the Jurassic spilitic sequence in the 8722 to 8890 foot interval. The production zone is associated with the range-front fault. Well 74-7 was the first well completed at Dixie Valley with 13 3/8" production casing set to a depth below the flash zone. Since completion this well has been extensively tested. Its maximum initial flow rate was 1,350,000 lbs/hr at a wellhead pressure of 162 psig. This well is currently producing as part of the 6 well flow test and will be one of the wells supplying the power plant.

32-18

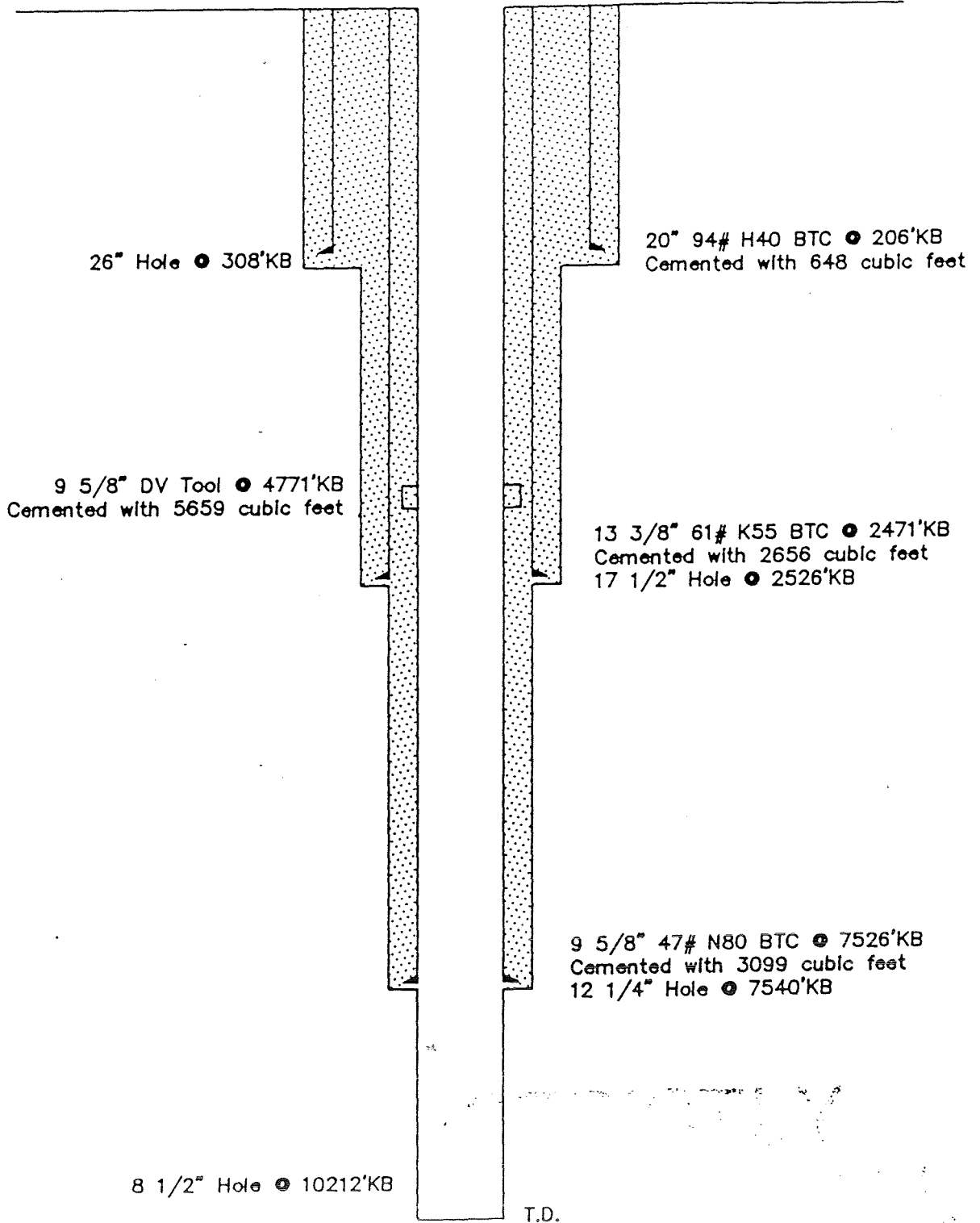
Well 32-18 was completed by Oxbow on March 31, 1986, to a total depth of 7461 feet (Figure 7.1.13). The well produces from the Miocene basalt in the 7360 to 7374 foot interval. The well was flow tested for a short period before the drill rig was released and later in 1986 during the six well flow

Well Completion Diagram Well 45-33

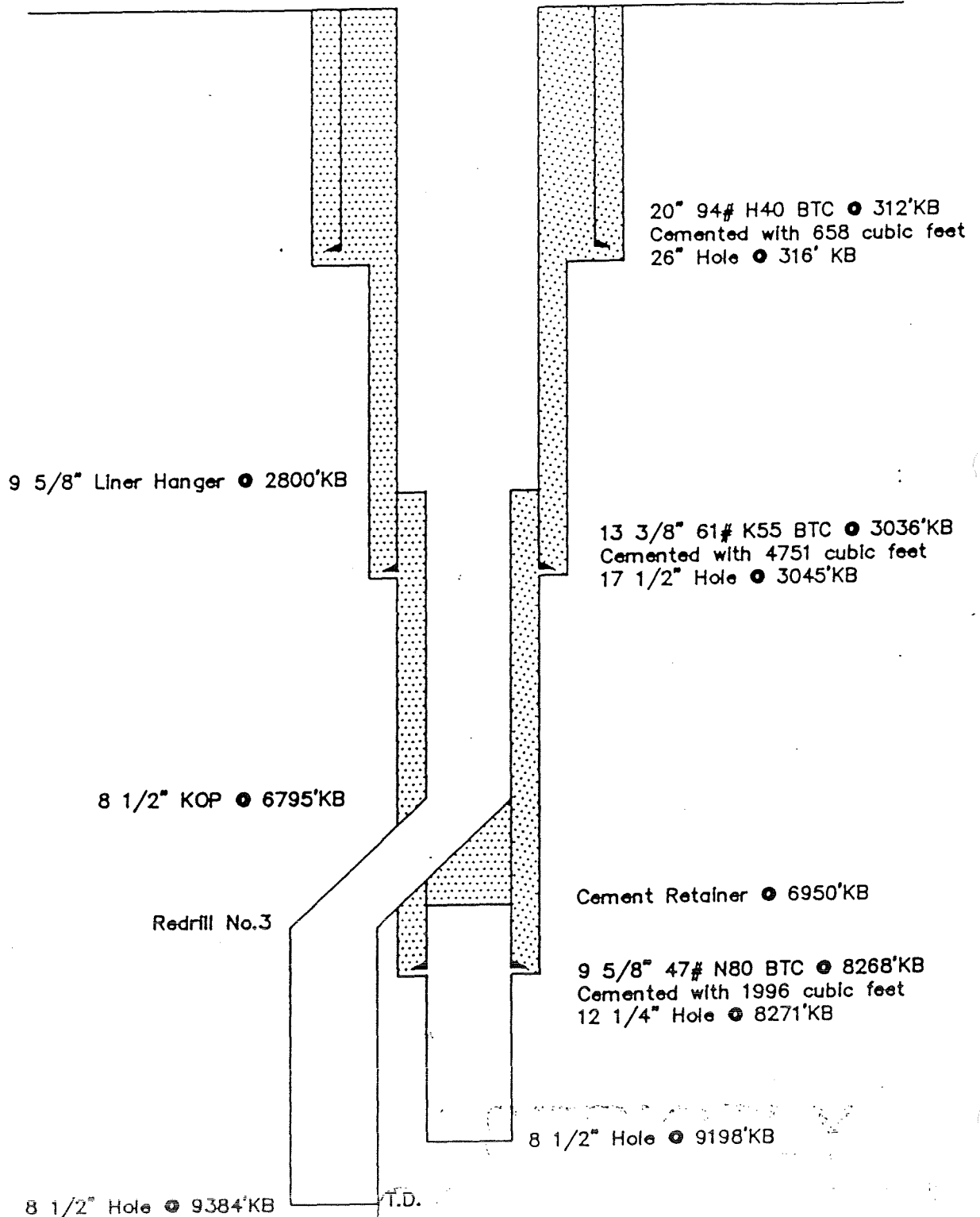
Location: NE-NE-SW Section 33-25N-37E
Churchill County, Nevada

Datum: 3471' KB, 23' Above Ground Level

Drilled: 12/31/83



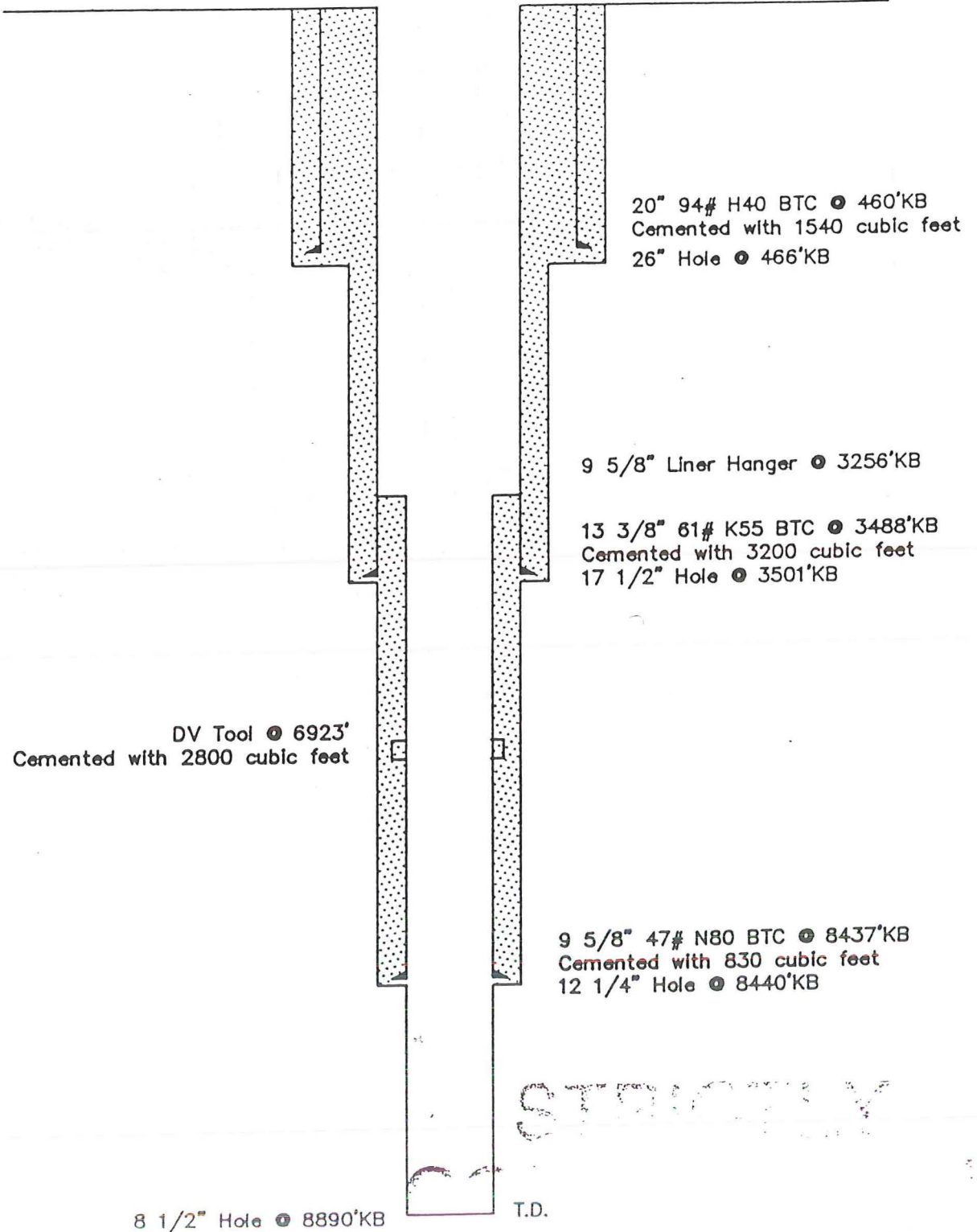
Well Completion Diagram Well 82-5
 Location: SE-NE-NE Section 5-24N-37E
 Churchill County, Nevada
 Datum: 3467' KB, 23' Above Ground Level
 Drilled: 02/18/86



Well Completion Diagram Well 74-7

Location: SE-SW-NE Section 7-24N-37E
Churchill County, Nevada

Datum: 3494.5' KB, 21' Above Ground Level
Drilled: 03/29/86

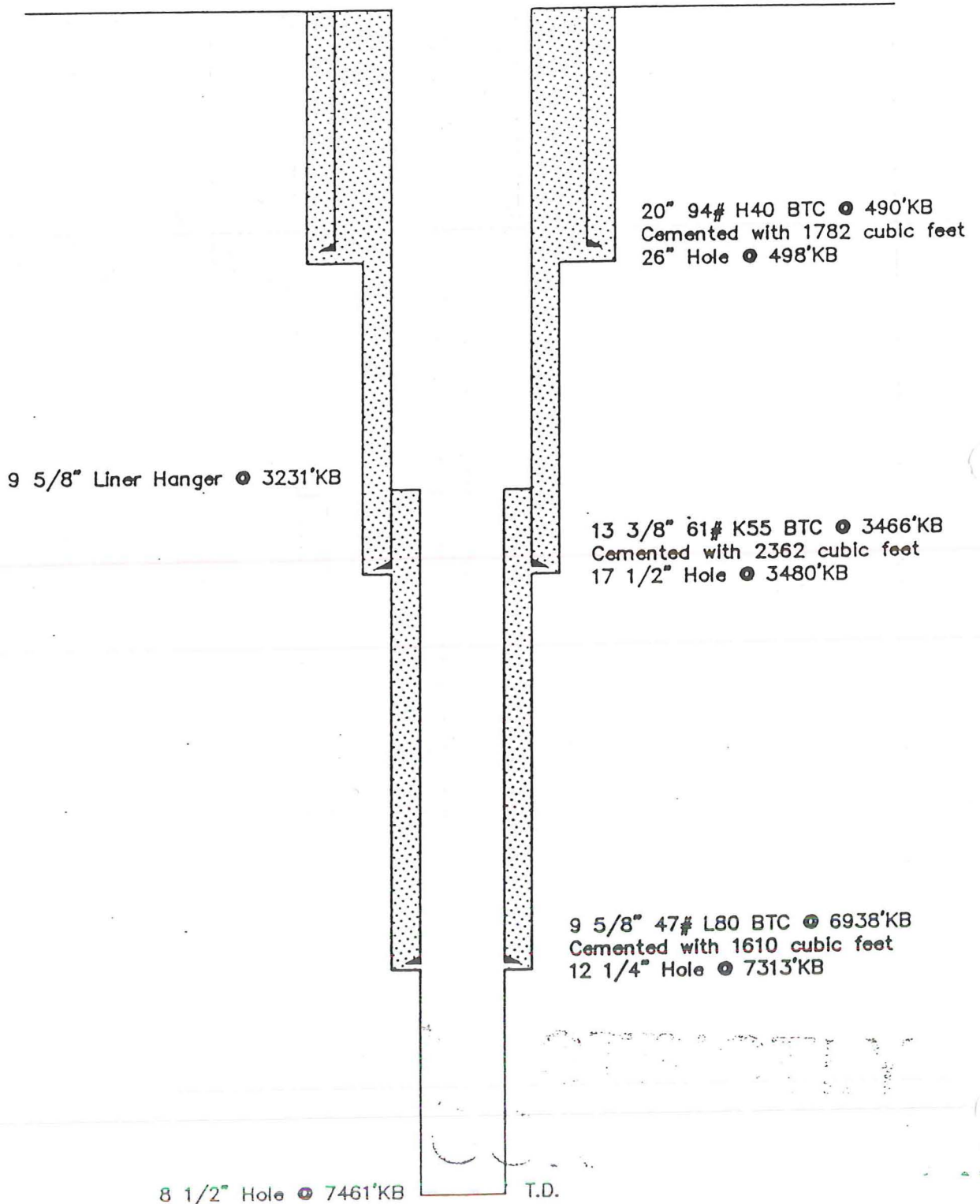


Well Completion Diagram Well 32-18

Location: SW-NE-NE Section 18-24N-37E
Churchill County, Nevada

Datum: 3467' KB, 30' Above Ground Level

Drilled: 02/20/86

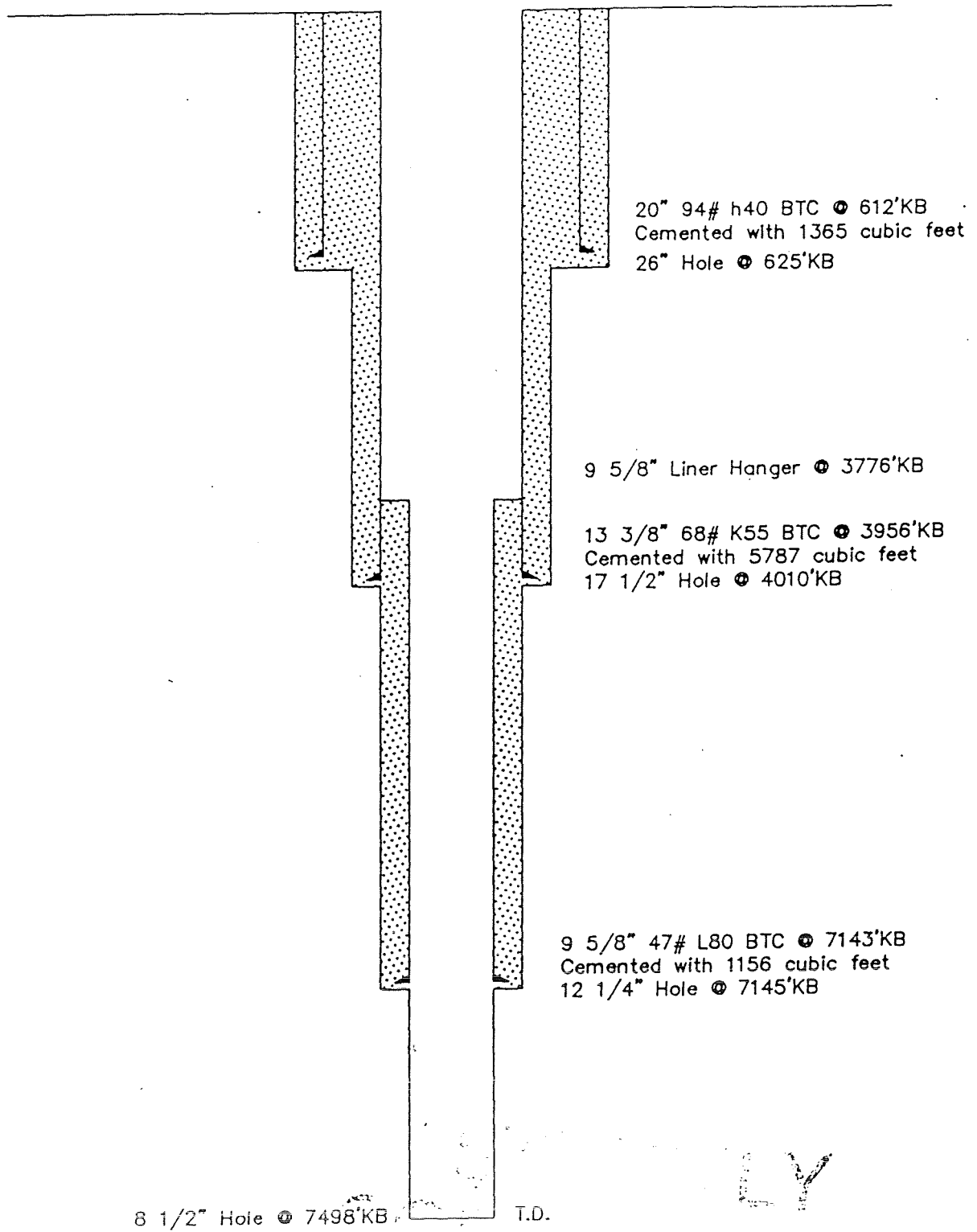


Well Completion Diagram Well 76-7

Location: SW-NE-SE Section 7-24N-37E
Churchill County, Nevada

Datum: 3491' KB, 28.5' Above Ground Level

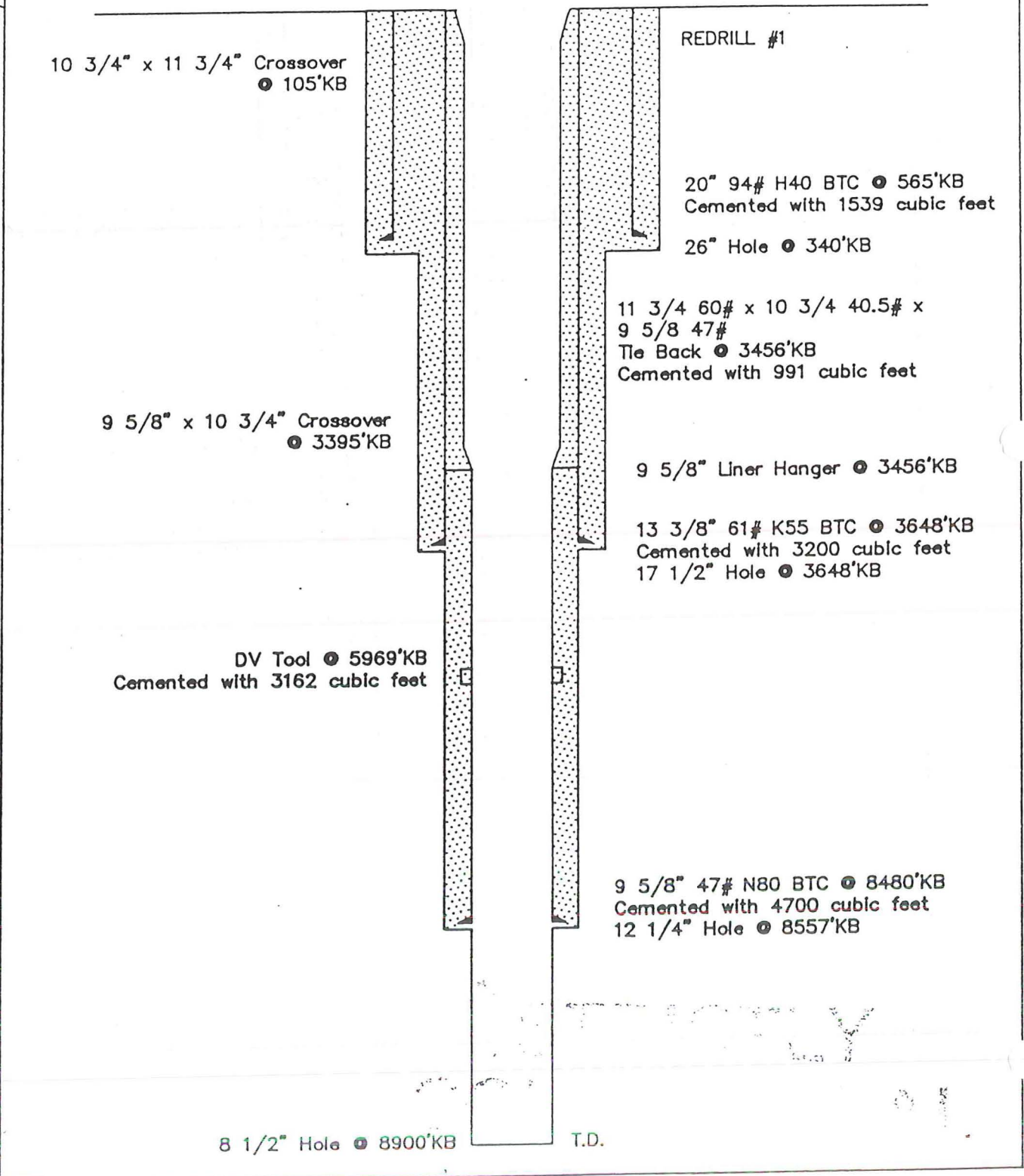
Drilled: 05/24/86



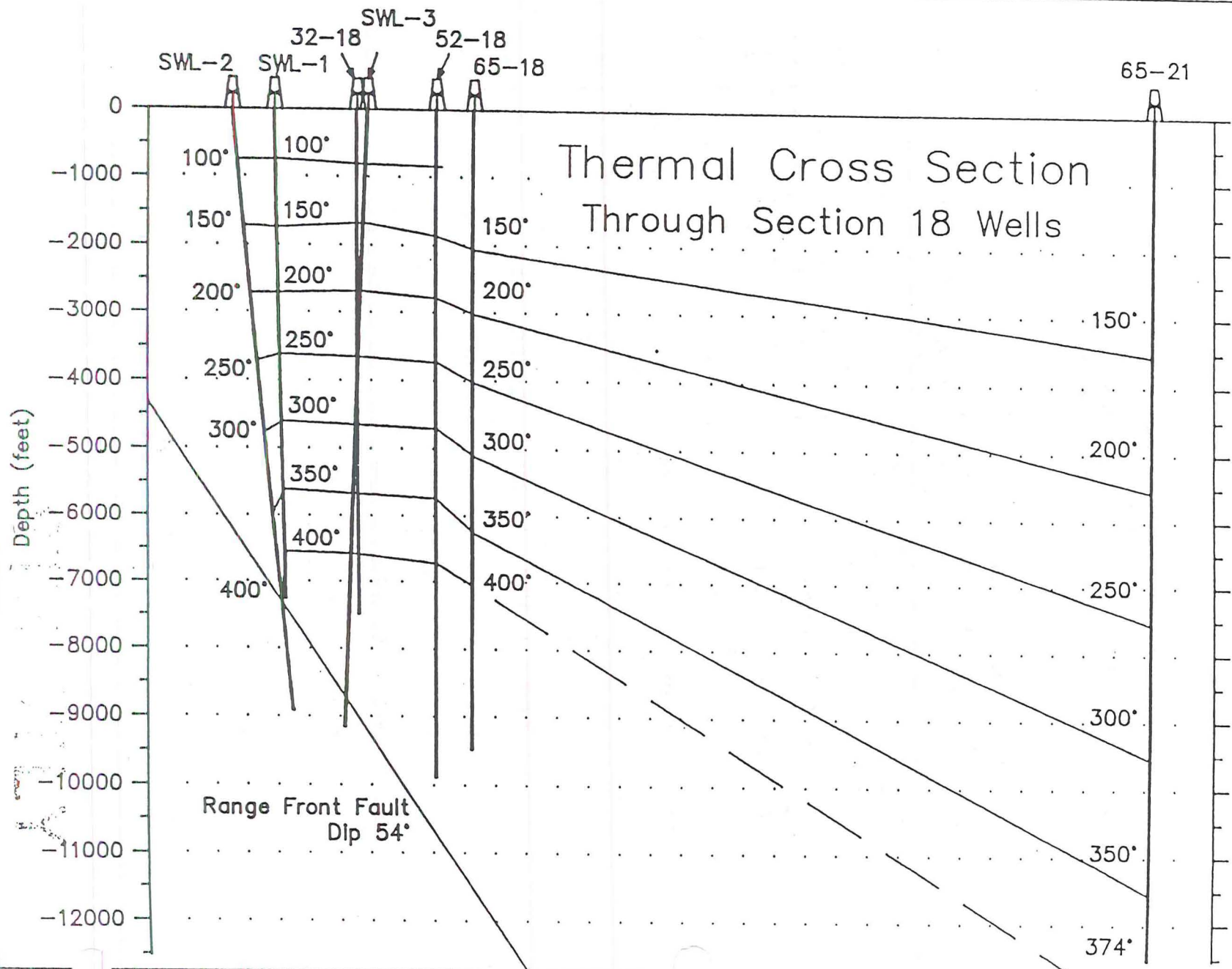
Well Completion Diagram Well 73-7

Location: NW-NW-SE Section 7-24N-37E
Churchill County, Nevada

Datum: 3508' KB, 32' Above Ground Level
Drilled: 08/07/86



Thermal Cross Section Through Section 18 Wells



34700

test. Initially this well produced 922,000lbs/hr at a wellhead pressure of 100 psig. This well is being evaluated as a possible injector.

76-7

Well 76-7 was completed by Oxbow on May 24, 1986, to a total depth of 7498 feet (Figure 7.1.14). The well produces from the Miocene basalt in the 7315 to 7461 foot interval. The initial production of well 76-7 was 1,700,000 lbs/hr at a wellhead pressure of 148 psig. This is by far the hottest of the wells to produce from the Miocene basalt and it is one of the wells currently flowing in the 6 well test. This will be one of the wells supplying the power plant.

73-7

Well 73-7 was completed by Oxbow on August 7, 1986 to a total depth of 8900 feet (Figure 7.1.15). The well produces from the Jurassic spilitic sequence in the 8528 to 8913 foot interval. The production zone is associated with the range front fault. A leak in the 13 3/8" casing required the well to be completed with 10 3/4" and 11 3/4" casing tie back set to a depth below the flash zone. This is one of the wells producing for the 6 well test. Well 73-7 initially flowed 1,080,000 lbs/hr at a wellhead pressure of 118 psig. This well will supply the power plant.

7.2 Previous Testing

7.2.1 SUNEDCO Geothermal Testing

SUNEDCO conducted a number of flow and interference tests in conjunction with its drilling during the period 1979 to 1982. The testing and results have been summarized by GeothermEx in a report titled "Estimation of Geothermal Energy Reserves Underlying Sun Geothermal Company Leases in Dixie Valley, Nevada. November 1984."

The testing showed that all the SUNEDCO wells except 62-21 are in good hydraulic communication and the transmissivity of the reservoir in the area of the wells is between 15,000 and 70,000 md ft. Table 7.3 summarizes the reservoir test data obtained by Sun.

GeothermEx concluded that the reservoir consisted of a permeable region associated with and generally confined to the range front fault. Thermal boundaries were placed on the reservoir on the basis of temperature contouring as shown in Figure 7.2.1.

7.2.2 Trans-Pacific Geothermal Testing

Trans-Pacific Geothermal Inc. (TGI) conducted interference tests between its two wells 27-33 and 45-33 in 1983-4. The tests are documented in a Berkeley Group Inc. report titled "Resource Characteristics, Dixie Valley, Nevada. August 1984." Figure 7.2.2 reproduced from the report shows the interference data obtained in 45-33 while 27-33 was flowing and Figure 7.2.3 shows the interference data when the roles of the two wells were reversed.

The test data were analytically interpreted by idealizing the reservoir as a homogeneous and infinite system containing a large uniform flux fracture. A diagram illustrating the conceptual model is shown in Figure 7.2.4. The two wells intersect the fracture and the fracture draws fluid from the reservoir along its length, delivering it to the wells.

The transmissivity of the reservoir given by type curve matching was about 70,000 md-ft and the storage-fracture length group (0chxj exp 2) was 25,000 ft/psi. Matches to the TGI test data using the fracture model are shown in Figures 7.2.5 and 7.2.6.

The model can be interpreted physically by considering the range-front fault to be representative of the uniform flux fracture in the analytical model. The fault acts as the very permeable conduit drawing fluid from surrounding lower permeability zones and delivering it to the wells.

The TGI and SUNEDCO activities were entirely separate, neither party having access to the other's data. However, once the two properties were consolidated by Oxbow, it was possible to integrate data from the two regions. Figure 7.2.7 and 7.2.8 show pressure measurements made in 45-5 and 52-18 by SUNEDCO during the period when TGI was conducting flow tests of 45-33 in 1983.

Well 45-5 is about 6000 feet and well 52-18 about 17,000 feet from well 45-33. Both wells showed a pressure response to flow at 45-33 with 52-18 exhibiting more direct communication even though it is three times further away. Also, the response in 52-18 was nearly half that observed in 27-33. This is not consistent with a homogeneous reservoir response when it is considered that 27-33 is only 500 feet from 45-33 compared with 17,000 feet to 52-18.

Pressures in Well 45-33
While Flowing Well 27-33

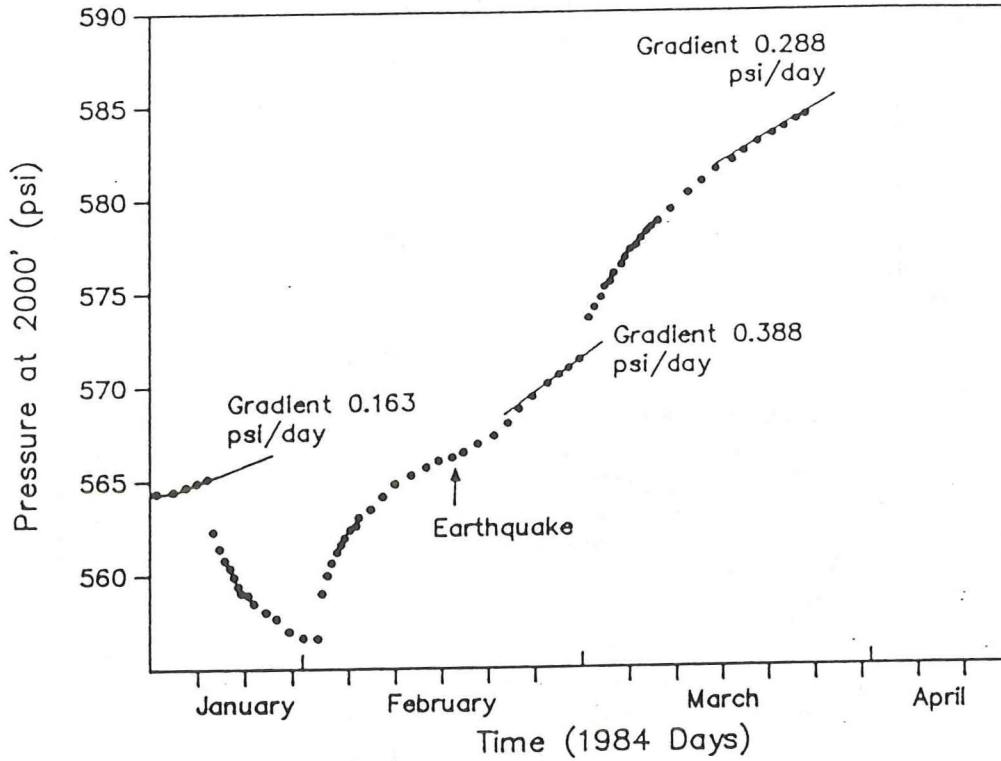


Figure 7.2.2

Pressures in Well 27-33
While Flowing Well 45-33

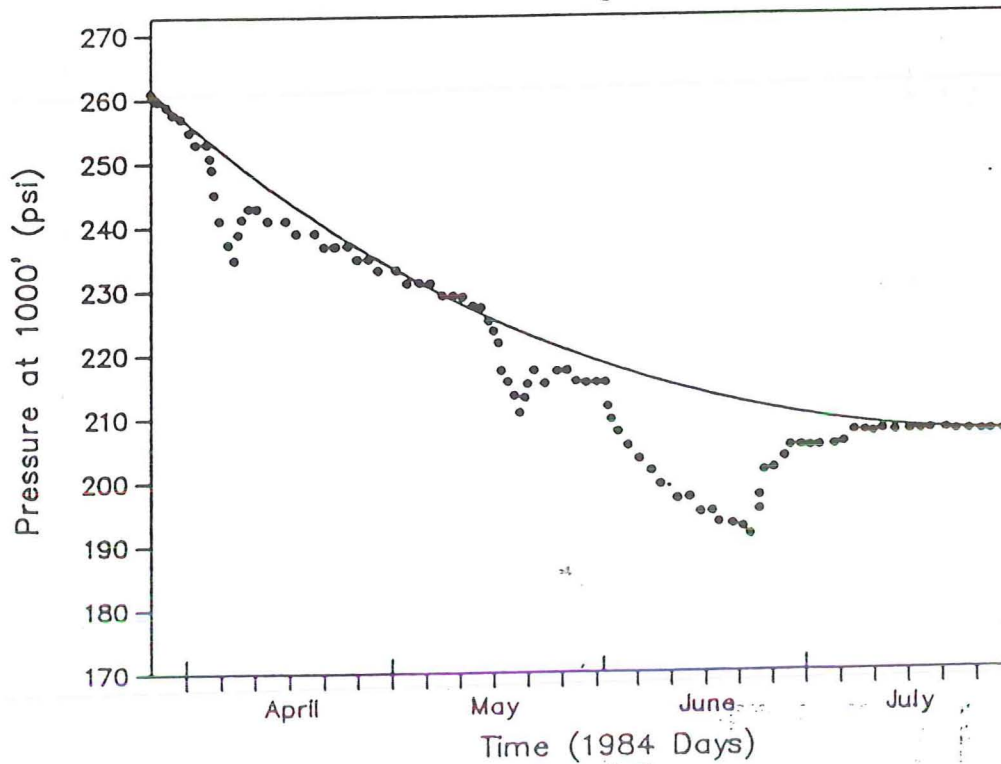


Figure 7.2.3

Pressures In Well 45-33 While Flowing Well 27-33

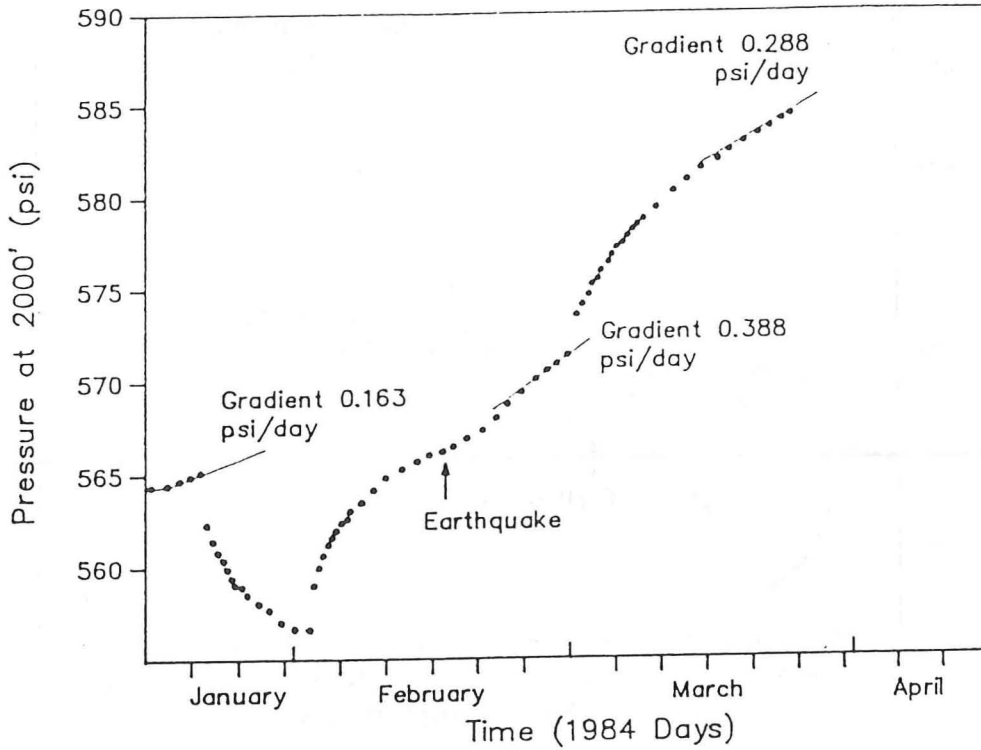


Figure 7.2

Pressures In Well 45-33 While Flowing Well 27-33

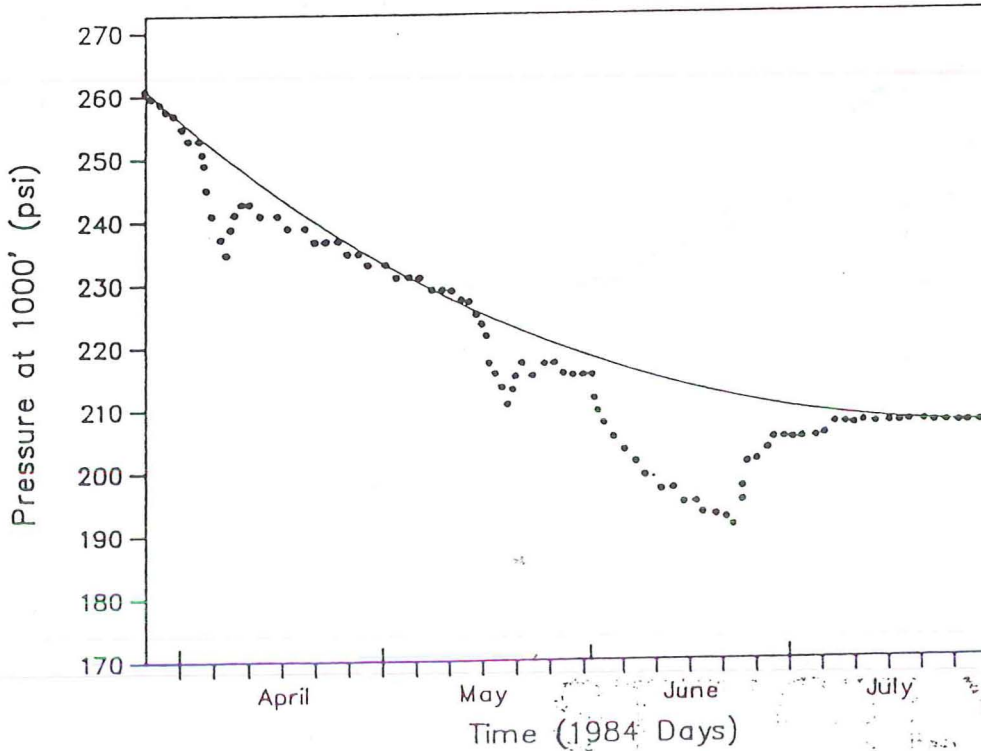


Figure 7.3

Conceptual Model of Dixie Valley Reservoir Evaluation of Transpacific Geothermal Test Data

Reservoir Properties
 $kh = 70,000 \text{ md-ft}$
 $\phi c h x_f^2 = 25,000 \text{ ft}^3/\text{psi}$

Wells



Uniform Flux
Fracture

History Match When 45-33 Was Producing and Subsequent Buildup

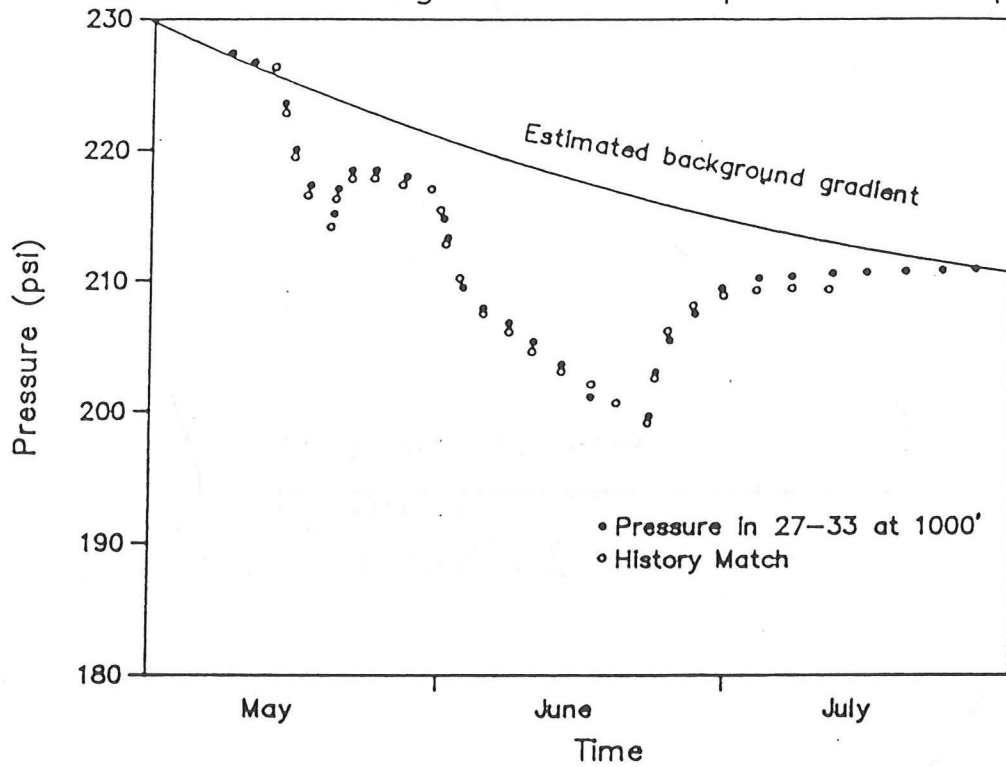


Figure 7.2.5

Drawdown in Well 45-33 Due to Flow Rate Increase of 27-33

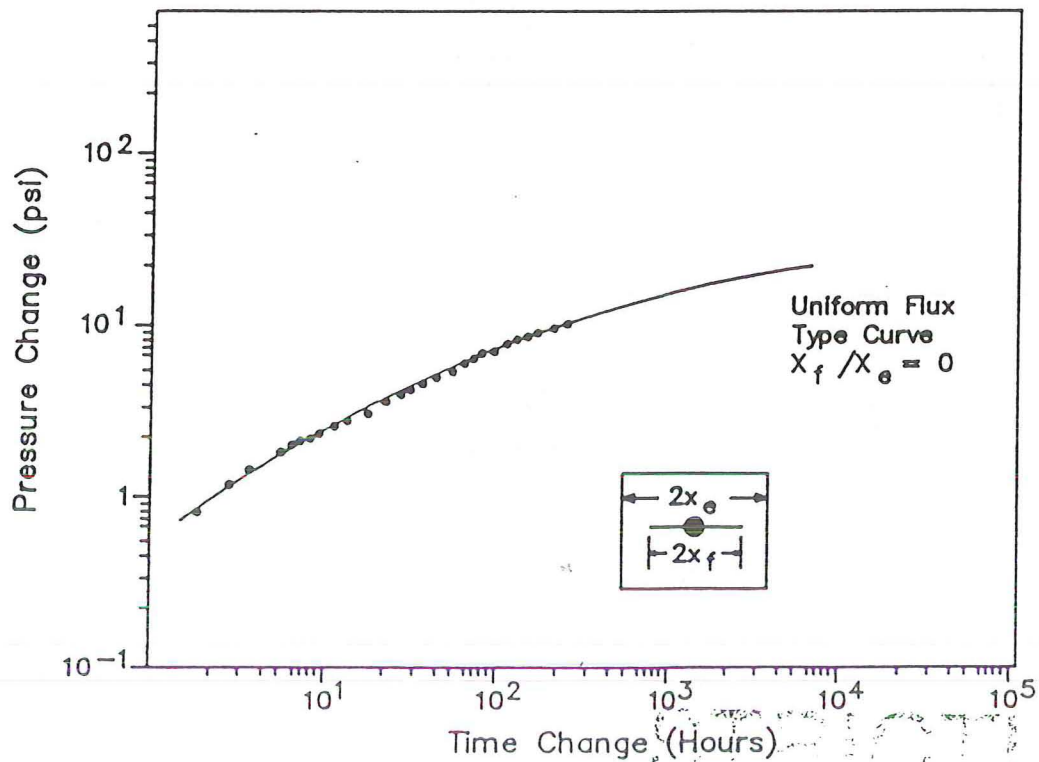


Figure 7.2.6

Downhole Pressure Monitoring Well SWL-1

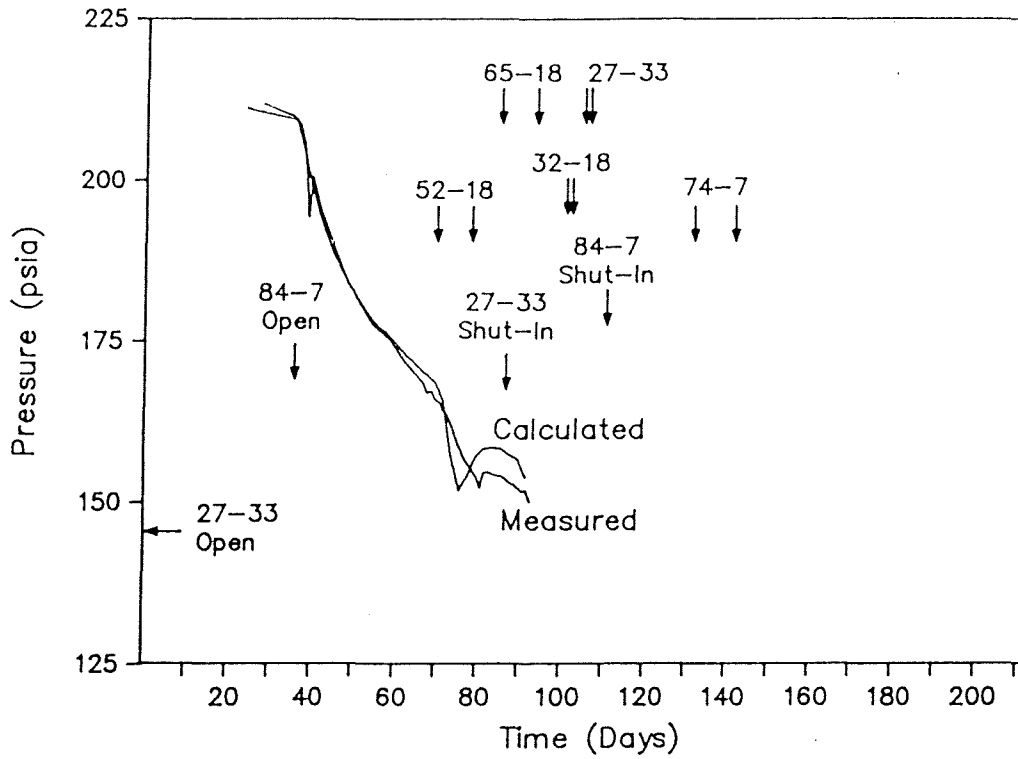


Figure 7.5.3

Downhole Pressure Monitoring Well SWL-3

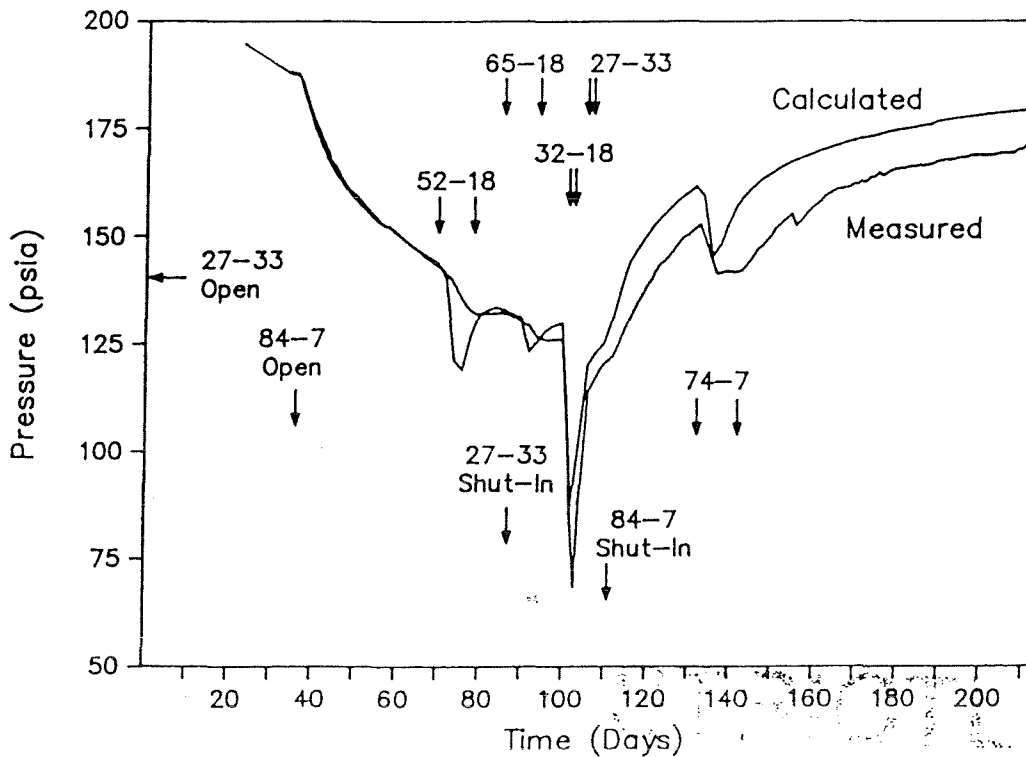


Figure 7.5.4

History Match When 45-33 Was Producing and Subsequent Buildup

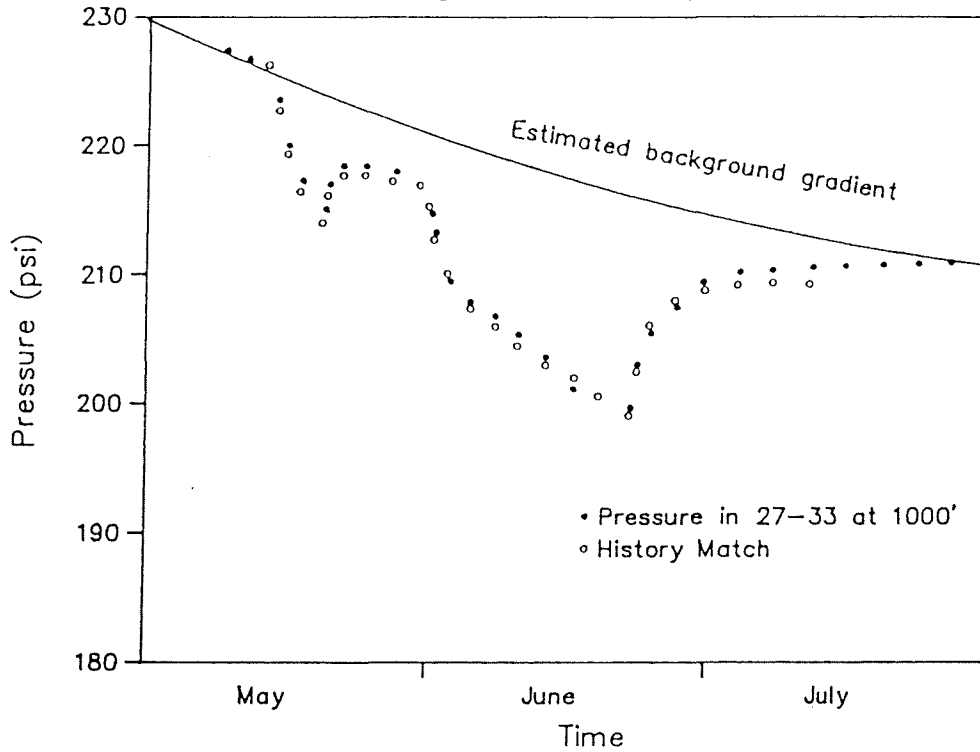


Figure 7.5

Drawdown In Well 45-33 Due To Flow Rate Increase Of 27-33

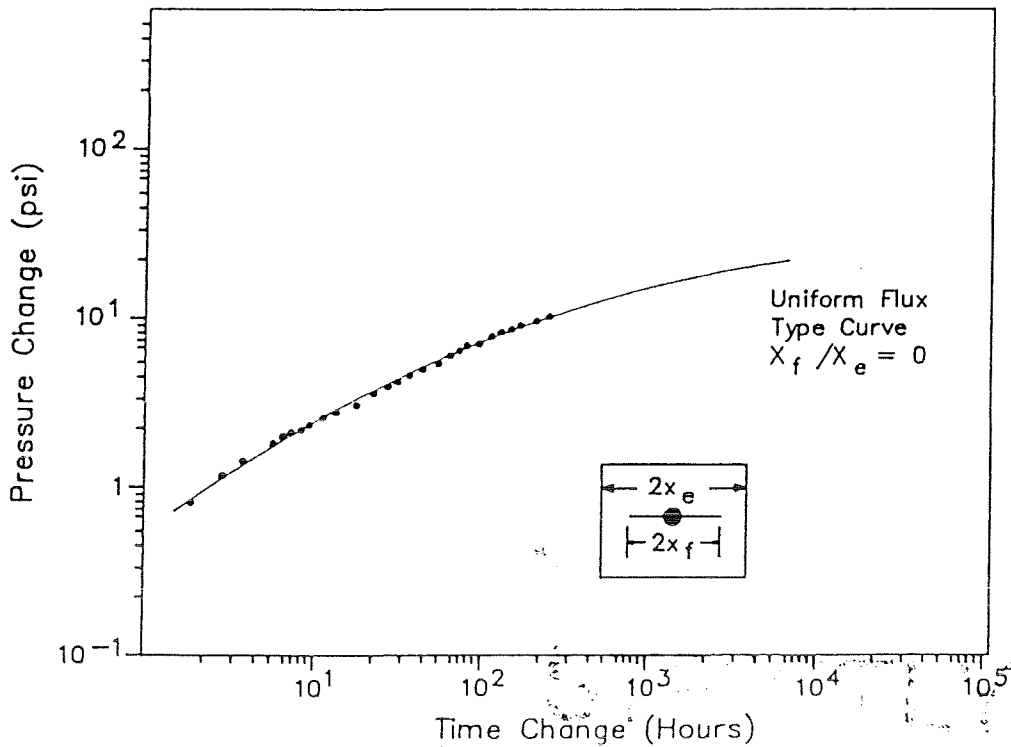


Figure 7.6

Pressure Response in Well 45-5 Due to Flow in 45-33

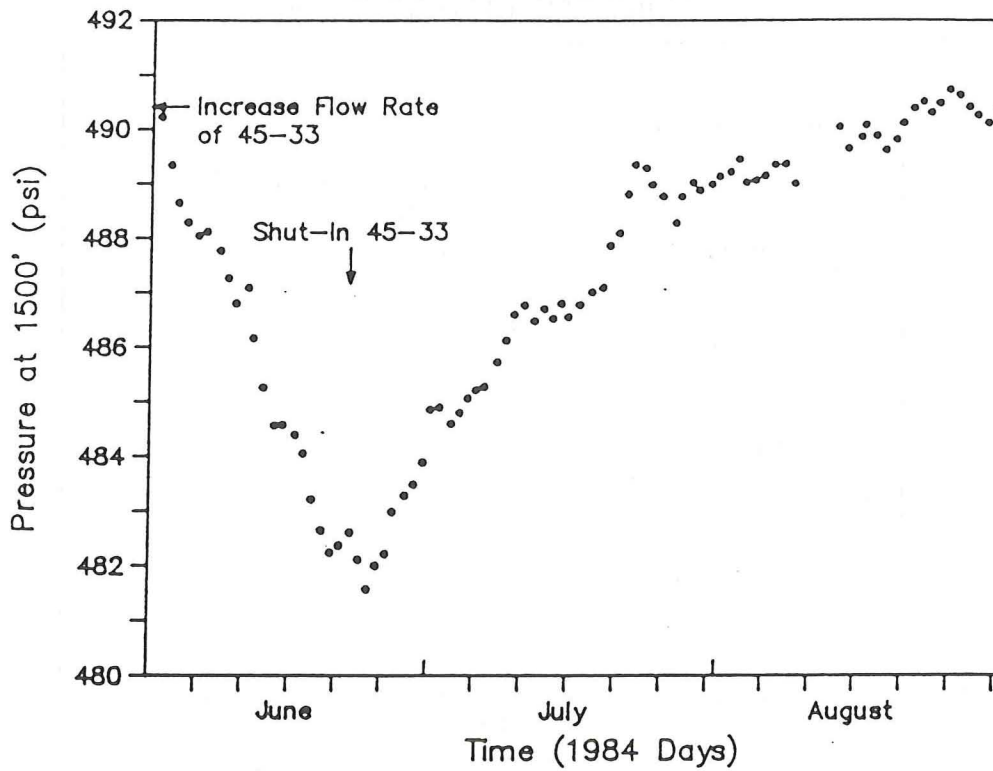
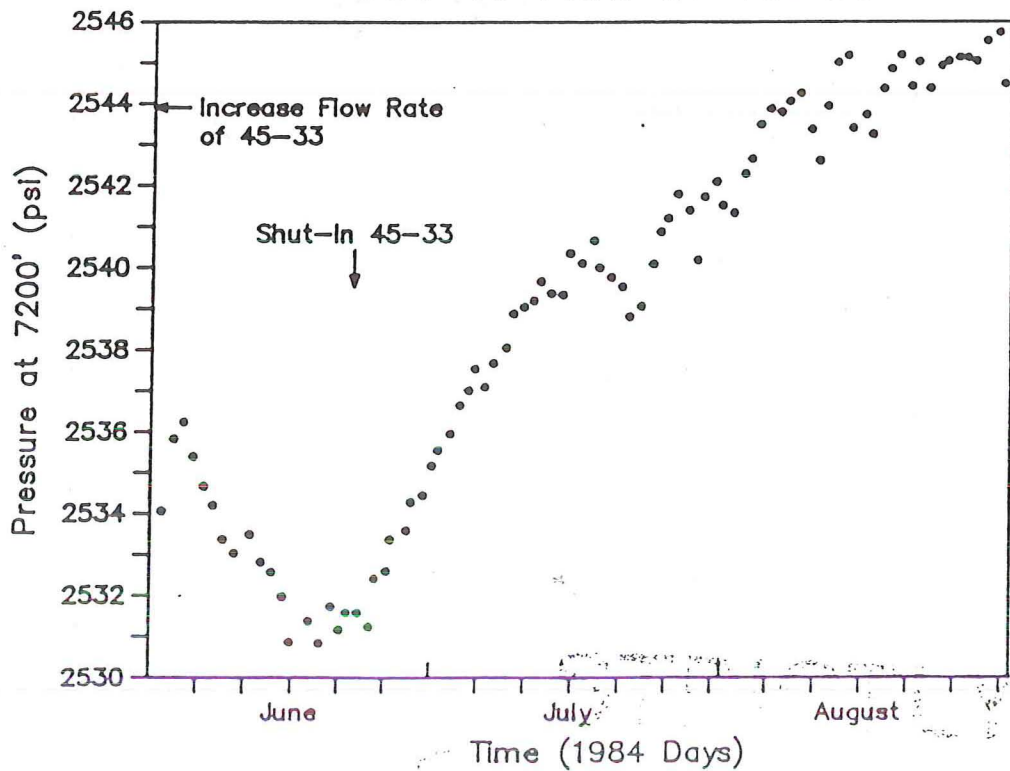


Figure 7.2.7

Pressure Response in Well 52-18 Due to Flow in 45-33



*

Figure 7.2.8

Pressure Response In Well 45-5 Due To Flow In 45-33

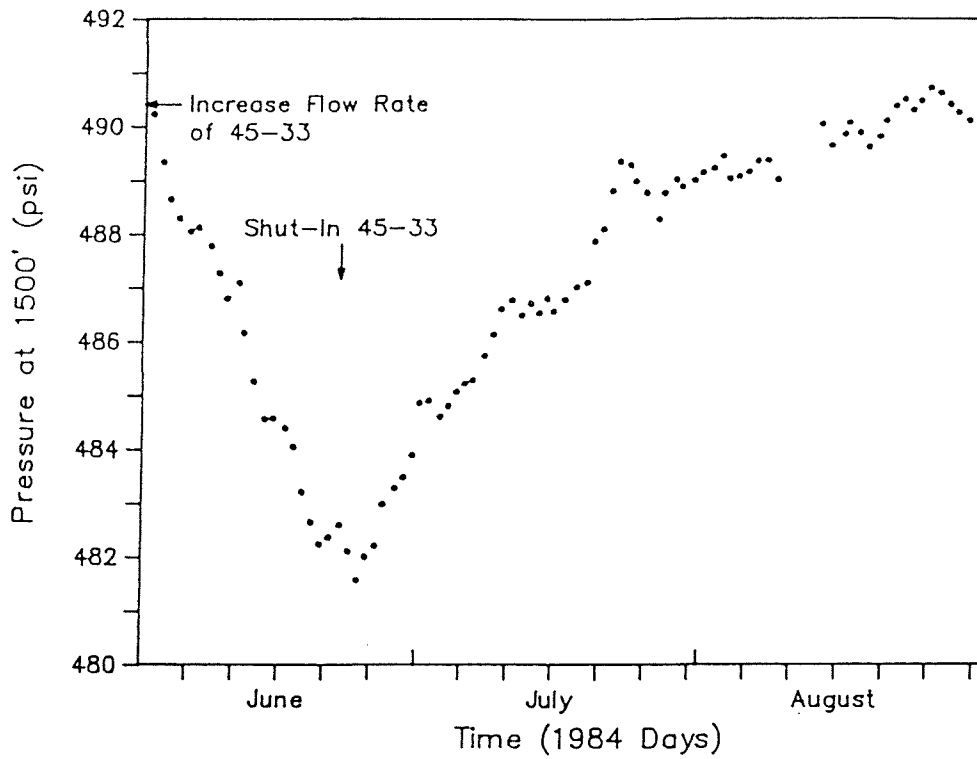


Figure 7.7

Pressure Response In Well 52-18 Due To Flow In 45-33

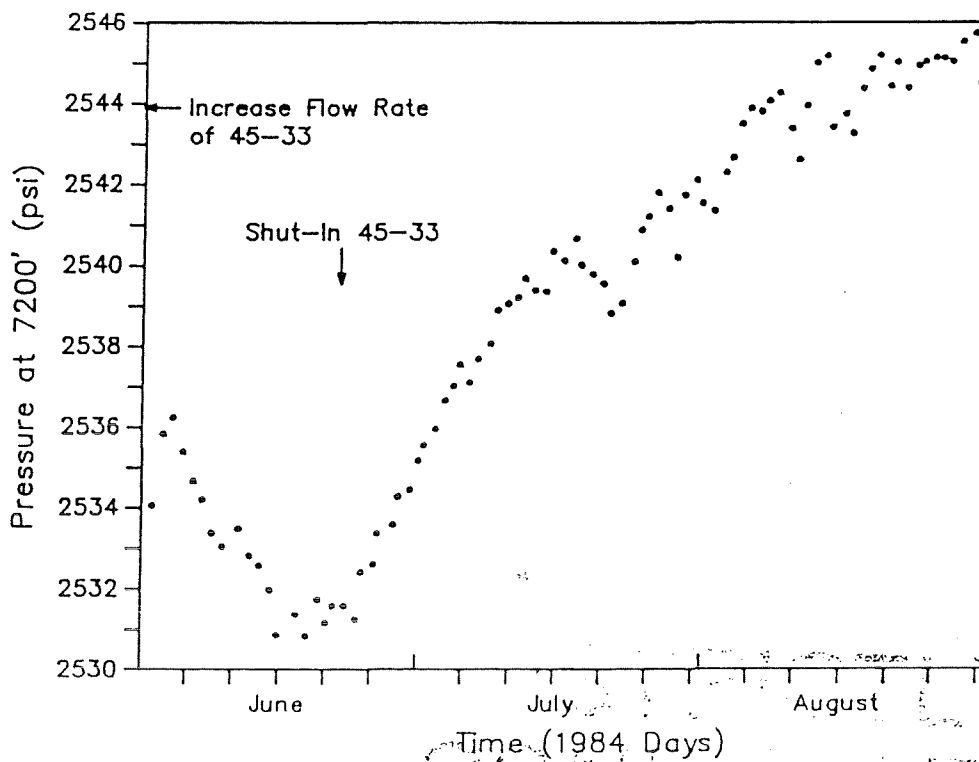


Figure 7.8

In summary, the overall character of the pre-1986 data suggests considerable anisotropy in the reservoir and is consistent with the fault-dominated behavior discussed earlier.

7.3 Description of Oxbow Reservoir Test

The flow and interference test performed by Oxbow during the first half of 1986 consisted of flowing wells 27-33 and 84-7 for a combined period of 4 months while pressures were monitored in the surrounding nine wells. (For location of wells see Figure 2.2).

In addition, short flow tests were conducted in other wells after completion of drilling or rework operations. The nonflowing wells were instrumented prior to the flow test to provide background reservoir pressure data.

Well 27-33 was kicked-off on December 17, 1985 and produced continuously at 370,000 lbs/hr until March 13, 1986. Well 84-7 was kicked off on January 22, 1986 and produced continuously at 650,000 lbs/hr until April 7, 1986. Various other wells were flowed for periods of between one and seven days. The flow test history is summarized in Table 7.4 and shown graphically in Figure 7.3.

7.4 Pressure Monitoring Data

7.4.1 Instrumentation

The observation wells were instrumented using a downhole pressure chamber and capillary tubing system. The system is shown diagrammatically in Figure 7.4. The chamber is hung on capillary tubing below the water level in the well. The chamber and tubing are charged with helium gas from the surface. A quartz pressure transducer or high resolution pressure gage is connected to the tubing at the surface and measures the hydrostatic pressure in the well at the chamber level.

Changes in reservoir pressure produce changes in the hydrostatic column and hence changes in pressure at the chamber. Quartz pressure transducers with a resolution better than 0.01 psi were used during the majority of the test. Pressures were transmitted to a central computerized logging unit where they were logged on disk and printed at regular (usually 20 minute) intervals.

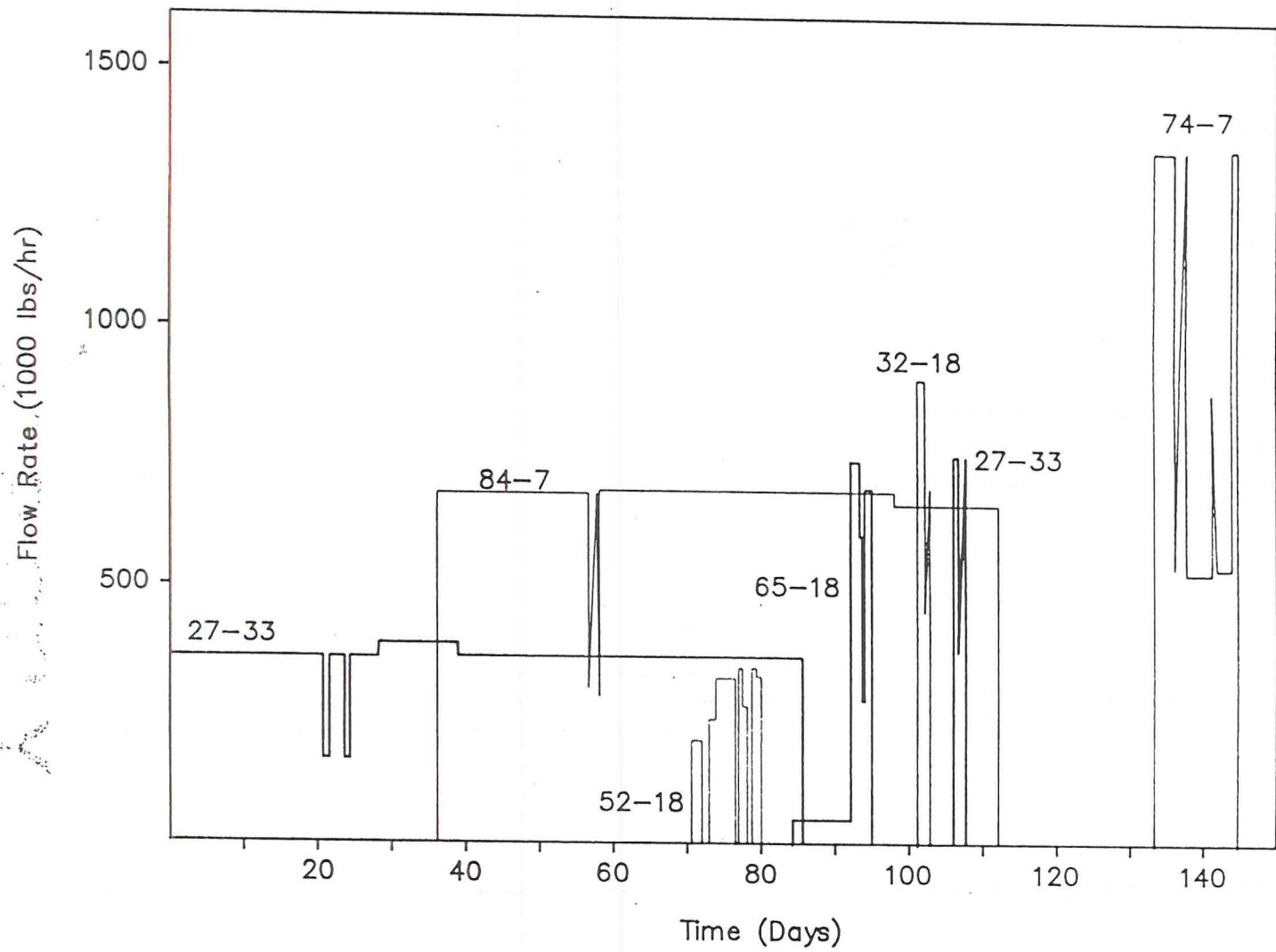
CONFIDENTIAL

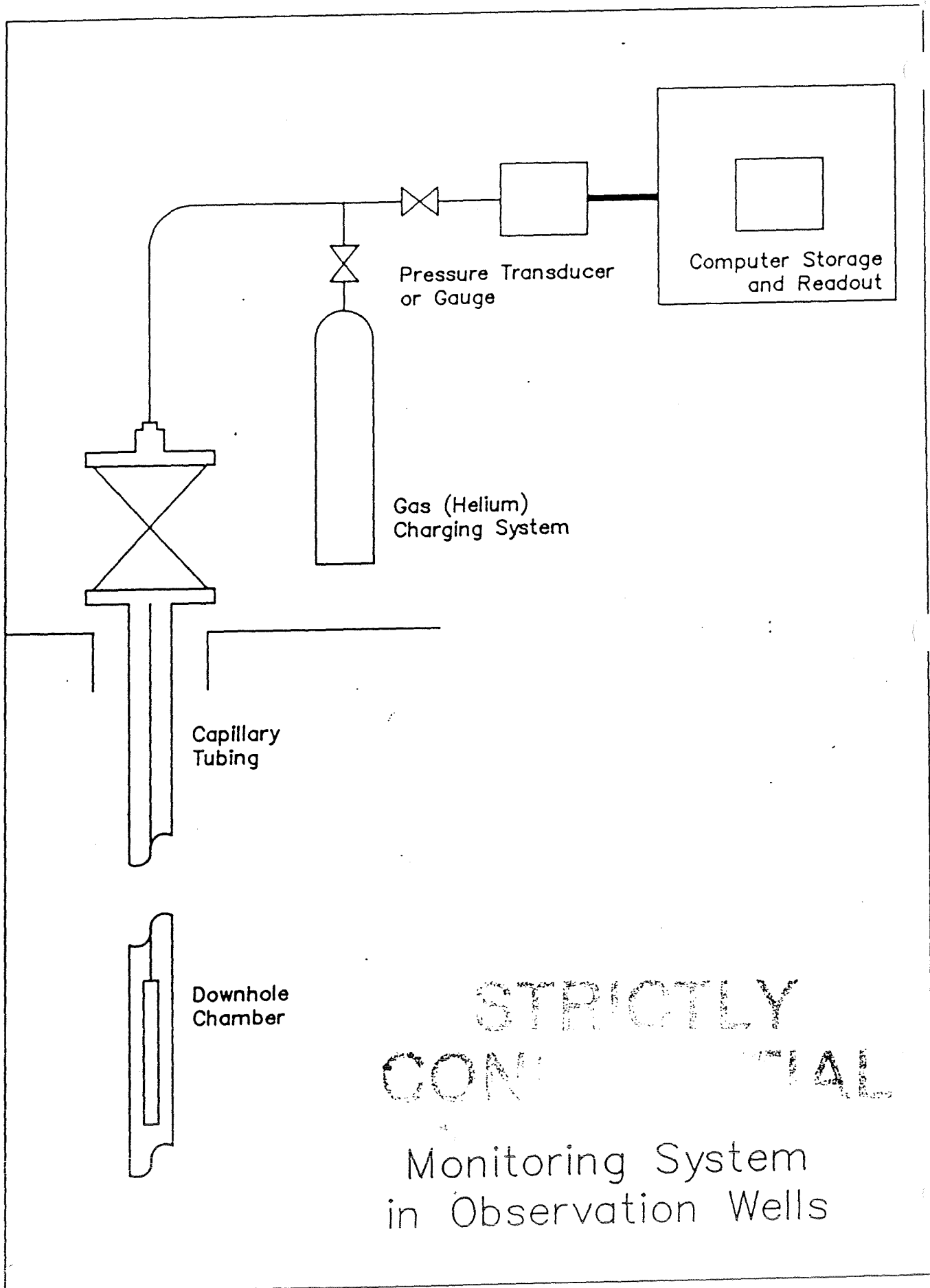
Table 7.4
Oxbow Reservoir Test History

WELL	DATES	TIME FLOWED	PURPOSE
27-33	12/17/85-3/13/86	86 days	Long term test
27-33	4/2/86-4/3/86	31 hours	Test after workover
84-7	1/22/86-4/7/86	75 days	Long term test
52-18	2/25/86-3/5/86 (Intermittent)	139 hours	Test after workover
65-18	3/12/86-3/18/86 (Intermittent)		Air drilling
65-18	3/8/86-3/19/86	25.5 hours	Test after workover
32-18	3/26/86-3/28/86		Air drilling
32-18	3/28/86-3/29/86	24 hours	Initial flow test
SWL-1	3/27/86	7 hours	Test after workover
74-7	3/27/86	1 hour	Rig test
74-7	4/29/86-5/8/86	9 days	Initial flow test
76-7	5/20/86-5/27/86 (Intermittent)		Air drilling
76-7	5/22/86	1 hour	Rig test
45-33	6/29/86-7/3/86 (Intermittent)		Air drilling
45-33	7/3/86	4 hours	Test after workover

SECRET
CONFIDENTIAL

Reservoir Test Flow Rate History





Toward the end of the test, the quartz transducers were replaced with Heise pressure gages with a resolution of about 0.1 psi. These were logged manually approximately once per day.

7.4.2 Monitor Wells and Monitoring Period

The periods during which monitoring was installed in the various wells is summarized in Table 7.5. The instrumentation was removed from a number of wells in December 1985 in order to conduct logging operations in preparation for rework operations. In some cases the instrumentation was reinstalled and then later removed when the rig was moved on to conduct the rework operations.

Three wells, 45-5, 45-33 and SWL-3, were instrumented during the entire test period and provide the major data base for the reservoir assessment and modeling effort.

Pressure monitoring instrumentation was installed at 6,000 feet in well 27-33 on January 10, 1986 while it was flowing and remained in the well until March 16, 1986, when it was removed in order to conduct a workover.

Well 74-7 was instrumented between April 3 and April 23, 1986 to monitor pressure recovery after nearby well 84-7 was shut in. The instrumentation was subsequently installed in 84-7 between April 23 and May 23, 1986 to monitor the interference during the flowtest of 74-7. The objective in these cases was to evaluate the interference effects between these two closely spaced wells and help determine appropriate well spacing for future wells in Section 7.10.

7.5 Results and Analytical Interpretation of Long Term Interference Test Data

Figures 7.5.1, 7.5.2, 7.5.3, and 7.5.4 show the monitoring data in wells 45-5, 45-33, SWL-1 and SWL-3 respectively. Calculated matches to the data employing a computer model that treats the reservoir as homogeneous and infinite, and has the capability of dealing with multiple flowrates and multiple wells, are shown on the same figures. Good matches were obtained to the drawdown portion of the data when 27-33 and 84-7 were producing. The transmissivities (kh) used to obtain these matches are given in Table 7.6 and ranged between 30,000 and 70,000 md ft. In general, it appears that the transmissivity decreases from north to south. The storage coefficient (0ch) used in the various cases ranged between 1×10^{-4} ft/psi and 4×10^{-4} ft/psi.

CONFIDENTIAL

CONFIDENTIAL

Table 7.5
 Periods During Which Pressures
 Were Monitored in Non-Flowing Wells

WELL	MONITORING PERIOD
45-5	8/31/85 - Present
SWL-3	11/25/85 - Present
45-33	12/19/85 - 6/20/86
62-21	10/10/85 - Present
52-18	8/31/85 - 2/3/86 5/29/86 - Present
SWL-1	12/24/85 - 12/27/85 1/9/86 - 3/20/86 5/12/86 - Present
SWL-2	8/2/86 - 5/20/86 6/17/86 - Present
65-18	12/22/85 - 3/10/86
66-21	10/30/85 - Present Intermittent Monitoring of WHP
74-7	4/4/86-4/24/86
84-7	4/24/86-5/26/86

STRICTLY
 CONFIDENTIAL

Downhole Pressure Monitoring Well 45-5

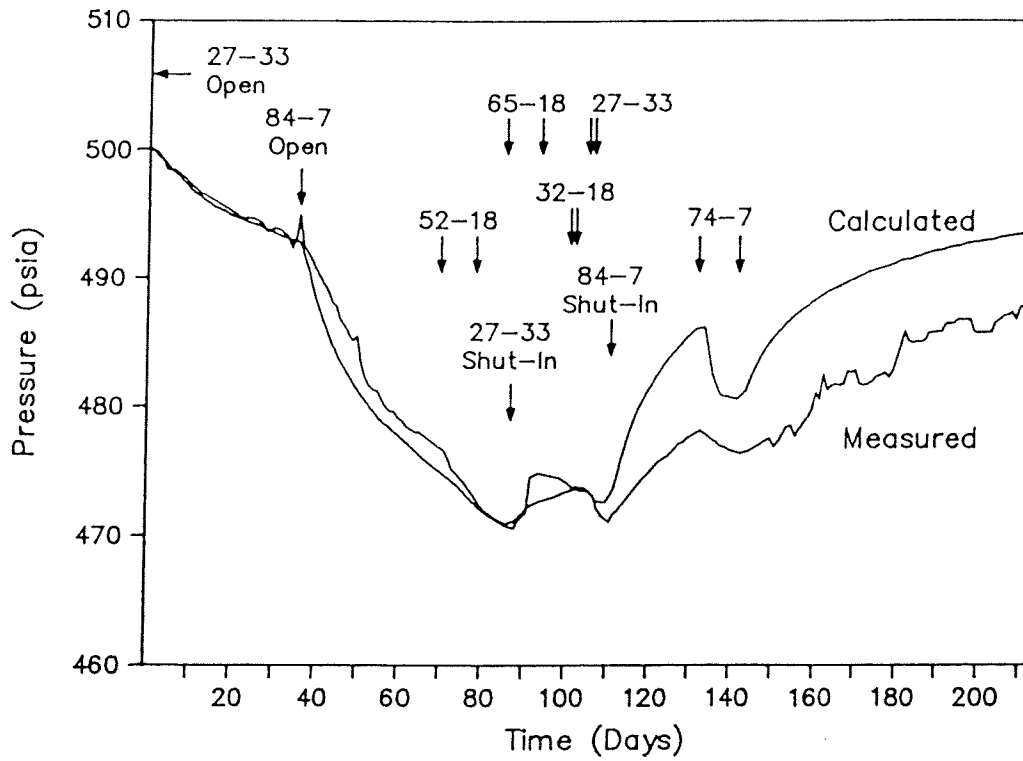


Figure 7.5.1

Downhole Pressure Monitoring Well 45-33

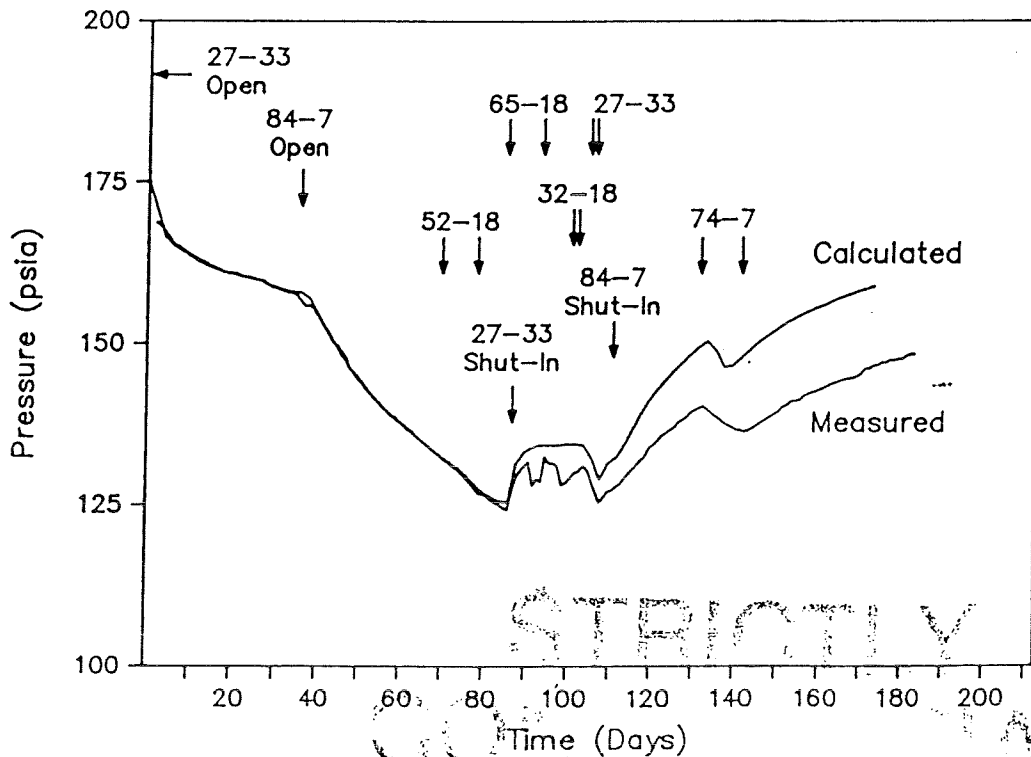


Figure 7.5.2

Table 7.6
 Summaries of Reservoir Properties
 Used to Match Oxbow Reservoir
 Test Data

OBSERVATION WELL	TRANSMISSIVITY (MD-FT)	STORAGE COEFFICIENT
45-33	68,000 (27-33) 30,000 (OTHERS)	1X10 exp-3 (27-33) 2X10 exp-4 (OTHERS)
SWL-3	15,000 (32-18) 30,000 (OTHERS)	3,75 X 10 exp-4
45-5	68,000	1X10 exp-3
SWL-1	30,000	4X10 exp-4

STRICTLY
 CONFIDENTIAL

The interference between closely spaced well-pairs 27-33 and 45-33, and 32-18 and SWL-3 could not be matched using the same regional transmissivity employed between the more widely-spaced wells. Well 27-33 is only 500 feet from 45-33. The next nearest flowing well during the test was 84-7 which is about 12,000 feet from 45-33. Similarly 32-18 is 600 feet from SWL-3. The nearest well that was flowed for any appreciable time during the test is 74-7, which is about 4800 feet from SWL-3.

Interference between closely spaced wells strongly reflects local reservoir conditions (probably the fault zone in this case). Therefore, interference in 45-33 and SWL-3 produced by their near neighbors (27-33 and 32-18 respectively) was calculated separately and added to the interference produced by the more distant flowing wells. Adding effects in this way has little physical justification; however, it is believed reasonable if the relative distance between the nearby and the distant wells is large. It is important to note that these matches do not take into account any structural controls that may produce hydraulic anisotropy in the reservoir.

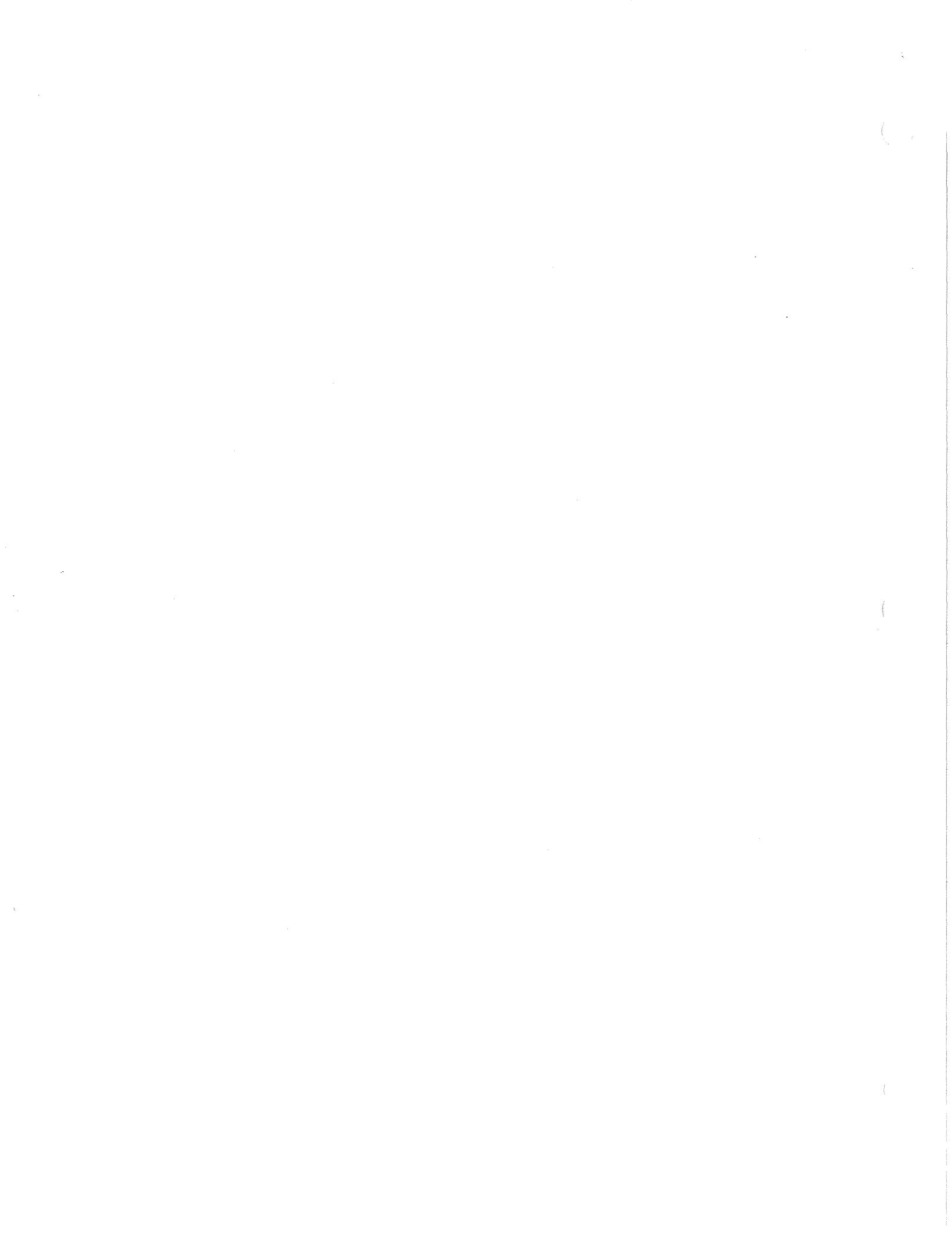
The same approach employed in matching the drawdown data was used to predict the pressure recovery after the wells were shut in. In all three cases (45-33, SWL-3 and 45-5) the observed pressure recovery was slower than the calculated recovery.

The measured pressures in 45-33 and SWL-3 two months after 84-7 was shut in are about 9 to 11 psi below the calculated pressures for a uniform permeability infinite system. (Figures 7.5.2 and 7.5.4). Pressures in 45-5 (Figure 7.5.1) also show a slower recovery than predicted. In this case, the overall interference effects were less pronounced than those in 45-33 and SWL-3, and the difference between the predicted recovery and observed recovery is about 6 psi.

Monitoring was continued in 45-5 and SWL-3 until the end of July when the six-well flow test was begun. It is interesting to note that in both cases the difference between the observed recovery and the predicted recovery decreases somewhat during July. For SWL-3 the difference was 9.3 psi on June 23 and 8.5 psi on July 17. Similarly, for 45-5 the difference was 6.7 psi on June 23 and 5.7 on July 17. The significance of these observations is discussed in Section 7.6.2.

STRICTLY

CONFIDENTIAL



Fluid pressure transients on seismogenic normal faults

W.T. Parry and R.L. Bruhn

*Department of Geology and Geophysics, College of Mines and Earth Science, University of Utah, 717 W.C. Browning Building,
Salt Lake City, UT 84112-1183 (U.S.A.)*

(Received August 31, 1989; revised version accepted March 5, 1990)

ABSTRACT

Parry, W.T. and Bruhn, R.L., 1990. Fluid pressure transients on seismogenic normal faults. *Tectonophysics*, 179: 335–344.

Fluid inclusions in hydrothermally altered footwall rocks of the Dixie Valley fault, Nevada, and the Wasatch fault, Utah, indicate that pore fluid pressure fluctuated. Minimum entrapment pressures for fluid inclusions consisting of H₂O–CO₂–NaCl ranged from 295 MPa to 60 MPa in the temperature range 350° to 170° C on the Wasatch fault, and from 158 to 35 MPa in the temperature range 350° to 200° C on the Dixie Valley fault. Scatter in the pressure estimates at constant temperature is interpreted as paleo-fluid pressure transients at depths of up to 11 km on the Wasatch fault and 3 to 5 km on the Dixie Valley fault.

Observed pressure transients range from 5 MPa, within the limits of error in pressure determination, to 120 MPa on the Wasatch fault and 7 to 126 MPa on the Dixie Valley fault. The pressure transients are greatest on both faults in the temperature range 270° to 310° C.

The fluids represented by fluid inclusions play a key role in nucleation and propagation of earthquake ruptures. High fluid pressures may initiate rupture, then dilatancy, pore-pressure reduction, and dilatant hardening may arrest the rupture. However, decompression of the fluids and phase separation produces a decrease in fluid bulk modulus of 41 to 90% which reduces the dilatant hardening effect and may permit ruptures to propagate.

Introduction

Conceptual (Ismail and Murrell, 1976; Murrell, 1977; Sibson, 1981), theoretical (Rice, 1980; Roeloffs and Rudnicki, 1985; Mase and Smith, 1985), experimental (Scholz, 1978; Walder and Nur, 1984), and observational (Sibson, 1981) models of faulting at upper crustal levels clearly predict that fluid flow and pressure fluctuations accompany faulting. Direct field evidence of faulting-related fluid flow includes changes in spring flow and hydrothermal vein systems (Sibson, 1981). Fluid inclusions trapped in quartz in hydrothermally altered rocks on the Wasatch fault, Utah, show minimum fluid pressures from lithostatic to hydrostatic (Parry and Bruhn, 1986; Parry et al., 1988) which were interpreted to result from displacement of the footwall from near the brittle–

ductile transition to shallower, cooler, more brittle regimes. However considerable scatter was apparent in pressure–temperature points for individual fluid inclusions. New fluid inclusion data on the Dixie Valley fault, Nevada, shows a similar scatter but at lower pressures. These fluid inclusion measurements in exhumed fault rock exposed within the footwall of two large seismogenic normal faults in the western U.S. are interpreted as evidence for significant paleofluid pressure transients perhaps generated during earthquakes. Fluids present on the faults were trapped as fluid inclusions in healed microfractures in the fault rock (Parry and Bruhn, 1986; Parry et al., 1988) and record variable pressures in the deformed rock.

The Wasatch fault in central Utah and the Dixie Valley fault in western Nevada are each

parts of zones of active normal faulting and extension that are more than 300 km long. Individual segments of the Wasatch fault are capable of generating magnitude 7 to 7.5 earthquakes (Schwartz and Coppersmith, 1984), and a magnitude 6.9 earthquake produced spectacular surface rupture on the Dixie Valley fault in 1954 (Slemmons, 1957). Exhumation of hydrothermally altered and tectonically deformed footwall fault rock on these two faults provides an opportunity for direct observation of pore fluid characteristics in fluid inclusions formed at seismogenic depths on the faults.

The Dixie Valley fault

The Dixie Valley fault is part of the 300 km long Central Nevada Seismic Belt (Wallace and Whitney, 1984) that extends from Pleasant Valley, Nevada, to Owens Valley, California. Historic seismicity resulting in surface rupturing events includes earthquakes (from north to south) at Pleasant Valley (1915), Fairview Peak–Dixie Valley (1954), Wonder (1903), Cedar Mountains (1932), Excelsior Mountain (1934), Mammoth Lakes (1980), and Owens Valley (1972). The Dixie Valley fault system forms the eastern margin of the Stillwater Mountains. A multiphase Oligocene granodiorite–quartz monzonite–granite intrusion emplaced at 28 Ma (Speed and Armstrong, 1971; Willden and Speed, 1974) that has been tectonically deformed and hydrothermally altered, is exposed in the footwall of the 1954 rupture segment.

Cataclasite, the dominant deformed rock near the fault, includes pervasive fracturing of meter-sized volumes of rock near the trace of the fault and thin tabular bodies of fine cataclasite within the footwall. A series of temporally distinct, but spatially overlapping hydrothermal alteration mineral assemblages is related to tectonic events on the Dixie Valley fault. The earliest assemblage of hydrothermal minerals includes hydrothermal biotite and a replacement of igneous plagioclase by K-feldspar leaving patchy remnants of twinned plagioclase. Next in the alteration sequence is chlorite and epidote associated with calcite, hematite, sericite, and prehnite. Latest hydrothermal minerals are laumontite, stilbite, kaolinite,

smectite, and illite. Hematite is hydrolyzed to limonite. Silicification accompanies alteration stages from early, coarse quartz–calcite veins to later replacement of rock units with fine grained quartz, feathery chalcedony, and latest deposition of opal.

Minimum displacement of 3 km on the Dixie Valley fault is established by correlation of basalt buried in the basin with basalt capping the Stillwater mountains (Okaya and Thompson, 1985).

The Wasatch fault

The Wasatch fault is a 370 km long zone of active normal faulting that extends from southern Idaho to central Utah (Gilbert, 1928; Cluff et al., 1975; Swan et al., 1980). The Oligocene Little Cottonwood quartz monzonite stock, exposed in the footwall, is 31.1 ± 0.9 Ma by K/Ar dating of hornblende (Crittenden et al., 1973). Wasatch fault footwall rock has been subjected to multiple alteration and deformation episodes with progressive displacement. Mechanical deformation is ductile to brittle in character in early alteration stages and becomes successively more brittle with later lower temperature alteration.

Cataclasite, the dominant rock within the Wasatch fault zone, occurs as large, tabular and lensoidal bodies forming a partly preserved carapace tens of meters thick on the western and southern margins of the Little Cottonwood stock, and as meter to millimeter thick zones associated with individual normal faults in the interior of the footwall. The cataclastic fabric has been superimposed on a remnant phyllonite fabric (Parry and Bruhn, 1986).

Hydrothermal alteration in the footwall occurs in overlapping alteration facies. Hydrothermal biotite and K-feldspar are the earliest alteration minerals followed by hydrothermal alteration of the host quartz–monzonite to chlorite, epidote, sericite, calcite, and magnetite. The youngest alteration consists of veins up to 1 cm thick of laumontite with prehnite and calcite that crosscut and offset earlier chlorite–epidote veins (Parry et al., 1988).

Tectonic deformation textures, hydrothermal minerals, fluid inclusion characteristics, and

footwall reconstruction indicate a minimum vertical displacement of 11 km for the Wasatch fault (Parry and Bruhn, 1987).

Fluid inclusions

Deformed igneous quartz grains in texturally intact granite between cataclastic zones within the footwall of the Dixie Valley and Wasatch faults show pronounced undulatory extinction, deformation lamellae, and abundant planes of secondary fluid inclusions that contain H₂O, NaCl, and CO₂ within healed microfractures. Fluid inclusion trains sometimes begin and end within a single grain but usually they cross grain boundaries. Inclusions with substantial CO₂ allows use of the CO₂-H₂O-NaCl phase relationships to estimate the minimum pressure of entrapment (Parry, 1986; Roedder and Bodnar, 1980) providing entrapment of a homogeneous fluid can be demonstrated and post entrapment changes have not altered fluid densities.

Fluid inclusions on the Wasatch fault, Utah contain 4.5 to 17.3 wt.% NaCl equivalent, 3 to 32 mol.% CO₂ and were trapped at minimum pressures of 60 to 295 MPa at temperatures of 170° to 350°C (Parry et al., 1988). Fluid inclusions on the Dixie Valley fault contain 0.6 to 6.8 wt.% NaCl equivalent, 3 to 17 mol.% CO₂ and were trapped at minimum pressures of 28 to 158 MPa at temperatures of 200° to 350°C. Minimum pressures and temperatures of entrapment are shown in Fig. 1.

Lithostatic and hydrostatic gradients on the Wasatch fault in Fig. 1 have been computed using a thermal gradient of 30°C/km consistent with the present thermal gradient characteristic of the Basin and Range province (Sass et al., 1981). The thermal gradient on the Dixie Valley fault is probably higher. The Battle Mountain heat flow high (Sass et al., 1971) lies at the northern end of the central Nevada seismic belt, and the Dixie Valley geothermal area is 47 km northeast of the 1954 rupture segment. Thermal gradients in the Battle Mountain high are 40° to 50°C per km (Sass et al., 1981), and gradients of 75°C per km and above have been measured in drill holes in northern Dixie Valley (Bell et al., 1980) due to local

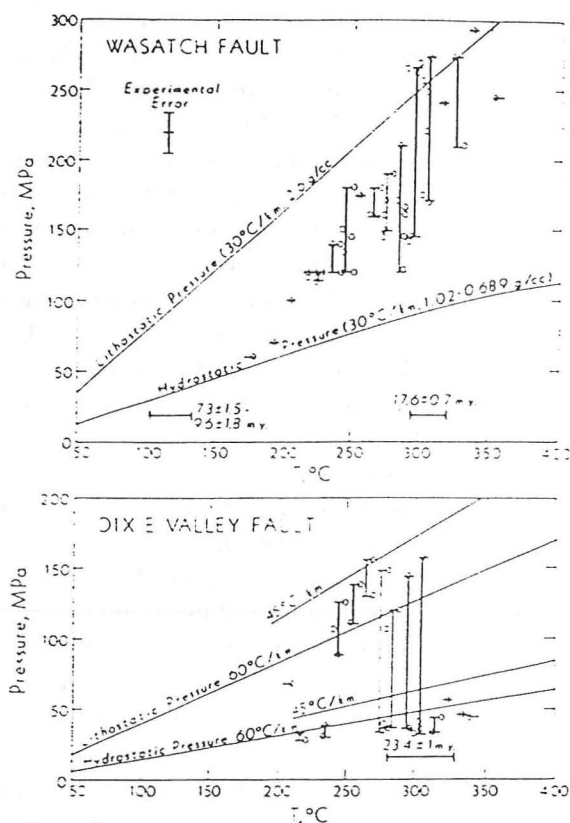


Fig. 1. Pressure variations at constant temperature on the Wasatch Fault, Utah, and the Dixie Valley Fault, Nevada, U.S.A. Open circles are pressure and temperature determinations from individual fluid inclusions. Vertical bars represent pressure variations observed in 10°C increments. A typical error bar for temperature and pressure is shown in the upper plot. Reasonable hydrostatic and lithostatic pressures profiles are shown for each fault system with temperature gradients and assumed densities included in the respective curves. Fluid densities on the Wasatch fault were calculated for a fluid containing 6 wt.% NaCl relative to H₂O saturated with CO₂ using the equations and data of Bowers and Helgeson (1983a). K-Ar ages of hydrothermal muscovites are shown as bars representing closure temperature errors at about 300°C on each diagram, and the apatite fission track age on the Wasatch fault is shown near its closure temperature of 120°C.

hydrothermal convection. On the Wasatch fault, the highest observed pressures are near lithostatic pressure for a thermal gradient of 30°C/km. The *P-T* points on the Dixie Valley fault lie between lithostatic and hydrostatic pressure for thermal gradients of 45° to 60°C/km.

The scatter in *P-T* points apparent in Fig. 1 could result from errors in temperature measurement and pressure estimation, from post entrap-

ment changes in the fluid inclusions, from entrapment of a non-homogeneous fluid, from real temperature variation in the fault fluid, or from variations in fluid pressure. The experimental error in temperature measurement is $\pm 5^\circ\text{C}$ and the error in pressure estimation is about $\pm 15\text{ MPa}$.

The greatest source of error in fluid inclusion measurements is a consequence of post entrapment changes in secondary inclusions described by Roedder (1984) and termed maturation by Bodnar et al. (1985). These changes result from dissolution and reprecipitation of host mineral surrounding the trapped fluid. The initial fluid inclusion may be irregular in shape but in time necks down to form many smaller inclusions with more regular shapes, often with widely varying liquid to vapor ratios. We have avoided measurements of necked inclusions (Parry et al., 1988).

The main criterion for identification of trapping of a homogeneous liquid is constancy of the ratios of volumes of liquid and vapor phases in inclusions in the same healed fracture. Groups of fluid inclusions in individual samples have similar compositions, liquid-vapor ratios, CO_2 liquid-vapor homogenization temperatures, and salinities as shown by Parry and Bruhn (1987). Fluid inclusions containing CO_2 of varying densities occur in parallel fractures within individual quartz grains but individual fractures contain fluids of a single density. High and low density CO_2 never occur within the same fracture.

Entrapment of the carbon dioxide bearing fluids near the two-phase boundary for these fluids is indicated by three separate observations. First, the CO_2 content of the fluids decreases systematically as temperature decreases (Parry et al., 1988) indicating that CO_2 has separated from the fluid as temperature and pressure is reduced. This can only happen if P - T conditions cross the two-phase boundary on the phase diagram into the two-phase region. Two-phase boundary curves for representative fluids are shown in Fig. 2. Second, the latest alteration mineral facies includes the zeolite laumontite on both the Dixie Valley and Wasatch faults requiring that CO_2 be less than 0.75 mol.% (Thompson, 1971). Third, a few fluid inclusions contain only CO_2 that represents the separated phase (Parry et al., 1988).

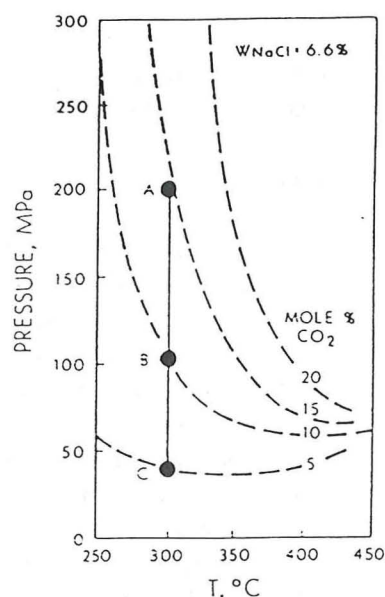


Fig. 2. Pressure-temperature projection of phase relations in the $\text{H}_2\text{O}-\text{CO}_2-\text{NaCl}$ system showing the two-phase boundary (heavy dashed curves) for a solution with constant weight percent NaCl relative to H_2O and 5 to 20 mol.% CO_2 and example isothermal decompression paths for typical fluids on seismogenic normal faults. Two-phase boundary curves are from Bowers and Helgeson (1983b). The pressure-temperature region in the upper right of each curve is the one-phase region and in the lower left region, a CO_2 rich vapor coexists with an aqueous liquid. Decompression of fluids from A to B to C discussed in the text.

The temperature variations observed are interpreted to reflect cooling of the footwall of the faults as displacement progresses. Both temperature and pressure are used to estimate the amount of displacement of the footwall. The displacement of the Wasatch fault is estimated to be at least 11 km at a thermal gradient of $30^\circ\text{C}/\text{km}$ (Parry and Bruhn, 1987). The displacement of the Dixie Valley faults is estimated to be 3 to 5 km at a thermal gradient near $60^\circ\text{C}/\text{km}$. We have chosen to illustrate lithostatic and hydrostatic pressure gradients on Fig. 1. Most of the pressure-temperature points lie between the two limiting pressures.

Pressure transients

Pressure ranges within 10°C temperature increments, shown as heavy bars on Fig. 1, and listed as the observed transients in Table 1, represent isothermal pressure variations that exceed the

TABLE 1

Isothermal pressure transients (in MPa) on the Dixie Valley fault, Nevada, and the Wasatch fault, Utah *

T range (°C)	Wasatch fault			Dixie Valley fault		
	P_{min}	P_{max}	ΔP range	P_{min}	P_{max}	ΔP range
171-180	60	60	0			
181-190		n.o.				
191-200	70	70	0			
201-210	100	100	0	68	68	0
211-220	115	120	5	28	35	7
221-230	114	120	6		n.o.	
231-240	120	140	20	30	40	10
241-250	120	180	60	88	127	39
251-260	174	174	0	110	140	30
261-270	160	180	20	130	156	26
271-280	150	190	40	34	148	114
281-290	120	210	90	38	120	82
291-300	145	265	120	38	145	107
301-310	170	272	102	32	158	126
311-320	240	240	0	32	45	13
321-330	210	274	64	56	56	0
331-340	292	292	0	46	46	0
341-350	244	244	0	44	44	0

* n.o. = no observations.

error limits of pressure determinations. Observed pressure transients range from 5 MPa, within the limits of error in pressure determination, to 126 MPa. The pressure transients are greatest on both faults in the temperature range 270° to 310° C.

The fluid inclusion record of pressure transients is incomplete. Fluid inclusions indicating pressures above approximately 200 MPa are poorly represented in the data set because internal pressures cause them to decrepitate before the homogenization temperature is reached. Because fluid inclusion sizes were generally very small, measurements could only be made on the largest inclusions, leaving many small inclusions from which no pressure-temperature data could be obtained.

Correlation of different healed fractures containing fluid inclusions with a single tectonic event is not possible. However, a number of fluid inclusions in common samples homogenize near the same temperature at widely differing pressures. Thus different fluid pressures and fluid compositions are inferred to have existed at the same depth on the faults.

The time required for entrapment of fluids in a

healed fracture in a quartz grain by precipitation of quartz depends on initial width of the fracture, temperature, and degree of supersaturation. Sealing times were calculated from Rimstidt and Barnes (1980, equation 63) at 300° C. At supersaturation of the solution with quartz resulting from a pressure reduction of 60 MPa and a fracture width of 10 μ m, the sealing time is about 1 year. Pressure reductions that are larger would result in more rapid entrapment and wider fractures would require more time.

A maximum time over which the pressure transients occurred is the time required for uplift of the footwall to produce 10° C cooling. The rate of footwall uplift and cooling has been established for the Wasatch fault by fission track ages of apatite that average 8.5 ± 1.7 Ma and K-Ar age of muscovite of 17.6 ± 0.7 Ma (Evans, et al., 1985; Parry et al., 1988). The closure temperatures are 120 ± 15 ° C (Naeser 1979, 1981) and 350 ± 50 ° C (Hunziker, 1979) for apatite and muscovite respectively. Formation temperature for the muscovite estimated from cogenetic fluid inclusions is 309 ± 13 ° C (Parry et al., 1988). These

time to know

because of 10° spread in T_{Home}

data show that the footwall cooled 190°C in 9.10 m.y. or 10°C per 0.5 m.y. However, it is likely that the time represented by the pressure transients is far less, possible as short as a few thousand years, the recurrence interval for large earthquakes.

Discussion

Alternative mechanisms that could account for the pressure transients include fluid pressure increases that result from porosity reduction due to strain and precipitation of hydrothermal minerals (Sibson, 1981; Walder and Nur, 1984; Roeloffs and Rudnicki, 1985), fluid pressure reduction as a result of porosity increases from dilatant fractures (Sibson, 1981) or fluid pressure draining away along the rupture zone as in the fault-valve model of Sibson et al. (1988), and fluid pressure induced by heating of the fault during slip (Mase and Smith, 1985). Fracture permeability in the faulted carapace of the Wasatch fault (exclusive of the highly sheared cataclasite) was estimated to be between 10^{-14} and 10^{-12} m^2 for average fracture apertures of 50 to 200 μm (Thompson, 1988). Calculations show that frictional melting would occur before thermal pressurization of the fluid for permeabilities greater than 10^{-15} m^2 (Mase and Smith, 1985). Fractures are even more abundant at Dixie Valley suggesting higher permeabilities, yet no evidence of melting has been observed. Thermal pressurization is therefore unlikely.

Fluid pressure changes and microfracturing may occur over a large range in deformation rates from aseismic creep to dynamic rupturing during earthquakes. In saturated fault rock with fluid pressure P_f , the frictional strength of the fault may be approximated by a Coulomb-type failure criterion modified to account for effective stress: $\tau = C_0 + \mu(\sigma_n - P_f)$ where τ and σ_n are shear and normal stresses on the fault surface, μ is the coefficient of friction, and C_0 is cohesive strength. Application of compressive stress causes a reduction in porosity and a rise in pore-pressure (Ismail and Murrell, 1976; Murrell, 1977), but when rock becomes dilatant, pore-pressure tends to fall and rock behavior then depends on whether it is in a drained or undrained condition. In undrained conditions di-

latancy hardening occurs and strength tends to increase with deformation. (Murrell, 1977). Dilatancy is produced by formation and propagation of cracks within the rock and begins to occur at stresses as low as one-half the breaking strength (Sholz et al., 1973). When effective stress becomes large enough to begin producing dilatancy at a rate faster than the rate at which pore fluid can flow into newly created volume, the pore pressure in the dilatant region drops and effective stress rises causing a strengthening of the rock and stabilization of the fault rupture by increasing effective normal stress (Rice, 1980; Rudnicki and Chen, 1988). Abrupt increases in crack volume and fault permeability produced during dynamic rupture has been observed in laboratory experiments to cause abrupt decreases in fluid pressure leading to boiling or effervescence of gases (Scholz, 1978).

Fluid pressure is thus seen to play an active role in seismic events. Reduction of pore volume due to strain during aseismic creep and precipitation of hydrothermal minerals causes fluid pressure to rise to near lithostatic values. The formation of an impermeable cap due to mineral precipitation is necessary to maintain high fluid pressures (Etheridge et al., 1983; Cox et al., 1986). Elevated pore pressure then leads to dynamic rupturing during earthquakes with partial relief of high pore pressures, communication of fluids with shallower, lower pressure reservoirs (the fault valve model of Sibson et al., 1988), separation of the fluid into CO_2 gas and H_2O liquid, and escape of CO_2 .

Effect of pressure reduction and phase separation on K_f

Rudnicki and Chen (1988, equation 23) have shown that the relationship between shearing stress and displacement during frictional slip may be accounted for by two terms in the governing equation. The first term includes factors for drained response, and the second term reflects hardening due to the decrease in pore pressure induced by dilatancy. This hardening effect is proportional to the friction coefficient and the pore fluid bulk modulus K_f .

The dependence of the hardening effect on the

thefting =
No. phys/bulk
if a mechanism
degradation

do
class

TABLE 2
Densities and bulk moduli of fluids on seismogenic faults

Fluid composition			T (°C)	P (MPa)	Density (g/cm ³)	K _f (MPa)
XCO ₂	WNaCl	XH ₂ O				
<i>Wasatch fault</i>						
0.18	6.6	0.804	300	255	0.975	1.91 × 10 ³
Decompressed fluids						
0.12	7.3	0.847	302	175	0.935	1.33
1.00	0.0	0.0	302	175	0.860	0.478
Two-phase fluid						1.12
Decrease on decompression and phase separation:						41%
<i>Dixie Valley fault</i>						
0.165	3.6	0.8255	294	145	0.892	1.03
Decompressed fluids						
0.062	4.3	0.9252	303	37	0.799	0.520
1.00			303	37	0.345	0.0422
Two-phase fluid						0.107
Decrease on decompression and phase separation:						90%
<i>Pure water</i>						
0	0	1	300	100	0.824	1.07
0	0	1	300	200	0.882	1.69
0	0	1	300	8.6	0.712	0.304
<i>Steam</i>						
0	0	1	300	8.6	0.0461	0.005
<i>Pure carbon-dioxide</i>						
1	0	0	300	45	0.410	0.0559 × 10 ³
1	0	0	300	100	0.683	0.206
1	0	0	300	150	0.813	0.388
1	0	0	300	200	0.904	0.570
<i>Carbon-dioxide-water-sodium-chloride</i>						
0	6.6	0.979	300	100	0.903	1.13
0	6.6	0.979	300	200	0.978	1.53
0.1	6.6	0.881	300	100	0.871	0.846
0.1	6.6	0.881	300	200	0.949	1.54
0.15	6.6	0.831	300	200	0.943	1.57

fluid bulk modulus is related to three crucial points in the derivation of Rudnicki and Chen (1988). Work hardening and weakening of the rock is related to slip distance, and instability occurs if the slope of the shear stress versus the slip distance curve is more negative than the unloading stiffness of the surrounding material. Coulomb friction applies; shear stress at failure is proportional to the effective normal stress. If dilatancy occurs as a function of slip distance, and effective normal stress is partly controlled by pore pressure,

then a decrease in bulk modulus of the fluid may cause the slope of the shear stress versus the slip distance curve to become negative leading to instability, even though the increase in pore volume by fracturing tends to stabilize the fault by decreasing the pore pressure. Decreases in fluid pressure that result in boiling or that allow dissolved gases to effervesce reduce K_f substantially.

Bulk moduli of fluids present in the Wasatch and Dixie Valley faults have been calculated together with the moduli for water, salt water, carbon

dioxide, and steam. For CO_2 -NaCl- H_2O fluids, the moduli were calculated using the MRK equation of state, data presented by Bowers and Helgeson (1983a), and a finite difference approximation for the derivative. For H_2O -NaCl fluids, equations and data of Potter and Brown (1977) were used. For CO_2 , equations and data of Angus et al. (1976) were used, and equations and data of Keenan et al. (1978) were used for water and steam. Densities and bulk moduli for representative fluids on the Wasatch and Dixie Valley faults are shown in Table 2 together with water, steam, carbon dioxide, and salt solutions for comparison purposes.

The bulk modulus of a two-phase fluid was computed from the moduli of the gas and liquid phases and their respective volume fractions. Application of a pressure increment to the two-phase fluid would produce a volume change that is the sum of the volume changes of the gas and liquid phases:

$$\Delta V_f = \Delta V_l + \Delta V_g \quad (1)$$

$$\Delta V_f = V_f \Delta P / K_f \quad (2)$$

$$\Delta V_l = V_l \Delta P / K_l \quad (3)$$

$$\Delta V_g = V_g \Delta P / K_g \quad (4)$$

where ΔV is the volume change, ΔP is the pressure increment, V is volume and K is bulk modulus, and the subscripts f , l , and g refer to fluid, liquid, and gas respectively. Substitution of 2, 3, and 4 into 1 and simplifying for a unit volume of fluid produces:

$$1/K_f = V_l/K_l + V_g/K_g$$

where V_l and V_g are the volume fractions of liquid and gas respectively.

Table 2 illustrates the reduction of fluid bulk modulus that results from decompression of various fluids. A homogeneous fluid consisting of 10 mol.% CO_2 that decompresses from 200 MPa to 100 MPa (A to B on Fig. 2) would undergo a reduction in bulk modulus from 1.54×10^3 to 0.846×10^3 MPa, a decrease of 45%. A fluid containing 15 mol.% CO_2 that decompresses from 200 to 100 MPa would separate into two phases, a CO_2 rich gas and an aqueous liquid. The aqueous liquid would have a bulk modulus of 0.846×10^3

MPa but the CO_2 gas would have a bulk modulus of 0.206×10^3 MPa and would comprise 12 vol.% for an overall bulk modulus of the two-phase fluid of 0.616×10^3 MPa, a decrease of 50%. Further decompression to point C on Fig. 2 would result in separation of additional CO_2 and a corresponding reduction in bulk modulus.

Examples

One representative example fluid on the Wasatch fault shown in Table 2 consists of a homogeneous fluid containing 18 mol.% CO_2 , 80.4 mol.% H_2O with 6.6 wt.% dissolved NaCl. The fluid density is 0.975 g/cm^3 . This fluid was trapped as a homogeneous fluid at a minimum of 300°C and 255 MPa. Isothermal decompression of 1 kg (1025 cm^3) of the fluid to 175 MPa, well within the observed pressure transient at 300°C in Table 1, permits effervescence of CO_2 resulting in two phases: 113 cm^3 of CO_2 with a density of 0.860 and 965 cm^3 of a fluid consisting of 12 mol.% CO_2 , 85 mol.% H_2O with 7.3 wt.% dissolved NaCl. The volume increase of 5% is well within the increase in porosity due to dilatancy observed in laboratory experiments (Brace, 1978). The bulk modulus of the combined two-phase system is 41% lower than the bulk modulus of the original fluid, cancelling almost half of the dilatant hardening effect produced by the increase in crack volume.

An example fluid on the Dixie Valley fault consists of 16.5 mol.% CO_2 and 83 mol.% H_2O with 3.6 wt.% dissolved NaCl. This fluid was trapped at a minimum of 145 MPa at a temperature of 249°C at a density of 0.892. On decompression of 1 kg to 37 MPa, CO_2 effervesces resulting in a two-phase system consisting of 535 cm^3 of CO_2 with a density of 0.345 g/cm^3 , and 1020 cm^3 of a fluid with 6.2 mol.% CO_2 and 92.5 mol.% H_2O with dissolved salt. The decrease in bulk modulus is 90%. The increase in volume is 39%, also within the range of observed dilatant volume increases (Brace, 1978).

Table 2 shows that decompression of pure water from 200 to 100 MPa at 300°C produces a decrease in bulk modulus of 37% and no phase separation would occur. Phase separation in pure water would not occur at 300°C until the pressure

crack modulus
porosity
if bulk modulus
decreases then
the compressibility
is greater

fell to 8.6 MPa where a drastic reduction in bulk modulus would occur depending on the volume fraction steam produced. The bulk modulus of saturated steam at 300°C is 2% of that of water (Table 2). Separation of 10 vol.% steam would result in a weighted average bulk modulus of 0.044×10^3 MPa which is a reduction of 85%.

The pore pressure variations observed in fluid inclusions on seismogenic normal faults are thus seen to destabilize the fault by reduction of normal stress as fluid pressure rises to near lithostatic values. The faults may then be stabilized by dilatant hardening, but effervescence of CO₂ and a decrease in fluid bulk modulus decreases this stabilizing effect.

Conclusions

Fault domains at a depth of up to 11 km on the Wasatch fault and up to 5 km on the Dixie Valley fault containing a CO₂-rich fluid may play a key role in nucleation and propagation of earthquake ruptures. Ruptures may be initiated by high pore pressures caused by porosity reduction. New pore volume produced by dilatancy coupled with low rock permeability then results in decompression of the fluid that may stabilize rupture by dilatant hardening. Separation of CO₂-H₂O-NaCl fluids into two phases results in a drastic reduction in fluid bulk modulus that diminishes the dilatant hardening effect and permits ruptures to propagate.

Acknowledgments

Financial support was received from the National Science Foundation EAR-8618250 and the U.S. Geological Survey. The manuscript was reviewed by D.S. Chapman, J.D. Pechman, F.H. Brown, R.H. Sibson, and P.E. Brown.

References

- Angus, S., Armstrong, B., De Reuck, K.M., Altunin, V.V., Gadetskii, O.G., Chapela, G.A. and Rowlinson, J.S., 1976. International Thermodynamic Tables of the Fluid State. Vol. 3. Carbon Dioxide. Pergamon, London, 385 pp.
- Bell, E.J., Campana, M.E., Jacobson, R.L., Larson, L.T., Slemmons, D.B., Bard, T.R., Bohm, B.W., Ingraham, N.L., Juncal, R.W. and Whitney, R.A., 1980. Geothermal reservoir assessment and case study, northern Basin and Range province, northern Dixie Valley, Nevada. Rep. Mackay Minerals Research Institute, University of Nevada, Reno, Nev., 223 pp.
- Bodnar, R.J., Reynolds, T.J. and Kuehn, C.A., 1985. Fluid-inclusion systematics in epithermal systems. In: B.R. Berger and P.M. Bethke (Editors), *Geology and Geochemistry of Epithermal Systems*. Rev. Econ. Geol., 2: 73-97.
- Bowers, T.S. and Helgeson, H.C., 1983a. Calculation of the thermodynamic and geochemical consequences of nonideal mixing in the system H₂O-CO₂-NaCl on phase relations in geologic systems: Equation of state for H₂O-CO₂-NaCl fluids at high pressures and temperatures. *Geochim. Cosmochim. Acta*, 47: 1247-1275.
- Bowers, T.S. and Helgeson, H.C., 1983b. Calculation of the thermodynamic and geochemical consequences of nonideal mixing in the system H₂O-CO₂-NaCl on phase relations in geologic systems: metamorphic equilibria at high pressures and temperatures. *Am. Mineral.*, 68: 1059-1075.
- Brace, W.G., 1978. Volume changes during fracture and frictional sliding: a review. *Pure Appl. Geophys.*, 116: 603-614.
- Cluff, L.S., Hintze, L.F., Brogan, G.E. and Glass, C.E., 1975. Recent activity of the Wasatch fault, northwestern Utah, U.S.A. *Tectonophysics*, 29: 161-168.
- Cox, S.F., Etheridge, M.A. and Wall, V.J., 1986. The role of fluids in syntectonic mass transport and the localization of metamorphic vein-type ore deposits. *Ore geol. Rev.*, 2: 65-86.
- Crittenden, M.D., Jr., Stuckless, J.S., Kistler, R.W. and Stern, T.W., 1973. Radiometric dating of intrusive rocks in the Cottonwood area, Utah. *J. Res. U.S. Geol. Surv.*, 1: 172-178.
- Etheridge, M.A., Wall, V.J. and Vernon, R.H., 1983. The role of the fluid phase during regional metamorphism and deformation. *J. Metamorph. Geol.*, 1: 205-226.
- Evans, S.H., Parry, W.T. and Bruhn, R.L., 1985. Thermal, mechanical, and chemical history of Wasatch fault cataclastic and phyllonite, Traverse Mountains area, Salt Lake City, Utah: age and uplift rates from K/Ar and fission track measurements. *U.S. Geol. Surv., Open File Rep.* 86-31: 410-415.
- Gilbert, G.K., 1928. Studies of Basin-Range structure. *U.S. Geol. Surv., Prof. Pap.*, 153: 92 pp.
- Hunziker, J.C., 1979. Potassium argon dating. In: E. Jäger and J.C. Hunziker (Editors), *Lectures in Isotope Geology*. Springer, Berlin, pp. 52-76.
- Ismail, I.A.H. and Murrell, S.A.F., 1976. Dilatancy and the strength of rocks containing pore water under undrained conditions. *Geophys. J.R. Astron. Soc.*, 44: 107-136.
- Keenan, J.H., Keyes, F.G., Hill, P.G. and Moore, J.C., 1978. *Steam Tables. Thermodynamic properties of water including vapor, liquid and solid phases*. Wiley, New York, N.Y., 156 pp.
- Mase, C.W. and Smith, L., 1985. Pore-fluid pressures and frictional heating on a fault surface. *Pure Appl. Geophys.*, 122: 583-607.

- Murrell, S.A.F., 1977. Natural faulting and the mechanics of brittle shear failure. *J. Geol. Soc. London*, 133: 175-189.
- Naeser, C.W., 1979. Fission-track dating and geologic annealing of fission tracks. In: E. Jager and J.C. Hunziker (Editors), *Lectures in Isotope Geology*. Springer, Berlin, pp. 154-169.
- Naeser, C.W., 1981. The fading of fission tracks in the geologic environment—data from deep drill holes. *Nuclear Tracks*, 5: 248-250.
- Okaya, D.A. and Thompson, G.A., 1985. Geometry of Cenozoic extensional faulting: Dixie Valley, Nevada. *Tectonics*, 4: 107-125.
- Parry, W.T., 1986. Estimation of X_{CO_2} , P, and fluid inclusion volume from fluid inclusion temperature measurements in the system $NaCl-CO_2-H_2O$. *Econ. Geol.*, 81: 1009-1013.
- Parry, W.T. and Bruhn, R.L., 1986. Pore fluid and seismogenic characteristics of fault rock at depth on the Wasatch fault, Utah. *J. Geophys. Res.*, 91: 730-744.
- Parry, W.T. and Bruhn, R.L., 1987. Fluid inclusion evidence for minimum 11 km vertical offset on the Wasatch fault, Utah. *Geology*, 15: 67-70.
- Parry, W.T., Wilson, P.N. and Bruhn, R.L., 1988. Pore-fluid chemistry and chemical reactions on the Wasatch normal fault, Utah. *Geochim. Cosmochim. Acta*, 52: 2053-2063.
- Potter, R.W., II and Brown, D.L., 1977. The volumetric properties of aqueous sodium chloride solutions from 0°C to 500°C at pressures up to 2000 bars based on regression of available data in the literature. *U.S. Geol. Surv. Bull.*, 1421-C: 36 pp.
- Rice, J.R., 1980. The mechanics of earthquake rupture. In: A.M. Dziewonski and E. Boschi (Editors), *Physics of the Earth's Interior*. North-Holland, Amsterdam, 555-659.
- Rimstidt, J.D. and Barnes, H.L., 1980. The kinetics of silica-water reactions. *Geochim. Cosmochim. Acta*, 44: 1683-1699.
- Roedder, E., 1984. *Fluid Inclusions*. Rev. Mineral., 12. Mineralogical Society of America, Washington, D.C., 644 pp.
- Roedder, E. and Bodnar, R.J., 1980. Geologic pressure determinations from fluid inclusion studies. *Annu. Rev. Earth Planet Sci.*, 8: 263-301.
- Roeloffs, E. and Rudnicki, J.W., 1985. Coupled-deformation diffusion effects on water level changes due to propagating creep events. *Pure Appl. Geophys.*, 122: 560-582.
- Rudnicki, J.W. and Chen, C.J., 1988. Stabilization of rapid frictional slip on a weakening fault by dilatant hardening. *Geophys. Res.*, 93: 4745-4757.
- Sass, J.H., Lachenbruch, A.H., Monroe, R.J., Greene, G.W. and Moses, T.J., Jr., 1971. Heat flow in the western United States. *J. Geophys. Res.*, 76: 6376-6413.
- Sass, J.H., Blackwell, D.D., Chapman, D.S., Costain, J.K., Decker, E.R., Lawver, L.A., and Swanberg, C.A., 1981. Heat flow from the crust of the United States. In: Y.S. Touloukian, W.R. Judd and R.F. Roy (Editors), *Physical Properties of Rocks and Minerals*. McGraw-Hill/CINDAS Data Series on Material Properties, Vol. II-2. McGraw-Hill, New York, pp. 503-548.
- Scholz, C.H., 1978. Velocity anomalies in dilatant rock. *Science*, 201: 441-442.
- Scholz, C.H., Sykes, L.R. and Aggarwal, Y.P., 1973. Earthquake prediction. A physical basis. *Science*, 181: 803-810.
- Schwartz, D.L. and Coppersmith, K.J., 1984. Fault behavior and characteristic earthquakes. Examples from the Wasatch and San Andreas fault zones. *J. Geophys. Res.*, 89: 5681-5698.
- Sibson, R.H., 1981. Fluid flow accompanying faulting: field evidence and models. In: D.W. Simpson and P.G. Richards (Editors), *Earthquake Prediction: an International Review*. Maurice Ewing Ser., Am. Geophys. Union, 4: 593-603.
- Sibson, R.H., Robert, F. and Poulson, K.H., 1988. High-angle reverse faults, fluid-pressure cycling, and mesothermal gold-quartz deposits. *Geology*, 16: 551-555.
- Stemmons, D.B., 1957. Geological effects of the Dixie Valley-Fairview Peak Nevada, earthquakes of December 16, 1954. *Seismol. Soc. Am. Bull.*, 47: 353-375.
- Speed, R.C. and Armstrong, R.L., 1971. Potassium-argon ages of some minerals from igneous rocks of western Nevada. *Isochron/West*, no. 71-1: 1-8.
- Swan, R.H., III, Schwartz, D.P. and Cluff, L.S., 1980. Recurrence of moderate to large magnitude earthquakes produced by surface faulting on the Wasatch fault zone. *Utah. Bull. Seismol. Soc. Am.*, 70: 1431-1462.
- Thompson, A.B., 1971. P_{CO_2} in low-grade metamorphism: zeolite, carbonate, clay mineral, prehnite relations in the system $CaO-Al_2O_3-SiO_2-CO_2-H_2O$. *Contrib. Mineral. Petrol.*, 33: 145-161.
- Thompson, T.R., 1988. Fracturing in the Wasatch fault zone: implications for fluid flow, rock mass strength, and earthquake processes. M.S. Thesis, University of Utah, Salt Lake City, Utah, 186 pp.
- Walder, J. and Nur, A.J., 1984. Porosity reduction and crustal pore pressure development. *Geophys. Res.*, 89: 11539-11548.
- Wallace, R.E. and Whitney, R.A., 1984. Late Quaternary history of the Stillwater seismic gap, Nevada. *Bull. Seismol. Soc. Am.*, 74: 301-314.
- Willden, R. and Speed, R.C., 1974. Geology and mineral resources of Churchill County, Nevada. *Nevada Bur. Mines Geol. Bull.*, 83: 95 pp.

Fluid Inclusions and Hydrothermal Alteration on the Dixie Valley Fault, Nevada

W.T. PARRY, D. HEDDERLY-SMITH, AND R. L. BRUHN

Department of Geology and Geophysics, University of Utah, Salt Lake City

Footwall rocks of the 1954 rupture segment of the Dixie Valley fault show extensive hydrothermal alteration related to fluids that were present on the fault during tectonic events. Hydrothermal alteration of granitic host rocks consists of temporally and spatially overlapping mineral assemblages. An early, biotite-feldspar assemblage is followed by later Fe-chlorite and epidote. Both chlorite and epidote are replaced by hydrothermal sericite and cross-cut by calcite-hematite and quartz-calcite veins. Biotite is partially replaced by prehnite. The latest hydrothermal minerals are stilbite, laumontite, kaolinite, alunite, smectite, illite, and pervasive replacement of rock units with fine grained quartz, chalcedony, and opal. Secondary fluid inclusions trapped in healed microfractures in igneous quartz include type I inclusions that contain a moderate salinity aqueous liquid and vapor, type II inclusions that contain a moderate salinity aqueous liquid and CO₂, type III inclusions that show eutectic melting temperatures below the NaCl-H₂O eutectic and contain substantial CaCl₂, and type IV inclusions containing halite and other daughter minerals. Microthermometric measurements on these inclusions yield variable compositions and homogenization temperatures. Salinities of type I inclusions vary from 0.1 to 12.9 wt % NaCl with the mode in the interval 0 to 1%. Salinities of type II CO₂ bearing inclusions range from 0.62 to 6.81 wt % NaCl relative to H₂O, and salinities of type III inclusions with low eutectic melting temperatures are 12.9 to 25.3 NaCl equivalent wt %. Salinities of halite-bearing inclusions are 30.1 to 39.2 wt % NaCl. Homogenization temperatures span the range 120° to 400°C. The processes of isochemical cooling with upward displacement of the footwall, mixing of cool low-salinity water with hotter components, and mixing of cool, evaporite brine with hotter components could be responsible for variable fluid inclusion compositions, homogenization temperatures, and densities. The P-T path of the fault fluids is established by mineral equilibria and fluid inclusion characteristics. The path includes a lithostatic fluid pressure at 305°C and 1570 bars. Along with cooling and escape of CO₂ from fluids, the fluid P-T path probably approaches hydrostatic pressure conditions at lower temperatures. Hydrothermal alteration product minerals, fluid temperatures, pressures, and compositions in the footwall of the Dixie Valley fault constrain minimum fault age to 20 to 25 Ma, displacement to 6 km with about 3 km of pre-10 to 13 Ma and 3 km of post-10 Ma uplift. Fluid compositions and P-T data suggest the following mechanism for rupture initiation and arrest. Ruptures may be initiated as a result of high fluid pressures, then opening of dilatant fractures causes drastic decrease in fluid pressure, separation of steam and CO₂. The drastic reduction in fluid bulk modulus that accompanies volatile phase separation permits propagation of the ruptures even though fluid pressure is reduced. In areas where fluid pressure reduction is not accompanied by phase separation, fractures are arrested by dilatant hardening.

INTRODUCTION

Hydrothermal fluids play a significant role in the mechanical stability of faults. Increased fluid pressure reduces the frictional shear strength of an existing fault where failure is governed by effective stress [Hubbert and Rubey, 1959]. Alteration of the fault rock to mineral assemblages such as muscovite with lower frictional or flow strength decreases stability [Janecke and Evans, 1988; Kirby and Kronenberg, 1987]. Increased pore volume produced during dynamic rupturing with accompanying reduction in fluid pressure [Ismail and Murrell, 1976; Rudnicki and Chen, 1988; Roeloffs and Rudnicki, 1985], and healing and sealing of cracks with precipitated minerals increase stability. Fault stability is also related to the temperature and pressure of the fault zone and the constitutive properties of fault zone rock and fluids. New pore volume produced by dilatancy coupled with low rock permeability can result in decompression of the fluid and may stabilize rupture. Separation of the fluid into gas and liquid phases results in drastic reduction in fluid bulk modulus that diminishes the dilatant hardening effect and may permit rupture propagation [Rudnicki and Chen, 1988; Parry and Bruhn, 1990].

Copyright 1991 by the American Geophysical Union.

Paper number 91JB01965.
0148-0227/91/91JB-01965\$05.00

Evidence of hydrothermal fluid circulation and chemical interaction of fluids with fault zone rocks is evident in fault zones exhumed by erosion [Sibson, 1981; Sibson et al., 1988; Parry et al., 1988]. Microscopic to megascopic fractures filled with precipitated minerals are common, and fluid inclusions trapped within these minerals represent samples of the pore fluids. Characteristics of fluid inclusions together with associated hydrothermal alteration product minerals may be used to infer the physical state of the fault zone at depth, estimate constitutive properties of fault zone materials such as fluid bulk modulus which control fault stability [Parry and Bruhn, 1990], constrain the fluid pressure [Parry and Bruhn, 1986; Parry et al., 1988; Parry and Bruhn, 1990], and estimate fault displacement using pressure and temperature constraints [Parry and Bruhn, 1987].

The Dixie Valley fault system is part of a 300-km-long active seismic belt in central Nevada [Wallace, 1984] with individual segments capable of producing magnitude 7 earthquakes. Exhumed footwall rocks on segments of this fault display the effects of hydrothermal alteration and provide an opportunity for observation of fluid characteristics in fluid inclusions and alteration product mineralogy near seismogenic depths on the fault.

The objectives of this study are to characterize and map hydrothermal alteration assemblages on the footwall of the 1954 rupture segment of the Dixie Valley fault Nevada, to determine the characteristics of fault pore fluids using fluid inclusions and

alteration mineralogy, and to relate these characteristics to fault behavior and history. We have chosen the 1954 rupture segment for study because the footwall exposes Tertiary age granitic rocks in which aluminosilicate minerals provide an excellent record of chemical interaction of fluids and because the age of the alteration must postdate the emplacement of the igneous host rock.

THE DIXIE VALLEY FAULT

The Dixie Valley fault in the western Basin and Range province of Nevada lies in an area of high heat flow, late Cenozoic volcanic activity, and recent seismic activity. Historic seismicity has resulted in surface rupturing events (from north to south) at Pleasant Valley (1915), Fairview Peak-Dixie Valley (1954), Wonder (1903), Cedar Mountains (1932), Excelsior Mountain (1934), Mammoth Lakes (1980), and Owens Valley (1972) [Wallace and Whitney, 1984].

The Dixie Valley fault system forms the eastern margin of the Stillwater Mountains shown in Figure 1, and close spatial correlation between the 1954 and older fault scarps indicates that repeated surface-rupturing earthquakes have created the structural relief between the Stillwater mountains and Dixie Valley. Footwall rocks exposed in the Stillwater range shown in Figure 1 include Mesozoic sedimentary rocks intruded by the Jurassic gabbroic Humboldt lopolith [Willden and Speed, 1974] a multiphase Oligocene granodiorite-quartz monzonite-granite intrusion emplaced at 28 Ma [Speed and Armstrong, 1971], and a small Cretaceous granitic intrusion. These rocks are overlain by Tertiary volcanic rocks.

Dixie Valley is a graben system consisting of an inner graben with valley fill 2 to 3.2 km deep and a shallower outer graben containing 150 to 1500 m of fill [Meister, 1967; Thompson and Burke, 1973; Okaya and Thompson, 1985; Anderson et al., 1983]. Fault displacement has taken place along a normal fault at the base of the Stillwater range (the range front fault) and along a zone of normal faults a few km east of the range front (the piedmont fault zone) [Bell and Katzer, 1987, 1990]. Small scarps of the Piedmont fault zone shown on Figure 1 mark the inner graben.

The topographic low in Dixie Valley is dominated by a large playa and the Humboldt salt marsh occupies 46 square miles (119 km²) of Dixie Valley at an elevation of 3365 feet (1026m) [Baleman and Hess, 1978]. The brine is 28.7 to 38.7 wt % salt.

EXPERIMENTAL PROCEDURES

Our studies focus on hydrothermal alteration and fluid inclusion characteristics in footwall granitic and volcanic rocks of the 1954 rupture segment of the Dixie Valley range front fault. Samples were collected from outcrop of the intrusive and volcanic rocks in the footwall of the Dixie Valley fault at localities shown in Figures 2a, 2b, and 2c. Hydrothermal alteration mineral assemblages, tectonic textures, and fluid inclusions were studied in 183 thin sections of rocks collected during the course of mapping footwall alteration. Alteration mineralogy and tectonic textures were determined by a combination of petrographic microscope and X ray diffraction techniques. Clay minerals were identified by X ray diffraction of oriented smears of clay size material following vapor glycolation at

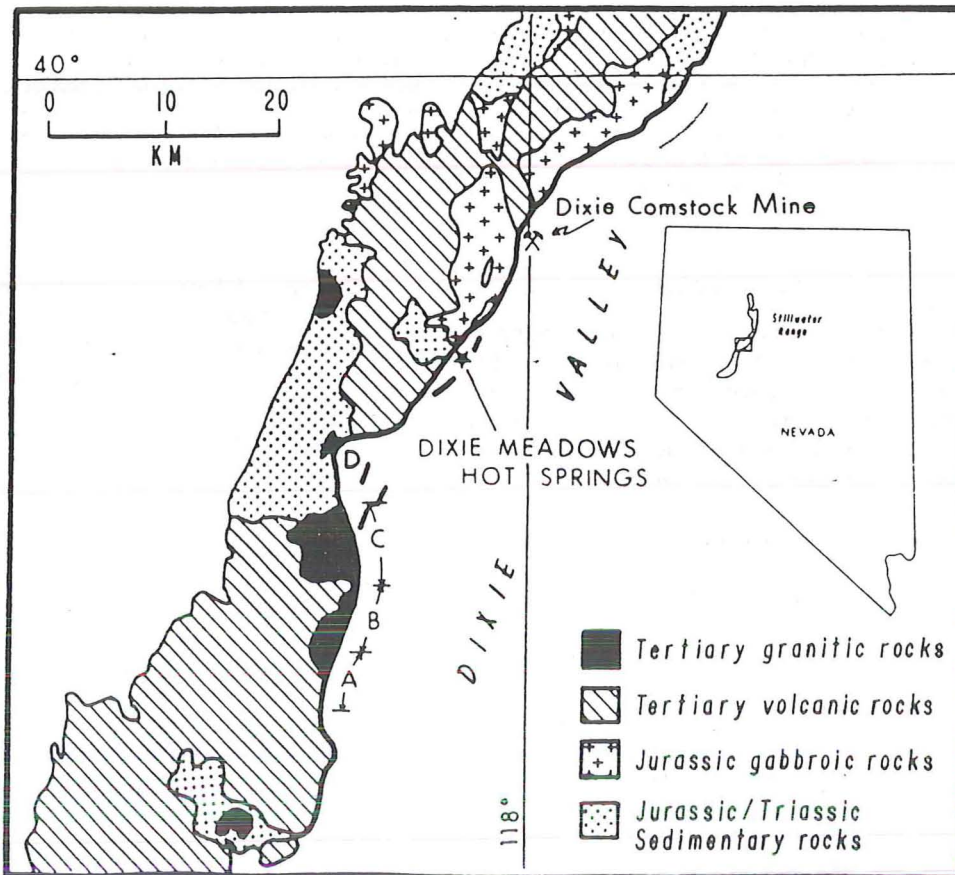


Fig. 1. Index map of Nevada showing the Stillwater Mountain Range and generalized geologic map of a portion of the Stillwater Mountain range modified from Page [1965]. The range front fault is shown as a heavy line. A, B, and C are sections of the Dixie Valley fault and footwall shown in detail in Figure 2.

60°C and heating to 250° and 550°C. The relative ages of alteration assemblages is established from crosscutting and replacement relationships.

Identity, density, and homogenization temperatures of fluid inclusion contents were determined by observation of phase changes in doubly polished plates on a Fluid Incorporated heating-freezing microscope stage and procedures outlined by *Roedder* [1984], *Parry and Bruhn* [1986], *Parry* [1986] and *Parry et al.* [1988]. Temperature calibration for the microscope stage was accomplished using synthetic fluid inclusions of known composition [*Sterner and Bodnar*, 1984]. Phase changes that were used to characterize fluid inclusion fluids were the CO₂ triple point temperature; melting of clathrate [*Collins*, 1979; *Bozzo et al.*, 1975]; melting of ice, hydrohalite, and halite; CO₂ liquid-vapor homogenization; and overall homogenization of fluid inclusion contents.

Fluid inclusion salinities were estimated from ice melting temperatures, from clathrate melting temperatures, and from halite melting temperatures as appropriate. Salinities of fluids in inclusions with no detectable CO₂ were calculated using freezing point depression estimated from ice melting temperatures and the regression equation of *Potter et al.* [1978]. Salinities for fluid inclusions on the halite liquidus were calculated using the equation and coefficients of *Sterner et al.* [1988]. Salinity of fluid inclusions showing eutectic temperatures below the NaCl-H₂O eutectic were estimated using the equations and coefficients for total salinity of *Oakes et al.* [1990].

The greatest source of error in fluid inclusion measurements is a consequence of post entrapment changes in secondary inclusions described as necked inclusions by *Roedder* [1984] and termed maturation by *Bodnar et al.* [1985]. These changes result from dissolution and reprecipitation of host mineral surrounding the trapped fluid. The initial fluid inclusion may be irregularly shaped but in time necks down to form many smaller inclusions with more regular shapes. If necking takes place after separation of a vapor phase, then the result is varying liquid to vapor ratios. All secondary fluid inclusions have undergone necking, but generally, the necking takes place before separation of a vapor phase or other daughter phases [*Roedder*, 1984]. We have avoided measurements of fluid inclusions with liquid-vapor ratios affected by necking using the following procedures: first, fluid inclusions in close proximity to one another with widely varying liquid to vapor ratios

were not measured; second, inclusions near one another with apparently similar liquid-vapor ratios were checked to insure similar homogenization temperatures.

FAULT ROCK PETROGRAPHY AND ALTERATION

Four separate plutons in the intrusive complex shown in Figures 1 and 2 were recognized in the footwall of the 1954 rupture segment during our field investigations, but the contacts between these plutons were not mapped. They are, from south to north, granite (40% plagioclase, 33% K-feldspar, 25% quartz, 2% biotite) outcropping in the vicinity of A in Figure 1; granodiorite (62% plagioclase, 12% K-feldspar, 19% quartz, 7% biotite) outcropping in the vicinity of B in Figure 1; biotite quartz monzonite (26% plagioclase, 34% K-feldspar, 27% biotite, 8% hornblende, 9% quartz) outcropping in the vicinity of C in Figure 1; and a small granite to granodiorite stock near Alameda Canyon (D on Figure 1) that consists of 33% quartz, 43% plagioclase, 17% K-feldspar, and 7% biotite. The K-Ar age of biotite from the biotite quartz monzonite at locality 108, Figure 2c, is 28±2 Ma (Table 1) [*Speed and Armstrong*, 1971]. The granite is younger than the granodiorite, but the relative age of the granodiorite with respect to the biotite quartz monzonite is not known due to the lack of outcrop. The K-Ar age of muscovite from the Alameda Canyon pluton at D on Figure 1 is 78.4±2.9 Ma (Table 1). Additional smaller intrusive rocks are also present at map localities shown in Figure 2 and include an altered quartz latite porphyry dike at 37, a diorite dike at 17, a quartz diorite dike at 65 and a diorite dike at 97. These smaller bodies are too small to map at the scale of Figure 2.

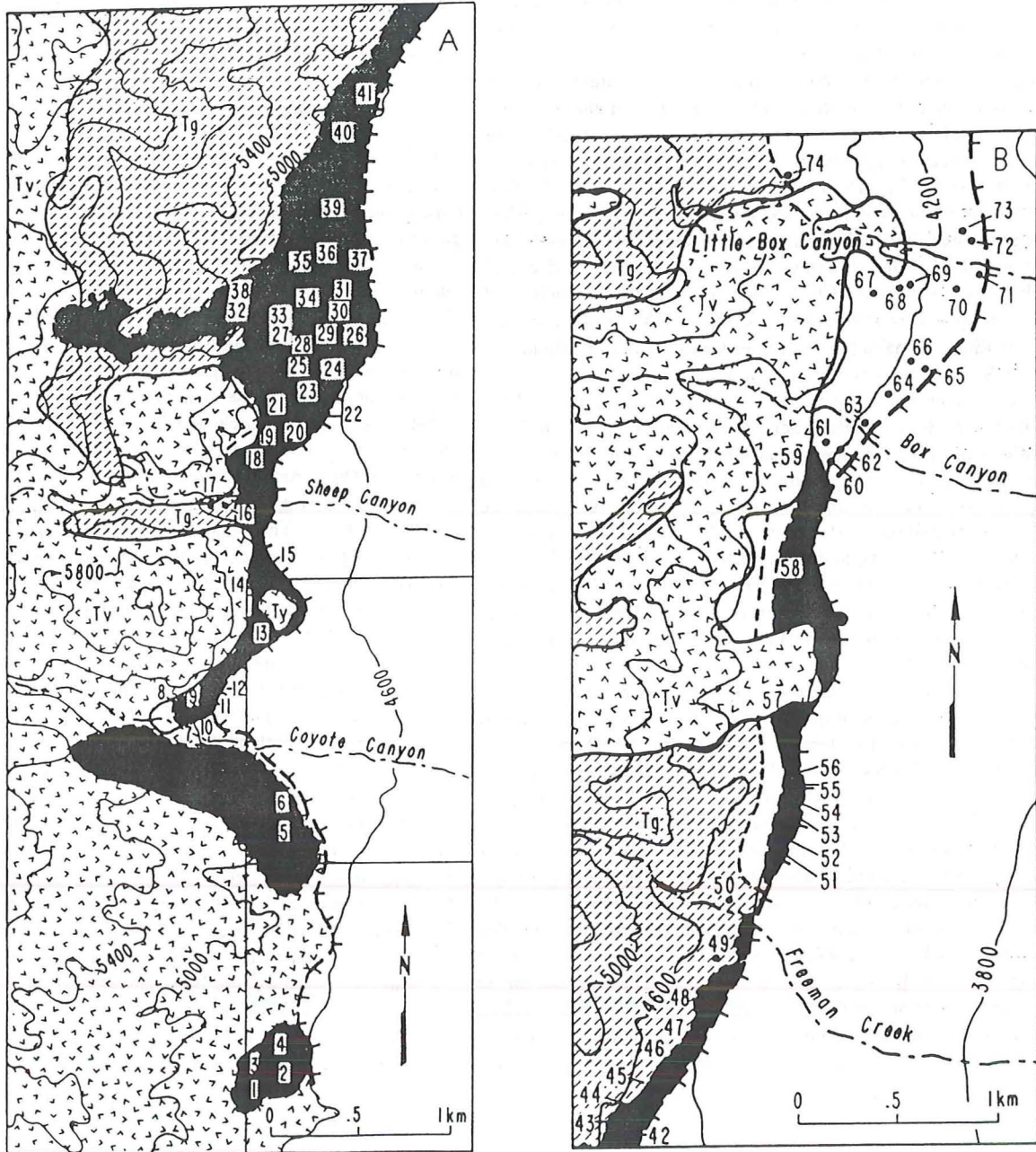
Fault breccia and cataclasite developed within the granitic protolith directly overlie the footwall granitic rocks. A pervasive set of closely spaced extension fractures is concentrated in the footwall immediately adjacent to the fault. Spacing between these steeply east dipping extension fractures is only a few centimeters and these fractures are present throughout the breccia and within the footwall for several meters to tens of meters. Thin discontinuous shear planes subparallel to the main fault plane also extend into the footwall and coexist with the penetrative fracture set.

Cataclasite is the dominant fault rock. Cataclastic textures include pervasive fracturing of large volumes of rock and veins. Cataclastic veins are thin tabular and branching bodies of fine cataclasite

TABLE 1. Potassium-Argon Age Data

Map No	Sample	Description	Dated Mineral	K, wt %	⁴⁰ Ar*/ ⁴⁰ Ar Total, %	⁴⁰ Ar*, x10 ⁻¹⁰ mol/g	Age, Ma±σ
108	IXL Pluton	fine to coarse plag K-feldspar, quartz 30°41'27"N 118°08'02"W	biotite	6.91	69	3.40	28±2.0
D	DV87-59	very coarse muscovite +quartz vein in granite	muscovite	8.91	82.1 89.7	12.37	78.4±2.9
18	DV87-7	sericite completely replacing feldspars in granite	muscovite	7.72	26.5 35.3	3.37	25.0±1
20	DV87-5b	near quantitative replacement of feldspars in granite	muscovite	7.07	54.6	2.69	21.8±0.9

Analyses by Geochron Laboratories. $\lambda\beta=4.962\times 10^{-10}/\text{yr}$. $\lambda\epsilon+\lambda\epsilon'=0.581\times 10^{-10}/\text{yr}$. $^{40}\text{K}/\text{K}=1.193\times 10^{-4}/\text{g}$. $^{40}\text{Ar}^*$ =radiogenic Ar.



EXPLANATION

- R s. Triassic sedimentary rocks
- T v. Tertiary volcanic rocks
- T g. Least altered granitic rocks
- Quaternary alluvium

- Chlorite and epidote alteration
- Sericite alteration
- Zeolite alteration
- Dixie Valley Fault
- 23 Sample locality

Fig. 2. Geologic, alteration, and sample location map of portions of the Dixie Valley fault. Temporally and spatially overlapping hydrothermal alteration mineral assemblages in footwall rocks are shown. (a) Coyote Canyon area, (b) Box Canyon area, and (c) IXL Canyon area.

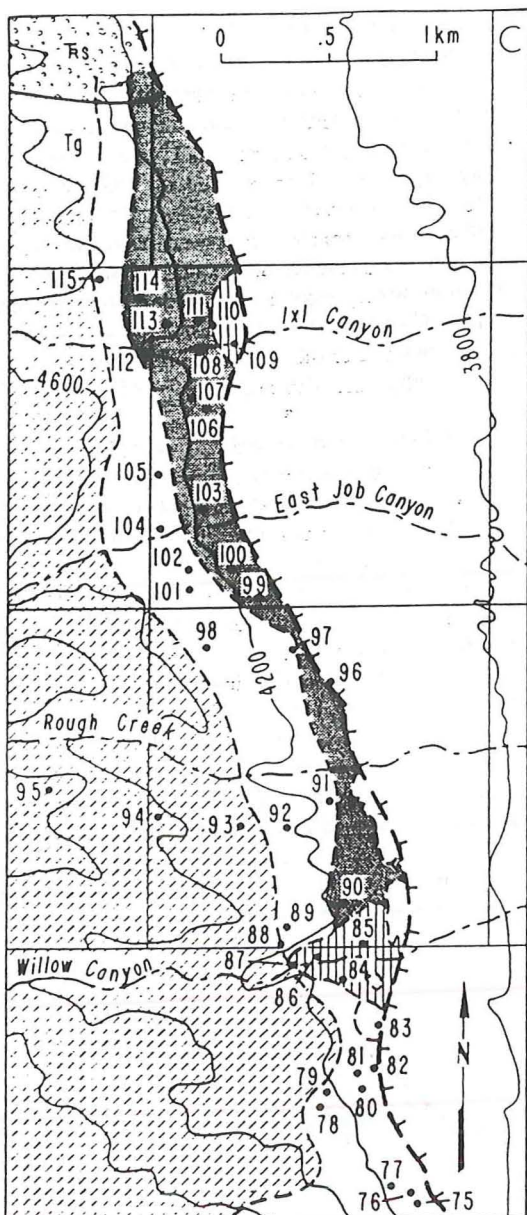


Fig. 2. (continued)

consisting of angular fragments of quartz and feldspar occasionally with a matrix of sericite or chlorite. No shear displacement of the fracture walls is apparent in thin section even though the fractures are crowded with angular fragments of quartz and feldspar and the quartz may be stretched and recrystallized. We infer that the cataclasite was emplaced as a suspension of fine rock particles possibly during hydraulic fracturing.

Temporally and spatially overlapping hydrothermal alteration mineral assemblages occur as a narrow band near the 1954 rupture in the fault footwall. Geometric association of the alteration with the fault and association with tectonic textures indicate alteration mineral assemblages are related to tectonic events on the Dixie Valley fault. From earliest to latest, these assemblages are biotite+K-feldspar, chlorite+epidote, sericite+kaolinite+ smectite, prehnite+laumontite+stilbite+kaolinite+smectite. The spatial distribution of areas dominated by sericite, chlorite+epidote, and zeolite assemblages is shown in Figure 2. The sericitic alteration is superimposed on chlorite and epidote, traces of which remain in the rock. Prehnite,

laumontite, stilbite, and clay minerals have also been superimposed on earlier alteration mineralogies with traces of the earlier minerals remaining in the rock.

The earliest assemblage of hydrothermal minerals includes a pervasive, partial to complete replacement of igneous plagioclase by K-feldspar, leaving patchy remnants of twinned plagioclase crosscut by K-feldspar veins visible in thin sections. Hydrothermal K-feldspar also occurs as selvages on quartz veins and as quartz+K-feldspar veins. Later veins of albite also crosscut plagioclase. Hydrothermal K-feldspar was not mapped but is widely distributed along the fault footwall. Hydrothermal biotite also forms early in the sequence, though the relative age of biotite cannot be unequivocally tied to the K-feldspar replacement of plagioclase. Hydrothermal biotite occurs as thin veins, as replacement of hornblende and as a replacement of igneous biotite. Hydrothermal biotite is more abundant in more mafic rocks where biotite vein networks occur in plagioclase and pyroxene. Hydrothermal biotite is not volumetrically abundant anywhere in the fault footwall.

The dominant alteration mineralogy on the Dixie Valley fault footwall is Fe-chlorite and epidote associated with local areas of calcite, hematite, sericite, and prehnite. Chlorite replaces hornblende and biotite and occurs in veins with actinolite, green biotite, calcite, quartz, or epidote. Epidote forms a selvaige to quartz+epidote veins that reach thicknesses of several centimeters. Cataclasite and breccia consisting of epidote and chlorite form the faces of some of the faceted spurs.

Hydrothermal sericite (dioctahedral white mica) replaces all previously formed minerals except quartz. In the most intense sericitic alteration, feldspars have been nearly completely replaced by sericite and fine-grained quartz. The resulting altered rock consists of up to 58% sericite, relict igneous quartz, and fine-grained hydrothermal quartz. Biotite, hornblende, chlorite, and epidote are completely replaced by sericite. With decreasing intensity of alteration sericite occurs as disseminated grains within the feldspars and as isolated veins. X ray diffraction of clay-sized separates from sericitized rocks shows both kaolinite and smectite associated with the sericite. However, thin section examination shows the kaolinite and smectite are later than the sericite. good.

Prehnite occurs locally as fibrous, radiating masses with typical bow-tie extinction which partially replaces biotite.

Latest hydrothermal minerals are laumontite, stilbite, kaolinite, smectite, and very fine grained illite that occur on the fronts of faceted spurs at exposures of the 1954 rupture trace of the range front fault (Figure 2c). Silicification of both volcanic and plutonic rocks is the latest alteration event. Chalcedony, kaolinite, alunite, smectite, and opal occur in volcanics both north and south of the 1954 rupture segment.

Deep exploration wells in northern Dixie Valley crossed the Dixie Valley fault. Well data indicate that volcanic and alluvial material is altered to albite, chlorite, illite, epidote, and clay. Plagioclase is altered to albite, illite, epidote, calcite, and clay, and hornblende is altered to biotite, chlorite, magnetite, epidote, and calcite. In the meta sediments, illite forms from andalusite, and biotite alters to vermiculite and calcite. Quartz, laumontite, and adularia veins are observed [Bell et al., 1980].

JOINT AND VEIN SYSTEMS

Mineral assemblages precipitated in veins and on joint surfaces occur in several sets of variably oriented fractures that formed over an extended period of time. The youngest mineral assemblages consist of prehnite-laumontite-stilbite-clay, and calcite-filled

↑ higher P

This is prehnite after biotite but not the same as the rocks in the area

not 8/21

need ref.

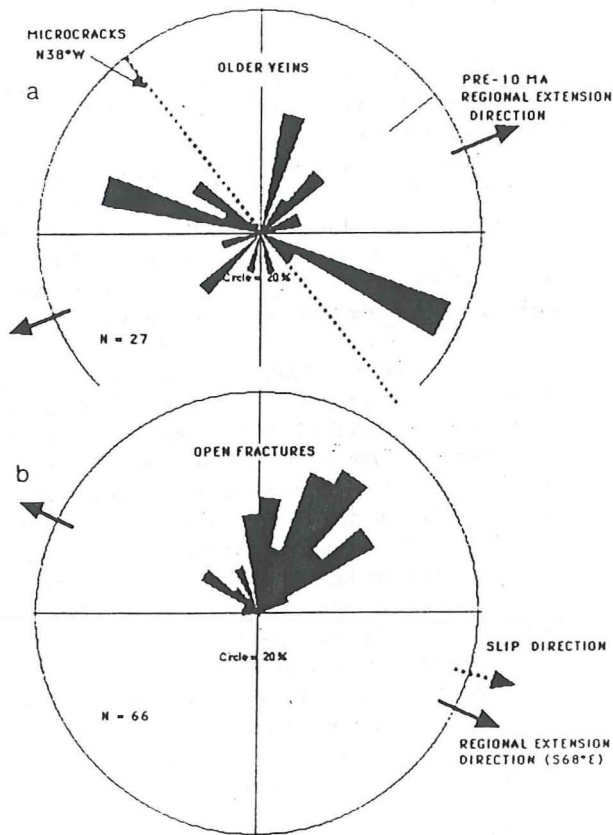


Fig. 3. (a) Rose diagram of strike directions of open fractures on the Dixie Valley fault, Nevada. (b) Rose diagram of strike directions of hydrothermal veins.

veinlets. This assemblage is concentrated in north to NE trending fractures that parallel the Dixie Valley fault trace (Figure 3a). Sericite-clay and older mineral assemblages are concentrated in NW to WNW striking veins that strike at a high angle to the contemporary fault zone and in a secondary set of NNE to NE striking veins (Figure 3b). These older mineral assemblages form bands of alteration several tens to hundreds of meters wide that either parallel the Dixie Valley fault zone or cut into the footwall at a high angle to the fault zone (Figures 1 and 2). Two samples of hydrothermal sericite were dated using the K-Ar method; one yielded an age of 21.8 Ma and the other 25 Ma (Table 1), indicating that this alteration occurred during late Oligocene to early Miocene.

The sericite-clay alteration assemblage is younger than the chlorite-epidote and biotite-K-feldspar assemblages based on crosscutting relationships seen in the field and in thin section. The epidote-chlorite assemblage is best preserved from Little Box Canyon to Willow Canyon (Figure 2), but remnants of this assemblage extend along almost the entire length of the fault zone in the study area. In most locales along the range front, the sericite-clay assemblage overprints the epidote-chlorite mineralization. Near Sheep Canyon, in the southern part of the study area (Figure 2), sericite-clay mineralization extends about 1 km into the footwall along a closely spaced set of WNW to west striking joints and veins.

Orientations of mineral-filled veins suggest that an early stage of activity on the Dixie Valley fault with an ENE to WSW extension direction is associated with mineral-filled extension veins of quartz, epidote, quartz-sericite, clay minerals, and hematite. Fractures with dustings of euhedral quartz, stilbite, chlorite, calcite, epidote, and hematite are parallel to present-day extension fractures.

FLUID INCLUSION PETROGRAPHY

Healed microcracks in both igneous quartz and vein quartz contain thin planar trails of numerous secondary fluid inclusions that often crosscut boundaries between adjacent quartz grains. In least altered rocks there are a few trains of small ($<1\mu\text{m}$) fluid inclusions, but most quartz grains near the fault show many intersecting planar arrays of secondary fluid inclusions. While numerous intersections of fluid inclusion trains are apparent, it is not possible to determine a fluid inclusion chronology from crosscutting relationships. Necking is a common phenomena. Fluid inclusions appear as irregular, immature to very regular mature inclusions with negative crystal shapes. Nearby fluid inclusions in linear arrays that are mature and display negative crystal outlines often have similar liquid to vapor ratios suggesting that necking preceded separation of a vapor phase.

The abundance of secondary fluid inclusions larger than $1\mu\text{m}$ can be correlated with proximity to the mapped trace of the Dixie Valley fault. Quartz grains nearest the fault trace contain up to 2×10^5 fluid inclusions per cubic millimeter. Fluid inclusion abundance decreases to 3×10^4 fluid inclusions per cubic millimeter within 6 m of the fault at Coyote Canyon and 400 m of the fault at IXL canyon. Here the broader distribution is due to the presence of several subsidiary faults.

Arrays of secondary fluid inclusions are subparallel to cataclastic veins with a second set at high angles to cataclastic veins. The orientations of fluid inclusion trails that define partly healed microfractures were measured on oriented samples of granitic rock using a universal stage (Figure 4). Poles to these trails are shown in Figure 4 contoured in terms of standard deviations (σ) from a uniform distribution of points. Three areas of high point density are apparent. The most prominent crack orientation, point density of $8-10\sigma$, represents nearly vertical planes striking $N38^\circ W$ about 15°

how many trails?

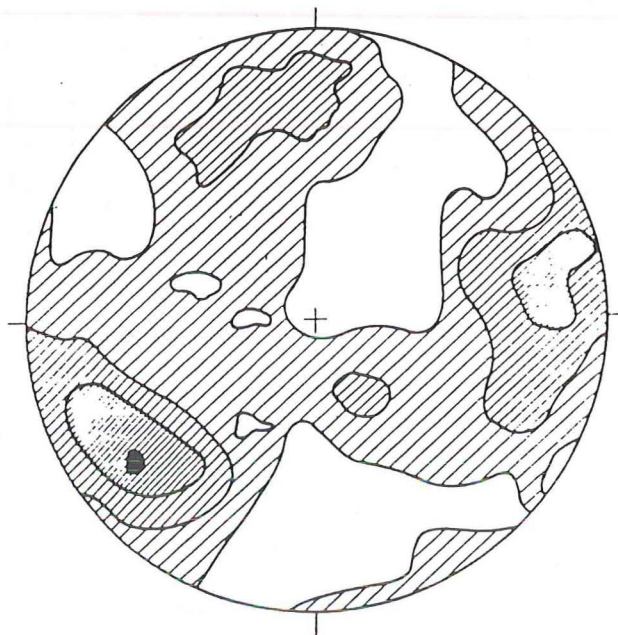


Fig. 4. Equal-area stereographic plot of poles to fluid inclusion trails, lower hemisphere. Contoured in terms of standard deviations from a uniform distribution of points [Kamb, 1959] with the contour interval of 2σ indicated by width of ruled lines. A uniform distribution is represented by 3σ , so the unruled area representing $2\sigma-4\sigma$ represents the area of the diagram in which the counting circle contained a distribution of points equivalent to 1σ on either side of the density of a uniform distribution of points.

TABLE 2. Characteristics of Major Fluid Inclusion Groups

Property	Type I Moderate Salinity	Type II CO ₂ -Bearing	Type III Low Eutectic	Type IV Halite
Phases at room temperature	40-90%l 10-60%v	60-90% H ₂ Ol 10-40% CO ₂ l +CO ₂ v	80-90%l 6-20%v	H ₂ Ol H ₂ Ov 2-10% NaCl
Aqueous phase at low temperature	freeze at -30° to -40°C melting of last solid (ice) 0° to -11°C		freeze at -60° -80°C coarsens -40°C visible melt -40°C melting of last solid ice -26° to -9°C	
Bubble behavior at low temperature	no change	CO ₂ melts -57.5° to -54.4°C		
Gas hydrates	none	clathrate melts 6.4° to 9.7°C		
Heating behavior	homogenization to l at 125°-400°C	CO ₂ l-v 22.5°-29.3°C(v) CO ₂ l-v 25.4°-29.4°C(l) homogenization to l at 197°-358°C	homogenization to liquid 129°-283°C	TmNaCl 160°-356°C Thl-v 275°-382°C
Number of measurements	256	45	17	7

v, homogenizes to vapor phase; l, homogenizes to liquid phase.

clockwise of the dominant NW to WNW concentration of older veins observed in outcrop. The next most prominent, 6-8σ, represents planes N10°W and the third set, 4-6 σ, represents planes striking N72°E.

The K-Ar age of hydrothermal illite in the area is 21 to 25 Ma (Table 1) corresponding to the earlier episode of extension where the extension direction is WSW-ENE consistent with mode I microcracks hosting fluid inclusions striking N38°W. Fluid inclusion fluids on this section of the Dixie Valley fault must therefore be associated with the early phase of Basin and Range extension. The orientations of fluid inclusion trails are subperpendicular to the inferred Oligocene to early Miocene regional stress field.

FLUID INCLUSION MEASUREMENTS

Phase changes observed in fluid inclusions on the heating-freezing microscope stage have revealed a diverse assemblage of chemically distinct fluids on the Dixie Valley fault. Fluid inclusions are categorized by their contents into liquid+vapor, moderate salinity inclusions (type I); carbon dioxide bearing inclusions (type II); low eutectic temperature inclusions (type III); halite bearing inclusions (type IV); and one-phase (liquid) inclusions. A few inclusions contain solid phases in addition to halite. The one-phase (liquid) inclusions are the youngest. The thermometric measurements are summarized in Table 2. The majority of fluid inclusions measured consist of an aqueous phase and a vapor bubble usually comprising 10 to 30 vol % (type I). Ice is the last phase to melt on warming. A second and possibly related type of inclusion contains a large vapor bubble (more than 60 vol %) and a small volume of low-salinity liquid. These two types of inclusions are occasionally in close proximity to one another and may show similar homogenization temperatures, the first to liquid and the second to vapor. These characteristics could be considered evidence for boiling of fluids at some stage of fault development. However, the widespread occurrence of necked inclusions suggests that necking probably accounts for this association. CO₂-bearing inclusions (type II) are present on some sections of the fault.

Two types of high-salinity inclusions are present. A few inclusions consisting of only vapor and liquid showed eutectic temperatures well below the NaCl-H₂O eutectic (type III). The fourth type of fluid inclusions contain daughter minerals (type IV). These daughter minerals include an isometric salt probably halite, a small, high-relief unidentified salt, and a platy, birefringent mineral that may be sericite.

Moderate Salinity Inclusions (Type I)

Microthermometric measurements of type I fluid inclusions have revealed wide diversity in chemical composition and homogenization temperatures. Salinities in NaCl equivalent wt % calculated from ice melting temperatures are shown for 265 fluid inclusions in the histogram of Figure 5. Salinity data form a highly skewed distribution with most frequent values in the low salinity range 0 to 1% NaCl. However significant numbers of higher salinity fluid inclusions were observed.

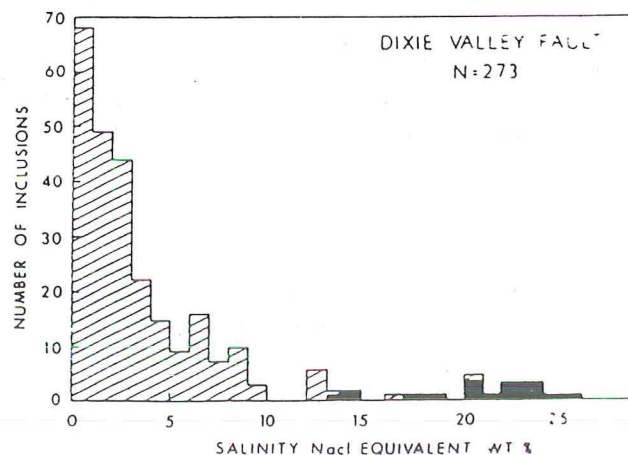


Fig. 5. Histogram of salinities of Type I (ruled lines) and Type III (solid) fluid inclusions calculated from ice melting temperatures using the regression equation of Potter et al. [1978].

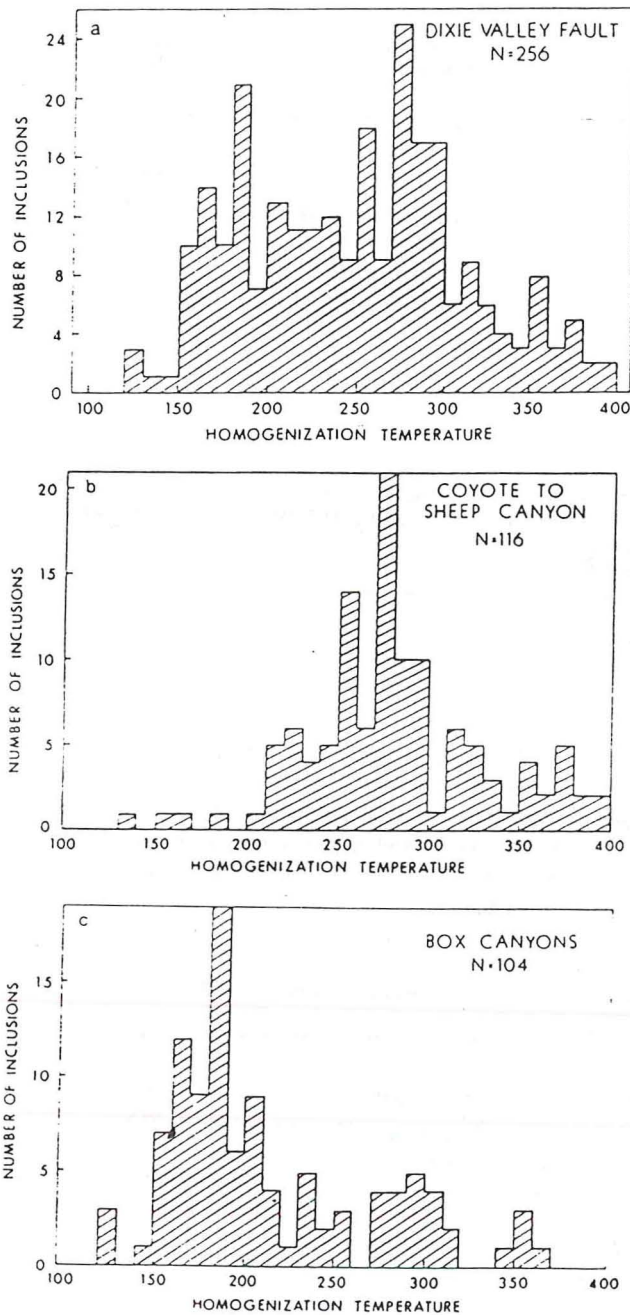


Fig. 6. (a) Homogenization temperatures of type I aqueous fluid inclusions from the Dixie Valley fault footwall. (b) Homogenization temperatures of fluid inclusions from the Coyote Canyon area of Figure 2a. (c) Homogenization temperatures of fluid inclusions from the Box Canyons area (Figures 2b and 2c).

Homogenization of type I fluid inclusions occurred by disappearance of the vapor bubble. The range in homogenization temperatures is 120° to 400°C (Figure 6). The mode of T_h values is 270°-280°C in the southern area near Coyote and Sheep Canyon (Figure 2a) and 180°-190°C in the Box Canyons area (Figure 2b), an area dominated by chlorite and epidote alteration (Figure 6), although both areas have homogenization temperatures that span nearly the full range.

Homogenization temperature is plotted versus salinity for type I, type II, and type III fluid inclusions in Figure 7. The data points on Figure 7 indicate no apparent trends of cooling and dilution. Homogenization temperature and salinity define the fluid density

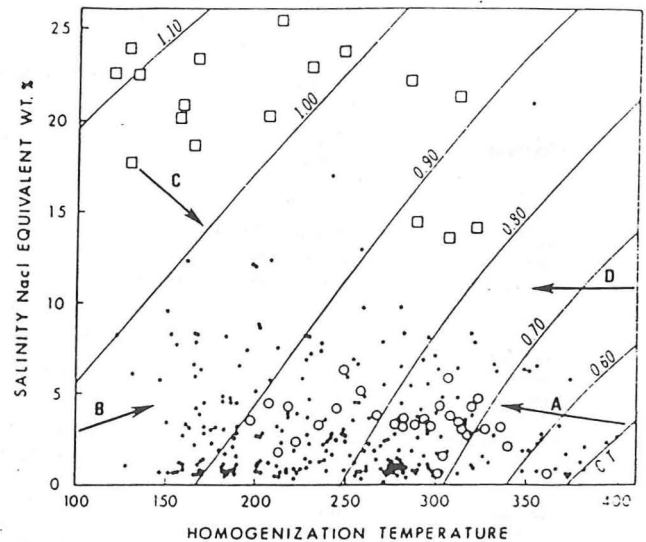


Fig. 7. Temperature of homogenization of fluid inclusions plotted versus salinity. Symbols are open squares, low eutectic inclusions (type III); open circles, CO₂ inclusions (type II); solid circles, moderate salinity aqueous inclusions (type I). Moderate salinity aqueous inclusions (type I) are contoured in terms of density (g/cm³) using the equations and coefficients of Potter and Brown [1977]. Density contours do not apply to CO₂ inclusions shown as open circles. Trends in the diagram indicated by arrows and discussed in the text are A, boiling; B, cool, low-salinity water mixing; C, cool evaporite mixing; and D, isochemical cooling of the fault footwall.

and Figure 7 is contoured in terms of density. Because fluids trapped in inclusions are constant density systems, the fluids must be trapped along isochores defined by these density values.

CO₂-Bearing Fluid Inclusions (Type II)

Secondary fluid inclusions containing CO₂ are present in several areas of the Dixie Valley fault footwall. These inclusions contain a recognizable meniscus separating liquid CO₂, vapor CO₂, and an aqueous liquid at room temperature. Thermometric properties of these inclusions are shown in Table 3. The liquid CO₂ phase that is frozen by supercooling to below -90°C, melts in the presence of CO₂ vapor at temperatures of -57.6°C to -54.4°C. The most frequent melting temperature is within 0.2°C of -56.6°C, the triple point temperature of pure CO₂. Lower melting temperatures could be accounted for by small amounts of methane. The melting temperatures above -56.6°C can not be accounted for by any known phase equilibria, but these temperatures are reproducible and not the result of experimental error.

Clathrate melting temperatures of CO₂-bearing inclusions yield salinities of 0.62 to 6.8 wt % NaCl relative to H₂O (Table 3). These salinities together with the homogenization temperatures are plotted on Figure 7 for comparison with aqueous inclusions, but the density contours on Figure 7 apply only to the aqueous inclusions.

The CO₂ component of these inclusions homogenized to liquid at 25.4°-29.5°C or to vapor at 20.5°-29.3°C. Homogenization to the liquid implies a greater density of CO₂ and entrapment at higher pressure.

Overall homogenization of CO₂ bearing inclusions occurred over nearly as wide a range (197°-371°C) as the moderate salinity inclusions (Table 2 and Figure 7).

Low Eutectic Temperatures (Type III)

Fluid inclusions with ice melting temperatures between -10.1°C and -26.0°C had very low initial melting temperatures as low as

TABLE 3. Microthermometric Properties of CO₂-Bearing Fluid Inclusions

Map	Sample	No.	T _m CO ₂	T _m CO ₂ Clath	T _h CO ₂ L-V	T _h	Volume Percent %CO ₂	WNaCl	XNaCl	XH ₂ O	XCO ₂	P, bar
12	DV87-1f	1	-56.5	9.2	28.0v	304	30	1.63	0.005	0.931	0.065	390
		4	-56.9	8.4	20.5v	313	29	3.19	0.010	0.942	0.049	320
		8	-56.8	7.9	26.5v	297	27	4.14	0.012	0.933	0.055	360
		14	-57.4	9.7	27.9v	300	30	0.62	0.002	0.934	0.064	340
		15	-56.4	9.6	29.3v	278	25	0.82	0.002	0.939	0.058	340
		16	-57.6	7.9	28.0v	335	39	4.14	0.012	0.902	0.086	450
		17		9.0	27.1v	340	40	2.03	0.006	0.909	0.085	440
22	DV87-4	17	-56.8		29.4	270v						
		18	-56.7	9.7	22.5v	371v	80	0.62	0.001	0.726	0.272	
		19	-57.2	8.0	28.4l	239D	17	3.95	0.012	0.921	0.068	
20	DV87-5a	8	-56.4			307		3.19				
		11	-57.0	8.5	26.6l	312D	42	3.10	0.008	0.810	0.182	
		12	-57.5	8.5	26.2l	254D	25	3.10	0.008	0.890	0.102	
		13		8.2	29.0l	197	9	3.67	0.011	0.947	0.042	540
18	DV87-7	5	-56.3	8.5	27.2v	312v		3.10	0.009	0.066	0.068	
		6	-56.3	8.5	26.4v	280	23	3.10	0.009	0.943	0.048	350
		7	-56.3	8.1	27.5v	308	31	3.86	0.011	0.924	0.065	380
		8	-56.3	8.6	22.5v	318	32	2.91	0.008	0.935	0.056	340
43	DV87-19	1	-56.4	7.1	24.7v	80v?	90	5.59	0.009	0.479	0.512	
		2	-56.9	6.9	24.0v	210D	15	6.03	0.018	0.948	0.033	
		6	-57.0	6.8	27.5v	250D	26	6.12	0.019	0.926	0.055	
		7	-57.1	7.9	28.0	261D	28	4.14	0.012	0.927	0.060	
D	DV87-54a	1	-55.4	8.5	26.5l	240D	21	3.00	0.009	0.906	0.085	
		2	-55.1	9.1	27.2l	252D	25	1.83	0.005	0.895	0.100	
		3	-54.9	8.1	25.4l	280	31	3.76	0.010	0.856	0.134	1480
		4	-54.4	8.0	27.0l	268	27	3.95	0.011	0.881	0.108	1300
		5	-56.7	7.6	28.7v	324	34	4.69	0.014	0.910	0.076	550
		6	-56.5	7.8	28.4v	320	36	4.32	0.013	0.907	0.080	430
		7	-56.8	7.8	27.5v	303	30	4.32	0.013	0.924	0.063	370
D	DV87-55	1	-56.7	8.3	30.0v	234	14	3.38	0.010	0.950	0.039	360
		3	-56.5	7.7	29.4l	208	10	4.51	0.014	0.939	0.047	670
		5		7.9	29.0v	244	21	4.14	0.012	0.908	0.082	880
D	DV87-59	1	-56.0	7.9	27.5v	219	10	4.14	0.013	0.958	0.030	280
		2	-56.0	9.2	29.5v	216	10	1.63	0.005	0.963	0.032	310
		3	-55.6	8.9	28.9v	222	11	2.22	0.007	0.961	0.033	300
		4	-56.6	8.4	29.4l	279	33	3.19	0.009	0.866	0.126	1060
		5	-56.6	8.4	29.5l	287	32	3.19	0.009	0.866	0.125	1200
		7	-56.7	6.4	24.1l	268D	25	6.81	0.020	0.875	0.105	
		9	-55.2	6.7	27.3l	248	18	6.29	0.019	0.908	0.073	1250
		10	-56.8	7.4	27.6l	259	19	5.05	0.015	0.909	0.076	1380
		11	-56.8	6.9	28.3l	305	32	5.94	0.017	0.857	0.126	1570
		12	-55.6	8.2	26.2l	294	39	3.57	0.009	0.824	0.167	1450

v, homogenizes to vapor phase; l, homogenizes to liquid phase; D, decrepitated. Map number on Figures 1 and 2.

45°C and ice crystal nucleation temperatures as low as -60°C to -80°C. These characteristics suggest the presence of a significant CaCl₂ component in the fluid. These fluid inclusions have salinities of 13.6-25.3 wt % CaCl₂+NaCl (Figure 5). In two cases, fluid inclusions were sufficiently large and visible to observe hydrohalite and ice melting temperatures. In these two fluid inclusions the weight fraction NaCl relative to CaCl₂ was 0.3 and 0.55. Homogenization of liquid and vapor in fluid inclusions with low eutectic temperatures ranged from 120° to 321°C. Homogenization temperatures and salinities of these inclusions are shown as open squares in Figure 7.

Inclusions Containing Halite (Type IV)

Several fluid inclusions that contain a vapor bubble, a halite crystal and liquid at 25°C were observed. These inclusions homogenize by disappearance of the vapor bubble or by dissolution of the halite crystal. The homogenization of liquid and vapor occurred at a temperature below the halite melting temperature in several of these inclusions. Because halite melting occurred in the

presence of liquid only, estimated salinity is only approximate because of the unknown slope of isopleths in P-T space (Stern *et al.*, 1988).

Fluid inclusions with a halite daughter salt are the highest salinity fluid inclusions. Salinities determined from halite melting temperatures of 160°-297°C for inclusions that homogenize by vapor disappearance are 30.1 to 37.9 NaCl equivalent wt %. In some halite-bearing inclusions, however, halite was present at the temperature of vapor bubble disappearance. Some of these inclusions decrepitated before all halite had dissolved. The few halite-bearing inclusions that homogenized by dissolution of halite yielded salinities of 39.2 to 43 NaCl equivalent wt %.

Discussion

Evidence that fluid inclusions and alteration mineral assemblages represent fluids and their interaction with rocks related to faulting, includes occurrence of alteration bands in the fault footwall, spatial orientation of fluid inclusions trails consistent with the stress system producing the faulting, and correlation of fluid inclusion abundance

with proximity to the fault. All fluid inclusions measured and all observed alteration minerals are in the footwall of the Dixie Valley fault, and all postdate the intrusion of the granitic rocks at 28 Ma so that the fluid inclusion fluids and alteration have a maximum age near the inception of extension.

The diversity in salinity of fluid inclusions could result from mixing of low-salinity and high-salinity components. These components may include cool, low-salinity meteoric water, saline water formed in evaporite basins, moderate salinity thermal water, and a high-temperature boiling fluid with temperature and salinity variations caused by steam separation. Lower temperatures resulting from boiling would correspond to higher salinities as shown by the temperature-salinity mixing lines labeled A on Figure 7. Mixing of low-temperature, low-salinity meteoric water with boiling fluids at any stage in their evolution toward lower T and higher salinity is labeled B on Figure 7. The present-day Dixie Valley contains evaporites in Humboldt Salt Marsh, and the extensive evaporites of Carson and Humboldt Sinks lie 30 km to the west.

Dixie Meadows hot springs (Figure 1) near the 1954 rupture termination consists of 35 springs and seeps over 4 square miles (10 km²) with wide variations in temperature and salinity. Springs emerge from alluvium in the hanging wall of the Dixie Valley fault. Temperature and salinity are inversely correlated in these springs suggesting that dissolution of evaporites by cold water and mixing with low salinity hot water accounts for the variation in temperature and salinity [Bell *et al.*, 1980]. Halite-cemented breccias are present in the fault in the vicinity of the hot springs area. Saline, gypsiferous clays occur in the Truckee formation of upper Miocene age in western Nevada [Morrison, 1964]. Mixing of cool, salty fluid with higher-temperature, lower-salinity fluids is illustrated by the trend labeled C on Figure 7. A fourth alternative is suggested by continuous displacement of the fault footwall to shallower, cooler depths. This trend is labeled D on Figure 7.

Geothermal fluids at depth in Dixie Valley presently contain CO₂. Fluid in the deep wells contains 312-396 mg/L Na, 37-54 mg/L K, and CO₂ comprises 0.12-0.22 wt % of the fluid (0.09 mol %) at a temperature of 206°-249°C [Benoit, 1989]. High bicarbonate in springs emerging from igneous rocks near major faults [Bohm, 1984]; vast travertine deposits at Sou hot springs, 47 km northeast of the 1954 rupture segment; and high bicarbonate (870-936 mg/L at Hyder hot springs, 42 km northeast, may be the result of CO₂ leakage from a deeper geothermal reservoir.

Secondary fluid inclusions in granitic rocks often show final ice melting temperatures in the range below the NaCl-H₂O eutectic [Konnerup-Madsen, 1977, 1979]. These types of high-salinity fluids are common in granitic rocks, and their occurrence in healed microfractures in the Dixie Valley fault rocks together with an intrusive age near the time of inception of Basin and Range extension suggests they may have been important fault fluids.

CaCl₂-NaCl brines have been observed in retrograde Ca-rich amphibolite where retrograde reactions with muscovite, epidote, and chlorite as product minerals are suggested as a mechanism for concentrating Na, K, and Ca in fluids [Crawford *et al.*, 1979]. These Ca-rich compositions are most common in metamorphosed carbonate rich sediments [Roedder, 1984, p. 351]. Hydrothermal calcium chloride brines are also known from continental rift systems [Hardie, 1990].

FLUID TEMPERATURE AND PRESSURE

Fluid inclusion characteristics and mineral equilibria may be used to place constraints on the fluid pressure and temperature in the

Dixie Valley fault footwall. Minimum pressures of entrapment are estimated from CO₂ containing fluid inclusions and from inclusions containing a halite crystal.

The salinity, CO₂ density, and homogenization temperatures of type II fluid inclusions were used together with the CO₂-H₂O-NaCl phase diagram to estimate CO₂ content and minimum pressure of entrapment using the procedures of Parry [1986]. Carbon dioxide content ranges from 3 to 17 mol %, and estimated pressures on the two-phase boundary curve for inclusion compositions vary from 280 to 1570 bars. These pressures represent minimum entrapment pressures of a homogenous fluid. Homogenous fluids could have been trapped at higher temperatures and pressures along appropriate isochores for each fluid composition.

Roedder and Bodnar [1980] and Roedder [1984] showed that the minimum pressure of entrapment of a homogenous fluid can be estimated from halite-bearing fluid inclusions by first assuming the fluid properties are adequately represented by the NaCl-H₂O system and that NaCl solubility is independent of pressure. The bulk composition of the fluid inclusion fluid and its density were estimated from the melting temperature of NaCl using the regression equation of Sterner *et al.* [1988]. The composition and density of the halite saturated solution on the liquid-vapor curve at the temperature of vapor disappearance were calculated using equations from Haas [1976]. At the temperature of liquid-vapor homogenization, the inclusion volume is the volume of saturated solution of known density plus the volume of halite. The mass of halite crystal is obtained from the difference in salinity at the temperature of liquid-vapor homogenization and at the temperature of NaCl melting, and its volume is calculated from halite density. These calculations yield densities of 1.137 and 1.275 g/cm³ for inclusions homogenizing at the NaCl melting temperature of 313° and 356°C, respectively. Extrapolation of the density determinations of Urusova [1975] at 350°C to higher pressures indicate a minimum entrapment pressure of about 1500 bars, but extrapolation of the MRK equation of state using the coefficients of Bowers and Helgeson [1983] indicates a pressure of 800 bars at 350°C. Extrapolation of Urusova's [1975] density measurements to 300°C yields a pressure estimate of 240 bars for the inclusion homogenizing at 313°C.

We next assume that lithostatic pressure represents a reasonable maximum and hydrostatic pressure represents a reasonable minimum for fluid pressure. Second, we infer a thermal gradient so that pressure-temperature gradients maybe shown in Figure 8. The thermal gradient on the Dixie Valley fault is probably greater than the 30°C/km gradient that is characteristic of the Basin and Range Province [Sass *et al.*, 1981]. The northern end of the belt of historic seismicity in the central Nevada seismic belt is an area of conspicuously high heat flow called the Battle Mountain High [Sass *et al.*, 1971] where thermal gradients are 40° to 50°C/km [Sass *et al.* 1981].

Additional indications of elevated geothermal gradients include intense hydrothermal alteration along the range front fault, fumaroles and hot water within 30 m of the surface, As and Hg in soils of the valley near the range front fault [Juncal and Bell, 1981], and hot springs widely distributed in the hanging wall of the Dixie Valley fault. The Dixie Valley geothermal area is 47 km northeast of the 1954 rupture segment where gradients of 75°C/km and above have been measured in drill holes [Bell *et al.*, 1980] due to hydrothermal convection. These observations lend support to a thermal gradient in Dixie Valley that exceeds the normal Basin and Range gradient. Lithostatic and hydrostatic pressure gradients are shown on Figure 8 for thermal gradients of 45° and 60°C/km.

Soil at
1600 ft
2 km depth

The Molten Side of Info.

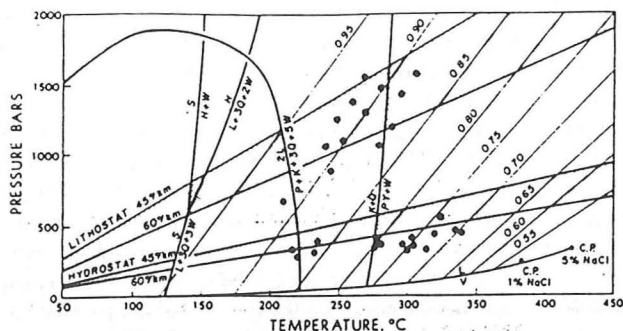


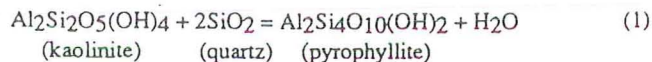
Fig. 8. Minimum pressure and temperature for entrapment of CO₂ fluid inclusions (solid circles), lithostatic and hydrostatic pressure gradients, mineral equilibria, and boiling curves. K, kaolinite; P, pyrophyllite; Q, quartz; W, water; L, laumontite; Pr, prehnite; S, stilbite; H, heulandite. Data for reactions: K+Q=P+W from Hemley et al. [1980]; L=Pr+K+3Q+5W from Bird and Helgeson [1981]; S=H+W and H=L+3Q+2W from Cho et al. [1987]; and S=L+3Q+3W from Liou [1971]. Isochores calculated for 1% NaCl solution and various homogenization temperatures from data of Potter and Brown [1977]. Boiling curve calculation used data and equations of Haas [1976].

A heat source for an elevated gradient is readily available. The earliest phase of extension before 18-15 Ma was synchronous with a generally southward migrating belt of intermediate to silicic volcanism [Sonder et al., 1987; Wernicke et al., 1987]. Major Cenozoic igneous activity in the Dixie Valley area began with andesitic lava flows 35 Ma [Riehle et al., 1972]. Voluminous eruptions of quartz latite to rhyolite ash flow tuffs are dated at 32-22 Ma [Riehle et al., 1972; Speed, 1976; Burke and McKee, 1979]. Basalt flows cap the sequence and have been dated at 13-17 Ma [Nosker, 1981]. Small igneous dikes and plutons of latite to diorite occur along the Dixie Valley fault zone. The Dixie Valley fault may be rooted within magmatic intrusion and further intrusion into the crust along the fault might allow for different subsidiary fault displacements and spreading of grabens [Thompson, 1966; Thompson and Burke, 1974; Okaya and Thompson, 1985].

The pressure and temperature of entrapment of type I moderate salinity inclusions must lie on isochores defined by the fluid density. Fluid density is calculated from salinity and homogenization temperature measurements shown in Figure 7. Representative isochores for densities of 0.55 to 0.95 g/cm³ are shown in Figure 8 corresponding to densities of 1 wt % NaCl solutions that homogenize by vapor disappearance at various temperatures. These fluids would have been trapped along their respective isochores at pressures and temperatures between lithostatic and hydrostatic pressures.

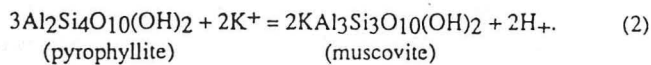
The minimum pressures and temperatures of entrapment of type II, CO₂-bearing inclusions are shown on Figure 8. These fluids, too, would have been trapped on isochores defined by the density of the fluid. The wide range in minimum pressures of entrapment has been interpreted to be the result of pressure transients accompanying dilatant fracturing [Parry and Bruhn, 1990]. The highest pressure values are near lithostatic pressure, and the lowest are near hydrostatic pressure.

Additional constraints are placed on P-T conditions by mineral equilibria. Equilibria among kaolinite, pyrophyllite, quartz, and water according to

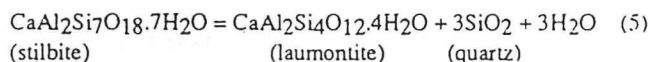
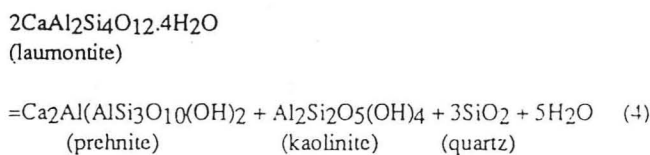
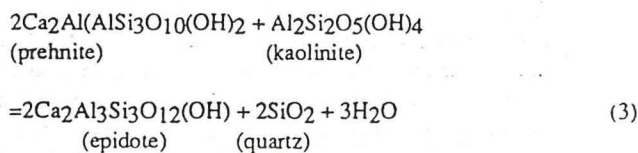


shown on Figure 8 indicate that the presence of kaolinite in these

quartz-rich rocks requires temperatures below about 270°C. Pyrophyllite has not been observed despite numerous fluid inclusion homogenization temperatures that exceed 270°C. The reason for this is that fluids contain sufficient K⁺ to stabilize muscovite according to



The low-temperature stability of epidote in the presence of quartz and an aqueous solution at pressures between 500 and 3800 bars is represented by reaction (3) [Bird and Helgeson, 1981]. Prehnite is stable relative to laumontite above about 220°C (reaction (4)) and stilbite is stable relative to laumontite below about 130°-140°C at pressures below 600 bars (reaction(5)):



Examination of equilibria (1), (4), and (5) on Figure 8 shows that mineral assemblages along with fluid inclusion properties record a systematic decrease in both temperature and pressure with displacement of the footwall during faulting. Fluid temperature at depth on the fault exceeded 350°C and pressure exceeded 1500 bars. K-feldspar, biotite, epidote, chlorite, and muscovite were the earliest formed stable mineral phases. As temperature and pressure decreased, kaolinite was stabilized relative to muscovite and pyrophyllite below about 270°C, prehnite was stabilized relative to epidote and then laumontite was stabilized relative to prehnite at about 220°C. At 140°C, stilbite is stable relative to laumontite and the fluid pressure must be lower than 600 bars, otherwise heulandite would occur. As pressure and temperature decreased, CO₂ separated so that zeolites were stabilized relative to calcite and clay.

REGIONAL IMPLICATIONS

The Stillwater Range lies in part of a regional WNW trending belt of mostly silicic volcanism that extended across southern Nevada from late Eocene through early Miocene time. This belt was characterized by widespread hydrothermal alteration and NW to WNW structural trends that included numerous dikes, caldera complexes, and high-angle fault and joint systems [Boden, 1986]. In some locales, NE trending faults formed as subsidiary features [Riehle et al., 1972; Boden, 1986; Hudson and Geissman, 1987]. Hudson and Geissman [1987] noted that counterclockwise rotation of rocks in the central Stillwater Range and Clan Alpine Mountains occurred as the result of movement on a complex array of strike-slip, oblique-slip, and dip-slip faults and suggested that rotation was accomplished by movement on NW-striking, right-lateral faults. Li et al. [1990] see paleomagnetic evidence for counterclockwise block rotations elsewhere in northern Nevada.

I don't understand that, now I understand

Regional extension in the great Basin dates from about 30 Ma and occurred in two episodes. The early episode of extension in northern Nevada was oriented $S68^{\circ}W-N68^{\circ}E$. At about 10 Ma the extension direction changed by clockwise rotation to the present-day extension direction of $N65^{\circ}W-S65^{\circ}E$ [Zoback *et al.*, 1981; Zoback and Thompson, 1978; Eaton, 1982]. The early phase of extension dated at 23-15 Ma based on angular unconformity and rotated high angle faults [John *et al.*, 1989] was accommodated by rotation of crustal blocks, strike slip motion on northwest trending faults, and normal faults that predate widespread basaltic volcanism dated at 13 to 17 Ma [Hudson and Geissman, 1987]. Remnants of this NW striking right-lateral fault set were preserved in the interior of the Stillwater Range near White Rock Canyon and Coyote Canyon and may be represented by the western fault branch in the "bend", within the present-day Dixie Valley fault zone (Figure 9). Hydrothermal activity and tectonic displacement on at least part of the Dixie Valley fault began during this early stage of extension. K/Ar ages of hydrothermal sericite on the fault are 21.8 to 25 Ma (Table 1) and mineral-filled veins and fluid inclusion train orientations are consistent with the earlier extension direction. The orientation and age of hydrothermal minerals in the older, NW to WNW trending

vein arrays indicate that these features probably reflect Oligocene to early Miocene deformation and hydrothermal activity, which occurred prior to the onset of NNE trending Basin and Range normal faulting [Stewart *et al.*, 1977].

The later episode of extension beginning at 10-13 Ma [Eddings *et al.*, 1987; Zoback *et al.*, 1981] is indicated by 10 Ma old basalt on the west flank of Job Peak that is tilted 10° west [Wallace and Whitney, 1984]. Basalt and andesite cap the Stillwater range at an elevation of 2200 m and also produce seismic reflections in Dixie Valley at an elevation 1280 m below sea level for a total of post-13-17 Ma displacement on the fault of 3.5 km [Wallace and Whitney, 1984] to 2.2 km farther north [Okaya and Thompson, 1985].

Moderate salinity fluid inclusions were trapped at the pressure and temperature defined by the isochore for the fluid density illustrated on Figure 8. Fluid inclusions containing CO_2 were trapped at minimum pressures as high as 1570 bars at a temperature of $305^{\circ}C$ (Table 3) shown in Figure 8 and corresponding to a lithostatic pressure at a depth of over 6 km. Aqueous fluid inclusions that homogenize at $380^{\circ}-400^{\circ}C$ then if trapped no deeper than 6 km must have been trapped at a thermal gradient of nearly $70^{\circ}C/km$.

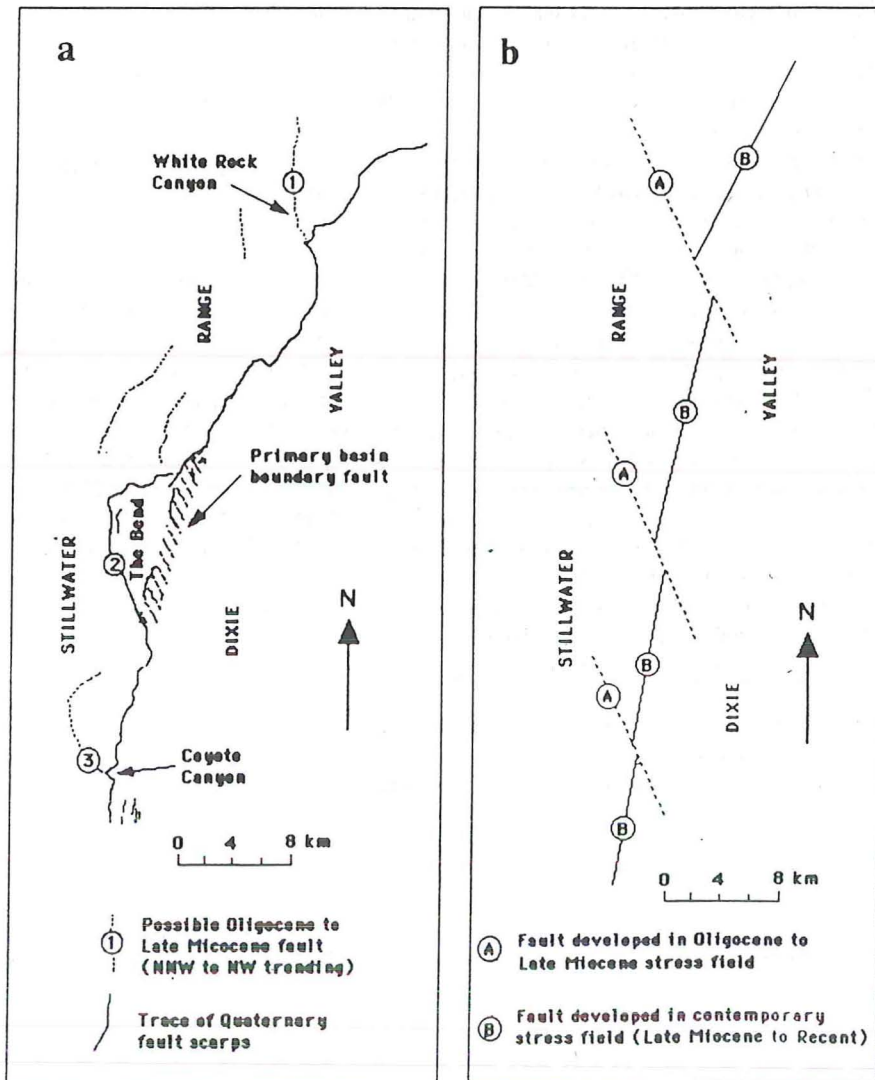


Fig. 9. (a) Map view of the rupture trace of the Dixie Valley fault. Localities referred to in the text are 1, White Rock Canyon; 2, The Bend; and 3, Coyote Canyon. (b) Map view of proposed development of the Dixie Valley fault from superposition of faults developed in contemporary stress field on Oligocene to late Miocene faults.

Supporting geological evidence for prebasalt displacement is evident on the 1:125,000 scale map of Page [1965] and the 1:250,000 scale map of Willden and Speed [1974]. Volcanic rock units on these maps include older Tertiary latite welded tuffs 0.6-1.8 km thick that are overlain by rhyolite to rhyodacite welded tuffs 0.6-3.0 km thick and rhyolite to rhyodacite. Basalt on the west flank of Job Peak directly overlies the older latite welded tuffs. Rhyolite to rhyodacite and up to 3.0 km of rhyodacite welded tuffs are missing. The older latite welded tuffs are exposed along a series of north to NW striking faults. Farther north, the basalt is in contact with Jurassic volcanics; rhyolite to rhyodacite, up to 3.0 km of rhyodacite welded tuffs, and 0.6 to 1.8 km of latite welded tuffs are missing. The older rock units are exposed on north to NW trending faults. The footwall of the Dixie Valley fault in the area C to D of Figure 1 also trends north to NW. Here Tertiary plutons have been unroofed, a Cretaceous pluton at D has been unroofed and the entire sequence of Tertiary volcanic rocks is missing exposing Mesozoic sedimentary rocks.

Evidence suggest that the present-day Dixie Valley fault zone began to form during Oligocene to early Miocene time and may have undergone two phases of extension. First, the fact that sericite-clay and older alteration mineral assemblages occur in a narrow band along the present-day fault trace suggests that a zone of intense fracturing and hydrothermal alteration with a geometry roughly similar to that of the Quaternary fault zone formed during Oligocene to early Miocene time. Second, paleofluid entrapment pressures estimated from measurements of high-temperature fluid inclusions indicate a minimum footwall uplift of 6 km. This is 3-4 km more vertical displacement than the post-13-17 ma displacement estimate of 3.5-2.2 km [Wallace and Whitney, 1984; Okaya and Thompson, 1985], suggesting that the early phase of vertical displacement was similar in magnitude to that of the later phase. Notably, the post-13-17 Ma displacement is estimated from offset of basalts that were extruded over a fairly flat surface. A period of tectonic quiescence must have occurred between the early and later phases of extension across the Dixie Valley fault zone. Third, we note that the Dixie Valley fault trace is highly sinuous, with two strong maxima in fault strike, one toward the WNW to NNW and the other NNE to NE (Figure 9). Perhaps this pattern is partly inherited from the earlier, Oligocene to early Miocene phase of extension, when deformation was concentrated on WNW striking strike-slip faults and subsidiary normal and normal-oblique-slip faults, many of which trended NNE to NE, forming a rectangular fault pattern when observed in map view [Riehle et al., 1972; Hudson and Geissman, 1987; Boden, 1986]. Presumably, rotation of extension from N68°E to S65°E about 10 Ma enhanced movement on NNE to NE trending normal faults, relative to older sets of WNW to NNW trending faults. Nevertheless, the distribution of hydrothermal alteration minerals, and the internal structure of the Dixie Valley fault zone indicate that part of the overall structural geometry is inherited from Oligocene and early Miocene deformation and hydrothermal circulation.

COMPARISONS WITH CONTEMPORARY FAULTS

Two well-studied contemporary fault systems in the Great Basin provide valuable comparisons. The Wasatch fault in the eastern Great Basin [Parry and Bruhn, 1986; Parry et al., 1988] and the Nevada Comstock fault in western Nevada [Vikre, 1989] are normal faults with displacement histories beginning in the Miocene.

Exhumation of the footwall at the southern end of the Salt Lake segment of the Wasatch fault has exposed hydrothermally altered granitic rocks. Vein filling and pervasive alteration mineralogy includes, from earliest to latest, biotite-K-feldspar, chlorite-epidote-

sericite, and laumontite-prehnite-clay. Secondary fluid inclusions present in healed fractures in quartz associated with syntectonic chlorite-epidote-sericite alteration contain 3 to 32 mol % CO₂ with 4.5 to 17.3 wt % NaCl solution. The mode of homogenization temperatures is 285°C. Estimated minimum entrapment pressures vary from 600 to 2950 bars. The mode of homogenization temperatures of secondary inclusions associated with the later laumontite-prehnite assemblage is 100°C, salinity ranges from 2.0 to 16.0 NaCl equivalent wt %, and no CO₂ was detected.

Fluid pressure and temperature within this segment of the Wasatch fault evolved along a path from lithostatic to hydrostatic with continued displacement of the footwall relative to the hanging wall. Age constraints are provided by a 17.6±0.6 Ma K-Ar age of hydrothermal sericite from a sample with mean Th of 309°C, and 7.3 to 9.6 Ma fission track ages of apatite (closure temperature 120°±15°C). Temperature and pressure estimates suggest post-17.6 Ma fault displacement is 11 km at a thermal gradient of 30°C/km [Parry and Bruhn, 1987].

The major tectonic consequence of the pore fluid and chemical reactions observed on the Wasatch fault is reduction of effective stress by pore fluid pressure. Elevated pressures are enhanced by chemical reactions that seal the tectonically induced cracks in the rock. The mechanical behavior of the rock is also modified by formation of chlorite and sericite with epidote in the fault rock at deeper levels, and vein fillings of zeolite, calcite, and clay minerals at shallower levels.

A contemporary fault system that has been examined in detail due to bonanza economic mineralization, the Comstock fault at Virginia City, Nevada, shows many similarities to the Dixie Valley fault. The Comstock fault is a major mineralized crustal structure 135 km southwest of Dixie Valley. This fault displaces Miocene volcanic rocks 762-1219 m [Vikre et al., 1988] and is mineralized over 4.6 km of strike length and to 1000 m below the present surface. Post-Miocene displacement is less than 183 m, and the fault is not presently active. Fault-related alteration and fluid characteristics date from the earlier episode of Basin and Range extension without superimposition of younger hydrothermal events. Alteration which is associated with precious metal veins and the Comstock fault includes strong silicification adjacent to the Comstock fault with accompanying sericite, chlorite, and pyrite. Near lode margins quartz, sericite, chlorite, montmorillonite, and pyrite overlie quartz + sulfide lodes. K-feldspar, albite, sericite, chlorite, and calcite locally occur with sulfides.

Chlorite, calcite, epidote, albite, quartz, and pyrite comprise a propylitic assemblage with no close association to the Comstock fault. A younger albite, natrolite, stilbite assemblage, and an assemblage of quartz, alunite, pyrophyllite, and clay are also not fault related.

Fluids circulated at least 2000 m below the Miocene paleosurface at temperature; from about 250°-300°C, with salinities of 1-6 % NaCl and up to 2.1 wt % CO₂. Fluids with recognizable CO₂ contain <3.2% NaCl, fluids with no CO₂ contain 0.4-6.1 % NaCl, and fluid inclusions with daughter NaCl and KCl contain 23% NaCl and 47% KCl. Boiling and mixing were invoked by Vikre [1989] to account for variable solution compositions, but the CO₂-bearing inclusions were determined to be later than those with no CO₂.

The Wasatch, Dixie Valley, and Comstock faults share several common characteristics. Fault fluids contain dissolved salts and CO₂, homogenization temperature modes are 250°-300°C. Fluid pressures on the Wasatch and Dixie Valley faults varied between lithostatic and hydrostatic pressures. Alteration minerals in the footwall include the common assemblages chlorite, epidote, sericite, prehnite, laumontite, zeolite, silicification, and clay.

this may provide the positive answer to the question of fluid and pore pressures

CONCLUSIONS

Detailed mapping, petrographic, and fluid inclusion work on the Dixie Valley fault and comparison with the Wasatch fault and Comstock fault suggests a model for Basin and Range seismogenic faults from which the relationship of fault behavior to fluid characteristics can be derived.

Hydrothermally altered footwall rocks have been exhumed by fault displacement and erosion on the Dixie Valley Fault, Nevada. Much of the footwall of the 1954 rupture segment consists of Tertiary age granitic rocks that provide aluminosilicate parent minerals for the alteration and constrain the maximum age of the alteration to be less than 28 Ma. Overlapping episodes of hydrothermal mineral formation were produced as displacement of the fault progressed. These mineral assemblages are from earliest to latest: hydrothermal biotite+K-feldspar, chlorite+epidote, sericite+kaolinite+smectite, prehnite+laumontite+stilbite+clay, and chalcedony, opal, smectite, alunite, and kaolinite. Microthermometric measurement of fluid inclusion characteristics indicate a diverse fluid chemistry, temperature, and pressure of entrapment. Hydrothermal alteration minerals and characteristics of secondary fluid inclusions trapped in healed microfractures in igneous quartz place constraints on fluid pressure and temperature during faulting.

Fluid inclusions in hydrothermally altered footwall rocks of the Dixie Valley fault, Nevada indicate that pore fluid pressure fluctuated from 1570 to 350 bars in the temperature range 350°-200°C. Scatter in the pressure estimates at constant temperature is interpreted as paleo-fluid pressure transients at depths of up to 3-5 km on the Dixie Valley fault. The pressure transients are greatest in the temperature range 270°-310°C.

Interaction of the pore fluid with host rock quartz monzonite on the Dixie Valley fault has resulted in a series of temperature dependent chemical reactions producing minerals that seal fractures and alter the mechanical properties of the rock. Ductile deformation combined with hydrothermal crack sealing must effectively prevent fluid communication with near surface fluids. As deformation becomes more brittle, rock fractures are less effectively sealed, the decrease in confining pressure allows fractures to be more open, and fluid pressures drop to hydrostatic conditions. Upward displacement of footwall rocks and decreasing fluid pressure permit open system conditions, effervescence of CO₂, and precipitation of calcite, zeolite, and other minerals in rock fractures.

Fault domains at a depth of up to 5 km on the Dixie Valley fault containing a CO₂-rich fluid may play a key role in nucleation and propagation of earthquake ruptures. Ruptures may be initiated by high pore pressures caused by porosity reduction. New pore volume produced by dilatancy coupled with low rock permeability would then result in decompression of the fluid and may stabilize the rupture by dilatant hardening. The dilatant hardening effect is proportional to the coefficient of friction and the pore fluid bulk modulus, $(\rho \, dP/d\rho)T$, where ρ is density, P is pressure, and T is temperature [Rudnicki and Chen, 1988]. Separation of CO₂-H₂O-NaCl fluids into two phases drastically reduces the fluid bulk modulus that diminishes the dilatant hardening effect and permits ruptures to propagate [Parry and Bruhn, 1990].

Acknowledgments. Financial support was provided by NSF grant EAR-8618250 to R.L.B. and W.T.P. The manuscript was carefully reviewed by Paula N. Wilson, John R. Bowman, and Ricardo Presnell. We are grateful to JGR reviewers E. Roedder and G. A. Thompson for their many helpful comments.

REFERENCES

- Anderson, R. E., M. L. Zoback, and G. A. Thompson, Implications of selected subsurface data on the structural form and evolution of some basins in the northern Basin and Range province, Nevada and Utah, *Geol. Soc. Am. Bull.*, **94**, 1055-1072, 1983.
- Bateman, R. L., and J. W. Hess, Hydrologic inventory and evaluation of Nevada playas, *Proj. Rep.* **49**, 137 pp, Water Resour. Cent., Desert Res. Inst., Univ. of Nev., Las Vegas, 1978.
- Bell, E. J., et al., Geothermal reservoir assessment case study, northern Basin and Range province, northern Dixie Valley, Nevada, report, 223 pp., Mackay Miner. Res. Inst., Univ. of Nev., Reno, 1980.
- Bell, J. W. and T. Katzer, Surficial geology, hydrology, and late Quaternary tectonics of the IXL Canyon area, Nevada, *Bull. Nev. Bur. Mines Geol.* **102**, 51 pp., 1987.
- Bell, J. W., and T. Katzer, Timing of late Quaternary faulting in the 1954 Dixie Valley earthquake area, central Nevada, *Geology*, **18**, 622-625, 1990.
- Benoit, W. R., Carbonate scaling characteristics in Dixie Valley, Nevada geothermal well bores, *Geothermics*, **18**, 41-48, 1989.
- Bird, D. K., and H. C. Helgeson, Chemical interaction of aqueous solutions with epidote-feldspar mineral assemblages in geologic systems, II, Equilibrium constraints in metamorphic/geothermal processes, *Am. J. Sci.*, **281**, 576-614, 1981.
- Boden, D. R., Eruptive history and structural development of the Toquima caldera complex, central Nevada, *Geol. Soc. Am. Bull.*, **97**, 61-74, 1986.
- Bodnar R. J., T. J. Reynolds, and C. A. Kuehn, Fluid-inclusion systematics in epithermal systems, in *Geology and Geochemistry of Epithermal Systems*, *Rev. Econ. Geol.*, vol. 2, edited by B.R. Berger and P. M. Bethke, pp. 73-97, Society of Economic Geologists, El Paso, Tex., 1985.
- Bohm, B., Possible relations between anomalous spring water chemistry in the Stillwater Range, and the Dixie Valley geothermal system, northern Nevada, *Trans. Geotherm. Resour. Council.*, **8**, 369-371, 1984.
- Bowers T. S. and H. C. Helgeson, Calculation of the thermodynamic and geochemical consequences of nonideal mixing in the system H₂O-CO₂-NaCl on phase relations in geologic systems: Equation of state for H₂O-CO₂-NaCl fluids at high pressures and temperatures, *Geochim. Cosmochim. Acta*, **47**, 1247-1275, 1983.
- Bozzo A. T., H-S Chen, J. R. Kass, and A. J. Barduhn, The properties of the hydrates of chlorine and carbon dioxide, *Desalination*, **16**, 303-320, 1975.
- Burke, D. B., and E. H. McKee, Mid-Cenozoic volcano-tectonic troughs in central Nevada, *Geol. Soc. Am. Bull.*, **90**, 181-184, 1979.
- Cho, M., S. Maruyama, and J. G. Liou, An experimental investigation of heulandite-laumontite equilibrium at 1000 to 2000 bar P fluid, *Contrib. Mineral. Petrol.*, **97**, 43-50, 1987.
- Collins, P. L. F., Gas hydrates in CO₂-bearing fluid inclusions and the use of freezing for estimation of salinity, *Econ. Geol.*, **74**, 1435-1444, 1979.
- Crawford, M. L., J. Filer, and C. Wood, Saline fluid inclusions associated with retrograde metamorphism, *Bull. Mineral.*, **102**, 562-568, 1979.
- Eaton, G. P., The Basin and Range province: Origin and tectonic significance, *Annu. Rev. Earth Planet. Sci.*, **10**, 409-440, 1982.
- Eddington, P. K., R. B. Smith, and C. Renggli, Kinematics of Basin and Range intraplate extension, in *Continental Extensional Tectonics*, edited by M. P. Coward, J. F. Dewey, and P. L. Hancock, *Geol. Soc. Spec. Pub. London*, **28**, 371-392, 1987.
- Haas, J. L., Jr., Physical properties of the coexisting phases and thermochemical properties of the H₂O component in boiling NaCl solutions, *U. S. Geol. Surv. Bull.*, **1421-A**, 73 pp., 1976.
- Hardie, L. A., The roles of rifting and hydrothermal CaCl₂ brines in the origin of potash evaporites: An hypothesis, *Am. J. Sci.*, **290**, 43-106, 1990.
- Hemley, J. H., J. W. Montoya, J. W. Marinenko, and R. W. Luce, Equilibria in the system Al₂O₃-SiO₂-H₂O and some general implications for alteration/mineralization processes, *Econ. Geol.*, **75**, 210-228, 1980.
- Hubbert, M. K. and W. W. Rubey, Role of fluid pressure in the mechanics of overthrust faulting, *Geol. Soc. of Am. Bull.*, **70**, 115-205, 1959.
- Hudson, M. R., and J. W. Geissman, Paleomagnetic and structural evidence for middle Tertiary counterclockwise block rotation in the Dixie Valley region, west-central Nevada, *Geology*, **15**, 638-642, 1987.

- Ismail, I. A. H., and S. A. F. Murrell, Dilatancy and the strength of rocks containing pore water under undrained conditions., *Geophys. J. R. Astron. Soc.*, 44, 107-136, 1976.
- Janecke, S. U., and J. P. Evans, Feldspar-influenced rock rheologies, *Geology*, 16, 1064-1067, 1988.
- John, D. A., R. E. Thomason, and E. H. McKee, Geology and K-Ar geochronology of the Paradise Peak mine and the relationship of pre-Basin and Range extension to early Miocene precious metal mineralization in west central Nevada, *Econ. Geol.*, 84, 631-649, 1989.
- Juncal, R. W., and E. J. Bell, Solid-sample geochemistry study of western Dixie Valley, Churchill County, Nevada, part II, Soil geochemistry, *Trans. Geotherm. Resour. Council.*, 5, 51-54, 1981.
- Kamb, W. B., Petrofabric observations from Blue Glacier, Washington, in relation to theory and experiment, *J. Geophys. Res.*, 64, 1891-1909, 1959.
- Kirby, S. H. and A. K. Kronenberg, Rheology of the lithosphere: Selected topics, *Rev. Geophys.*, 25, 1219-1244, 1987.
- Konnerup-Madsen, J., Composition and microthermometry of fluid inclusions in the Kleivan granite, south Norway, *Am. J. Sci.*, 277, 673-696, 1977.
- Konnerup-Madsen, J., Fluid inclusions in quartz from deep-seated granitic intrusions, south Norway, *Lithos*, 12, 13-23, 1979.
- Li, Y., J. W. Geissman, A. Nur, R. Hagai, and Q. Huang, Palcomagnetic evidence for counter clockwise block rotation in the north Nevada rift region, *Geology*, 18, 79-82, 1990.
- Liou, J. G., Stilbite-laumontite equilibrium, *Contrib. Mineral. Petrol.*, 31, 171-177, 1971.
- Meister, L. J., Seismic refraction study of Dixie Valley, Nevada, Ph. D. thesis, 72 pp., Stanford Univ., Stanford, Calif., 1967.
- Morrison, R. B., Lake Lahontan: Geology of the southern Carson Desert, Nevada, *U.S. Geol. Surv. Prof. Pap.*, 401, 156 pp., 1964.
- Nosker, S. A., Stratigraphy and structure of the Sou Hills, Pershing County, Nevada, M. S. Thesis, 60 pp., Univ. of Nev., Reno, 1981.
- Oakes, C. S., R. J. Bodnar, and J. M. Simonson, The system NaCl-CaCl₂-H₂O, I, The ice liquidus at 1 atm total pressure, *Geochim. Cosmochim. Acta*, 54, 603-610, 1990.
- Okaya, D. A., and G. A. Thompson, Geometry of Cenozoic extensional faulting: Dixie Valley, Nevada, *Tectonics*, 4, 107-125, 1985.
- Page, B. M., Preliminary geologic map of a part of the Stillwater Range, Churchill County, Nevada, *Map 28*, Nev. Bur. of Mines and Geol., Reno, 1965.
- Parry, W. T., Estimation of XCO₂, P, and fluid inclusion volume from fluid inclusion temperature measurements in the system NaCl-CO₂-H₂O, *Econ. Geol.*, 81, 1009-1013, 1986.
- Parry W. T., and R. L. Bruhn, Pore fluid and seismogenic characteristics of fault rock at depth on the Wasatch fault, Utah, *J. Geophys. Res.*, 91, 730-744, 1986.
- Parry, W. T., and R. L. Bruhn, Fluid inclusion evidence for minimum 11 km vertical offset on the Wasatch fault, Utah, *Geology*, 15, 67-70, 1987.
- Parry, W. T., and R. L. Bruhn, Fluid pressure transients on seismogenic normal faults, *Tectonophysics*, 179, 335-344, 1990.
- Parry, W. T., P. N. Wilson, and R. L. Bruhn, Pore-fluid chemistry and chemical reactions on the Wasatch normal fault, Utah, *Geochim. et Cosmochim. Acta*, 52, 2053-2063, 1988.
- Potter, R. W., II, and D. L. Brown, The volumetric properties of aqueous sodium chloride solutions from 0°C to 500°C at pressures up to 2000 bars based on regression of available data in the literature, *U.S. Geol. Surv. Bull.*, 1421-C, 36 pp., 1977.
- Potter R. W. II, M. A. Clyne, and D. L. Brown, Freezing point depression of aqueous sodium chloride solutions, *Econ. Geol.*, 73, 284-285, 1978.
- Riehle, J. R., E. H. McKee, and R. C. Speed, Tertiary volcanic center, west-central Nevada, *Geol. Soc. of Am. Bull.*, 83, 1383-1396, 1972.
- Roedder E., Fluid inclusions, *Rev. Mineral.*, 12, 644 pp, 1984.
- Roedder, E., and R. J. Bodnar, Geologic pressure determinations from fluid inclusion studies, *Annu. Rev. Earth Planet. Sci.*, 8, 263-301, 1980.
- Roeloffs, E., and J. W. Rudnicki, Coupled-deformation diffusion effects on water level changes due to propagating creep events, *Pure Appl. Geophys.*, 122, 560-582, 1985.
- Rudnicki, J. W., and C. J. Chen, Stabilization of rapid frictional slip on a weakening fault by dilatant hardening, *J. Geophys. Res.*, 93, 4745-4757, 1988.
- Sass, J. H., A. H. Lachenbruch, R. H. Monroe, G. W. Greene, and T. J. Moses, Jr, Heat flow in the western United States, *J. Geophys. Res.*, 76, 6376-6413, 1971.
- Sass, J. H., D. D. Blackwell, D. S. Chapman, J. K. Costain, E. R. Decker, L. A. Lawver, and C. A. Swanberg, Heat flow from the crust of the United States, in *Physical Properties of Rocks and Minerals, McGraw-Hill/CINDAS Data Ser. on Mater. Prop.* Vol. II-2, edited by Y. S. Touloukian, W. R. Judd, and R. F. Roy, pp. 5681-5698, McGraw-Hill, New York, 1981.
- Sibson, R. H., Controls on low-stress hydro-fracture dilatancy in thrust, wrench and normal fault terrains, *Nature*, 289, 665-667, 1981.
- Sibson, R. H., Fluid flow accompanying faulting: Field evidence and models, in *Earthquake Prediction: An International Review, Maurice Ewing Ser.* vol. 4, edited by D. W. Simpson and P. G. Richards, pp. 593-603, AGU, Washington, D. C., 1981.
- Sibson, R. H., F. Robert, and K. H. Poulson, High-angle reverse faults, fluid-pressure cycling, and mesothermal gold-quartz deposits, *Geology*, 16, 551-555, 1988.
- Sonder, L. J., P. C. England, B. P. Wemick, and R. L. Christiansen, A physical model for Cenozoic extension of western North America, in *Continental Extensional Tectonics*, edited by M. P. Coward, J. F. Dewey, and P. L. Hancock, *Geol. Soc. London Spec. Publ.* 28, 187-201, 1987.
- Speed, R. C., Geologic map of the Humboldt Lopolith, scale 1:81050, *Map Chart Ser. MC-14*, Geol. Soc. of Am. Boulder, Colo., 1976.
- Speed, R. C., and R. L. Armstrong, Potassium-argon ages of some minerals from igneous rocks of western Nevada, *Isotopes*, 71(1), 1-8, 1971.
- Sterner S. M., and R. J. Bodnar, Synthetic fluid inclusions in natural quartz, I, Compositional types synthesized and applications to experimental geochemistry, *Geochim. Cosmochim. Acta*, 48, 2659-2668, 1984.
- Sterner, S. M., D. L. Hall, and R. J. Bodnar, Synthetic fluid inclusions, V, Solubility relations in the system NaCl-KCl-H₂O under vapor saturated conditions, *Geochim. Cosmochim. Acta*, 52, 989-1005, 1988.
- Stewart, J. H., Geology of Nevada, *Spec. Publ.* 4, 136 pp., Nev. Bur. of Mines and Geol., Reno, 1980.
- Stewart, J. H., W. J. Moore, and I. Zeitz, East-west patterns of Cenozoic igneous rocks, aeromagnetic anomalies, and mineral deposits, Nevada and Utah, *Geol. Soc. Am. Bull.*, 88, 67-77, 1977.
- Thompson, G. A., The rift system of the western United States, in *The World Rift System* edited by T. N. Irvine, *Tech. Surv. Pap.* 66-14, pp. 280-290, Geol. Surv. Can. Dep. of Mines, Ottawa, 1966.
- Thompson, G. A., Perspective from the Fairview Peak-Dixie Valley earthquakes of 1954, in *Proceedings of Workshop XXVIII on the Borah Peak Earthquake*, edited by R. S. Stein and R. C. Bucknam, *U.S. Geol. Surv. Open File Rep.*, 85-290, 27-42, 1985.
- Thompson, G. A., and D. B. Burke, Rate and direction of spreading in Dixie Valley, Basin and Range province, Nevada, *Geol. Soc. Am. Bull.*, 84, 627-632, 1973.
- Thompson, G. A., and D. B. Burke, Regional geophysics of the Basin and Range province, *Annu. Rev. Earth Planet. Sci.*, 2, 213-238, 1974.
- Urusova, M. A., Volume properties of aqueous solutions of sodium chloride at elevated temperatures and pressures, *Russ. J. of Inorg. Chem. Engl. Trans.*, 20, 1717-1721, 1975.
- Vikre, P. G., Fluid-mineral relations in the Comstock lode, *Econ. Geol.*, 84, 1574-1613, 1989.
- Vikre, P. G., E. H. McKee, and M. L. Silberman, Chronology of Miocene hydrothermal and igneous events in the western Virginia Range, Washoe, Storey, and Lyon counties, Nevada, *Econ. Geol.*, 83, 864-874, 1988.
- Wallace, R. E., Patterns and timing of late Quaternary faulting in the Great Basin province and relation to some regional tectonic features, *J. Geophys. Res.*, 89, 5763-5769, 1984.
- Wallace, R. E., and R. A. Whitney, Late Quaternary history of the Stillwater seismic gap, Nevada, *Bull. Seismol. Soc. Am.*, 74, 301-314, 1984.
- Wemick, B. P., R. L. Christiansen, P. C. England, and L. J. Sonder, Tectonomagmatic evolution of Cenozoic extension in the North American Cordillera in *Continental Extensional Tectonics*, edited by M. P. Coward, J. F. Dewey, and P. L. Hancock, *Geol. Soc. Spec. Publ. London*, 28, 203-221, 1987.
- Willden, R., and R. C. Speed, Geology and mineral resources of Churchill County, Nevada, *Nev. Bur. Mines Geol. Bull.* 83, 95 pp., 1974.

Marrion was: May 1976 series (65A)
 64352 H 82 CC 1976 56
 MC-14
 Bull of Soc of Am. Geol.
 87 4 1979
 Geol. Soc. of Am. Bull. 87 4 1979
 The Stillwater Basin, Nevada, 1979
 Geol. Soc. of Am. Bull. 87 4 1979
 1979

Zoback, M. L., and G. A. Thompson, Basin and Range rifting in northern Nevada: Clues from a mid-Miocene rift and its subsequent offsets, *Geology*, 6, 111-116, 1978.

Zoback, M. L., R. E. Anderson, and G. A. Thompson, Cainozoic evolution of the state of stress and style of tectonism of the Basin and Range province of the western United States, *Philos. Trans. R. Soc. London, Series A*, 300, 407-434, 1981.

W. T. Parry, D. Hedderly-Smith, and R. L. Bruhn, Department of Geology and Geophysics, University of Utah, Salt Lake City, UT 84112.

(Received February 1, 1991;
revised June 26, 1991;
accepted July 22, 1991.)

INFLUENCE OF FAULT SURFACE GEOMETRY ON THE LOCATION OF THE DIXIE VALLEY GEOTHERMAL AREA, DIXIE VALLEY, NEVADA

Gabriel Plank, Richard Schweickert¹, Dick Benoit², and Ardyth Simmons³

¹University of Nevada, Reno
MS-172
Reno, NV 89557
plank@seismo.unr.edu, richschw@unr.edu

²Oxbow Power Services Inc.
9790 Gateway Dr.
Reno, NV 89511

³Lawrence Berkeley National Laboratory
Earth Sciences Division
1 Cyclotron Road
Berkeley, CA 94720
asimmons@lbl.gov

ABSTRACT

Detailed geologic maps, seismic reflection surveys, and borehole lithologic data were used to construct geologic cross sections through the Dixie Valley geothermal field and adjacent rocks in the Stillwater Range. The cross sections give an interpretive but well constrained picture of the stratigraphic and structural relationships between the footwall and the hanging wall of the Dixie Valley fault. Most importantly, the cross sections model the geometry of the active strand of the Dixie Valley fault system (Dixie Valley fault, *sensu strictu*) and suggest a possible mechanical model for the development of subsidiary faults (ancestral and/or active) within that system. Both the geometric and mechanical fault models offer an explanation for the high permeability of the Stillwater segment of the Dixie Valley fault (relative to other segments), and hence for the location of the geothermal area.

INTRODUCTION

In the Dixie Valley Geothermal Area (DVGA) the tectonic setting has not been well studied. Though the DVGA supports the largest geothermal electricity plant in the state of Nevada, the development of the area as an energy resource has been slowed partly as a result of the lack of a detailed structural understanding. Therefore, to better characterize the strata and structures that influence geothermal circulation in the reservoir beneath Dixie Valley, we

mapped and interpreted the surface and subsurface distribution of faults and fractured rocks.

Primarily, this study aimed to help understand the structural geologic conditions that influence permeability. Also, it sought to clarify drilling targets. A secondary goal of this study was to understand the tectonic events that have shaped the regional geology since early Mesozoic time.

Plank (in review) presented detailed descriptions of the geology and tectonic implications of the Stillwater Range, as well as comprehensive discussions of the cross sections that are included herein as figures. In this paper, we present some of the conclusions we have drawn about the geologic and tectonic influences on the geothermal reservoir.

FIELD WORK AND DATA ANALYSIS

Detailed geologic mapping of the Stillwater Range has refined the previous work of Speed (1976). Speed mapped the locations of the rocks in the area, but he omitted many structural details. Our mapping project focused on the structural and tectonic aspects of the geology, using such modern mapping and analytical methods as those described in Ramsay and Huber (1983, 1987).

The geophysical investigation of the reservoir incorporated previously processed seismic images, and also took advantage of several recently developed processing techniques to create new seismic images. Both generations of images were interpreted. Where

possible, the new generation of images were validated by comparison with older images.

Borehole assessment involved the re-evaluation of lithologic data; in some cases, cuttings were reviewed to verify the lithologic interpretations of the original logging geologists. For the first time, the geometric and lithologic data from the boreholes were compiled and visualized within a computerized modeling program.

Geologic cross sections integrated surface maps, seismic reflection interpretation, seismic velocity models, and digitized borehole models. In these sections, faults and contacts that are based on observed data (surface relations, boreholes, and P-wave velocity models) are well constrained. The features that are based on reflection interpretation include some intuitive license. In parts of the cross sections that completely lacked data, structures and formational contacts were drawn using surface geology and/or the nearest control points as interpretive bases.

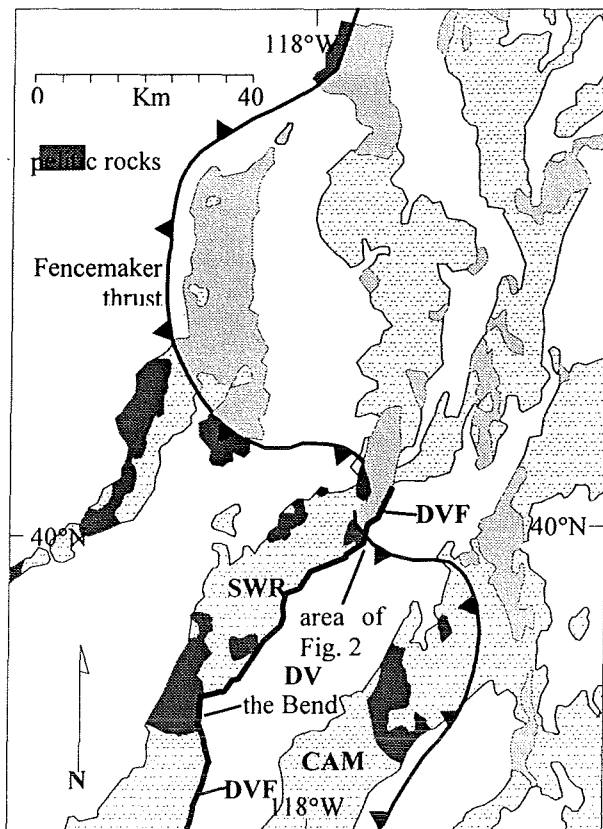


Fig. 1. Location map of the study area and regional geographic features. SWR, Stillwater Range; CAM, Clan Alpine Mountains; DV, Dixie Valley; DVF, Dixie Valley fault.

GEOMETRIC MODELS OF THE STILLWATER SEGMENT OF THE DIXIE VALLEY FAULT

Listric versus Ramp-Flat Geometry in Cross Sections

Geometric models of the Dixie Valley fault imply that the fault could have either a listric or a ramp-flat geometry (Figure 3). In cross section C-C' (Figure 4), both types of fault geometry can be drawn to conform with four very important observations:

- (1) Splays along the range front are inactive and cross-cut by the Dixie Valley fault.

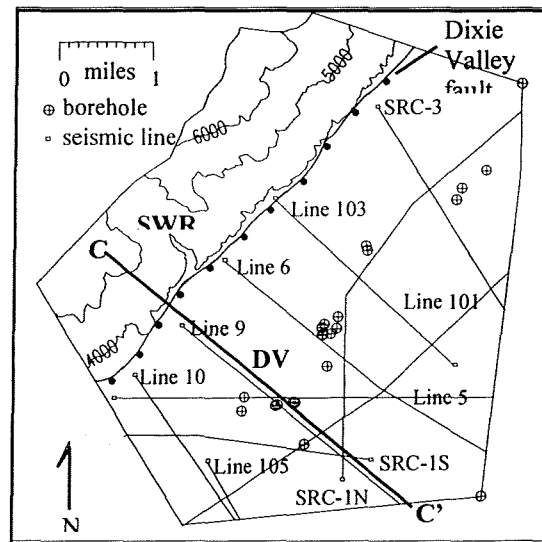


Fig. 2. Map of the study area showing lines of cross section, seismic surveys, and boreholes. SWR, Stillwater Range; DV, Dixie Valley.

- (2) Measurements along the trace of the Dixie Valley fault indicate that the range front fault dips between 52° and 65° toward Dixie Valley.
- (3) Highly accurate P-wave velocity models from several seismic lines indicate that a basement block is present at a shallow ($\approx 1\text{km}$) depth near the range front (Figure 5).
- (4) Three-point solutions to the top of the Cretaceous granite indicate that the range front fault dips 53° at reservoir depths.

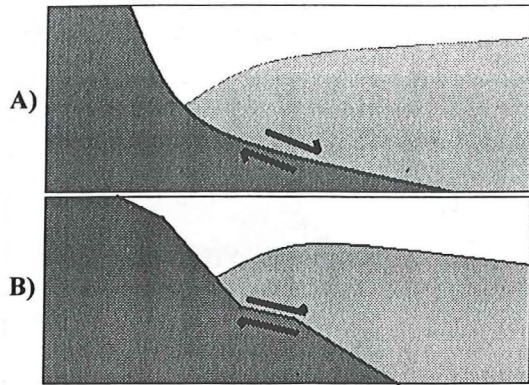


Fig. 3. A) Listric fault surface geometry. B) Ramp-flat fault surface geometry.

Fig. 4. Cross section C-C' through the Stillwater Range and Dixie Valley subsurface, using (A) a listric fault geometry, and B) a ramp-flat geometry for the Dixie Valley fault. **Mesozoic rocks:** QZG, quartzite and gabbro; PEL, pelitic rocks; MAR, marble; GR, granite; ARC, magmatic arc rocks; **Tertiary rocks:** VOL, volcanic rocks; BF, basin fill. BF, Boyer fault; FT, Fencemaker Thrust.

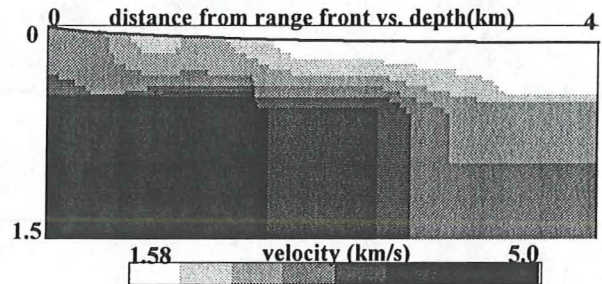
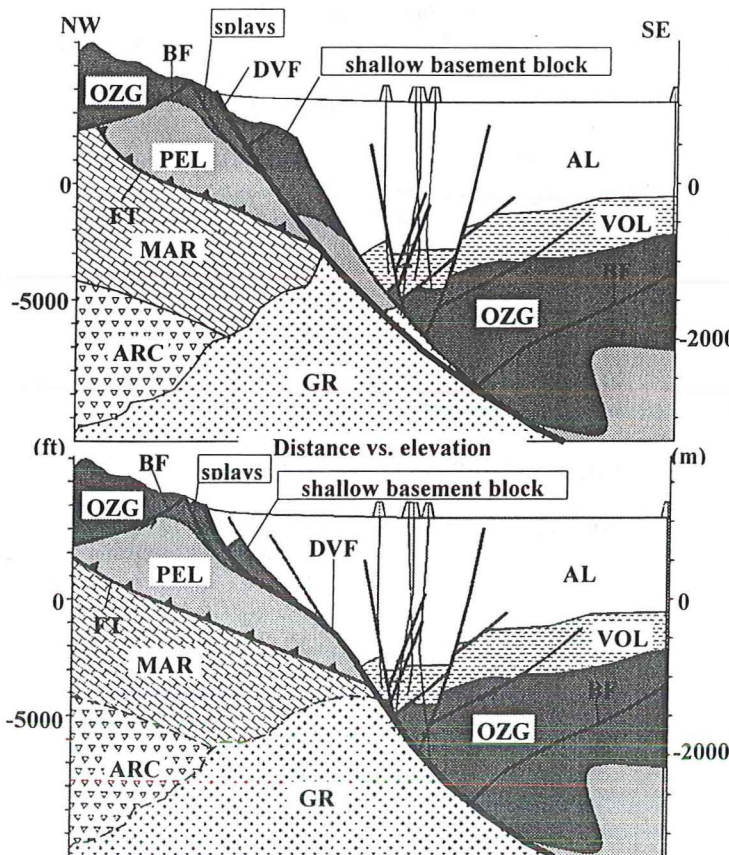


Fig. 5. P-wave velocity model from line 9, showing high velocity bedrock in the shallow subsurface near the range front. This high velocity block shows up in velocity models from several seismic surveys.



Surface Evidence Favors Ramp-Flat Fault Geometry

By themselves, the cross sections do not favor one geometric model over another. However, surface observations in the study area and in the Bend area (Figure 1) compel us to favor a ramp-flat model over a listric model.

Rheologic Contrasts in Exposed Rocks in the Geothermal Field

Along a ramp-flat fault, flats generally develop in incompetent pelitic rocks, while ramps cut across relatively more competent rocks. This rule applies to normal faults as well as thrust faults (Twiss and Moores, 1992). Ramp-flat normal faults have been modeled with clay (Cloos, 1968) and with balanced cross sections in the Basin and Range (Groshong, 1989).

Sharp, tectonostratigraphically-induced competence contrasts are apparent in the footwall of the Dixie Valley fault. These contrasts are demonstrated by exposed post-Miocene shear zones that crop out above producing geothermal field. Deformation in the shear zone of the Black Canyon fault shows that

the pelitic rocks behave semi-ductilely at shallow crustal levels (Figure 6). In the shear zone of the Boyer fault, quartzite and gabbro in the upper plate deform as rigid blocks, while pelitic rocks in the lower plate deform to an uncemented, clay-rich gouge.

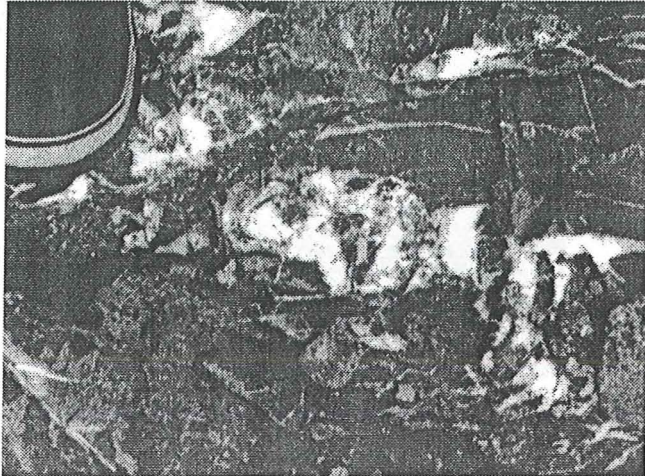


Fig. 6. Shears in the shear zone of the Black Canyon fault (post-Miocene age), demonstrating the brittle-ductile rheology of pelitic rocks in the Stillwater Range (Figure 1). At relatively shallow depths, these rocks are incompetent and do not maintain open fractures. The rocks may deflect fault surfaces toward the horizontal, forming a flat. Note boot for scale.

The competence contrasts between quartzite, gabbro, and pelitic rocks thus provide a rheological basis for the formation of ramps and flats. As predicted by the model in Figure 4(b), the incompetent pelitic rocks may deflect the fault surface toward the horizontal.

Fault Characteristics in the Bend Area

Caskey et al. (1996) presented detailed maps of the 1954 Dixie Valley surface ruptures along the Dixie Valley fault. In the Bend area (Figures 1 and 6), their study documented a section of the fault that dips at angles as low as 20° to the southeast (Figure 6). The low angle surface crops out in both bedrock and alluvium, and creates a series of listric piedmont faults that may merge into the low angle range front surface at seismic depths (Caskey, 1996).

Pelitic rocks in the footwall of the Dixie Valley fault crop out along the length of this low angle segment (Figure 1). To the northeast and southwest of the Bend, gabbroic and granitic rocks crop out along the

range front, and the Dixie Valley fault surface steepens to an average dip above 50° (Caskey, 1996).

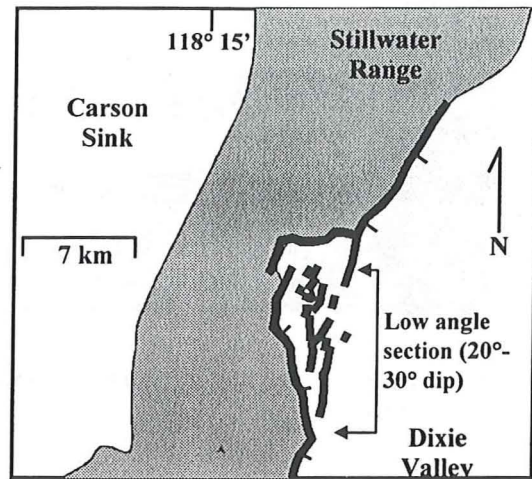


Fig. 7. Diagrammatic map of surface ruptures (dark lines) in the Bend area (Figure 1). Fault line surveys and seismic reflection lines in this area indicate that the Dixie Valley fault in this section dips at a low angle (modified from Caskey et al., 1996).

The correlation between the low angle fault segment at the Bend and exposed pelitic rocks in the footwall suggests that the Dixie Valley normal fault tends to form flats in incompetent footwall rocks.

MECHANICAL MODEL OF THE STILLWATER SEGMENT OF THE DIXIE VALLEY FAULT

Extensional Duplexes and Listric Fans

We propose a mechanical model for the development of the Dixie Valley fault that involves a combination of extensional duplexes and listric fans (Figure 8). Furthermore, we postulate that the development of these features is the strongest where pelitic rocks in the footwall crop out against the surface of the Dixie Valley fault.

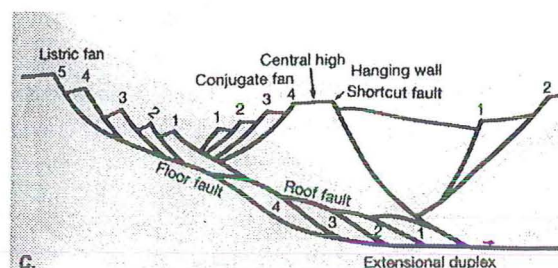


Fig. 8. *Listric Fans and Extensional Duplexes*(modified from Twiss and Moores, 1992).

Splays Along the Stillwater Range Front, Above the Geothermal Field

Five large splays of the Dixie Valley fault crop out in the bedrock adjacent to the producing geothermal field (Plank, in review). Several of these splays are included in the cross sections in Figure 4.

The splays are most widely spaced in proximity to the largest outcrops of pelitic rocks. They become more closely spaced or die out towards the farthest northeast and southwestern extents of the pelitic outcrops. Where the pelitic rocks are absent, the splays are nonexistent. The splays above the geothermal field thus delineate the footwall exposures of incompetent rocks, much in the way that the low angle range front fault and piedmont faults delineate incompetent rocks in the Bend.

It is difficult to say exactly how the the bedrock splays exposed adjacent to the geothermal field accord with the mechanical model in Figure 8. It is possible that the faults represent uplifted and eroded parts of either listric fans or extensional duplexes. Formation of extensional duplexes requires attrition of fault surface flats during migration of the active fault toward the footwall (Figure 8). In the range front above the geothermal area, the surface expression the outcrops of pelitic rocks does not include low angle surfaces, so there is no evidence of an uplifted segment of an ancestral fault flat. This suggests (1) that a fault flat that cut across the exposed pelitic rocks has been tectonically eroded during evolution of the Dixie Valley fault, and (2) that the rangefront splays may therefore have been floor faults in an extensional duplex system.

Piedmont Faults Along the Stillwater Range Front in the Bend area.

High-angle piedmont faults in the Bend area may merge at depth into a low-angle master fault (Caskey, 1996). With respect to the mechanical model in Figure 8, these piedmont faults may be a small-scale example of a listric fan.

IMPLICATIONS OF THE MECHANICAL MODEL ON PERMEABILITY

In our extensional duplex and extensional fan model, the number of fault splays is greatest in proximity to inflections along the surface of the active fault, and in areas where ramp-flat geometry is generally favored. Therefore, ramp-flat fault geometry, extensional duplexes, and/or listric fans probably

have affected and/or caused the formation of fault splays or subsidiary faults that are known to occur in the hanging wall of the Dixie Valley fault, where they have been penetrated by wellbores.

It is likely that these faults are oriented sub-parallel to the Dixie Valley fault, like those at the surface, and therefore that they are favorably oriented to be hydraulically conductive (Barton and Hickman, 1998; Hickman and Zoback, 1998). Because ramps and flats increase the number of favorably oriented faults in the system, the total permeability through the Dixie Valley fault system may be greatest along fault segments characterized by ramps and flats, and also by sharp competence contrasts in the wall rocks. This suggests in turn that less permeable segments of the Dixie Valley fault system may occur in places where the fault system has developed with a more planar or listric geometry.

ACKNOWLEDGEMENTS

Funding for this research was received jointly through a private grant from Oxbow Geothermal Inc. and a Department of Energy pass-through grant via Lawrence Berkeley National Laboratory. The seismic reflection data—and, in addition, borehole lithologic logs, well cuttings, and downhole logs—were also made available by Oxbow Inc. We wish to thank CEMAT at the University of Nevada at Reno for assistance in processing the seismic reflection data.

REFERENCES

- Barton, C., Hickman, S., Morin, R., Zoback, M., and Benoit, R. (1998), "Reservoir Scale Fracture Permeability in the Dixie Valley, Nevada, Geothermal Field", Proceedings 23rd Workshop on Geothermal Reservoir Engineering, Stanford Univ., Stanford CA.
- Caskey, S.J., Wesnousky, S.G., Zhang, P., and Slemmons, D.B. (1996), "Surface Faulting of the 1954 Fairview Peak (Ms=7.2) and Dixie Valley (Ms=6.9) Earthquakes, Central Nevada", Bull. Seism. Soc. Am., v.86, no.3, pp.761-787.
- Cloos, E. (1968), "Experimental Analysis of Gulf Coast Fracture Patterns", AAPG Bulletin, v.52, p. 420-444.
- Groshong, R.H. (1989), "Half Graben Structures: Balanced Models of Extensional Fault-Bend Folds", Geol. Soc. Am. Bull., v.101, p. 96-105.
- Hickman, S. and Zoback, M. (1998), "Tectonic Controls on Fracture permeability in a Geothermal Reservoir at Dixie Valley, Nevada", Proceedings 23rd

Workshop on Geothermal Reservoir Engineering,
Stanford Univ., Stanford CA.

Honjas, W., Pullamannappillil, S., Lettis, W., Plank, G.L., Louie, J.N., and Schweickert, R.A. (1997), "Predicting Shallow Earth Structure within the Dixie Valley, Nevada, Geothermal Field Using a Non-Linear Velocity Optimization Scheme", Proceedings 22nd Workshop on Geothermal Reservoir Engineering, Stanford Univ., Stanford CA, p. 147-152.

Plank, G.L. (in review), "Structure, Stratigraphy, and Tectonics of a Part of the Stillwater Escarpment and Implications for the Dixie Valley Geothermal Area", M.S. Thesis, University of Nevada, Reno.

Twiss, R.J. and Moores, E.M. (1992), "Normal Faults", in Structural Geology, W.H. Freman (ed.), p. 74-93.

The relationship between slickenside surfaces in fine-grained quartz and the seismic cycle

WILLIAM L. POWER* and TERRY E. TULLIS

Department of Geological Sciences, Brown University, Providence, RI 02912, U.S.A.

(Received 12 December 1988; accepted in revised form 14 April 1989)

Abstract—Well polished or reflective fault surfaces, with or without linear striae indicating the sliding direction, are commonly referred to as slickensides. This study examines the development of slickensides which are now exposed along the surface trace of a large, seismically active normal fault zone in Dixie Valley, Nevada, U.S.A. Geologic and mineralogic constraints indicate the slickenside surfaces formed at depths of less than 2 km and temperatures less than 270°C. The slickenside surface material is composed of greater than 98% quartz, with less than 2% kaolinite and iron oxide. Transmission electron microscope (TEM) observations reveal that the slickenside surface material has an extremely fine yet variable grain size (0.01–1 µm), and an unusual, non-equilibrium texture characterized by irregular grain boundaries and low dislocation density. Angular fragments in the cataclasite to either side of the slickensides provide clear evidence of cataclasis. Crystallographic preferred orientation in the slickenside surface material indicates that non-brittle, continuous deformation occurred within 0.1–10 mm of the fault surfaces in many areas. Non-brittle, continuous deformation must have alternated with cataclasis, because some fragments in the cataclasite have strong preferred orientations. We suggest that in the Dixie Valley slickensides, continuous deformation and the development of crystallographic preferred orientations occurred at relatively low strain rates during the interseismic period, while cataclasis occurred at higher strain rates associated with seismic events. The wide range of strain rates occurring within a fault zone during the earthquake cycle may be an essential element in the formation of fine-grained, glassy slickensides, both at Dixie Valley, Nevada, and many other areas.

INTRODUCTION

SHINY, reflective fault surfaces often termed slickensides are common in many faulting environments, but have received relatively little study (Tjia 1968, Means 1987, Petit 1987). Following Fleuty (1975) and Means (1987) we refer to fault surfaces as slickensides, as distinct from slip-parallel striae found on many, but not all, fault surfaces. Slickensides form through a wide variety of mechanisms, including: (1) frictional wear and surface polishing (Avakian 1986, Hancock & Barka 1987); (2) pressure-solution slip leading to the formation of surfaces covered by felted mats of fibrous crystals (Durney & Ramsay 1973, Elliott 1976); (3) streaking or trailing of lightly cemented gouge material (Tjia 1968, Engelder 1974); (4) strain alignment of clay particles during expansion and contraction in clay soils (Gray & Nickelsen 1989); and (5) plastic yielding and strain alignment of layer silicates prior to the development of discontinuous faults (Will & Wilson 1989). Slickenside features have been widely utilized to determine the direction and, in some cases, the sense of slip on fault surfaces. This information is useful because it allows one to infer the strain history of large rock masses (Wojtal 1987, Hancock & Barka 1987) or, by inference, the state that caused faulting and deformation (Angelier 1979, Angelier *et al.* 1985, Zoback 1989).

Additionally, the study of slickensides has the potential to provide insights into the grain-scale deformation

mechanisms that are active along frictional rock surfaces, contributing to the understanding of the mechanical properties of fault zones and their evolution. One particularly important reason for studying the surfaces is that certain slickenside types or features may be indicative of different phases of the earthquake cycle. The earthquake cycle is often divided into four phases: an interseismic phase (quiescent period between earthquakes), a pre-seismic phase (foreshocks and accelerating creep), a co-seismic phase (rapid slip during earthquakes) and, finally, a post-seismic phase (aftershocks and decelerating creep). Some faults may not experience all four stages. Some examples of fault surface features that have been attributed to the seismic phase of the earthquake cycle include carrot-shaped asperity grooves (Engelder 1974), pseudotachylytes or friction melts (Sibson 1975) and crescent-shaped tension fractures (Petit 1987). Fibrous pressure-solution slip slickensides such as those described by Durney & Ramsay (1973) and Elliott (1976) probably develop during slow aseismic creep rather than during seismic events. The possibility of finding other features which can be directly linked to seismically or geodetically observed aspects of fault behavior is great, and should be pursued.

One important implication of the earthquake cycle for the development of fault zone materials is that an extremely wide range of strain rates will prevail along faults that experience seismic slip events (Sibson 1977). Relative slip rates along faults range from velocities as high as 1–2 m s⁻¹ during seismic events (Brune 1976) to 1–30 mm yr⁻¹ during steady, aseismic shearing (Thatcher 1979, Burford & Harsh 1980, Sibson 1983). If

* Present address: CSIRO Division of Geomechanics, P.O. Box 54, Waverley, Victoria 3149, Australia.

deformation during seismic faulting events is confined to relatively thin and discrete principal slip surfaces, as is often observed (Sibson 1986a), strain rates as high as 10^2 – 10^4 s^{-1} might occur in the fault zone. In contrast, strain rates more typical of deformation during the interseismic period probably range from 10^{-10} to 10^{-15} s^{-1} , or perhaps less (Sibson 1977, Pfiffner & Ramsay 1982).

Major fault zones with large displacements and significant components of dip-slip provide the opportunity to directly observe the effects of faulting on materials under non-surface conditions, because slip on the fault surfaces 'exhumes' materials from depth. In this study we describe and interpret textural and mineralogical features of exhumed normal fault surfaces from Dixie Valley, Nevada, U.S.A. The slickenside surfaces we describe, however, are not unique to the Dixie Valley area; we infer that many other glassy slickensides composed of fine-grained quartz formed in much the same way as those at Dixie Valley. We conclude by offering some preliminary inferences concerning the relationship of specific slickenside features to the earthquake cycle.

GEOLOGIC SETTING

Before describing the slickenside surfaces, we briefly review the geologic history of the Dixie Valley area (Fig. 1). More extensive information can be found in studies by Page (1965), Anderson *et al.* (1983), Wallace & Whitney (1984) and Okaya & Thompson (1985). The fault zone we investigated lies within an area termed the "Stillwater seismic gap" by Wallace & Whitney (1984), because major historic earthquakes occurred immediately to the north in Pleasant Valley in 1915, and immediately to the south in southern Dixie Valley in 1954. Fault scarps within the Stillwater seismic gap (Wallace & Whitney 1984), and offset shorelines of pre-historic lakes (Thompson & Burke 1973) provide evidence of displacement within the last 12,000 years. The Stillwater seismic gap is relatively quiet in terms of microearthquake activity, but areas to the north and

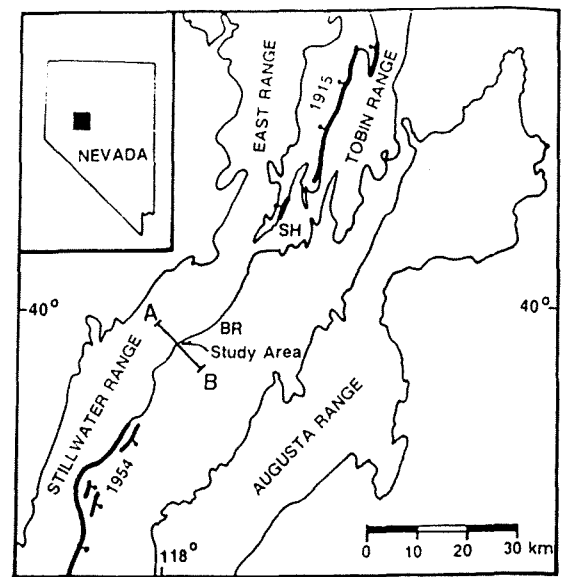


Fig. 1. Location map showing the Stillwater seismic gap and the slickenside study area. The line labeled A–B shows the location of the cross-section shown as Fig. 2. Surface ruptures of the 1915 and 1954 earthquakes are shown as heavy lines. Abbreviations as follows: SH—Sou Hills. BR—Boyer Ranch. Total normal slip on the Stillwater range-front fault is about 0.3 km in the Sou Hills (Fonseca 1988) and 3 km at Boyer Ranch (Okaya & Thompson 1985). Total normal slip on the Stillwater fault at the study area is 3–6 km.

south still show elevated levels of microearthquakes (Dozer 1986). It is clear that earthquakes will occur in the study area in the future, and that seismic faulting played an important part in the development of the fault zone materials now exposed in Dixie Valley.

For the purposes of this study, rock materials in the region are divided into three groups (Fig. 2): 'basement' rocks of Mesozoic age; volcanic and sedimentary rocks of early Tertiary age, which pre-date the development of the fault zone; and alluvial and lacustrine sediments of late Tertiary and Pleistocene age, which accumulated concurrently with faulting. The basement rocks consist of a wide variety of variably metamorphosed, primarily Cretaceous age rocks, including pelites, granodiorites and gabbros (Page 1965, Okaya & Thompson 1985).

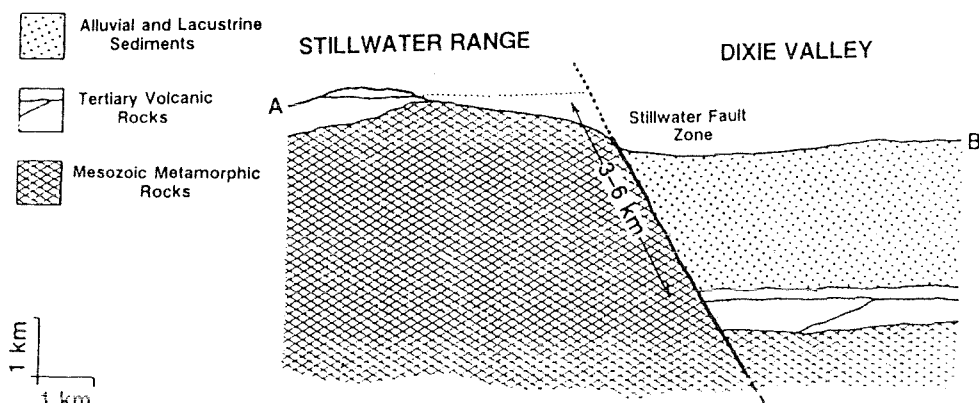


Fig. 2. Cross-section showing the geometry of the Stillwater fault zone in the study area. Total normal slip across the Stillwater fault can be estimated from the offset of the youngest part of the Tertiary section, a widespread and flat-lying basaltic flow which outcrops at the crest of the Stillwater range and underlies the syntectonic valley fill of alluvial and lacustrine sediments. Location of this section is shown on Fig. 1 as line A–B.

The basement rocks are unconformably overlain by a variety of Tertiary age sedimentary and volcanic rocks which pre-date the development of steep normal faults in the Dixie Valley area (Riehle *et al.* 1972, Hastings 1979). The Tertiary sequence is capped by an 11–17 Ma old unit of basaltic volcanic flows and pyroclastics (Hastings 1979, Fonseca 1988).

Late Cenozoic extension of the Dixie Valley area disrupted the Mesozoic and early Tertiary age rocks, resulting in the development of a major, range-front fault zone on the east side of the Stillwater Range. We refer to this fault as the Stillwater fault, following Wallace & Whitney (1984) and Fonseca (1988). The surface trace of the Stillwater fault at the current level of exposure is characterized by a variety of fault rocks that originally formed under different conditions. In most places there is no single fault surface. Rather, the fault zone consists either of a uniform clay gouge zone, or of many discrete surfaces separating fault bounded horses of cataclasite, breccia, or variably deformed and fractured wallrocks. In scattered locations along the fault trace, slickenside surfaces composed almost entirely of fine-grained quartz are present.

Slickenside locality

This study concentrates on a unique part of the fault zone where slickenside surfaces which developed in fine-grained, hydrothermal quartz are well exposed (Fig. 1—39.95° N. Lat., 117.95° W. Long.). In the study area, the most recent trace of the Stillwater fault juxtaposes alluvial sediments against metamorphosed Jurassic age gabbroic rocks (Fig. 3). Although the host rock for the slickenside surfaces is metamorphosed gabbro, the slickenside surfaces occur only in areas that have experienced extensive enrichment in silica due to the passage of hydrothermal fluids. The exposure of shiny, reflective fault surfaces is approximately 100 m long parallel to the strike of the fault zone. The largest exposures of a single surface are about 25 m². Other, similar slickenside surfaces can be found along the Dixie Valley fault zone, but none are as large as those described in this study.

We estimate that total normal slip on the Stillwater fault zone at the slickenside locality is 3–6 km. Gravity studies, combined with reflection seismology studies (Okaya & Thompson 1985) and unpublished well data (reviewed by Fonseca 1988), indicate that Dixie Valley is filled with alluvial and lacustrine sediments floored by the same sequence of early Tertiary volcanic rocks found on the top of the Stillwater Range (Fig. 2). Normal slip, estimated from the separation of the Tertiary volcanic sequence, varies from about 300 m in the Sou Hills (Fig. 1—approximately 23 km north of the study area) to 3 km at Boyer Ranch (approximately 8 km north of the study area). Because total normal slip varies along the fault zone, and generally increases southwards, total normal slip at the study area is probably between 3 and 6 km.

We conclude that the slickenside surfaces formed at a depth of less than 2 km because: (1) the current exposure level of the footwall materials is approximately 1 km

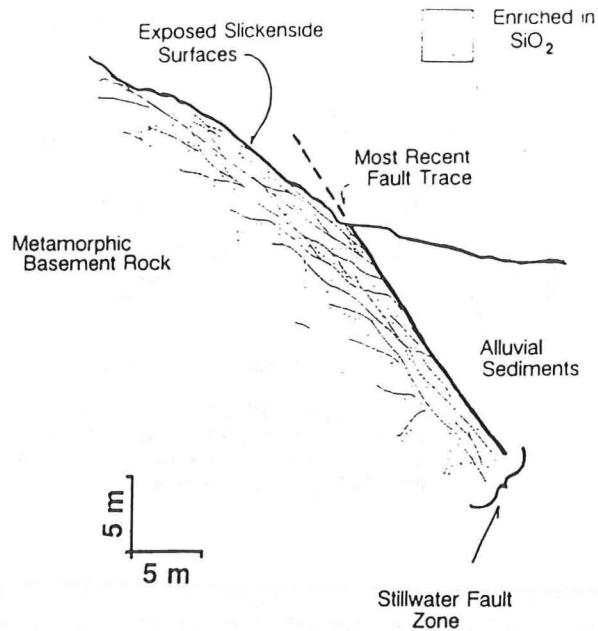


Fig. 3. Schematic outcrop scale cross-section illustrating the details of the slickenside study locality. In the study area, the fault zone juxtaposes Mesozoic metamorphic rock against alluvial sediments. The most recently active fault surface occurs at the base of the exposure of metamorphic rock. The slickenside surfaces are found in the footwall block, in areas that have been strongly enriched in quartz by precipitation from hydrothermal fluids.

below the base of the Tertiary volcanic sequence; (2) the total thickness of the Tertiary volcanic sequence is approximately 1 km; and (3) normal faults developed in the Dixie Valley area after the deposition of the Tertiary volcanic sequence (Fig. 2). Thermal gradients of 20–45°C km⁻¹ are typical of the Basin and Range Province (Lachenbruch & Sass 1977), but ongoing geothermal energy investigations in the Dixie Valley region indicate that gradients as high as 150–200°C km⁻¹ may prevail at least temporarily near the Stillwater fault zone (Parchman & Knox 1981). This range of thermal gradients suggests that the slickenside surfaces developed at temperatures between 50 and 400°C. Test wells drilled to depths of 3 km encountered temperatures of approximately 200°C (Denton *et al.* 1980), in general concurrence with this conclusion. The presence of the assemblage kaolinite + quartz in the slickenside surface material (discussed below) provides independent evidence that temperatures were below 270°C during slickenside formation.

SLICKENSIDE SURFACES

Surface roughness and striation features

The slickenside surfaces in the study area may be divided into a three-fold classification based on surface morphology. To illustrate the range of roughness of the fault surfaces, we show 0.5 m profiles from each of three surfaces (Fig. 4). These profiles were measured parallel

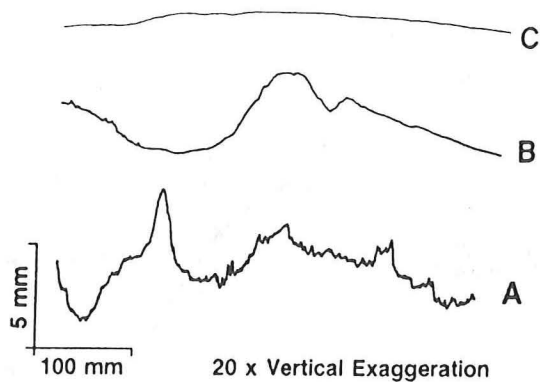


Fig. 4. Surface profiles of typical slickenside surfaces. The surfaces have a variety of roughnesses, ranging from moderately rough (A), through intermediate (B), to very smooth (C). The smoothest surfaces have the largest exposure areas.

to the slip direction, using equipment and techniques described by Power *et al.* (1987, 1988). The Dixie Valley surfaces range from moderately rough (A—Fig. 4), to intermediate (B—Fig. 4) and finally to very smooth (C—Fig. 4). As can be deduced from the surface profiles, the maximum amplitude to wavelength ratio of each surface profile varies from about 1/100 for the roughest surfaces to about 1/500 for the smoothest surfaces. The surfaces have a generally self-similar geometry. This means that surface profiles observed at an enlarged or reduced scale appear statistically similar (Power *et al.* 1988).

On the roughest surfaces (A—Fig. 4) much of the roughness is the result of small, hard clasts in the footwall surface (A—Fig. 5). Curiously, in the area we examined, all the clasts are in the footwall surface, while matching depressions or indentations are present in the hangingwall surface. The roughest surfaces are generally small in areal extent, and do not form prominent weathering or parting surfaces.

The intermediate roughness surfaces (B—Fig. 4) have a ridge and groove geometry (B—Fig. 5). Ridges from one surface match grooves from the opposing surface. Means (1987) described geometrically similar surfaces. The grooves and ridges decrease in height or depth along the slip direction gradually, rather than beginning or ending at discrete asperities or hard clasts. Most ridges or grooves are 10–100 times as long in the direction parallel to slip as in the direction perpendicular to slip.

The smoothest and most reflective slickensides (C—Fig. 4) have the thickest accumulations of fine-grained quartz to either side of their surfaces. These surfaces often have spoon-shaped depressions formed by localized deformation around a hard clast or asperity, which are commonly composed of either single crystals of quartz, or of fragments of well indurated but reworked cataclasite (C—Fig. 5). For the smoothest surfaces, it was not possible to examine both the hangingwall and footwall surfaces to determine how well the surfaces match one another. The smoothest fault surfaces form the largest, most continuous exposures, probably because their flatness allows large blocks of the hangingwall to part easily from the footwall.

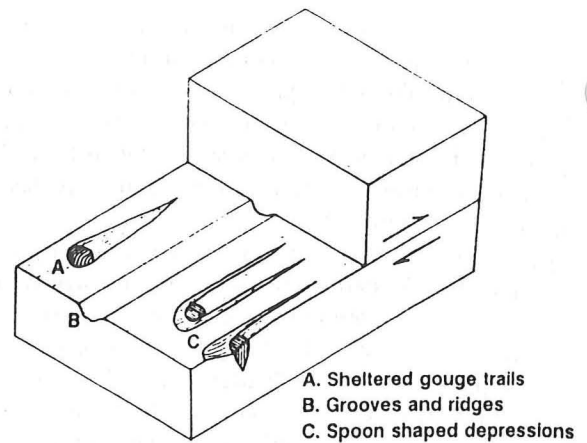


Fig. 5. Surface features of Dixie Valley slickenside surfaces. Features labeled are as follows: hard asperity, protruding above the surface, with lightly cemented gouge material on its lee side (A); interlocking ridges and grooves (B); spoon shaped depressions which form around small hard particles (C).

The difference in roughness of the various sub-parallel surfaces is difficult to explain. Although one tempting explanation is that rougher surfaces have less total displacement than the smoother surfaces, this possibility cannot be evaluated because it is difficult to estimate the total displacement for individual surfaces. Slip on most of the surfaces must be at least 1 m, based on color contrasts in the cataclasite to either side of many of the surfaces. Slip on any one surface must also be well under 3–6 km, because that is the total slip across the Stillwater fault zone. Another possible explanation for the difference in surface character is that the surfaces formed under different conditions of depth, confining pressure, temperature, strain rate or chemical environment.

Mineralogy, composition and temperature

The slickenside surfaces occur within a 1–10 m thick zone of cataclasite which has been considerably enriched in quartz relative to the gabbroic wallrock. The enrichment in silica is most extreme closest to the fault surfaces, and probably results from the passage of hydrothermal fluids through the fault zone. The fine-grained material within 1–10 mm of the fault surfaces consists of greater than 98% quartz. Energy dispersive X-ray composition determinations made with scanning and transmission electron microscopes reveal that the only common elements in the fine-grained slickenside material are Si, Fe and Al. The iron occurs in scattered iron oxide particles, particularly within 10–20 μm of the sliding surfaces. The aluminium occurs in fine-grained (0.01–0.1 μm) kaolinite flakes (Fig. 6a).

The slickenside surfaces must have formed at temperatures less than 270°C because both kaolinite and quartz are present in the fine-grained surface material. Kaolinite and quartz react to form pyrophyllite and water at temperatures of approximately 270°C over a wide range of pressures, under conditions where the

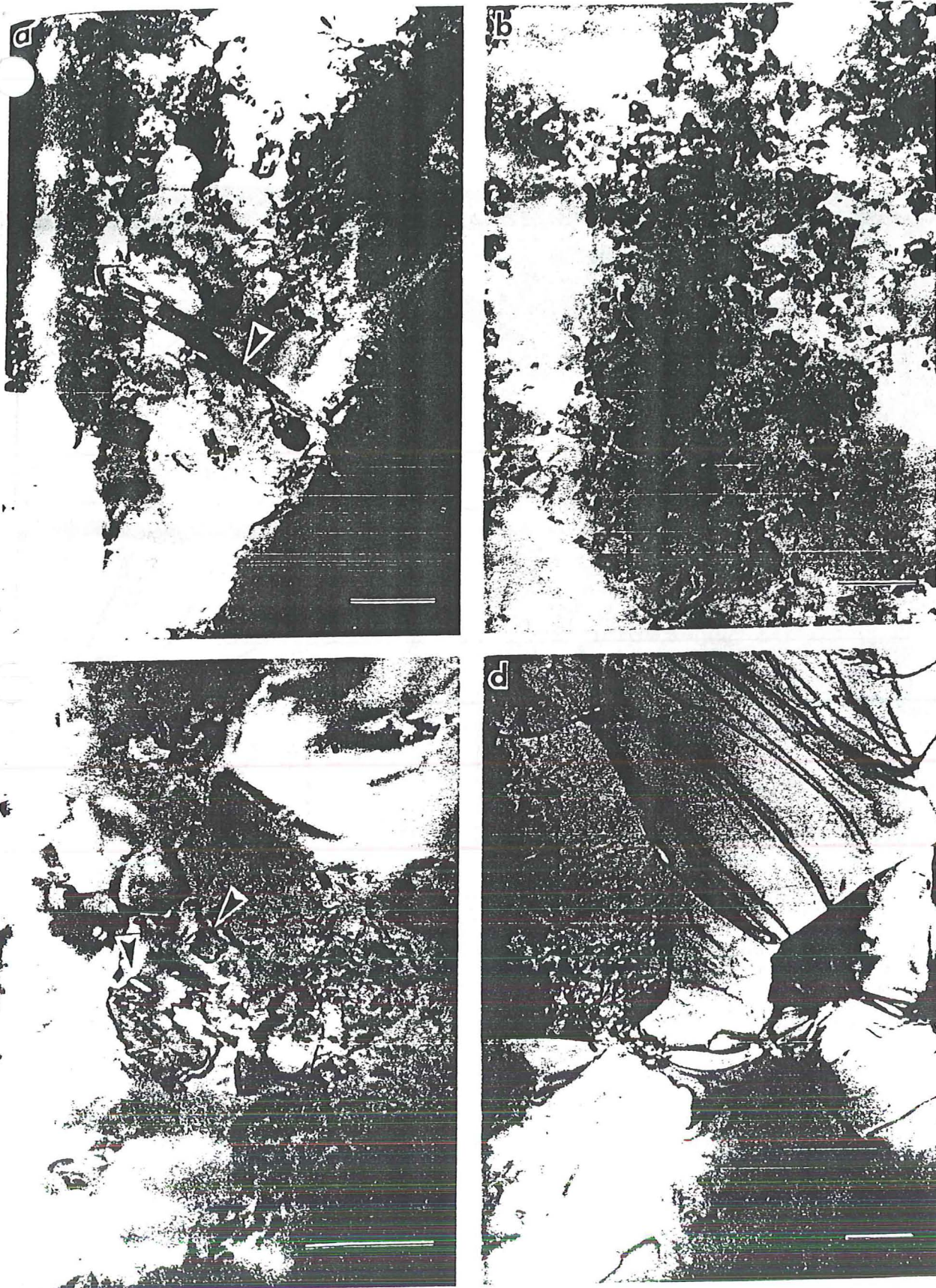


Fig. 6. Transmission electron microscope (TEM) micrographs of textural features found in fine-grained quartz. All scale bars 0.5 μm . (a) Slickenside surface material. Note kaolinite grain (arrow) surrounded by fine-grained quartz. This kaolinite grain is particularly large; most range in size from 0.01 to 0.1 μm . (b) Typical view of the slickenside surface material, which has a wide range of grain sizes (0.01–0.1 μm). (c) Smaller grains within the slickenside surface material (arrows) are often completely enclosed within larger grains, a configuration of high surface energy. (d) Micrographs of a fine-grained novaculite (not from the Stillwater fault zone) which was experimentally deformed in the dislocation creep field. In contrast to the slickenside material, the novaculite has a narrow range of grain sizes (1–5 μm), polygonal grain shapes and straight grain boundaries.

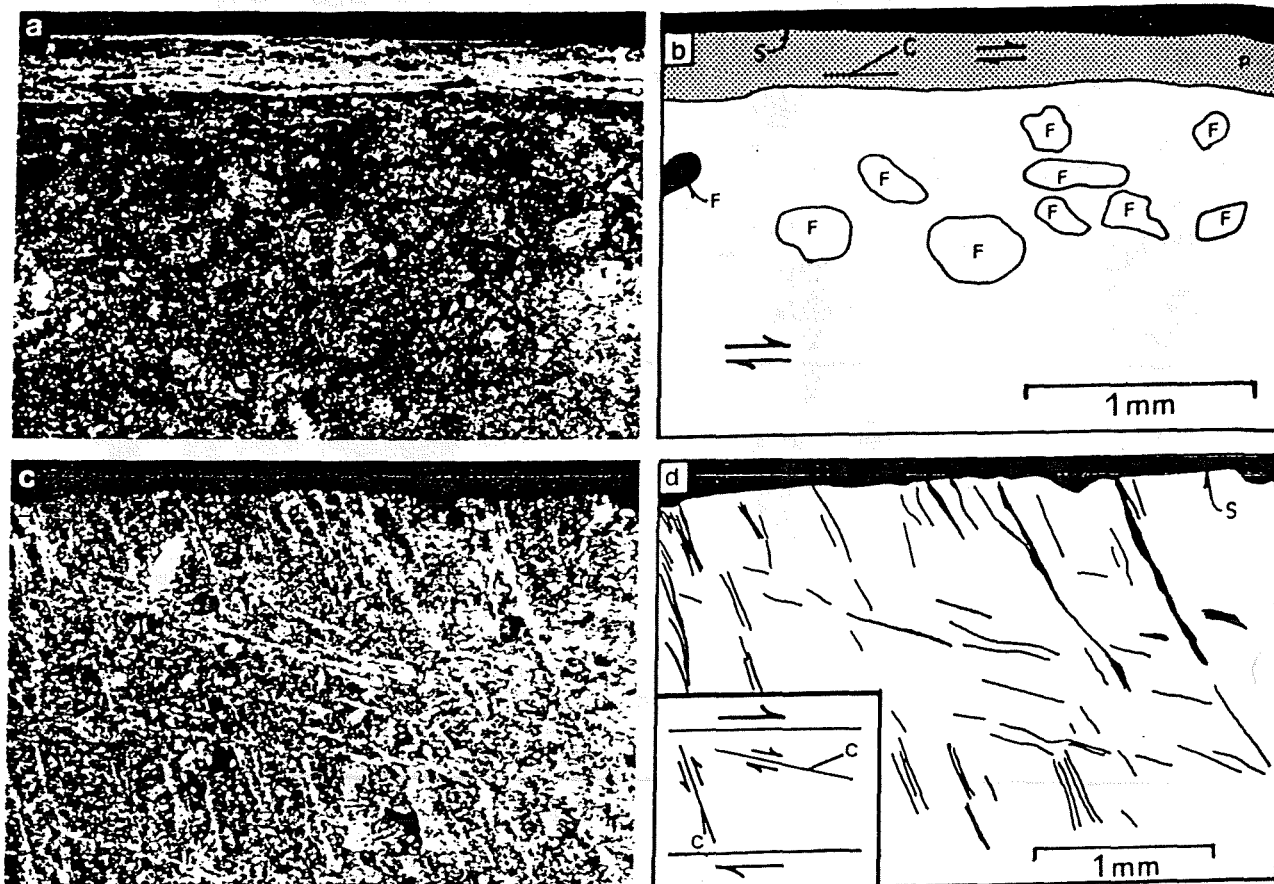


Fig. 7. Optical photomicrographs illustrating crystallographic preferred orientation in fine-grained quartz along the fault surfaces. The photomicrographs were taken with crossed polarizers; areas of the samples with preferred orientation appear either lighter or darker than the background. (a) A simple, 0.2 mm thick, preferred orientation zone with essentially one orientation of quartz *c*-axes. (b) Schematic view of (a). The fault surface (S) is developed on/in an area of strong crystallographic preferred orientation (P—shaded). Quartz *c*-axes are inclined in the direction of shear. Fragments in the cataclasite (F) are visible beneath the zone of preferred orientation. (c) A more complex array of preferred orientation zones. (d) Schematic view of (c). The fault surface (S) is underlain by a zone of fine-grained quartz with an array of preferred orientation zones reminiscent of Riedel shear geometry (Logan *et al.* 1979). The position of the quartz *c*-axes within each preferred orientation zone is consistent with slip on each shear zone in the sense shown (inset), but there is no independent evidence that actual displacement occurred across either the steeply or shallowly inclined surfaces.

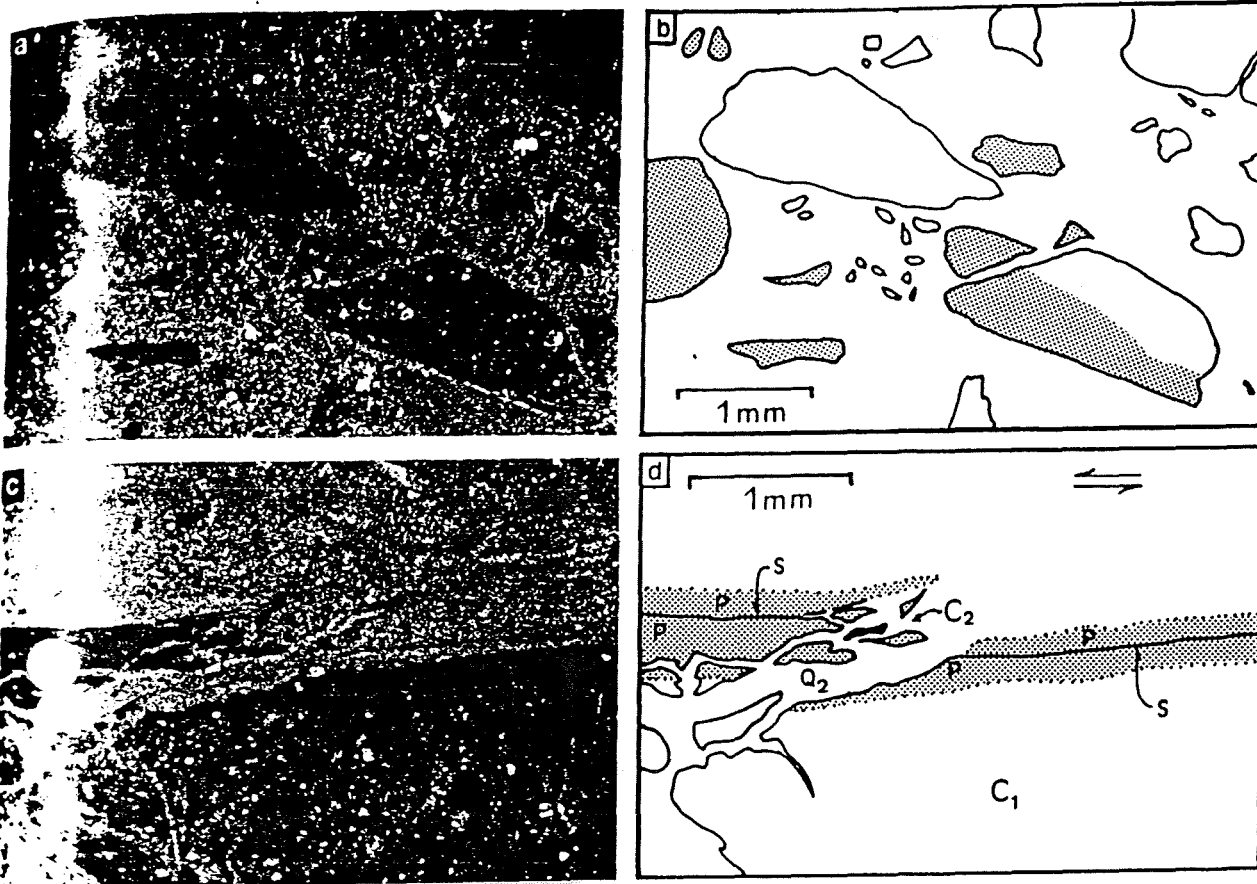


Fig. 9. Photomicrographs illustrating textural features of the cataclasite that forms the slickenside surfaces. (a) Cataclasite fragments cemented together with fine-grained hydrothermal quartz. (b) Schematic view of (a). Some fragments consist of earlier cataclasites which have crystallographic preferred orientation zones very similar to those shown in Fig. 7(a). Shaded areas have strong crystallographic preferred orientation. These textures indicate that conditions favorable for continuous, non-brittle deformation and the development of crystallographic preferred orientations alternated with conditions favorable for discontinuous cataclasis. (c) Well preserved textures along the fault surfaces indicate repetitive cycles of continuous and discontinuous deformation. (d) Schematic view of (c). An early cataclasite (C_1), truncated by a fault surface (S) are the earliest textural features visible. Associated with the fault surface (S) are preferred orientation zones which are shown shaded (P). Preferred orientation developed in both the early cataclasite and in the hydrothermal quartz. The fault surface and associated preferred orientation zones were fragmented, offset and then cemented together with new hydrothermal quartz (Q_2) to form a second generation cataclasite (C_2).

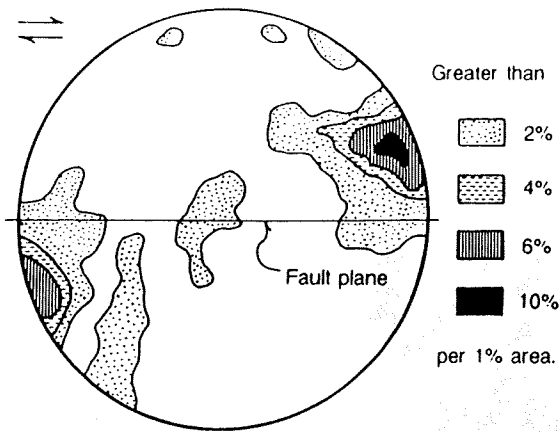


Fig. 8. *c*-Axis pole figure for the fine-grained slickenside surface material. The great circle represents the fault plane, with sense of slip shown at upper left. *c*-Axis data were measured using the photometric technique of Price (1980).

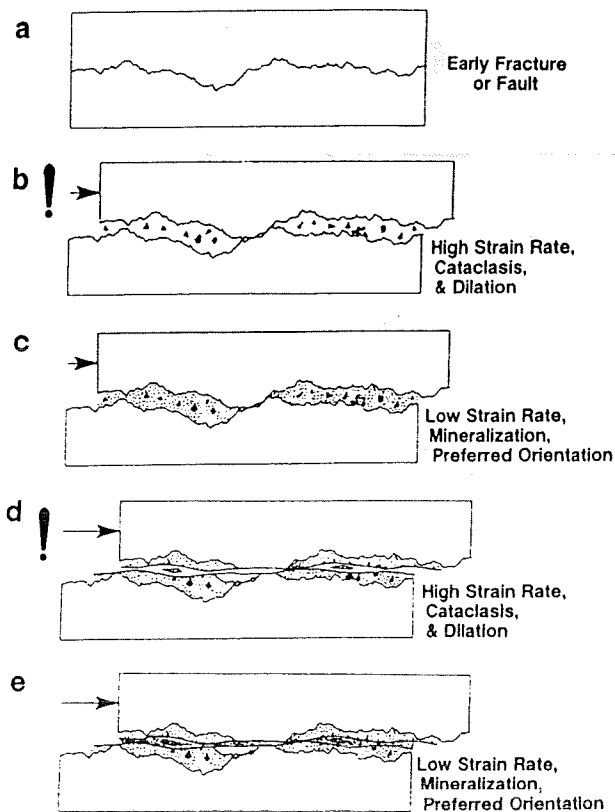


Fig. 10. Schematic diagrams illustrating the inferred development sequence for slickenside fault surfaces in Dixie Valley, Nevada. Alternating episodes of both discontinuous and continuous deformation are responsible for textural and mineralogic features preserved in the slickenside surface material and the cataclasis to either side of the surfaces. (a) We infer that the surface developed from pre-existing fracture or fault surfaces. (b) During seismic events, rapid translation of the surfaces relative to one another caused cataclasis and dilation along the fault surfaces. (c) Enhanced fluid flow after faulting resulted in the deposition of fine-grained hydrothermal quartz. Continued slow deformation caused the development of crystallographic preferred orientations. (d) and (e) Repeated episodes of cataclasis during seismic events, precipitation of hydrothermal minerals, and continuous deformation during the non-seismic phases of the earthquake cycle led to complex textures within the fault zone.

water pressure is equal to the lithostatic pressure (Hemley *et al.* 1980). If fluid pressure is less than the lithostatic pressure, or the fluid is not composed entirely of water, the reaction occurs at lower temperatures. The temperature estimate from the kaolinite plus quartz assemblage (less than 270°C) is consistent with the depth and temperature we inferred for slickenside formation from geologic constraints and geothermal investigations.

Transmission electron microscopy

The microstructure of the fine-grained quartz within the slickenside surface material is unusual. Examination by transmission electron microscopy (TEM) reveals that most of the grains are between 0.01 and 1.0 μm . Although the grains are approximately equant, they often have very irregular grain boundaries (Fig. 6b) and large surface areas. Smaller quartz grains and iron oxide grains are entirely included within larger quartz grains (Fig. 6c), a configuration of high surface energy. All the grains are essentially free of dislocations. Dislocations were rarely observed even after tilting and rotation of the ion-thinned specimens in the TEM. This microstructure is not typical of quartz which has been deformed within the dislocation creep field, nor of quartz which has been thermally annealed. The slickenside surface material contains no evidence for static grain growth or recrystallization. The samples shown in Figs. 6(a)–(c) were taken from the area with a strong crystallographic preferred orientation shown in Fig. 7(a).

In order to provide a contrast to the microstructure of the slickenside material, we include a TEM micrograph of a fine-grained quartz sample (novaculite) which was deformed experimentally in the dislocation creep field at 850°C, 1525 MPa confining pressure, a strain rate of 10^{-5} s^{-1} and to about 30% strain (Kronenberg & Tullis 1984). The sample (Fig. 6d) has undergone dynamic recrystallization and has straight grain boundaries, polygonal grains with approximately 120° grain junctions and a variable dislocation density. Annealing of this microstructure would only decrease the dislocation density and/or produce growth of new strain-free grains: the low energy configuration of the grain boundaries would be preserved. Thus the absence of dislocations and the presence of small grains with very irregular boundaries in the slickenside surface material is not consistent with deformation by dislocation creep or post-tectonic annealing.

Crystallographic preferred orientation

In many areas along the slickenside surfaces, a strong, optically visible, crystallographic preferred orientation is present in the fine-grained quartz material nearest the slickenside surface (Figs. 7a & b). The preferred orientation is usually confined to within 1–10 mm of the fault surfaces, and is most strongly developed along the smoother surfaces which have the greatest thickness of

fine-grained quartz. Individual quartz grains within the area of preferred orientation are too fine-grained to measure crystallographic orientations with a U-stage, but the approximate location of the majority of *c*-axes in two dimensions was determined using a gypsum plate. The majority of *c*-axes are inclined in the direction of shear, and lie close to the plane perpendicular to the sliding surface which includes the sliding direction (Fig. 7b). Observations of one sample made with an X-ray pole figure device provide independent confirmation that the quartz has a crystallographic preferred orientation. Full *c*-axis pole figures were measured using the photometric technique of Price (1980). The computer reduction technique used in the photometric method assumes that individual quartz grains are as thick as the sample (7–20 μm). Because the slickenside surface material is extremely fine-grained (0.01–1 μm), this condition was not satisfied. This may cause the results to be slightly less accurate than would be obtained for coarser-grained materials. The results from the photometric technique (Fig. 8) confirm the conclusions obtained from optical observations using the gypsum plate; the *c*-axis pole figures showed single *c*-axis maxima. The orientations of the maxima are unusual, however, because they occur in the direction of extension, rather than in the direction of maximum shortening, as is often observed (Tullis *et al.* 1973, Schmid & Casey 1986).

Some of the slickensides display more complex patterns of preferred orientation (Figs. 7c & d) which are reminiscent of Riedel shear geometries described and interpreted by Logan *et al.* (1979). Features similar to both the shallowly inclined (R_1 type) and steeply inclined (R_2 type) Riedel shear zones are present. No evidence which precludes or demonstrates slip of the R_1 and R_2 zones was found. The *c*-axis orientations within the R_1 and R_2 zones, as determined with the gypsum plate, have the same relationship to the sense of shear inferred for R_1 and R_2 zones as is observed for the overall shear zone, namely the *c*-axes are inclined in the direction of shear (Figs. 7c & d).

Very similar crystallographic preferred orientations including Riedel shear geometries have been observed by Higgs (1981) in ultra fine-grained quartz (grain size < 1 μm) deformed experimentally in shear at temperatures of 450 and 600°C, and shear strain rates of 10^{-2} – 10^{-4} s^{-1} . The experiments which generated the preferred orientations were performed at confining pressures of 250 MPa and fluid (water) pressures of 100 MPa, while other experiments were performed at 150 MPa confining pressure with no water or fluid. Higgs observed some textural evidence of diffusive mass transfer (pressure solution) in the form of recrystallization and the formation of quartz veins in the wet experiments. Microscopic evidence for pressure solution or preferred orientation fabrics was not observed in the dry samples. Higgs offered no explanation for the development of the preferred orientation. Wenk & Kolodny (1968) described preferred orientation in a fine-grained chert which probably formed as a result of deformation during diagenesis. They concluded that the preferred orien-

tation fabric they observed also must have formed at very low temperatures: the mechanism that produced the preferred orientations was unclear.

Interplay of continuous and discontinuous deformation

Outside the region of crystallographic preferred orientation, angular fragments in the cataclasite provide evidence of brittle deformation (Figs. 9a & b). The fragments range in size from 0.2 mm to larger than 10 cm, and include fragments of intact wallrock, fragments of earlier cataclasites, and of single crystal grains, usually quartz. The matrix between the angular fragments consists of randomly oriented, fine-grained quartz, which is texturally indistinguishable from the strongly oriented material which forms the slickenside surfaces.

Textural features of the slickenside surfaces provide clear evidence that cataclasis alternated with ductile deformation. Some of the angular fragments in the cataclasite are clearly derived from earlier fault surfaces which had crystallographic preferred orientations (Figs. 9a & b), providing evidence that conditions favorable for cataclasis alternated with conditions favorable for the development of preferred orientation. In some cases striking evidence of more than one cycle of alternating cataclastic and continuous deformation is well preserved (Figs. 9c & d). Stel (1981) described a similar history of alternating brittle failure, crystal growth and ductile deformation in cataclasites formed in granite rock.

None of the slickenside material we examined contains evidence for fiber growth either through the crack-seal mechanism (Ramsay 1980) or through pressure-resolution slip (Elliott 1976). Some portions of the cataclasite to either side of the slickenside surfaces consist of dilation breccias with exploded-jigsaw textures, similar to those described by Sibson (1986b). Exploded-jigsaw texture means that angular cataclasite fragments appear as if they could be re-assembled if the intervening matrix material were removed. Sibson (1986b) inferred that exploded-jigsaw texture results from implosion brecciation, which is caused by the rapid opening of dilatant cavities along fault surfaces during seismic slip.

Figure 10 schematically illustrates the sequence of events which we believe caused the formation of the slickenside surfaces. The earliest history of the fault surfaces is difficult to ascertain (Fig. 10a). We presume the fault surfaces develop initially from either pre-existing fracture or fault surfaces. Textural features in the cataclasite (discussed above) indicate at least two phases of deformation were important in slickenside development. In the first phase (Fig. 10b) cataclasis and/or dilation between the surfaces caused the creation of new porosity, the disruption of pre-existing fault surfaces and the formation of angular fragments. The important elements of the second phase (Fig. 10c), include healing of the fault zone by the precipitation of new, hydrothermal quartz and the development of crystallographic preferred orientations. Precipitation of hydrothermal quartz may have been aided by enhanced

fluid flow from seismically induced fluid pressure gradients (Nur & Booker 1972, Sibson *et al.* 1988), or from the development of marked disequilibrium between fluid phase and the wallrock as a result of seismic faulting (Fournier 1985). Many repetitions of the two phases are responsible for the development of the slickenside surfaces (Figs. 10d & e).

DISCUSSION

Development of crystallographic preferred orientation in fine-grained quartz

Two features of the fine-grained quartz which forms the slickenside surfaces remain enigmatic. The first is the extremely fine-grained and non-equilibrium texture, and the second is the presence of crystallographic preferred orientation. In this section we discuss possible mechanisms for the development of these features. The preferred orientation and unique grain scale microstructure may have developed via a non steady-state mechanism. As we discuss above, it is quite possible that the fine-grained material which now forms the slickenside surfaces originally precipitated as ultra fine-grained amorphous silica, cristobalite or chalcedony. If the present microstructure developed from material of this type, a phase change and considerable grain coarsening have occurred. If the preferred orientation developed during grain coarsening, or concurrently with a phase change, a steady-state mechanism would not have been responsible. Possible steady-state mechanisms include: (1) crystalline plasticity or dislocation creep; (2) strain alignment of sub-microscopic crystals; and (3) pressure solution. Although we favor pressure solution, a final conclusion as to which mechanism occurred is not possible, because few experimental studies have focused on exceedingly fine-grained quartz aggregates, because it is unclear whether the deformation was steady-state, and because it is unclear if important textural features of the slickenside material have been annealed or obliterated.

To place the conditions we infer for slickenside formation in context with relevant experimental data on deformation mechanisms, we show a plot of differential stress vs strain rate (Fig. 11). We can estimate the maximum differential stress during slickenside development because we know the depth at which the slickenside surfaces formed (2 km or less). Because Dixie Valley is characterized by normal faulting, we infer that the greatest principal compressive stress was vertical, and had a value consistent with a lithostatic pressure gradient (26 MPa km⁻¹) typical of average crustal rock densities (2.65 g cm⁻³). The frictional strength of rock or Coulomb failure theory can be used to constrain average total differential stress to 40 MPa or less (Brace & Kohlstedt 1980). Higher differential stresses may have been realized for short intervals during seismic events, or near asperities and irregularities in the fault zone. As mentioned earlier, strain rates during faulting may have varied from values as low as 10⁻¹⁵ s⁻¹ or less

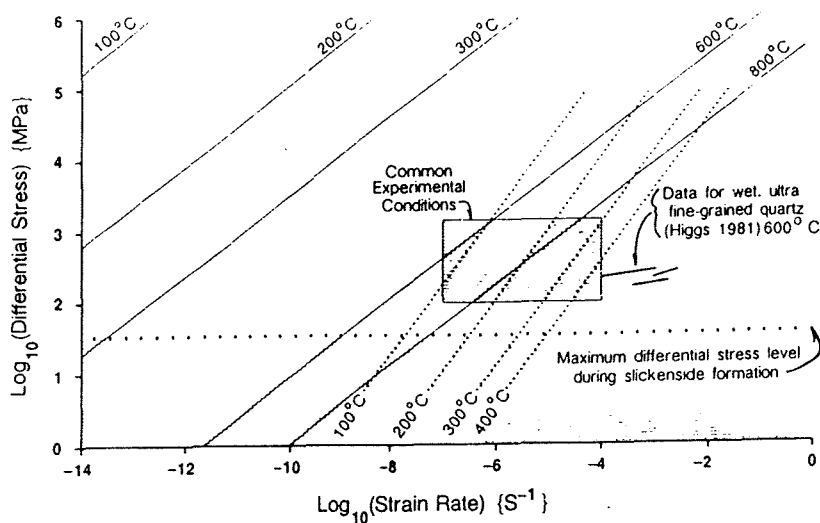


Fig. 11. Plot of differential stress vs strain rate, encompassing differential stress levels and strain rates for relevant experimental studies and for formation of natural slickenside surfaces. Differential stress levels and strain rates during slickenside formation in Dixie Valley are indicated by the shaded area below the heavy dotted line. Differential stress during slickenside formation can be constrained with knowledge of the depth of slickenside formation (less than 2 km—see text). Estimated strength of wet, coarse-grained (100 μm) quartz deforming by dislocation creep at different temperatures (solid lines) was calculated using equation (1) and the parameters given by Jaoul *et al.* (1984). Estimated strength of wet, fine-grained (1 μm) quartz deforming by pressure solution at different temperatures (fine dotted lines) was taken from Rutter (1983, fig. 10), and extrapolated to smaller grain size. Experiments on wet, ultra fine-grained quartz (grain size <1 μm) by Higgs (1981) were done at considerably higher strain rates than most experimental work. Recrystallization and the formation of aligned veins in Higgs samples suggests that some portion of their strain was accomplished by pressure solution. Extrapolation of stresses required for deformation by dislocation creep and by pressure solution suggest that at the conditions we infer for slickenside formation, pressure solution is more likely than dislocation creep.

(increase seismic period) to values as high as 10^2 s^{-1} during seismic events.

Crystalline plasticity. The most common way that crystallographic preferred orientations develop is by slip of dislocations combined with material rotations required by continuity and the conservation of vorticity (Tullis *et al.* 1973, Lister *et al.* 1978, Schmid & Casey 1986). In a deforming aggregate, work hardening is prevented either by syntectonic recrystallization or by dislocation climb (Tullis & Yund 1985). Because both of these processes are thermally activated, dislocation creep is highly temperature sensitive. Based on extrapolation of laboratory data and study of naturally deformed rocks for which the temperatures during deformation can be well constrained, many studies have concluded that dislocation creep in quartz at typical geologic strain rates is only important at temperatures greater than about 300°C (Tullis *et al.* 1982, Sibson 1983, Simpson 1985). Flow laws for steady-state deformation of quartz (and many other minerals) typically have the form

$$\frac{d\epsilon}{dt} = A\sigma^n e^{-(Q/RT)}, \quad (1)$$

where ϵ is strain, σ is differential stress, Q is an activation energy, T is temperature, R is the universal gas constant, and A and n are dimensionless constants (the 'pre-exponential term' and the stress exponent, respectively). Experimental results can be extrapolated to other temperatures and strain rates if the estimates of A , Q and n come from experiments which achieved steady-

state conditions. Estimates of A , Q and n have been provided by Jaoul *et al.* (1984) for steady-state dislocation creep of coarse-grained quartzite (100 μm) in the presence of water (Fig. 11).

Extrapolation of predictions from Jaoul *et al.* (1984) to lower strain rates suggests that dislocation creep is an unlikely explanation for the development of crystallographic preferred orientations in the slickenside surface material in Dixie Valley, Nevada, because temperatures during slickenside formation were less than 270°C . Moreover, micron-scale textural features of the fine-grained surface material, most notably the complex grain-boundary geometries and the lack of visible dislocations, are inconsistent with deformation by dislocation motion. Additionally, the texture of the fine-grained quartz is not what would be expected for a fine-grained aggregate which first deformed by dislocation creep and then annealed statically. Both dislocation creep and static annealing mechanisms produce equigranular textures with simple, straight grain boundaries rather than the complex grain-boundary geometry observed in the slickenside surface material.

Strain alignment of sub-microscopic quartz grains. Another possibility for the development of crystallographic preferred orientations in the slickenside material is strain reorientation of rod-shaped crystals (Jeffery 1923, March 1932, reviewed by Tullis 1976 and Oertel 1985). The mechanism was originally proposed to explain the development of preferred orientation in quartz-rich metamorphic rocks by Sander (1930) and Schmidt (1932) (reviewed in Griggs & Bell 1938). In

order for a strain alignment mechanism to cause the development of preferred orientation in a quartz aggregate, individual grains must have non-equant shapes, the *c*-axes must be statistically aligned with one axis of the grains and grain-boundary sliding must be possible. Elongate, sub-microscopic quartz grains might form either by precipitation from an aqueous solution due to faster growth rates parallel to the *c*-axis, a possibility which we discuss below, or perhaps by comminution of pre-existing quartz grains. Although Griggs & Bell (1938) concluded that comminution of quartz grains produced fragments which are statistically elongate parallel to the *c*-axis, the dominant control on the orientation of the fragments in their experiments was the stress direction. In addition, Frondel (1962, pp. 104–109) and Dunning *et al.* (1984) both concluded that fracture and cleavage in quartz preferentially followed the *r* and *z* faces rather than the prism or *m* faces that would be required to create fragments elongated parallel to the *c*-axis. Because strain alignment could occur at very low temperatures, it is an attractive explanation for the formation of preferred orientation in the slickenside surface materials at Dixie Valley. Strain alignment seems unlikely, however, because there is no evidence of elongate quartz crystals in the Dixie Valley slickenside surface material (Figs. 6a–c).

Pressure solution. A third possibility for the development of crystallographic preferred orientation involves low-temperature crystallization of quartz directly from a fluid phase or colloid. Chalcedony, cristobalite, opal and other silica polymorphs are common in near surface hydrothermal deposits (Fournier 1985). These materials are particularly interesting for two reasons. First, these silica phases are very fine-grained, much like the slickenside surface material. Second, they often precipitate from supersaturated fluids that are in a state of disequilibrium with the wallrock, as seems to be the case in the Stillwater fault zone.

We suggest that crystallographic preferred orientations in fine-grained quartz may develop because of the tendency for quartz to grow and dissolve fastest in the direction parallel to the *c*-axis. The anisotropy in dissolution is easily demonstrated in strong acid (Meyer & Penfield 1889, Liang & Readey 1987), but we are not aware of completed experimental studies which document an anisotropy in water, although such studies are currently underway (H. Westrich, personal communication 1989). Preferred orientations in crack–seal veins of quartz (Cox & Etheridge 1983) are thought to be caused by crystallographically controlled anisotropy in crystal growth rates. Preferred orientations are also observed in fibrous chalcedony. Chalcedony fibers are usually aligned either parallel or perpendicular to the *c*-axes of the submicroscopic quartz that forms the fibers (Folk & Pittman 1971). Under experimental conditions, the orientation of the *c*-axes relative to the fiber axes can be controlled by changing the chemical environment (Oehler 1976, Kastner 1980). Precipitation of chalcedony with aligned *c*-axes has been observed experimentally at temperatures as low as 150–165°C (Oehler 1976,

Kastner 1980). Because the crystallization of both quartz and chalcedony has been observed to form preferred orientations at low temperatures, we suggest crystallization mechanism may explain the development of preferred orientation in the slickenside surface material from Dixie Valley. The question is, if crystallization and dissolution of quartz occurs simultaneously with strain of the rock, can a preferred orientation be produced that reflects the deformation?

In crack–seal or pressure-solution slip fibers, a preferred orientation of quartz can occur that reflects deformation and is due to precipitation from solution. Individual fibers in crack–seal veins or pressure-solution slickensides may have crystallographic orientations that are random, or that have the same crystallographic orientations as 'seed' crystals in the fracture walls (Durney & Ramsay 1973, Ramsay 1980, Cox & Etheridge 1983). In some cases, however, anisotropies in growth kinetics cause certain fiber orientations to be favored over others. This presumably occurs because fibers with their fast-growth directions essentially normal to the crack walls or parallel to the extension or opening direction impede or occlude fibers with other crystallographic orientations (Buckley 1951, pp. 262–263). Durney & Ramsay (1973, p. 73) and Spry (1969, p. 162) suggested that for quartz, fibers with their *c*-axes parallel to the fibers would predominate. Cox & Etheridge (1983) described two natural examples where the *c*-axis of crack–seal fibers had a small circle distribution with an opening angle of ~40°, which they attributed to preferential growth in the [1012] direction. Although this mechanism may explain preferred orientations in crack–seal veins and pressure-solution slip slickensides, it does not seem likely that the preferred orientation in the slickensides from the Stillwater fault zone is inherited from pressure-solution slip fibers, because no evidence of relict fibers was found in any of the fault zone materials.

Although it is unlikely that pressure-solution slip fibers existed on the slickensides from the Stillwater fault zone, it is possible that deformation by pressure solution in very fine-grained aggregates could produce a crystallographic preferred orientation of quartz by a similar process. As mentioned above, the rate of precipitation and dissolution in quartz depends on crystallographic orientation. We suggest that if the anisotropy is strong enough, crystallization and dissolution during pressure solution will depend on the orientations of the grain boundaries as well as the magnitude of stress across them, and that crystallographic preferred orientations might result. If the fastest growth direction in quartz is parallel to the *c*-axis, then grains with their *c*-axes oriented in the direction of extension should grow faster than grains of other orientations, whereas grains with their *c*-axes oriented in the direction of compression would undergo faster dissolution than others (Tullis 1989). One attraction of this mechanism as an explanation for the preferred orientations in the Dixie Valley slickensides is that it predicts that the *c*-axes should be oriented in the extension direction, as observed in the

slickenside surfaces (Figs. 7 and 8). One potential problem with this mechanism is that it should cause the development of elongate quartz grains, a feature which we did not observe.

Kamb (1959) used non-hydrostatic thermodynamics to develop a mechanism for the development of crystallographic preferred orientations during deformation by pressure solution. The driving force for solution transfer during pressure solution results from variations in normal stress across differently oriented grain boundaries. These normal stress variations cause variations in chemical potential. In Kamb's mechanism, small additional differences in chemical potential due to elastic anisotropy of the crystalline material are responsible for some grains growing at the expense of others. In the mechanism we propose above, the preferred orientation results from anisotropies in the kinetics of dissolution and growth, a different mechanism. To the best of our knowledge, there are no experimental or natural examples in which Kamb's mechanism has been shown to be responsible for an observed preferred orientation; the driving energy for this mechanism may be too small to be important. Kamb's predicted patterns of preferred orientation do not match those we observe, although, as discussed by Paterson (1973), the predictions of Kamb's model can be quite dependent on details of the processes that are allowed to operate.

As discussed above, Higgs (1981) has performed a set of experiments on ultra fine-grained quartz (grain size $< 1 \mu\text{m}$), both with excess water and dry. In the wet experiments, Higgs observed both preferred orientations and evidence of pressure solution or diffusive mass transfer. Microscopic evidence for pressure solution or preferred orientation fabrics was not observed in the dry samples. Higgs observed that the wet samples were considerably weaker than the dry samples, suggesting that different deformation mechanisms contributed to the strain in the wet and dry experiments. The combination of the textural evidence, the change in mechanical behavior in the presence of water, and the lower strength of the ultra fine-grained quartz relative to coarser-grained material suggests that the mechanism of pressure solution was active. Because Higgs (1981) observed preferred orientations that are very similar to those observed in the slickenside surface material from Dixie Valley, Nevada, we suggest that the same mechanism is responsible for the preferred orientation in both the experimental and natural cases, and that this mechanism involves both pressure solution and a growth/dissolution rate anisotropy in quartz, as discussed above.

Unfortunately, the mechanical data from the study by Higgs (1981) do not allow accurate estimates of the strength exponent or the activation energy, precluding extrapolation of the observed strengths to lower strain rates and temperatures. Estimates of the strength of quartz aggregates deforming by pressure solution have been provided by Rutter (1983). Figure 11 shows Rutter's predictions, which were extrapolated to a grain size of $1 \mu\text{m}$ using an inverse cubic dependence of strain rate

on grain size (Rutter 1983, equation 4). Rutter's predictions, the results of Higgs' experiments, and the predictions from extrapolation of dislocation creep flow laws (Fig. 11) suggest that for the slickenside surface material deformation by pressure solution is more likely than deformation by dislocation creep. The results of Higgs' (1981) experimental study, coupled with the observations reported in this study, suggest that additional experimental work on fine-grained quartz aggregates would be worthwhile.

Summary. We cannot argue conclusively for a single explanation for the development of the crystallographic preferred orientation in the fine-grained slickenside surface material. Crystalline plasticity is an unlikely mechanism because the temperatures we infer for slickenside formation seem too low and because the extreme variation in grain size, the complex grain-boundary geometries, and the extremely low dislocation density observed in the slickenside surface material are inconsistent with dislocation motion. Strain alignment of sub-microscopic quartz fragments elongate in the *c*-axis direction seems unlikely, because the texture of the fine-grained slickenside material shows no elongate grains. Crystallographic preferred orientation in the slickenside material is probably not inherited from pressure-solution slip fibers, because relict fibers were not found in any of the slickenside surface materials. It seems most likely that a mechanism associated with pressure solution and the growth/dissolution rate anisotropy of quartz caused the preferred orientations in the slickenside material.

CONCLUSIONS

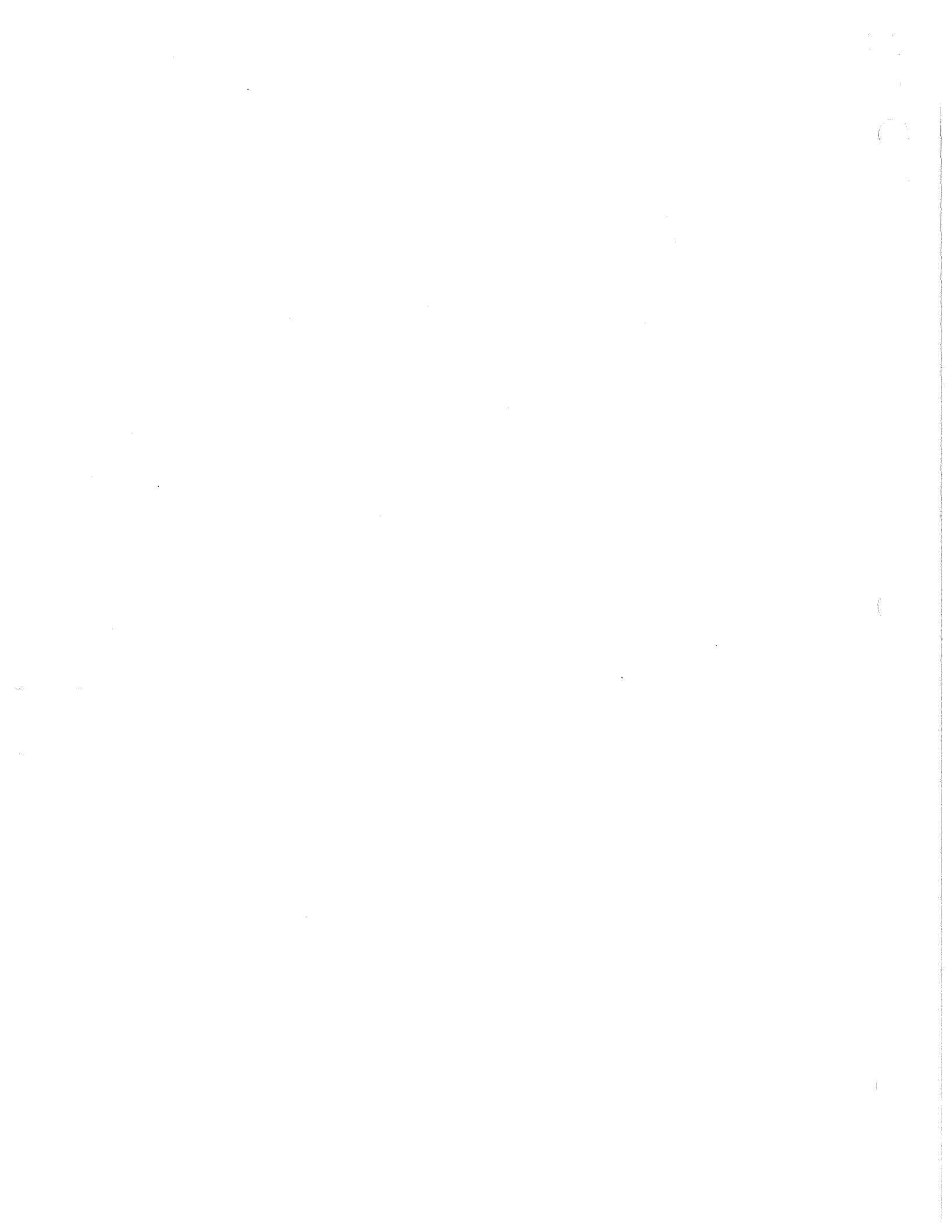
Slickenside surfaces along the Stillwater fault zone in the Dixie Valley area of Central Nevada, U.S.A., formed at depths of less than about 2 km and temperatures that were less than 270°C . The slickenside surface material is composed of very fine-grained ($0.01\text{--}1.0 \mu\text{m}$) quartz with small amounts of iron oxide and kaolinite. Evidence of both continuous and discontinuous deformation processes are present in the slickenside surface material, and textural features in the slickenside surface material indicate that the continuous and discontinuous processes alternated in time. Because the crystallographic preferred orientation is probably related to strain, and probably developed at relatively low strain rates, we correlate the continuous deformation phase of slickenside formation with the low-strain-rate phases of the earthquake cycle. We tentatively correlate the discontinuous deformation phase characterized by cataclasis, with the higher-strain-rate, seismic portion of the earthquake cycle. The wide range of strain rates which occur during the seismic cycle may be an essential element in the formation of fine-grained, glassy slickensides observed at Dixie Valley, Nevada, and many other areas.

Acknowledgements—We wish to express special thanks to Dick Yund for electron microscope work, Maura Weathers for X-ray observations, and Paul Williams for measuring quartz *c*-axis preferred orientations. Dick Yund, Bill Parry, Fred Chester, Greg Hirth, Jan Tullis and Tim Byrne provided helpful comments and suggestions. Tim Byrne, Mike Blanpied, Melissa Huther and Eileen Brennan provided indispensable assistance in the field. This work was supported by National Science Foundation grants EAR-8509014 and EAR-8610088.

REFERENCES

- Anderson, R. E., Zoback, M. L. & Thompson, G. A. 1983. Implications of selected subsurface data on the structural form and evolution of some basins in the northern Basin and Range province, Nevada and Utah. *Bull. geol. Soc. Am.* **94**, 1055–1072.
- Angelier, J. 1979. Determination of the mean principal directions of stresses for a given fault population. *Tectonophysics* **56**, T17–T26.
- Angelier, J., Colletta, B. & Anderson, R. E. 1985. Neogene paleostress changes in the Basin and Range: a case study at Hoover Dam, Nevada–Arizona. *Bull. geol. Soc. Am.* **96**, 347–361.
- Avakian, A. J. 1986. Mirror-quality polished fault surfaces from the Last Chance Range, East-Central California. *Geol. Soc. Am. Abs. w. Prog.* **18**, 530.
- Brace, W. F. & Kohlstedt, D. L. 1980. Limits on lithospheric stress imposed by laboratory experiments. *J. geophys. Res.* **85**, 6248–6252.
- Brune, J. 1976. The physics of earthquake strong motion. In: *Seismic Risk and Engineering Decision* (edited by Lomnitz, C. & Rosenblueth, E.). Elsevier, Amsterdam, 141–177.
- Buckley, H. E. 1951. *Crystal Growth*. John Wiley, New York.
- Burford, R. O. & Harsh, P. W. 1980. Slip on the San Andreas fault in central California from alignment array surveys. *Bull. seism. Soc. Am.* **70**, 1233–1261.
- Cox, S. F. & Etheridge, M. A. 1983. Crack–seal fibre growth mechanisms and their significance in the development of oriented layer silicate microstructures. *Tectonophysics* **92**, 147–170.
- Denton, J. M., Bell, E. J. & Jodry, R. L. 1980. Geothermal reservoir assessment case study: northern Dixie Valley, Nevada. Southland Royalty Co., Fort Worth, Texas, U.S.A.
- Dozer, D. I. 1986. Earthquake processes in the Rainbow Mountain–Fairview Peak–Dixie Valley, Nevada, Region 1954–1959. *J. geophys. Res.* **91**, 12572–12586.
- Dunning, J. D., Schuyler, J. & Owens, A. 1984. The effects of aqueous chemical environments on crack propagation in quartz. *J. geophys. Res.* **89**, 4115–4123.
- Durney, D. W. & Ramsay, J. G. 1973. Incremental strains measured by syntectonic crystal growths. In: *Gravity and Tectonics* (edited by DeJong, K. A. & Scholten, R.). John Wiley, New York, 67–96.
- Elliott, D., 1976. The energy balance and deformation mechanisms of thrust sheets. *Phil. Trans. R. Soc. Lond.* **A283**, 289–312.
- Engelder, J. T. 1974. Microscopic wear grooves on slickensides: indicators of paleoseismicity. *J. geophys. Res.* **79**, 4387–4392.
- Fleuty, M. J. 1975. Slickensides and slickenlines. *Geol. Mag.* **112**, 319–322.
- Folk, R. L. & Pittman, J. S. 1971. Length-slow chalcedony: a new testament for vanished evaporites. *J. sedim. Petrol.* **41**, 1045–1058.
- Fonseca, J. 1988. The Sou Hills: a barrier to faulting in the Central Nevada Seismic Belt. *J. geophys. Res.* **93**, 475–489.
- Fournier, R. O. 1985. The behavior of silica in hydrothermal solutions. In: *Geology and Geochemistry of Epithermal Systems* (edited by Berger, B. R. & Bethke, P. M.). *Rev. Econ. Geol.* **2**, 45–59.
- Fronдел, C. 1962. *The System of Mineralogy, Volume III. Silica Minerals*. John Wiley, New York.
- Gray, M. B. & Nickelsen, R. P. 1989. Pedogenic slickensides, indicators of strain and deformation processes in redbed sequences of the Appalachian foreland. *Geology* **17**, 72–75.
- Griggs, D. & Bell, J. F. 1938. Experiments bearing on the orientation of quartz in deformed rocks. *Bull. geol. Soc. Am.* **49**, 1723–1746.
- Hancock, P. L. & Barka, A. A. 1987. Kinematic indicators on active normal faults in Western Turkey. *J. Struct. Geol.* **9**, 573–584.
- Hastings, D. D. 1979. Results of exploratory drilling, northern Fallon Basin, western Nevada. In: *Basin and Range Symposium* (edited by Newman, G. W. & Good, H. D.). *Rocky Mountain Ass. Geol.–Utah Geol. Ass.* Denver, Colorado, 515–522.
- Hemlev, J. J., Montoya, J. W., Marinenko, J. W. & Luce, R. W. 1980. Equilibria in the system $\text{Al}_2\text{O}_3\text{--SiO}_2\text{--H}_2\text{O}$ and some general implications for alteration/mineralization processes. *Econ. Geol.* **75**, 210–228.
- Higgs, N. G. 1981. Mechanical properties of ultrafine quartz, chlorite and bentonite in environments appropriate to upper-crustal earthquakes. Unpublished Ph.D. thesis, Texas A&M University, College Station, Texas, U.S.A.
- Jaoul, O., Tullis, J. & Kronenberg, A. 1984. The effect of varying water contents on the creep behavior of Heavittree Quartzite. *J. geophys. Res.* **89**, 4298–4312.
- Jeffery, G. B. 1923. The motion of ellipsoidal particles immersed in a viscous fluid. *Proc. R. Soc. Lond.* **A102**, 161–179.
- Kamb, W. B. 1959. Theory of preferred crystal orientation developed by crystallization under stress. *J. Geol.* **67**, 153–170.
- Kastner, M. 1980. Length-slow chalcedony: the end of the new testament. *Eos, Trans. Am. Geophys. Un.* **61**, 399.
- Kronenberg, A. K. & Tullis, J. 1984. Flow strengths of quartz aggregates: grain size and pressure effects due to hydrolytic weakening. *J. geophys. Res.* **89**, 4281–4297.
- Lachenbruch, A. H. & Sass, J. H. 1977. Heat flow in the United States and the thermal regime of the crust. In: *The Earth's Crust* (edited by Heacock, J. G.). *Am. Geophys. Un. Washington, DC*, 626–675.
- Liang, D.-T. & Readey, D. E. 1987. Dissolution kinetics of crystalline and amorphous silica in hydrofluoric–hydrochloric acid mixtures. *J. Am. Ceram. Soc.* **70**, 570–577.
- Lister, G. S., Paterson, M. S. & Hobbs, B. E. 1978. The simulation of fabric development in plastic deformation and its application to quartzite: the model. *Tectonophysics* **45**, 107–158.
- Logan, J. M., Friedman, M., Higgs, N., Dengo, C. & Shimamoto, T. 1979. Experimental studies of simulated fault gouge and their application to studies of natural fault zones. *U.S. Geol. Surv. Open-File Rep.* **79-1239**, 305–343.
- March, A. 1932. Mathematische theorie der regelung nach der korn-gestalt bei affiner deformation. *Z. Kristallogr.* **81**, 285–298.
- Means, W. D. 1987. A newly recognized type of slickenside striation. *J. Struct. Geol.* **9**, 585–590.
- Meyer, O. & Penfield, S. L. 1889. Results obtained by etching a sphalerite and crystals of quartz with hydrofluoric acid. *Trans. Conn. Acad.* **158**–165.
- Nur, A. & Booker, J. R. 1972. Aftershocks caused by pore fluid flow? *Science* **175**, 885–887.
- Oehler, J. H. 1976. Hydrothermal crystallization of silica gel. *Bull. geol. Soc. Am.* **87**, 1143–1152.
- Oertel, G. 1985. Reorientation due to grain shape. In: *Preferred Orientation in Deformed Metals and Rocks: An Introduction to Modern Texture Analysis* (edited by Wenk, H.-R.). Academic Press, New York, 259–265.
- Okaya, D. A. & Thompson, G. A. 1985. Geometry of Cenozoic extensional faulting: Dixie Valley, Nevada. *Tectonics* **4**, 107–125.
- Page, B. M. 1965. Preliminary geologic map of a part of the Stillwater Range, Churchill County, Nevada. Map 28, Nevada Bureau of Mines and Geology, Reno, Nevada, U.S.A.
- Parchman, W. L. & Knox, J. W. 1981. Exploration for geothermal resources in Dixie Valley, Nevada. *Bull. Geotherm. Resources Council* **10**, 3–6.
- Paterson, M. S. 1973. Nonhydrostatic thermodynamics and its geologic applications. *Rev. Geophys. & Space Phys.* **11**, 355–389.
- Petit, J. P. 1987. Criteria for the sense of movement on fault surfaces in brittle rocks. *J. Struct. Geol.* **9**, 597–608.
- Pfiffner, O. A. & Ramsay, J. G. 1982. Constraints on geological strain rates: arguments from finite strain states of naturally deformed rocks. *J. geophys. Res.* **87**, 311–321.
- Power, W. L., Tullis, T. E., Brown, S. R., Boitnott, G. N. & Scholz, C. H. 1987. Roughness of natural fault surfaces. *Geophys. Res. Lett.* **14**, 29–32.
- Power, W. L., Tullis, T. E. & Weeks, J. D. 1988. Roughness and wear during brittle faulting. *J. geophys. Res.* **93**, 15,268–15,278.
- Price, G. P. 1980. The analysis of quartz *c*-axis fabrics by the photometric method. *J. Geol.* **88**, 181–195.
- Ramsay, J. G. 1980. The crack–seal mechanism of rock deformation. *Nature* **284**, 135–139.
- Riehle, J. R., McKee, E. H. & Speed, R. C. 1972. Tertiary volcanic center, west-central Nevada. *Bull. geol. Soc. Am.* **83**, 1383–1396.
- Rutter, E. H. 1983. Pressure solution in nature: theory and experiment. *J. geol. Soc. Lond.* **140**, 725–740.
- Sander, B. 1930. *Gefugekunde der Gesteine*. Springer, Wien.
- Schmid, S. M. & Casey, M. 1986. Complete fabric analysis of some commonly observed quartz *c*-axis patterns. In: *Mineral and Rock Deformation: Laboratory Studies* (edited by Hobbs, B. E. & Heard, H. C.). *Am. Geophys. Un. Geophys. Monogr.* **36**, 263–286.

- Schmidt, W. 1932. *Tektonik und Verformungslehre*. Geb. Borntraeger, Berlin.
- Sibson, R. H. 1975. Generation of pseudotachylyte by ancient seismicity. *Geophys. J. R. astr. Soc.* **43**, 775-794.
- Sibson, R. H. 1977. Fault rocks and fault mechanisms. *J. geol. Soc. Lond.* **133**, 191-231.
- Sibson, R. H. 1983. Continental fault structure and the shallow earthquake source. *J. geol. Soc. Lond.* **140**, 741-767.
- Sibson, R. H. 1986a. Earthquakes and lineament infrastructure. *Phil. Trans. R. Soc. Lond.* **A317**, 63-79.
- Sibson, R. H. 1986b. Brecciation processes in fault zones: inferences from earthquake rupturing. *Pure & Appl. Geophys.* **124**, 159-175.
- Sibson, R. H., Robert, F. & Poulsen, K. H. 1988. High-angle reverse faults: fluid pressure cycling, and mesothermal gold-quartz deposits. *Geology* **16**, 551-555.
- Simpson, C. 1985. Deformation of granitic rocks across the brittle-ductile transition. *J. Struct. Geol.* **7**, 503-511.
- Spry, A. 1969. *Metamorphic Textures*. Pergamon, London.
- Stel, H. 1981. Crystal growth in cataclases: diagnostic microstructures and implications. *Tectonophysics* **78**, 585-600.
- Hatcher, W. 1979. Systematic inversion of geodetic data in central California. *J. geophys. Res.* **84**, 2283-2295.
- Thompson, G. A. & Burke, D. B. 1973. Rate and direction of spreading in Dixie Valley, Basin and Range province, Nevada. *Bull. geol. Soc. Am.* **84**, 627-632.
- Tjia, H. D. 1968. Fault-plane markings. *XXIII Int. Geol. Congr.* **13**, 279-284.
- Tullis, T. E. 1976. Experiments on the origin of slaty cleavage and schistosity. *Bull. geol. Soc. Am.* **87**, 745-753.
- Tullis, T. E. 1989. Development of preferred orientation due to anisotropic dissolution/growth rates during solution-transfer creep. *EOS, Trans. Am. Geophys. Un.* **70**, 457-458.
- Tullis, J., Christie, J. M. & Griggs, D. T. 1973. Microstructures and preferred orientations of experimentally deformed quartzites. *Bull. geol. Soc. Am.* **84**, 297-314.
- Tullis, J., Snoke, A. W. & Todd, V. R. 1982. Significance and petrogenesis of mylonitic rocks. *Geology* **10**, 227-230.
- Tullis, J. & Yund, R. A. 1985. Dynamic recrystallization of feldspar: a mechanism for ductile shear zone formation. *Geology* **13**, 238-241.
- Wallace, R. E. & Whitney, R. A. 1984. Late Quaternary history of the Stillwater Seismic Gap, Nevada. *Bull. seism. Soc. Am.* **74**, 301-314.
- Wenk, H. R. & Kolodny, Y. 1968. Preferred orientation of quartz in a chert breccia. *Proc. natn. Acad. Sci. U.S.A.* **59**, 1061-1066.
- Will, T. M. & Wilson, C. J. L. 1989. Experimentally produced slickenside lineations in pyrophyllitic clay. *J. Struct. Geol.* **11**, 657-667.
- Wojtal, S. 1986. Deformation within foreland thrust sheets by populations of minor faults. *J. Struct. Geol.* **8**, 341-360.
- Zoback, M. L. 1989. State of stress and modern deformation of the northern Basin and Range province. *J. geophys. Res.* **94**, 7105-7128.



Numerical Simulation of a Tracer Test at Dixie Valley, Nevada

P. E. Rose¹, K. D. Apperson¹, S. D. Johnson², and M. C. Adams¹

¹Energy and Geoscience Institute, University of Utah,
423 Wakara Way, Salt Lake City, UT 84108

²Oxbow Power Services, Inc., 5250 S. Virginia St, Ste 304, Reno, Nevada 89502

Abstract

A tracer test was conducted at the Dixie Valley, Nevada, geothermal reservoir using fluorescein. Four of 9 production wells showed fluorescein breakthrough during the first 200 days of the test. Reconstructed fluorescein return curves are presented that correct for the thermal decay of the tracer assuming an average reservoir temperature of 227°C. In order to examine the feasibility of using numerical simulation to model tracer flow, we developed simple, two-dimensional models of the geothermal reservoir using the numerical simulation programs TETRAD and TOUGH2. By fitting model outputs to measured return curves, we show that numerical reservoir simulations can be calibrated with the tracer data. Both models predict the same order of elution, approximate tracer concentrations, and return curve shapes. Using these results, we propose a method for using numerical models to design a tracer test.

Introduction

With the increased use of reinjection in geothermal reservoirs, tracers have become an important tool in developing reservoir management strategies. If injectors are positioned too close to producers, a risk of short circuiting develops, resulting in the possibility of premature thermal breakthrough. If injectors are placed too far away, the injected water will not provide sufficient pressure support to the reservoir. Since chemical breakthrough is more rapid than thermal breakthrough, a tracer test can provide important interwell flow data that can be used to optimize injection well placement and injection flow rates.

In tracing the flow of geothermal water along injection-production flow paths, a chemical compound is typically injected as a pulse into a selected well. The tracer enters the reservoir and is diluted as it is connected through fractures and diffuses into the pore matrix. The surrounding production wells are then

sampled over an appropriate duration in order to determine the arrival times and concentrations of the tracer produced at each well. From an analysis of the tracer-return curves, it is possible to derive valuable information concerning the potential for thermal breakthrough between injection and production wells.

Perhaps the most challenging aspect of tracer test design is the determination of the appropriate quantity of tracer required for a test. The use of an insufficient quantity results in no detected tracer at the production wells, and no flow path information is obtained. The use of excessive quantities of tracer, which is often done in order to insure breakthrough, is not only expensive, but leads to the use of even greater quantities of that chemical for any subsequent tests in order to overcome the induced high background levels.

An accurate estimation of the quantity of tracer required for a tracer test requires a knowledge of reservoir well spacing, well fluid-entry positions, injector and producer flow rates, fluid temperatures, matrix and fracture porosity, and reservoir volume. Such information is contained in the input data file of a calibrated reservoir simulation model. The simulator uses this input information to calculate flow patterns, production well pressures, and produced fluid temperatures. It follows that the simulation model might be a valuable tool in tracer test design. In addition, the tracer return curves can be used to provide constraints that will aid in model calibration. The recalibrated model might then be used to improve tracer-return predictions for subsequent tracer tests.

Our objective is to demonstrate the feasibility of using numerical simulation to model the flow of tracer throughout a geothermal reservoir. Models of the geothermal reservoir at Dixie Valley, Nevada, were developed using the two finite difference simulators, TOUGH2 and TETRAD. Predicted tracer return data are compared to those measured in a recent tracer test conducted at the Dixie Valley geothermal reservoir.

Using these data and results, we developed a method for estimating the minimum quantity of tracer required to obtain reliable interwell tracer-break-through data.

Geology of Dixie Valley

Dixie Valley, located in west-central Nevada, is an asymmetric Basin and Range graben. It is bounded on the west by the Stillwater Range and on the east by the Clan Alpine Mountains. The Dixie Valley geothermal field is located on the west side of the valley. Production in the geothermal field is defined primarily by fracture permeability associated with the Stillwater range front fault and related secondary faults (Fig. 1).

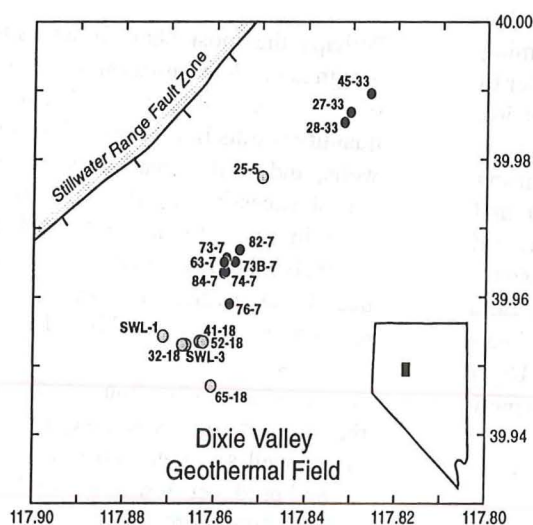


Figure 1. Wellhead locations in Dixie Valley, Nevada, geothermal field. Injection wells shaded grey, production wells shaded black. Approximate location of Stillwater Range normal fault zone, dipping 52-54° to the southeast, is shown in upper left.

Seismic data indicate that the young NNE-striking normal faults that presently define the structural topography of Dixie Valley are high angle, planar, and may extend to depths of 14 km. In the vicinity of the Dixie Valley Geothermal Field, the Stillwater range front fault is known to dip 52-54° to the SE with a roughly planar geometry to depths of 3 km (Benoit, 1995).

Sibson (1977) and Chester and Logan (1986) developed a conceptual fault zone model consisting of a fault core and damage zone surrounded by relatively undeformed protolith (see also Caine et al., 1996). In

any individual fault zone segment, the fault core and damage zone can be spatially heterogeneous, and either may be absent. Fault cores, which accommodate most of the fault displacement, typically consist of fine-grained gouge and cataclasite. Associated damage zones are typically faulted and fractured. Fractures and faults in the damage zone oriented sub-parallel to the main fault increase the permeability in the plane of the fault (Forster and Evans, 1991). As Caine et al. (1996) suggest, permeability in the fault core may be limited by the fine grain size, whereas it is the hydraulic properties of faults and fractures in the damage zone which control permeability there.

The Tracer Test

On May 29, 1996, 169 kg of a 50% by weight aqueous solution of the dipotassium salt of fluorescein and 100 kg of the disodium salt of 7-amino-1,3-naphthalene disulfonic acid (amino G acid) were mixed with approximately 3000 kg of produced reservoir brine and pumped into injector 25-5 over a period of about 20 minutes. The 9 production wells were sampled weekly and the samples were analyzed for fluorescein using a Perkin Elmer LS-30 luminescence spectrometer at excitation and emission wavelengths of 475 nm and 510 nm respectively.

The mean temperature of the brine at the Dixie Valley reservoir was recently shown to be between 225°C and 230°C (Adams and Davis, 1991). For the purposes of this exercise, it is assumed that the mean brine temperature is 227°C, which is within the range of this recent measurement. Adams and Davis (1991) showed that, at 227°C, fluorescein has a half-life of about 95 days. At about 300 days, when the first return-curve maxima are expected, more than 90% of the originally injected fluorescein will have thermally decayed. From a knowledge of fluorescein decay kinetics, it is possible to correct for thermal decay and to reconstruct "conservative" fluorescein return curves. Of course, after the fluorescein has decayed below the detection limit of the spectrofluorometer, it will not be possible to correct for decay, and the tracer test will necessarily end.

The decay-rate constant, k , varies with temperature according to the Arrhenius relationship:

$$k = Ae^{-E_a/RT} \quad (1)$$

where E_a is the activation energy, A is a pre-expo-

tial factor and R is the gas constant. Based upon parameters obtained in the study by Adams and Davis (1991), the rate constant at 227°C was found to be:

$$k = 7.92 \times 10^{-3} \text{ da}^{-1} \quad (2)$$

The concentration of fluorescein in the reservoir varies with time according to the first-order rate expression:

$$C = C_0 e^{-kt} \quad (3)$$

where C is fluorescein concentration, C_0 is initial fluorescein concentration, and t is time. By substituting equation 2 into equation 3, the rate expression for decay at 227°C becomes:

$$C = C_0 e^{-0.00792t} \quad (4)$$

Finally, by correcting the measured fluorescein return-curve concentrations using expression 4, it is possible to construct conservative tracer return data. Figure 2a shows the uncorrected return curves for all of the wells where fluorescein appeared, and Figure 2b shows the return curves after correcting for thermal decay. Since the minimum measurable concentration was approximately 10 parts per trillion (ppt), only the return curves for wells showing fluorescein concentrations greater than 10 ppt are shown in Figure 2b.

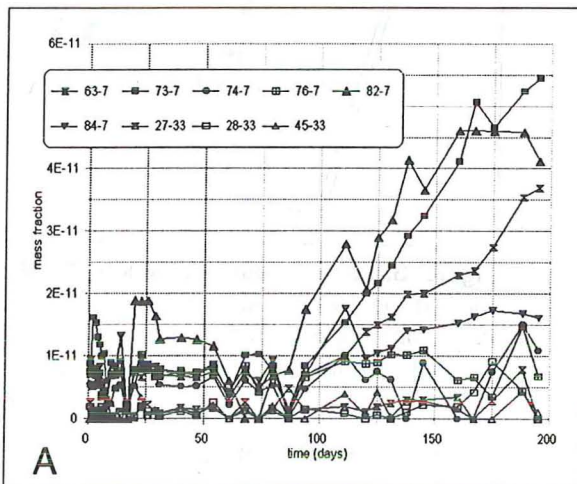


Figure 2. (a) Fluorescein mass fractions measured at 9 production wells.

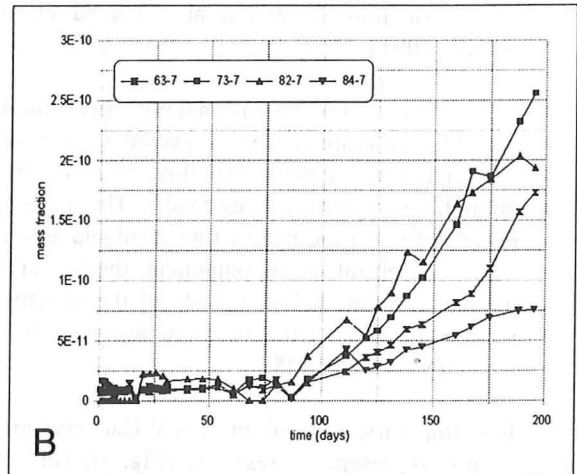


Figure 2. (b) Fluorescein mass fractions at 4 production wells after correcting for thermal decay.

The Reservoir Models

Models of the reservoir at Dixie Valley were developed using the finite difference, numerical simulation programs TOUGH2 (Preuss, 1991) and TETRAD (Vinsome, 1995). The models were configured to simulate the flow of a short pulse of tracer injected into well 25-5 (Fig. 1). The model outputs were then fit to the actual tracer production data by adjusting reservoir thickness, permeability and porosity, within reasonable limits.

Both TOUGH2 and TETRAD allow for the separate tracking of two aqueous components. The "first water" represents all of the water initially present in the reservoir as well as essentially all of the water that is reinjected. The "second water" is injected into an appropriate injection well over a very short period of time at the beginning of the simulation. It represents the pulse of tracer that is used to trace the flow of injectate. After the injection of the tracer pulse, the injector is immediately switched back to injection of the first water. Although the two aqueous components mix thoroughly as they are convected throughout the reservoir, the second water emerges as dispersed pulses in the production wells.

TOUGH2 is a numerical simulation program that was developed for the purpose of modeling the multiphase and multicomponent flow of fluid and heat through porous and fractured media. Among the specific applications for which the code was designed are geothermal reservoir engineering, nuclear waste disposal and unsaturated zone hydrology. Its architecture and

method of implementation are detailed elsewhere (Preuss, 1991).

TETRAD is a three dimensional numerical simulation computer program that was developed to model the multiphase, multicomponent flow of heat and fluid through porous or fractured media. The name "TETRAD" refers to the code's four available application modes: black oil, multicomponent, thermal and geothermal flow modeling. Details of the structure and implementation of the program are provided elsewhere (Vinsome, 1995).

For simplicity, a two-dimensional Cartesian grid was used to represent the reservoir (Fig. 3). This is justified since the reservoir is defined largely by a set of fractures closely associated with the Stillwater Fault, which possesses remarkably constant dip and strike angles within the Dixie Valley geothermal field and which therefore can be reasonably approximated as a plane. In addition, all of the wells except one are completed within this highly fractured fault zone.

The 442-element grid that was used in both the TOUGH2 and TETRAD models is shown in Figure 3. This figure shows the locations of the completion intervals of the seven injection wells and nine production wells that were active during the tracer test. Tracer was injected only into well 25-5. With a flow rate of about 284 kg/sec, this well alone accounts for over half of the total injection into the field. The remaining injectors are distributed between shallow and deep completion intervals in section 18. Six of the nine production wells are clustered in section 7; the remaining three are located in the northeast end of the reservoir in section 33.

The top of the grid was positioned 1676 m below the ground surface, and the initial pressure within the grid was hydrostatic. The initial temperature was set at 227°C uniformly throughout the reservoir, whereas the reinjected water had a temperature of 100°C.

In the case of the TOUGH2 model, Neumann (no-flow) boundary conditions were maintained on all surfaces except for the uppermost blocks at either end of the reservoir. At these blocks, the elements were given Dirichlet (constant temperature and pressure) boundary conditions. In the case of the TETRAD model, the columns of blocks at either end were designated as steady-state aquifer elements, which allow for flow into the reservoir. Such conditions were chosen because only about 82% of the produced water is returned as injectate. If the boundaries were entirely

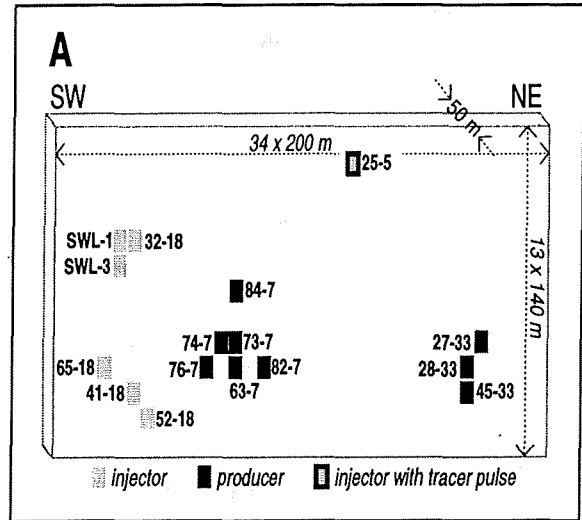


Figure 3. (a) Schematic grid used in both TETRAD and TOUGH2 numerical simulations. Well positions (based on wellhead location) are projected onto the assumed planar fault zone. Completion intervals for production wells (black) and injection wells (grey) are shown.

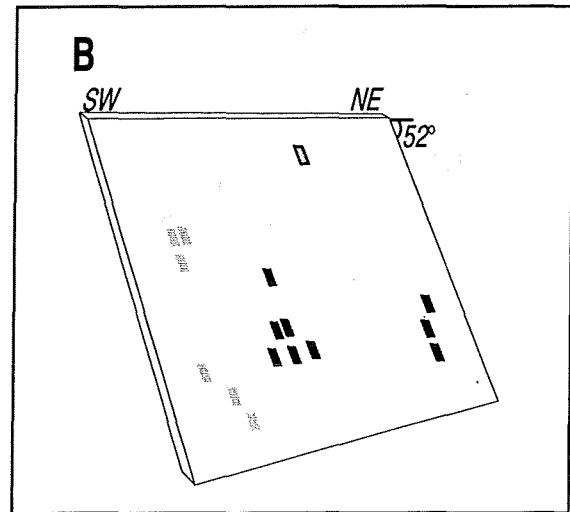


Figure 3. (b) In both simulation models, we rotated the gravity vector to simulate the planar fault zone dipping 52° to the southeast. Well symbols are the same as in Figure 3a.

closed, two-phase conditions would soon develop in the reservoir and likewise in the model. The choice of these boundary conditions allows for flow throughout the reservoir to be dominated by the injection and production wells, while allowing for make-up flow into the reservoir as needed to maintain single-phase (liquid) conditions.

Although the Dixie Valley reservoir consists of a complex network of faults and fractures extending throughout a heterogeneous rock matrix, it was defined for the purposes of this modeling exercise as an isotropic and homogeneous porous medium

Results and Discussion

Using the input parameters and boundary conditions described above, the TOUGH2 and TETRAD models were run for a period of three years. Plots of tracer concentration vs time for all of the wells showing return are shown in Figure 4. It is apparent that both models predict the same order of elution and approximate relative tracer quantity for the section-7 production wells, although the TETRAD returns are all slightly greater than the TOUGH2 returns. Both models predict that the section-7 wells show return well in advance of the section-33 wells. Interestingly, the relative quantity of returning tracer is reversed for the section-33 wells, with the TOUGH2 model showing a greater return than the TETRAD model. The differences between the model predictions are slight, however, as revealed by a plot of cumulative tracer production vs time in Figure 5. Figure 6 shows the first 200 days of tracer-return data, corrected for thermal decay, and simulation results from TOUGH2.

Although the match is imperfect, the simulated curves reflect the general order of elution, position, size and shape of the measured curves. The match is particularly good for the producer 82-7, which shows the strongest return, whereas the simulated returns underpredict to varying degrees the measured returns for the remaining section-7 wells.

Figure 7 shows the return-curve data in combination with the simulation results for the TETRAD model. Again, the simulated curves reflect the general order of elution, position, size and shape of the measured curves. The TETRAD-generated curves bracket the measured data, with two curves (wells 82-7 and 84-7) being overpredicted and two curves (wells 73-7 and 63-7) being underpredicted. Since both models represent a two-dimensional, homogeneous and isotropic porous medium and the reservoir is doubtlessly a three-dimensional, anisotropic, heterogeneous, and fractured medium, the similarity between both the TOUGH2 and TETRAD modeled results and the data is remarkable.

Tracer Test Design

In designing a tracer test, the reservoir engineer must estimate the minimum quantity of tracer required for

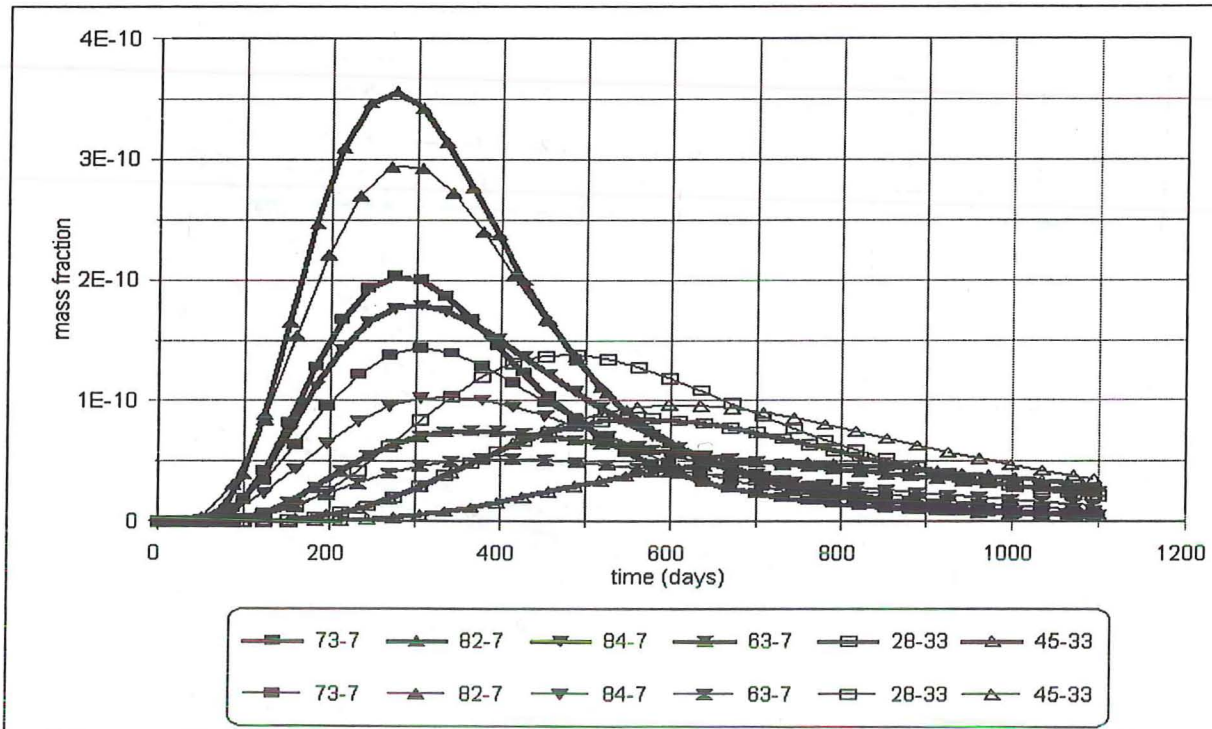


Figure 4. Simulated tracer return curves for TETRAD (thick lines) and TOUGH2 (thin lines).

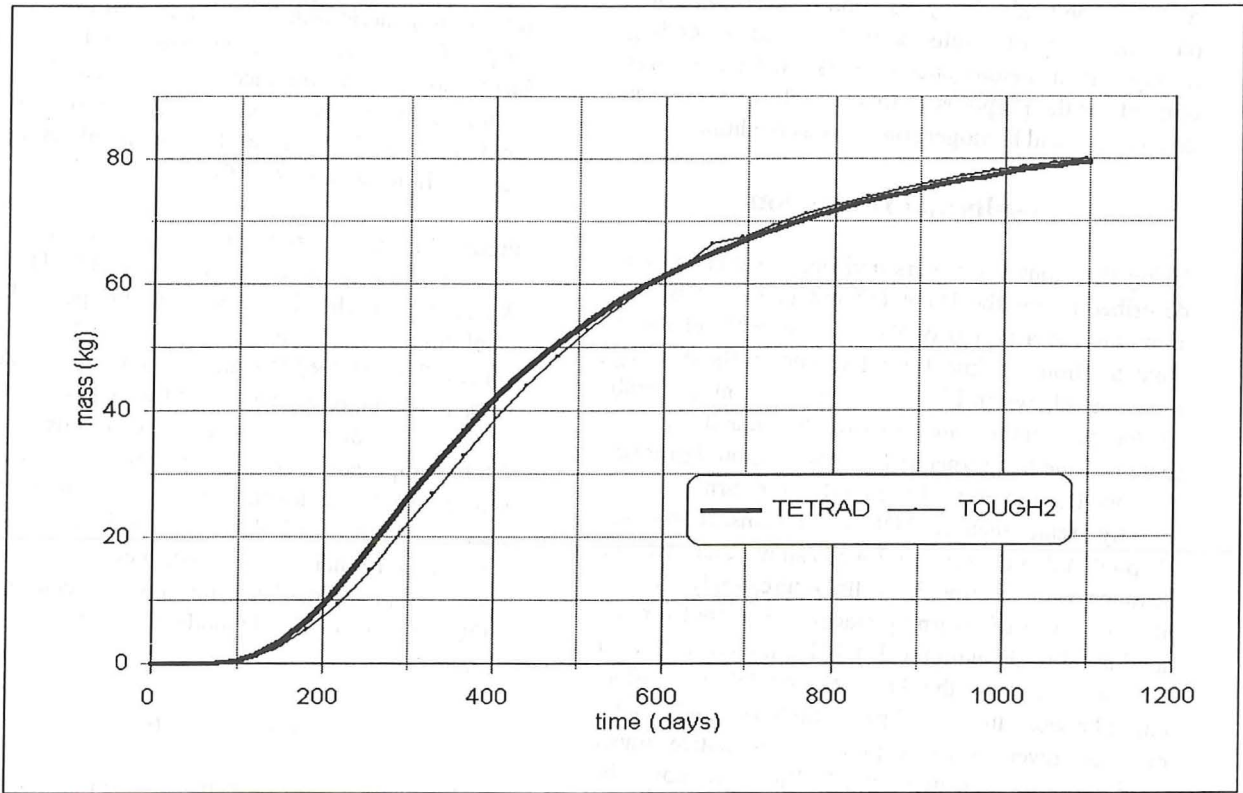


Figure 5. Cumulative tracer returns for TETRAD and TOUGH2.

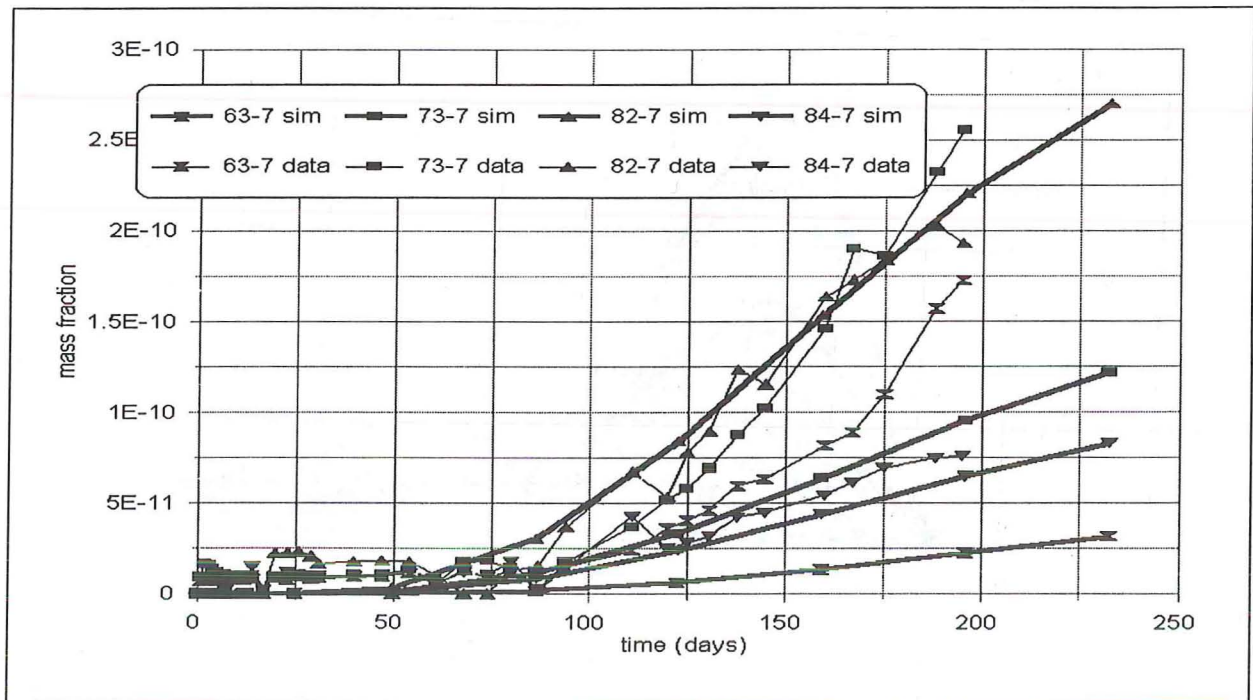


Figure 6. Measured return curves (thin lines) and simulated return curves using TOUGH2 (thick lines)

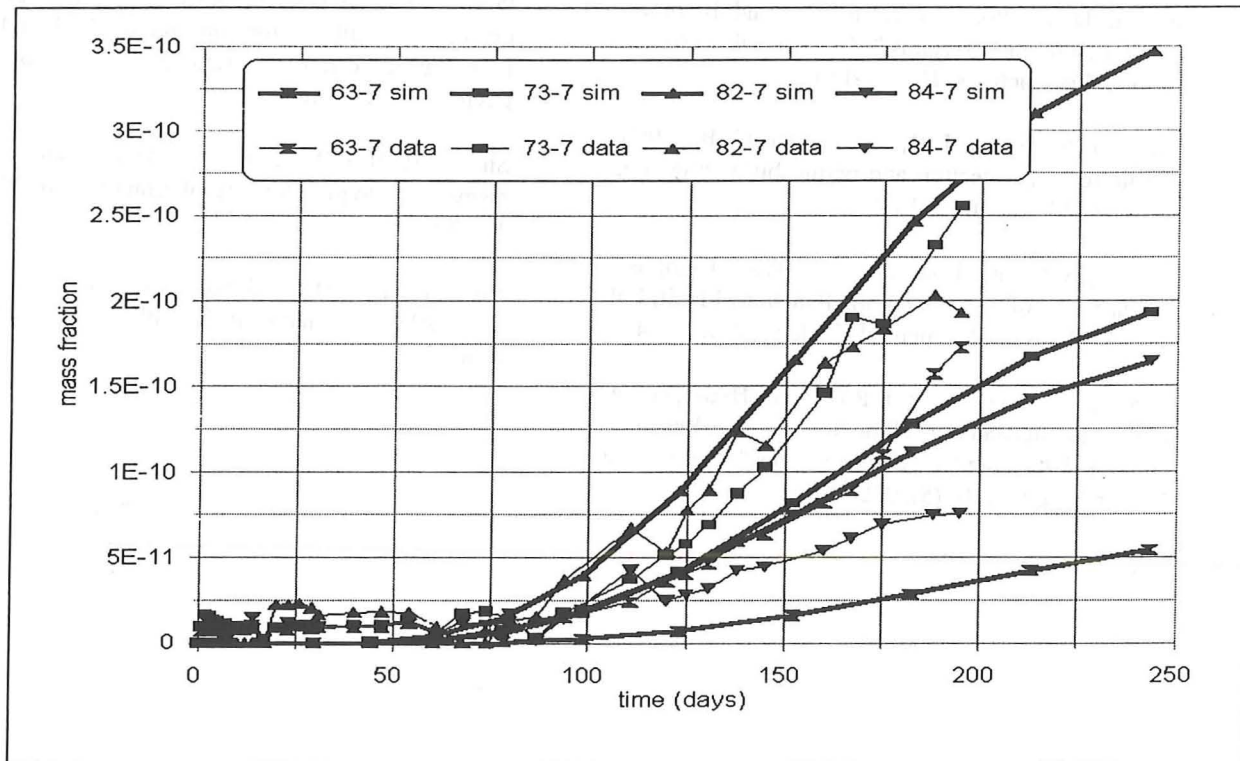


Figure 7. Measured return curves (thin lines) and return curves simulated using TETRAD (thick lines).

breakthrough at the producers and the probable injectate flow patterns. A knowledge of flow patterns is required in order to estimate the first arrival times and peak arrival times of tracer, which in turn are used to determine appropriate sampling locations and sampling frequency. In order to estimate the minimum amount of tracer, the reservoir engineer needs only to minimize the duration of the simulated tracer-injection pulse, since, for a constant flow rate, the pulse duration is directly proportional to the mass of tracer injected. The minimum pulse duration occurs when enough tracer has been injected to result in return curve concentrations at the production wells that exceed the minimum measurable concentration of the detector by a comfortable margin. Of course, if thermally unstable tracers are used, the tracer decay kinetics must be determined and accounted for.

Summary and Conclusions

A tracer test was conducted at the Dixie Valley, Nevada, geothermal reservoir in order to determine the destiny of reinjected reservoir fluids. Fluorescein breakthrough was evidenced at 4 of the reservoir's 9 production wells. Using TOUGH2 and TETRAD, relatively simple two-dimensional models of the tracer

flow patterns were developed by fitting model outputs to measured return curves. Since fluorescein decays rapidly at the average reservoir temperature of approximately 227°C, it was necessary to correct the return curves for tracer decay, using kinetics developed under conditions that simulate the geothermal environment. Both models were equally successful at simulating the return curve shapes and elution order as well as the approximate concentrations of produced tracer. We have proposed a method for using numerical models to design a tracer test.

Acknowledgements

This work was supported by the U.S. Department of Energy under contract number DE-HC07-90ID12929. Such support does not constitute an endorsement by the U.S. Department of Energy of the views expressed in this publication.

References

Adams, M. C. and Davis, J. (1991), "Kinetics of fluorescein decay and its application as a geothermal tracer," *Geothermics*, 20 (1/2), 53-66.

Benoit, D. (1995), "Forced folding and basin and range geothermal systems," *Geothermal Resources Council Transactions*, **19**, 155-163.

Caine, J. S., Evans, J. P., and Forster, C. B. (1996), "Fault zone architecture and permeability structure," *Geology*, **24** (11), 1025-1028.

Chester, F. M. and Logan, J. M. (1986), "Composite planar fabric of gouge from the Punchbowl fault, California," *Journal of Structural Geology*, **9**, 621-634.

Forster, C. B. and Evans, J. P. (1991), "Hydrogeology of thrust faults and crystalline thrust sheets: Results of combined field and modeling studies," *Geophysical Research Letters*, **18** (5), 979-982.

Preuss, K. (1991), TOUGH2--a general-purpose numerical simulator for multiphase fluid and heat flow. Lawrence Berkeley Laboratory, Earth Sciences Division, LBL-29400.

Sibson, R. H. (1977), "Fault rocks and fault mechanisms," *Geological Society of London Journal*, **133**, 191-231.

Vinsome, K. (1995) Tetrad user's manual, version 11.5, ADA International Consulting Ltd., Alberta, Canada.

Tracer Testing at Dixie Valley, Nevada, Using Pyrene Tetrasulfonate, Amino G, and Fluorescein

P.E. Rose¹, W.R. Benoit², and M.C. Adams¹

¹ Energy and Geoscience Institute, University of Utah,
423 Wakara Way, Salt Lake City, UT 84108

²Oxbow Power Services, Inc., 5250 S. Virginia St, Ste 304, Reno, Nevada 89502

ABSTRACT

A series of four tracer tests was recently conducted at the Dixie Valley, Nevada, geothermal reservoir in order to determine fluid-flow processes and to evaluate candidate tracers for use in hydrothermal systems. These tests have resulted in the first successful use of the compounds amino G and pyrene tetrasulfonate as tracers in a geothermal reservoir. The tracer candidates were first subjected to simulated hydrothermal conditions in laboratory reactors at temperatures as high as 300°C in order to determine their thermal stabilities. They were next injected as pulses into the target injection wells. Fluids from the surrounding production wells were then sampled and analyzed in order to determine injectate flow patterns. The tracer data indicate that injected fluids flow only to a cluster of production wells in the south-central portion of the field; no tracer was produced in the producers located in the northeast section of the reservoir. Tracer returns from fluids injected into one of the wells indicate a much shorter residence time and a more heterogeneous flow pattern than traced fluids from the other three injectors.

Introduction

With the increased use of injection in geothermal reservoir management strategies, tracer testing has become an increasingly important tool in determining flow patterns between wells. If injectors are positioned too close to producers, a risk of short circuiting develops, resulting in the possibility of premature thermal breakthrough. If injectors are placed too far away, the injected water will not provide sufficient pressure support to the reservoir. Since chemical breakthrough is more rapid than thermal breakthrough, a tracer test can provide important interwell flow data that can be used to optimize well placement and flow rates.

The main limitation to tracer testing in hydrothermal systems has been the limited number of tracers possessing a combination of good thermal stability, detectability, and

affordability. Due to their excellent detectability, fluorescent compounds have been used extensively as groundwater tracers. Until recently, however, fluorescein was the only fluorescent compound possessing sufficient thermal stability for intermediate-temperature (200-250°C) applications.

The first tracer testing at the Dixie Valley, Nevada, geothermal reservoir was conducted in 1989 (Adams et al., 1989; Benoit, 1992). These tests were largely unsuccessful, however, due to poor tracer detectability and an underestimation of the length of time required for tracer breakthrough. More recently, tracer testing was reinitiated at Dixie Valley for the purpose of demonstrating greatly enhanced fluorescent-tracer detectability, and of testing the viability of new fluorescent tracers in a well studied resource (Rose et al., 1997).

Recently, two new classes of fluorescent tracers, the polyaromatic sulfonates and the amino-substituted polyaromatic sulfonates, have been shown to possess excellent thermal stability upon exposure to simulated hydrothermal conditions in laboratory experiments (Rose and McPherson, 1997). In the current study, a compound from each category, pyrene tetrasulfonate and amino G, is used in combination with the well characterized companion dye, fluorescein, to characterize the flow patterns of water injected through four injection wells at the Dixie Valley hydrothermal system. The reservoir at Dixie Valley is an excellent laboratory for verifying the thermal stability of candidate tracers, since the 248°C brine temperature and long residence times of injected fluids provide an environment for challenging the most refractory fluorescent compounds.

Geologic Setting of Dixie Valley

The Dixie Valley geothermal field, located in west-central Nevada, is perhaps the classical hydrothermal system located along a narrow fault zone (Fig. 1). Dixie Valley is an asymmetric Basin and Range graben that is bounded on the

west by the Stillwater Range and on the east by the Clan Alpine Mountains. The geothermal field is located on the west side of the valley.

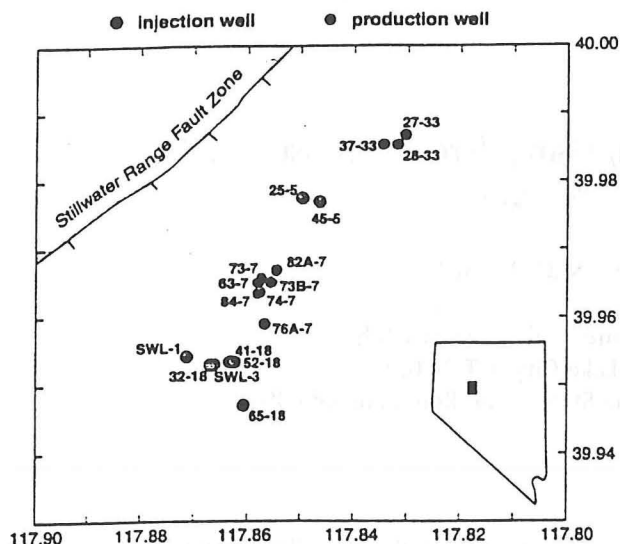


Figure 1. Wellhead locations at the Dixie Valley, Nevada, geothermal field.

Sibson (1977) and Chester and Logan (1986) developed a conceptual fault zone model consisting of a fault core and damage zone surrounded by relatively undeformed protolith (see also Caine et al., 1996). In any individual fault zone segment, the fault core and damage zone can be spatially heterogeneous, and either may be absent. Fault cores, which accommodate most of the fault displacement, typically consist of fine-grained gouge and cataclasite. Associated damage zones are typically faulted and fractured. Fractures and faults in the damage zone oriented subparallel to the main fault increase the permeability in the plane of the fault (Forster and Evans, 1991). As Caine et al. (1996) suggest, permeability in the fault core may be limited by the fine grain size, whereas it is the hydraulic properties of faults and fractures in the damage zone which control permeability there.

Production in the Dixie Valley geothermal field is defined primarily by fracture permeability associated with the Stillwater range-front fault and related secondary fractures or faults (Fig. 1). In the vicinity of the geothermal field, the Stillwater range-front fault is known to dip 52°-54° to the SE with a roughly planar geometry to depths of 3 km (Benoit, 1995). Most production wells produce up to 2,000 gpm from three to six individual fractures located between depths of 2500 and 3100 m (Hickman and Zoback, 1998). Injection is into three different environments (Benoit, 1992): an areally restricted basalt aquifer at a depth of 2225 m, the main fault zone at a depth of about 1860 m, and the deep fault zone between depths of 2700 and 2950 m.

Experimental Methods

The candidate tracers 7-amino-1,3-naphthalenedisulfonic acid, monosodium salt (amino G) and

1,3,6,8-pyrenetetrasulfonic acid, tetrasodium salt (PTSA) were tested for resistance to thermal degradation by subjecting them to autoclave conditions of temperature and pressure that simulate a geothermal reservoir (Rose and McPherson, 1997). The candidate compounds were dissolved in buffered aqueous solutions at a concentration of 25 ppm by weight and adjusted to a room-temperature pH of 6.5. The buffer consisted of 0.747 gm/l of KH_2PO_4 and 0.403 gm/l of Na_2HPO_4 .

Eighteen-ml aliquots of the buffered tracer solution were transferred to 30-ml quartz ampules and purged with argon to remove elemental oxygen. The ampules were carefully sealed using an oxymethane flame, while being purged with argon.

The sealed vials were transferred to a water-filled, one-liter autoclave (Autoclave Engineers, Philadelphia, PA), which was heated to the target temperature. The time required for the autoclave to attain operational temperature was between 1.5 and 2 hours, whereas the cool-down time was about 4 hours. In all cases, the interior of the reactor was maintained within 1°C of the target temperature for a duration of one week. The pressure inside the autoclave was the pressure of steam under saturated conditions at the target temperature.

The fluorescein samples were analyzed using a Perkin Elmer LS30 spectrofluorometer, with a detection limit of 10 parts per trillion. The spectrofluorometer was also used to obtain spectral scans of the reacted amino G and pyrene tetrasulfonate both for compound verification, as well as the identification of excitation and emission peak maxima.

A spectrofluorometer is generally inadequate for analyzing fluorescent compounds in solution with other fluorescent compounds, since excitation and emission bands often overlap. In addition, geothermal reservoir water contains significant interferences in the ultraviolet spectrum, which is the region employed for the analysis of naphthalene sulfonates and amino-naphthalene sulfonates. For analyzing amino G and pyrene tetrasulfonate, we used a High Performance Liquid Chromatograph (HPLC) with a fluorescence detector (Waters Corporation, Milford, MA). In order to take advantage of the high resolution of reverse-phase chromatography, we used a C18 column (e.g., Waters NovaPak 150 mm x 4.6 mm) and ion-pairing agents. The mobile phase consisted of a pH 7.5, phosphate-buffered, 5 Mmol solution of tetrabutyl ammonium phosphate (TBAP) in varying proportions of methanol and water. The use of this HPLC method allows for the chromatographic separation of analytes both from each other and from reservoir interferences.

From the laboratory studies described above, it was determined that amino G decays under high-temperature geothermal conditions to a stable fluorescent compound. Whereas this compound is not as fluorescent as amino G, it is nevertheless very stable, in that it was able to resist thermal degradation upon exposure to simulated geothermal conditions for one week at 295°C. We analyzed samples for the decay product of amino G using excitation and emission wavelengths of 220 and 350 nm, respectively. The mobile phase consisted of an isocratic, phosphate-buffered, 5Mmol solution of TBAP in 62.5% methanol and 37.5% water.

Pyrene tetrasulfonate also reacts to form a stable and very fluorescent product upon exposure to reservoir conditions for one week at 300°C. The analysis of pyrene tetrasulfonate was similar to that of the decay product of amino G. We used an isocratic, phosphate-buffered, 5Mmol TBAP mobile phase of 38.5% methanol and 61.5% water. A spectral scan revealed that the excitation and emission maxima for fluorescence were at 346 nm and 386 nm, respectively.

The Tracer Tests

The first tracer test was initiated on May 29, 1996 (Rose et al, 1997). One hundred seventy kg of a 50% by weight aqueous solution of uranine (the dipotassium salt of fluorescein) was mixed with 100 kg of amino G in a tank containing approximately 3000 kg of produced reservoir brine. The solution was pumped into injector 25-5 over a period of about 20 minutes. In the second test, 91kg of powdered uranine was added to well SWL-1 on July 15, 1997 over a period of about one hour. For the third test, 100 kg of powdered amino G was poured into well 65-18 on July 15, 1997 over a period of approximately one hour. In the fourth test, 1818 kg of a 10 wt% aqueous solution of pyrene tetrasulfonate was injected into well 45-5 on September 3, 1997 over a period of about 20 minutes. Ten production wells were sampled twice weekly throughout the tests.

Results and Discussion

Figure 2 shows the return curves for each of the four tracer tests. The mass fractions of amino G and pyrene tetrasulfonate are both shown in parts per billion, whereas the fluorescein results are plotted in parts per trillion. Based upon laboratory-determined decay kinetics (Adams and Davis, 1991), we estimate that approximately 90% of the fluorescein had decayed in the 248°C reservoir fluid by the time that the tracer first arrived at the production wells. In contrast, amino G and PTSA are both much more thermally stable, and, as a result, were produced at significantly higher concentrations.

Figure 2(a) shows the tracer return curves for the five production wells with the strongest responses from the first tracer test, in which fluorescein and amino G were injected into well 25-5. Only trace concentrations were measured at any of the remaining wells in section 7, and no tracer return was observed in the three section-33 wells. There was a small background fluorescence that was generally below about 10 parts per trillion. First arrival occurred about 90 days into the test, with the strongest returns to wells 73-7 and 73B-7. The next strongest returns were to wells 82A-7 and 63-7. No amino G was observed in any of the production wells, since the produced concentration was apparently below its detection limit of 500 parts per trillion.

Figure 2(b) shows the fluorescein returns to the section 7 wells during the second tracer test, in which fluorescein was injected into well SWL-1. This test was initiated 14 months after the previous injection of fluorescein into well 25-5. This long hiatus between the two tests allowed for the fluorescein

from the first test to decay within the reservoir before the subsequent use of fluorescein in the SWL-1 test.

As shown in Figure 2(b), the first arrival of fluorescein from SWL-1 to four of the section-7 producers occurred at about 30 days, a significantly shorter duration than the first arrival of tracer in any of the other tests. The peak fluorescein concentrations occurred at about 140-150 days into the test, which is also significantly earlier than the maxima for any of the three other tests. These data indicate that, among the four wells tested, the most rapid return of injectate to section 7 occurs via well SWL-1.

Figure 2(b) shows that injection well SWL-1 is most strongly connected to well 82A-7. In addition, the spikes within the 82A-7 return curve indicate the existence of three or four distinct fracture flow paths within a more homogeneously distributed set of fractures. Return from well SWL-1 to wells 76A-7, 73B-7, 63-7, and 84-7 is much more evenly distributed, with the tracer return to each being approximately half that observed for well 82A-7. Flow to well 74-7 from SWL-1 is relatively weak. Since injection-well SWL-1 is located within the southwest portion of the field, no connection was either expected or observed between it and the producers in section 33 in the northeast section of the field.

In the third test, amino G was injected into well 65-18 on the same day that fluorescein was injected into SWL-1. The returns of amino G are shown in Figure 2(c). The first arrival of tracer to section 7 occurred approximately 100 days after injection. The strongest return is to well 74-7, which showed only weak returns from the other tagged wells. Slightly weaker concentrations were measured in wells 63-7, 73-7, 76A-7, and 73B-7. Still weaker but significant tracer concentrations were measured in wells 82A-7 and 84-7. In general, flow of tracer to section 7 from 65-18 was observed to be much more delayed and more evenly distributed among the producers than flow of tracer from injector SWL-1.

Figure 2(d) plots the return curves of PTSA injected into well 45-5 during the fourth test. This is the first documented use of PTSA in either a groundwater or hydrothermal environment. The graph shows that the PTSA-tagged water follows a similar flow pattern to the fluorescein-tagged water that returned from well 25-5 a year earlier. This is not unreasonable since the completion intervals of the two injection wells are close together. The first arrival is at about 90 days, with the strongest return to well 73-7. The next strongest returns are to wells 73B-7 and 63-7, followed by 82A-7. No PTSA was observed in any of the section-33 wells.

Figure 3 shows the dominant flow patterns of the traced injection fluids for each of the four tracer tests. Each of the four smaller figures in Figure 3 shows a cross section of the reservoir along the Stillwater fault and through the completion intervals of the seven injection wells and ten production wells that were active either continuously or intermittently during the tracer tests. All of the wells are completed in close proximity to the Stillwater fault, with the notable exception of the shallow injection wells in section 18, wells SWL-1, SWL-3, and 32-18.

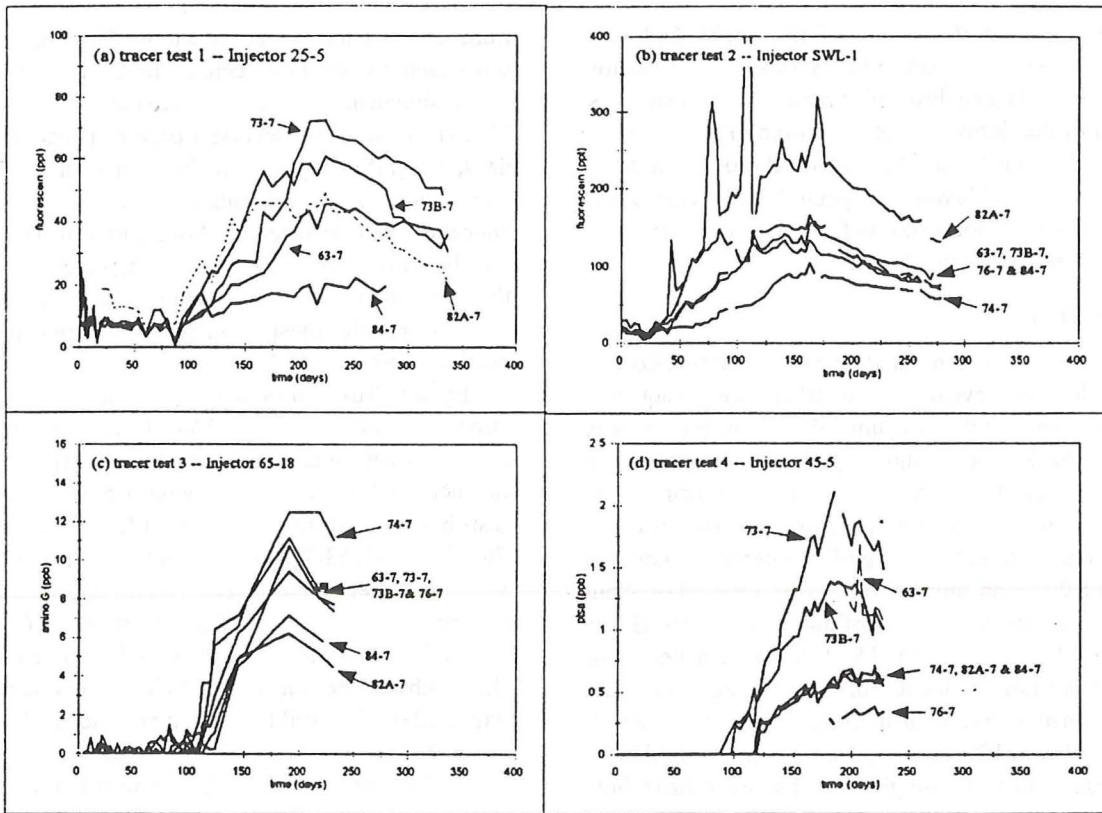


Figure 2. Return curves for the four tracer tests.

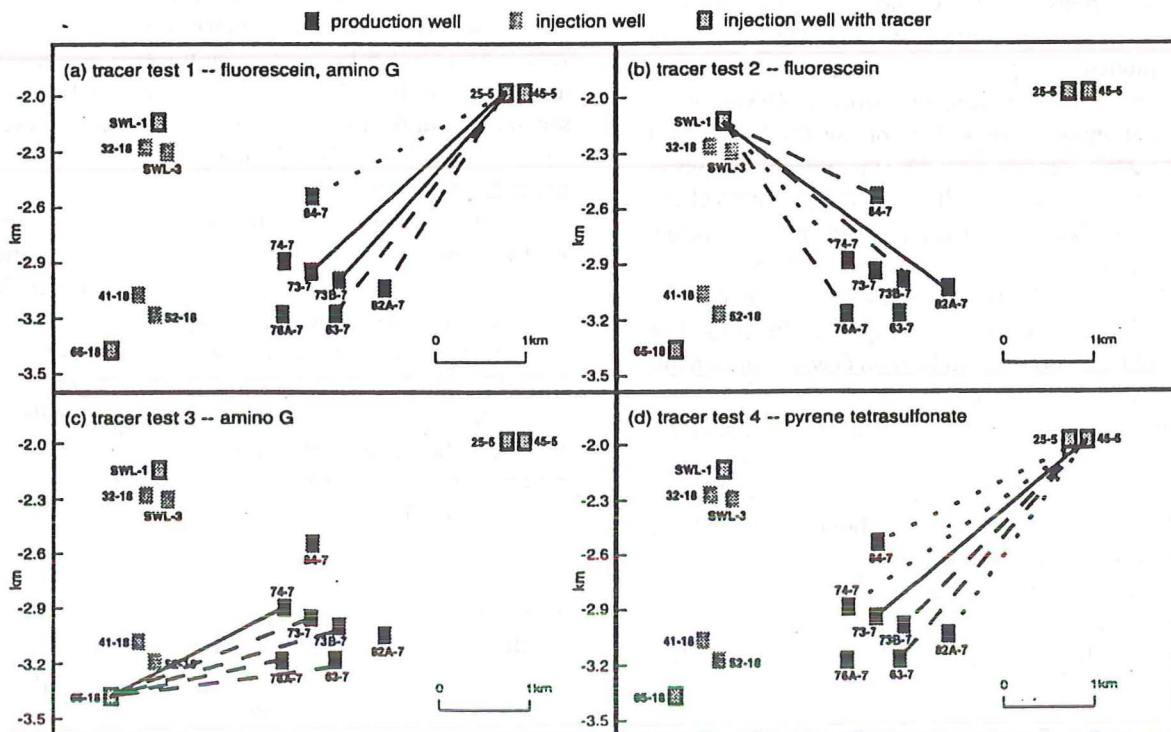


Figure 3. Schematic cross sections of the Dixie Valley reservoir along the Stillwater Fault zone showing the approximate completion intervals of the active wells. The lines connecting each tagged injector to various producers shows the relative tracer returns for the four tests. The relative strength of return for each tracer test is represented by the line type. A solid line represents the strongest return. The dashed line is intermediate, and the dotted line is the weakest.

These wells were completed within a basalt aquifer and out of the plane of the fault zone.

The relative strength of return for each tracer is represented by the line type. A solid line represents the strongest relative return, whereas the dashed line is of intermediate strength, and the dotted line is weakest. It is apparent that the flow pattern of fluid injected into 25-5, shown in Figure 3(a), is quite similar to the flow of fluid injected via well 45-5, shown in Figure 3(d). A likely interpretation is that the water from these two wells mixes in close proximity to the injectors and follows a common flow path towards the section-7 producers. In contrast, the two tagged injection wells in section 18 (SWL-1 and 65-18) have flow patterns that are almost mutually exclusive. Two of the production wells showing the highest return of tracer from injector SWL-1 (82A-7 and 84-7) were wells that produced no tracer from injector 65-18. Likewise, the three wells (63-7, 73-7, and 74-7) that produced very strong returns from 65-18 showed only modest returns from SWL-1. There were only two production wells, 73B-7 and 76A-7, that received moderate tracer returns from both SWL-1 and 65-18.

The return curve patterns in Figure 3 emphasize the heterogeneous nature of flow in a fractured medium. The production well that is closest to 25-5 is well 82A-7. It is therefore the well that might be expected to show the strongest and fastest tracer return. In contrast, it showed a relatively weak return during the first and fourth tracer tests. Even more striking is the anomalous flow pattern of tracer from injector SWL-1 in the second tracer test. The well that evidenced the strongest return was well 82A-7, whose completion interval is the farthest removed of all the section-7 producers. Likewise, the flow of tracer from 65-18 in the third test was strongest to well 74-7, whose completion interval is further removed from well 65-18 than well 76A-7, which showed a weaker return.

Summary and Conclusions

A series of tracer tests was conducted at the Dixie Valley, Nevada, geothermal reservoir, involving four injection and ten production wells. It was determined that the dominant flow pattern for all of the tagged injection fluid was towards the cluster of seven production wells in the south-central portion of the field. No tracer production was observed in the three producers at the northeast boundary of the reservoir, due, perhaps, to the fact that pressures in the northeast region are somewhat higher than those in the southwest part of the reservoir.

These tests document the first successful use of the fluorescent tracers amino G and pyrene tetrasulfonate in a hydrothermal system. With detection limits below one part per trillion and possessing excellent thermal stabilities, these compounds are now qualified for use in moderate-temperature (~250°C) hydrothermal systems. We are proceeding with laboratory and field experiments to determine the suitability of these and other polyaromatic sulfonates for use as tracers in high temperature (>300°C) hydrothermal environments.

Acknowledgments

This work was supported by the U.S. Department of Energy under contract number DE-HC07-90ID12929. Such support does not constitute an endorsement by the U.S. Department of Energy of the views expressed in this publication.

References

- Adams, M.C., Benoit, W.R., Doughty, C., Bodvarsson, G.S. and Moore, J.N. (1989), "The Dixie Valley, Nevada, tracer test," *Geothermal Resources Council Transactions*, 13, 215-220.
- Adams, M.C. and Davis, J. (1991), "Kinetics of fluorescein decay and its application as a geothermal tracer," *Geothermics*, 20(1-2), 53-60.
- Benoit, W.R. (1992), "A case history of injection through 1991 at Dixie Valley, Nevada," *Geothermal Resources Council Transactions*, 16, 611-620.
- Benoit, W.R. (1995), "Forced folding and basin and range geothermal systems," *Geothermal Resources Council Transactions*, 19, 155-163.
- Caine, J. S., Evans, J. P., and Forster, C. B. (1996), "Fault zone architecture and permeability structure," *Geology*, 24 (11), 1025-1028.
- Chester, F. M. and Logan, J. M. (1986), "Composite planar fabric of gouge from the Punchbowl fault, California," *Journal of Structural Geology*, 9, 621-634.
- Forster, C. B. and Evans, J. P. (1991), "Hydrogeology of thrust faults and crystalline thrust sheets: Results of combined field and modeling studies," *Geophysical Research Letters*, 18 (5), 979-982.
- Rose, P. E., Apperson, K. D., Johnson, S. D., and Adams, M. C. (1997), "Numerical simulation of a tracer test at Dixie Valley, Nevada," *Proceedings, Twenty-Second Workshop on Geothermal Reservoir Engineering*, Stanford University, January 27-29, 169-176.
- Rose, P.E. and McPherson, P.A. (1997), "New fluorescent tracers for use in geothermal reservoirs," *Geothermal Resources Council Transactions*, 21, 249-253.
- Sibson, R. H. (1977), "Fault rocks and fault mechanisms," *Geological Society of London Journal*, 133, 191-231.

()

()

()

TRACER TESTING AT DIXIE VALLEY, NEVADA, USING 2-NAPHTHALENE SULFONATE AND 2,7-NAPHTHALENE DISULFONATE

Peter E. Rose¹, Stuart D. Johnson², and Phaedra Kilbourn¹

¹Energy and Geoscience Institute at the University of Utah
423 Wakara Way suite 300
Salt Lake City, Utah, 84108

²Caithness Energy Corporation
9790 Gateway Drive suite 220
Reno, Nevada 89511

ABSTRACT

The decay kinetics of the candidate tracers 2-naphthalene sulfonate and 2,7-naphthalene disulfonate was studied under laboratory conditions that simulate a hydrothermal environment, with neither compound exhibiting any decay after one week at 330°C. These data indicate that these compounds are more thermally stable than any of the previously studied polyaromatic sulfonates. Both of the tracer candidates were successfully tested in a field study at the Dixie Valley, Nevada, geothermal reservoir. In addition to being environmentally benign, affordable and very thermally stable, these two compounds were shown to have excellent detection limits of approximately 200 parts per trillion by standard HPLC and fluorescence detection methods.

INTRODUCTION

The uv-fluorescent polyaromatic sulfonates are excellent candidates for geothermal tracing applications because they are environmentally benign, very detectable by fluorescence spectroscopy, affordable, and thermally stable. The first successful use of the polyaromatic sulfonates as geothermal tracers occurred in recent tracer tests at Dixie Valley (Rose *et al.*, 1998). 1,3,6,8-pyrene tetrasulfonate was shown to possess sufficient thermal stability for use in 300°C geothermal systems and to have a detection limit of approximately 200 parts per trillion. 1,5-naphthalene disulfonate has also been investigated in the laboratory and in the field and been shown to be suitable for groundwater environments (Rose, unpublished results), low-temperature geothermal reservoirs (Rose *et al.*, 1999) and high-temperature geothermal reservoirs (Rose *et al.*, 2000). Likewise, 1,3,6-naphthalene trisulfonate has been studied in the laboratory and the field and found to be useful for

high temperature geothermal applications (Rose *et al.*, 2000). In this paper, we report the laboratory and field study of two additional naphthalene sulfonate candidate tracers, 2-naphthalene sulfonate and 2,7-naphthalene disulfonate.

EXPERIMENTAL METHODS

2-naphthalene sulfonate and 2,7-naphthalene disulfonate, whose structural formulas are shown in Figure 1, were selected for study based upon commercial availability. Also shown in Figure 1 are three additional polyaromatic sulfonate compounds, 1,3,6,8-pyrene tetrasulfonate, 1,5-naphthalene disulfonate, and 1,3,6-naphthalene trisulfonate, which have recently been tested in the laboratory and the field and found to be viable geothermal tracers. The excitation and emission band maxima for each compound are listed in column 3, indicating that all fluoresce in the ultraviolet.

The naphthalene sulfonates were analyzed using High Performance Liquid Chromatography (HPLC) with fluorescence detection (Waters Corporation, Milford, MA). In order to take advantage of the high-resolution capability of a reverse-phase C-18 column (30 mm x 4.6 mm Keystone BetaBasic-18, 3 μ m), paired-ion chromatography (PIC) was employed. The mobile phase consisted of a pH-7.5, phosphate-buffered, 5 Mmol solution of tetrabutyl ammonium phosphate (TBAP) in 25% MeOH. This HPLC method allowed for the chromatographic separation of analytes both from each other and from reservoir interferences.

The decay kinetics of the five polyaromatic-sulfonate tracer candidates was studied using autoclave batch reactors under controlled conditions designed to simulate a geothermal environment. The compounds were dissolved in buffered aqueous solutions at target concentrations of 25 ppm by weight and adjusted to a

Compound	Structure	Excitation / Emission (nm)
2-naphthalene sulfonic acid		220 / 336
2,7-naphthalene disulfonic acid		226 / 339
1,5-naphthalene disulfonic acid		218 / 334
1,3,6-naphthalene trisulfonic acid		228 / 342
1,3,6,8-pyrene tetrasulfonic acid		346 / 386

Figure 1. Chemical names, structures, and excitation and emission band maxima for five polyaromatic sulfonates studied in the laboratory and in the field.

room-temperature pH of 6.5. The buffer consisted of 0.747 gm/l of KH_2PO_4 and 0.403 gm/l of Na_2HPO_4 .

Eighteen-ml aliquots of the buffered tracer solution were transferred to 30-ml quartz ampules and purged with argon to remove elemental oxygen. The ampules were carefully sealed using an oxymethane flame, while being purged with argon. For each experiment, four ampule-solutions were prepared: three samples and one control.

The sealed vials were transferred to a water-filled, one-liter autoclave (Autoclave Engineers, Philadelphia, PA), which was heated to the target temperature. The time required for the autoclave to attain operational temperature was between 1.5 and 2 hours, whereas the cool-down time was about 4 hours. In all cases, the interior of the reactor was maintained within 1°C of the target temperature for a duration of one week. The pressure inside the autoclave was the pressure of steam under saturated conditions at the target temperature. The control and was stored at 2°C for the duration of the autoclave experiment.

DECAY KINETICS OF THE POLYAROMATIC SULFONATES

No decay was observed for either 2-naphthalene sulfonate or 2,7-naphthalene disulfonate upon

exposure to simulated geothermal conditions for one week at 330°C . Other polyaromatic sulfonate tracers that have been evaluated for use as geothermal tracers, however, have been observed to decay considerably under comparable laboratory conditions (Rose *et al.*, 2000). For purposes of comparison, the decay kinetics of three less refractive polyaromatic sulfonates (1,3,6,8-pyrene tetrasulfonate, 1,3,6-naphthalene trisulfonate, and 1,5-naphthalene disulfonate) is summarized below.

The thermal decay kinetics of the polyaromatic sulfonates was modeled by the first-order differential equation:

$$-dC_n/dt = k_n \cdot C_n \quad (1)$$

where C_n is the concentration of naphthalene sulfonate and k_n is the first-order rate constant. Solution of this equation results in the following relationship between C_n and t :

$$\ln\left(\frac{C_n}{C_n^0}\right) = -k_n \cdot t \quad (2)$$

where C_n^0 is the initial concentration of polyaromatic sulfonate. The temperature dependence of k_n can be described by the Arrhenius relationship:

$$k_n = A e^{(-E_a/RT)} \quad (3)$$

where A is the pre-exponential factor, E_a is the energy of activation, R is the gas constant and T is absolute temperature. A linearization of the Arrhenius expression results in the following:

$$\ln k_n = \ln A - \frac{E_a}{RT} \quad (4)$$

Figure 2a shows Arrhenius plots of $\ln k_n$ vs. inverse temperature between 300°C and 330°C for the three compounds 1,5-naphthalene disulfonate, 1,3,6-naphthalene trisulfonate, and 1,3,6,8-pyrene tetrasulfonate. A fairly linear relationship between $\ln k_n$ and inverse temperature was observed for the three compounds, indicating that the Arrhenius equation provides a reasonably good means of expressing the temperature dependence of the decay rate constant.

Using the Arrhenius data, the half-lives of these three polyaromatic sulfonates were calculated as functions of temperature (Figure 2b). For comparison, the half-lives of two xanthene dyes that have been used as geothermal tracers, fluorescein and rhodamine WT, are also plotted. In addition, a curve representing the half-life vs. temperature relationship for 2-naphthalene sulfonate and 2,7-naphthalene

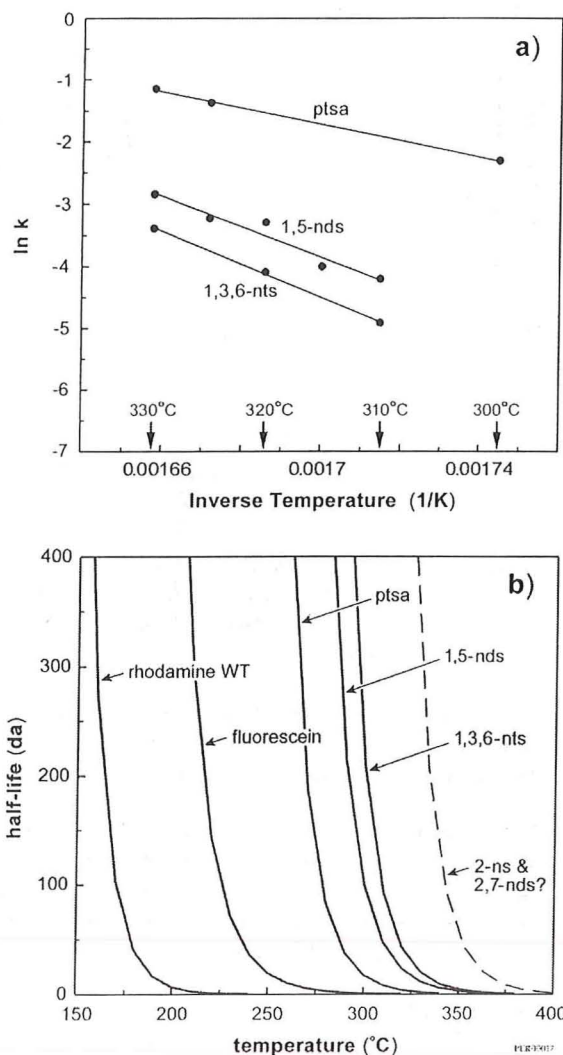


Figure 2. a) Arrhenius plots of $\ln(k)$ vs. inverse temperature between 300°C and 330°C for the three compounds 1,5-naphthalene disulfonate, 1,3,6-naphthalene trisulfonate and 1,3,6,8-pyrene tetrasulfonate. b) Plots of half-life vs. temperature based in part upon the Arrhenius plots shown in a).

disulfonate is included in Figure 4b. Obviously, this latter curve does not accurately reflect the thermal stability of these two compounds, since these data are not known. It is intended only to indicate that they are somewhat more thermally stable than the other compounds studied.

TRACER TESTING AT DIXIE VALLEY

The Dixie Valley geothermal field, located in west-central Nevada, is perhaps the classical hydrothermal system located along a narrow fault zone (Figure 3). Dixie Valley is an asymmetric Basin and Range graben that is bounded on the west by the Stillwater

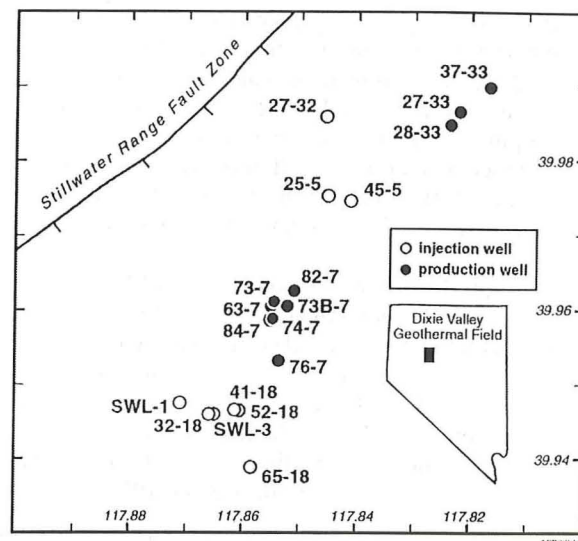


Figure 3. A plan view of the Dixie Valley geothermal reservoir, showing the injection and production wellhead locations.

Range and on the east by the Clan Alpine Mountains. The geothermal field is located on the west side of the valley. For a review of conceptual, structural and numerical models of the Dixie Valley hydrothermal system see Benoit (1999).

Sibson (1977) and Chester and Logan (1986) developed a conceptual fault zone model consisting of a fault core and damage zone surrounded by relatively undeformed protolith (see also Caine *et al.*, 1996). In any individual fault zone segment, the fault core and damage zone can be spatially heterogeneous, and either may be absent. Fault cores, which accommodate most of the fault displacement, typically consist of fine-grained gouge and cataclaste. Associated damage zones are typically faulted and fractured.

Fractures and faults in the damage zone oriented subparallel to the main fault increase the permeability in the plane of the fault (Forster and Evans, 1991). As Caine *et al.* (1996) suggest, permeability in the fault core may be limited by the fine grain size, whereas it is the hydraulic properties of faults and fractures in the damage zone which control permeability there.

Until recently, the prevailing structural model for interpreting flow patterns within the Dixie Valley geothermal field was based upon a single range-front fault dipping 52°-54° to the SE with a roughly planar geometry to depths of 3 km (Benoit, 1995). According to this model, it was assumed that production is controlled primarily by fracture permeability associated with this range-front fault and its related secondary fractures or faults.

A recent study based primarily upon Bouguer gravity data suggests a more complex model with a steep-dipping range front fault that accommodates most of the topographic displacement and a series of steep-dipping piedmont faults that account for most of the displacement at depth within the reservoir (Blackwell *et al.*, 1999). According to this model, the reservoir is primarily associated with the piedmont faults.

Most production wells produce up to 125 kg/sec from three to six individual fractures located between depths of 2500 and 3100 m (Barton *et al.*, 1998). Injection is into three different environments: an areally restricted basalt aquifer at a depth of approximately 2225 m, the main fault zone at a depth of about 1860 m, and the deep fault zone between depths of 2700 and 2950 m (Benoit, 1992).

The first tracer tests at the Dixie Valley, Nevada, geothermal reservoir were conducted in 1989 (Adams *et al.*, 1989; Benoit, 1992). These tests were largely unsuccessful, however, due to poor tracer detectability and an underestimation of the length of time required for tracer breakthrough.

A series of tracer tests was conducted at Dixie Valley between 1996 and 1999 using fluorescein, 7-amino-1,3-naphthalene disulfonate (amino G), 1,3,6,8-pyrene tetrasulfonate (Rose *et al.*, 1997; Rose, 1998; Rose *et al.*, 1998) and 1,5-naphthalene disulfonate and 1,3,6-naphthalene trisulfonate (Rose *et al.*, 2000). Two tests using 2-naphthalene sulfonate and 2,7-naphthalene disulfonate that were initiated in 1999 are reported here.

On 17 November, 1999, 198 kg of 2,7-naphthalene disulfonate (Yick-Vic Chemicals, Hong Kong) was slurried with approximately 400 liters of flashed reservoir water and injected over a period of about 4 minutes into well 27-32 (see Figure 3). Water was continuously injected into the well at a rate of approximately 70 kg/sec. Similarly, on 18 November, 1999, 199 kg of 2-naphthalene sulfonate (Yick-Vic Chemicals, Hong Kong) was dissolved into approximately 400 liters of flashed reservoir water and injected over a period of 2 minutes into injector 25-5 (see Figure 3), which was flowing at a rate of approximately 310 kg/sec. All of the producing wells in the field were subsequently monitored for the two naphthalene sulfonates over the subsequent year.

The return curves for the candidate tracer 2,7-naphthalene disulfonate that was injected into well 27-32 are plotted in Figure 4. These return curves show tracer production in three producers in section 33 only, as no tracer was observed in any of the production wells monitored further to the southeast in section 7. This represents the first observation of tracer production ever to section 33. The tracer first arrived to two producers (28-33 and 37-33)

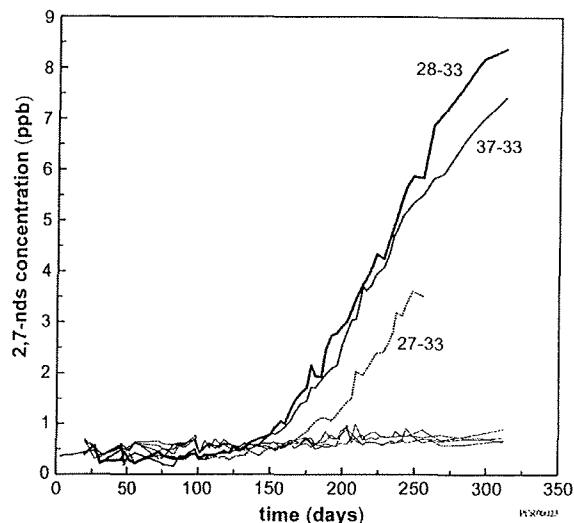


Figure 4. 2,7-naphthalene disulfonate returns observed from the testing of injector 27-32 at the Dixie Valley geothermal reservoir.

approximately 135 days after tracer injection. This is the longest duration before first arrival of tracer in any tracer tests conducted at Dixie Valley.

The return curves for the candidate tracer 2-naphthalene sulfonate that was injected into well 25-5 are plotted in Figure 5. These return curves show tracer production in all of the operating producers in section 7 except well 76A-7 (see Figure 3). No tracer was observed in any of the production wells monitored further to the northeast in section 33. The tracer first arrived to two producers, 63-7 and 73B-7, approximately 100 days after tracer injection.

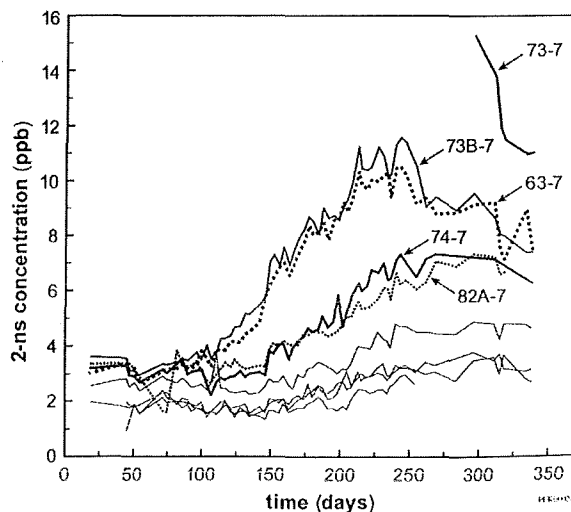


Figure 5. 2-naphthalene sulfonate returns observed from the testing of injector 25-5 at the Dixie Valley geothermal reservoir.

Shown in the plot of return curves of 2,7-naphthalene disulfonate (see Figure 4) is a significant background concentration of approximately 0.5 ppb in all of the wells monitored during the test. The identity of this background contaminant is not known, although it is possible that it is 2,7-naphthalene disulfonate, which was created as either an isomerization product or partial decomposition product of other naphthalene sulfonates injected in previous tracer tests.

As shown in Figure 5, there is also a significant background concentration between approximately 2 ppb and 3.8 ppb of an apparent contaminant that is chromatographically indistinguishable from 2-naphthalene sulfonate. The identity of this compound is not known, but it is possible that it is either 2-naphthalene sulfonate or a similar compound that co-elutes with 2-naphthalene sulfonate.

Neither 2,7-naphthalene disulfonate nor 2-naphthalene sulfonate had ever been used as tracers at Dixie Valley. The existence of strong background contaminant concentrations is therefore somewhat troubling. Since all of the water produced at the Dixie Valley reservoir is reinjected, however, conservative tracers such as the naphthalene sulfonates remain in the reservoir until they leak into surrounding aquifers. And, due to a management scheme that (until recently) produced more fluid than was reinjected, the main production areas are underpressured relative to the injection zones, resulting in very little leakage into surrounding aquifers. Therefore, conservative tracers tend to remain in solution in the reservoir for a long time.

In addition to the candidate tracers 2-naphthalene sulfonate and 2,7-naphthalene disulfonate reported here, 1,5-naphthalene disulfonate, 1,3,6-naphthalene trisulfonate, 1,3,6,8-pyrene tetrasulfonate, and the amino-substituted naphthalene disulfonate, amino G, were also recently tested. Therefore, the background concentrations could possibly be attributed to a combination of isomerization and/or partial decomposition of a number of polyaromatic sulfonates and an amino-substituted naphthalene disulfonate tested at the Dixie Valley reservoir over the past few years. This illustrates the risk of using conservative tracers in reservoirs where all of the produced fluids are reinjected and where there is very little natural fluid leakage into surrounding aquifers. If the background tracer concentration is relatively constant, however, tracer pulses can nevertheless be detected above the background, as illustrated in figures 4 and 5.

CONCLUSIONS

The naphthalene sulfonates show excellent potential for use as tracers in geothermal reservoirs. In addition to being environmentally benign and very affordable,

these fluorescent compounds have detection limits of approximately 200 parts per trillion.

A decay kinetics study of the candidate tracers 2-naphthalene sulfonate and 2,7-naphthalene disulfonate revealed that neither compound showed any decay after being exposed for one week to simulated geothermal conditions at 330°C, indicating that they are the most stable organic tracers tested to date.

A tracer test at the Dixie Valley geothermal reservoir using 2-naphthalene sulfonate confirms that water injected in well 25-5 flows toward the main production area in section 7. Similarly, a tracer test using 2,7-naphthalene disulfonate revealed that water injected into the recently drilled well 27-32 flows to the section-33 producers. This is the first tracer confirmation of injectate flowing to section 33 in the Dixie Valley reservoir.

ACKNOWLEDGEMENTS

We thank Caithness Energy Corporation (formerly Oxbow Power Services) for their participation in this project. Their support in providing access to the Dixie Valley reservoir and in conducting the field tests has been essential for the successful testing of these candidate tracers. We also acknowledge the continued support of the Department of Energy (under contract number DE-HC07-90ID12929), without which this project could not have been accomplished. Such support does not constitute an endorsement by the U.S. Department of Energy of the views expressed in this publication.

REFERENCES

- Adams, M.C., Benoit, W. R., Doughty, C., Bodvarsson, G.S. and Moore, J.N. (1989), AThe Dixie Valley, Nevada, tracer test, @ *Geothermal Resources Council Transactions*, 13, 215-220.
- Barton, C.A., Hickman, S., Morin, S., Zoback, M.D., and Benoit, W.R. (1998) "Reservoir-scale fracture permeability in the Dixie Valley, Nevada, geothermal field," *Proceedings, Twenty-Second Workshop on Geothermal Reservoir Engineering*, Stanford Geothermal Program Workshop Report SGP-TR-158, 299-306.
- Benoit, W.R. (1992), AA case history of injection through 1991 at Dixie Valley, Nevada, @ *Geothermal Resources Council Transactions*, 16, 611-620.
- Benoit, W.R. (1995), "Forced folding and basin and range geothermal systems," *Geothermal Resources Council Transactions*, 19, 155-163.



TRACER TESTING AT DIXIE VALLEY, NEVADA USING 1-NAPHTHALENE SULFONATE AND 2,6-NAPHTHALENE DISULFONATE

Peter E. Rose¹, Stuart D. Johnson², Phaedra Kilbourn¹, and Christian Kasteler¹

¹Energy and Geoscience Institute at the University of Utah
423 Wakara Way suite 300
Salt Lake City, Utah, 84108

²Caithness Energy Corporation
9790 Gateway Drive suite 220
Reno, Nevada 89511

ABSTRACT

The decay kinetics of the candidate tracers 1-naphthalene sulfonate and 2,6-naphthalene disulfonate was studied under laboratory conditions that simulate a hydrothermal environment. Neither of the naphthalene sulfonates exhibited any thermal decay after one week at 330°C, indicating that they are suitable for use in geothermal settings having temperatures of 330°C or hotter. Both tracers were successfully tested in a field study at the Dixie Valley, Nevada geothermal reservoir. In addition to being environmentally benign, affordable and very thermally stable, these two compounds were shown to have excellent detection limits of less than 0.1 ppb by standard HPLC and fluorescence detection methods. Currently, six naphthalene sulfonates have been tested for use as geothermal tracers. A detailed method for the simultaneous HPLC analysis of all six is presented.

INTRODUCTION

The uv-fluorescent polyaromatic sulfonates have proven to be excellent tracers in high temperature geothermal reservoirs because they are environmentally benign, very detectable by fluorescence spectroscopy, affordable, and thermally stable. The first successful use of the polyaromatic sulfonates as geothermal tracers involved 1,3,6,8-pyrene tetrasulfonate at the Dixie Valley geothermal system in west-central Nevada, USA (Rose *et al.*, 1998).

The naphthalene sulfonates, a subset of the polyaromatic sulfonates, have been used extensively as tanning agents, cement dispersants, and intermediates in the synthesis of dyes. Studies on surfactant toxicity indicate that the naphthalene

sulfonates are neither carcinogenic nor mutagenic (Greim *et al.*, 1994). We have studied six naphthalene sulfonates (see Figure 1) in the laboratory and have found them to be suitable for use as conservative tracers in high temperature (>300°C) reservoirs (Rose *et al.*, 2001). Field tests in a number of geothermal reservoirs with temperatures up to 250°C further confirm the long-term stability of these chemicals (Rose *et al.*, 2001). The excitation and emission peak maxima for each compound are listed in column 3, indicating that all fluoresce in the ultraviolet.

In this paper we summarize data on the thermal stability of the naphthalene sulfonates, and provide details of their analysis in the laboratory. We then present some results of a recent tracer test at the Dixie Valley, Nevada geothermal field that further confirms the utility of these chemicals in a well characterized geothermal system.

HPLC ANALYSIS OF THE NAPHTHALENE SULFONATES

The naphthalene sulfonates were analyzed using High Performance Liquid Chromatography (HPLC) with fluorescence detection (Waters Corporation, Milford, MA). HPLC allows for the separation of the polyaromatic sulfonates not only from each other but also from interferences that occur naturally in the reservoir. Using HPLC, any number of polyaromatic sulfonate tracers can, in principle, be analyzed in each other's presence.

In HPLC, high resolution means that compounds can be efficiently separated from each other. In order to take advantage of the high-resolution capability of a reverse-phase C-18 column (e.g., 50 mm x 4.6 mm Keystone BetaBasic-18, 3 µm), paired-ion chromatography (PIC) was employed.

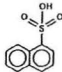
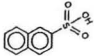
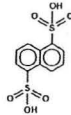
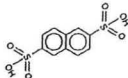
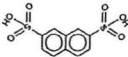
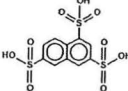
Compound	Structure	Excitation / Emission (nm)
1-naphthalene sulfonic acid		217 / 333
2-naphthalene sulfonic acid		220 / 336
1,5-naphthalene disulfonic acid		218 / 334
2,6-naphthalene disulfonic acid		225 / 342
2,7-naphthalene disulfonic acid		226 / 339
1,3,6-naphthalene trisulfonic acid		228 / 342

Figure 1. Chemical names, structures, and excitation and emission band maxima of six naphthalene sulfonate geothermal tracers studied in the laboratory and in the field.

Using PIC reagents in the mobile phase, the very anionic polyaromatic sulfonates are 'paired' in solution with polar cations, or, in our case, tetrabutyl ammonium phosphates. The pairing of negatively charged compounds with positively charged compounds creates neutral, nonpolar compounds with pendant *n*-butyl chains. Those alkyl chains then are free to interact with the stationary C-18 chains as they flow through the column. It is the interaction of the paired nonpolar *n*-butyl chains with the stationary nonpolar C-18 stationary phase that allows for the separation of the polyaromatic sulfonates one from another.

The mobile phase consisted of a phosphate-buffered solution of tetrabutyl ammonium phosphate (TBAP) in various proportions of methanol. The higher the proportion of methanol in the mobile phase, the faster the neutral ion-pairs elute from the column. Through trial and error, the proportion of methanol to water can be optimized to allow for the efficient separation and subsequent simultaneous analysis of several polyaromatic sulfonate tracers.

The excitation and emission peak maxima are shown in Figure 1. These are the detector settings required for the greatest sensitivity for each compound. If the detector cannot be programmed for each analyte's wavelength pair individually, then it is possible to obtain reasonable sensitivity in the simultaneous

analysis of all six naphthalene sulfonates by using an excitation setting of 222 nm and an emission setting of 338 nm. Obviously, the compounds 1,3,6-naphthalene trisulfonate, which has an excitation peak maximum at 228 nm, and 1-naphthalene sulfonate, which has an excitation peak maximum at 217 nm, are the two compounds whose sensitivity would be most effected. For maximum sensitivity, each compound can be analyzed separately, using the appropriate wavelengths for each.

In order to protect the column, all samples should be filtered. We have found that a 0.45- μm Whatman cellulose nitrate membrane filter is adequate for most brines. Columns occasionally deteriorate, regardless of sample and mobile phase filtering. As a means of prolonging column life, we recommend a thorough rinse after analyzing a set of samples and before shutting down the pump. The composition of the rinsate should resemble that of the mobile phase without salts (e.g., 25% *meOH* and 75% water). In most cases, a rinse time of approximately 45 min is adequate. If, over time, peak shapes deteriorate and backpressure increases, it may mean that the column is partially plugged. It may be possible to clean the column by back flushing a 50% methanol/50% water mix at a high flow rate, holding the column temperature constant at 55°C.

With isocratic liquid chromatography, the composition of the mobile phase remains constant throughout each chromatographic analysis. With gradient liquid chromatography, however, the composition of the mobile phase is varied during the run, allowing for an optimization of the mobile phase composition over time.

The six naphthalene sulfonates shown in Figure 1 can be separated isocratically using a 50-mm reverse phase C-18 column as described above in combination with an appropriate guard column. Figure 2 shows an isocratic chromatogram of the six analytes with a mobile phase consisting of 20% HPLC-grade methanol and 80% HPLC-grade water. The injection volume was 200 μl and the flow rate of the mobile phase was maintained at 2.5 ml/min. The concentrations of Na_2HPO_4 and KH_2PO_4 in the mobile phase were 3.17 mM and 6.21 mM respectively and the concentration of the TBAP ion-pairing agent was 5.0 mM. Using these concentrations of salts, the pH of the mobile phase was about 6. The mobile phase was filtered through a 0.45- μm nylon filter. The column temperature was constant at 35°C. The column backpressure was approximately 2800 psi.

The long run time shown in Figure 2 was required, since the 1,3,6-naphthalene trisulfonate contained fluorescent contaminants (possibly isomers of 1,3,6-naphthalene trisulfonate) that had to be eluted before

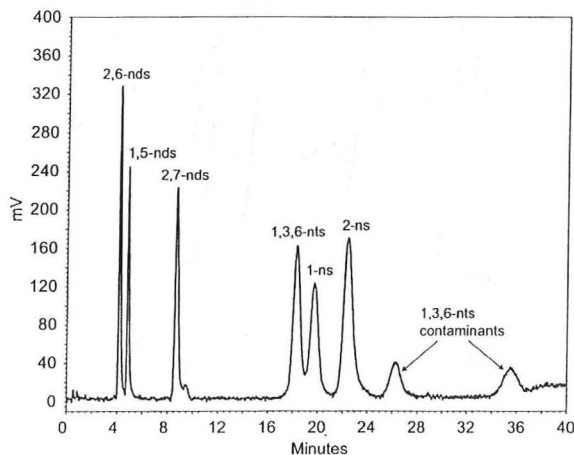


Figure 2. Chromatogram of six naphthalene sulfonate analytes obtained using an isocratic method.

a subsequent injection. An even longer run time would be required to obtain baseline separation between 1,3,6-naphthalene trisulfonate and 1-naphthalene sulfonate. Such long run times require large volumes of mobile-phase solvents and result in poorer resolution and lower sensitivity due to peak broadening.

Using gradient chromatography, however, it is possible to reduce the run time from 40 minutes to less than 10 minutes, as shown by the chromatogram in Figure 3. The first mobile phase consisted of a solution of 3.17 mM Na_2HPO_4 , 6.21 mM KH_2PO_4 , and 5.0 mM TBAP in 25%/75% methanol/water. The second mobile phase consisted of the same concentrations of salts in 30%/70% methanol/water. Each mobile phase was filtered through a 0.45- μm nylon filter. The pH of each mobile phase was naturally about 6.

The chromatogram in Figure 3 was obtained by first flowing phase one at a rate of 2.5 ml/min. At 2.25 minutes into the run, a control valve switched mobile phases from phase one to phase two, allowing phase two to flow through the column for the next five minutes. At 7.25 minutes into the run, the control valve switched back to phase one for the remaining 2.25 minutes of the analysis, for a total run time of 10 minutes. The column temperature was constant at 35°C. The maximum backpressure was approximately 2800 psi.

Using the gradient method, the two 1,3,6-naphthalene trisulfonate contaminants now elute before and after 1-naphthalene sulfonate, respectively. With a run time that is only one fourth as long as required by the

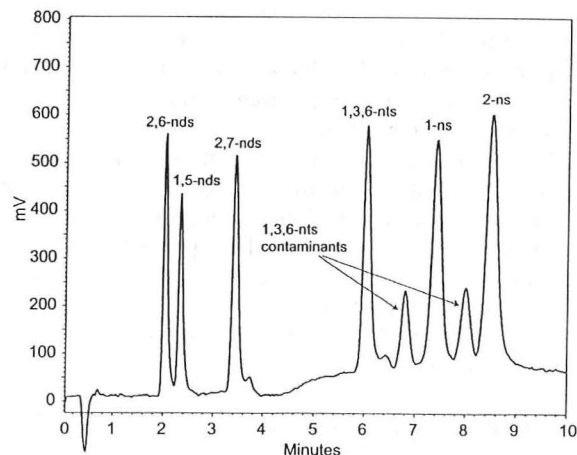


Figure 3. Chromatogram of six naphthalene sulfonate analytes obtained using a gradient method.

isocratic method, only one fourth of the mobile phase solvent volume is likewise required. In addition, the resolution is improved.

Larger injection volumes result in lower detection limits, since, for a given concentration, larger injection volumes result in more analyte flowing through the detector flow cell. Lower detection limits allow for a reduction in the mass of tracer required to achieve measurable breakthrough. It is therefore preferable to use the largest injection volume that the instrument and the chromatographic conditions will allow. Using an injection volume of 200 μl with the conditions described above, the detection limit of each of the naphthalene sulfonates was less than 0.1 ppb. By optimizing the detector excitation and emission wavelengths for each tracer, the detection limits can be reduced even further.

DECAY KINETICS OF 1-NAPHTHALENE SULFONATE AND 2,6-NAPHTHALENE DISULFONATE

The decay kinetics of the two naphthalene-sulfonate tracer candidates was studied using autoclave batch reactors under controlled conditions designed to simulate a geothermal environment. The compounds were dissolved in buffered aqueous solutions at target concentrations of 25 ppm by weight and adjusted to a room-temperature pH of 6.5. The buffer consisted of 0.747 gm/l of KH_2PO_4 and 0.403 gm/l of Na_2HPO_4 .

Eighteen-ml aliquots of the buffered tracer solution were transferred to 30-ml quartz ampules and purged with argon to remove elemental oxygen. The ampules were carefully sealed using an oxymethane flame, while being purged with argon. For each experiment, four ampule-solutions were prepared: three samples and one control.

The sealed vials were transferred to a water-filled, one-liter autoclave (Autoclave Engineers, Philadelphia, PA), which was heated to the target temperature. The time required for the autoclave to attain operational temperature was between 1.5 and 2 hours, whereas the cool-down time was about 4 hours. In all cases, the interior of the reactor was maintained within 1°C of the target temperature for a duration of one week. The pressure inside the autoclave was the pressure of steam under saturated conditions at the target temperature. The control and was stored at 2°C for the duration of the autoclave experiment.

No decay was observed for either 1-naphthalene sulfonate or 2,6-naphthalene disulfonate upon exposure to simulated geothermal conditions for one week at 330°C. Other naphthalene sulfonate tracers that have been evaluated for use as geothermal tracers, however, have been observed to decay considerably under comparable laboratory conditions (Rose *et al.*, 2001). The less stable fluorescent compounds appear to decay according to the first-order differential equation:

$$-dC_n/dt = k_n \cdot C_n \quad (1)$$

where C_n is the concentration of naphthalene sulfonate and k_n is the first-order rate constant. Solution of this equation results in the following relationship between C_n and t :

$$\ln\left(\frac{C_n}{C_n^0}\right) = -k_n \cdot t \quad (2)$$

where C_n^0 is the initial concentration of polyaromatic sulfonate. The temperature dependence of k_n can be described by the Arrhenius relationship:

$$k_n = Ae^{(-E_a/RT)} \quad (3)$$

where A is the pre-exponential factor, E_a is the energy of activation, R is the gas constant and T is absolute temperature.

By solving for the Arrhenius rate constant coefficients, it is possible to determine the half-life vs. temperature for each compound (see Figure 4). The dotted line approximates half-life data for the two compounds 1-naphthalene sulfonate and 2,6-naphthalene disulfonate, which are the object of this study, as well as two other compounds, 2-naphthalene sulfonate and 2,7-naphthalene disulfonate that have been recently studied. We suspect that these compounds are sufficiently stable to be suitable for use in geothermal reservoirs with fluid temperatures of 330°C or hotter. Also shown for

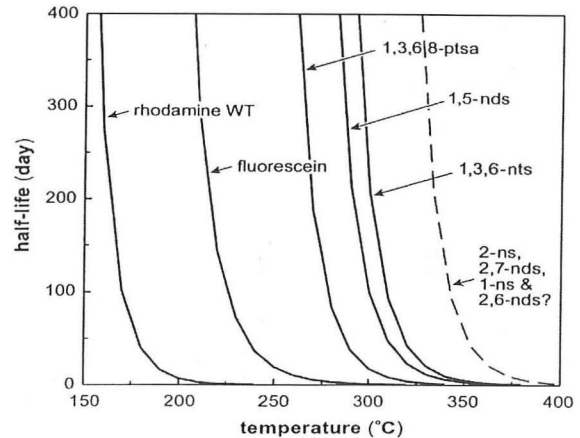


Figure 4. Plots of half-life vs. temperature for several polyaromatic sulfonate tracers as well as for two xanthene dyes as determined from decay kinetics data measured at EGI.

comparison in Figure 4 are the half-life vs. temperature plots for the two xanthene dyes fluorescein and rhodamine WT, as well as the polyaromatic sulfonate 1,3,6,8-pyrene tetrasulfonate.

TRACER TESTING AT DIXIE VALLEY

The Dixie Valley geothermal field, located in west-central Nevada, is perhaps the classical hydrothermal system located along a narrow fault zone (Figure 5). Dixie Valley is an asymmetric Basin and Range graben that is bounded on the west by the Stillwater Range and on the east by the Clan Alpine Mountains. The geothermal field is located on the west side of the valley. For a review of conceptual, structural and numerical models of the Dixie Valley hydrothermal system see Benoit (1999).

Extensive tracer testing has been conducted over the past several years at Dixie Valley using the polyaromatic sulfonates. These tests have served to verify the laboratory studies that were conducted to predict the field performance of these tracers (Rose *et al.*, 2001).

On July 10, 2001, 143 kg of 1-naphthalene sulfonate (Yick-Vic Chemicals, Hong Kong) was injected into well 45-5, which was flowing at approximately 100 kg/sec. Similarly, on July 10, 2001, 150 kg of 2,6-naphthalene disulfonate (Yick-Vic Chemicals, Hong Kong) was injected into the recently drilled well 38-32, which was flowing at a rate of approximately 110 kg/sec. All of the producing wells in the field were subsequently monitored for the two naphthalene sulfonates over the subsequent six months.

The return of the candidate tracer 2,6-naphthalene disulfonate that was injected into well 38-32 is plotted in Figure 6. These return curves show tracer

production in section 33 only, as no tracer was observed in any of the production wells monitored further to the southwest in section 7. This flow pattern is similar to the one observed from tracer testing of the nearby well 27-32 that was initiated in November 1999 (Rose *et al.*, 2001).

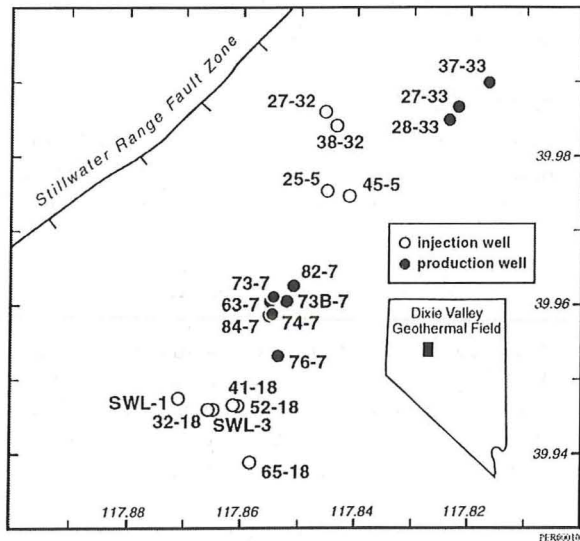


Figure 5. A plan view of the Dixie Valley geothermal reservoir, showing the injection and production wellhead locations.

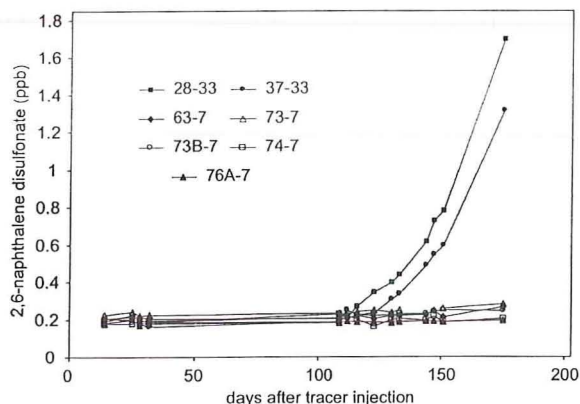


Figure 6. 2,6-naphthalene disulfonate returns observed from the testing of injector 38-32 at the Dixie Valley geothermal reservoir.

The returns of the candidate tracer 1-naphthalene sulfonate that was injected into well 45-5 are plotted in Figure 7. These return curves show tracer breakthrough in the operating producers in section 7 (see Figure 5). No tracer was observed in any of the production wells monitored further to the northeast in section 33. These curves are very similar to those observed from a September, 1997 test of injector 45-5 using pyrene tetrasulfonate (Rose *et al.*, 1998).

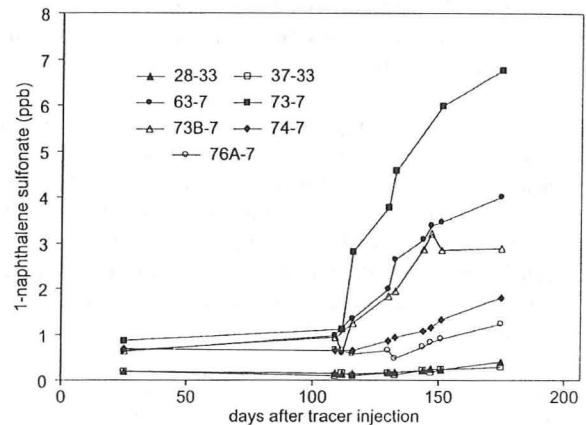


Figure 7. 1-naphthalene sulfonate returns observed from the tracer testing of injector 45-5 at the Dixie Valley geothermal reservoir.

Shown in the plot of the 2,6-naphthalene disulfonate return curves (Figure 6) is a slight background concentration of approximately 0.2 ppb in all of the wells monitored during the test. Likewise, in the plot of the 1-naphthalene sulfonate return curves (Figure 7), there is a background concentration as high as 1 ppb of an apparent contaminant that is chromatographically indistinguishable from 1-naphthalene sulfonate. The identity and origin of these compounds is not known, but it is likely that they were introduced as contaminants during previous tracer tests at Dixie Valley (Rose *et al.*, 2001). It is also possible they were created in the reservoir as either isomerization products or partial decomposition products, again from tracers introduced during those previous tests.

Since essentially all of the water produced at the Dixie Valley reservoir is reinjected, conservative tracers such as the naphthalene sulfonates remain in the reservoir until they leak into surrounding aquifers. And, due to a management scheme that (until recently) produced more fluid than was reinjected, the main production areas are underpressured relative to the injection zones, resulting in very little leakage into surrounding aquifers. Therefore, conservative tracers tend to remain in solution in the reservoir for a long time. This illustrates the risk of using conservative tracers in reservoirs where all of the produced fluids are reinjected and where there is very little natural fluid leakage into surrounding aquifers. If the background tracer concentration is relatively constant, however, tracer pulses can easily be detected above the background, as illustrated in figures 6 and 7, allowing for some reuse of conservative tracers.

CONCLUSIONS

The naphthalene sulfonates show excellent potential for use as tracers in geothermal reservoirs. In addition

to being environmentally benign and very affordable, these fluorescent compounds have detection limits less than 0.1 ppb.

Six of the naphthalene sulfonates can be simultaneously analyzed using either isocratic or gradient HPLC methods. A gradient method was shown to provide for baseline separation between the six compounds with a run time less than 10 minutes. An isocratic method could also be used to separate and analyze all six, but the run time was increased to 38 minutes.

A decay kinetics study of the candidate tracers 1-naphthalene sulfonate and 2,6-naphthalene disulfonate revealed that neither compound showed any decay after being exposed for one week to simulated geothermal conditions at 330°C, indicating that they are among the most stable organic tracers tested to date.

A tracer test at the Dixie Valley geothermal reservoir served to confirm the laboratory predictions of both excellent detectability and excellent thermal stability of the candidate tracers 1-naphthalene sulfonate and 2,6-naphthalene disulfonate. Returns of 1-naphthalene sulfonate injected in well 45-5 indicate flow toward the main production area in section 7. Similarly, returns of 2,6-naphthalene disulfonate revealed that water injected into the recently drilled well 38-32 flows to the section-33 producers.

ACKNOWLEDGEMENTS

We thank Caithness Energy for their participation in this project. Their support in providing access to the

Dixie Valley reservoir and in conducting the field tests has been essential for the successful testing of these candidate tracers. We also acknowledge the continued support of the Department of Energy (under contract number DE-HC07-90ID12929), without which this project could not have been accomplished. Such support does not constitute an endorsement by the U.S. Department of Energy of the views expressed in this publication.

REFERENCES

- Benoit, W.R. (1999), "Conceptual models of the Dixie Valley, Nevada geothermal system," *Geothermal Resources Council Transactions*, 23, 505-511.
- Greim H., Ahlers, R., Bias, R., Broecker, B., Hollander, H., Gelbke, H.P., Klimisch, H.J., Mangelsdorf, I., Paetz, A., Schon I., Stropp, G., Vogel, R., Weber, C., Ziegler-Skylakakis, K., and Bayer, E. (1994) Toxicity and Ecotoxicity of Sulfonic Acids: Structure-Activity Relationship: *Chemosphere*, 28(12), 2203-2236.
- Rose, P.E., Benoit, W.R., and Adams, M.C. (1998) Tracer testing at Dixie Valley, Nevada, using pyrene tetrasulfonate, amino G, and fluorescein: *Geothermal Resource Council Transactions*, 22, 583-587.
- Rose, P.E., Benoit, W.R., and Kilbourn, P.M., (2001) The application of the polyaromatic sulfonates as tracers in geothermal reservoirs: *Geothermics*, 30(6), 617-640.

Benoit, W.R. (1999), "Conceptual models of the Dixie Valley, Nevada geothermal system," *Geothermal Resources Council Transactions*, 23, 505-511.

Blackwell, D.D., Wisian, K.W., Benoit, W.R., and Gollan, B. (1999), "Structure of the Dixie Valley geothermal system, a 'typical' Basin and Range geothermal system, from thermal and gravity data," *Geothermal Resources Council Transactions*, 23, 525-531.

Caine, J. S., Evans, J. P., and Forster, C. B. (1996), "Fault zone architecture and permeability structure," *Geology*, 24 (11), 1025-1028.

Chester, F. M. and Logan, J. M. (1986), "Composite planar fabric of gouge from the Punchbowl fault, California," *Journal of Structural Geology*, 9, 621-634.

Forster, C. B. and Evans, J. P. (1991), "Hydrogeology of thrust faults and crystalline thrust sheets: Results of combined field and modeling studies," *Geophysical Research Letters*, 18 (5), 979-982.

Rose, P.E., Apperson, K.D., Johnson, S.D., and Adams, M.C. (1997) Numerical simulation of a tracer test at Dixie Valley, Nevada: *Proceedings, Twenty-Second Workshop on Geothermal Reservoir Engineering*, Stanford Geothermal Program Workshop Report SGP-TR-155, 169-176.

Rose, P.E., Benoit, W.R., and Adams, M.C. (1998) Tracer testing at Dixie Valley, Nevada, using pyrene tetrasulfonate, amino G, and fluorescein: *Geothermal Resource Council Transactions*, 22, 583-587.

Rose, P.E. (1998) The use of polyaromatic sulfonates as tracers in high temperature geothermal reservoirs: *Proceedings 20th NZ Geothermal Workshop*, 239-243.

Rose, P.E., Goranson, C., Salls, D., Kilbourn, P.M. (1999) Tracer testing at Steamboat Hills, Nevada, using fluorescein and 1,5-naphthalene disulfonate: *Proc. Twenty-Fourth Workshop on Geothermal Reservoir Engineering*, Stanford University, SGP-TR-162.

Rose, P.E., Benoit, W.R., Bacon, L., Tandia, B., Kilbourn, P.M., (2000) Testing the naphthalene sulfonates as geothermal tracers at Dixie Valley, Ohaaki, and Awibengkok: *Proc. Twenty-Fifth Workshop on Geothermal Reservoir Engineering*, Stanford University, SGP-TR-165.

Sibson, R. H. (1977), "Fault rocks and fault mechanisms," *Geological Society of London Journal*, 133, 191-231.

Smith, J. S., Bloggs, R. T. and Jones, E. R. (1974), "Magnetic Anomalies in Geothermal Systems," *Journal of Fluid Mechanics*, 254, 73-79.



Sub Part-Per-Trillion Detection of a Fluorescent Tracer at the Dixie Valley and Beowawe Geothermal Reservoirs

Peter E. Rose¹, Stuart D. Johnson², Yee Lam Wong¹, Troy Carter¹, Christian Kasteler¹, and Phaedra Kilbourn¹

¹Energy and Geoscience Institute at the University of Utah
423 Wakara Way suite 300
Salt Lake City, Utah, 84108

²Caithness Energy Corporation
9790 Gateway Drive suite 220
Reno, Nevada 89511

Abstract

A highly sensitive laser fluorimeter was designed and fabricated using emerging technologies of fiber optics, charge-coupled-device (CCD) spectrometry, and laser light sourcing. Using conventional High Performance Liquid Chromatography (HPLC) in combination with the highly sensitive detector, a detection limit of 40 parts per quadrillion (ppq) was demonstrated for the geothermal tracer fluorescein. A family of fluorescein derivatives was screened for resistance to thermal degradation using high-temperature batch autoclave reactors and conditions that simulate a geothermal reservoir. One of the fluorescein derivatives, 6-carboxyfluorescein, was shown to possess comparable thermal stability to fluorescein and was therefore selected for use in field tests at the Dixie Valley and Beowawe geothermal reservoirs. The field tests confirmed the laboratory predictions that the detection limit of fluorescein and fluorescein derivatives could be enhanced by a factor of 100 over conventional fluorescence techniques.

Introduction

Fluorescent compounds are among the most detectable tracers used in the geothermal industry. However, hundreds of kilograms of a tracer are still typically required for each injection well that is tagged during a tracer test. As detection limits are lowered, however, the amount of tracer required is proportionally reduced, with a concomitant reduction in tracer cost. Likewise, since a chemically distinct tracer is required for each injector that is tagged, many tracers are needed in order to simultaneously tag all of the injectors within a reservoir. And, since most candidate fluorescent tracers are not manufactured in bulk, an increase in detectability results in an expansion of the list of candidate tracers. The objective of this research project is to increase the detectability of fluorescent tracer candidates by a factor of 100. This will result in not only a great reduction in the cost of performing a tracer test, but also a significant increase in the number of candidate tracer compounds available. Also, many of these technologies are relevant to the development of rugged, affordable, on-line tracer detection at the well head, something geothermal operators have long desired.

Our experimental approach has developed along multiple pathways. The first was the design and fabrication of the analytical equipment, based upon the concepts of laser-induced fluorescence. Second has been the selection and evaluation of candidate fluorescent tracer compounds. These compounds are sufficiently similar to fluorescein that they require the same excitation

wavelength, serving to greatly simplify the analytical apparatus. A third activity was the demonstration of the application of a candidate fluorescein-derivative in tracer tests in geothermal reservoirs.

Equipment Design, Fabrication, and Testing

With the advent of intense laser light sources and very efficient charge-coupled-device (CCD) spectrometers, it is possible to greatly enhance the detectability of fluorescent tracers. In addition, conventional high performance liquid chromatography (HPLC) allows for the efficient separation of fluorescent tracers not only from each other but also from naturally fluorescing contaminants present in geothermal reservoir water. Shown in Figure 1 is a schematic drawing of an HPLC/laser-fluorimeter assembly that was designed and fabricated in our laboratory.

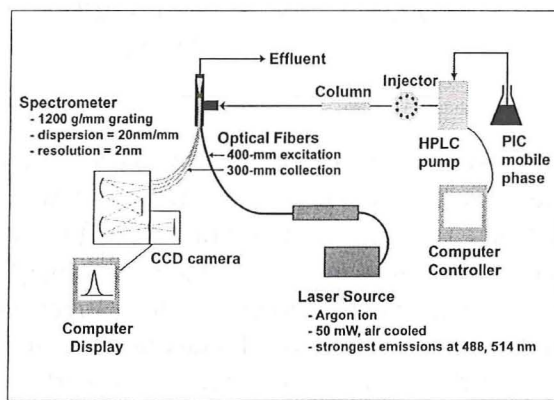


Figure 1. The HPLC/laser fluorimeter assembly.

One of the advantages of the fluorimeter shown in Figure 1 is that the CCD detector allows for the collection of an entire fluorescence emission spectrum with each chromatogram. The raw emission spectra for fluorescein at concentrations between 50 parts per quadrillion and 750 parts per quadrillion are plotted as functions of wavelength in Figure 2. By integrating over the entire wavelength for each curve at each time step, the chromatograms in Figure 3 were created. Finally, by integrating each curve in Figure 3, the calibration curve in Figure 4 was obtained, indicating that a reasonably linear relationship between concentration and fluorescence emission can be obtained over this concentration range. The detection limit for fluorescein was determined to be 40 ppq, which represents an increase in detectability over conventional HPLC instruments by a factor of approximately 100 (Kleimeyer et al., 2001).

Candidate Tracer Evaluation

Fluorescein has been extensively used as a tracer in hydrothermal systems. Not only is it very detectable by conventional fluorescent spectroscopy techniques, but it is also quite thermally stable and can be used in geothermal reservoirs as hot as about 250°C (Adams and Davis, 1991). Several derivatives of fluorescein have recently been synthesized for biochemical applications. We have therefore evaluated this family of compounds with the expectation that some of the fluorescein derivatives would possess similar properties of thermal stability and detectability (Wong and Rose, 2000; Wong, 2000).

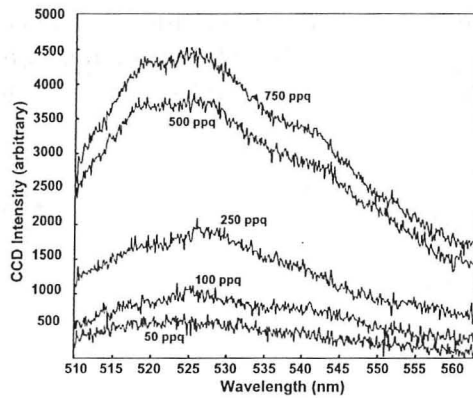


Figure 2. Raw CCD spectra for fluorescein between 50 and 750 parts per quadrillion.

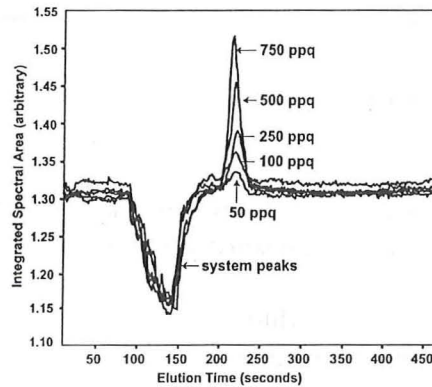


Figure 3. Chromatograms of fluorescein solutions between 50 and 750 parts per quadrillion obtained by integrating over the entire emission spectrum of each solution.

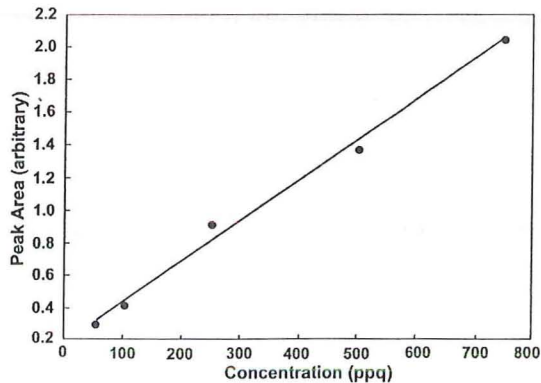


Figure 4. Calibration curve for fluorescein showing a linear relationship between concentration and peak area over the range of interest.

Nine candidate tracers were identified from among the fluorescein derivatives. Those nine were screened by exposing them to conditions that simulate a hydrothermal environment in laboratory reactors at a temperature of 270°C for 48 hours. Of the nine, four were shown to possess reasonably good thermal stability. The residual undecayed percentage for the four most stable

compounds is shown in Figure 5. For comparison, fluorescein is also shown. It is evident from the figure that one of the compounds, 6-carboxyfluorescein is comparable in stability to fluorescein. We therefore selected this compound for a detailed thermal stability study in anticipation of its use in a field test.

Compound	Structure	% Undecayed (2 days at 270°C)
fluorescein		78
6-carboxyfluorescein		83
fluorescein-5-sulfonic acid		59
Oregon Green 488		40
Oregon Green 500 carboxylic acid		30

Figure 5. The structural formula for fluorescein and four fluorescein derivatives and their residual undecayed percentages upon exposure to geothermal conditions for two days at 270°C.

The thermal decay kinetics of 6-carboxyfluorescein was modeled by the first-order differential equation (Wong, 2000; Wong and Rose, 2000):

$$-dC_c/dt = k_c \cdot C_c \quad (1)$$

where C_c is the concentration of naphthalene sulfonate and k_c is the first-order rate constant. Solution of this equation results in the following relationship between C_c and t :

$$\ln\left(\frac{C_c}{C_c^0}\right) = -k_c \cdot t \quad (2)$$

where C_c^0 is the initial concentration of polyaromatic sulfonate. The temperature dependence of k_c can be described by the Arrhenius relationship:

$$k_c = Ae^{(-E_a/RT)} \quad (3)$$

where A is the pre-exponential factor, E_a is the energy of activation, R is the gas constant and T is absolute temperature. A linearization of the Arrhenius expression results in the following:

$$\ln k_c = \ln A - \frac{E_a}{RT} \quad (4)$$

Figure 6 shows an Arrhenius plot of $\ln k_c$ vs. inverse temperature between 270°C and 290°C for 6-carboxyfluorescein. A fairly linear relationship between $\ln k_c$ and inverse temperature was observed, indicating that the Arrhenius equation provides a reasonably good means of expressing the temperature dependence of the decay rate constant. The constants A and E_a were determined to be $7.54E4 \text{ s}^{-1}$ and $1.11E5 \text{ J/mol}$, respectively.

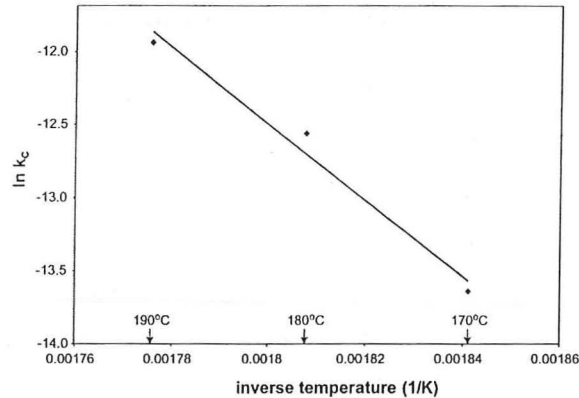


Figure 6. Arrhenius plot for 6-carboxyfluorescein based upon first-order decay rate kinetics.

Tracer Testing at the Beowawe Geothermal Field

On July 12, 2001, 530 g of 6-carboxyfluorescein was injected into well 85-18 at the Beowawe (Caithness Corporation) geothermal field (Figure 7). The injector was flowing at approximately 220 kg/sec. The reservoir's three production wells were subsequently monitored and analyzed for 6-carboxyfluorescein using conventional HPLC methods over the subsequent several months.

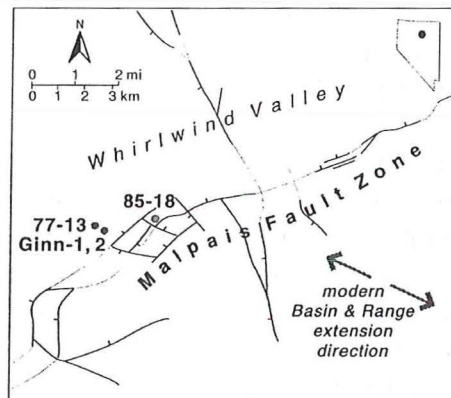


Figure 7. A plan view of the Beowawe geothermal reservoir, showing the injection (85-18) and production (Ginn 1, Ginn 2, and 77-13) wellhead locations.

The tracer test in 2001 was not the first at Beowawe involving injector 85-18. Almost seven years to the day (July 13, 1994), 91 kg of fluorescein was mixed with approximately 23 m^3 of reservoir water and injected as a slug at a rate of approximately 220 kg/sec into 85-18 (Rose et al., 1995). The surrounding production wells were sampled and analyzed for fluorescein over the subsequent several years.

Figure 8 shows the return of the tracers to the reservoir's three production wells (Ginn 1, Ginn 2, and 77-13) for each test. In both cases, the returns were normalized by dividing by the mass of tracer injected. The curves do not overlie each other perfectly, which may result from an incorrect knowledge of the mass of tracer injected—at least in the first test. In the 1994 test, 91 kg of fluorescein was mixed with produced brine in a 6,000-gal tank prior to injection into the reservoir. An unknown volume of tracer solution was left in the tank, but the normalized return curve shown in Figure 8 was based on a 91-kg injection mass.

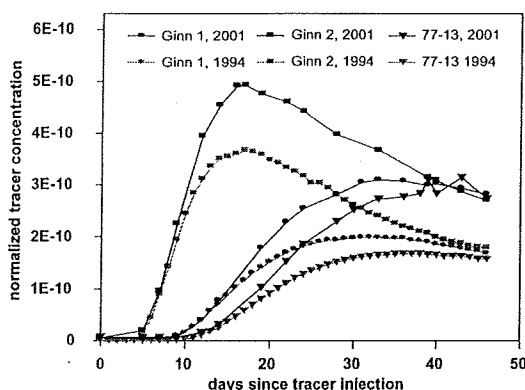


Figure 8. Normalized returns for the 1994 and 2001 tracer tests at the Beowawe geothermal field.

In the case of the 2001 test, the mass of tracer was measured quite accurately as 530 g and essentially all of the 530 g of 6-carboxyfluorescein was injected. Therefore, the normalized values shown for 6-carboxyfluorescein for the 2001 test are considered to be more accurate than the normalized fluorescein values for the 1994 test. Regardless of the differences, the return curves for each well pair are quite similar with first arrivals and peak maxima almost identical, indicating that reservoir flow patterns changed very little during the seven years between tests.

The tracer-return data shown for the 2001 test in Figure 8 were obtained using HPLC with conventional fluorescence detection. After analyzing the tracer-return data, we observed that much less tracer than the amount used would have been necessary to measure tracer breakthrough at Beowawe's three production wells. In order to demonstrate this, we diluted the samples by a factor of 1,000 and reanalyzed them for 6-carboxyfluorescein using the HPLC with LIF detection. Shown in Figure 9 are plots of tracer concentration both for undiluted Ginn-2 samples, as measured by conventional HPLC, and diluted Ginn-2 samples, as measured by HPLC with LIF detection. The curves do not overlie each other perfectly but reproduce each other reasonably well. This demonstrates that only one thousandth as much tracer (0.53 g of 6-carboxyfluorescein) would have been required to produce measurable breakthrough. This represents a reduction in tracer mass by a factor of approximately 170,000 compared to the quantity used in the 1994 test!

Tracer Testing at the Dixie Valley Geothermal Field

The Dixie Valley geothermal system presents a more challenging hydrothermal environment for organic tracers than the Beowawe reservoir. Not only are the fluid temperatures somewhat hotter, but the interwell residence times are significantly longer. On July 10, 2001, 530 g of 6-

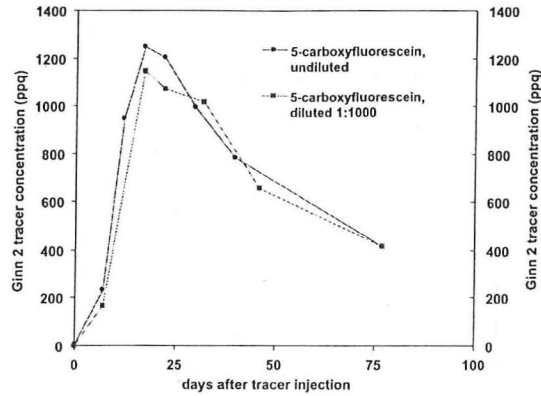


Figure 9. Undiluted and diluted tracer returns to Beowawe producer Ginn 2, analyzed using conventional fluorescence and laser-induced fluorescence detection methods, respectively.

carboxyfluorescein was injected into well 38-32 at the Dixie Valley (Caithness Corporation) geothermal field (Figure 10). Simultaneously, 150 kg of the candidate tracer 2,6-naphthalene disulfonate was injected as a companion tracer into the same well, which was flowing at about 110 kg/sec (1650 gpm). All of the reservoir's production wells were sampled and analyzed for 2,6-naphthalene disulfonate during the subsequent several months using conventional HPLC techniques (Rose et al., 2002).

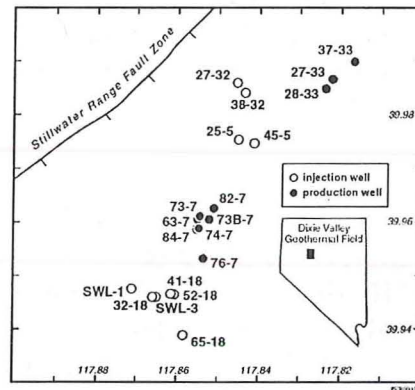


Figure 10. A plan view of the Dixie Valley geothermal reservoir, showing the injection and production wellhead locations.

Shown in Figure 11 are the returns of the two tracers to well 28-33. The values in this figure were normalized by dividing the measured concentrations by the mass of each tracer injected. If both tracers behaved conservatively, their normalized return curves would overlie each other. It is evident that the 6-carboxyfluorescein values are considerably lower than those of the conservative tracer, 2,6-naphthalene disulfonate, indicating that this tracer was extensively thermally degraded as it traveled through the reservoir. Also shown in Figure 11 is the corrected return curve for 6-carboxyfluorescein. The points on this curve were calculated based upon the thermal decay kinetics reported in this paper, assuming an effective temperature of 217°C. This temperature is between the approximate bottom-hole temperatures of 200°C and 242°C for the injection well (38-32) and production well (28-33), respectively.

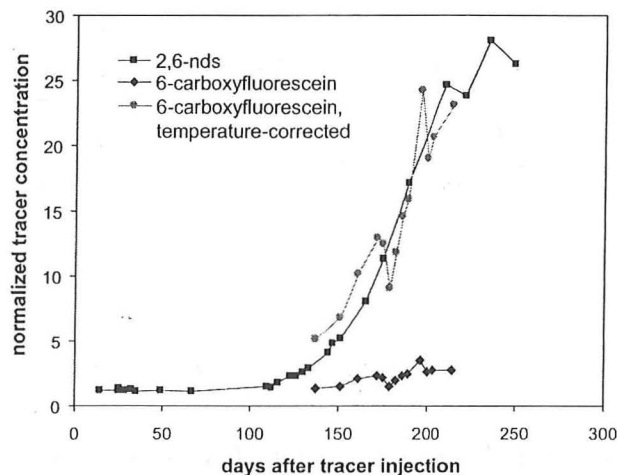


Figure 11. Return of tracers 2,6-naphthalene disulfonate and 6-carboxyfluorescein from well 38-32 to well 28-33 at the Dixie Valley geothermal reservoir. The temperature-corrected 6-carboxyfluorescein curve was calculated based upon the measured decay kinetics of 6-carboxyfluorescein, assuming an effective temperature of 217°C.

Acknowledgements

We thank Caithness Energy Corporation for their participation in this project. Their support in providing access to their reservoirs and in conducting the field tests has been essential for the successful testing of these candidate tracers. We also acknowledge the continued support of the Department of Energy (under contract number DE-HC07-90ID12929), without which this project could not have been accomplished.

References

- Adams, M.C. and Davis, J., 1991. Kinetics of fluorescein decay and its application as a geothermal tracer. *Geothermics* 20(1-2), 53-60.
- Kleimeyer, J.A., Rose, P.E., and Harris, J.M., 2001, Determination of ultratrace-level fluorescent tracer concentrations in environmental samples using a combination of HPLC separation and laser-excited fluorescence multiwavelength emission detection: application to testing of geothermal well brines: *Applied Spectroscopy*, **55(6)**, 690-700.
- Rose, P.E., Johnson, S.D., and Kilbourn, P.M., and Kasteler, C. (2002) Tracer Testing at Dixie Valley, Nevada Using 1-Naphthalene Sulfonate and 2,6-Naphthalene Disulfonate: *Proc. Twenty-Sixth Workshop on Geothermal Reservoir Engineering*, Stanford University, SGP-TR-171.
- Rose, P.E., Adams, M.C., and Benoit, W.R. (1995) A tracer test at the Beowawe geothermal field, Nevada, using fluorescein and tinopal CBS: *Geothermal Resource Council Transactions*, **19**, 217-221.
- Wong, Y.L. and Rose, P.E. (2000) The testing of fluorescein derivatives as candidate geothermal tracers: *Geothermal Resource Council Transactions*, **24**, 637-640.
- Wong, Y.L. (2000) An Evaluation of Fluorescein-Derived Compounds for Use as Geothermal Tracers, M.S. Thesis, Department of Chemical and Fuels Engineering, University of Utah.